TECHNISCHE UNIVERSITÄT DRESDEN

Deutsches Zentrum für Luft- und Raumfahrt
German Aerospace Center

Entwicklung von Perowskitmaterialien für zweistufige solar-thermochemische Redoxzyklen

Perovskite Materials Design for Two-Step Solar-Thermochemical Redox Cycles

Von der Fakultät für Maschinenwesen
der Technischen Universität Dresden
angenommene

Dissertation

zur Erlangung des akademischen Grades

Doktoringenieur (Dr.-Ing.)

von

M.Sc. Josua Vieten

geboren am 14.10.1991 in Freising

Gutachter:	Prof. Dr. Christian Sattler	TU Dresden
	Prof. Dr. Gianaurelio Cuniberti	TU Dresden
Vorsitzende:	Prof. Dr. rer. nat. et Ing. habil. K. Eckert	TU Dresden
Eingereicht am:	19.11.2018	
Verteidigt am:	07.05.2019	

Contents

Abstract

Solar-thermochemical redox cycles are a promising technological option in the framework of utilization and conversion of renewable energy. By reducing metal oxides at high temperature and/or low oxygen partial pressure, one can generate a material in a state which can be used to capture oxygen from a gas stream or split water or carbon dioxide. By this means, air can be separated, oxygen can be pumped, or so-called solar fuels can be generated. One especially attractive materials class for application in such redox cycles is constituted by perovskites. These materials form stable phases over a large compositional range. Within this work, we show how these perovskite oxides can be applied in thermochemical redox cycles and study the mechanisms behind these redox reactions using *in-situ* X-Ray techniques. We also show that the kinetic properties of the oxidation reaction are very appealing. It is furthermore presented how perovskite solid solutions can be formed over a large compositional range and how phase formation and stability are affected by the perovskite composition. Based on this knowledge, the focus of this work is set on the materials thermodynamics. A new method of rational perovskite materials design is developed by adjusting the tolerance factor of the perovskites and their thermodynamics. Both experimental and theoretical materials development are conducted, the latter based on density functional theory (DFT) within the framework of the online resource "Materials Project". Over 240 perovsite-brownmillerite pairs are included in the search. Detailed models describing the thermodynamics of such perovskite solid solutions are established which allow describing the perovskite redox properties as a function of the temperature, oxygen partial pressure, and oxygen non-stoichiometry δ. Using these functions, we developed an interactive tool within the framework of Materials Project, which can be used to model materials properties for a large range of conditions and also serves as a perovskite search engine. This search engine uses a simplified process model to evaluate the material-specific energy demand of a thermochemical redox process and allows finding the most efficient materials choice for a large range of different operational parameters. We could identify new redox materials for application in such processes and found that perovskites can lead to more efficient thermochemical fuels production than the state of the art, especially if the reduction temperature is lowered to 1300-1400 °C to reach higher reactor longevity. It is also discussed which factors affect the overall process efficiency to which extent, and suggestions are given which steps are necessary for a commercialization of such redox processes. The most important factor is the solid-solid heat recovery efficiency. By making all this data publicly available in the framework of MPContribs/Materials Project through providing user-controlled interactive graphs, we are providing a valuable resource for accelerating the discovery and use of new redox materials.

Zusammenfassung

Solar-thermochemische Redoxzyklen stellen eine vielversprechende Technologieoption zur Nutzung und Umwandlung von erneuerbaren Energiequellen dar. Durch Reduktion von Metalloxiden bei hoher Temperatur und/oder niedrigem Sauerstoffpartialdruck kann ein Material in einen Zustand überführt werden, der dazu geeignet ist, Sauerstoff aus einem Gasstrom zu entfernen oder Wasser bzw. Kohlenstoffdioxid zu spalten. Dadurch ist es möglich, Luft zu zerlegen oder Sauerstoff zu pumpen, sowie sogenannte solare Brennstoffe zu erzeugen. Eine besonders vielversprechende Materialklasse stellen dabei die Perowskite dar. Diese Materialien bilden stabile Phasen mit sehr unterschiedlichen Zusammensetzungen. In dieser Arbeit wird gezeigt, wie diese Perowskit-Oxide in thermochemischen Redoxzyklen verwendet werden können und die Mechanismen hinter diesen Redoxreaktionen werden mit *in-situ*-Röntgenuntersuchungen aufgeklärt. Es wird auch gezeigt, dass die kinetischen Parameter der Oxidationsreaktion sehr vielversprechend sind. Zudem wird demonstriert, wie feste Lösungen aus Perowskiten in einem weiten Bereich verschiedener Zusammensetzungen hergestellt werden können und wie die Zusammensetzung der Perowskite die Phasenbildung und Stabilität beinflusst. Mit diesem Wissen wird ein Schwerpunkt dieser Arbeit auf die thermodynamischen Eigenschaften dieser Perowskite gelegt. Eine neue Methode der gezielten Materialentwicklung wird demonstriert, welche darauf basiert, den Toleranzfaktor und die thermodynamischen Eigenschaften der Perowskite gezielt einzustellen. Sowohl experimentelle, als auch theoretische Untersuchungen werden durchgeführt, letztere basierend auf Dichtefunktional-theorie (DFT) im Rahmen von „Materials Project“. Über 240 Perowskit-Brownmillerit-Paare wurden untersucht. Detaillierte Modelle wurden entwickelt, um die thermodynamischen Eigenschaften solcher fester Lösungen aus Perowskiten als eine Funktion der Temperatur, des Sauerstoff-partialdrucks, und der Sauerstoff-Fehlstellenkonzentration δ zu beschreiben. Mit Hilfe dieser Funktionen wurde ein interaktiver Beitrag im Rahmen von Materials Project entwickelt, mit dem Materialeigenschaften in einem weiten Bereich verschiedener Bedingungen untersucht werden können. Darin ist auch eine Perowskit-Suchmaschine enthalten. Diese verwendet ein vereinfachtes Prozessmodell, um den materialspezifischen Energiebedarf von Redoxzyklen auszuerwerten und ermöglicht es so, das effizienteste Material basierend auf den Prozessbedingungen auszuwählen. Es konnten neue Redoxmaterialien zur Anwendung in thermochemischen Kreisprozessen identifiziert werden und es wurde festgestellt, dass Perowskite die Effizienz der solaren Brennstofferzeugung bei vergleichsweise niedrigen Reduktionstemperaturen von 1300-1400 °C erhöhen können. So soll eine höhere Reaktorlebensdauer erreicht werden. Es wird auch diskutiert, welche Faktoren die Prozesseffizienz beeinflussen und es werden Ideen präsentiert, welche Schritte nötig sind, um eine kommerzielle Nutzung zu ermöglichen. Der wichtigste Faktor ist dabei die Wärmerückgewinnungseffizienz zwischen Feststoffen. Durch die Veröffentlichung aller Daten im Rahmen von MPContribs/Materials Project durch das Erstellen von interaktiven Graphen wird eine wertvolle Ressource zur schnelleren und zielgerichteten Materialentwicklung bereitgestellt.

1. Introduction

1.1 Motivation and Challenges

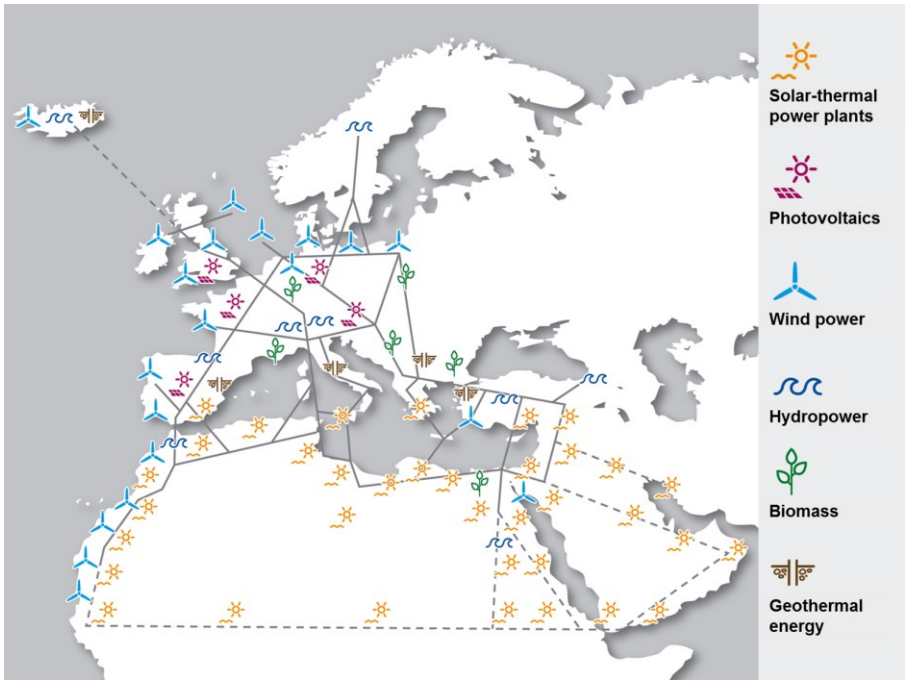

Fig. 1.1. The potential of renewable energy sources across Europe, Northern Africa, and the Middle East, including a long-distance electricity network. Concentrated Solar Power can be used in regions with high solar irradiance, and can also be applied for the direct utilization of heat to create solar fuels. Image adapted from DLR (CC-BY 3.0).

Global warming is widely considered one of the main challenges of the 21st century. The reduction of greenhouse gas emissions constitutes one of the key objectives of research in the field of materials science, engineering, chemistry, and energy technology, and whole research institutes centered on this topic are founded around the globe every year. While many promising new technological approaches are described in journal articles and patents every day, seeing such technology in practical application has been rare for a long time. This is no longer the case: For example, the share of renewable energy sources in the total electricity production is rising every year, reaching an average as high as 36 % in Germany in the first half of 2018. [1] A combination of different renewable energy sources has the potential to supply electricity for the whole of Europe (Fig. 1.1). Moreover, the transportation sector is facing one of the largest transitions in the past centuries, which will lead to a boost in the share of renewable energy sources with respect to the total energy demand. Renewable energy technology becomes more and more widespread, and associated with that, costs are decreasing due to economies of scale, rendering former niche technologies economically viable. [2]

Despite the promising progress in renewable energy generation, one major practical issue is its inherent intermittent character, meaning that solar energy can only be captured if the sun shines, and wind power is not continuously available either. This is becoming more and more of a limiting factor in the growth of the renewable energy sector. For instance, if a low power demand meets high solar irradiation and strong winds, almost the entire electricity demand of Germany is met using renewable energy, with record highs of 85 % renewable energy share on a Sunday afternoon in 2017. [3] However, conventional energy sources currently remain crucial for a steady energy supply, as energy storage options remain limited, and further expansion of renewable energy generation is futile if the peaks in supply cannot be smoothed out through decoupling demand and supply. A possible remedy of this issue is the storage of chemical or thermal energy. Both can be achieved using concentrated solar power (CSP, Fig. 1.2), a power source mainly used in areas with high solar irradiance. In contrast to most other renewable energy sources, the primary form of energy supplied in such power plants is heat, generated through focusing solar radiation on a small area. Heat is much easier to store on a large scale than electricity, as demonstrated in Marocco's Noor III CSP plant in Ouarzazate, which will be capable of supplying electricity up to 7 hours after sunset. [4]

Fig. 1.2. Concentrated solar power tower facility with heliostats focusing the sunlight in order to concentrate heat for electricity generation or in solar-thermochemical redox cycles. Image: DLR/Ernsting.

Another appealing option is to convert the heat to chemical energy, which is stored in carbon-neutral renewable fuels. These include hydrogen [5, 6] as well as hydrocarbon-based fuels [7, 8] or ammonia. [9] Such fuels are particularly interesting for applications in the transportation sector, specifically in aviation. For the foreseeable future, the high gravimetric power densities required for intercontinental flights are only conceivable through combustion of fuels. [10] Moreover, these fuels could be used to transport renewable energy while using the existing infrastructure for conventional fossil fuels. So-called solar fuels, for example hydrogen, can be prepared through several pathways: electrolysis, [11] photoelectrochemistry, [12] or thermochemical routes. [13, 14] While all of these routes have their specific advantages, the latter offers the only option of directly converting heat to chemically stored energy, making it an ideal candidate for application in CSP plants by avoiding conversion losses. In this case, solar fuels are produced through thermochemical water splitting as the first step. Although the direct thermolysis of water is in principle feasible, the high temperature required to thermally dissociate water (2500-3500 K) is setting practical limitations. [15] Therefore, a two-step thermochemical cycle involving a redox material can be used alternatively (see Fig. 1.3).

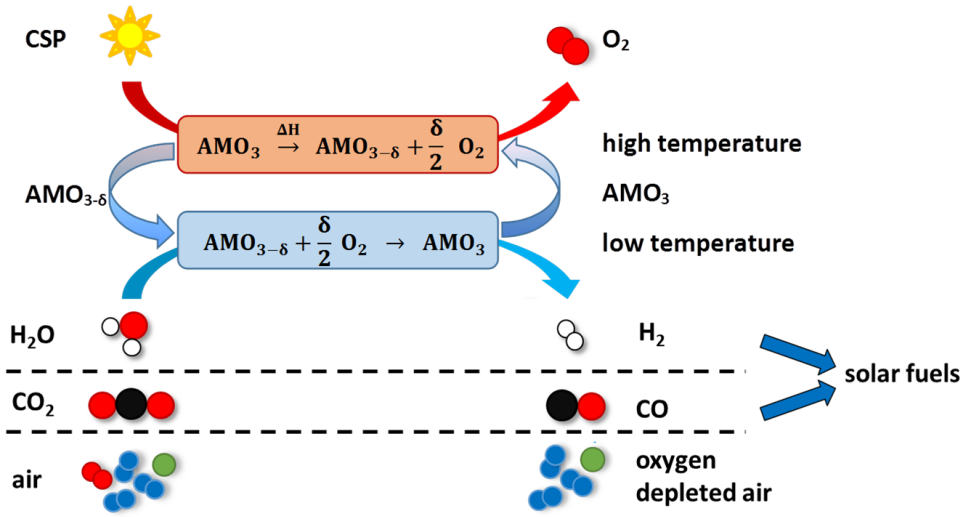

Fig. 1.3. Two-step thermochemical cycles are a versatile option for the direct conversion of heat from concentrated solar power (CSP) into chemical energy or separation work. A redox material, in this case a metal oxide $AMO_{3-\delta}$, is partially reduced at high temperature under the release of oxygen, and subsequently re-oxidized at lower temperature. Potential oxidants for re-oxidation include water, carbon dioxide, or air, which allow the sustainable generation of hydrogen, carbon monoxide, or oxygen depleted air, respectively. Taken from Vieten et. al. [16]

At high temperatures and/or low oxygen partial pressures, the redox material (typically a metal oxide) is partially reduced under the release of oxygen. The redox material is then re-oxidized in a second step at lower temperature and/or increased oxygen partial pressure. If water is used as an

oxidant, some redox materials such as ceria [17] or ferrites [18] are capable of splitting it under the release of hydrogen. This two-step cycle also offers the advantage that oxygen and hydrogen can be easily separated, as the two gases are produced in different process steps. Moreover, if carbon dioxide is used as an oxidant instead of steam, carbon monoxide can be produced as a product, which together with hydrogen can serve as the feedstock for the generation of hydrocarbons as fuels through the Fischer-Tropsch process or methanol-based routes. [7, 19-21] If that carbon dioxide has previously been captured from the air, combustion of the produced fuel is carbon-neutral. Another application of these two-step solar-thermochemical cycles is separation of air into a stream of mostly inert gas and oxygen if air is used as an oxidant, or the storage or pumping of oxygen in general. [22-24] The so-prepared nitrogen can be used in combination with hydrogen to prepare ammonia through the Haber-Bosch process. All these cycles share the common principle that heat is directly converted into chemically stored energy or separation work. The origin of the thermal energy is irrelevant for the chemistry involved, but concentrated solar plants are an ideal heat source due to their carbon-neutral operation and the direct generation of heat without any intermediate steps.

While research on these two-step thermochemical cycles has been performed for a long time, [25] their practical application remains challenging. One reason for that are constraints in engineering: For solar-thermochemical water splitting, the operation of a reduction chamber at temperatures of up to 1500 °C under vacuum or with an inert sweep gas is required when the state-of-the-art redox material ceria is used. Only high temperature refractory materials can be applied, but what is even more important and challenging, the reaction chamber needs to remain gas tight while allowing solar radiation to enter through a window. [26] Another issue is the currently relatively low efficiency of the overall process, although it is theoretically one of the most efficient means to generate renewable fuels. [25, 27, 28] For an economically competitive redox process, it is necessary to improve the solar field and receiver efficiency, the energy demand to maintain a low oxygen partial pressure during reduction, and the work required to separate hydrogen from steam. Apart from that, one crucial factor determining the viability of the entire process is the choice of a suitable redox material. As explained in further detail in chapter 2, the thermodynamic and kinetic properties as well as the chemical stability of the materials decide over their applicability under a given set of process conditions. The redox enthalpy and entropy change upon redox operation govern the material's ideal redox temperature and oxygen partial pressure levels. A redox material which is perfectly suitable for water splitting under certain conditions is far from ideal for air separation, and not even well applicable for water spitting under different conditions, such as different temperature levels. Therefore, it is necessary to control the thermodynamic properties of these materials. At the same time, their chemical stability as well as their redox kinetics need to allow the reaction to occur reversibly and quickly. With these prerequisites in mind, it is possible to specifically design perovskite redox materials for different thermochemical applications, as demonstrated in this work.

1.2 Scope of this Work

As mentioned before, cerium(IV)-oxide (ceria) and ferrites have been used for solar-thermochemical water splitting in many research projects, even on the larger pilot scale. [29] Their properties are well known, which renders experiments easily comparable while offering an overall good performance. [30, 31] However, materials with potentially better properties are studied on the laboratory scale, and it is likely that the state-of-the-art redox materials will eventually be replaced. [32, 33] Ceria is part of the class of non-stoichiometric redox materials, which are capable of releasing or absorbing oxygen gradually upon change of the chemical potential of oxygen around them, typically allowing for fast redox kinetics. The non-stoichiometry of $CeO_{2-\delta}$ is expressed by δ. Another promising material class with similar behavior is constituted by perovskites with the general formula $AMO_{3-\delta}$. The amount of possibly stable combinations of different A and M metals on the perovskite lattice sites leads to this oxide class being one of the most versatile. Depending on the choice of cations, the perovskite's chemical and thermodynamic properties change. This has been exploited by researchers in the last couple of years to successfully generate new redox materials for solar-thermochemical water or carbon dioxide splitting or air separation. [33-37] However, many of the efforts in this direction are characterized either by incremental improvements of existing materials, such as by adding different dopants, or by trial and error based exploration. In addition, some theoretical studies have been performed as well, which allow a more systematic materials selection based on computational methods such as density functional theory (DFT), but only on ternary oxides. [38, 39]

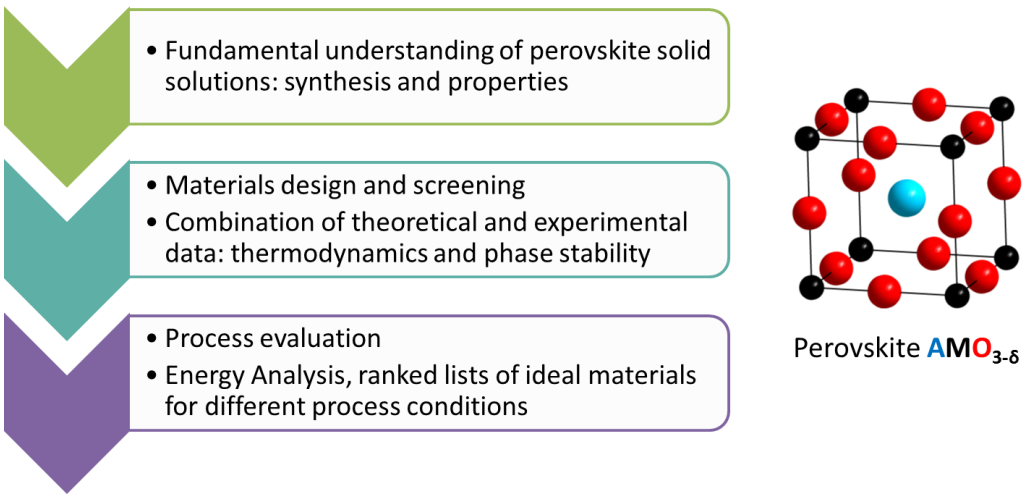

Fig. 1.4. Scope of this work: A fundamental understanding of perovskite materials and their application as redox materials is developed step-by-step in order to rationally design perovskite solid solutions for application in solar-thermochemical cycles. Experimental and theoretical data is combined in a model creating a ranked list of ideal materials for different process conditions.

In a first step, it is necessary to get a general understanding of perovskites as redox materials and their redox behavior when one species is gradually exchanged by another. By preparing some perovskites and simple solid solutions where only one species is replaced partially by another, the fundamental properties of perovskite solid solutions shall be studied. The perovskites shall be prepared and characterized using standard methods of solid state chemistry and analytics. Additionally, it is necessary to monitor the perovskite's oxidation state during reduction and oxidation *in-situ*, in order to verify that the reduction and oxidation takes place under the conditions foreseen for application in thermochemical cycles.

With this knowledge, stable perovskite materials with solid solutions containing two different species on the A site as well as two other species on the M site shall be both studied experimentally, as well as through DFT. By extending the realm of possible solid solutions to two different species on both perovskite sites, it should be possible to control their redox properties as well as their crystal structure and chemical stability using the tolerance factor. This so-called Goldschmidt tolerance factor plays a key role in pre-selecting potentially stable materials, and the ionic radii of the solid solution components are chosen accordingly (tolerance factor adjusted materials design).

By combining both theoretical and experimental data, it is possible to study the thermodynamics of a large set of materials, derive theoretical models describing the reduction and oxidation process, and verify the theoretical models using the experimental data. Ideally, one could derive equations and physical expressions describing the change in the Gibbs free energy in order to predict the equilibrium state of these materials under different conditions. Using this data in combination with an analysis of the redox process and its energetics, one is then able to rank materials according to their suitability for specific process conditions and the energy demand of the entire redox process. With the help of computational data handling in collaboration with the Lawrence Berkeley National Laboratory (USA), this large dataset is transformed into an interactive online resource. For the first time, perovskite solid solutions with up to four different cations are systematically explored based on their thermodynamic data, and combined into an interactive database which is freely accessible to the public.

By creating solid solutions with more than one species on the A or M lattice site in the perovskite, the range of possibly stable perovskites is significantly increased, yet no systematic studies of a large set of perovskite solid solutions have been published so far. The aim of this work is to change this. This work will go into the details of thermodynamics and materials properties. By this means, the knowledge about the redox behavior of perovskites and their solid solutions shall be deepened to allow for the targeted design of redox materials for different two-step thermochemical redox cycles and different process conditions.

2. Background and theoretical considerations

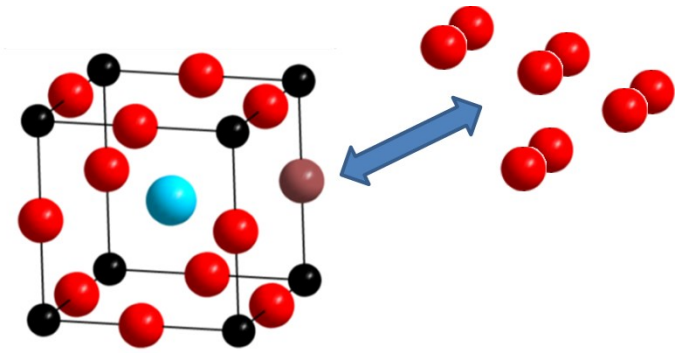

$$\Delta G = \Delta H - T \cdot \Delta S + \frac{1}{2} RT \cdot \ln\left(\frac{p_{O_2}}{p_0}\right)$$

Fig. 2.1. Perovskites can form oxygen vacancies, and their concentration is dependent on the temperature and oxygen partial pressure of the environment and the thermodynamic properties of the perovskite, which depend on the composition. The state of the chemical equilibrium is defined by the Gibbs-Helmholtz equation.

The choice of suitable redox materials is of paramount importance for the performance of two-step thermochemical cycles in terms of their productivity and efficiency. Therefore, the rationale behind selecting these materials is explained in this chapter. After a summary of the state of the art in perovskite application for thermochemical cycles and a comparison to other redox materials, the chemistry of perovskites is explained in detail. This includes their chemical stability, as well as their redox kinetics and thermodynamics. This chapter introduces new concepts in describing the thermodynamics of perovskite solid solutions. Based on these properties, it is shown how redox materials can be selected according to the specific requirements of each type of application, a process also known as Materials Design. Moreover, the different contributions to the energy demand of an entire redox cycle are explained, including their derivation from theoretical and experimental properties. An emphasis is set on the chemistry and physics of the materials independent of specific reactor concepts.

This chapter is partially based upon the following peer-reviewed publications authored and co-authored by the author of this work:

Vieten, J.; Bulfin, B.; Huck, P.; Horton, M.; Guban, D.; Zhu, L.; Youjun, L.; Persson, K.; Roeb, M.; Sattler, C., Materials design of perovskite solid solutions for thermochemical appplications, Energy & Environmental Science 2019, 12, 1369-1384.

Vieten, J.; Bulfin, B.; Call, F.; Lange, M.; Schmücker, M.; Francke, A.; Roeb, M.; Sattler, C., Perovskite oxides for application in thermochemical air separation and oxygen storage. Journal of Materials Chemistry A 2016, 4, (35), 13652-13659.

Bulfin, B.; Vieten, J.; Agrafiotis, C.; Roeb, M.; Sattler, C., Applications and limitations of two step metal oxide thermochemical redox cycles; a review. Journal of Materials Chemistry A 2017, 5, (36), 18951-18966.

2.1 Perovskites in Thermochemical Cycles

Apart from perovskites, many other material classes have been discussed for application in two-step thermochemical cycles. Many of them have been successfully tested on the laboratory scale, and some even beyond. However, perovskites offer some unique advantages over all these materials, which are elaborated in the following. In this work, only redox cycles with oxygen as transported species are discussed, such as water splitting, carbon dioxide splitting, or air separation and oxygen pumping. All these require an oxygen storage material (OSM), which releases oxygen during the reduction step and re-captures it during the oxidation step. However, other (solar)-thermochemical cycles for further applications have been proposed, such as carbon dioxide sequestration from the air or from flue gas, which are based on materials storing other species. [40] These are beyond the scope of this work, but could be a subject of future studies. Moreover, we only consider redox cycles where the release and uptake of oxygen is the main objective of the reaction, as opposed to thermochemical heat storage cycles where only the storage of heat is relevant and pure oxygen is just a byproduct.

The reduction of the OSM can proceed either in one step and stoichiometrically, or gradually and non-stoichiometrically. An example for an OSM with **stoichiometric** reduction is iron(II,III)-oxide (magnetite), which can be applied as redox material for solar-thermochemical water splitting. [41] At high temperature and/or under low oxygen partial pressure, it is reduced to iron(II)-oxide under the release of oxygen:

$$Fe_3O_4 \overset{\Delta T}{\rightarrow} 3\,FeO + \frac{1}{2}\,O_2 \qquad \text{(Reduction)} \tag{2.1}$$

The reduced metal-oxide can then be re-oxidized at lower temperature using water under the release of hydrogen:

$$3\,FeO + H_2O \rightarrow Fe_3O_4 + H_2 \quad \text{(Oxidation)} \tag{2.2}$$

Non-stoichiometric wustite phases may be formed as well. [41] The stoichiometric reaction, however, is characterized by the release of a well-defined amount of oxygen during reduction, and the formation of one product oxide with lower oxygen content than the educt. The reaction proceeds spontaneously as soon as the Gibbs free energy is below zero. In most cases, no reaction is observed until a certain temperature or oxygen partial pressure level is reached. Another example for a stoichiometric reaction is the reduction of cobalt(II,III)-oxide Co_3O_4 to cobalt(II)-oxide CoO. This reaction is

considered for solar-thermochemical heat storage and may also be suitable for air separation. [42-44] The reaction only occurs in a small temperature window, and the temperature at which the material is oxidized or reduced depends on the oxygen partial pressure level. The conversion from one stoichiometric oxide to another is characterized by a complete change of the crystal structure under re-arrangement of atoms. Therefore, the redox reactions are typically slower than when non-stoichiometric oxides are used, and it usually takes some minutes until chemical equilibrium is reached. [45] Stoichiometric metal oxides considered for fuel production (solar thermochemical water splitting or carbon dioxide splitting) include iron oxides, [41, 46] zinc oxide, [30] tin oxide, [30, 47] and magnesioferrites. [48] Moreover, other oxides such as manganese oxides, [22, 49] cobalt oxides, [22, 44] copper oxides, [22, 50] and lead oxides [30] are considered for solar-thermochemical air separation.

Non-stoichiometric compounds consist of non-integer amounts of atoms per formula unit. Although non-stoichiometry of metal species in oxides is also possible, [51] we focus here on oxides with non-stoichiometric oxygen content. These oxides are characterized by a gradual release or uptake of oxygen as a response to a change in temperature or oxygen partial pressure. If the oxygen partial pressure or temperature is changed, this has a direct effect on the oxygen vacancy concentration. The amount of released oxygen depends on the magnitude of the temperature and oxygen partial pressure change. In contrast to stoichiometric oxides, it is not necessary to reach a certain threshold temperature for a reaction to occur, but the higher the temperature or oxygen partial pressure change is, the higher the amount of released/captured oxygen. However, as the non-stoichiometry range is limited, non-stoichiometric oxides typically show a lower overall oxygen storage capacity. The crystal structure of non-stoichiometric oxides usually only changes slightly upon release or uptake of oxygen. The general structural motif is maintained while some oxygen sites are “filled” with vacancies instead of oxygen. Along with the very high oxygen diffusion rates in perovskites, [52-54], this leads to very high reaction speeds and usually good reversibility of the solar-thermochemical process. [23] Moreover, the mechanical stress induced by a change in crystal structure leads to a usually lower mechanical stability of structured materials made from stoichiometric oxides.

The advantages and disadvantages of stoichiometric and non-stoichiometric oxides as redox materials in two-step solar thermochemical cycles are summarized in Table 2.1. While there are some applications where stoichiometric oxides are beneficial (i.e. oxygen storage with high storage density or thermal storage within a small temperature window), the advantages of using non-stoichiometric oxides outweigh their disadvantages in many cases considering their performance for thermochemical fuels production and air separation. However, there are exceptions from these general trends. For instance, the phase change of stoichiometric oxides may involve melting or evaporation of an oxide at high temperature, which can lead to very appealing thermodynamic properties despite the potential challenges in engineering. [30]

Table 2.1. Advantages and disadvantages of stoichiometric oxides (with phase change upon reduction) and non-stoichiometric oxides (with maintained crystal structural motif during redox cyclization) as redox materials in two-step solar-thermochemical cycles.

	Stoichiometric oxides		**Non-stoichiometric oxides**	
Reaction speed	usually slow (within minutes)	–	fast (typically within seconds)	+
Reversibility	degradation due to phase change possible	–	usually high	+
Mechanical stability	sudden expansion/contraction possible (phase change)	–	gradual expansion/contraction	+
Oxygen storage capacity	potentially very high	+	limited	–
Temperature/pressure change neccessary	low	+	high	–
Temperature/pressure window in which the reaction occurs	small	–	large	+

One of the most well-known **non-stoichiometric** oxides is cerium(IV)-oxide, also known as ceria. The amount of oxygen in the lattice varies as a function of temperature and oxygen partial pressure, which is well-defined and characterized. [31, 55] The non-stoichiometry is denoted by δ in the general formula $CeO_{2-\delta}$. Two-step thermochemical cycles for solar fuels production involving ceria and its doped variants are well-known. [14, 17, 20, 30, 56-58] However, other materials may be used to reach higher efficiencies in fuel production, as explained in more detail in chapter 2.5. One of these materials classes are perovskites with the general formula $AMO_{3-\delta}$, where A is a cation with larger and M a cation with smaller ionic radius. Moreover, perovskites may also be applied for air separation and oxygen pumping processes, as mentioned before. The non-stoichiometry δ is typically between 0 and 0.5, but may in some cases also reach higher or negative values (meaning that additional oxygen is incorporated with respect to the original perovskite structure). [59, 60]

A typical redox cycle for air separation with the perovskite material $SrMnO_{3-\delta}$ starts with $SrMnO_3$ at room temperature. In the reduction step, oxygen vacancies are formed depending on the temperature:

$$SrMnO_3 \xrightarrow{\Delta T} SrMnO_{3-\delta} + \frac{\delta}{2} O_2 \quad \text{(Reduction)} \tag{2.3}$$

The reduced perovskite can then be re-oxidized at lower temperature by capturing oxygen from the air, which can be written as the reverse reaction to the reduction:

$$SrMnO_{3-\delta} + \frac{\delta}{2} O_2 \rightarrow SrMnO_3 \quad \text{(Oxidation)} \tag{2.4}$$

Perovskites which are easily reducible, such as $SrFeO_{3-\delta}$, show an initial non-stoichiometry at room temperature in air. $SrFeO_{3-\delta}$ synthesized in air therefore has a non-stoichiometry of approx. 0.19, i.e. a composition of $SrFeO_{2.81}$. [61] In fact, all perovskite oxides always show at least some small oxygen non-stoichiometry at any temperature above 0 K, but it is in many cases negligible.

Among the different types of non-stoichiometric oxides, perovskites constitute the most promising class of oxides for materials design. Their wide range of compositions offers an almost unlimited range of different compositions. As explained later, the A site in $AMO_{3-\delta}$ perovskites can be occupied by a multitude of different cation species including numerous alkali, alkali earth, lanthanide, and actinide species, whereas the M site can be filled with various transition metals or main group elements. [62] Even organic species may occupy cation sites in perovskites. [63] The preparation of perovskite solid solutions further extends the spectrum of potential compositions. Perovskites have been investigated for application in two-step thermochemical cycles by many researchers. For instance, in the case of **Air Separation**, a study by Yang *et al.* concludes that $La_{0.1}Sr_{0.9}Co_{0.5}Fe_{0.5}O_{3-\delta}$ and $La_{0.1}Sr_{0.9}Co_{0.9}Fe_{0.1}O_{3-\delta}$ are promising materials for the removal of trace oxygen from gases or for the production of high-purity nitrogen or extremely pure oxygen from air. [64] The latter perovskite is also mentioned by Yin *et al.* as a material with minimal heat release upon oxygen sorption. [37] $SrCoO_{3-\delta}$ and $SrFeO_{3-\delta}$ are mentioned in studies by Ezbiri *et al.* and Marek *et al.,* repectively. [36, 65] Meng *et al.* mention hollow fibre membranes consisting of LSFCM ($La_{0.3}Sr_{0.7}Fe_{0.7}Cu_{0.2}Mo_{0.1}O_{3-\delta}$) as another possible air separation material. All these studies have in common that air separation is possible at rather low temperatures compared to the reduction of ceria for fuels production (reduction of the perovskites at 1000 °C or less) and that the selectivity for oxygen is extremely high, which allows preparation of oxygen with very little or no contaminants. Moreover, an oxygen-containing stream of gases can be separated into mostly inert gases and oxygen very effectively. These studies, however, do not include the targeted design of materials for specific applications, i.e. in a certain temperature range with a certain target oxygen concentration of the purified gas stream.

Air separation with high purity levels is especially appealing for applications in ammonia production, as the Haber-Bosch process requires very low oxygen levels in the nitrogen feed to avoid catalyst poisoning. [66, 67] By applying efficient methods for air separation, the energy demand of the entire process may be reduced, and if the heat for air separation is supplied from renewable sources, the greenhouse gas emissions of ammonia and fertilizer production can be significantly lower than today. This is especially important considering that more than 1 % of the world's primary energy demand is attributed to ammonia production only. [68] The oxygen produced through solar-thermochemical air separation may also be used in a second step after ammonia synthesis in the Ostwald process for the production of ammonium nitrate as fertilizer (see Fig. 2.2). This process chain is currently under investigation in the project DÜSOL funded by Klimaschutzwettbewerb NRW and the European EFRE fund.

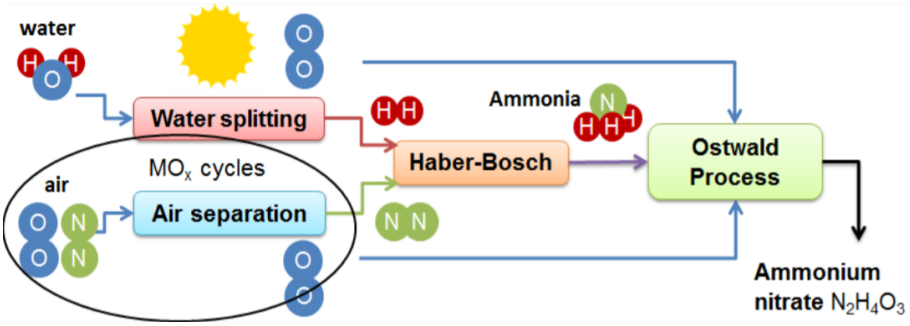

Fig. 2.2. Envisioned process for solar-thermochemical fertilizer production in the project Düsol. After solar-thermochemical air separation, nitrogen is used in the Haber-Bosch process in combination with hydrogen produced by water splitting. The oxygen as the second product of the air separation process is combined with ammonia to produce ammonium nitrate by preparing nitric acid in the Ostwald process. Taken from Guban et al. [69]

Moreover, ammonia may also be used directly as a carbon-free fuel, which is easier to transport than hydrogen due to its liquefaction at lower pressures. Upon combustion, nitrogen and water are formed:

$$4\,NH_3 + 3\,O_2 \rightarrow 2\,N_2 + 6\,H_2O \tag{2.5}$$

Ammonia is interesting as an alternative jet fuel. However, nitrogen oxides may also be formed as a byproduct, and the use of ammonia as a jet fuel may contribute to the depletion of the ozone layer. [9] Further research and development is necessary to study the use of ammonia as a fuel and its potential environmental impact. Nevertheless, it is a promising fuel in gas turbines and for naval applications, and near-zero NO_x emissions can be achieved. [a] The use of perovskites for air separation and/or solar-thermochemical water splitting could have a positive impact on the specific greenhouse gas emissions of the overall process.

For **Fuels Production** through the splitting of water and carbon dioxide, other perovskite materials come into play. In order to split these molecules, the Gibbs free energy ΔG of the re-oxidation reaction must be below zero, which typically requires a higher enthalpy change than for air separation. Perovskites with suitable thermodynamic properties include lanthanum strontium manganese oxides with or without aluminium on one of the lattice sites, i.e. LSMA (lanthanum strontium manganese aluminium oxide), [34, 35, 70] or lanthanum strontium iron oxides with different dopants on the Fe site. [71] These perovskites usually show reduction at lower temperatures than ceria under the same oxygen partial pressures, but a large excess of steam may be necessary to produce a

[a] *NH3 Energy Implementation Conference,* Pittsburgh, USA, 2018.

significant amount of hydrogen. Further perovskites for fuel production have been studied using DFT (density functional theory). [38, 72] Emery *et al.* first calculate whether those perovskites are expected to be stable, followed by an assessment of their structural distortions and oxygen vacancy formation energies. [72] They find a multitude of potentially stable new perovskite phases, yet their study shows some limitations when compared to experimental findings. For instance, $CaMnO_{3-\delta}$ is not predicted to be stable at all, yet it undoubtedly is a synthesizable perovskite compound. [73] All theoretical studies may include some inaccuracies inherent to the calculation methods and initial assumptions made. Moreover, some perovskites may be metastable, which means that thermodynamically they are expected to decompose, but they do not decompose at a notable rate unless certain conditions are met. For an effective study of these materials properties, it is therefore necessary to combine both experimental and theoretical materials screenings. Moreover, the published theoretical studies on $ABO_{3-\delta}$ perovskites are complimented by investigating the role of solid solutions for the preparation of novel perovskite phases, as described in this work.

The synthesis of hydrogen and carbon monoxide is especially appealing for the production of hydrocarbons. As the natural reserves of crude oil are limited, alternatives to classical petrochemical routes are promising future technologies. One option for the preparation of alkanes is the Fischer-Tropsch process: [74, 75]

$$n\,\mathrm{CO} + (2\mathrm{n}+1)\mathrm{H_2} \xrightarrow{\Delta T, cat.} \mathrm{C_nH_{2n+2}} + n\,\mathrm{H_2O} \qquad (2.6)$$

As a catalyst, several transition metal based materials can be used, for instance based on cobalt. [76] Another option is the preparation of methanol from syngas using copper-based catalysts. [7, 19] Despite these routes being very appealing for fuel preparation, especially in aviation, it has to be noted that they are only carbon-neutral if all the energy required for their production is generated via renewable sources, and the carbon dioxide required for carbon monoxide production is captured from the air. This is possible, as recently demonstrated, but only economically viable if the cost of greenhouse gas emissions increases significantly. [77]

2.2 Perovskite Chemistry and the tolerance factor

Perovskites are known since the 19th century, and the then-discovered mineral "perovskite" has the composition $CaTiO_3$. [62] Although this is not the case for the prototype perovskite calcium titanate, the ideal perovskite structure is cubic (see Fig. 2.3).

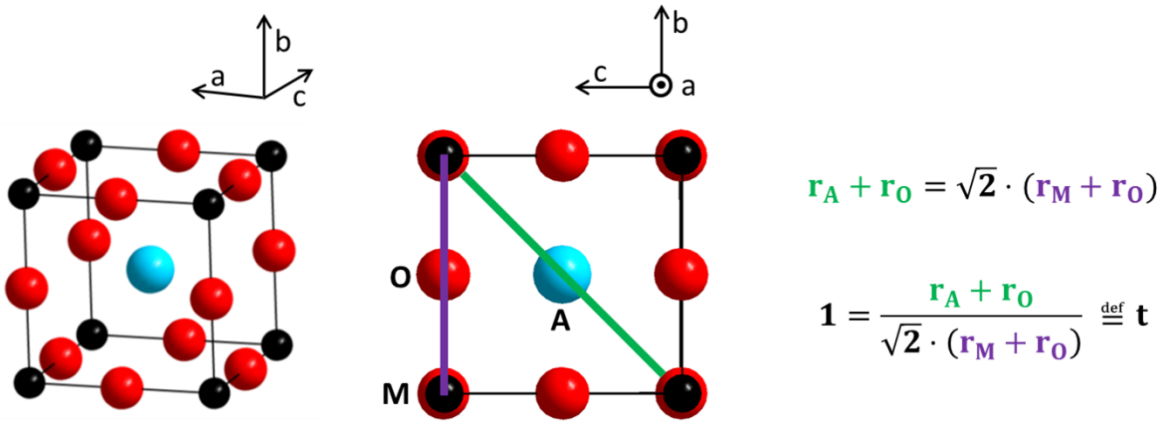

Fig. 2.3. An ideal cubic perovskite structure with the composition AMO_3, where A is the cation with larger ionic radius and M is the cation with smaller ionic radius. The length of the diagonal crossing the A cation is longer (by a factor of $\sqrt{2}$) than the distance of two M cations on the edge. From these purely geometric considerations, the ratio between the ionic radii can be determined for an ideal cubic perovskite structure, and the tolerance factor t (also known as Goldschmidt tolerance factor) is defined as '1' in this case. Please note that the ions are not drawn space-filling to maintain a better overview. In reality, the edges of the two neighboring ions are in direct contact.

The perovskite lattice consists of the A cation in the center with the M cations (often also referred to as B cations) at the corner of the cube and an anion ion in-between two M cations on the edges of the cube. In our case, these anions are always oxide ions, O^{2-}. To achieve charge neutrality, different combinations of cations are possible. As the A cation has a larger ionic radius, it often carries a lower charge than the M cations due to the decrease in ionic radii associated with an increase in positive charge of the species. In most cases, either alkali metals, alkali earth metals, or rare earth metals (lanthanides and actinides) occupy the A sites, whereas the M site is occupied by transition metal cations. This leads to the respective perovskite compositions $A^{+}M^{5+}O_3$, $A^{2+}M^{4+}O_3$, and $A^{3+}M^{3+}O_3$. However, other combinations are possible, for instance main group species such as Al^{3+} on the M site, [70] as well as large main group species such as Bi^{3+} or Tl^{3+} or organic cations in the perovskite. [63, 78, 79] Moreover, it is possible to form related structures such as double perovskites or structures with even more complex stacking variants. [80] For instance, the first discovered high temperature

superconductor YBaCuO ($YBa_2Cu_3O_{7-x}$) shows a crystal structure which is based on the perovskite structural motif. [81]

From geometrical considerations (see Fig. 2.3), it can be derived that the ionic radii in a perovskite need to be in a certain ratio to achieve an ideal cubic crystal structure. V.M. Goldschmidt derived a tolerance factor *t*, which is exactly 1 if this condition is met. [62, 82] The Goldschmidt tolerance factor can be calculated for any perovskite to give a first indication about its stability. If the tolerance factor is smaller than one, a perovskite-like structure may still be formed, but it will be distorted with respect to the ideal cubic structure to accommodate ions with different size. However, if the deviation is too large, other structure types may be more stable. It is important to note that the tolerance factor gives a first indication about the stability of the perovskite, but reality often is more complex. For instance, the stability of a perovskite also depends on the oxidation states and nature of the ions involved, and the bond strength, polarizability, and electronegativity difference between the species have an effect. [62, 83, 84] As the tolerance factor is a rather simplistic method of perovskite stability prediction, it has been modified by various researchers in order to achieve better predictions. [85-87] Nevertheless, the classic Goldschmidt tolerance factor is used in this work for an initial assessment of the perovskite stability, as it is the most well-known metric and it is surprisingly accurate for many different perovskite oxides.

In order to calculate the tolerance factor, the ionic radii of the involved species need to be known. For this purpose, we use Shannon's database of ionic radii, which has been published in 1976 and cited more than 45000 times since then. [88] As usual, a coordination number (CN) of 6 is assumed for the M species and oxide anions to represent their octahedral coordination. [62] For partially reduced perovskites, the size of an oxide vacancy is assumed to be 131 pm according to Chatzichristodoulou *et al.*, who determined this value for $LaGaO_3$. [89] Transition metal species are assumed to be in high spin configuration, if applicable, which is the case for most perovskites. Spin transitions may occur especially at low temperatures (often below ambient temperature), but as this work is only considering high temperature applications, only the high spin configuration is considered. [90] The A species are coordinated 12-fold in an ideal perovskite structure. However, smaller coordination numbers than 12 can be used to account for the distortion of the perovskite lattice from the ideal structure (compare section 4.4). [89, 91] Despite the accuracy of the results gained with this method, it can be argued that the tolerance factor already accounts for this distortion, and using a CN different from 12 is erroneous. [89] In this work, this issue is approached from an empirical point of view. If a coordination number of CN = 12 is assumed, a tolerance factor of $t = 1.001$ results for $SrFeO_{2.81}$, which is the composition reached after synthesis in air. [61] This would indicate a cubic crystal structure due to the near-ideal tolerance factor. However, this non-stoichiometric strontium ferrite is found as a mixture between tetragonal and orthorhombic phases, which indicates some extent of distortion with respect to the ideal perovskite structure. [92] To account for this, the A site CN

is adjusted slightly by assuming a mixed state between CN 12 and CN 10 with 80 % of the Sr^{2+} ions in 12-fold coordination and 20 % in 10-fold coordination. The A ionic radius is then calculated as a weighted average between these two. This leads to a tolerance factor of t = 0.995, which corresponds well to the observed slight distortion. Moreover, using this modified A site CN yields accurate predictions for the crystal structures of Mn-substituted $SrFeO_{3-\delta}$ perovskites, which are further discussed in chapter 4.4. [92] Although this method is arbitrary to some extent and purely based on reaching a mathematically accurate result, it yields good results for this perovskite system. Another way to approach this would be to say that the ionic radii or crystal structures formed are slightly variable in different environments or that they are not defined accurately enough in the literature. In addition, it is important to note that this method may only give accurate results for this specific perovskite system. However, it is used here as a method to give a first prediction on the stability of different perovskites with respect to the crystal structure.

Another word of caution needs to be stated regarding temperature effects. An increase in temperature leads to an increase in the tolerance factor in many systems. [93] For manganates with Sr^{2+}, Ca^{2+}, or Ba^{2+} on the A site, as a rule of thumb according to Fig. 6 in a publication by Dabrowski *et al.*, one can state that the tolerance factor increases by approx. 0.002 at 800 K, by 0.010 at 1000 K, and by 0.020 at 1300 K (all with respect to the calculated tolerance factor at 0 K). [93] For this specific perovskite system, Dabrowski *et al.* derived an equation to calculate the tolerance factor increase. As density functional theory calculations are always only valid for 0 K, and these calculations are used to predict the perovskite stability in this work, those temperature effects are neglected.

Within this work, some perovskites with highly unstable metal species are studied theoretically, such as Cu^{4+} or highly coordinated Mg^{2+}. Moreover, the ionic radii of highly coordinated lanthanides are not known for all species. For this reason, it is necessary to estimate ionic radii not included in Shannon's original work. This is possible using the Pauling bond strengths: [94]

$$r = a - b \cdot \log_{10}(z/\mathrm{CN}) \tag{2.7}$$

z refers to the charge of the ion, whereas a and b are fitted parameters using z/CN pairs with known ionic radii. [88] The calculated ionic radii are summarized in Table 2.2.

Table 2.2. Ionic radii for Mg, Eu, Sm, and Cu. Values printed in bold are estimated using the Pauling bond strengths based on known z/CN pairs with a and b obtained from linear fits of $log_{10}(z/CN)$ vs. r. The other ionic radii are taken from Shannon.[88] Adapted from Vieten *et. al.* (supporting information).[95]

Mg, a = 0.24298, b = 1.05058			**Sm, a = 0.67517, b = 0.94435**		
z	**CN**	**r(Å)**	**z**	**CN**	**r(Å)**
2	4	0.57	3	6	0.958
2	5	0.66	3	7	1.02
2	6	0.72	3	8	1.079
2	8	0.89	3	9	1.132
2	10	**0.98 (calc.)**	3	10	**1.17 (calc.)**
2	12	**1.06 (calc.)**	3	12	1.24
Eu, a = 0.65086, b = 0.97932			**Cu, a = 0.66666, b = 0.13288**		
z	**CN**	**r(Å)**	**z**	**CN**	**r(Å)**
3	6	0.947	1	6	0.77
3	7	1.01	2	6	0.73
3	8	1.066	3	6	**0.71 (calc.)**
3	9	1.12	4	6	**0.69 (calc.)**
3	10	**1.16 (calc.)**			
3	12	**1.24 (calc.)**			

Upon non-stoichiometric reduction of a perovskite, the transition metal (M) oxidation state decreases. In principle, a decrease in the A ion oxidation state would also be possible, but does not occur in the case of most alkali and alkali earth metals, which are most stable in the oxidation states +1 and +2, respectively. For cesium and rubidium, suboxides are known with the alkali metal in a lower oxidation state than +1,[96] so it might be possible to reduce the A site species as well in this case. However, this possibility is not further considered within this work as it is speculative and beyond the scope of this study. The reduction of M metal species leads to the formation of oxygen vacancies. At $\delta = 0.5$, the oxidation state of the transition metals is decreased by 1 with respect to $\delta = 0.0$, and the defect structure formed at $\delta = 0.5$ is referred to as brownmillerite.[97] In-between these two points, structures with mixed valence of the M cations are formed. For instance, a mixed formal valance of Fe^{3+} and Fe^{4+} is formed in $SrFeO_{3-\delta}$.[98] Including the non-stoichiometric phases, the perovskites considered in this work can be written as $A^{+}M^{4/5+}O_{3-\delta}$, $A^{2+}M^{3/4+}O_{3-\delta}$, and $A^{3+}M^{2/3+}O_{3-\delta}$. Please note that the oxygen vacancies formed upon reduction may either be randomly distributed over the lattice, or there may be some additional vacancy ordering. This depends on the specific perovskite composition.[99] The reduction of metal species in these perovskites is directly proportional to an increase in the average ionic radii of the M species. Due to this increase, the Goldschmidt tolerance factor decreases upon reduction, which leads to a change in the expected degree of distortion of the crystal structure. In most cases, this effect outweighs the impact of a temperature change on the tolerance factor. The reduction-induced change in tolerance factor is shown exemplarily for the reduction of $SrFeO_{3-\delta}$ in Fig. 2.4. This explains the transition from a cubic perovskite structure for the fully oxidized $SrFeO_3$ over a tetragonal to an orthorhombic structure upon reduction to $SrFeO_{2.5}$.[61, 99] Moreover, the effect of different M cations is explained

exemplarily using both $SrMnO_3$ and $SrFeO_3$. By choosing different compositions, it should be possible to design different perovskite structures with different degrees of distortion on purpose.

As mentioned before, ideal cubic structures should be formed for t ~ 1.00. Firstly, above t ~ 1.02 we assume hexagonal or rhombohedral structures. As the rhombohedral structure can be seen as a combination of hexagonal and cubic stacking variants, these structures are often formed at the transition between ideal cubic structures and fully hexagonally stacked lattices. [100-102] Then, if the tolerance factor falls below 1.00, tetragonal or different forms of orthorhombic structures can be formed. The octahedral coordination spheres of the M cations and oxide ions are tilted, and a large variety of different tilt systems leads to an according number of different orthorhombic structures. [103-105] Finally, at very low tolerance factors (below ~ 0.94-0.95), another type of orthorhombic structure may be formed, which is known as post-perovskite and occurs in the earth's mantle. [106, 107] It is not clear, however, whether the Goldschmidt tolerance factor is a reasonable means of predicting the formation of this post-perovskite structure. If the tolerance factor is even lower, other non-perovskite structures become more stable, as mentioned before. Phase transitions between different perovskite and non-perovskite structures deep down in the earth's mantle are considered as a potential cause of earthquakes and influence the convection in the earth's mantle. [108, 109] As these phase changes can have a such large effects on the expansion and contraction of materials, avoiding these phase changes will increase the perovskite's stability in redox cycles, especially with respect to their mechanical durability. Therefore, these phase changes are avoided within this work for the most part, but nevertheless the effect of a targeted induction of these phase changes is studied as well, as it may be beneficial from a thermodynamic point of view, as mentioned later.

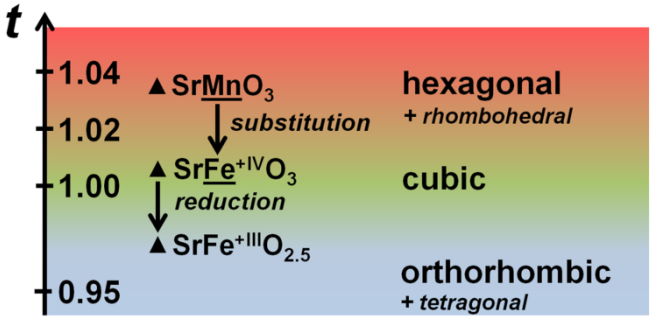

Fig. 2.4. Tolerance factor of some exemplary perovskites and the effect of substitution and reduction of the M species. Cubic perovskites are formed if the tolerance factor t is ~ 1, whereas orthorhombic and tetragonal structures are reached if $t < 1$, whereas hexagonal and rhombohedral structures are formed at $t > 1$. Adapted from Vieten *et al*. [95]

2.3 Perovskite materials design

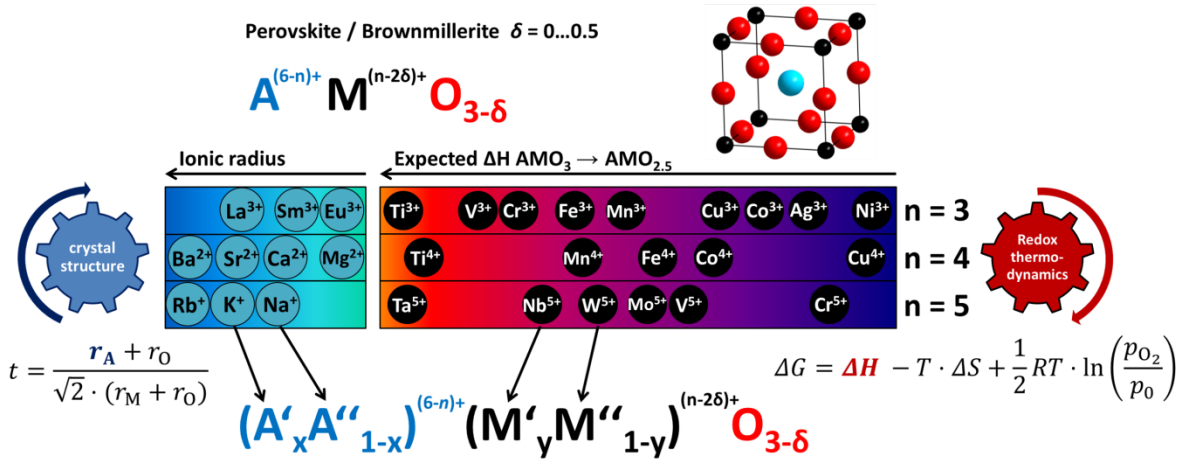

Fig. 2.5. Design principles for perovskite solid solutions. Different perovskite systems are investigated, denoted by n = 3, 4, and 5. The choice of M metals has a significant impact on the redox thermodynamics defined by the Gibbs-Helmholtz equation, while the A metals are chosen accordingly to maintain a stable crystal structure according to the Goldschmidt tolerance factor. Taken from Vieten *et al*. [95]

In the previous paragraphs, the stability and crystal structure of pure perovskites (without solid solution formation) has been described. It has been shown how the perovskite's composition influences its crystal structure, and how the reduction may lead to phase changes. These principles are extended to perovskite solid solutions in the following. Considering a solid solution with two different A species and two different M species, the general composition of the perovskite can be described as $(A'_xA''_{1-x})^{(6-n)+}(M'_yM''_{1-y})^{(n-2\delta)+}O_{3-\delta}$ with n = 3, 4, or 5 and δ = 0...0.5. The variable n can only have integer values in our case, and is used to describe the type of perovskite system. It is equal to the positive charge of the M site ions in the fully oxidized state of the perovskite. In this work, no perovskites with mixed valence on the A site are considered, such as lanthanum strontium manganese oxides. These compounds are beyond the scope of this study. Considering that there is already a rich collection of published work on this topic available (mainly due to the application of such perovskite systems in solid oxide fuel cells and on LSMA perovskites for water splitting), the interested reader is referred to those publications. [110-112]

Within this work, the following rationale is applied to design perovskite solid solutions as redox materials (taken from the accompanying peer-reviewed publications, see also Fig. 2.5): [95, 113]

1. **Tolerance factor engineering**
   ⇨ Define a stable perovskite structure
2. **Selection of M site species**
   ⇨ Define reducibility (redox thermodynamics)
3. **Selection of A site species**
   ⇨ Match ionic radii to reach target tolerance factor

Tolerance factor Engineering

It is assumed that the species in these perovskite solid solutions are statistically distributed (ideal solid solutions). It is a generally accepted paradigm that isomorphic mixtures are formed if the difference in ionic radii does not exceed 15 %. This rule of thumb also originates in the work of V.M. Goldschmidt, in fact it has been introduced in the same publication as the tolerance factor. [82] These considerations are still valid today, nevertheless many exceptions from these rules have been found, mainly attributed to covalent bonding. [114] For most of the compositions studied in this work, covalent bonding does, however, not play a significant role. As the ionic radii of most species considered for solid solutions on the perovskite sites differ by less than 15 %, we can assume ideal solid solution formation for the most part. Larger differences in ionic radii occur for A site cations, but as we are only mixing species with small differences in radii, i.e. only Ca^{2+} with Sr^{2+}, never Ca^{2+} with Ba^{2+}, ideal solid solutions should still form. The ionic radii of $(A'_xA''_{1-x})^{(6-n)+}\left(M'_yM''_{1-y}\right)^{(n-2\delta)+}O_{3-\delta}$ solid solutions can then be calculated using a modified tolerance factor with weighted averages between the ionic radii of the A'/A'' and M'/M'' species: [95]

$$t = \frac{[r_{A'} \cdot x + r_{A''} \cdot (1-x)] + r_O}{\sqrt{2} \cdot ([r_{M'} \cdot y + r_{M''} \cdot (1-y)] + r_O)} \tag{2.8}$$

The M site composition is chosen according to thermodynamic considerations (see later section). A target value for the tolerance factor *t* is then defined. This target value is chosen based on the fully oxidized state of the perovskite ($\delta = 0$). For our large scale materials screening with many different perovskite species, we define the target tolerance factors in such a way that no phase change is to be expected during reduction, especially no transition between hexagonal or rhombohedral and cubic forms. Naturally, some distortion of the perovskite will occur during reduction, but by defining target tolerance factors around 1 or slightly above 1 for $n = 4$, and 5 and around 0.945 for n = 3, stable perovskite structures should form. If the tolerance factor decreases upon reduction, no phase

transitions should occur (see Fig. 2.4). If, however, phase transitions shall be caused deliberately, a target tolerance factor at the lower end of the stability range of a certain type of structure is chosen, i.e. 1.02-1.03 to induce a transition to cubic structures upon reduction. After choosing the target tolerance factor and defining the M site composition, the average ionic radius of the A site ions can be calculated which is necessary to reach a certain tolerance factor. We can then choose those two A site species which lead to an overall charge neutrality of the perovskite and use their ionic radii $r_{A'}$ and $r_{A''}$ to solve Eq. 2.8 for *x*. By this means, we obtain a composition on the A site based on the composition of the M site and on a target tolerance factor. In Fig. 2.6, this is shown exemplarily for perovskite solid solutions with a target t = 1.006 in the n = 4 system, i.e., with alkali earth metal ions on the A site. The target tolerance factor 1.006 is chosen as it is the tolerance factor of $SrFeO_3$, which is used as a reference here.

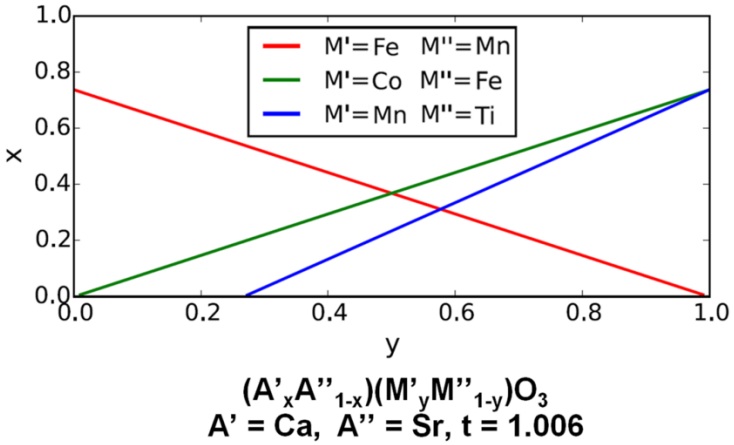

Fig. 2.6. Relation between A and M site composition in a perovskite solid solution based on a common target tolerance factor of 1.006. For high titanium concentrations in the Mn-Ti system, the ionic radius of Sr^{2+} is not sufficient and a mixed Sr^{2+}/Ba^{2+} occupation is necessary to reach the target tolerance factor. Adapted from Vieten *et. al.* [95]

Selection of M site species

For the M site species, we select those elements which show a stable oxidation state both for the perovskite and for the brownmillerite state. Moreover, elements with no stable isotopes and heavier elements with ionic radii too large to form stable perovskites with most A site species are excluded. Some elements show a clear preference for either oxidation state, i.e. Ag^{3+} and Cu^{4+} are rather unstable. [115] The stability of each redox state can be described using the standard redox potential or the redox enthalpies of compounds with species in those oxidation states can be compared. The latter approach is used in this work, mainly by comparing the redox enthalpies of different perovskites AMO_3 for the complete reduction to the brownmillerite $A_2M_2O_5$, i.e., the conversion from a state with δ = 0.0 to a state with δ = 0.5:

$$4\,AMO_3 \rightarrow 2\,A_2M_2O_5 + O_2 \tag{2.9}$$

The same A site cation is chosen in order to allow for a reasonable comparison of reducibilites. These reactions are calculated using *Materials Project*, an online resource containing data on a large amount of inorganic compounds, including redox enthalpies based on DFT calculations. [116, 117] If this data is not available for a certain species, we use data for binary oxides with the same oxidation states instead. By this means, the expected redox enthalpies can be ranked for different species in different redox systems (see Fig. 2.5). The redox enthalpies can then be tuned based on the requirements of a specific application for a perovskite. The two M site species chosen are always those with minimal difference in redox enthalpy, i.e. Mn^{4+} and Fe^{4+} for the $n = 4$ system, or Cr^{3+} and Fe^{3+} for the $n = 3$ system. The goal of this materials engineering process is to be able to reach any target redox enthalpy just by mixing the two species with redox enthalpies closest to the target value in the according ratio. The choice of A site species should only have a small effect on the materials thermodynamics, as those are not involved in the redox reaction. Therefore, these can be used to adjust the tolerance factor. This novel materials design method is further explained in section 2.3 and justified by the experimental results of this work.

Selection of A site species

As A site species, those ions are used which are likely to form stable perovskites with the before-mentioned transition metals according to the tolerance factors. Three different species are selected for each redox system (n = 3, 4, 5) to account for small, medium, and large ionic radii on the M site. Additionally, Mg^{2+} is selected as a potential constituent of perovskite solid solutions, as it might be possible to incorporate at least small amounts of Mg into the lattice, despite its small radius which makes it difficult to achieve high coordination numbers. It is definitely possible to form perovskite phases with only Mg^{2+} on the A site under high pressures, and the mineral bridgmanite ($MgSiO_3$) which exists in the earth's mantle is actually the most abundant solid phase in earth. [118] For the lanthanides, we only use those species which show no stable oxidation state of +4 to achieve a fixed +3 oxidation state at all times. Moreover, Pm is excluded, as no stable isotopes exist, and Gd as well as all heavier elements are not used, as these have very small ionic radii ("Gadolinium break" [119]) which would make it difficult to prepare stable perovskite structures. From this pre-selection process, the elements La, Sm, and Eu are left.

2.4 DFT-based perovskite screening

Theoretical methods nowadays allow accelerating materials science significantly. By avoiding laboratory experiments based on trial and error and partially replacing them by computational materials screening, many work hours can potentially be saved and innovative materials can be found much faster. One method of computational chemistry is referred to as density functional theory (DFT). It is based upon simulating the structure of the electron shell around atoms, as the electronic charge density is crucial for the chemical properties of materials. [120] The electrons are arranged around the atoms in orbitals, which are zones where an electron can be found with a certain probability. If time-dependent interactions and relativistic effects are not regarded, one can use the time-independent Schrödinger equation to describe an isolated *N*-electron system consisting of atoms or molecules in Born-Oppenheimer approximation: [120]

$$\hat{H}\,\Psi = E\,\Psi \tag{2.9}$$

Ψ is the wave function describing the electron density, the electronic energy is expressed by E, and the Hamiltonian operator $\hat{H}$ describes the sum of kinetic and potential energies in the system, in the simplest case (the hydrogen atom) consistent of an operator for the kinetic energy of the electron and the potential energy of electron-nucleus attraction. [120] In the case of multi-electron systems, electron-electron repulsion has to be considered as well. The electron density around an atom is not the same in every direction (except for *s* orbitals). Therefore, it is necessary to determine the spatially dependent electron density using spatially dependent wave functions. Hohenberg and Kohn showed that the properties of an *N*-electron system in the ground state are determined by the electron density with only 3 *N* spatial coordinates. [121] This simplifies the problem significantly. To describe the wave function of the electron system, different approaches to solve the many-body Schrödinger equation have been developed over the past decades. [122] The simplest method is the Hartree-Fock approximation, in which products of single-particle wavefunctions (Slater determinants) are applied, which are then used to find the minimum energy. However, this method becomes very computationally expensive when applied to larger many electron systems. By using functionals describing the electron density (hence the name density functional theory), DFT provides an alternative. Despite DFT being an exact method itself, the central problem in DFT is that for real systems the exchange and correlation functionals decribing the interaction of the electrons between each other are not known explicity and need to be approximated. [123] Many methods exist for doing so, and one of these methods is referred to as GGA (generalized gradient approximation), which considers that the electron density is not homogenously distributed over space. It is used within this work as the total energy of the system is given quite accurately using GGA. [124] As we are

interested mainly in redox enthalpies between different phases, this is a paramount feature. Despite GGA providing a good approximation, it introduces the so-called self-interaction error, which refers to a non-physical electron self-interaction energy being used. This error is particularly large for localized electron states such as *d* and *f* orbitals, which occur in many cases in our perovskites. [117] By adding an energy correction for these cases, this error can be mitigated. This method is referred to as GGA + *U*. Jain *et al.* developed a method to accurately predict formation enthalpies of compounds by mixing GGA and GGA + *U* calculations. [117] This method is used within *Materials Project* and as the work presented herein is closely related to and partially based upon *Materials Project*, it is also used in the following. Details on the calculation methods can be retrieved through https://materialsproject.org/docs/calculations. By calculating the difference between the formation enthalpies of the products and educts of a reaction, one can calculate reaction enthalpies. The so-calculated reaction enthalpies are referred to in the following as ΔH_{DFT}.

To begin calculating the structure and energy of a new compound such as our solid solutions, one must first know some similar crystal structure as a starting point, including the explicit positions of all atoms without any partial occupancies. This is a problem for true solid solutions, as it cannot be said exactly which atom occupies a certain lattice site, but only a probablity can be given to find one species or the other. Therefore, an approximation can be used by defining superstructures of the ideal perovskite lattice. We use the crystal structure of the cubic perovskite $SrFeO_3$ as a starting point, which crystallizes in space group 221 ($Pm\bar{3}m$). Upon reduction to the brownmillerite, another structure is obtained, in the case of $Sr_2Fe_2O_5$ an orthorhombic structure in space group 46 (Ima2). These two structures are used to create 2x2x2 supercells, which with respect to the original unit cells have exactly the double lattice constant in each direction and contain 8 times as many atoms. In the case of the brownmillerite, the amount of atoms per unit cell reaches 144, which is a high but still manageable number. The perovskite compositions are then rounded to fractions of 1/8 and thus discretized. This means that there will be some small error in composition (and thus, also in the achieved tolerance factor), but the error in composition is smaller than ± 1/16, and this simplification allows us to compute these structures at all. The alternative would be to create a gigantic unit cell to account for compositions such as $Ca_{0.29}Sr_{0.71}FeO_{3-\delta}$, and run out of computation time very quickly. Moreover, the scaling matrix of the unit cell (in our case a 3x3 diagonal matrix with a (2 2 2) diagonal vector) must scale the original unit cell to the same extent in either direction to not create anisotropic effects unrelated to the real situation. The unit cells prepared as input structures for the DFT calculations are shown in Fig. 2.7 for a perovskite with exemplary composition $Sr_{0.75}Ca_{0.25}Mn_{0.375}Fe_{0.625}O_{3-\delta}$, which converted to a 2x2x2 superstructure corresponds to a composition of $Sr_6Ca_2Mn_3Fe_5O_{24}$ for the perovskite, and $Sr_{24}Ca_8Mn_{20}Fe_{12}O_{80}$ for the brownmillerite. By this means, only integer site occupancies are used.

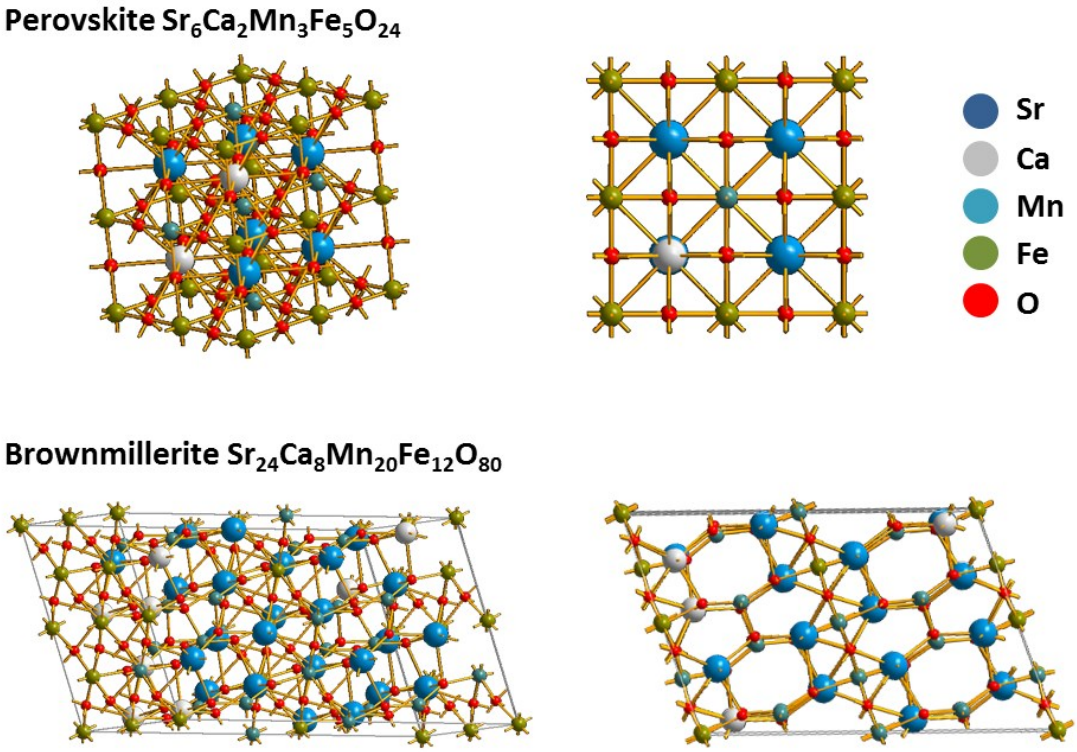

Fig. 2.7. Exemplary crystal structures of perovskites (top two images) and brownmillerites (bottom two images) used as starting points for DFT calculations within this work, in this case for $Sr_{0.75}Ca_{0.25}Mn_{0.375}Fe_{0.625}O_3$ and $Sr_{0.75}Ca_{0.25}Mn_{0.375}Fe_{0.625}O_{2.5}$. The structures are based upon a basic cubic perovskite structure and the orthorhombic brownmillerite structure of $Sr_2Fe_2O_5$. The views on the right are from the side with one lattice vector in viewing direction, whereas the views on the left are tilted projections of the three-dimensional structure.

An almost endless amount of possibilities exist for distributing the atoms on the different A and M sites, and we can only pick one of them for DFT calculations, as our atom positions are fixed. To find a good representation of the actual structure which yields energy values comparable to the actual values for real solid solutions, we can use different methods. One of them includes the calculation of the electrostatic energy, which is referred to as the Ewald method and yields the so-called Ewald sum. [125] By minimizing the Ewald sum, one should find the ordered structure with lowest energy and therefore the highest probability. This method is carried out using *pymatgen*, with details given in the experimental section. [126] An alternative would be to use so-called special quasirandom structures (SQS). [127, 128] These structures represent the actual properties of a solid solution much more accurately, but the computational effort for getting these structures increases significantly for the large structures we are investigating. Therefore, it is not used within this work, but considered an appealing option for future studies on select systems.

In summary, mixed GGA and GGA + U DFT calculations based on superstructures of prototype perovskites can be an effective method to retrieve properties of quinary perovskite phases (two different species on either metal site + oxygen) as solid solutions based on known phases. Despite all efforts, however, theoretical data may be flawed due to incorrect assumptions and inaccuracies of the models used. Therefore, these methods cannot (yet) entirely replace experimental testing, but at least they help streamline the process. Based on a theoretical pre-selection, a much smaller amount of materials has to be tested experimentally, and the probability of positive results in experimental tests is significantly increased.

2.5 Thermodynamics and Kinetics

It is generally known that any chemical reaction proceeds spontaneously if the Gibbs free energy is below zero. The Gibbs free energy results from a transformation of the Gibbs-Helmholtz equation:

$$\Delta G = \Delta H - T \cdot \Delta S \tag{2.10}$$

ΔH refers to the change in reaction enthalpy, i.e., the heat effect of the reaction, whereas the change in entropy is given by ΔS. The entropy can be described as the extent of disorder in the system. The change in Gibbs free energy is temperature dependent, which means in the case of endothermal reduction reactions, for instance of perovskites in air, an increase in temperature causes a decrease of ΔG. Naturally, this means that thermal reduction reactions occur at high temperature. In addition to that, both ΔH and ΔS may show a temperature dependence. As oxygen gas is one of the reaction products of the reduction of our redox materials, the Gibbs free energy also depends on the oxygen partial pressure p_{O_2}. The Gibbs free energy at any oxygen partial pressure can be calculated from the Gibbs free energy at standard conditions ΔG^0:

$$\Delta G = \Delta G^0 + \frac{1}{2} RT \cdot \ln\left(\frac{p_{O_2}}{p^0}\right) \tag{2.11}$$

And in combination with Eq. 2.10:

$$\Delta G = \Delta H - T \cdot \Delta S + \frac{1}{2} RT \cdot \ln\left(\frac{p_{O_2}}{p^0}\right) \tag{2.12}$$

R refers to the ideal gas constant, and p^0 is the reference oxygen partial pressure, i.e. the oxygen partial pressure under the conditions ΔG^0 is defined for. Throughout this work, we use p^0 = 1 bar. The factor ½ in Eq. 2.12 originates from the fact that we use ΔH, ΔS *and* ΔG as per mol of oxygen O, not per mol of molecular oxygen O_2. Therefore, the enthalpy and entropy are also referred to as ΔH^O and ΔS^O in this work. However, the gas partial pressure refers to molecular oxygen. The redox enthalpy change per mol of oxygen can also be defined as vacancy formation energy. The key element of this work is to determine ΔH^O and ΔS^O for different perovskites, as these quantities can be used to predict their redox properties. For non-stoichiometric perovskites, both of these quantities depend on the oxygen non-stoichiometry δ and on the temperature T. As the non-stoichiometry itself is a function of p_{O_2} and T, we have to find expressions for the functions $\Delta H^O(\delta, T, p_{O_2})$ and $\Delta S^O(\delta, T, p_{O_2})$. For the experimental datasets, these are determined by measuring this data and fitting it to empirical model functions, as demonstrated in section 5.1.1. To determine these theoretically from DFT data and thermochemical databases, we use the method presented in the following which is partially based on earlier work done for ceria [55, 129], but is novel in terms of treating solid solutions of perovskites.

Theoretical redox enthalpies as a function of δ, T

We first assume that the redox enthalpy of a perovskite solid solution depends on its non-stoichiometric oxygen content. A perovskite consisting of two species on the M site with different redox potential, i.e. Fe^{4+} and Mn^{4+} is expected to be reduced more readily as long as the amount of Fe^{4+} species available is still high. After most of the Fe^{4+} is reduced to Fe^{3+}, the only way to achieve a significant increase in δ would be to reduce Mn^{4+} to Mn^{3+}, which should be associated with an increase in redox enthalpy. This assumption is put to the test in a later section of this work. Based on this assumption, one can define a minimum and maximum redox enthalpy for any perovskite solid solution as limiting values $\Delta H_{\min}$ and $\Delta H_{\max}$ for $\delta \to 0$ and $\delta \to 0.5$, respectively. Furthermore, a solid solution of the type $(A'_xA''_{1-x})(M'_yM''_{1-y})O_3$ can be described as an ideal mixture of four pure perovskite species, i.e. for $Sr_{0.3}Ca_{0.7}Mn_{0.4}Fe_{0.6}O_3$: [95]

$$\begin{array}{ccc} SrMnO_3 \searrow & & \swarrow SrFeO_3 \\ & \mathbf{Sr_{0.3}Ca_{0.7}Mn_{0.4}Fe_{0.6}O_3} & \\ CaMnO_3 \nearrow & & \nwarrow CaFeO_3 \end{array} \tag{2.13}$$

It has been mentioned earlier that the redox enthalpy is mainly governed by the choice of M species, and the choice of A species has only little effect. For instance, the reduction of $CaMnO_3$ to the brownmillerite form occurs with a redox enthalpy change of 173 kJ/mol_O, whereas $SrMnO_3$ is reduced at 170 kJ/mol_O according to DFT data from *Materials Project*. [116, 117] Moreover, differences in

redox enthalpy induced by different *A* cations should be independent of the redox extent of the perovskite, as these species are not reduced. Therefore, we can use a weighted average of the reaction enthalpies of endmembers containing the same M species. In the example (Eq. 2.13), this means that: [95]

$$\Delta H_{min} = 0.3 \cdot \Delta H_{\mathrm{SrFeO_3}} + 0.7 \cdot \Delta H_{\mathrm{CaFeO_3}} \tag{2.14}$$

$$\Delta H_{\mathrm{max}} = 0.3 \cdot \Delta H_{\mathrm{SrMnO_3}} + 0.7 \cdot \Delta H_{\mathrm{CaMnO_3}} \tag{2.15}$$

Based on the redox enthalpies of the four pure perovskite species mentioned above (with respect to a complete reduction to the brownmillerite), the redox enthalpy of the solid solution can be approximated based on data for the solid solution endmembers (see Fig. 2.8):

$$\Delta H_{(\mathrm{A'_xA''_{1-x}})(\mathrm{M'_yM''_{1-y}})\mathrm{O_3}} = \Delta H_{\mathrm{min}} \cdot \mathrm{y} + \Delta H_{\mathrm{max}} \cdot (1 - \mathrm{y}) = \Delta H_{\mathrm{endmembers}} \tag{2.16}$$

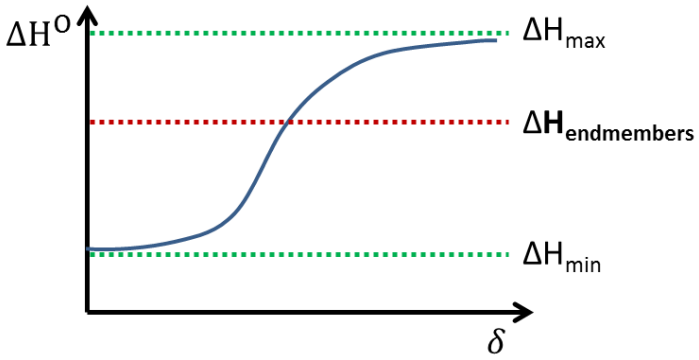

Fig. 2.8. Approximation of the redox enthalpy of a solid solution based on limiting values ΔH_{min} and ΔH_{max} for the solid solution endmembers with a generic function $\Delta H(\delta)$ (blue).

This approximation is only valid if M' is the more redox active species and thus defines ΔH_{min}. In this case, y is the stoichiometry of the more redox active species, which shall be defined as *act* in the following, and Eq. 2.16 is then only valid if $y = act$. If the $\Delta H_{\mathrm{endmembers}}$ value is the correct average redox enthalpy of the solid solution, the integral of the real function $\Delta H(\delta)$ over the full non-stoichiometry range (0-0.5) must correspond to the integral of $\Delta H_{\mathrm{endmembers}}$ in the same range: [b]

$$\int_0^{0.5} \Delta H(\delta, \mathrm{T})\, \mathrm{d}\delta = \int_0^{0.5} \Delta H_{\mathrm{endmembers}}\, d\delta \tag{2.17}$$

[b] As we see later, this integral also corresponds to the amount of heat necessary for the reduction (and released during re-oxidation in air).

However, this is not necessarily the case. The so-approximated redox enthalpy, which is denoted by $\Delta H_{\mathrm{endmembers}}$, may deviate from the value obtained for the solid solution using DFT (ΔH_{DFT}). The solid solution does not always act like the sum of its constituents. Nevertheless, it is still necessary to know enthalpy values not just for the complete reduction from perovskite to brownmillerite, which can be obtained by using DFT as explained before, but also the limiting values for the extreme cases. If those are not known, it is not possible to obtain a function for $\Delta H(\delta)$, as we see later. To resolve this issue, one can correct the values for ΔH_{min} and ΔH_{max} by the difference between $\Delta H_{\mathrm{endmembers}}$ and ΔH_{DFT}:

$$\Delta H_{\mathrm{min,corr}} = \Delta H_{\mathrm{min}} + (\Delta H_{\mathrm{DFT}} - \Delta H_{\mathrm{endmembers}}) \tag{2.18}$$

$$\Delta H_{\mathrm{max,corr}} = \Delta H_{\mathrm{max}} + (\Delta H_{\mathrm{DFT}} - \Delta H_{\mathrm{endmembers}}) \tag{2.19}$$

If these corrected values are used to calculate a mean ΔH using Eq. 2.16, the result is equal to the value obtained using DFT, but now we also have estimated values for the extreme points δ = 0 and δ = 0.5. This method, however, may fail in some cases. Let's assume that ΔH_{min} = 100 kJ/mol and ΔH_{max} = 400 kJ/mol based on the redox enthalpies of the endmembers, and that act = 0.5. The result for $\Delta H_{\mathrm{endmembers}}$ is then 250 kJ/mol according to the equations stated before. Now we assume that ΔH_{DFT} differs significantly from this value, i.e. ΔH_{DFT} = 130 kJ/mol. Then, using Eqn. 2.18 and 2.19, we get $\Delta H_{\mathrm{min,corr}} = -20$ kJ/mol and $\Delta H_{\mathrm{max,corr}} = 280$ kJ/mol. As the redox enthalpy is negative for small values of δ according to the limiting value $\Delta H_{\mathrm{min,corr}}$, this would indicate that it is impossible to fully oxidize the material at 1 bar oxygen partial pressure. This result most likely does not describe the real situation accurately (although, of course, some perovskites show this behavior, but those would also have much lower ΔH_{DFT} values). Therefore, this method fails if the difference between ΔH_{DFT} and $\Delta H_{\mathrm{endmembers}}$ becomes too large. In this case it would be more accurate to use the DFT-calculated value both for ΔH_{min} and ΔH_{max}, even though this leads to a δ-independent function for ΔH. Of course it is difficult to say what "too large" means in this case. A cutoff value of 30 kJ/mol$_O$ is defined for the maximum difference between ΔH_{DFT} and $\Delta H_{\mathrm{endmembers}}$, above which a a δ-independent function for ΔH is used instead of the values from Eqn. 2.18 and 2.19. This cutoff value leads to reasonable results in most cases.

Now that the minimum and maximum of $\Delta H(\delta)$ are defined for every case, one needs to find a model describing the increase of ΔH in-between these values and also the temperature dependence of ΔH, i.e., we need to find $\Delta H(\delta, T)$. First, one can state that the total non-stoichiometry as a function of the temperature T and the oxygen partial pressure p_{O_2} in an ideal solid solution of two perovskites is the sum of the non-stochiometries induced in both individual sub-lattices: [95]

$$\delta\left(T, p_{O_2}, \Delta H_{\min}, \Delta H_{\max}\right) = \delta_1\left(T, p_{O_2}, \Delta H_{\min}\right) + \delta_2\left(T, p_{O_2}, \Delta H_{\max}\right) \tag{2.20}$$

The non-stoichiometry in one sub-lattice δ_n is given by: [95, 129, c]

$$\delta_n(T, p_{O_2}, \Delta H_n) = \frac{\delta_{max,n} \cdot \exp\left(\frac{1}{2} \cdot \frac{S_{0,O_2}(T)}{R} \delta_{max,n}\right) \cdot p_{O_2}^{\left(-\frac{1}{2}\delta_{max,n}\right)} \cdot \exp\left(-\Delta H_n \cdot \frac{\delta_{max,n}}{RT}\right)}{1 + \exp\left(\frac{1}{2} \cdot \frac{S_{0,O_2}(T)}{R} \cdot \delta_{max,n}\right) \cdot p_{O_2}^{\left(-\frac{1}{2}\delta_{max,n}\right)} \cdot \exp\left(-\Delta H_n \cdot \frac{\delta_{max,n}}{RT}\right)} \tag{2.21}$$

with $\delta_{max,1} = act/2$, $\delta_{max,2} = (1 - act)/2$, $\Delta H_1 = \Delta H_{min,corr}$, $\Delta H_2 = \Delta H_{max,corr}$, $\delta_1 \geq \delta_2$, the ideal gas constant R, and the partial molar entropy of oxygen as a function of temperature $S_{0,O_2}(T)$. This partial molar entropy can be calculated using literature values, for instance from the NIST-JANAF thermochemical tables. [130, 131] Using the Shomate equation and the constants published in these tables, a function $S_{0,O_2}(T)$ results. The total non-stoichiometry is given by Eq. 2.20. For a given set of T and δ, the oxygen partial pressure p_{O_2} can be calculated by finding where Eq. 2.20 is zero:

$$0 = \delta\left(T, p_{O_2}, \Delta H_{\min}, \Delta H_{\max}\right) - \delta \tag{2.22}$$

The result describes $p_{O_2}(\delta, \Delta H_{min}, \Delta H_{max}, T)$. Then, $\Delta H(\delta, T)$ is calculated as a numerical derivative of p_{O_2} with respect to the temperature: [95, c]

$$\Delta H(\delta, T) = \frac{-\frac{1}{2} \cdot \ln p_{O_2}(\delta, \Delta H_{min}, \Delta H_{max}, T) - \frac{1}{2} \cdot \ln p_{O_2}(\delta, \Delta H_{min}, \Delta H_{max}, T + 0.01)}{\frac{1}{RT} - \frac{1}{R \cdot (T + 0.01)}} \tag{2.23}$$

We now have a function for $\Delta H(\delta, T)$. It can easily be seen that calculating this numerical derivative to find the solution of this function can become tedious for large datasets, so the amount of data points for which the solution is calculated needs to be limited. Using this model, the steepness of the increase in redox enthalpy upon reduction is temperature-dependent. At low temperatures (well below ambient temperature), it is very steep, almost resembling a step function. At higher

[c] Dr. Brendan Bulfin, ETH Zurich, personal communication (2017).

temperatures (those relevant for solar-thermochemical cycles), the result resembles the blue curve in Fig. 2.8.

Theoretical redox entropies as a function of δ, T

The redox entropy change in perovskite solid solutions – similar to the redox entropy change in ceria – can be divided into three contributions. The total entropy change can be written as the sum of the partial molar entropy of oxygen $S_{0,O_2}(T)$, the vibrational entropy change $\Delta s_{\mathrm{vib}}(T)$, and the configurational entropy change $\Delta s_{\mathrm{conf}}(\delta, T)$: [95, 129, 132]

$$\Delta S(\delta, T) = \frac{1}{2} S_{0,O_2}(T) + \Delta s_{\mathrm{vib}}(T) + \Delta s_{\mathrm{conf}}(\delta, T) \tag{2.24}$$

$S_{0,O_2}(T)$ is often the largest factor in this summation. The release of gaseous oxygen which was bound in a solid lattice before the reduction reaction leads to a phase change and thus to a dramatic increase in entropy. As explained before, it is can be determined relatively easily using the Shomate equation and the NIST-JANAF thermochemical tables. [131] The change in vibrational entropy is more complex. The vibrational entropy, also referred to as phonon entropy, results from the excitation of vibrational modes in the lattice. At higher temperature, more of these modes are excited until finally all of them are excited and the vibrational entropy stays constant. This is very closely related to the heat capacity of a solid, as the extent of phonon mode excitation determines the amount of heat which is stored by the solid. To calculate the change in vibrational entropy we use the Debye model. [133] According to the Debye model, absolute vibrational entropy values as a function of the temperature ($s_{\mathrm{vib}}(T)$) can be determined for a given material using the Debye temperatures $\Theta_{\mathrm{D},\delta}$ of these phases with $y_\delta = T/\Theta_{\mathrm{D},\delta}$ and the ideal gas constant R: [133]

$$\mathrm{D}(y) = \frac{3}{y_\delta^3} \int_0^{y_\delta} \frac{x^3}{e^x - 1}\, dx \tag{2.25}$$

$$s_{\mathrm{vib},\delta}(T) = \mathrm{R} \cdot \left[-3 \cdot \ln\left(1 - e^{-\left(\frac{T}{\Theta_{\mathrm{D},\delta}}\right)} \right) \right] + 4 \cdot \mathrm{D}\left(\frac{T}{\Theta_{\mathrm{D},\delta}} \right) \tag{2.26}$$

The Debye temperatures of the phases need to be known for any non-stoichiometry value δ. To obtain these, we first determine the Debye temperatures of the fully oxidized and fully reduced brownmillerite phases. Using *pymatgen*, these can be determined from the elastic tensors of these phases, and those can be determined using DFT (see *Materials Project*). [126, 134] The Materials Project website contains elastic tensors for many materials, and they are being calculated for all of the

materials in our study. As this is a very lengthy and computationally expensive process, some of the materials still lack elastic data. It is gradually being added, and in the meantime, the elastic tensors for the model system $SrFeO_{3-\delta}$ are used as an approximation. As the vibrational entropy change is usually the smallest contribution and all perovskites show similar crystal structures (i.e., similar vibrational modes), the error introduced by doing so is negligible for the most part, especially at high temperatures where all vibrational modes are excited ($T >> \Theta_{D,\delta}$).

Now that the absolute entropies for the fully oxidized and fully reduced state are known, one can use this data to get the change in entropy during reduction. For this purpose, it is assumed that the vibrational entropy and the Debye temperature $\Theta_{D,n}$ depend linearly on δ. This assumption is very accurate, as the amount of vibrational modes scales with the amount of atoms in the unit cell. This is demonstrated below using data for different intermediate phases in the model system $SrFeO_{3-\delta}$.

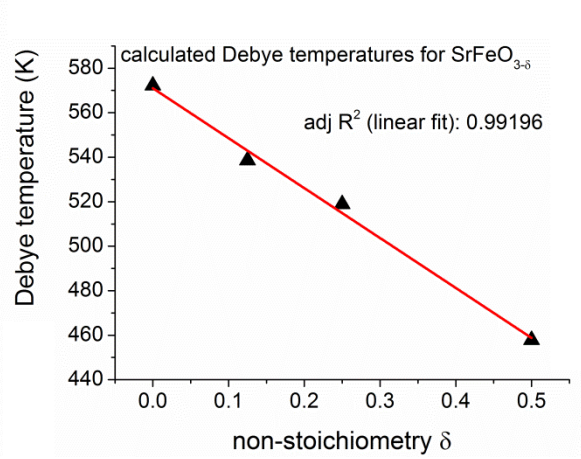

Fig. 2.9. Debye temperatures calculated for different $SrFeO_{3-\delta}$ phases based on elastic tensors from *Materials Project* and pymatgen. [126, 134] The linear fit shows a very good dependence of the Debye temperature on the non-stochiometry δ (see the adjusted R^2). Taken from the supporting information of Vieten *et al*. [95]

Using this linear correlation between the vibrational entropy and δ, the change in vibrational entropy does not depend on δ anymore as the derivative of the vibrational entropy vs. δ is zero:

$$\Delta s_{\mathrm{vib}} = 2 \cdot s_{\mathrm{vib},\delta}(T) \frac{\partial}{\partial \mathrm{T}} \frac{\partial}{\partial \delta} = 2 \cdot (s_{\mathrm{vib},\delta=0}(T) - s_{\mathrm{vib},\delta=0.5}(T)) \tag{2.27}$$

The factor 2 is owing to the fact that two mol of a perovskite with composition AMO_3 are required to release one mol of monatomic oxygen. It could be omitted if the entropy change would be given per mol of O_2 instead.

Finally, the change in configurational entropy (which describes the amount of possible locations in the lattice where the oxide vacancies can form) is calculated. Perovskites typically show lower changes in redox entropy than ceria, as only half of the cations in the lattice are involved in the reduction reaction, as opposed to all of the cations being involved in the case of ceria. This decreases the amount of possible locations of oxygen vacancies, and therefore decreases the configurational entropy change. Moreover, the electronic structure of cerium favors a high change in electronic entropy, which contributes to the configurational entropy. [135] Despite the typically higher entropy change of ceria, the thermodynamic properties of perovskites can be tuned much more accurately to match the specific application. Additionally, it could be possible to increase the change in entropy for perovskites by inducing additional disorder due to phase changes between different perovskite structures using tolerance factor engineering as described before, or by involving the A site species in the redox reaction.

For an ideal solid solution with two individual sub-lattices, the change in configurational entropy for the solid solution corresponds to the weighted sum of the entropy changes in each of the sub-lattices. In analogy to non-stoichiometric ceria, a so-called dilute species model can be used to describe the configurational entropy change of a perovskite in general: [129, 132]

$$\Delta s_{\mathrm{conf,general}} = 2 \cdot a \cdot R \cdot \left[\ln\left(\frac{1}{2} - \delta\right) - \ln \delta\right] \tag{2.28}$$

The factor of 2 is used in analogy to Eq. 2.27, and a is a dimensionless constant used to describe the vacancy ordering of the non-stoichiometric phase according to Bulfin *et al.* If a = 2, a random distribution of oxygen vacancies is assumed without any defect ordering. [129, 132] Using this dilute species model in with $\delta_{\mathrm{max},1} = act/2, \delta_{\mathrm{max},2} = (1 - act)/2, \delta_1 \geq \delta_2$, and Eq. 2.21 for $\delta_{\mathrm{n}}(T, p_{\mathrm{O_2}}, \Delta H_{\mathrm{n}})$ with $\mathrm{p_{O_2}}(\delta, \mathrm{dH_{min}}, \mathrm{dH_{max}}, \mathrm{T})$ derived using Eq. 2.22, one can determine the configurational entropy change in one sub-lattice: [129]

$$\Delta s_{\mathrm{conf,n}}(\delta, \delta_{\mathrm{n}}, T, \Delta H_{\mathrm{n}}) = \frac{1}{\delta_{\mathrm{max,n}}} \cdot \frac{\mathrm{a}}{2} \cdot \mathrm{R} \cdot \left[\ln\left(\delta_{\mathrm{max,n}} - \delta_{\mathrm{n}}(T, p_{\mathrm{O_2}}, \Delta H_{\mathrm{n}})\right) - \ln \delta_{\mathrm{n}}(T, p_{\mathrm{O_2}}, \Delta H_{\mathrm{n}})\right] \cdot \frac{\delta_n(T, p_{O_2}, \Delta H_n)}{\delta} \tag{2.29}$$

In this work, we assume a = 2, i.e., no oxygen vacancy ordering. In any case, the configurational entropy change of the perovskite solid solution is given by:

$$\Delta s_{\mathrm{conf}}(\delta, T) = \Delta s_{\mathrm{conf},1}(\delta, \delta_1, T, \Delta H_{\mathrm{min}}) + \Delta s_{\mathrm{conf},2}(\delta, \delta_2, T, \Delta H_{\mathrm{max}}) \tag{2.30}$$

As mentioned before, this is holds true assuming that the individual sub-lattices do not interact. This concludes the set of entropic contributions necessary to calculate the total entropy change according to Eq. 2.24. [95] This model is very accurate in terms of predicting the change in vibrational and partial molar entropy, and uses an approximation for the configurational entropy change assuming no interaction between the solid solution sub-lattices and no defect ordering. It is very challenging to predict the latter properties from first principles for any perovskite solid solution, and this is a subject of further studies as discussed in section 5. Moreover, second order phase transitions which may lead to a change in the vibrational properties are not accounted for. [136] By using the before-mentioned description of the entropic effects in perovskite solid solutions based on the partial molar entropy of oxygen, the vibrational entropy, and the configurational entropy, and by combining this theoretical data with a description of the redox enthalpy in dependence of the non-stoichiometry δ, the equilibrium state of perovskite solid solutions can be predicted. The types of graphs derivable from the thermodynamic data, such as isotherms and isobars, are listed in the appendix (section 8.5).

Kinetics

The reduction and oxidation kinetics in redox reactions are closely related to the reaction mechanism. While the detailed reaction mechanism of perovskite solid solutions may be complex, it consists of three principal steps:

1. **Diffusion of oxygen to/from the perovskite within the reaction medium**
   The area around the perovskite should be oxygen-depleted as soon as the perovskite is oxidized. It can be expected that a gradient in oxygen concentration exists within the reaction medium as long as the reaction is proceeding. Conversely, for the reduction reaction, the gradient is reversed and oxygen must diffuse away from the sample in order for the reaction to proceed. The oxygen gradient has been modelled very accurately by Lapp *et. al.* for ceria as a redox material. [137]
   In any case, the reaction cannot proceed faster than the rate at which oxygen can travel within the reaction medium. If this is the slowest of all processes involved, this step is referred to as the rate-limiting step. As an alternative to the free diffusion within a closed reactor, the oxygen movement can also be forced by using a sweep gas or pumps.

2. **Adsorption/desorption of oxygen on the perovskite's surface**
   At the interface between the perovskite and its environment, the oxygen is bound to the surface of the perovskite, or released from it in case of reduction. According to literature for other perovskites and similar oxides, the process of oxygen absorption and desorption on the surface is assumed to take place in the following steps: [138-140]

$$O_2\,(g) \leftrightarrow O_2^* \overset{+e^-}{\longleftrightarrow} O_2^{-*} \overset{+e^-}{\longleftrightarrow} O_2^{2-*} \leftrightarrow 2\,O^{-*} \overset{+2e^-}{\longleftrightarrow} 2\,O^{2-}\,(\text{lattice}) \tag{2.31}$$

Species marked with an asterisk are surface species. The uptake or release of electrons by the oxygen species corresponds to the oxidation or reduction of transition metal species in the perovskite. Apart from the species listed in Eq. 2.31, other oxygen-containing species may occur on the perovskite surface as well, such as OH^- or CO_3^{2-}. [140] The carbonate is ubiquitous on surfaces of alkali earth (and most likely also alkali) metal based perovskites, as these metals form very stable carbonates (such as $BaCO_3$, for instance). These carbonates may be detrimental for the long-term reversibility of these materials as oxygen carriers in thermochemical CO_2 splitting. [141] However, not all perovskites show carbonate formation to the same extent, and it may also be possible to remove carbonates from the surface to restore the redox activity of these species (see section 4.1).

3. Internal diffusion of oxide ions within the perovskite lattice

The oxide ions diffuse within the perovskite bulk to decrease local gradients in oxide ion concentration, and from the surface and surface-near regions to the bulk. Without this diffusion process, the perovskites could only be oxidized on the surface. [d] In the case of most perovskites, the diffusion rates of oxide ions through the lattice are considerably high. [142, 143] Moreover, diffusion rates may be anisotropic. [144] However, in the simplest case and considering cubic oxides, the oxide ion conductivity σ_O is exponentially proportional to the negative ratio of the activation energy for oxygen migration E_A and the thermal energy, where k_B is the Boltzmann constant: [143]

$$\sigma_O \sim \exp\left(-\frac{E_A}{k_B T}\right) \tag{2.32}$$

In the case of more complex structures such as orthorhombic perovskite oxides, the situation becomes more difficult to describe theoretically. Using methods of molecular dynamics (MD), the oxygen diffusion in these perovskites can be studied. [145] However, this is beyond the scope of this work and may be subject of future studies. The kinetic studies in this work are limited to measuring experimentally determined half-lives of the oxidation reaction for exemplary perovskites and drawing some conclusions from this data.

[d] In fact, this happens in the case of some other materials such as aluminum, which is only oxidized on the surface as diffusion rates for oxide ions in the oxide are very low. This effect is also known as passivation.

If either the adsorption/desorption or the internal diffusion of oxide ions are rate-limiting, the particle size should influence the reaction speed. Moreover, intrinsic factors such as the material composition and crystal structure also have an effect on diffusion and adsorption/desorption rates, but not on the diffusion within the reaction medium. Moreover, if other atoms besides oxygen are re-arranged during the redox reaction, the overall reaction rates are also dependent on the rate of diffusion of these atoms. Also, when comparing redox reactions of perovskites to redox reactions involving a phase change, it is worth noting that some oxides allow only very slow diffusion of oxygen within their lattice. For these reasons, perovskites and other non-stoichiometric oxides are some of the fastest-reacting oxides when it comes to thermochemical redox reactions. To distinguish regimes of different rate-limiting steps, one can plot an observable of the reaction, such as the reaction half-life, vs. $1/T$ (Arrhenius plot). Regions with different slopes indicate different diffusion activation energies, and therefore, different rate-limiting steps. By this means, these regimes can be distinguished qualitatively.

2.6 Energy analysis of thermochemical cycles

To choose an ideal redox material for a specific thermochemical process, it is necessary to determine the amount of energy necessary for each different material per redox cycle. The goal of this work is neither to give details on a specific reactor design, nor to develop an optimal reactor design for different thermochemical cycles. The interested reader is referred to existing studies on different reactor designs. [27, 146-158] Instead of using a specific reactor setup and limiting the applicability of the model to this design, a generic concept for the operation of the redox cycle is applied to all materials in order to compare them. By modifying properties such as the heat recovery efficiency or the pumping energy, different reactor concepts can be mimicked if those properties are known for these reactor types. By using this generic energetic analysis, we can define which material is the most suitable for an existing reactor under known conditions, but we cannot define which kind of reactor to use in the first place.

First, we start by defining the conditions for the reduction and oxidation reaction. The **reduction** reaction occurs at the temperature T_{red} and under the oxygen partial pressure p_{red}. It is assumed that a constant oxygen partial pressure is reached at the end of the reduction process, and that the material is in chemical equilibrium with its environment at this point. As the material releases oxygen upon reduction, the released oxygen must be continuously removed to maintain p_{red}. This can be performed either by using a pump or a sweep gas with low $p_{\mathrm{O_2}}$. To compare different redox materials, it does not matter which method is used as long as the amount of energy required for maintaining a constant partial pressure is known, but we specifically calculate the energy demand for pumps only.

The **oxidation** reaction occurs at the temperature T_{ox} and under the oxygen partial pressure p_{ox}. For water splitting and CO_2 splitting, there is no defined oxygen partial pressure, but a target ratio of H_2/H_2O or CO/CO_2 partial pressures shall be used instead. These product-educt pressure ratios can be directly converted to equivalent oxygen partial pressure values. The equivalent oxygen partial pressure is the p_{O_2} which would be reached in equilibrium without the presence of water or carbon dioxide as an oxidant. The equilibrium δ in the perovskite is the exact same – whether the oxidation is carried out under this equilibrium partial pressure in a gas mixture or under the presence of this oxidant does not matter for calculating this equilibrium. In fact, one could also describe solar-thermochemical water splitting as water dissociation at low oxygen partial pressures achieved using a thermochemical pump. For the calculation to be valid, it is assumed that the steam or CO_2 is oxygen-free, or at least contains oxygen in such small amounts that it does not contribute significantly to the oxidation reaction. This is usually implied in studies on thermochemical water or CO_2 splitting – otherwise the observed oxidation of the redox material would have to be attributed to the oxygen present in the oxidant stream instead of the splitting reaction. A good indicator as to whether this assumption is true is to compare the amount of hydrogen produced to the amount of oxygen released during reduction. If those differ significantly from the expected 2:1 ratio, it means that there must be another oxygen source apart from water or carbon dioxide molecules, which can have many reasons such as leakage, a contaminated oxidant stream, or irreversible redox reactions. Trustworthy and reputable studies therefore are never based only on measurements of the oxygen produced, but instead on the actual hydrogen or carbon monoxide production.

To calculate the equivalent oxygen partial pressure p_{eq} for splitting reactions, we first consider the equilibrium constants. For water, we have:

$$K_{eq,ws} = \exp\left(-\frac{\Delta G^0_{ws}(T)}{RT}\right) \tag{2.33}$$

$\Delta G^0_{ws}(T)$ refers to the formation enthalpy of water at the temperature T. It can be found in standard textbooks such as *Barin – Thermochemical Data of Pure Substances.* [159] To get a function of ΔG^0_{ws} of the temperature, the tabulated values in the range from 298.15 K to 2000 K are fitted linearly. [e] The resulting function is:

$$\Delta G^0_{ws}(T) = (-0.052489 \cdot \mathrm{T} + 245.039) \cdot 1000\ \mathrm{Jmol^{-1}} \tag{2.34}$$

[e] Dr. Nicole Knoblauch, Institute of Materials Research (DLR), personal communication (2018).

The equivalent oxygen partial pressure for the water splitting reaction as a function of the temperature and the partial pressure ratio between hydrogen and steam is then given as: [113, 160]

$$p_{\mathrm{eq,ws}}\left(T, \frac{p_{\mathrm{H_2}}}{p_{\mathrm{H_2O}}}\right) = \left(\frac{K_{\mathrm{eq,ws}}(T)}{\frac{p_{\mathrm{H_2}}}{p_{\mathrm{H_2O}}}}\right)^2 \tag{2.35}$$

This data is only valid for gaseous water (steam). Analogously, for CO_2 splitting we can define:

$$K_{\mathrm{eq,cs}} = \exp\left(-\frac{\Delta G^0_{\mathrm{cs}}(T)}{RT}\right) \tag{2.36}$$

$$p_{\mathrm{eq,cs}}\left(T, \frac{p_{\mathrm{CO}}}{p_{\mathrm{CO_2}}}\right) = \left(\frac{K_{\mathrm{eq.cs}}(T)}{\frac{p_{\mathrm{CO}}}{p_{\mathrm{CO_2}}}}\right)^2 \tag{2.37}$$

In this case, ΔG^0_{cs} is the Gibbs free energy change of the reaction

$$\mathrm{CO_2} \leftrightarrow \mathrm{CO} + \frac{1}{2}\mathrm{O_2} \tag{2.38}$$

It can be calculated from the Gibbs free energies of formation for CO_2 and CO (the Gibbs free energy of formation for O_2 is zero by definition):

$$\Delta G^0_{\mathrm{cs}}(T) = -\Delta G^0_{\mathrm{f\,CO_2}}(T) + \Delta G^0_{\mathrm{f\,CO}}(T) \tag{2.39}$$

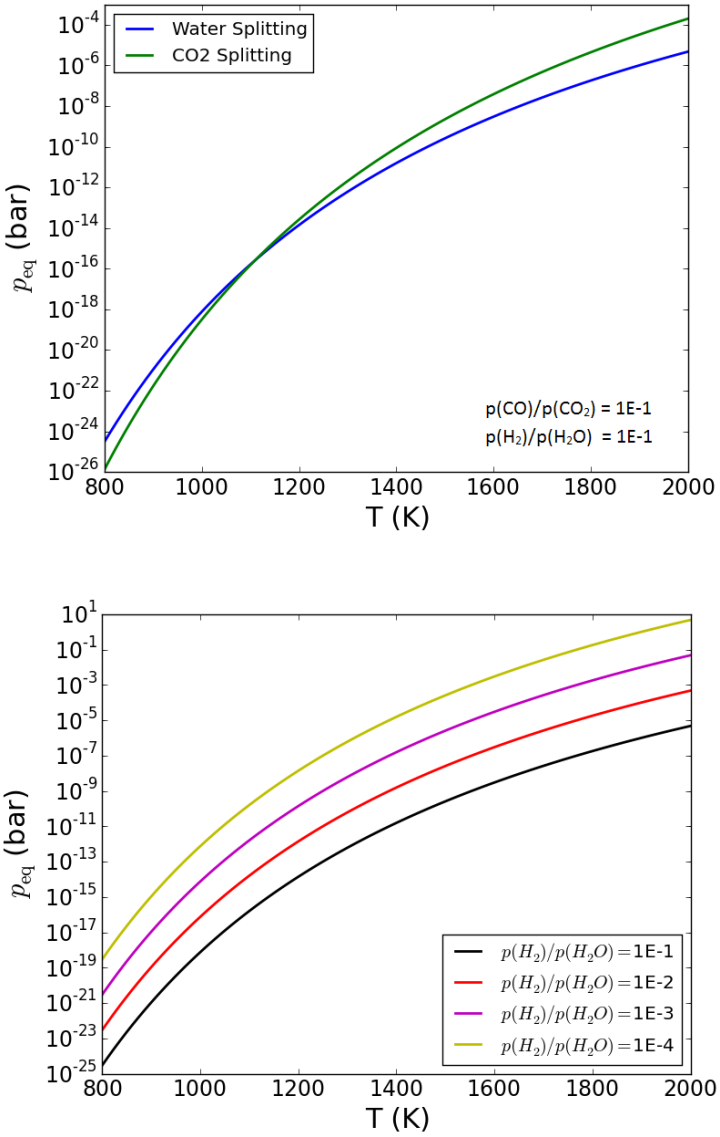

Fig. 2.10. Equivalent oxygen partial pressures for water and carbon dioxide splitting at a partial pressure ratio $p(H_2)/p(H_2O)$ of 0.1 (above) and for water splitting at different partial pressure ratios (below). The CO_2 splitting reaction is favored over the water splitting reaction at high temperatures.

The formation energies can again be taken from *Barin* at T = 298.15 – 2000 K using the following fit functions:

$$\Delta G^0_{f\,CO_2}(T) = (9.44 \cdot 10^{-7} \cdot T^2 - 0.0032113 \cdot T - 393.523) \cdot 1000\ \mathrm{Jmol^{-1}} \quad (2.40)$$

$$\Delta G^0_{f\,CO}(\mathrm{T}) = (-0.0876385 \cdot T - 111.908) \cdot 1000\ \mathrm{Jmol^{-1}} \quad (2.41)$$

Using this data and the before-mentioned equations, the equivalent oxygen partial pressures can be defined for different partial pressure ratios of product vs. educt (see Fig. 2.10). For the overall process, we consider only the usable energy at the material. This means that the reactor efficiency, the solar field efficiency, and heat losses due to re-radiation, conduction, and convection are not investigated. The only heat flow rate considered in our process scheme is the heat used by the thermochemical process itself, denoted by $\dot{Q}_{total}$. Losses have to be added to this value in order to get the heat flow of total thermal energy from concentrated solar power used ($\dot{Q}_{CSP}$). Under these assumptions, we can formulate an energy balance (see Fig. 2.11): [113]

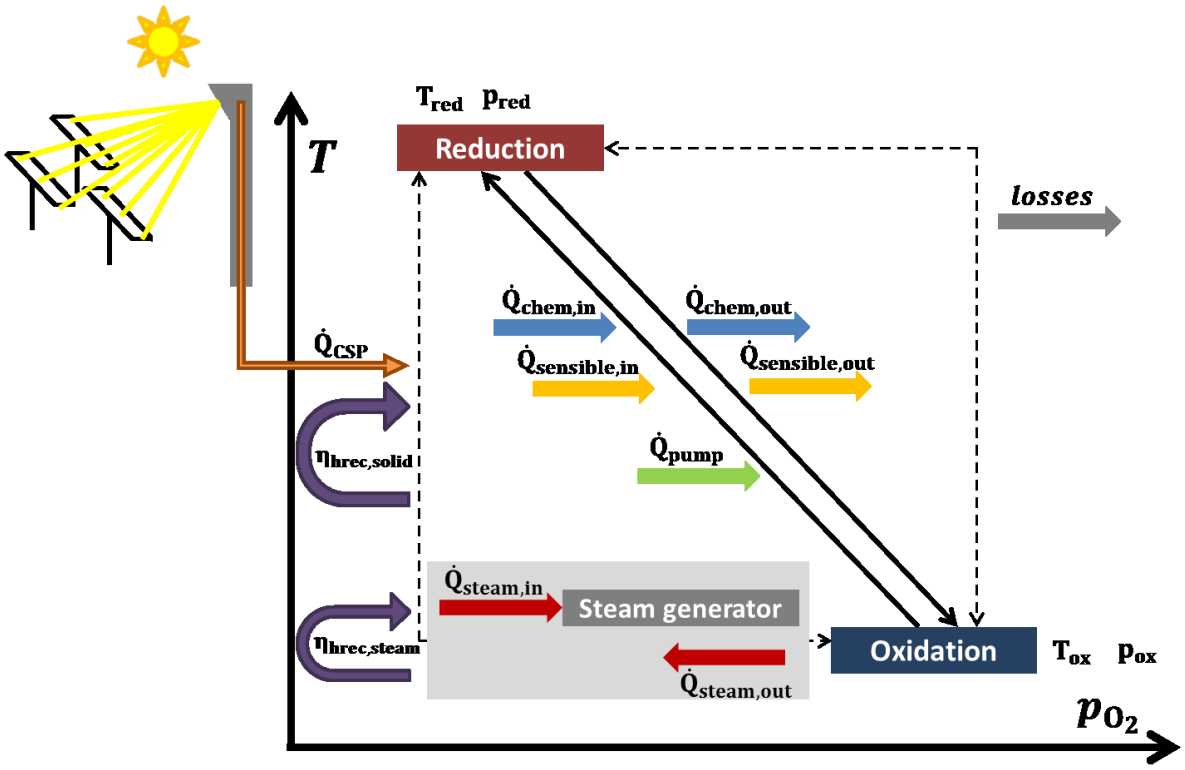

Fig. 2.11. Process scheme for the operation of a two-step thermochemical redox cycle. Solar energy is captured using heliostats and brought to a receiver in a solar tower, which transports heat into a cycle. The heat stream reaching the redox material is denoted by $\dot{Q}_{CSP}$. Chemical, sensible, and pumping energy penalties contribute to the total energy demand of the cycle, and part of the heat required for reduction can be restored during re-oxidation. Water splitting requires steam generation energy additionally. T and p_{O_2} are assumed to change gradually (solid arrows), but could also be changed one after another (dashed arrows). Taken from Vieten *et. al.* [113]

$$\dot{Q}_{\mathrm{CSP}} = \underbrace{\dot{Q}_{\mathrm{chem}} + \dot{Q}_{\mathrm{sensible}} + \dot{Q}_{\mathrm{pump}} \left(+\dot{Q}_{\mathrm{steam}}\right)}_{\dot{Q}_{\mathrm{total}}} + \mathrm{losses} \tag{2.42}$$

The pumping energy is not directly supplied as heat in the case of mechanical pumps, but usually as electrical energy, which can be generated from thermal energy via turbines and generators. All contributions to the total amount of energy according to Eq. 2.42 are addressed in the following. For the upcoming considerations, we use the amount of total energy required to drive the process instead of the heat flows, so the thermal energy Q instead of $\dot{Q}$. As mentioned before, thermal losses are not further considered, and we focus in the following on getting values for each of the contributions to Q_{total}.

The energy required to drive the chemical reaction is defined by the heat effect of the reaction, which is again defined by the redox enthalpy. It is referred to as **Chemical Energy** in the following, or Q_{chem}. The amount of energy which needs to be supplied during the **reduction** reaction to partially reduce the perovskite can be calculated as the integral of $\Delta H(\delta, T)$ over the change in non-stoichiometry and the change in temperature (compare Eq. 2.17): [113]

$$Q_{\mathrm{chem,red}} = \int_{\delta_{\mathrm{ox}}}^{\delta_{\mathrm{red}}} \Delta H(\delta, T)\, d\delta \tag{2.43}$$

In the case of non-stoichiometric phases the reduction reaction takes place over the entire temperature range, meaning that oxygen is released as soon as the temperature is larger than T_{ox}. This also implies that theoretically, the reduction reaction is already completed as soon as T_{red} and p_{red} are reached. In practice, it will take some time until the equilibrium is reached, but for all purposes in this section, it is irrelevant how long this takes, as we are considering the total energy required and not the heat flow rates. As the change in redox enthalpy is temperature-dependent, we must define how the redox cycle is operated in-between T_{ox} and T_{red}. The result of Eq. 2.43 is slightly different depending on whether

a) the pressure is first changed isothermally from p_{ox} to p_{red}, then the temperature is changed from T_{ox} to T_{red} (lower-left dashed arrow in Fig. 2.11), *or*

b) the reverse of (a), i.e. the temperature is changed from T_{ox} to T_{red}, the pressure is then changed from p_{ox} to p_{red} (upper-right dashed arrow in Fig. 2.11), *or*

c) both temperature and pressure are changed simultaneously (solid diagonal arrows in Fig. 2.11).

Within this work, only case (c) is considered as the thermal energy is supplied steadily in this case, instead of the intermittent heat supply necessary in cases (a) or (b). This should allow the most efficient use of the solar energy supplied by the solar field, which usually does not vary

significantly within these relatively short cycle times. To calculate Eq. 2.43 we assume a linear change of T and $ln(p_{O_2})$ and define sets of T and p_{O_2} between T_{ox}/p_{ox} and T_{red}/p_{red}. Using Eqn. 2.10, 2.23, and 2.24, one can find for which values of δ the Gibbs free energy is zero at each given set of T and p_{O_2}. The resulting δ can then be used along with the temperature T to calculate $\Delta H(\delta, T)$, which can then be integrated over $d\delta$.

The amount of **Chemical Energy** released during the **oxidation** reaction is equivalent to the chemical energy supplied during reduction in the case of air separation, as it is the exact reverse process. However, if the chemical energy is partially stored in a fuel, this fraction of the total energy is not released as heat. Therefore, the chemical energy released during the oxidation reaction is given as: [113]

$$Q_{\mathrm{chem,ox}} = -\left(\int_{\delta_{ox}}^{\delta_{red}} \Delta H(\delta, T)\, d\delta - \Delta H_{\mathrm{stored}}(T)\right) \tag{2.44}$$

Interestingly, this amount of energy does not depend on the redox entropy change, but ΔG does. Therefore, two materials with the same ΔH can show a different amount of oxygen release under the same reduction conditions, but require the same amount of chemical energy. Naturally, it is beneficial to choose the material with highest ΔS if two materials with equal ΔH are available to increase the overall process efficiency.

$\Delta H_{\mathrm{stored}}(T)$ refers to the redox enthalpy of water splitting (ws) or carbon dioxide splitting (cs) as a function of the temperature, and is zero for air separation. $\Delta H_{\mathrm{ws}}(T)$ is equal to the formation enthalpy of water. It can be calculated using the respective Shomate equation and the constants published in the NIST-JANAF thermochemical tables. [130, 131] As defined here, T changes linearly during the whole reduction process, so as a good approximation we can use $T = 0.5\,(T_{ox} + T_{red})$, i.e., we are using the mean temperature of the process. For carbon dioxide spitting, $\Delta H_{\mathrm{cs}}(T)$ can be calculated as the difference of the formation enthalpies of CO_2 and CO according to Hess's law. These formation enthalpies at the temperature T can again be found using the NIST-JANAF thermochemical tables and with T as the mean temperature of the process. The chemical energy released during oxidation can partially be used to drive the reduction reaction by using a heat exchanger. The transport medium can be the heated product gases as well as solid inert particles as heat exchange medium, [161, 162] or just adjacent reduction and oxidation chambers allowing heat transfer. The heat recovery efficiency (or heat recovery rate) of the transfer of chemical and/or latent heat from the oxidation to the reduction cycle is in the following denoted simply by $\eta_{\mathrm{hrec,solid}}$ to indicate that the heat originates from reactions of the solid redox material. It is important to note that the real heat recovery efficiency will depend

on the temperature, [163] but in our case we are using $\eta_{\mathrm{hrec,solid}}$ as an average value. According to literature data, $\eta_{\mathrm{hrec,solid}} = 0.6$ seems realistic, [163] but the real value has to be determined for each reactor concept individually. Taking into account heat recovery, the total chemical energy required to drive a full redox cycle per mol of redox material can be written as: [113]

$$Q_{\mathrm{chem}} = (1 - \eta_{\mathrm{hrec,solid}}) \cdot \int_{\delta_{\mathrm{ox}}}^{\delta_{\mathrm{red}}} \Delta H(\delta, T)\, d\delta \; - \; \Delta H_{\mathrm{stored}}(T) \qquad \eta_{\mathrm{hrec,solid}} = 0 \dots 1 \qquad (2.45)$$

As the heat recovery efficiency influences all materials to the same extent in our model, the relative differences between different materials are independent of $\eta_{\mathrm{hrec,solid}}$ – the heat recovery efficiency only affects the absolute amount of energy consumed by the redox cycle.

The amount of **Sensible Energy** refers to the material's specific heat capacity. Any material requires some energy to be heated from a lower to a higher temperature level, and it stores this amount of heat as long as it rests at this high temperature level (latent heat storage). The amount of sensible energy required is initially completely independent of the chemical energy, and would have to be supplied even if no chemical reaction occured. The heat capacity of perovskites may be determined using the Debye model. Second order phase transitions are ignored in this case, but the Debye model still offers a good method to get the heat capacities for a large amount of different phases without any further knowledge about these second order phase transitions such as magnetic order-disorder transitions. These transitions also often occur at temperatures below those relevant for thermochemical cycles. [136] As explained before in the section on the vibrational entropy, the Debye temperatures $\Theta_{\mathrm{D},\delta}$ of the involved materials are calculated based on DFT data using their elastic tensors. As we are using solid oxides only, we assume $C_{\mathrm{v}} = C_{\mathrm{p}}$ and only use the value C in the following to denote the heat capacity. With $y_\delta = T/\Theta_{\mathrm{D},\delta}$ and the ideal gas constant R, the heat capacity per mol of redox material can be calculated: [113, 133, 164]

$$C(y_\delta) \approx C_{\mathrm{v}}(y_\delta) = 9 \cdot R \cdot \; y_\delta^3 \cdot \int_0^{\frac{1}{y_\delta}} \frac{y_\delta^4 \cdot \; e^{y_\delta}}{(e^{y_\delta} - 1)^2}\; dy_\delta \; \cdot \; n_{\mathrm{a}} \qquad (2.46)$$

The amount of atoms per formula unit is represented by n_{a}. Although we are using large unit cells with up to 144 atoms, we normalize the composition to $AMO_{3-\delta}$, or, for solid solutions, $(A'_xA''_{1-x})^{(6-n)+}\left(M'_yM''_{1-y}\right)^{(n-2\delta)+}O_{3-\delta}$ with n = 3, 4, or 5 as explained before and $\delta = 0 - 0.5$. It follows that $n_a = 4.5 + \delta$. The Debye temperatures $\Theta_{\mathrm{D},\delta=0}$ and $\Theta_{\mathrm{D},\delta=0.5}$ can be determined indirectly via DFT from the elastic tensors as explained in section 2.5. At high temperatures ($T >> \Theta_{\mathrm{D},\delta}$), the heat capacity only depends on n_a. By using the Debye model, we

assume that all perovskites with the same crystal structure have the same amount of excitable phonon modes, and their composition only influences at which temperature which fraction of them is excited. As mentioned before, the Debye temperature as a function of the non-stoichiometry δ can be estimated accurately using a linear interpolation between $\delta = 0$ and $\delta = 0.5$. After substituting y_δ by $T/\Theta_{\mathrm{D},\delta}$, we can therefore use the following expression for the heat capacity as a function of the temperature T and the non-stoichiometry δ:

$$C(T,\delta) = C\left(T,\delta=0,\Theta_{\mathrm{D},\delta=0}\right)\cdot\frac{0.5-\delta}{0.5} + C\left(T,\delta=0.5,\Theta_{\mathrm{D},\delta=0.5}\right)\cdot\frac{\delta}{0.5} \tag{2.47}$$

The specific molar heat capacity as a function of temperature according to the Debye model is exemplarily shown in Fig. 2.12 for different intermediate phases from *Materials Project* in the $SrFeO_{3-\delta}$ phase space. The values are in good agreement with literature data, but second order phase transitions are not accounted for. [165]

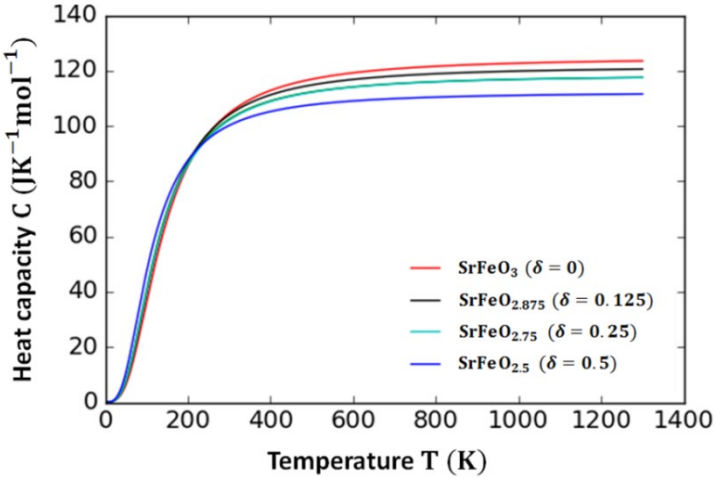

Fig. 2.12. Specific molar heat capacity of different $SrFeO_{3-\delta}$ phases according to the Debye model using Debye temperatures generated indirectly via DFT using elastic tensors as present in *Materials Project* database. Taken from Vieten *et. al.* (supporting information). [113]

The change in heat capacity between the fully oxidized and the fully reduced phase is rather small, and usually the perovskite is not even cyclized between $\delta = 0$ and $\delta = 0.5$, but the change in δ is smaller. As the change in δ is small, the total change in heat capacity can be approximated by assuming a linear correlation between δ and T. The specific molar heat capacity then only depends on T, δ_{ox}, and δ_{red}. The sensible heat input from the reduction reaction may be partially recovered during oxidation using solid-solid heat recovery, which lowers the total demand in sensible energy by a factor of $\eta_{\mathrm{hrec,solid}}$. Both the chemical and the sensible energy are recovered in the same process

step with the same method, so it is reasonable to couple the heat recovery efficiency for both contributions.

The demand in sensible energy per mol of redox material can then be determined by integration of the heat capacity over the temperature between T_{ox} and T_{red} : [113]

$$Q_{\mathrm{sensible}} = \int_{T_{\mathrm{ox}}}^{T_{\mathrm{red}}} C(T, \delta_{\mathrm{ox}}, \delta_{\mathrm{red}})\, dT \cdot (1 - \eta_{\mathrm{hrec,solid}}) \tag{2.48}$$

As mentioned before, the amount of sensible energy required *per mol of redox material* is completely independent of the chemical reaction. However, the amount of sensible energy *per mol of product gas* is not. As the molar amount of product gas (oxygen, hydrogen, carbon monoxide) produced depends on the change in the perovskite's non-stoichiometry between oxidation and reduction, the amount of sensible energy per mol of product gas will also depend on the change in non-stoichiometry under the conditions applied. Therefore, the sensible heat energy input per mol of product gas is indirectly dependent on the thermodynamic properties of the material. For perovskites, the sensible heat input often is even the largest fraction of all contributions to the total energy demand of the cycle seen per mol of product gas. This is owing to the fact that the amount of oxygen stored in one mol of perovskite is rather small compared to stoichiometric phase change redox reactions. For this reason, all perovskites showing a very small change in non-stoichiometry under given conditions are not a good option as a redox material, although the amount of chemical energy necessary for reduction may be low. The advantage of a low chemical energy input is more than compensated by the fact that a very large amount of material would be necessary to produce an appreciable amount of product gas, leading to a very large input in sensible energy.

Another contribution to the total energy demand of such redox cycles is the **Pumping Energy**. It is only relevant for the **reduction** step, and we assume that it cannot be recovered. The amount of pumping energy required strongly depends on the type of pump used and the individual setup of the whole process. Nevertheless, one can distinguish two primary types of pumps. Firstly, mechanical pumps are the state of the art pump used to create low oxygen (partial) pressures. The energy demand of these pumps per mol of gas pumped increases significantly with decreasing pressure of the gas. While each pump will have a different energy demand, it is possible to define an empirical envelope function using data for some mechanical pumps describing their lower limit in terms of energy demand. This has been done by Brendelberger *et al.*, and we rely on the data gathered by these authors in the following. [24] The envelope function is defined as follows and only valid in the

pressure range $10^{-6} < p_{\mathrm{red}} < 0.7$ bar, and the pressures are converted using $p_0 = 10^5$ and $p = p_{\mathrm{red}} \cdot p_0$: [24, f]

$$q_{\mathrm{iso}} = R \cdot T \cdot \ln(p_0/p) \tag{2.49}$$

$$\begin{aligned} eff = 0.30557 \; - \; 0.17808 \cdot \ln\left(\frac{p}{p_0}\right) \quad - 0.15514 \cdot \left[\ln\left(\frac{p}{p_0}\right)\right]^2 \\ - 0.03173 \cdot \left[\ln\left(\frac{p}{p_0}\right)\right]^3 - 0.00203 \cdot \left[\ln\left(\frac{p}{p_0}\right)\right]^4 \end{aligned} \tag{2.50}$$

$$q_{\mathrm{pump}}\left[\frac{\mathrm{kJ}}{\mathrm{mol_O}}\right] = \frac{q_{\mathrm{iso}}}{eff \cdot 0.4 \cdot 2000} \tag{2.51}$$

A temperature of T = 473 K is assumed as operating temperature of the pump (the temperature of the gas while it is pumped). *eff* is an empirical function for the efficiency of the pump and q_{iso} refers to the work of isothermal compression of an ideal gas. The factor 0.4 refers to an assumed conversion efficiency from thermal to electrical energy of 40 %, as the pumping energy is always considered as thermal energy in our case. [24] The factor 2000 is needed to convert J/$\mathrm{mol_{O2}}$ to kJ/$\mathrm{mol_O}$. The resulting value of Eq. 2.55 in kJ/$\mathrm{mol_O}$ is converted to kJ/mol of material by multiplying it with the amount of oxygen released per mol of redox material, which is known according to the non-stoichiometry change between oxidation and reduction. Please note that the pumping energy is not zero at ambient pressure, as pumping is required to remove the oxygen produced during the reduction reaction in order to maintain a constant oxygen partial pressure.

Another appealing option for maintaining a low oxygen partial pressure is thermochemical pumping. This idea is relatively new, and it may be promising for application at low oxygen partial pressures in water splitting or carbon dioxide splitting, as the energy demand per mol of oxygen pumped is significantly lower than when using a mechanical pump. [24, 166] The principle of such thermochemical pumps is based upon a second redox cycle with a material that is reduced at lower temperatures. This material serves as an oxygen absorber during the reduction process in the splitting cycle, and requires a lower amount of energy to be reduced than the material used for water or carbon dioxide splitting itself. Moreover, due to the direct use of heat in both cycles, no conversion losses in electricity generation occur, and by coupling both processes, the heat released in one process can partially be re-used in the other process. The potential of such thermochemical pumps can be roughly estimated by using constant redox enthalpies for some exemplary oxygen carrier materials based on DFT calculations in *Materials Project* ($SrFeO_3$: 84.6 kJ/$\mathrm{mol_O}$, $SrMnO_3$: 170.3 kJ/$\mathrm{mol_O}$, and

[f] Dr. Stefan Brendelberger, Institute of Solar Research (DLR), personal communication (2018).

$EuFeO_3$: 282.5 kJ/mol$_O$) and assuming a temperature-independent heat capacity of C_p = 120 J/molK (per mol of redox material). [116, 117, 165, 166] This means that the vibrational entropy change is zero, and the sensible energy demand is simply given by $C_p \cdot \Delta T$. Assuming no heat recovery, a dilute species model for the configurational entropy change, and using the Gibbs-Helmholtz equation (see section 2.5) to calculate the state of the chemical equilibrium, one can determine the amount of energy required to pump one mol of oxygen for different types of pumps (see Fig. 2.13).

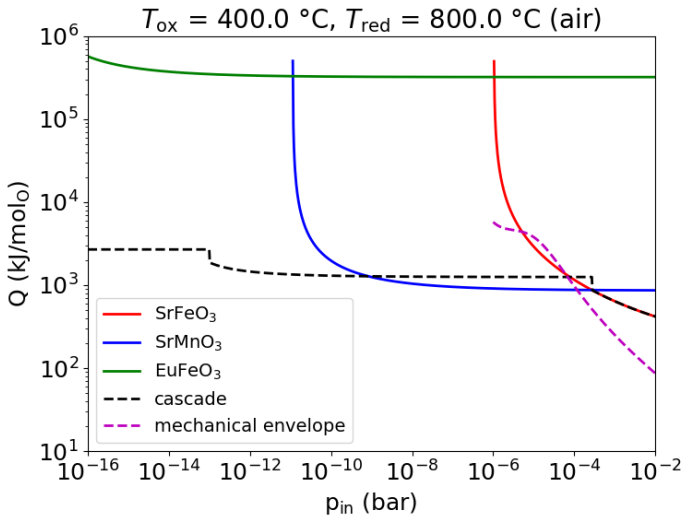

Fig. 2.13. Energy demand to pump one mol of oxygen for mechanical pumps (magenta, only defined at $10^{-6} < p_{red} < 0.7$) and thermochemical pumps based on different redox materials. The dashed black line refers to a cascade of reactors using all three materials. Thermochemical pumps are more efficient than the best mechanical pumps at pressures oxygen partial pressures below 10^{-4} – 10^{-5} bar. Adapted from Vieten *et. al.* [166]

The mechanical envelope function as previously defined describes the lower limit of energy demand of mechanical pumps, taking into account conversion losses from thermal to electrical energy. $SrFeO_3$ and $SrMnO_3$ appear to be ideal as redox materials for such applications, and the energy demand of a pump based on such materials is lower than the energy demand of mechanical pumps if the oxygen partial pressure is below 10^{-4} – 10^{-5} bar. Nevertheless, if δ comes close to 0.5 during reduction of these materials, a high amount of redox material would be needed to generate a significant amount of oxygen and the energy demand of pumping increases significantly. Due to its high redox enthalpy change, the reduction extent of $EuFeO_3$ is negligible in air, which leads to a very high energy demand per mol of oxygen. [166] However, if all three materials are combined in a cascade of reactors, each of them can be operated in the ideal pressure range. This means that $SrFeO_3$ is used to initially lower the oxygen partial pressure, and then $SrMnO_3$ further lowers the partial pressure level from there to the next lowest level, and so on. As mentioned before, the energy demand of thermochemical pumps is calculated without considering heat recovery in our brief estimation. Using solid-solid heat recovery, these pumps could be even more efficient. [166] In summary, thermochemical pumps seem to

be a viable option for vacuum pumping in thermochemical processes, and should be considered whenever reduction pressures in the sub-millibar range are required. Within this work, we do not consider the option of using a sweep gas to lower the oxygen partial pressure. It has been shown that sweep gas operation leads to even lower overall process efficiencies than mechanical vacuum pumping. [150] However, if the sweep gas is recovered using a redox material, the process could be calculated the same way as the thermochemical pump, with the added penalty of sweep gas pumping.

Only in the case of thermochemical water splitting, we need to consider a fourth contribution to the total energy demand of the redox cycle: The energy penalty of **Steam Generation**. The steam used as an oxidant needs to be pre-heated in order to maintain the oxidation temperature of the redox material. Moreover, water at ambient temperature first has to be evaporated to generate steam. The energy necessary for steam generation is reverse proportional to the target ratio of hydrogen vs. water. In other words, this means that if the steam is only converted to a small extent in the reactor, a large amount of steam needs to be generated in order to create a given amount of hydrogen. When considering the whole process efficiency, this contribution must not be neglected. Many materials apparently offer the possibility to save energy with respect to the state of the art as they can be reduced at lower temperatures or higher oxygen partial pressures, but at the expense of low conversion rates. It is difficult to reach a low steam generation energy demand and a low chemical, thermal, and pumping energy demand at the same time, therefore, the overall energy demand must be considered and minimized. The energy for steam generation can be directly supplied as thermal energy using state-of-the-art technology, as solar-thermal power plants rely on evaporating steam to drive turbines and generators.

To calculate the steam generation energy Q_{steam}, we start by defining the mean temperature of the oxidation process $T = 0.5\ (T_{\mathrm{ox}} + T_{\mathrm{red}})$. This is the temperature the steam needs to be heated to on average, which can be used as a good approximation, similar to the calculation of $\Delta H_{\mathrm{stored}}(T)$. Moreover, the water feed temperature T_{feed} is defined as a starting point. The heat capacities of liquid water ($C_{\mathrm{p,water}}$) and steam ($C_{\mathrm{p,steam}}$) are calculated by using the Shomate equations with constants from the NIST-JANAF thermochemical tables. [130, 131] The heat of vaporization ΔH_{vap} of water at 100 °C is 40.79 kJ/mol. [167] Please note that all values are considering water at ambient pressure. The steam generation energy can then be given as:

$$\mathrm{Q_{steam}}' = \left(\int_{\mathrm{T_{feed}}}^{373.15\ \mathrm{K}} \mathrm{C_{p,water}}\ \mathrm{dT} + \Delta \mathrm{H_{vap}} + \int_{373.15\ \mathrm{K}}^{0.5\ (\mathrm{T_{ox}}+\mathrm{T_{red}})} \mathrm{C_{p,steam}}\ \mathrm{dT} \right) \cdot (1 - \eta_{\mathrm{hrec,steam}}) \qquad (2.52)$$

If $\mathrm{T_{feed}} > 373.15$ K, Eq. 2.52 must be replaced by: [113]

$$Q_{\mathrm{steam}}{}' = \left(\int_{T_{\mathrm{feed}}}^{0.5\,(T_{\mathrm{ox}}+T_{\mathrm{red}})} C_{\mathrm{p,steam}}\, dT \right) \cdot (1 - \eta_{\mathrm{hrec,steam}}) \tag{2.53}$$

This energy demand is given per mol of water. To obtain the energy demand per mol of hydrogen produced, it needs to be divided by the target partial pressure ratio of hydrogen vs. water:

$$Q_{\mathrm{steam}} = \frac{Q'_{\mathrm{steam}}}{p(\mathrm{H_2})/p(\mathrm{H_2O})} \tag{2.54}$$

The resulting value can be converted to a value per mol of redox material using the non-stoichiometry change of the redox material. The energy demand can be lowered if the heat necessary to generate steam is (partially) recovered from the steam leaving the reactor. In this work, this heat recovery efficiency is denoted by $\eta_{\mathrm{hrec,steam}}$.

This concludes the contributions to the total energy demand of the redox cycle. On the previous pages, equations have been stated to calculate the energy demand per mol of redox material or per mol of product gas. For water splitting, one can also calculate the heat-to-fuel efficiency of the process, considering hydrogen as a fuel. This efficiency $\eta_{\mathrm{heat/fuel}}$ is given as the quotient of the heating value of hydrogen and total demand in thermal energy per mol of hydrogen as Q_{total} (consisting of the contributions mentioned before):

$$\eta_{\mathrm{heat/fuel}} = \frac{\mathrm{HHV}}{Q_{\mathrm{total}}} \tag{2.55}$$

For the heating value of hydrogen, we can use the higher heating value (HHV), considering that heat is regenerated from the product gases after combustion.[168] It is important to point out that this efficiency value is the upper limit for the efficiency of the real process, and does not correspond to the solar-to-fuel efficiency. This value is typically significantly lower than our calculated value, as the solar field efficiency, the receiver efficiency, and thermal losses are not further considered. Especially at the high temperatures necessary for thermochemical water splitting, these losses become substantial.

Besides the heat to fuel efficiency and the energy demand per mol of redox material, the total energy demand can also be given in other units. The conversion between those is given in Table 2.3. Using the theoretical description of the perovskite chemistry, the redox thermodynamics, and the energetics of redox cycles described in this chapter, new perovskite materials are prepared and

analyzed within this work. The experimental methods necessary to prepare these materials and gather experimental and theoretical data are summarized in the following chapter.

Table 2.3. Conversion of energy values in different units for analysis of different redox cycles. Taken from the supporting information of Vieten *et al.* [113]

	Air Separation	**Water Splitting**	**CO_2 Splitting**
kJ/mol of redox material	Q_{total}	Q_{total}	Q_{total}
kJ/kg of (oxidized) redox material	$\frac{Q_{\mathrm{total}} \cdot 1000 \frac{\mathrm{kg}}{\mathrm{g}}}{n_{\mathrm{ox}}\ (\mathrm{g/mol})}$	$\frac{\mathrm{Q_{total}} \cdot 1000 \frac{\mathrm{kg}}{\mathrm{g}}}{\mathrm{n_{ox}\ (g/mol)}}$	$\frac{Q_{\mathrm{total}} \cdot 1000 \frac{\mathrm{kg}}{\mathrm{g}}}{n_{\mathrm{ox}}\ (\mathrm{g/mol})}$
Wh/kg of (oxidized) redox material	$\frac{Q_{\mathrm{total}} \cdot 1000 \frac{\mathrm{kg}}{\mathrm{g}}}{n_{\mathrm{ox}} \cdot 3.6 \frac{\mathrm{kJ}}{\mathrm{Wh}}}$	$\frac{Q_{\mathrm{total}} \cdot 1000 \frac{\mathrm{kg}}{\mathrm{g}}}{n_{\mathrm{ox}} \cdot 3.6 \frac{\mathrm{kJ}}{\mathrm{Wh}}}$	$\frac{Q_{\mathrm{total}} \cdot 1000 \frac{\mathrm{kg}}{\mathrm{g}}}{n_{\mathrm{ox}} \cdot 3.6 \frac{\mathrm{kJ}}{\mathrm{Wh}}}$
kJ/mol of product	$\frac{Q_{\mathrm{total}}}{\delta_{\mathrm{red}}-\delta_{\mathrm{ox}}}$ (kJ/mol O)	$\frac{Q_{\mathrm{total}}}{\delta_{\mathrm{red}}-\delta_{\mathrm{ox}}}$ (kJ/mol H_2)	$\frac{Q_{\mathrm{total}}}{\delta_{\mathrm{red}}-\delta_{\mathrm{ox}}}$ (kJ/mol CO)
kJ/L of product (ideal gas at SATP)	$\frac{2 \cdot Q_{\mathrm{total}}}{(\delta_{\mathrm{red}}-\delta_{\mathrm{ox}}) \cdot 24.465 \frac{\mathrm{L}}{\mathrm{mol}}}$ (kJ/L O_2)	$\frac{Q_{\mathrm{total}}}{(\delta_{\mathrm{red}}-\delta_{\mathrm{ox}}) \cdot 24.465 \frac{\mathrm{L}}{\mathrm{mol}}}$ (kJ/L H_2)	$\frac{Q_{\mathrm{total}}}{(\delta_{\mathrm{red}}-\delta_{\mathrm{ox}}) \cdot 24.465 \frac{\mathrm{L}}{\mathrm{mol}}}$ (kJ/L CO)
Wh/L of product (ideal gas at SATP)	$\frac{2 \cdot Q_{\mathrm{total}}}{(\delta_{\mathrm{red}}-\delta_{\mathrm{ox}}) \cdot 24.465 \frac{\mathrm{L}}{\mathrm{mol}} \cdot 3.6 \frac{\mathrm{kJ}}{\mathrm{Wh}}}$ (Wh/L O_2)	$\frac{Q_{\mathrm{total}}}{(\delta_{\mathrm{red}}-\delta_{\mathrm{ox}}) \cdot 24.465 \frac{\mathrm{L}}{\mathrm{mol}} \cdot 3.6 \frac{\mathrm{kJ}}{\mathrm{Wh}}}$ (Wh/L H_2)	$\frac{Q_{\mathrm{total}}}{(\delta_{\mathrm{red}}-\delta_{\mathrm{ox}}) \cdot 24.465 \frac{\mathrm{L}}{\mathrm{mol}} \cdot 3.6 \frac{\mathrm{kJ}}{\mathrm{Wh}}}$ (Wh/L CO)

Abbreviations and Units in Table 2.3

Q_{total}: Energy in kJ/mol of redox material

δ_{ox}: Oxygen non-stoichiometry of the perovskite in the oxidized state

δ_{red}: Oxygen non-stoichiometry of the perovskite in the reduced state

$\delta_{\mathrm{red}} - \delta_{\mathrm{ox}} = \Delta\delta$ Change in oxygen non-stoichiometry during the redox cycle operation; can also be interpreted as $\mathrm{mol_O/mol_{redox\ material}}$

n_{ox}: Molar mass of the redox material in its oxidized state (at δ_{ox}) in g/mol

3. Methods and Materials

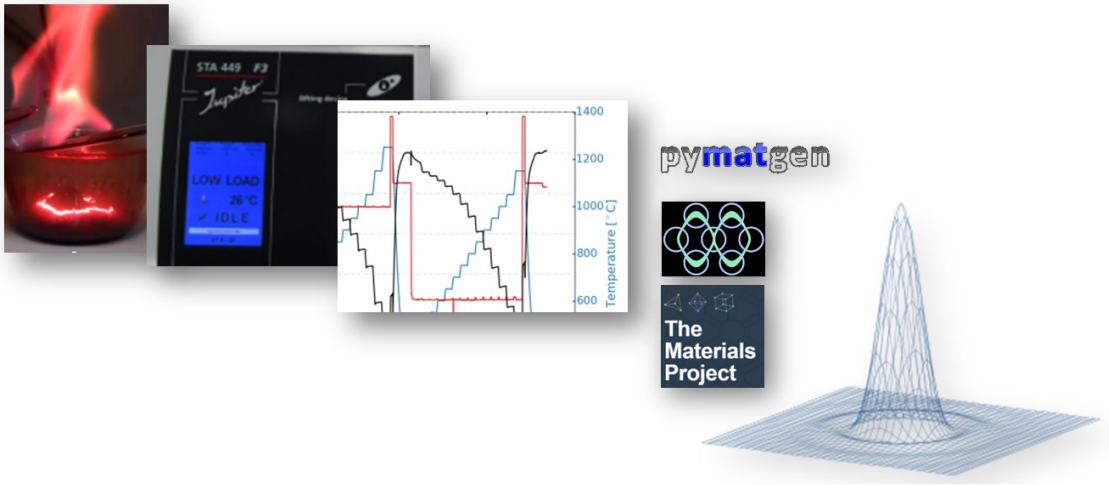

Fig. 3.1. Illustrative representation of some of the methods used within this work. Perovskites are synthesized via citric-acid autocombustion and their mass change is analyzed using thermogravimetry. Theoretical data is gathered via pymatgen and *Materials Project* using Computational Chemistry. Adapted from Vieten *et. al*. [169]

Perovskite solid solutions with different composition are synthesized and characterized within this work. Methods of characterization include thermogravimetry, X-Ray diffraction, and X-Ray spectroscopy. In parallel, theoretical data is gathered using *Materials Project*, *pymatgen* and density functional theory. The data is used for modelling in a custom python™ program, which can be used to predict the redox properties of over 200 perovskites under different conditions, and rank the materials by energy demand in different thermochemical processes. The methods used for experimental synthesis and computational chemistry are explained in this section. As the methods are generically applied for all samples with only minor composition-dependent changes, they allow screening a large set of different perovskite materials with different redox properties.

This chapter is partially based upon the following peer-reviewed publications authored and co-authored by the author of this work:

Vieten, J.; Bulfin, B.; Huck, P.; Horton, M.; Guban, D.; Zhu, L.; Youjun, L.; Persson, K.; Roeb, M.; Sattler, C., Materials design of perovskite solid solutions for thermochemical appplications, Energy & Environmental Science 2019, 12, 1369-1384.

Vieten, J.; Bulfin, B.; Senholdt, M.; Roeb, M.; Sattler, C.; Schmücker, M., Redox thermodynamics and phase composition in the system $SrFeO_{3-\delta}$-$SrMnO_{3-\delta}$. Solid State Ionics 2017, 308, 149-155.

Vieten, J.; Bulfin, B.; Starr, D.E.; Hariki, A.; de Groot, F.M.F.; Azarpira, A.; Zachäus, C.; Hävecker, M.; Skorupska, K.; Knoblauch, N.; Schmücker, M.; Roeb, M.; Sattler, C., Redox behavior of solid solutions in the $SrFe_{1-x}Cu_xO_{3-\delta}$ system for application in thermochemical oxygen storage and air separation. Energy Technology 2019, 7 (1), 131-139.

Vieten, J.; Bulfin, B.; Roeb, M.; Sattler, C., Citric acid auto-combustion synthesis of Ti-containing perovskites via aqueous precursors. Solid State Ionics 2018, 315, 92-97.

3.1 Synthesis of perovskite solid solutions

Perovskite solid solutions can be synthesized via different routes. It is possible to prepare many perovskites directly from binary oxides by just mixing these oxides and treating them at high temperature. This so-called ceramic method has proven to be very useful in many cases. [170, 171] However, the temperature necessary to get the target perovskite is composition-dependent, which makes it difficult to use one method for all perovskites in a large screening. Moreover, some perovskites cannot be produced via this method, such as Cu-doped $SrFeO_{3-\delta}$ or Ti-containing perovskites. [16, 172] Also, some perovskites require many intermediate powdering and re-heating steps in order to get a phase-pure substance using the ceramic method. [173] A better option is the use of precursors for the synthesis. One of the most well-known and versatile precursor-based methods for perovskite synthesis is known as the citric acid auto-combustion route or Pechini method, which is named after Maggio P. Pechini who introduced this wet-chemical synthesis route in 1966. [174-178] The different cations are supplied as aqueous solutions of metal nitrates mixed according to the target composition, and citric acid is added as a complexant and chelating agent. After evaporating most of the water from the solution, a gel forms, which spontaneously ignites at higher temperatures. The citrate ions therefore also act as a "fuel", which is oxidized at high temperature using the nitrates as oxidizers. The resulting metal oxide powder contains the metal ions as oxides in homogeneous dispersion, serving as an excellent precursor for the subsequent high temperature treatment. [172] This method is elaborated in the following, and consists of four principal steps (see Fig. 3.2).

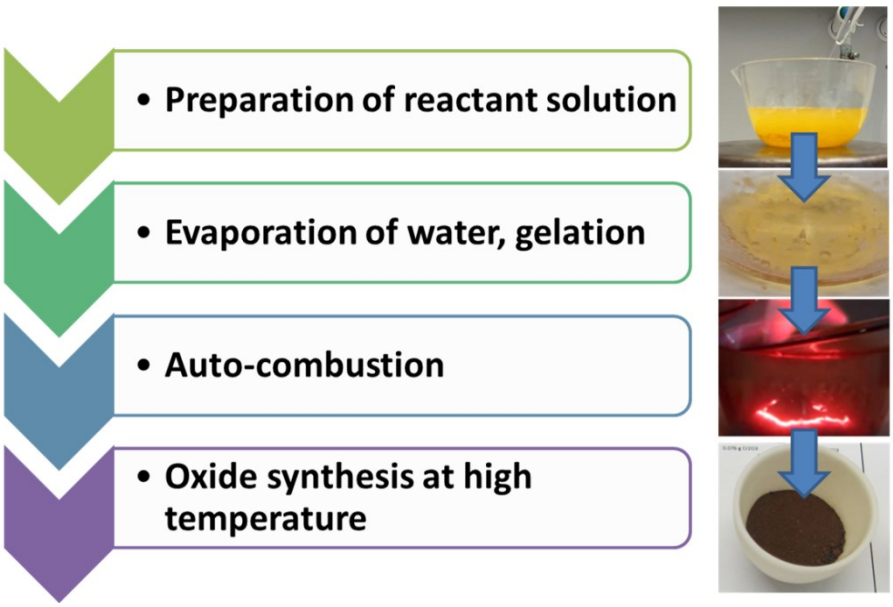

Fig. 3.2. Synthesis procedure for perovskites using a citric acid auto-combustion route. Adapted from publications by Vieten *et al.* [23, 172, 179]

1. Preparation of reactant solutions (aqueous metal citrate/nitrate mixtures)

To prepare perovskites using the citric acid auto-combustion route, metal nitrates are dissolved in water to yield 0.1 M solutions. The used starting materials are listed in the appendix (see section 8.1). Alternatively, metal species can be supplied as carbonates, which readily dissolve in an acidic environment at elevated temperature. This is done in case of the initial studies using Cu-doped $SrFeO_{3-\delta}$ complexes, where Sr has been supplied as $SrCO_3$ solution. After mixing the metal salt solutions in the stoichiometric ratios according to the intended perovskite composition, 4 mL of a 2.5 M citric acid solution are added (from anhydrous citric acid, 99 %, Merck). In any case, it is necessary that enough nitrate species are present as an oxidant, and the fuel (citric acid) is used in excess. The exact ratio between nitrate and citrate ions varies, but does not have an effect on the success of the synthesis in our case, as all precursor materials are treated at high temperature after citric acid auto-combustion. However, this ratio affects the reaction speed of the auto-ignition and the particle size of the resulting precursor oxides. [180]

For most of the metals used within this work, stable nitrates are available and can easily be dissolved in water. However, this is not the case for titanium. Chemically stable titanium nitrates do not exist, which makes it necessary to use different precursors. [181] The most common alternative is to use titanium alkylates such as titanium iso-propoxide. [182] However, these alkylates are very easily hydrolyzed in water, which would make it necessary to work in a non-aqueous medium. [172] Alternatively, titanium chloride or sulfide could be used as starting materials, but at the disadvantage of having to remove these ions in a second step. For instance, if chloride ions are not removed, these ions can be incorporated into the perovskite lattice on the oxygen sites and potentially alter the perovskite's properties. [172, 183] For this reason, a novel synthesis method has been developed as part of this work. It is based upon preparing the well-known peroxo-citrate complex of titanium via dissolution of titanium species in alkaline hydrogen peroxide. [184] For a residue-free product, ammonia is used to alkalize the solution. However, the previously-known methods involve the dissolution of titanium in this mixture, which is either very slow if titanium is supplied as granules or as a coarse powder, or the reaction has to be performed under protective gas to avoid self-ignition of fine pyrophoric titanium powder. However, it has been found that titanium(II)-oxide dissolves readily in a mixture of hydrogen peroxide and ammonia at moderate temperatures. [172] For this purpose, an aqueous mixture of hydrogen peroxide and ammonia in the volume ratio of 3:1 is prepared and titanium(II)-oxide (99.5 %, Alfa Aeasar, -325 Mesh powder) is added slowly in the amount according to the intended perovskite composition. Typically, 30 mL of 30 % H_2O_2 (30 %, Merck, stabilized) are mixed with 10 mL of 28-30 % NH_3 (reagent grade, 28-30 %, Merck) in a large beaker to account for the strong gas evolution and foam generation. For perovskites with high titanium content, it may be necessary to use a larger amount of this mixture to completely dissolve all of the titanium(II)-oxide. The beaker should have at least 10 times more volume than the solution

before the titanium(II)-oxide is added. Moreover, it is useful to partially close the beaker with a lid. After adding the titanium monoxide while stirring, the solution is slowly heated until the hydrogen peroxide notably decomposes, which is indicated by vigorous gas evolution (see Fig. 3.3) and a color change to bright yellow showing the formation of the titanium peroxo complex. [185] Heating is then suspended, and the gas evolution stops after a few minutes. If not all the titanium(II)-oxide is dissolved at this point, the previous steps are repeated by adding more of the hydrogen peroxide/ammonia mixture. After dissolving all of the metal oxide, 4 mL of a 2.5 M citric acid solution (from anhydrous citric acid, 99 %, Merck) are added while the solution is still hot, which leads to a color change from bright to dark yellow/orange, most likely indicating the formation of the (ammonium) titanium peroxo complex. [172, 184, 186] The other metals are then added as nitrate solutions as explained above.

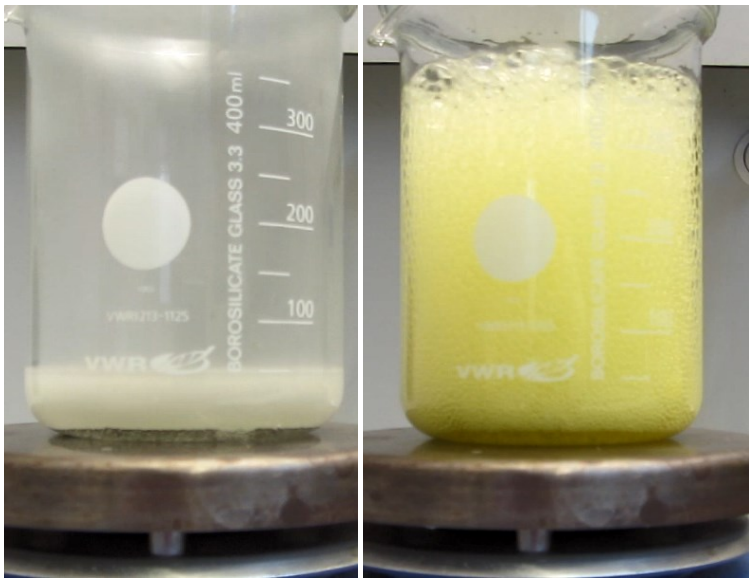

Fig. 3.3. Left: Titanium(II)-oxide (grey powder on the bottom of the beaker) is added to a mixture of hydrogen peroxide and ammonia in the volumetric ratio 3:1. Right: At elevated temperature, the hydrogen peroxide partially decomposes under vigorous gas evolution while forming a yellow titanium peroxo complex.

2. Evaporation of water/gelation

The citric acid in the solution enables the formation of chelating metal complexes, which are present in aqueous solution. [177, 187] Most of the water from these solutions is then removed by evaporation of the reaction mixture in an open glass beaker under continuous stirring. When almost all of the water is removed, the viscosity of the mixture increases significantly and a gel forms. For this reason, this

protocol is also characterized as a so-called so-gel synthesis method. This gel contains the metal nitrates as large polymer-like agglomerates interlinked by chelating citric acid ions.

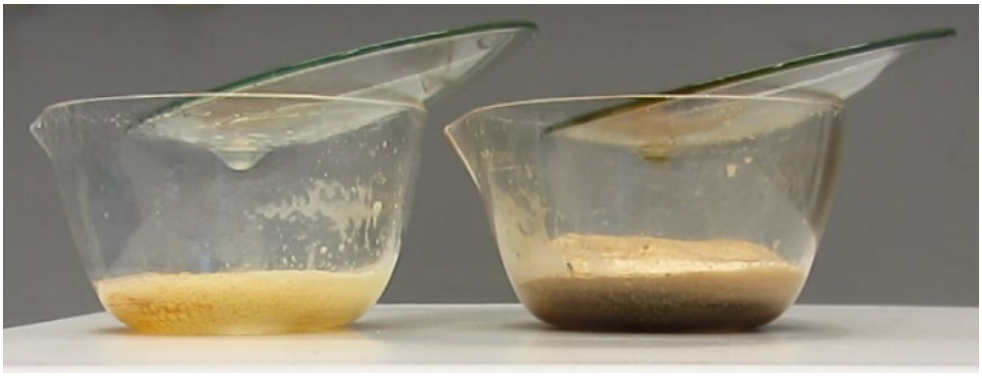

Fig. 3.4. Partially closed reaction vessels with expanding and decomposing gel. In the left beaker, the gel is still containing a large amount of water and in the liquid state, whereas on the right side the gel is already dried completely and forms a foamy solid.

3. Auto-combustion

As soon as the gel is formed, the stirring bar is removed from the mixture, and the reaction vessel is partially closed with a lid (see Fig. 3.4). Partial closure of the reaction vessel has proven to be the optimal compromise between a too vigorous reaction in air with some of the fine powder being ejected from the beaker, and a too slow reaction under isolation from the air. [23, 172, 179] The reaction mixture is then transferred on an IKA C-MAG HP 10 hot plate (according to the manufacturer the maximum temperature of this hot plate is 500 °C), and further heated. The temperature is first increased to 130-200 °C in steps of 10-20 °C within one minute, then to 300 °C after 3-5 min (according to the thermostat setting). After 2 min, the thermostat is set to 500 °C, which leads to a temperature of 400 °C in the center of the hot plate and 200-300 °C in the reaction mixture (pyrometer readings). [172] The gel decomposes at elevated temperature under volume expansion, releasing nitrogen oxides and decomposition products of the citrate ions. [172, 188] The expansion of the gel depends on its composition. Ultimately, at 200-300 °C, the gel ignites in a spontaneous auto-combustion reaction, in some cases accompanied by a flame of burning organic matter, sometimes in a less vigorous reaction with a glowing reaction front traveling through the reaction mixture within some seconds (see Fig. 3.5). After auto-combustion, an oxide powder remains, showing a dark brown to black color. The powder is then pestled to yield a uniform fine mixture.

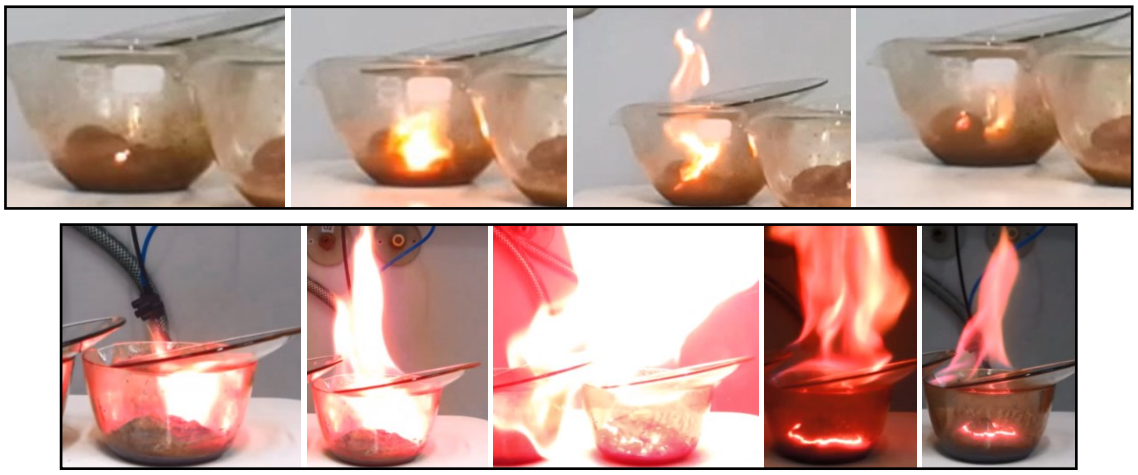

Fig. 3.5. Citric acid auto-combustion reaction to create perovskite precursors. Top row, from left to right: Reaction of a Calcium strontium iron cobalt oxide mixture. Bottom row, from left to right: Reaction of a strontium iron oxide mixture. The intensity of the reaction and its speed depend on the composition of the reactive mixture. All images are still frames extracted from a video and cover a time span of < 5 s. The video used for the lower row has previously been published as supplementary material in Vieten *et. al.* [23]

4. Oxide synthesis at high temperature

The fine oxide powder remaining from auto-combustion is transferred into alumina crucibles. Afterwards, the samples are treated at high temperature in a muffle furnace (Carbolite® RHF 14/35). The crucibles are kept open, as synthesis is performed in ambient air. The furnace is initially heated to 800 °C, and this temperature is maintained for 10 h. An initial heating rate of only 2 K/min is chosen to slowly decompose potentially remaining carbonaceous species without causing vigorous reactions. After the treatment at 800 °C, the furnace is turned off for 4 h (reaching 300-400 °C at the end of this period [172]), and then re-heated to 800 °C at 5 K/min. This temperature is again maintained for 10 h, and the furnace is turned off for 4 h. As the final step, the samples are heated to 1300 °C at 5 K/min, and this temperature is maintained for 20 h. The samples are then cooled down to ambient temperature at 5 K/min or less (natural cooling at low temperature, as the furnace is not actively cooled). The synthesis program is summarized in Fig. 3.6. The temperature steps are chosen to allow optimal solid-solid diffusion during the reaction. The reaction temperature in a solid state chemical reaction should be chosen at around 2/3 of the melting point of the lowest-melting reactant (in our case manganese oxides). [172, 189] Therefore, the first two steps are chosen to be at 800 °C. The final step is at about 2/3 of the typical melting temperature of perovskites and is chosen to allow crystal growth, which should yield a purer and more crystalline product. This upper temperature step is selected according to reports in the literature. [190] Due to the relatively low melting point of cobalt-

containing ferrites, the final step has to be modified to 1100 °C for those samples. Apart from that, all perovskites are synthesized using the same temperature program.

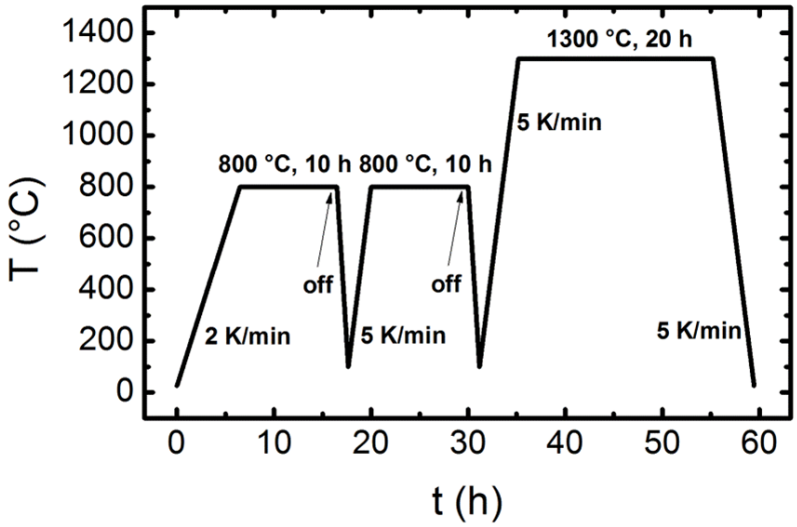

Fig. 3.6. High temperature synthesis program for perovskite phases. The maximum temperature in the third step is changed to 1100 °C for Co-containing samples. Taken from Vieten *et al.* [23, 172, 179]

This concludes the set of steps necessary for perovskite synthesis using the citric acid auto-combustion route. For comparison, solid state routes are applied as well. An attempt is made to synthesize $CaTi_{0.6}Mn_{0.4}O_3$ using a combination of the ceramic method and the citric acid auto-combustion method. Citric acid auto-combustion is carried out as mentioned above, but without a titanium source. Before the powder resulting from auto-combustion is treated at high temperature in the furnace, the stoichiometric amount of titanium(IV)-oxide powder (99.995 %, Alfa Aesar Puratronic, -22 Mesh) is added and thoroughly mixed with the precursor oxide powder in a mortar. [172] The high temperature synthesis is then carried out using the same steps as mentioned before.

The perovskites synthesized include mostly solid solutions in the $n = 3$ system (see section 2.3) with tolerance factors of t = 0.995 (tolerance factor of $CaMnO_3$ as a reference), 1.006 (reference: $SrFeO_3$), and 1.015, in order to study the effect of tolerance factor variations. All synthesized perovskites are listed in the appendix (see section 8.2).

3.2 Phase analysis

The composition of the prepared oxides is studied using standard methods of solid state analytical chemistry. With the help of X-Ray diffraction (XRD), the crystal structure of the samples can be studied using the diffraction of X-Rays on the lattice planes causing angle-dependent interference patterns. X-Ray diffractometers by Siemens (model D-5000) and Bruker (model D8 Advance) are used to study the diffractograms of polycrystalline powdered samples placed on Si single crystals. Both devices are equipped with X-Ray tubes producing Cu-K_α radiation. The Siemens diffractometer is applied to scan samples in a 2ϑ-range from 10° to 90° in steps of 0.02° with 6 s exposure time per step. Due to the relatively long measurement times, it is only used to study individual samples within the initial tests of this work, and for the studies on perovskite phase transitions. In contrast, the Bruker diffractometer allows faster measurements due to its area detector, and is therefore used for materials screening with shorter exposure times (2 s) and larger step sizes (0.05°), and for the tests using Cu-doped $SrFeO_{3-\delta}$ (2.5 s exposure, 0.03° step size to achieve higher resolution). [16, 172] *In-situ* X-Ray diffraction experiments are carried out in atmospheric air at temperatures between 400 and 1200 °C in steps of 40 °C using a high temperature chamber HTK 1200N by Anton Paar and the D8 Advance diffractometer using a Göbel mirror. The phase composition is studied using the ICDD PDF-2 database in combination with Bruker Diffrac.Suite™, where the $K_{\alpha 2}$ signal and the background are removed electronically. Subsequently, the lattice parameters of some of the samples with high quality XRD data are refined according to the Rietveld method with the help of reference cif files from the Crystallography Open Database (COD) for known perovskite phases and using the software MAUD. [179, 191-193]

Furthermore, the composition of some samples is investigated using energy-dispersive X-Ray spectroscopy (EDX). Powdered samples are coated with Pt for 15-30 s to increase their surface electronic conductivity using Ar-sputtering. The samples are then placed in a Zeiss Ultra-55 SEM microscope equipped with an Oxford INCA® X-Ray detector, [16, 23] where the energy of the photons emitted by the sample is measured. This energy is characteristic of the composition at the area of the sample irradiated by the electron beam, and by scanning over the sample, maps of the distribution of elements over the sample can be drawn. However, the surface morphology may lead to some errors. For some more detailed studies, samples are not used as powders but as annealed pellets, which are prepared using a hydraulic press, treated at 1300 °C for 10h in a muffle furnace, and then are cleaved, polished, and coated with Pt using sputtering as explained before. [16]

3.3 *In-situ* X-Ray photoelectron spectroscopy (XPS) and X-Ray absorption spectroscopy (XAS)

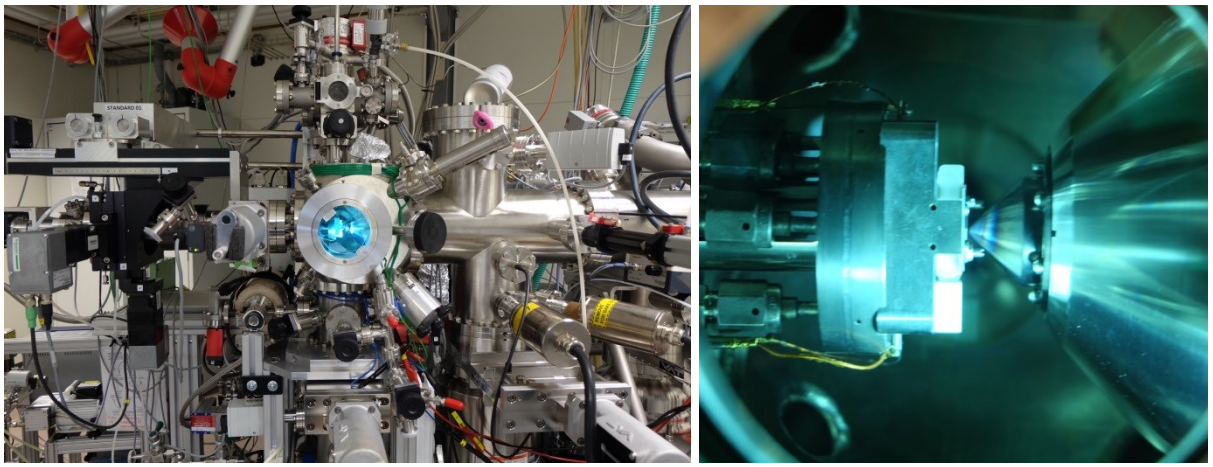

Fig. 3.7. *In-situ* synchrotron XPS/XAS setup. The X-Ray beam is inserted from the right side through a nozzle. The chamber (close-up view on the right) contains the sample in the center heated via a tantalum back sheet and an infrared laser from the back (left). [194] Images: B. Bulfin. [132]

The redox reaction is studied *in-situ* using X-Ray photoelectron spectroscopy (XPS) and X-Ray absorption spectroscopy (XAS). XPS is based on the interaction of X-Ray photons with the electrons in the material, which leads to the excitation of electronic states and their subsequent relaxation under the release of photoelectrons with characteristic energies. XAS has a similar working principle, but is based upon the absorption of X-Rays by the sample due to electronic excitation. Whereas XPS uses secondary radiation emitted by the sample, XAS is based upon measuring the intensity of the primary radiation weakened by the sample to create absorption spectra. Due to their different electronic energy and occupation of energy bands, different chemical elements can be distinguished using X-Rays interacting with the samples both in XPS and XAS. Moreover, different oxidation states of the same element can be distinguished in the same way. Due to the subtle differences in electronic structure in these cases, and to allow detecting elements in small concentrations, all these measurements are carried out using synchrotron radiation. The ISISS beamline at the HZB (Helmholtz-Zentrum Berlin) synchrotron source BESSY II is used, as it allows studying the samples under redox conditions using pure oxygen atmospheres with total pressures of up to 1.0 mbar (see Fig. 3.7). [16, 132, 194] Due to the considerably high operation pressure compared to vacuum XPS/XAS, this setup is also referred to as near-ambient pressure XPS/XAS (NAP-XPS, NAP-XAS). The samples are studied as compressed pellets prepared using a hydraulic press without further treatment. The sample holders and the setup are described in the literature in further detail. [195] To study the materials properties at elevated temperature, the samples are irradiated using an infrared laser,

reaching temperatures of up to 700 °C. This temperature is significantly lower than the maximum temperature achievable in the thermobalance, but the rather low oxygen partial pressures in the XPS setup nevertheless allow reduction to a substantial extent. The temperature is monitored using a pyrometer and a type K thermocouple in contact with the sample. XAS data is measured as total electron yield (TEY) and calibrated using the mirror currents. To check for beam damage, the O 1*s* XPS signal is monitored. In the case of XPS measurements on $Ca_{0.8}Sr_{0.2}MnO_{3-\delta}$ samples, the photon energies are calibrated using the Ca 2*p* XPS signals and their respective second order peaks. In the case of $SrFe_{1-x}Cu_xO_{3-\delta}$ samples, the Sr 2*p* XPS signal is monitored instead to check for systematic variations and errors. [16, 132] The spectra are analyzed using the software XPSPeak 4.1 and SpecsLab Prodigy. A Shirley-type background is subtracted in the case of XPS, and the peaks are fit using symmetric functions of mixed Lorentzian and Gaussian type (80 % Lorentzian). [16]

3.4 Extraction of thermodynamic data *via* the van't Hoff method using thermogravimetric experiments

The central method used for analysis of the redox behavior of perovskites within this work is thermogravimetry. The mass change of perovskites is monitored in dependence of the temperature and oxygen partial pressure, and as this mass change is induced by the release or uptake of oxygen in the samples, measuring the change in mass allows determining the change in non-stoichiometry of the perovskites. The relationship between the mass change in g (Δm) and the change in non-stoichiometry $\Delta\delta$ is given as: [92]

$$\Delta\delta = \frac{\Delta m}{M_{\mathrm{O}}} \cdot \frac{M_{\mathrm{P}}}{m_{\mathrm{s}}} \tag{3.1}$$

M_{O} refers to the molar mass of oxygen, M_{P} is the molar mass of the perovskite, and m_s is the initial mass of the sample. Thermogravimetric analysis is performed using a thermobalance by Netzsch, model STA 449 F3 Jupiter using a silicon carbide furnace. The balance is continuously kept at constant temperature with water to maintain a temperature of the weight measurement device of 27.0 °C. The oxygen partial pressure is monitored using an integrated oxygen pump/sensor system containing a lambda probe. The system is manufactured by SETNAG, and also allows small changes in the oxygen concentration by using an oxygen pump based on a ceramic membrane. By changing gas flow rates using mass flow controllers, the oxygen partial pressure can be regulated in a range of $\sim 10^{-4}$ to 0.9 bar. Ar (Linde, grade 5.0), synthetic air (Linde, 80:20 mol% mixture of N_2 and O_2), and

O_2 (Linde, grade 4.5) are used as purge gases, and the Ar is also used as a protective gas. Ceramic sample holders covered with Pt foil are used. The samples are placed onto these sample holders as powders in an amount of ~ 100 – 300 mg. The maximum oxygen partial pressure which can be measured by the lambda probe is 0.25 bar. Some measurements are carried out at 0.9 bar, and in these cases, the oxygen partial pressure used for further analysis is calculated using the flow rate ratios of the gases. [92] All measurements of redox thermodynamics are intended to be carried out in equilibrium, meaning that Δm is zero if ΔT and Δp_{O_2} are zero. In some cases, especially at low p_{O_2}, the state of constant mass is reached only slowly, as it takes some time until the target oxygen partial pressure is reached. For this reason, the sample is over-heated for a short period of time (70 K above the intended temperature level) to reach the equilibrium state faster. [92, 132] Further analysis is performed using a standardized method and a python script developed for this purpose. [g]

Different programs with different T and p_{O_2} steps are used to analyze different samples with different redox enthalpy. The steps are set to cover a large range of $\Delta\delta$ according to the expected ΔH of the perovskites. All measurements using different measurement programs typically take about 30-40 h in total. In all cases, an empty measurement (same configuration but with empty sample holder) is subtracted first to account for systematic errors induced by the sample holder itself and its different buoyancies in different gases (see Fig. 3.8). [23]

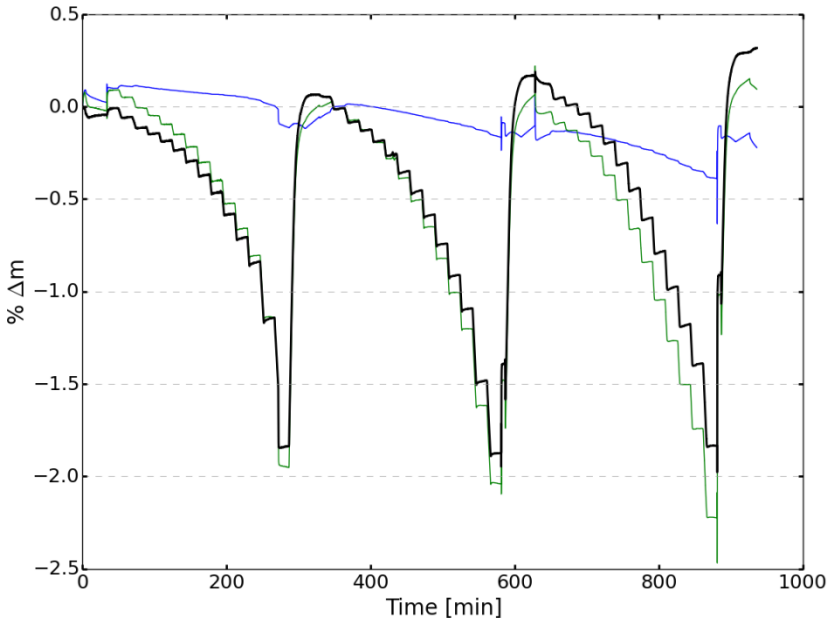

Fig. 3.8. Raw data from thermogravimetric analysis of a perovskite sample, mass change in % vs. time in minutes. Green: original data, blue: empty measurement, black: corrected data.

[g] Scripts for thermogravimetric analysis developed by Dr. Brendan Bulfin, currently ETH Zurich, and partially adapted by the author of this work.

All measurement programs contain steps at p_{O_2} = 0.18 bar and T = 400 °C. These data points are used as a reference and as the zero point of the data, i.e., $\Delta\delta$ is defined as zero at these points. In Fig. 3.8 it can be seen that the maxima of the data drift to higher values with each cycle. This is attributed to a systematic error of the thermobalance, which shows a near-linear drift of the mass change values over some hours, which can be positive or negative in different magnitudes. The drift appears to be dependent on the time of the day and may therefore be attributed to temperature or pressure changes in the room. Long-term measurements with over 40 redox cycles using perovskites in the same thermobalance show that this drift is not induced by irreversible reactions of the samples, as the mass change between two fixed temperature points at constant oxygen partial pressure remains constant over all these cycles.[179] Therefore, this drift is corrected using the before-mentioned reference points (see Fig. 3.9).

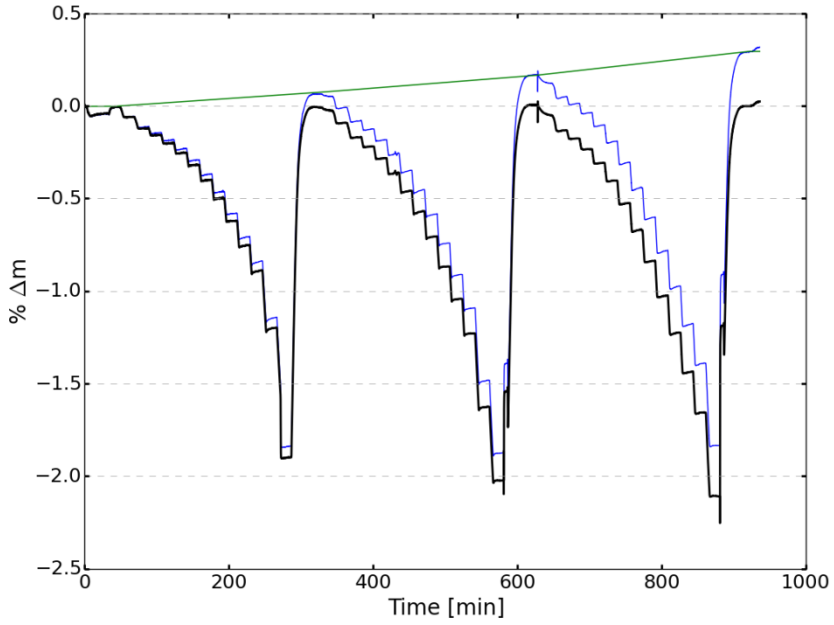

Fig. 3.9. Drift correction of the thermogravimetric data using fixed reference points at T = 400 °C and p_{O_2} = 0.18 bar. Blue: data before correction, green: correction curve, black: corrected data.

The resulting data including the oxygen partial pressure values (see Fig. 3.10) is then used to extract sets of Δm, p_{O_2}, and T at the equilibrium points. The mass change is converted to $\Delta\delta$ using Eq. 3.1 and the p_{O_2} values are adapted for p_{O_2} > 0.25 bar, as mentioned before. Please note that the pressure data contains some spikes induced by the lambda probe which are not considered for extraction of the equilibrium data.

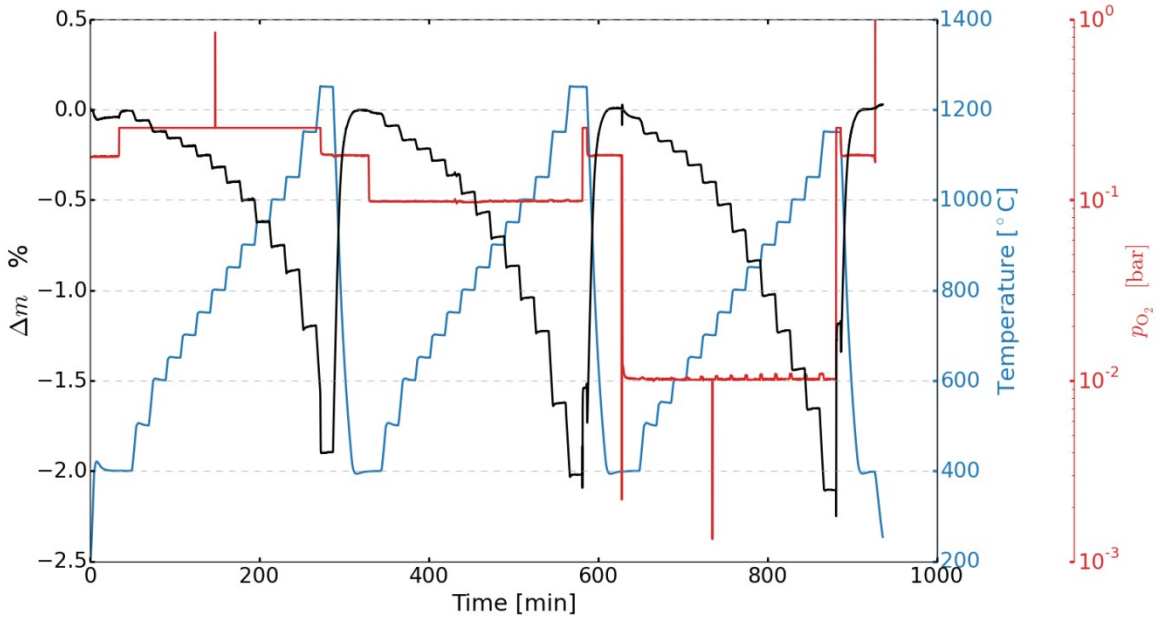

Fig. 3.10. Processed mass change data extracted from a thermogravimetric measurement containing temperature and oxygen partial pressure values. The mass change values are extracted at the equilibrium points with constant temperature and oxygen partial pressure.

These datasets are then used to create plots of p_{O_2} vs. $\Delta\delta$ at constant temperature (see Fig. 3.11). Between the measured data points a linear interpolation is used. Parallels to the x-axis represent values with constant $\Delta\delta$. The experimental datasets contain a large amount of different $\Delta\delta$ values. Going through this data, a new parallel to the x-axis is drawn for each set of consecutive $\Delta\delta$ values at the mean value of the two. Let's assume we are looking at two experimental values $\Delta\delta_1$ = 0.10 and $\Delta\delta_2$ = 0.12. The line is then drawn at $\Delta\delta$ = 0.11. This procedure is repeated for every set of consecutive $\Delta\delta$ values. By using this method, the amount of parallels to the x-axis is proportional to the density of the experimental data. Additionally, for the systematic materials screening of perovskite solid solutions these parallels are only drawn under the condition that they intercept the experimental data at least at five points (and at least at three points in the initial studies).[92] The intercepts of these lines with the experimental data are then used to generate correlated datasets of $\Delta\delta$, T, and p_{O_2}. Therefore, a set of at least five (or three in case of the initial studies) T-p_{O_2} pairs exists for each value of $\Delta\delta$. This means that the redox state denoted by a certain value $\Delta\delta$, i.e. $\Delta\delta = 0.11$ in our example, can be reached under five different conditions – it is possible to use a low temperature level and a low oxygen partial pressure, or a high temperature level at higher oxygen partial pressure – or some values in-between resulting in the same ΔG.

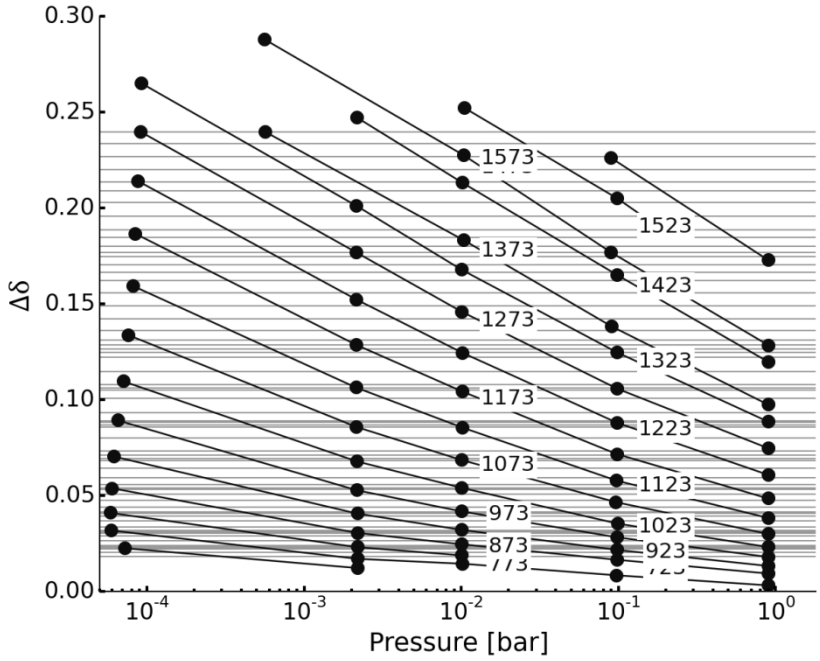

Fig. 3.11. Plot of experimental data points (solid circles) vs. the change in non-stoichiometry $\Delta\delta$ and the oxygen partial pressure p_{O_2} at different temperatures T (in K). The parallels to the x-axis at constant $\Delta\delta$ are used to extract $T - p_{O_2}$ datasets with the same $\Delta\delta$, which are defined as the intercept of these parallels of constant $\Delta\delta$ with the experimental data.

When plotting each dataset at constant $\Delta\delta$ in a diagram of -1000/RT vs. 0.5 p_{O_2} (see Fig. 3.12), one can use a version of the Gibbs-Helmholtz equation to extract the thermodynamic properties of the material, assuming $\Delta G = 0$ in equilibrium. This procedure is referred to as the van't Hoff method. [31, 92, 129, 132, 196] At constant $\Delta\delta$, the enthalpy change ΔH and entropy change ΔS per mol of oxygen O are given as (compare Eq. 2.12): [92]

$$\frac{1}{2}\ln\left(\frac{p_{O_2}}{p^0}\right) = -\frac{\Delta H}{RT} + \frac{\Delta S}{R} \qquad \Delta\delta = \text{const.} \tag{3.2}$$

In the van't Hoff plot (see Fig. 3.12) each dataset of constant $\Delta\delta$ values is then fit linearly. The confidence intervals of these fits are determined using the square roots of the covariance matrices to determine the experimental measurement errors. [95] Using Eq. 3.2., we can extract a value for ΔH for each value $\Delta\delta$, which can be calculated from the slope of the respective linear fit, and ΔS at each value $\Delta\delta$ is dependent on the y-intercept of these fits. Fig. 3.13 shows an exemplary plot of the so-extracted values for $\Delta H(\Delta\delta)$ and $\Delta S(\Delta\delta)$ per mol of oxygen.

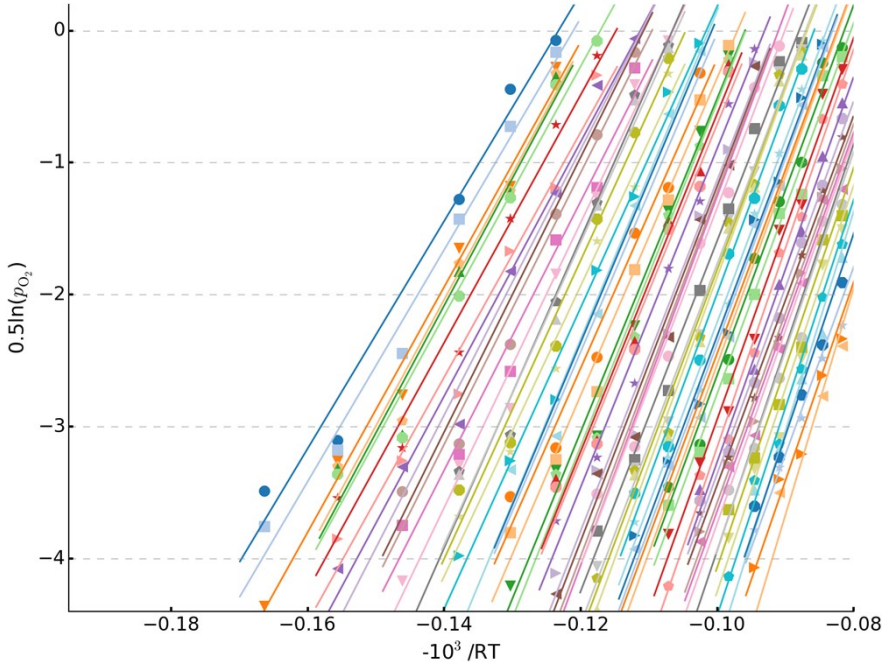

Fig. 3.12. Van't Hoff plot to extract thermodynamic data from thermogravimetric measurements. Each color represents a different $\Delta\delta$ value, and each point of the same color is defined as the intercept with of a parallel with constant $\Delta\delta$ with the experimental data. The linear fits are then used to determine ΔH and ΔS at this $\Delta\delta$ value using Eq. 3.2.

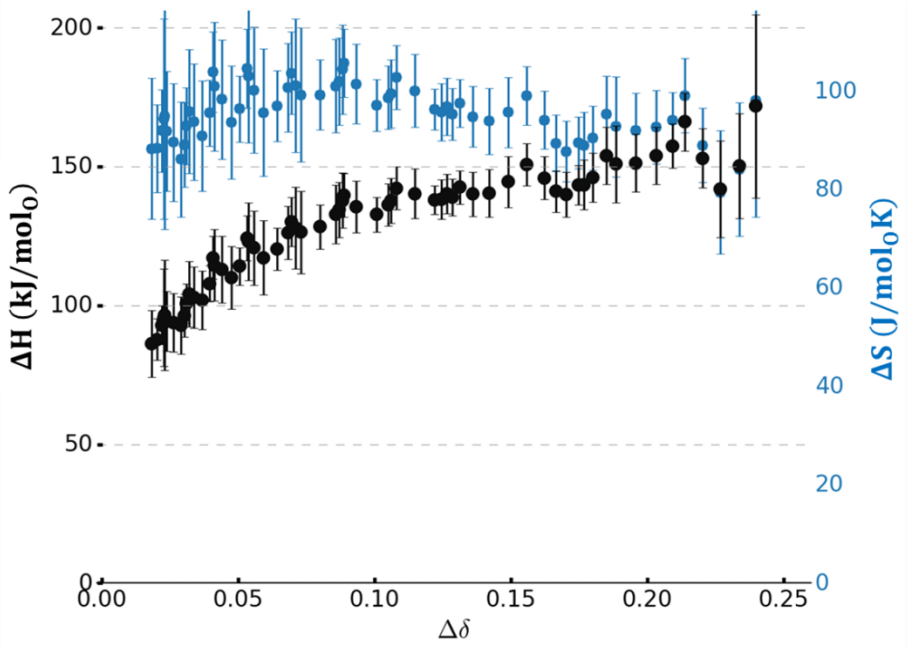

Fig. 3.13. Data points for $\Delta H(\delta)$ and $\Delta S(\delta)$ extracted from the van't Hoff plot. The measurement uncertanties are given using the covariance matrices of the linear fits in the van't Hoff plot.

Please note that although the thermodynamic properties are temperature-dependent, this temperature dependence is not considered when extracting data through this method. The temperature dependence can only be extracted if multiple measurements are carried out within small temperature windows at many different oxygen partial pressure levels, and this measurement is then repeated in as many different temperature windows as possible. However, this would increase the time necessary to characterize one material from days to weeks, which is counteracting the idea of a fast materials screening. Moreover, we only get thermodynamic data as a function of $\Delta\delta$ relative to a pre-defined reference point where $\Delta\delta = 0$. For most applications, this is the most relevant value, as only the absolute amount of oxygen released is of interest to the user. However, to get the absolute δ describing the amount of vacancies in the lattice, one has to determine the absolute δ value at $\Delta\delta = 0$. This value is derived either by using literature data or from the entropy as shown in chapter 5.1. In addition to that, it is also necessary to consider that by measuring thermodynamic data experimentally, the enthalpy and entropy can be interlocked and never be measured completely independent from each other. This well-known effect is referred to as enthalpy-entropy compensation in the literature.[197] Although there are some limitations when extracting thermodynamic data using the van't Hoff-method, which are also further discussed in the following chapters, this method is still very useful to characterize redox materials and to get experimental data defining the chemical equilibrium in these perovskite samples.

3.5 Thermogravimetric kinetic studies

Using the same thermobalance and setup as described before, the samples can also be studied in terms of their redox kinetics. As chemical reactions typically proceed faster at higher temperatures, the oxidation reaction is usually slower than the reduction reaction. To measure composition-dependent oxidation kinetics such as in the case of $SrFe_{1-x}Cu_xO_{3-\delta}$ solid solutions, 260.0 mg of the powdered samples are placed onto the sample holders. The samples are first heated to 860 °C under pure argon, and then cooled down to different oxidation temperatures.[16] The maximum heating and cooling rates of the setup (50 K/min) are applied to minimize re-oxidation effects before the measurement. As soon as the samples have reached the oxidation temperature, oxygen gas is added to reach an oxygen partial pressure of 0.9 bar and allow quick re-oxidation (total gas flow rate: 100 mL/min). The mass change is observed, and the progress of the reaction over time is monitored. The oxidation extent of the samples is denoted by α, and $\alpha = 0$ refers to the samples before re-oxidation, whereas $\alpha = 1$ is the limiting value describing a fully re-oxidized sample. The reaction half-life can be determined by finding at which time $\alpha = 0.5$. By comparing the reaction half-lives at different re-oxidation temperatures and for different samples, composition-dependent differences in

the reaction speed can be shown, and different regimes with different rate-limiting steps can be distinguished.

Reduction kinetics can be determined by using an opposite process where the samples are heated to the reduction temperature under a high oxygen partial pressure, and the atmosphere is then switched to argon. However, only very slow reactions can be measured in this way, and other methods have been developed to study the reduction kinetics of faster reactions.[198] However, the thermogravimetric method is used in this work to verify that the reaction is faster than what can be measured in the thermobalance, which means that it is fast enough for all solar-thermochemical applications.

3.6 Calculations and computational chemistry

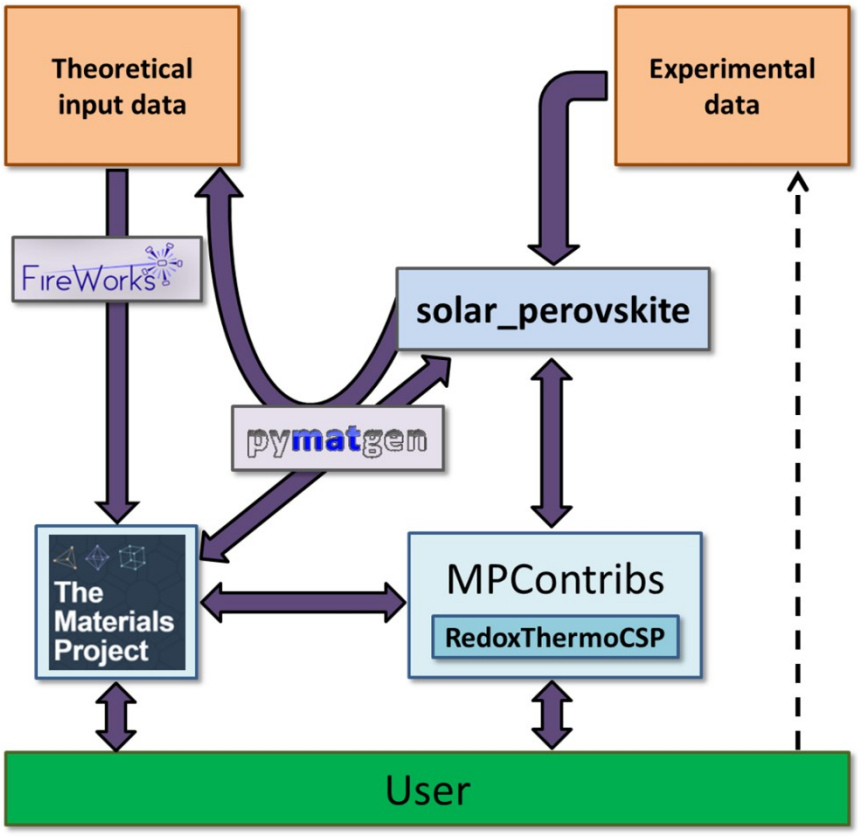

Fig. 3.14. Scheme describing the interaction between the users and the data with the help of *Materials Project* and its user contribution portal *MPContribs*. The data contributed within this work is collected in the *RedoxThermoCSP* contribution, which is based upon a custom python program called "solar_perovskite". The experimental data is evaluated and fit using this program, and the theoretical data previously contributed to *Materials Project* through *FireWorks* is retrieved with the help of *pymatgen*. Taken from Vieten *et. al.*[113]

Within a large scale materials screening, both theoretical and experimental data are made available to the public (see Fig. 3.14). The contributed theoretical materials data is available through www.materialsproject.org and the experimental and theoretical thermodynamic data is integrated through the interface for user contributions *MPContribs*. Data can be used free of charge after registration. All calculations as described in sections 2, 5, and 6 are carried out in a custom python library referred to as "solar_perovskite". The scripts are written in python 3.5, but compatible with python 2k. Part of the "solar_perovskite" code is used in the *RedoxThermoCSP* package, which is one of the user contributions within *MPContribs*. The data in *RedoxThermoCSP* is presented on interactive html pages using javascript, which are interacting with the python code in the background using Django.

Contribution of theoretical data

The theoretical dataset consists of DFT calculations. As a starting point of these calculations, data on the perovskite and brownmillerite superstructures is prepared using *pymatgen*. Pymatgen is an open-source python software library for materials analysis with an interface to Materials Project. [126] The initial cif (crystallographic information) files are retrieved from the Crystallography Open Database. [192] As explained in section 2.4, the crystal structures of $SrFeO_3$ (space group 221, $Pm\bar{3}m$) and $Sr_2Fe_2O_5$ (space group 46, Ima2) are expanded with pymatgen using a 2x2x2 scaling matrix to obtain a supercell. The ions in these supercells are then replaced by other species according to the intended perovskite compositions without partial occupancies (stoichiometries rounded to multiples of 1/8). The perovskite compositions are generated so they reach tolerance factor values of stable perovskites as explained in section 2.3. For n = 3, a tolerance factor of t = 0.945 is used to obtain a stable orthorhombic structure, as the rather small ionic radii of the lanthanides do not allow the formation of cubic perovskites with most transition metal species. In the case of n = 4, t = 1.000 is defined to form cubic structures, but to match the theoretical data with different experimental datasets ans to study the effect of tolerance factor variations, t = 0.995, 1.006, and 1.015 are used as well. For n = 5, t = 1.015 is used to account for the rather large ionic radius of most alkali metal species. Additionally, ternary perovskites with just one metal species on both sites are screened irrespective of their tolerance factors in order to gather DFT data on solid solution endmembers. A list of the over 240 perovskite-brownmillerite pairs studied theoretically is included in the appendix (section 8.3), and the corresponding materials are available through the DOI 10.17188/1475589. [199]

The so-generated structures are ordered by minimizing their Ewald sum using the pymatgen function "OrderDisorderedStructureTransformation" with the setting algo = 2 ("best first" due to large unit cell size, see the pymatgen online documentation; www.pymatgen.org). By preparing these supercell structures as starting points, the composition, occupancy, and initial cell parameters of the new phases are defined, which is necessary as a starting point for the DFT calculations. These structures are then submitted to *Materials Project* using a workflow generated with *FireWorks* in the framework of *atomate*. [200, 201] The development of this workflow is not part of this work, as it is used for most DFT calculations in the framwork of *Materials Project* and not changed for this specific contribution. This work is limited to providing the input structures and using the resulting DFT data, especially the ground state energies, crystal structures, and elastic tensors. The workflow contains the DFT calculations using the well-known *VASP* environment and combines GGA and GGA + U calculations, as explained before. [117, 202, 203] Within this workflow, the new structures are automatically added to Materials Project database, as long as they are not duplicates of existing entries. *Materials Project* is a repository of data on inorganic materials with currently over 80000 different materials and their crystal structures, and this work contributes some new calculations of perovskite solid solutions based on their superstructures.

Using the theoretical data

Using the so-called *MPRester*, a part of *pymatgen*, the contributed data is retrieved from Materials Project. With *pymatgen.analysis.reaction_calculator*, the redox enthalpies for a complete reduction from perovskite to brownmillerite under the release of oxygen are calculated according to the ground state energies of the involved species. The solar_perovskite code searches *Materials Project* using the *MPRester* based on the composition of this perovskite, and if more than one entry exists with the same composition, it uses the most stable of these entries. For oxygen as a reaction product, the most stable entry for biatomic oxygen (O_2) is used. Thermodynamically, O_8 would be slightly more stable than O_2, but it is only stable at very low temperatures, and therefore not considered. [117, 181] Please note that the result of these DFT calculations always yields energies for a temperature of 0 K.

The reaction enthalpies retrieved by this means are saved in an internal database, and the values for ΔH_{min} and ΔH_{max} are calculated as explained in section 2.4 in order to calculate $\Delta H(\delta, T)$. Together with the theoretical redox entropy change $\Delta S(\delta, T)$, the equilibrium thermodynamics can be calculated for any of the perovskite solid solutions at any temperature and oxygen partial pressure. This data is used to prepare *Isographs* as explained in section 8.5, and to perform an energy analysis as explained in section 2.6. The user is able to define the conditions of any specific redox cycle and plot graphs showing the resulting equilibrium state and ranking the materials by energy demand. In order to decrease the response time of this online calculation, the values for ΔH_{min}, ΔH_{max}, ΔH_{DFT} (redox enthalpy for complete reduction), and the Debye temperatures are saved in a database and not calculated again each time a user requests data.

For the energy analysis section, the thermal energy required to carry out the chemical reaction (Chemical Energy) and the sensible energy are calculated and saved for over 10000 pre-defined parameter sets consisting of different values of p_{ox}, p_{red}, T_{ox}, and T_{red}, as well as for different processes (Air Separation, Water Splitting, and CO_2 Splitting). This is further explained in sections 5.3 and 6.1 of this work. These fixed values for the oxidation and reduction conditions are chosen so they match the most likely reaction conditions of interest for the user. The integrals for the energy analysis are solved by approximating the change from p_{ox} and T_{ox} to p_{red} and T_{red} by splitting the range between T_{ox} / p_{ox} and $T_{\mathrm{red}}/p_{\mathrm{red}}$ into 20 equidistant sections and calculate the resulting $\Delta H(\delta, T)$ and $C(\delta, T)$ only once for each of these sections using the average temperature and pressure between these steps. The integration can then be performed by calculating the sum of the areas under each of these sections. This allows accelerating the calculation without decreasing the accuracy of the results notably (which has been verified by using different amounts of intermediate steps). This data is then loaded from the database and the energy demand of the process is calculated according to the user inputs for the heat recovery efficiencies (and the water

feed temperature in case of Water Splitting). Moreover, the Pumping Energy and Steam Generation energy are calculated live according to the user inputs. Using pre-calculated data, the response time to generate a full energy analysis of all perovskites included in this work is decreased from several min to ~ 1 sec. However, it is not possible for the user to perform an energy analysis outside these pre-defined sets of p_{ox}, p_{red}, T_{ox}, and T_{red}.

Contribution and use of experimental data

The experimental data is contributed as datasets containing values for $\Delta H(\delta)$ and $\Delta S(\delta)$ as described in section 3.4. Each of the contributed experimental datasets including the raw data can be viewed using the *RedoxThermoCSP* user interface in *MPContribs* [h]. To use this data for thermodynamic equilibrium calculations, the experimental values for $\Delta H(\delta)$ and $\Delta S(\delta)$ are fit using empirical functions, as explained later in section 5.1.1. This data is then used to calculate *Isographs* and perform an *Energy Analysis* by calculating where ΔG is zero under the given conditions. For the Energy Analysis, only data for Air Separation is calculated, as most of the studied perovskites are only applicable for this purpose. As the empirical equilibrium thermodynamic functions for the experimental data are not as complex as for the theoretical datasets, all of the calculations are performed live without relying on pre-saved data. However, the amount of sensible energy used for a redox reaction of one of these materials cannot be given using the experimental data, as no heat capacity values are measured. Therefore, the sensible energy demand is calculated using theoretically calculated Debye temperatures, as mentioned before.

User interaction with the database

Users can access all thermodynamic data including *Isographs* and the *Energy Analysis* for all materials included in the materials screening presented herein. The data is accessed interactively, meaning that the process conditions can be changed by the user in order to model a specific thermochemical redox cycle. Additionally, the structural and DFT data can also be accessed through *Materials Project* website directly. In principle, it is also be possible to include experimental thermodynamic data on more materials generated by other users. This is indicated by the dashed arrow in Fig. 3.14. Such data could be integrated in future versions of the *RedoxThermoCSP* database.

[h] https://materialsproject.org/mpcontribs and https://contribs.materialsproject.org/redox_thermo_csp, source code: https://github.com/materialsproject/MPContribsUsers/tree/master/redox_thermo_csp

4. Fundamental understanding of perovskite solid solutions

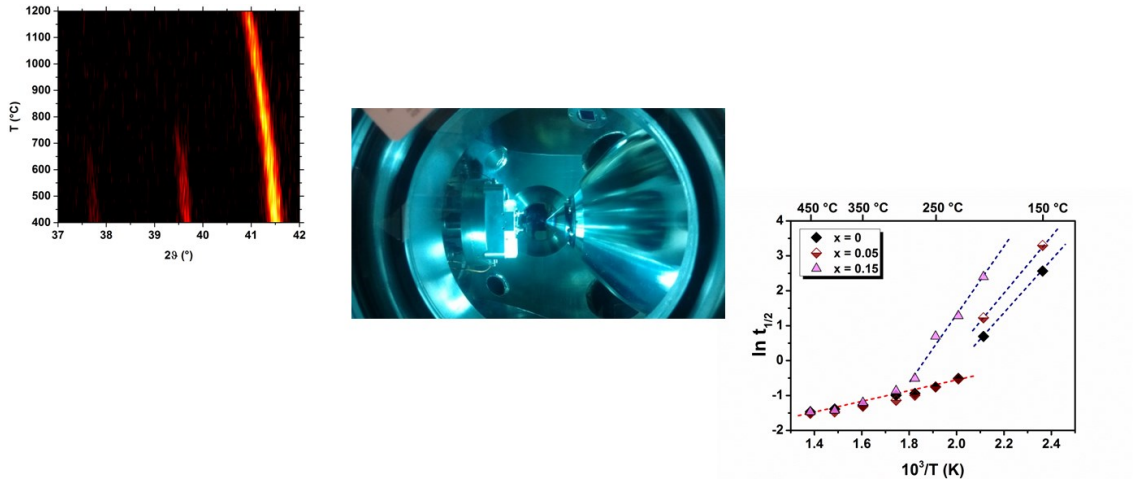

Fig. 4.1. The redox reaction in perovskites is studied using methods of *in-situ* analysis such as *in-situ* X-Ray diffraction (top left) and *in-situ* X-Ray photoelectron spectroscopy (middle). Fundamental properties such as the redox kinetics of perovskites are investigated through relaxation experiments based on thermogravimetric experiments (bottom right). Adapted from Vieten *et. al* and Bulfin *et. al*. [16, 23, 132]

After some perovskites with simple composition are synthesized, it is shown that these compounds in fact show reversible and non-stoichiometric oxygen release and uptake and that the re-oxidation occurs at high reaction rates. It is presented how solid solution formation and doping influence the properties of the perovskites by using the reference systems $Ca_{0.8}Sr_{0.2}MnO_{3-\delta}$/$CaMnO_{3-\delta}$, $SrFe_{1-x}Cu_xO_{3-\delta}$, $SrMnO_{3-\delta}$-$SrFeO_{3-\delta}$, and $CaTiO_{3-\delta}$-$CaMnO_{3-\delta}$. The influence of the tolerance factor on phase formation and phase transitions in these perovskites is investigated and discussed. Based on these results, solid solutions of perovskite phases can be formed in order to fine-tune their redox properties while maintaining control over their crystal structure.

This chapter is partially based upon the following peer-reviewed publications authored and co-authored by the author of this work:

Vieten, J.; Bulfin, B.; Call, F.; Lange, M.; Schmücker, M.; Francke, A.; Roeb, M.; Sattler, C., Perovskite oxides for application in thermochemical air separation and oxygen storage. Journal of Materials Chemistry A 2016, 4, (35), 13652-13659.

Bulfin, B.; Vieten, J.; Starr, D.E.; Azarpira, A.; Zachäus, C.; Hävecker, M.; Skorupska, K.; Schmücker, M.; Roeb, M.; Sattler, C., Redox chemistry of $CaMnO_3$ and $Ca_{0.8}Sr_{0.2}MnO_3$ oxygen storage perovskites. Journal of Materials Chemistry A 2017, 5, (17), 7912-7919.

Vieten, J.; Bulfin, B.; Senholdt, M.; Roeb, M.; Sattler, C.; Schmücker, M., Redox thermodynamics and phase composition in the system $SrFeO_{3-\delta}$-$SrMnO_{3-\delta}$. Solid State Ionics 2017, 308, 149-155.

Vieten, J.; Bulfin, B.; Starr, D.E.; Hariki, A.; de Groot, F.M.F.; Azarpira, A.; Zachäus, C.; Hävecker, M.; Skorupska, K.; Knoblauch, N.; Schmücker, M.; Roeb, M.; Sattler, C., Redox behavior of solid solutions in the $SrFe_{1-x}Cu_xO_{3-\delta}$ system for application in thermochemical oxygen storage and air separation. Energy Technology 2019, 7 (1), 131-139.

Vieten, J.; Bulfin, B.; Roeb, M.; Sattler, C., Citric acid auto-combustion synthesis of Ti-containing perovskites via aqueous precursors. Solid State Ionics 2018, 315, 92-97.

4.1 Initial studies of the redox process based on manganate systems

Based on a pre-selection of perovskites in an earlier study, $AMO_{3-\delta}$ systems containing an alkali earth metal on the *A* site and a 3*d* transition metal on the *M* site ($A^{2+}M^{3/4+}O_{3-\delta}$) exhibit excellent redox properties for application as oxygen carriers in two-step thermochemical cycles for air separation. [179] Manganese-containing alkali earth metal perovskites are especially appealing due to their redox enthalpy being in a range which allows reducing them in air at 1000 °C or below. At the same time, a high oxygen affinity is maintained in the reduced state, as opposed to (for instance) cobalt-containing perovskites which often are very easy to reduce but are not re-oxidized in air to an appreciable amount. [36] The expected redox enthalpies per mol of O (data from Materials Project) for some alkali $A^{2+}M^{3/4+}O_{3-\delta}$ systems are shown in Fig 4.2.

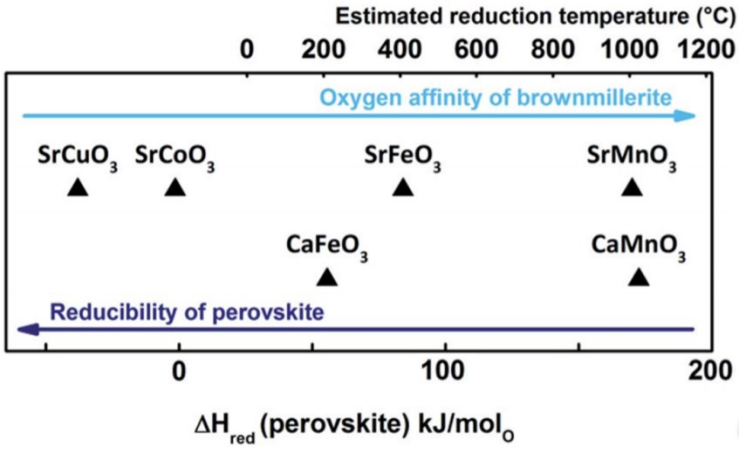

Fig. 4.2. Theoretical reduction enthalpies for the complete reduction of $A^{2+}M^{3/4+}O_3$ perovskites to the $A^{2+}M^{3/4+}O_{2.5}$ brownmillerite phases per mol of O based on Materials Project and reduction temperatures approximated by considering only the partial molar entropy of oxygen. Adapted from Vieten *et al.* [23]

Thermogravimetric scans show a mass change of over 2 % between 400 and 1200 °C at p_{O_2} = 0.16 bar. [23, 179] $Ca_{0.8}Sr_{0.2}MnO_{3-\delta}$ showed slightly higher mass changes than $CaMnO_{3-\delta}$ under these conditions. The full reversibility of the mass change has been confirmed for $Ca_{0.8}Sr_{0.2}MnO_{3-\delta}$ by executing 40 redox cycles, which revealed no significant changes in Δm. The microstructure of the material showed only minor changes in the porosity after these 40 redox cycles according to SEM images, and the particle size remained constant. [179]

Phase composition and stability limits

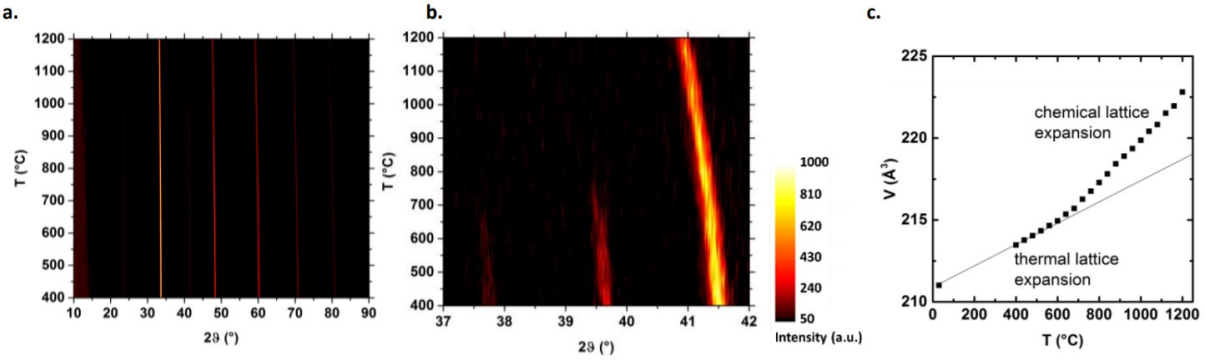

Fig. 4.3. *In-situ* X-Ray diffractograms of $Ca_{0.8}Sr_{0.2}MnO_{3-\delta}$ recorded in air at 400-1200 °C. (a) The shift of the reflections to lower 2ϑ angles indicates the lattice expansion. This can also be observed using a more detailed representation with the $K_{\alpha 2}$ signal removed electronically (b). Reflections with smaller intensity disappear at higher temperatures in this case. The refined unit cell parameters indicate the lattice expansion (c), which can be separated into two distinct regimes: thermal expansion only, and a combination of thermal and "chemical" expansion owing to the reduction reaction. The thermal expansion is shown with a line as a guide to the eye. Room temperature data is added to complement the results. Taken from Vieten *et al.* [23]

In-situ X-Ray diffraction measurements of the $Ca_{0.8}Sr_{0.2}MnO_{3-\delta}$ perovskite have already been part of an earlier study. [179] The samples are subjected to 400-1200 °C in air, and the change in the X-Ray diffraction signal is observed (see Fig. 4.3). The shift of reflections to lower 2ϑ angles indicates an expansion of the lattice. The calculated cell volume from refined diffraction data shows the volume expansion, which amounts to about 5% between 400 °C and 1200 °C in air. The onset of the reduction at about 600 °C in air can clearly be observed due to the stronger change in cell volume at 600-1200 °C w.r.t. lower temperatures and agrees well with thermogravimetric data. [23, 179] The lattice expansion at lower temperatures is attributed to thermal expansion only, whereas at higher temperatures, the stronger lattice expansion can be explained with increased ionic radii of Mn^{3+} ions compared to Mn^{4+} ions ("chemical lattice expansion"). This expansion in principle occurs during the non-stoichiometric reduction of any perovskite, and needs to be considered when manufacturing pellets or any structured materials, as they may not withstand such changes in volume.

It is noteworthy that looking at the data in detail (Fig. 4.3 b), reflections with smaller intensity disappear at higher temperatures. The reason for this may be a (minor) phase change, i.e., a decrease of the orthorhombic lattice distortion. Another explanation would be the thermal broadening of the XRD reflections, rendering reflections with small intensities invisible at high temperatures as they are below the background noise level. The understanding of these features in the XRD can be facilitated by comparing room temperature X-Ray diffractograms of $Ca_{0.8}Sr_{0.2}MnO_{3-\delta}$ and $CaMnO_{3-\delta}$ (see Fig. 4.4). The occurrence of more than one reflection between 34 and 48° 2ϑ indicates the

presence of an orthorhombic phase for $CaMnO_{3-\delta}$, as expected according to the literature. [204] The Sr-doped sample exhibits smaller intensities of these small reflections, which may show its lower degree of distortion. This is in good agreement with the calculated tolerance factors of 0.995 and 1.004 for $CaMnO_3$ and $Ca_{0.8}Sr_{0.2}MnO_3$, respectively, which indicate that the fully oxidized $Ca_{0.8}Sr_{0.2}MnO_3$ phase should exhibit a near-ideal cubic perovskite structure (compare Fig. 2.4). It has been reported in the literature that pure $CaMnO_{3-\delta}$ maintains its orthorhombic structure even during (moderate) reduction. [204] This is not the case for all perovskites, as the tolerance factor is also a function of the temperature. From Fig. 6 in Dabrowski *et. al*, [93] one can estimate an increase of the tolerance factor by 0.01 w.r.t. room temperature at 800 K, and by 0.02 at 1300 K for these perovskite systems. In some cases, this small increase may be enough to induce a phase transition, but this cannot be concluded definitively from our data for $Ca_{0.8}Sr_{0.2}MnO_{3-\delta}$. In most cases, the effect of the reduction on the tolerance factor counteracts and outweighs the temperature effects. The Sr doping stabilizes the phase in its reduced state, as the larger ionic radius of Sr^{2+} with respect to Ca^{2+} allows a larger *M* site ionic radius (Mn^{3+}/Mn^{4+}) in a stable cubic perovskite structure. With this information, we can confirm the effect of the tolerance factor on the perovskite phase formation and stability. By replacing some of the Ca^{2+} ions by Sr^{2+} in $Ca_{0.8}Sr_{0.2}MnO_{3-\delta}/CaMnO_{3-\delta}$, one can decrease the degree of distortion in the perovskite structure. One can therefore foresee that tolerance factor engineering as it is introduced within this work may be a viable means of controlling the perovskite's crystal structure.

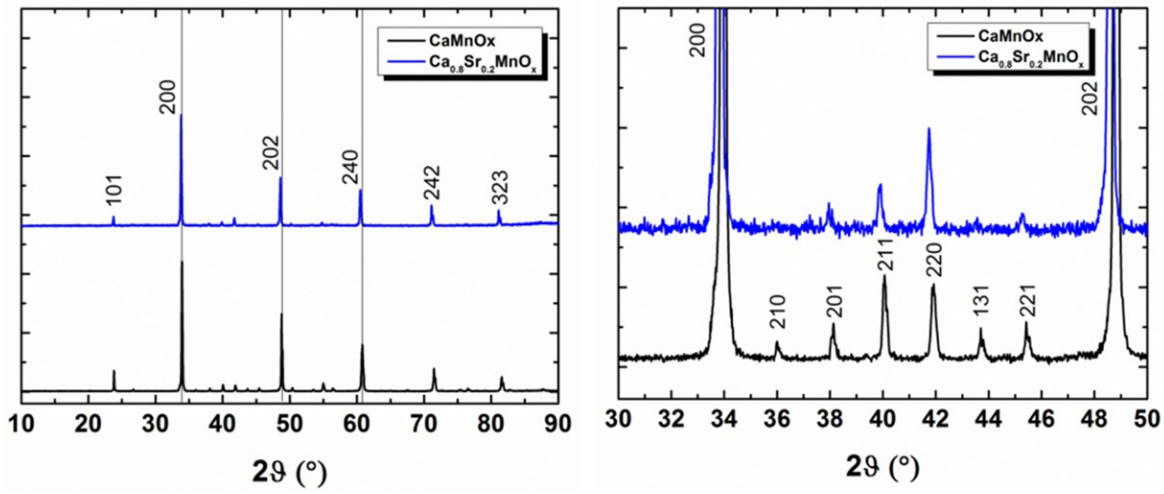

Fig. 4.4. Room temperature X-Ray diffractograms of $Ca_{0.8}Sr_{0.2}MnO_{3-\delta}$ and $CaMnO_{3-\delta}$ indexed in the orthorhombic space group 62 (*Pnma*). Not all indices shown in the case of overlapping reflections (for instance, 200 and 121). For undistorted cubic perovskite phases, only one reflection should be present between 34 and 48° 2ϑ (compare DFT-calculated materials mp-19201 and mp-1017467 on Materials Project, DOI: 10.17188/1194051 and 10.17188/1349742, respectively [116, 205]). Adapted from Bulfin *et al.* (supplementary information). [132]

For $Ca_{0.8}Sr_{0.2}MnO_{3-\delta}/CaMnO_{3-\delta}$, this can be very well observed in case of strong reduction at elevated temperatures and low oxygen partial pressures (see thermogravimetric data, Fig. 4.5). $CaMnO_{3-\delta}$ is known for its reductive disproportionation into $Ca_2MnO_{4-\delta}$ and $CaMn_2O_{4-\delta}$.[206] This decomposition reaction can be suppressed by stabilizing the perovskite structure using Sr, which leads to a higher oxygen storage potential of the Sr-doped perovskite sample (up to 4 wt%).

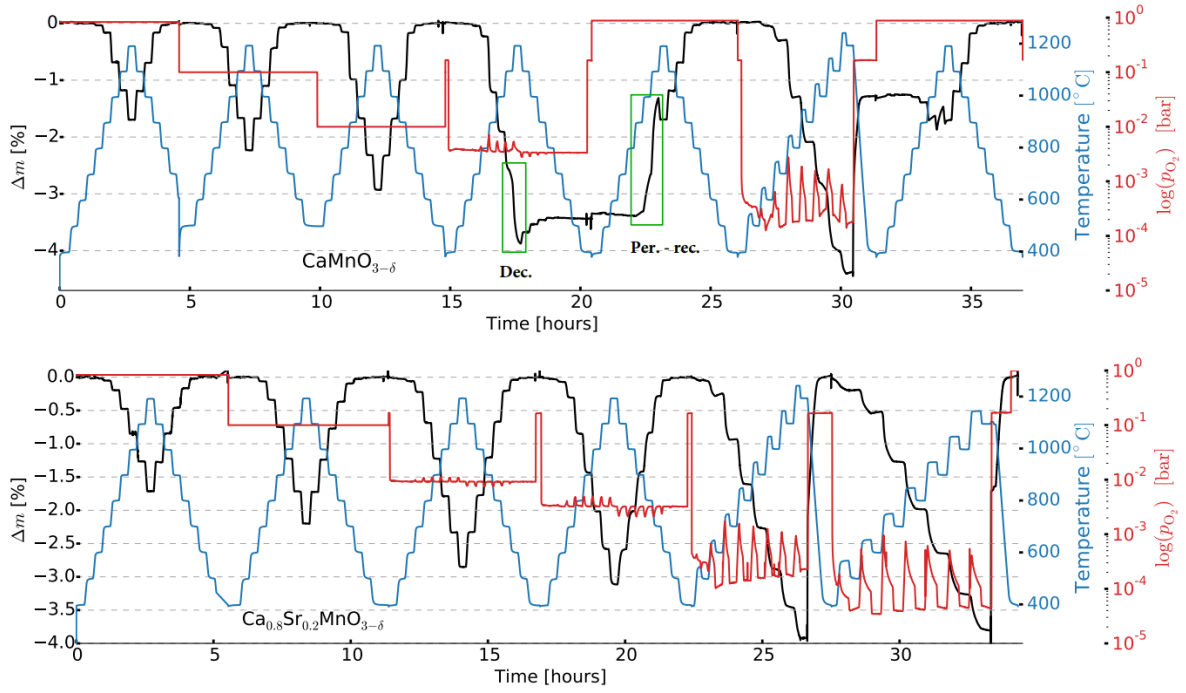

Fig. 4.5. Thermogravimetric data of $CaMnO_{3-\delta}$ and $Ca_{0.8}Sr_{0.2}MnO_{3-\delta}$ at different temperatures and oxygen partial pressures. The decomposition of $CaMnO_{3-\delta}$ (Dec.) and the recovery of the perovskite (Per.-rec.) can be distinguished from the non-stoichiometric redox reaction as the system is not in equilibrium during the phase change. Taken from Bulfin *et al.* (supplementary information).[132]

Thermodynamic properties

Data on the thermodynamics of these systems is recorded using the van't Hoff method. As predicted using DFT (see Fig. 4.2), the Sr content only has a small effect on the redox enthalpy change ΔH (see Fig. 4.6). The redox enthalpy change shows no significant dependence on the non-stoichiometry δ. The values for the redox enthalpy are in good agreement with DFT data ($CaMnO_{3-\delta}$ exp.: 161 ± 6 kJ/mol_O, DFT (Materials Project): 173 kJ/mol_O for the full reduction to the brownmillerite[117]). At least for the case of $Ca_{0.8}Sr_{0.2}MnO_{3-\delta}/CaMnO_{3-\delta}$, this confirms our initial assumption for materials design stating that the choice of *A* site cations has only little influence on the redox thermodynamics

of perovskite solid solutions. Furthermore, the change in redox enthalpy ΔS is not influenced significantly by the Sr content. It has to be stated, however, that the redox entropy change per mol of oxygen for perovskites is typically smaller than for ceria (see Fig. 4.7), as the configurational entropy change is lower in perovskites due to the redox-passive *A* cations and the unique electronic properties of cerium. [135] This means that if a perovskite and ceria had the same redox enthalpy change ΔH upon reduction, the perovskite would require a higher reduction temperature than ceria.

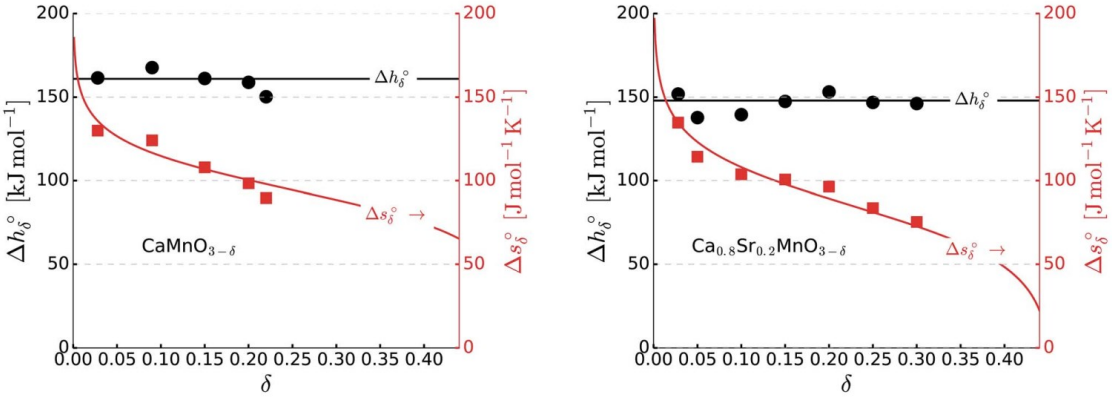

Fig. 4.6. Thermodynamics of the $CaMnO_{3-\delta}$ and $Ca_{0.8}Sr_{0.2}MnO_{3-\delta}$ redox reaction extracted from equilibrium thermogravimetric data using the van't Hoff method as a function of the non-stoichiometry δ. In the case of $CaMnO_{3-\delta}$, only data before the phase transition is used. All values given in terms of per mol of oxygen O. Adapted from Bulfin *et al.* [132]

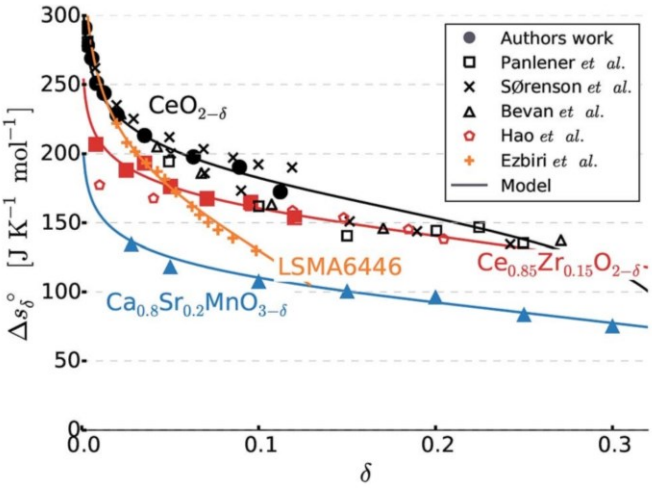

Fig. 4.7. Entropy change given per mol of oxygen O as a function of the non-stoichiometry δ for different redox materials using literature data [31, 110, 129, 207-209] compared to measurements on $Ca_{0.8}Sr_{0.2}MnO_{3-\delta}$ within this work. Data fit using dilute species model. [129, 132] Ceria and doped variants typically exhibit higher changes in entropy during the redox reaction. Taken from Bulfin *et. al.* [30]

***In-situ* XPS/XAS studies on the redox process and perovskite composition**

$Ca_{0.8}Sr_{0.2}MnO_{3-\delta}$ as a reference system is studied *in-situ* in order to investigate the redox process more in detail. As discussed later, this system shows better redox stability with respect to pure $CaMnO_{3-\delta}$. XAS (X-Ray absorption spectroscopy) studies performed on pressed pellets at the synchrotron source BESSY II show a decrease in the Mn^{4+} *L* edge absorption along with an increase in the Mn^{3+} signal correlating with increasing temperatures or decreasing oxygen partial pressures (see Fig 4.8). This process is fully reversible.

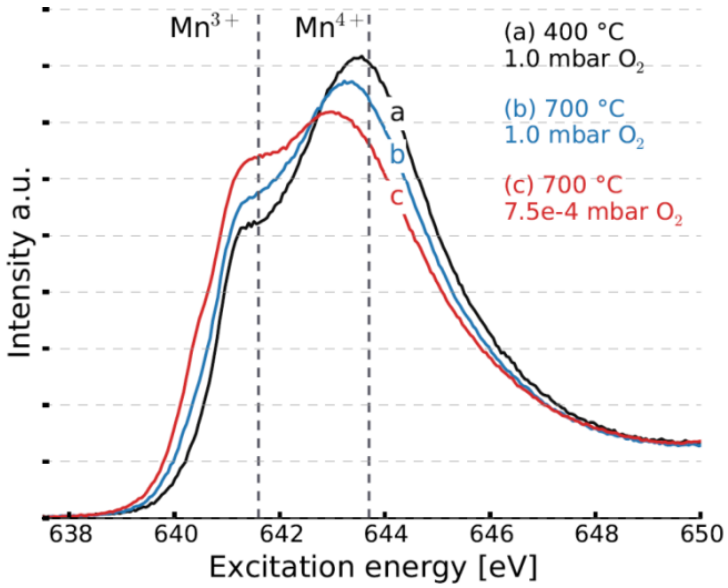

Fig. 4.8. XAS spectra recorded on the M *L* edge using $Ca_{0.8}Sr_{0.2}MnO_{3-\delta}$ samples showing the reduction of the perovskite *in-situ*. At increased temperatures and/or lower oxygen partial pressures (equal to total pressures in this case), the Mn^{3+} signal increases due to the partial reduction of Mn^{4+} (a-c). Intensities are normalized by peak area. A second set of peaks (not shown here) occurs at higher energy due to spin-orbit splitting. Taken from Bulfin *et. al.* [132]

The perovskite lattice is terminated by different oxygen containing species on the surface, which typically are less electron-rich than the bulk oxide O^{2-}. According to the literature, the perovskite oxidation mechanism occurs in several steps in which the oxygen molecules are first absorbed on the surface and then reduced before they diffuse into the perovskite bulk (see proposed mechanism in section 2.5). [138-140] The surface oxygen species can be clearly distinguished from the bulk species in $Ca_{0.8}Sr_{0.2}MnO_{3-\delta}$ using XPS (X-Ray photoelectron spectroscopy, see Fig. 4.9).

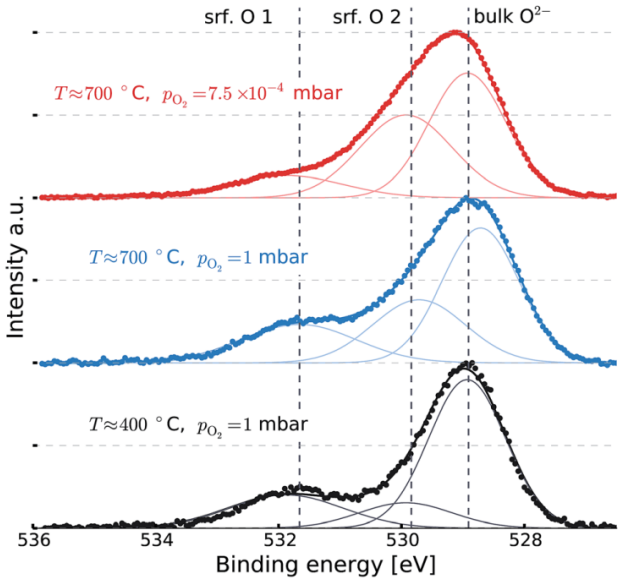

Fig. 4.9. XPS of the O 1*s* signal for $Ca_{0.8}Sr_{0.2}MnO_{3-\delta}$ measured *in-situ* at different temperatures and oxygen partial pressures. The peaks are fit using three Gaussian functions corresponding to the bulk oxide species and two distinct surface oxygen species (srf.) according to the literature. Taken from Bulfin *et. al*. [132]

While the signal at low binding energy (B.E.) corresponds to bulk oxide ions (O^{2-}), [138-140] the peak at medium binding energy is attributed to surface oxygen species such as O_2^{2-}, O^-, and O_2^-, [140, 210] whereas the peak at the highest binding energy corresponds to more easily reduced species. [132] The distribution of different bulk and surface species changes during reduction, and the amount of surface species seems to increase with increasing reduction extent compared to the bulk species. Moreover, the highest B.E. species seem to be less prevalent in the most reduced samples, which may indicate that these species are less stable under reducing conditions. It has been verified using depth profiling (XPS measurements at different photon energies) that these peaks in fact correspond to surface and bulk species. [132] However, the trends in prevalence of the three different species are not distinct and significant.

It is important to mention that an XPS study of pristine perovskite samples in many cases would not reveal the composition of the perovskite bulk accurately. Perovskites, especially those containing alkali earth metals, are often terminated by carbonate species on their surface due to the ubiquitous presence of carbon compounds in the environment. [141, 211] Due to the surface sensitivity of XPS, this issue affects the observed composition drastically. This effect has been observed for $Ca_{0.8}Sr_{0.2}MnO_{3-\delta}$, and the full XPS spectrum of the pristine sample clearly shows a high carbon content (see Fig. 4.10). However, upon heating the sample in a pure oxygen atmosphere (1 mbar, total pressure equals oxygen partial pressure), the carbon species disappear completely and do not re-appear as long as the sample is kept under vacuum or in an oxygen atmosphere.

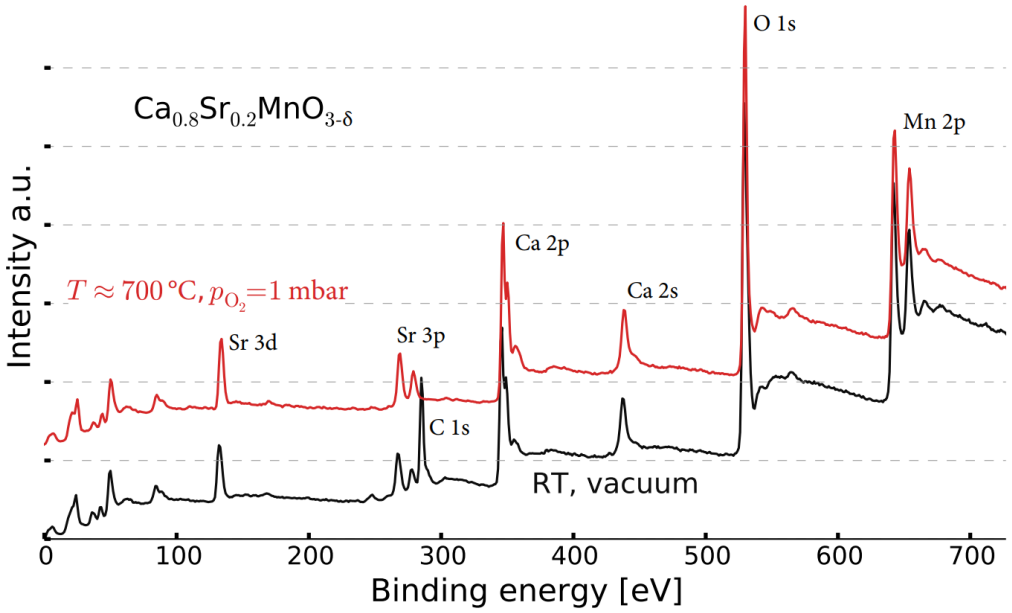

Fig. 4.10. Full XPS scan of a pristine $Ca_{0.8}Sr_{0.2}MnO_{3-\delta}$ sample which has been exposed to the environment (black) and at 700 °C in 1 mbar of oxygen (red). The carbonaceous species on the surface of the perovskite completely disappear after heating the sample in pure oxygen. Taken from Bulfin *et al.* (supplementary information). [132]

For comparison: The same effect has been observed for $SrFe_{1-x}Cu_xO_{3-\delta}$ (see Fig. 4.11). Carbon species are below the detection limit at temperatures above ≈ 300 °C when heating the sample in a pure oxygen atmosphere. The formation of carbonates may be an issue in particular for CO_2 splitting applications, as the perovskite is partially decomposed into the alkali earth carbonate and transition metal oxides in the presence of CO_2 at low temperatures. [141, 211] According to the literature, this issue occurs in atmospheres with high CO_2 concentration, [141, 211] but as mentioned above, carbonate species are present on the surface even if perovskites are kept in air. Carbonate formation therefore appears to be mainly a problem in CO_2 splitting cycles, but we cannot exclude a long term detrimental effect in air separation. Howsoever, the results presented herein show a potential remedy of this issue, as we demonstrated that heating the perovskite in pure oxygen leads to the full recovery of the initial structure. However, this might only be an option if the carbonate content of the perovskites is low, and further studies are required to clarify the suitability of an oxygen treatment to remove carbonates in perovskites.

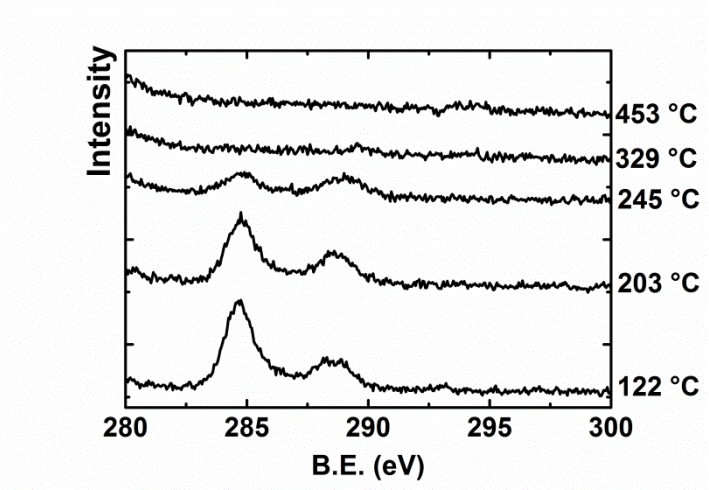

Fig. 4.11. XPS scans of the C 1*s* signal of $SrFe_{1-x}Cu_xO_{3-\delta}$ at different temperatures in 1 mbar of oxygen (x = 0.05). At high temperatures, carbonaceous species are below the detection limit. Taken from Vieten *et al.* (supplementary information). [16]

In summary, studies on manganate perovskites revealed that these materials can in fact be used for reversible oxygen storage in two-step thermochemical cycles, and that a reduction from Mn^{4+} to Mn^{3+} occurs upon heating, which is accompanied by an expansion of the lattice. This leads to a change in the tolerance factor, which can be influenced by choosing appropriate *A* site cations. By doing so, the stability of perovskites can be controlled. In terms of thermodynamics, the studied perovskites behave as expected, and the entropy change is smaller for perovskites than for ceria. Perovskites may be terminated by a carbonate layer, which can be removed by heating the samples in pure oxygen. This has been shown using *in-situ* XPS scans on $Ca_{0.8}Sr_{0.2}MnO_{3-\delta}$ and $SrFe_{1-x}Cu_xO_{3-\delta}$ samples. In the next section, the redox properties of the material $SrFe_{1-x}Cu_xO_{3-\delta}$ are studied in detail.

4.2 Doping perovskites on the transition metal site: Cu-doped $SrFeO_3$

After the fundamental properties of perovskites as redox materials for two-step thermochemical processes have been introduced in the previous section and the effect of a compositional variation on the *A* site has been studied, it shall now be investigated how their redox properties can be altered by doping on the *M* site. As the transition metals on the *M* site are involved in the redox reaction (as opposed to *A* site cations), *M* site doping is expected to have more drastic effects on the redox properties of perovskites. Initially, we demonstrate in the following how the exchange of one transition metal species by another in a limited amount (referred to as "doping" within this work, although this expression usually refers to smaller concentrations) can be used to modify the properties of $SrFeO_{3-\delta}$. The non-stoichiometric reduction of this material has been known for a long time, and its suitability for thermochemical air separation has been demonstrated. [23, 61, 65, 212, 213] It is very appealing that by replacing 5 % of the Fe ions by Cu, the redox properties of this material can be further improved, i.e., its gravimetric oxygen storage capacity is increased. [16, 23] This effect is further discussed in the following, especially with respect to details on the redox mechanism, phase formation, and the oxidation state of Cu in these solid solutions.

Phase composition and solubility limits

Cu ions show significantly larger ionic radii than Fe ions in all oxidation states. [88] It may therefore be expected to find a solubility limit of Cu in $SrFe_{1-x}Cu_xO_{3-\delta}$, i.e., that there is a maximum value *x* above which a two-phase mixture is formed instead of a solid solution. This has in fact already been observed by Zhang *et. al*, who noticed a phase segregation in $SrFe_{0.7}Cu_{0.3}O_{3-\delta}$ membranes. [214] The phase composition of systems with x = 0-0.33 is studied using X-Ray diffraction (XRD) and EDX (energy dispersive X-Ray spectroscopy). If a single phase is found in the XRD patterns and EDX indicates an even elemental distribution, this is a strong indicator for the formation of a solid solution without phase segregation. However, one needs to state that all experiments are carried out using polycrystalline materials, and that using single crystals may improve the accuracy of the information on phase composition and formation in future studies.

We first focus on the sample with x = 0.05, as it has shown beneficial oxygen storage properties even at low temperatures. [16, 23] It has been found that a side phase is formed in an appreciable amount if this sample is prepared by mixing the starting materials in the stoichiometric ratio, as revealed by EDX studies on cleaved and polished samples. [23] This issue can be resolved by using an excess of 5% Sr during preparation of the sample (see the supplementary information in Vieten *et. al.* [16]), and samples with even elemental distribution were formed successfully. One could assume that this effect may be induced by a Sr loss due to reaction with the crucible or due to the volatility of Sr-containing species at high temperatures, and/or that phase formation in the sample prepared with $x = 0.05$ is especially susceptible to small variations of the perovskite composition. [16]

The EDX analysis shows no significant difference between the A/M site ratio for different Cu contents. [16] A potential non-stoichiometry on the A site of the perovskites could not be observed. This makes it very unlikely that the observed redox behavior is related to the A site composition. However, even a small non-stochiometry on the A site may affect some properties of the perovskites, [215] and we cannot exclude small variations below the accuracy limit of EDX. Nevertheless, the phase formation could be studied successfully using an EDX study on powders. An even distribution of all elements is found for x = 0.05 and 0.15 (see Fig. 4.12). The XRD patterns also show no known side phases except for the brownmillerite at x = 0 – 0.15. At x = 0 and 0.05, one additional reflection appears at 2ϑ = 45°, which could not be assigned to any known phase and does not shift during the reduction reaction according to *in-situ* XRD on $SrFe_{0.95}Cu_{0.05}O_{3-\delta}$. [23] The origin of this reflection may be clarified in future studies. Looking at samples with higher Cu content, however, one can observe indications of phase segregation. XRD shows reflections assigned to CuO at x = 0.25 and 0.33, and the EDX maps show the formation of isolated Cu clusters for x = 0.25. Moreover, aluminium has been found in this sample (≈ 3 at%), which most likely originates from the alumina crucible being attacked by Cu species at elevated temperatures. [16] From these considerations, we can conclude that the solubility limit of Cu in $SrFeO_{3-\delta}$ is at or above 15 and below 25 at% w.r.t. Fe.

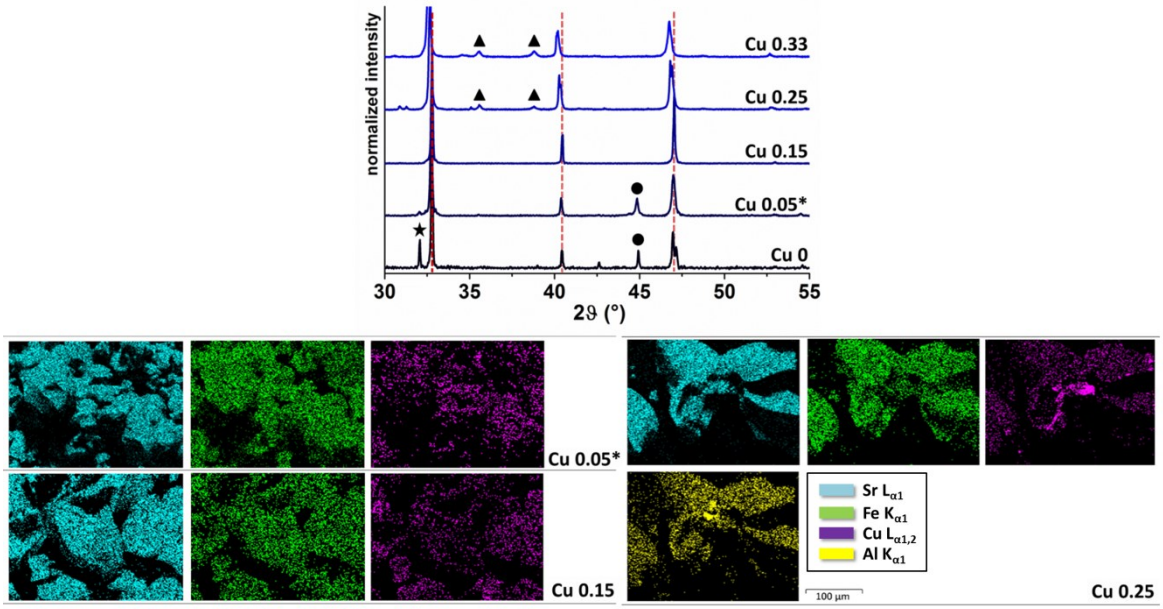

Fig. 4.12. Top: X-Ray diffraction patterns of $SrFe_{1-x}Cu_xO_{3-\delta}$ samples with the Cu content (based on the initial stoichiometry of the reaction mixture) indicated. The sample "Cu 0.05*" has been prepared with 5% Sr excess. Vertical lines are shown as guide to the eye. The reflection marked with ★ is assigned to the brownmillerite $Sr_2Fe_2O_5$, reflections assigned to CuO are denoted by▲, while the origin of the reflections marked as ● remains unclear, as discussed in the text. Bottom: EDX maps of three different phases show an even elemental distribution for samples with a Cu content of 15 at% w.r.t. Fe or below, and the formation of Cu clusters at 25 at%. Adapted from Vieten *et. al.* [16]

Redox kinetics

Perovskites typically exhibit very fast reaction kinetics due to high oxygen diffusion rates, but there are composition-dependent differences.[23] First, we consider the oxidation kinetics of undoped $SrFeO_{3-\delta}$ in the following. This data is gathered using relaxation experiments in a thermobalance. The oxidation reaction of pre-reduced materials is very fast even at lower temperatures (see Fig. 4.13). Significant temperature-dependent differences in the oxidation reaction rate could only be determined at $T \leq 200\,°C$. Even at 150 °C, the reduced sample can be half re-oxidized in only 13 min. Compared to stoichiometric oxides such as CuO/Cu_2O, the oxidation reaction is significantly faster in these non-stoichiometric perovskites.[45] However, one needs to clarify that these experiments are carried out using powders with crystallite sizes in the range of $\approx 10 - 200\,\mu m$ [179] and that bulk samples may exhibit slower reaction kinetics. This should be addressed in future studies. Nevertheless, the oxidation reactions in perovskite powders are significantly faster than in stoichiometric oxide powders with comparable particle size.[45]

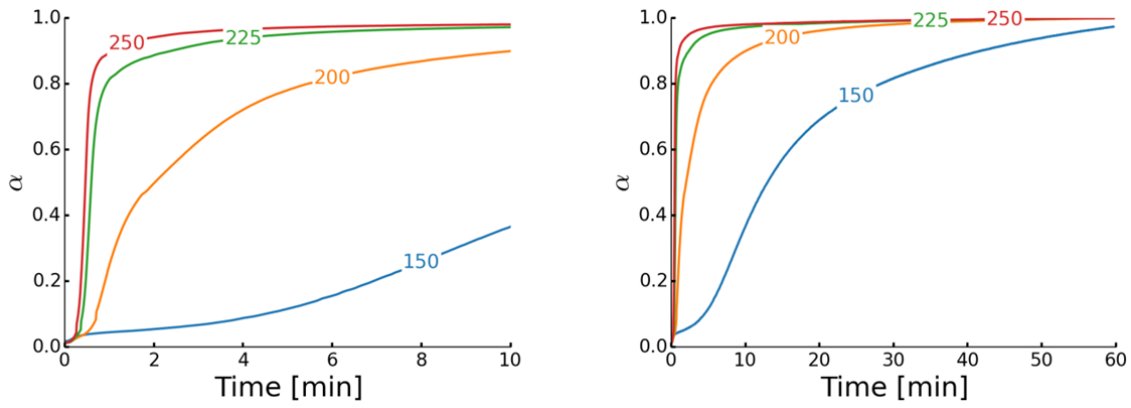

Fig. 4.13. Oxidation speed of $SrFeO_{3-\delta}$ as measured in thermobalance relaxation experiments at different temperatures after reduction in Ar and through re-oxidation in an oxygen-rich atmosphere (p_{O_2} = 0.9 bar). The oxidation extent is indicated as α, and temperatures are given in terms of °C. Adapted from Vieten *et. al.* (supplementary information).[16]

Comparing samples with different Cu content, it can be noted that a higher Cu content leads to slower reaction kinetics. Nevertheless, the reactions are still significantly faster than with stoichiometric oxides. Fig. 4.14 shows the reaction half lives $t_{1/2}$ (defined as the time t at $\alpha = 1/2$) for samples with Cu content x = 0, 0.05, and 0.15 drawn in an Arrhenius-like plot of $1/T$ vs. $\ln t_{1/2}$. Two distinct regimes can be observed. At high temperatures, the reactions are very fast (completed in about 20 seconds after the gas supply was switched) and independent of the perovskite composition. This implies that the reaction rates are limited by the supply of gas in the thermobalance and gas phase

diffusion. As the gas flow rate is set at 100 mL/min and the volume of the reaction chamber and the piping in the thermobalance is in the order of ~ 20-50 mL, it takes several seconds until the oxygen can reach the sample after the gas supply is switched. This means that the oxidation reaction at high temperatures is so fast that it cannot be measured within our relaxation experiments. At low temperatures, however, a clear temperature-dependent trend in the reaction half lives can be observed, and $\ln t_{1/2}$ is linearly proportional to $1/T$. This regime must therefore be controlled by internal diffusion and/or the oxygen adsorption rate on the surface. The slower reactions in samples with high Cu content might indicate higher activation barriers for internal oxide ion diffusion.

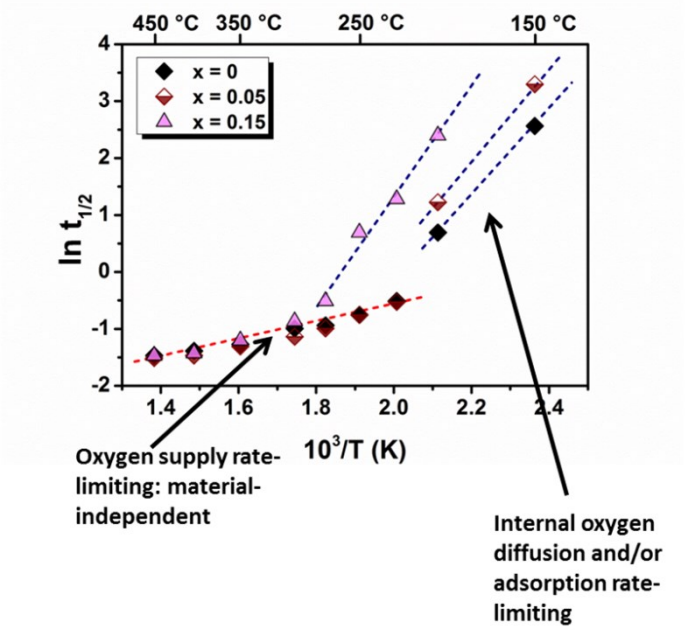

Fig. 4.14. Natural logarithm of the reaction half-lives $t_{1/2}$ determined in thermogravimetric relaxation experiments for different powdered $SrFe_{1-x}Cu_xO_{3-\delta}$ samples with Cu content x. Two distinct regimes can be observed: at high temperature, the reaction rates are composition independent, whereas at low temperature, different reaction rates for different materials indicate that the adsorption rate or internal oxygen diffusion rate are rate-limiting. Adapted from Vieten *et. al.* [16]

Redox state of Cu and oxygen storage capacity

Thermogravimetric experiments show that Cu-doped $SrFeO_{3-\delta}$ phases exhibit higher oxygen storage capacities than Cu-free $SrFeO_{3-\delta}$ under most conditions. The difference is in the order of 5-20 % (see Vieten *et al.* [16]). To gain a further understanding why this is the case and to elucidate the role of Cu in these perovskites, *in-situ* XPS and XAS measurements are carried out at the synchrotron source BESSY II, HZB Berlin. The redox state of Cu in these samples is of particular interest. Fe in $SrFeO_{3-\delta}$ occurs as Fe^{4+} and Fe^{3+} ions, depending on the oxygen non-stoichiometry. Mössbauer studies in the

literature suggest that Fe^{4+} in fact may disproportionate into Fe^{5+} and Fe^{3+},[216, 217] but the Fe oxidation state could not be resolved in our experiments using XAS or XPS due to the lack of significant differences of Fe spectra between different high oxidation states.[16, 218] It is particularly interesting to see whether Cu exhibits similarly high oxidation states in these perovskites. Cu^{4+} is only known in some rare metal complexes, and there are some indications of this oxidation state in perovskite phases prepared under high oxygen pressures.[115, 219, 220] However, according to DFT data, the reduction enthalpy of $SrCuO_3$ to $Sr_2Cu_2O_5$ is negative, meaning that very high oxygen partial pressures would be required according to Eq. 2.11 for reaching this high Cu oxidation state.[16, 117] The XAS and XPS spectra (Fig. 4.15 and 4.16, respectively) show a significant broadening of the Cu 2*p* signal towards higher energies, which indicates that at least two distinct oxidation states or chemical environments are present. The influence of the chemical environment on the peak structure should essentially be temperature-independent, and we therefore attribute the signals to two different Cu oxidation states. Higher binding energies in the same chemical environment correspond to a higher oxidation state.

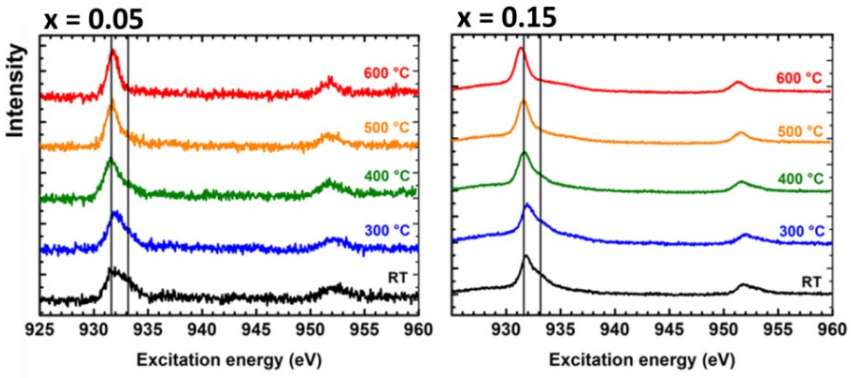

Fig. 4.15. Cu 2*p* XAS spectra measured at BESSY II (HZB Berlin) using $SrFe_{1-x}Cu_xO_{3-\delta}$ with the Cu contents *x* indicated. All samples are measured *in-situ* in an atmosphere of pure oxygen at a pressure of 1.0 mbar, and after the carbonate layer has been removed as explained in the previous section of this work. Vertical lines show the peak positions as a guide to the eye. At high temperatures, the intensity of the high energy peak decreases gradually, indicating the reduction of the perovskites. Taken from Vieten *et. al.* [16]

We first consider the XAS spectra. The lower Cu content in the sample with $x = 0.05$ compared to $x = 0.15$ is obvious due to the lower signal to noise ratio in the Cu-poor sample. The positions of the lower and higher energy signals (at 931.8 and ≈ 933 eV excitation energy, respectively) are indicated in Fig. 4.15 by black vertical lines. All measurements are carried out in pure oxygen atmospheres with 1.0 mbar oxygen (partial) pressure and at different temperatures. Both in the case of $x = 0.05$ and $x = 0.15$, the second (high energy) peak disappears gradually as the temperature is increased. We attribute this observation to the reduction of the perovskite. The observed peak positions are in

good agreement with literature data (typically 931-934 eV [221]). The XAS spectra show a very similar structure as in literature reports on mixed Cu^{2+}/Cu^{3+} perovskites. [222] To further study the oxidation state of Cu in these samples, XPS spectra recorded using the same setup are considered in the following (see Fig. 4.16).

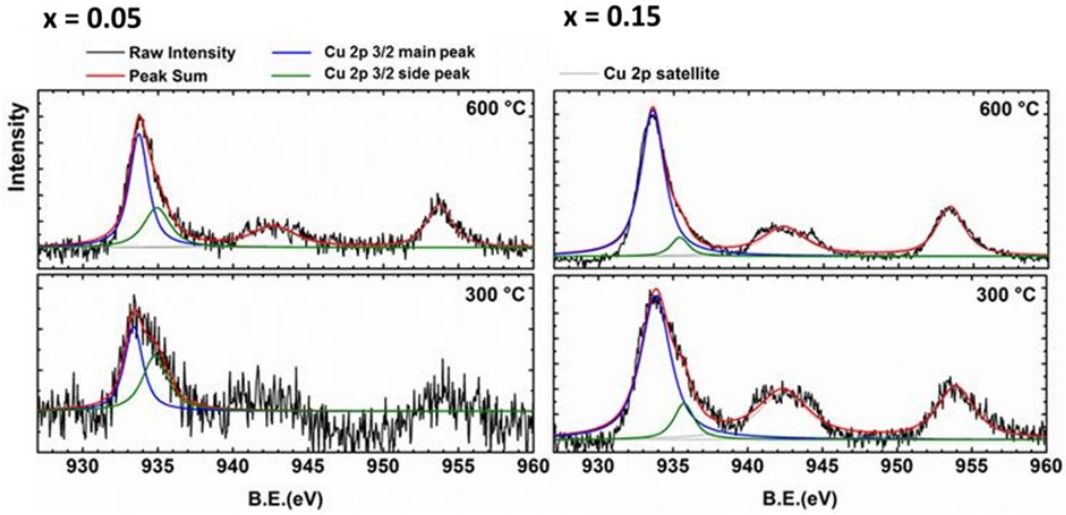

Fig. 4.16. Cu 2*p* XPS spectra measured under the same conditions as the XAS spectra for two $SrFe_{1-x}Cu_xO_{3-\delta}$ perovskite phases. Peaks are fit using mixed Gaussian-Lorentzian functions. The Cu $2p_{3/2}$ main peak at lower binding energy (B.E.) is overlapped with a feature at higher energies ("side peak"). A satellite peak is observed at 940-945 eV, and spin-orbit splitting generates the peak at > 950 eV (Cu $2p_{1/2}$), which is not further discussed here. Taken from Vieten *et. al.* [16] For data at further temperature levels: see the supporting information of the same publication. [16]

The temperature-dependent changes in XPS and XAS are very similar, and the Cu $2p_{3/2}$ main peak in XPS is located at a B.E. of 933.42 ± 0.20 eV and 933.71 ± 0.11 eV for $x = 0.05$ and $x = 0.15$, respectively, whereas a side peak corresponding to a higher energy is located at 935.61 ± 0.18 eV for $x = 0.15$ and at 935.61 ± 0.18 eV for $x = 0.15$. It has to be noted that these fitted peak positions may be affected by the curve fitting procedure applied. [16] Nevertheless, the observed peak positions are in good agreement with literature data. The lower energy peak at 933 eV is characteristic of a Cu^{2+} system, whereas the peak at approx. 935 eV is a signature of a ground state Cu^{3+} system. [16, 223] While the peak structure observed in our case is similar to data by Darracq *et al.,* [219] the observed structure can be explained without assuming an unusual Cu oxidation state such as Cu^{4+}. The peak position of Cu^{3+} is sensitive to the charge transfer energy, which explains different peak positions in different studies. [16, 223] In our case, the Cu^{3+} binding energy is relatively high. Moreover, one can exclude the presence of a significant amount of Cu^{+} ions (or Cu^{0}), as we always observe a satellite ("shake-up") peak with significant intensity, which can only occur if the system has empty *d* states. [224] The relatively high intensity ratio between this satellite peak and the main peaks indicates that a

relatively high formal Cu oxidation state must be present. [16, 225] Our XPS spectra are similar to those of $YBa_2Cu_3O_{7-\delta}$ annealed at different temperatures showing different δ values. In conclusion, the XPS and XAS data clearly indicates the presence of a mixed Cu^{3+}/Cu^{2+} valence, but no evidence for any higher oxidation states. This is also in good agreement with theoretical redox enthalpies for the reduction of $Sr_2Cu_2O_5$ to $SrCuO_2$ and from $SrFeO_3$ to $Sr_2Fe_2O_5$, which are very similar. [16, 117] The Cu valence decreases during reduction according to our XPS and XAS data. If we assume individual and independent sub-lattices, one could expect that the reduction reactions $Fe^{4+} \rightarrow Fe^{3+}$ and $Cu^{3+} \rightarrow Cu^{2+}$ occur in parallel. The relative peak intensities for x = 0.15 and x = 0.05 indicate that the system with 15 at% Cu substitution is more Cu^{2+}-like, and the sample with lower Cu content has a significantly higher share of Cu^{3+} w.r.t. the total amount of Cu. To further study the redox mechanism and oxidation state, one can correlate the data from thermogravimetric analysis (TGA) to the relative peak area ratios in XPS (see Fig. 4.17). For this purpose, we use data recorded at different temperatures and with comparable oxygen partial pressures (2 mbar in the TGA vs. 1 mbar in XPS, which amounts to a difference of only 10 % in terms of $\ln p_{O_2}$). The change in non-stochiometry $\Delta\delta$ according to TGA corresponds well to the observed change in XPS $2p_{3/2}$ peak area ratios for x = 0.05. In fact, a linear fit shows a correlation indicated by the adjusted R^2 of 0.9994 in this case. While it may be a coincidence that the correlation is near-ideal considering the measurement errors of XPS at these low Cu contents and given that only three data points are available, a direct dependence of the peak area ratios to the mass change seems reasonable if the Cu^{3+} content is directly proportional to the mass change of the perovskites. Since the Cu content is very low, it cannot account for the complete observed mass change, which indicates that Fe^{4+} and Cu^{3+} must be reduced in parallel in this case.

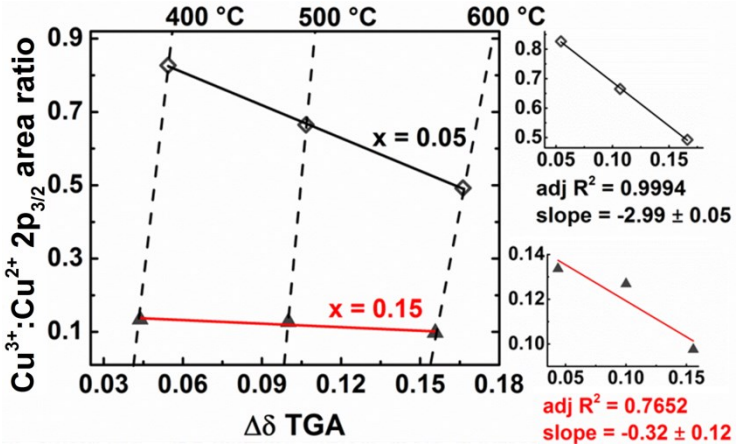

Fig. 4.17. Correlation between the change in the Cu^{3+}:Cu^{2+} $2p_{3/2}$ XPS peak area ratios and the observed change in non-stochiometry $\Delta\delta$ at different temperatures with comparable oxygen partial pressures. While the Cu^{3+} content changes drastically during the reduction of $SrFe_{0.95}Cu_{0.05}O_{3-\delta}$ and correlates with the thermogravimetric data, Cu in $SrFe_{0.85}Cu_{0.15}O_{3-\delta}$ appears more passive. Taken from Vieten *et. al.* [16]

This is a reasonable assumption according to thermodynamic considerations (see above). For $x = 0.15$ the correlation between mass changes in thermogravimetric studies and the observed change in the Cu $2p_{3/2}$ is not as clear as in the case of $x = 0.05$, which may be related to the relatively low intensity of the Cu^{3+} peak, but may also indicate that both properties in fact do not correlate as well as for the sample with lower Cu content. The slope of the linear fit is one order of magnitude lower for $x = 0.15$ than for $x = 0.05$, which shows that the Cu^{3+} content does not change strongly during reduction of the $x = 0.15$ sample. Therefore, the redox reaction in this case must be mainly driven by the Fe^{4+} reduction, whereas Cu is mainly redox-passive. Therefore, one could also write the chemical equation of the x = 0.15 sample as $(SrFe_{1-x'}Cu_{x'}O_{3-\delta})_{x'} \cdot (SrCuO_2)_{x-x'}$, where x′ denotes a small amount of Cu being involved in the redox process.[16] Whether this chemical equation represents the true structure of the perovskite (for instance, a layered structure with a perovskite solid solution containing isolated $SrCuO_2$ layers) could be clarified in the future by using high resolution single crystal XRD or neutron diffraction. So far, this is a rather speculative statement. Nevertheless, this data shows how two different samples with very similar composition can show a rather different behavior, which is controlled by the extent of doping. The increased oxygen storage capacity under some conditions may be explained by studying the thermodynamics of these systems using the van't Hoff method (see supporting information in Vieten *et. al.* [16]). As the redox enthalpies for isolated $Sr_2Cu_2O_5$ to $SrCuO_2$ and from $SrFeO_3$ to $Sr_2Fe_2O_5$ are comparable (see above), one would expect an increase in the entropy change as the reason for the improved oxygen storage capacity whereas the enthalpy change should remain unchanged. Within the confidence interval of our measurements, however, both the enthalpy and entropy change in all three materials are essentially equal, and reading trends from this data is not reliable. Nevertheless, it is likely that the parallel reduction of two different species leads to a higher change in entropy than if only one species is reduced.

In summary, it has been demonstrated using $SrFe_{1-x}Cu_xO_{3-\delta}$ as a reference system that the redox properties of perovskites can be tuned by changing the *M* site composition through solid solution formation. This has interesting implications for the Cu oxidation state in these samples, which is an attractive aspect of fundamental materials science. Our example also shows that phase formation in perovskite solid solutions can sometimes be more complex than it initially appears. According to the results for $SrFe_{1-x}Cu_xO_{3-\delta}$, no drastic changes in the redox properties are to be expected if the composition is only changed slightly – doping is a means of adjusting the perovskite's redox behavior gradually rather than changing it completely, but this will certainly depend on the perovskite composition and cannot be generalized. In this case, one could improve the oxygen storage capacity at low temperatures (400-600 °C) by doping $SrFeO_{3-\delta}$ with 5 at% Cu on the Fe sites, while 15 at% Cu allow for the material to be more suitable for applications at higher temperature (900 °C).[16] The oxidation kinetics of all studied $SrFe_{1-x}Cu_xO_{3-\delta}$ solid solutions are very appealing and render those perovskites suitable for air separation at low temperatures (oxidation at 150-250 °C).

4.3 Creating solid solutions on the transition metal site over the full stoichiometry range

After discussing the effect of replacing a small amount of one transition metal species by another in the previous section, it shall now be studied how phase formation and redox properties of perovskites are affected by preparing solid solutions over the full stoichiometry range. For this purpose, we first study a system where no major phase changes are expected according to the tolerance factor ($CaTiO_3$-$CaMnO_3$), and then another system ($SrFeO_3$-$SrMnO_3$) with a variety of different perovskite phases from orthorhombic and tetragonal over cubic to rhombohedral and hexagonal. Synthesis, solid solution formation and phase composition are studied along with the thermodynamics in dependence of the oxygen non-stochiometry δ and the composition of the solid solution.

4.3.1 $CaTiO_3$ – $CaMnO_3$ solid solutions as a prototype

$CaTiO_{3-\delta}$ – $CaMnO_{3-\delta}$ solid solutions are interesting for thermochemical applications, as the difference in redox enthalpy between the two endmembers is relatively large (per mol of oxygen: 173 kJ/mol_O for $CaMnO_3$ and 579 kJ/mol_O for $CaTiO_3$ for the full reduction to the brownmillerite [117]). Solid solutions between the two materials might therefore be used to span a wide range of redox enthalpies and fields of application, and furthermore, the formation enthalpy of water is situated in-between these two enthalpy values. However, before any further studies can be carried out, it has to be verified that solid solution can actually be formed, both in terms of the synthesis procedure and in terms of phase purity without segregation.

The preparation of $CaMnO_3$ and similar compounds through citric acid auto-combustion based routes is simple and has been demonstrated in the past, as also shown in section 4.1 of this work. [23, 179] The preparation of $CaTiO_3$ appears more challenging. Although the original patent of M.P. Pechini is dealing with the preparation of barium titanate specifically, the example in the patent describes the use of tetra isopropyl titanate as a precursor instead of nitrates. [178] These titanium alkylates are susceptible to hydrolysis. Moreover, Pechini described the use of barium chloride as a barium source, but using chlorides as starting materials requires thorough removal of the chloride ions, as they otherwise may be incorporated into the perovskite structure. [183] This may alter the properties of the perovskite. However, titanium nitrates cannot be used, as titanium does not form any stable nitrates. [181] For these reasons, a new synthesis method for titanates and solid solutions with other perovskites has been developed, which is described in detail in the experimental section of this work (see section 3.1). [172] It is based upon the well-known fact that titanium can be dissolved in alkaline

hydrogen peroxide solutions. [184, 226, 227] However, the dissolution of titanium metal beads or granules is very time consuming, if the usage of fine Ti powder shall be avoided, which is pyrophoric in air. Therefore, a titanium peroxo complex is formed in our case by dissolving titanium(II)-oxide (also known as titanium monoxide, TiO) in an aqueous hydrogen peroxide/ammonia mixture. [172] Titanium monoxide powder is dissolved much more readily and it is not flammable. By using this method and preparing a titanium peroxo citrate complex in a first step, the citric acid auto-combustion method can be used for the preparation of perovskites containing titanium. For the preparation of solid solutions, all other metal nitrates are added after preparing the peroxo citrate complex and all later steps are carried out the same way as for all other perovskite samples.

Alternatively, perovskites containing titanium can be prepared through solid state synthesis from the oxides, but this requires thorough mixing of the powders in a ball mill, and/or multiple high temperature steps with intermediate grinding and powdering of the intermediate products. [228] An attempt has been made to mix titanium(IV)-oxide powder with the Ca/Mn oxide precursors obtained through citric acid auto-combustion for the preparation of a $CaTi_{0.6}Mn_{0.4}O_{3-\delta}$ solid solution. The result of a high temperature treatment of this sample is compared to a sample prepared using our new method in Fig. 4.18 by studying the X-Ray diffractograms of the resulting powdered samples. The result of the new method is phase-pure orthorhombic $CaTi_{0.6}Mn_{0.4}O_3$, whereas the combined citric acid auto-combustion/solid state route yields a crude mixture of $CaTiO_3$ [229] and Ca_2MnO_4. [172, 230]

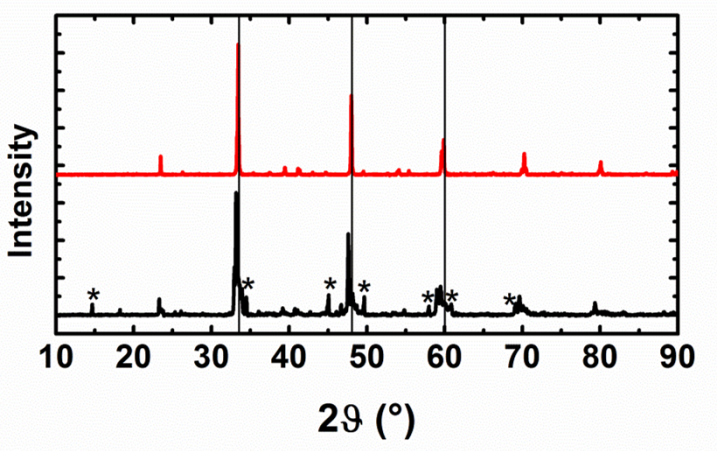

Fig. 4.18. X-Ray diffractograms of two samples with nominal starting composition $CaTi_{0.6}Mn_{0.4}O_n$ (n: unknown) after the high temperature treatment following two different synthesis methods. Whereas the sample prepared using titanium monoxide and the presented new method shows a pure orthorhombic phase assigned to $CaTi_{0.6}Mn_{0.4}O_3$ (red), the date on the sample prepared through a combined solid state/auto-combustion method with titanium dioxide as a precursor (black) shows the formation of $CaTiO_3$ mixed with Ca_2MnO_4 (marked with asterisks. Vertical lines added as a guide to the eye. Taken from Vieten *et. al.* [172]

This shows that a single phase $CaTi_{0.6}Mn_{0.4}O_{3-\delta}$ solid solution can be prepared using titanium monoxide based precursors. In a next step, the solid solution formation over the full range of $CaTi_xMn_{1-x}O_3$ compositions is studied. The X-Ray diffractograms of these phases with the Ti content x indicated are shown in Fig. 4.19. Over the full range of the solid solution phase space, no side phases are observed and only the pure orthorhombic phases are formed. The formation of orthorhombic phases is expected as the tolerance factors range from 0.958 to 0.996 for $CaTiO_3$ and $CaMnO_3$, respectively. The ionic radius of Ti^{4+} is 14 % larger than that of Mn^{4+}, and in the oxidation state +3 the difference is only 4 %. [88] As mentioned in section 2.3, a difference of less than 15 % in ionic radii leads to solid solution formation according to Goldschmidt's rule, which, however, needs to be considered as a "rule of thumb" only. Nevertheless, this rule is in good agreement with the findings within this work so far, as Cu^{3+} ions are 21 % larger in radius than Fe^{4+}, [88] and we in fact found a solubility limit in phases containing these two species (see previous section).

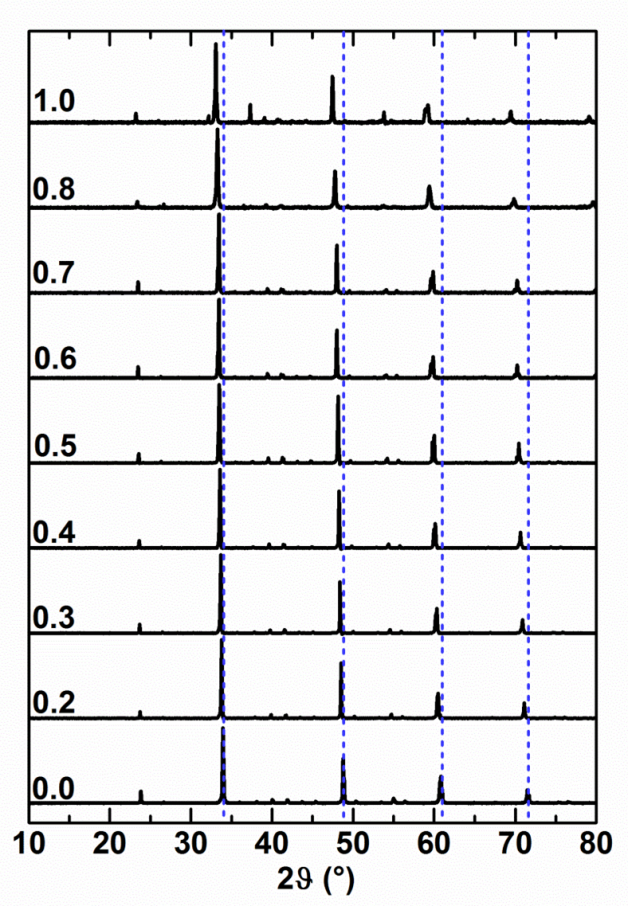

Fig. 4.19. X-Ray diffractograms of $CaTi_xMn_{1-x}O_3$ solid solutions with the Ti content x indicated. All materials are formed as pure orthorhombic phases, and no side phases are observed. Due to the higher ionic radius of Ti^{4+} compared to Mn^{4+}, the lattice gradually expands with increasing Ti content, indicated by the shift of all reflections towards lower 2ϑ angles. The position of the $CaMnO_3$ reflections is indicated using blue vertical lines. Taken from Vieten *et. al.* [172]

The formation of solid solutions is also indicated by looking at the shift of 2ϑ angles in the XRD pattern due to the different ionic radii of Ti^{4+} and Mn^{4+}. By refining the unit cell parameters based on these XRD patterns, it is found that the cell volume of these solid solutions is in good agreement with Vegard's law (see Fig. 4.20). These results show that the titanium monoxide based synthesis route is suitable to reliably prepare titanates and related solid solutions.

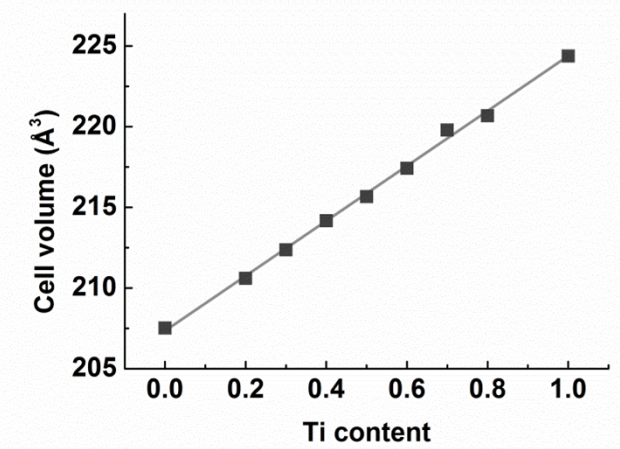

Fig. 4.20. Unit cell volumes of $CaTi_xMn_{1-x}O_3$ solid solutions in dependence of the titanium content obtained through Rietveld refinement of the XRD patterns. The change of the cell volume is in good agreement with Vegard's law, as indicated by the linear fit. Taken from Vieten *et. al.* [172]

Preliminary tests of the thermodynamics and redox properties of some of these materials with higher Mn content are carried out using the van't Hoff method. Similar studies using (Ca,Sr)(Ti,Mn) solid solutions are presented in section 5.1.2. It can be found that up to a Ti content of about 20-40 %, no significant increase in the redox enthalpy can be observed. This result seems counter-intuitive, as the addition of titanium should decrease the reducibility of the material. However, as we see later, these measurements are in good agreement with DFT data showing that a large amount of the Mn^{4+} ions needs to be replaced by Ti^{4+} to see a significant increase in redox enthalpies. Moreover, only the reduction at low δ values could be observed due to limitations in the minimum oxygen partial pressure and maximum temperature in the TGA system, and Ti^{4+} appears to be virtually redox-passive under these conditions.

In conclusion, it has been shown that perovskite solid solutions can be formed in any mixture ratio in the model system $CaTiO_3$-$CaMnO_3$, and that our modified citric acid auto-combustion route is suitable for obtaining these solid solutions. The lattice constants are in good agreement with Vegard's law. As expected according to the tolerance factors of these phases, perovskites with orthorhombic structure are formed in any of the studied cases. The titanium species are mostly redox-passive under the conditions applied here.

4.3.2 $SrMnO_3$ – $SrFeO_3$ solid solutions showing composition-dependent thermodynamics

Phase formation

While calcium titanate-manganates all have tolerance factors below one, $SrMnO_{3-\delta}$ – $SrFeO_{3-\delta}$ solid solutions show a different behavior. The tolerance factor for the phases with $\delta = 0$ varies from 1.006 for $SrFeO_3$ to 1.035 for $SrMnO_3$. According to literature data and the considerations in section 2.2 of this work, the Mn-rich phases should therefore show a hexagonal or rhombohedral structure, while the Fe-rich phases should be cubic. [101, 102, 231, 232] The difference in ionic radii is 10 % for Fe^{4+}/Mn^{4+}, while Fe^{3+} and Mn^{3+} both show an ionic radius of 64.5 pm according to Shannon. [88] Therefore, no miscibility gap is expected. In contrast to titanates and manganates, alkali earth metal perovskites containing Fe often show an initial non-stoichiometry δ at room temperature in air, which means that they cannot be synthesized without significant non-stoichiometry, except by using high oxygen partial pressures. [61] This leads to a mixed Fe^{4+}/Fe^{3+} valence which is present at all times under the conditions used within this work and which decreases the tolerance factor due to the larger ionic radius of Fe^{3+} w.r.t. Fe^{4+}. We first focus on phase formation of these perovskites in air, which are prepared using the citric acid auto-combustion method. In all cases, perovskites and distorted variants are formed as solid solutions according to the XRD patterns. In the case of $SrMn_{0.05}Fe_{0.95}O_{3-\delta}$, impurities assigned to $Sr_3Fe_2O_7$ are observed. Moreover, minor impurities can be found for some of the other samples, but these are all close to the detection limit in XRD. [92] The phases formed and their assignments to perovskites with different crystal structures are summarized in table 4.1.

Table 4.1. Perovskite phases and impurities formed in the $SrMnO_{3-\delta}$ – $SrFeO_{3-\delta}$ phase space according to X-Ray diffraction data. Taken from Vieten *et. al.* [92]

Composition	Main phase(s)	Side phase(s)
$SrFeO_{3-\delta}$	orthorhombic* ($Cmmm$)	tetragonal $SrFeO_{3-\delta}$ *, ($Sr_4Fe_6O_{13}$)
$SrMn_{0.05}Fe_{0.95}O_{3-\delta}$	tetragonal ($I4/mmm$)	$Sr_3Fe_2O_7$
$SrMn_{0.15}Fe_{0.85}O_{3-\delta}$	cubic perovskite ($Pm\bar{3}m$)	(-)
$SrMn_{0.33}Fe_{0.67}O_{3-\delta}$	cubic perovskite ($Pm\bar{3}m$)	(-)
$SrMn_{0.5}Fe_{0.5}O_{3-\delta}$	cubic perovskite ($Pm\bar{3}m$)	-
$SrMn_{0.67}Fe_{0.33}O_{3-\delta}$	cubic perovskite ($Pm\bar{3}m$)	(-)
$SrMn_{0.85}Fe_{0.15}O_{3-\delta}$	'γ-$SrMnO_3$', rhombohedral ($P31c$)	-
$SrMn_{0.95}Fe_{0.05}O_{3-\delta}$	'$SrMnO_3$', hexagonal ($P6_3/mmc$)	(-)
$SrMnO_{3-\delta}$	'$SrMnO_3$', hexagonal ($P6_3/mmc$)	-

*orthorhombic and tetragonal phase show very similar X-Ray diffraction patterns
In brackets: minor impurities

For **Mn-rich phases** ($SrMn_{1-x}Fe_xO_{3-\delta}$ with $\boldsymbol{x \leq 0.15}$), the average transition metal radius is too large to accommodate an undistorted perovskite structure, which leads to the formation of rhombohedral and tetragonal phases. Due to the low Fe content, an oxygen non-stochiometry is only expected to a small extent in these materials after synthesis in air. [102, 173] According to the literature, a metastable cubic $SrMnO_{3-\delta}$ phase can be formed in air if the synthesis temperature is 1525 °C or higher (most likely due to reduction and Mn^{3+} formation), but in all other cases, a hexagonal phase is formed. [173] As the synthesis temperature within this work is below 1525 °C, the hexagonal structure observed in the X-Ray diffractograms of $SrMnO_3$ is in good agreement with the literature. While the phase with x = 0.05 is still hexagonal, a rhombohedral structure is formed for x = 0.15 which shows essentially the same diffraction pattern as γ-$SrMnO_3$. [92, 233] Further rhombohedral stacking variants have been reported in the literature for phases with similar composition. [102] If $\boldsymbol{x}$ is **between 0.33 and 0.85**, cubic phases are formed. The XRD data within this work is in good agreement with data for previously studied perovskites with x = 0.33, 0.5, and 0.67 by Fawcett *et al.*, as the refined unit cell parameter a for the cubic cell is very similar (see Fig. 4.21). The perovskite with x = 0.85 is a special case as we can observe a cubic structure, but the deviation of the refined lattice parameter a from Vegard's law might indicate an onset of a distortion, and the cubic phase might be metastable. This seems also reasonable, as cubic, orthorhombic, and tetragonal phases show very similar X-Ray diffraction patterns, and the presence of an orthorhombic distortion, for instance, is usually indicated in the XRD patterns by the occurrence of additional reflections with small intensity (compare section 4.1), which may be below the detection limit for small degrees of distortion. Neutron diffraction experiments could help clarify these minor differences in the future and also allow distinguishing different oxygen vacancy ordered phases. [231] For **Fe-rich** compositions ($\boldsymbol{x = 0.95\text{-}1.00}$), the X-Ray diffractograms clearly show that tetragonal and orthorhombic phases are formed, [92] which is in good agreement with the literature. [61, 231]

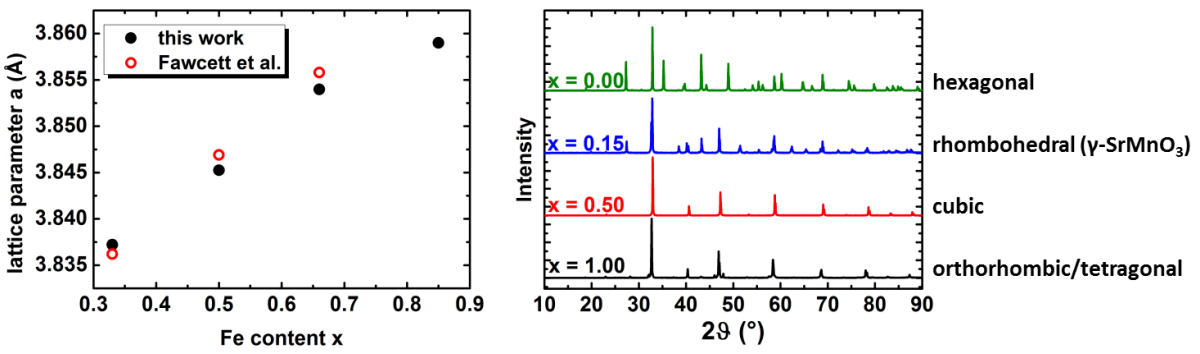

Fig. 4.21. Refined lattice parameters a for cubic unit cells (left) from this work in comparison to data by Fawcett *et. al.* [232] Right: Exemplary X-Ray diffraction patterns for the four different structure types observed in the $SrMn_{1-x}Fe_xO_{3-\delta}$ solid solution phase space with the Fe content x indicated. Adapted from Vieten *et al.* – for XRD patterns of all phases and detailed diffraction pattern indexing, please refer to the supporting information of that publication. [92]

Initial non-stochiometry δ_0

As mentioned before, most of the phases presented herein show an initial non-stochiometry δ_i. This value ranges between 0.19 and 0. [i] As only the change in non-stochiometry $\Delta\delta$ is determined through thermogravimetry, the value δ_i needs to be added to the measured $\Delta\delta$ in order to determine the absolute oxygen non-stoichiometry δ. The δ_i values used (see table 4.2) are partially taken from the literature, and interpolated in-between literature values. These values may of course not be accurate for all cases, and for many other phases discussed later within this work, literature data may not be available. Therefore, we present a different method to obtain δ_i from the entropy data later within this work (see section 5.1.1), but its accuracy is limited. Alternatives include iodometry, thermogravimetric reduction using hydrogen/argon mixtures, or volumetric gas analysis. [234]

Table 4.2. Initial non-stochiometry values δ_0 for $SrMnO_{3-\delta} - SrFeO_{3-\delta}$ solid solutions according to the literature and interpolated data. Adapted from Vieten *et. al* (supporting information). [92]

Composition	δ_i value	Source
$SrFeO_{3-\delta}$	0.19	Takeda et al. [61]
$SrMn_{0.05}Fe_{0.95}O_{3-\delta}$	0.19	(linear interpolation)
$SrMn_{0.15}Fe_{0.85}O_{3-\delta}$	0.18	(linear interpolation)
$SrMn_{0.33}Fe_{0.67}O_{3-\delta}$	0.16	Fawcett et al. [232]
$SrMn_{0.5}Fe_{0.5}O_{3-\delta}$	0.11	Fawcett et al. [232]
$SrMn_{0.67}Fe_{0.33}O_{3-\delta}$	0.08	Fawcett et al. [232]
$SrMn_{0.85}Fe_{0.15}O_{3-\delta}$	0.03	(linear interpolation)
$SrMn_{0.95}Fe_{0.05}O_{3-\delta}$	0.01	(linear interpolation)
$SrMnO_{3-\delta}$	0.00	Rørmark et al. [173]

Thermodynamics as a function of δ

The thermodynamic properties of the $SrMnO_{3-\delta} - SrFeO_{3-\delta}$ phases are determined from thermogravimetric data as a function of $\Delta\delta$ using the van't Hoff method, and $\Delta\delta$ is converted to δ using $\delta = \Delta\delta + \delta_i$ and the δ_i values from table 4.2. For the $SrMn_{0.05}Fe_{0.95}O_{3-\delta}$ phase, no thermogravimetric data is recorded due to the relatively high amount of a non-perovskite side phase present according to XRD. The resulting values for the enthalpy $\Delta H(\delta)$ are shown in Fig. 4.22. Comparing $SrFeO_{3-\delta}$ and $SrMnO_{3-\delta}$, it can be seen that the redox enthalpy of $SrMnO_{3-\delta}$ per mol of oxygen O is about twice as high as for $SrFeO_{3-\delta}$, which is in good agreement with DFT data and experimental data in the literature. [117, 173, 235] Data for $SrFeO_{3-\delta}$ and $SrMnO_{3-\delta}$ measured over a wider δ

[i] In fact, a certain amount of oxygen vacancies will also be present in the $SrMnO_{3-\delta}$ sample, but it is negligible according to the literature in air at room temperature in equilibrium.

range is included in section 5.13. The data on solid solutions is of particular importance. The redox enthalpy shows a strong dependence on δ in these cases. With increasing δ, $\Delta H(\delta)$ increases. This can be explained with the before-mentioned preferential reduction of Fe^{4+} over Mn^{4+}. At low values of δ, the oxygen loss is mainly driven by the reduction of Fe^{4+}, and the redox enthalpy change is close to the values for $SrFeO_{3-\delta}$. As δ increases, the redox enthalpy increases, as a lower amount of Fe^{4+} is available and the reduction reaction is governed more and more by the reduction of Mn^{4+}, yielding $\Delta H(\delta)$ values closer to those of $SrMnO_{3-\delta}$. Over a wide range of compositions, the observed change in non-stoichiometry, moreover, cannot be explained with the reduction of just one of the two species, but a certain extent of simultaneous Fe^{4+} and Mn^{4+} reduction must be present. The system does not act like Mn-doped $SrFeO_{3-\delta}$ or Fe-doped $SrMnO_{3-\delta}$, but like a solid solution with a mixture of the properties of both materials. This may not be the case for all the materials studied within this work, but at least in the case of this system, our assumption of forming a solid solution which exhibits δ-dependent changes in the redox properties due to the preferential reduction of one of the species (here Fe^{4+}) appears very reasonable.

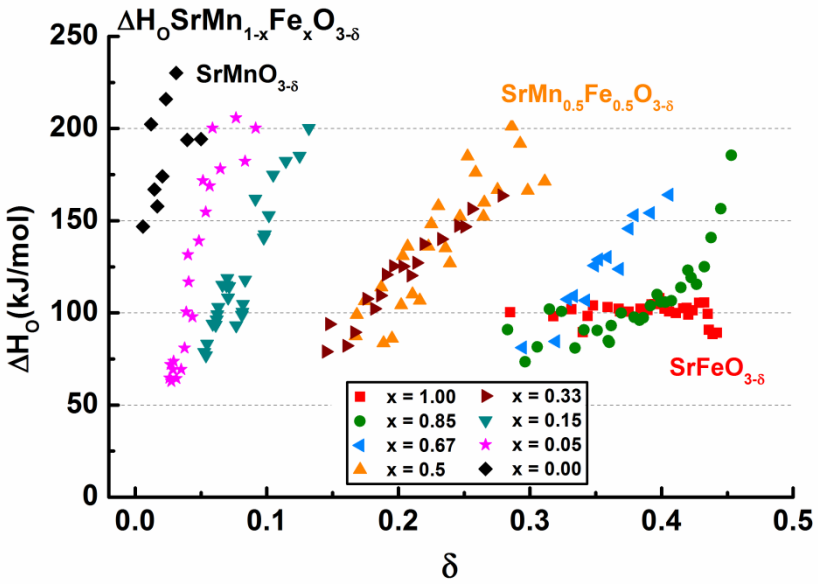

Fig. 4.22. Measured redox enthalpy change in terms of kJ per mol of oxygen O as a function of the non-stoichiometry δ in $SrMn_{1-x}Fe_xO_{3-\delta}$ perovskite solid solutions ($\Delta H(\delta)$) for different Fe contents x. Data is obtained from thermogravimetric scans in equilibrium at different temperature and oxygen partial pressure levels ($T = 400 - 1200$ °C, $p_{O_2} = 10^{-4} - 0.9$ bar). Graph adapted from Vieten *et al.* [92] For raw thermogravimetric data, please refer to the supporting information of the journal publication. [92]

The increase in redox enthalpies is gradual, meaning that there is a region in solid solutions where both Mn^{4+} and Fe^{4+} are reduced simultaneously and the redox enthalpy is between the values of $SrFeO_{3-\delta}$ and $SrMnO_{3-\delta}$. This observation can be explained by assuming two individual and independent sub-lattices in the solid solution consisting of $SrFeO_{3-\delta}$ and $SrMnO_{3-\delta}$ using a defect model. At low δ values, only the $SrFeO_{3-\delta}$ sub-lattice is reduced, whereas the $SrMnO_{3-\delta}$ sub-lattice is redox-passive. At the onset of the reduction of the $SrMnO_{3-\delta}$ sub-lattice, the redox enthalpy gradually increases and oxygen vacancies are formed in both sub-lattices. The $SrFeO_{3-\delta}$ reduction eventually reaches a saturation level, whereas $SrMnO_{3-\delta}$ is further reduced until $\delta = 0.5$. The redox enthalpy is then governed by the reduction of Mn^{4+} to Mn^{3+}. This is behavior is explained in Eqn. 2.20 through 2.23 in section 2.5, and our experimental data confirms the theoretical considerations presented there. Fig. 4.23 illustrates the change in $\Delta H(\delta)$ per mol of oxygen O. The region with simultaneous reduction of Fe^{4+} and Mn^{4+} (green area in Fig. 4.24) can be observed for all perovskite solid solutions shown in Fig. 4.22. Moreover, the region with preferential Fe^{4+} reduction (red area in Fig. 4.23) and the onset of Mn^{4+} reduction are visible for the sample with x = 0.85, as the Fe content is very high in this case and high values of δ are required to reduce Mn^{4+} significantly. However, we do not observe the full region of δ in our initial study, and therefore never record a curve as in Fig. 4.23 showing all three regimes of $\Delta H(\delta)$. Therefore, more data on other perovskite materials is shown in section 5.1, which confirms the statements made here. One of the main findings of this work is that the redox enthalpy of perovskite solid solutions depends on δ and that this behavior can be explained using a model of two individual perovskite sub-lattices as presented here. Our initial study on $SrMnO_{3-\delta}$ – $SrFeO_{3-\delta}$ confirms the δ-dependence of ΔH and indicates that the change in ΔH as a a function of δ might be explained by assuming two individual perovskite sub-lattices with different redox thermodynamics. However, this statement needs to be supported with more accurate thermodynamic data over a wider range of δ.

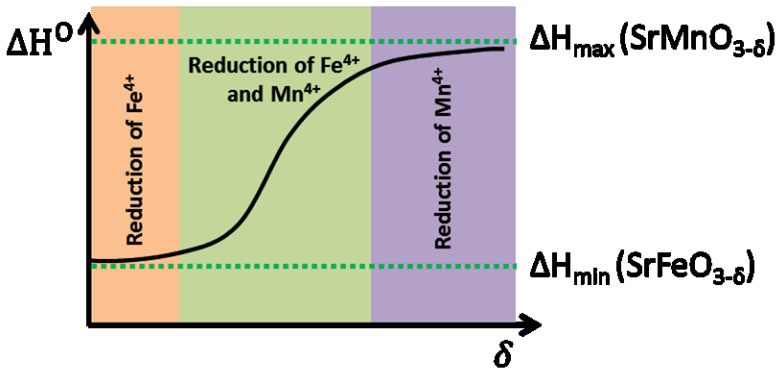

Fig. 4.23. Assumed redox behavior of $SrMnO_{3-\delta}$ – $SrFeO_{3-\delta}$ perovskite solid solutions based on experimental data and the considerations in chapter 2.5 (compare Fig. 2.8). The illustrative graph shows the redox enthalpy change per mol of oxygen as a function of the non-stoichiometry δ.

The change in redox enthalpy ΔS (see Fig. 4.24), is also dependent on the non-stoichiometry δ, as in all non-stoichiometric oxides. This is due to the change in configurational entropy, which depends on the amount of vacancies which are present in the lattice (see section 2.5), and can be explained using a dilute species model. [129, 132] The redox enthalpy change in $SrFeO_{3-\delta}$ is in good agreement with this model, as it decreases as δ approaches its limiting value 0.5 (compare also section 4.1 and Fig. 4.10 and 4.11). For solid solution phases, ΔS appears to be significantly lower than as expected by the dilute species model at low values of δ. This behaviour may be explained by assuming that only one of the two individual perovskite sub-lattices is redox active in those cases, which decreases the amount of possible vacancy configurations. This hypothesis is confirmed later in section 5.1 using data for more perovskite solid solutions recorded over a larger range of δ.

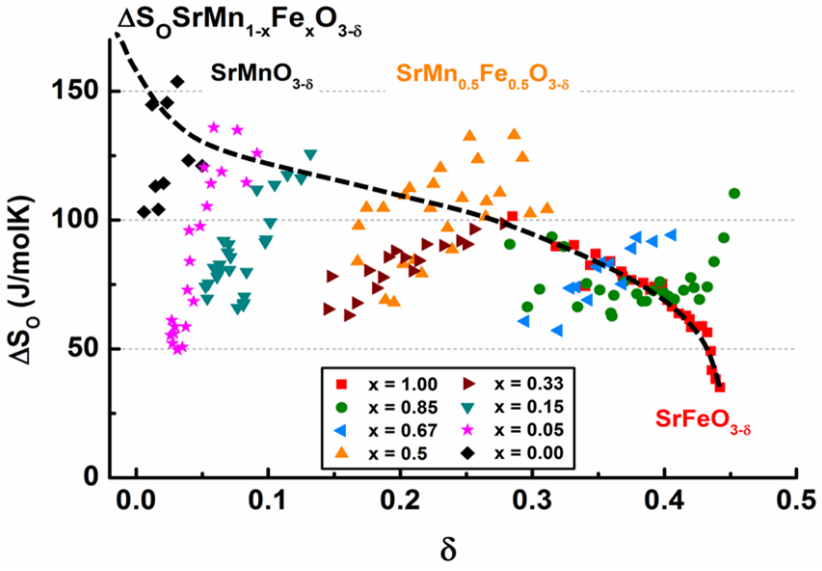

Fig. 4.24. Measured redox entropy change in terms of J per mol of oxygen O and Kelvin as a function of the non-stoichiometry δ in $SrMn_{1-x}Fe_xO_{3-\delta}$ perovskite solid solutions ($\Delta S(\delta)$) for different Fe contents x. $\Delta S(\delta)$ according to the dilute species model illustrated qualitatively using the dashed line. Graph adapted from Vieten *et al.* [92]

In summary, it has been shown within this section that perovskite solid solutions can be formed in high purity with any mixture ratio in the reference systems $CaTiO_{3-\delta}$ - $CaMnO_{3-\delta}$ and $SrMnO_{3-\delta}$ - $SrFeO_{3-\delta}$ using a citric acid auto-combustion method, which has been modified to allow the preparation of Ti-based precursors. The lattice constants follow Vegard's law and the formation of different perovskite phases can be explained using the Goldschmidt tolerance factor. The redox thermodynamics in $SrMnO_{3-\delta}$ - $SrFeO_{3-\delta}$ systems depend on the non-stoichiometry δ and indicate the preferential reduction of Fe^{4+} w.r.t. Mn^{4+}, which can be explained by assuming two individual sub-lattices in the perovskite solid solutions.

4.4 Tolerance factor engineering as a means to control the perovskite crystal structure

In the previous section, we have shown the occurrence of different perovskite phases and explained these phases using the Goldschmidt tolerance factor. In this section, we show more in detail where the stability limits of different perovskite phases are located in terms of their tolerance factors, and we show how phase transitions during the redox reactions can be avoided or induced on purpose by choosing the tolerance factors of the initial perovskite phases appropriately ("tolerance factor engineering"). This requires knowing the coordination number of the species in the perovskite, and we justify our calculation method of the tolerance factor as introduced in section 2.2 in the following by studying the reference system $SrMnO_{3-\delta}$ - $SrFeO_{3-\delta}$.

Coordination of the *A* site species in perovskites

For $SrMnO_{3-\delta}$ - $SrFeO_{3-\delta}$ solid solutions, we observed that Fe^{4+} is reduced preferentially. This means that when the oxygen non-stoichiometry δ is created in the perovskite, only Fe^{4+} is reduced initially until all Fe is present as Fe^{3+}. Only if no more Fe^{4+} is available, Mn^{4+} is reduced to Mn^{3+}. The tolerance factor is calculated as explained in section 2.2, and in non-stoiochiometric phases, the slightly smaller radius of oxygen vacancies is accounted for. [89] In the following, we justify the initial assumption in section 2.2 that the tolerance factor is calculated using *A* species with mixed 10- and 12-fold coordination (CN12/CN10 = 80:20).

The calculated tolerance factors in the $SrMn_{1-x}Fe_xO_{3-\delta}$ system are shown for different values of δ and different Fe contents x in Fig. 4.25. The tolerance factor is calculated both for a pure CN of 12 of the Sr^{2+} ions (dashed light blue lines), as well as for the mixed CN12/CN10 coordination assumed within this work (solid black line). The blue horizontal line indicates where t = 1.00, and the stability regions of different perovskite phases according to the literature and section 2.2 of this work are shown on the right. The transition region between cubic and rhombohedral or hexagonal phases is not defined strictly. For low values of δ, the tolerance factor gradually decreases with increasing Fe content due to the increasing average transition metal ionic radius. For higher values of δ, there are regions in which the tolerance factor does not depend on the Fe content, as both Fe^{3+} and Mn^{3+} have the same ionic radius. [88] Data for the experimentally prepared phases has been added to this graph (red and green triangles, for CN12 and CN10/CN12 = 0.8, respectively). For this purpose, the determined values δ_0 from table 4.2 are used to show the tolerance factor of these phases after synthesis in air in equilibrium.

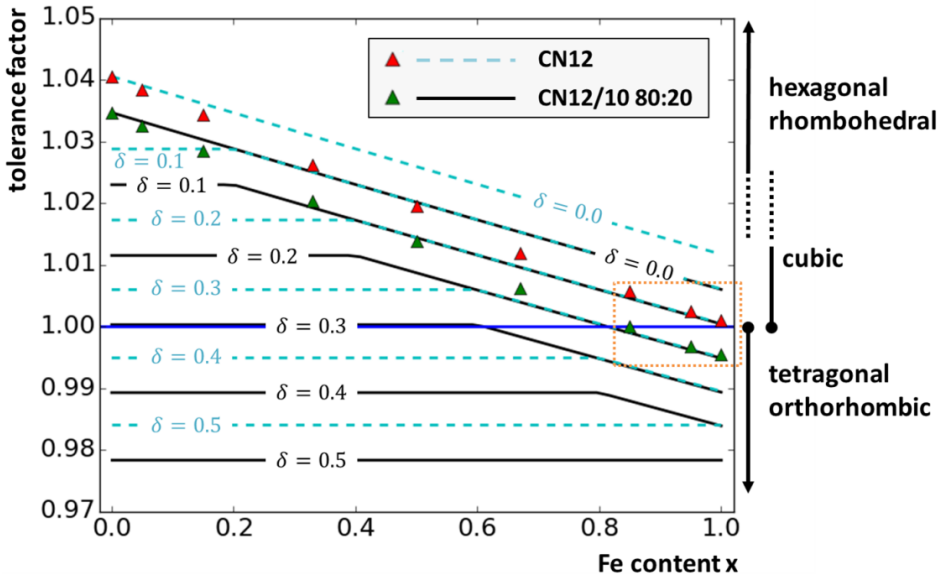

Fig. 4.25. Calculated tolerance factors for $SrMn_{1-x}Fe_xO_{3-\delta}$ perovskites for different Fe contents x and different non-stoichiometry values δ assuming a coordination number (CN) of 12 for Sr^{2+} (dashed blue lines and red triangles) in one case and a mixed CN of 12 and 10 (80 % of the Sr^{2+} in 12-fold coordination, 20 % in 10-fold coordination, solid lines and green triangles) in the other case. The δ_i values from table 4.2 are used to calculate the tolerance factors of the synthesized $SrMn_{1-x}Fe_xO_{3-\delta}$ phases in equilibrium with ambient air at room temperature (triangles). The mixed CN leads to tolerance factors in better agreement with our experimental data, especially for high Fe contents (highlighted in orange box). These assumptions are purely empirical and used only to calculate the tolerance factor.

It can clearly be seen that for CN12, the tolerance factor of all phases is above 1, whereas at CN10/CN12 = 0.8, phases with high Fe content show tolerance factors below 1. If we consider the $SrFeO_{3-\delta}$ phase only, which is formed as $SrFeO_{2.81}$ according to the literature, [61] using CN12 for Sr^{2+} would result in a near-ideal cubic perovskite structure. There would be no reason to assume that this phase shows an orthorhombic or tetragonal distortion, as the ratio of radii is ideal for a cubic structure according to the tolerance factor. However, we observe a mixture of tetragonal and orthorhombic phases, which cannot be explained with a t near 1. The phases we observe are in good agreement with literature studies on the tetragonal phase $Sr_8Fe_8O_{23}$ and the orthorhombic phase $Sr_4Fe_4O_{11}$. [99] If we assume in our calculation that 20 % of the Sr^{2+} is in 10-fold coordination and calculate the tolerance factor based on the average ionic radius of Sr^{2+} in this case, we reach tolerance factors below one, which agree well with the observed distortion. Moreover, looking at the phases with lower Fe content x, a tolerance factor of 1 is reached if x = 0.85, which is exactly where we observe a transition to a cubic structure. Therefore, we empirically reach the most accurate results if we assume this mixed coordination number in our calculation of the tolerance factor, a property which of course is not necessarily in line with the actual crystal structure and coordination environment in these phases. Temperature effects can also not be used to explain this behavior, as

the tolerance factors are calculated for 0 K, and any increase in temperature would only lead to an increase in the tolerance factor which would make an orthorhombic or tetragonal structure of $SrFeO_{3-\delta}$ even less likely for CN12. [93] Moreover, the value of δ_i is known accurately enough to justify our statements, as our thermogravimetric scans show a decrease in ΔS towards $\delta = 0.5$ which can only be explained if the value of δ_i assumed to calculate δ from the measured $\Delta\delta$ is correct. Moreover, literature studies support the assumed δ_i value for $SrFeO_{3-\delta}$, [61] and the tetragonal phase $Sr_8Fe_8O_{23}$ shows an even lower δ, but does not form a cubic perovskite in equilibrium in air at room temperature. [99] Furthermore, the assumed preferential reduction of Fe^{4+} does not affect the tolerance factor for the pure $SrFeO_{3-\delta}$ phase.

Based on these considerations, we can only assume that the tolerance factor of the actual phases must be lower than when using values for CN12. This, of course, could also be explained with inaccuracies of the ionic radii. [88] The ionic radius in any case is just a value which is determined in a certain crystal environment, and deviations in different materials may occur. By assuming a mixed CN12/CN10, we reach a slightly lower value for the radius of the *A* species, and empirically reach a good agreement with our experimental data on the $SrMnO_{3-\delta}$-$SrFeO_{3-\delta}$ system. We extend this methodology to all perovskites within this work due to the lack of accurate literature data on phase formation and non-stoichiometry, but this may of course not always yield a correct result. This method is purely empirical and only applied for the purpose of tolerance factor calculation. One could argue that the tolerance factor is not the only factor determining the crystal structure, that the crystal ionic radii may not be known accurately enough, or that assuming such a mixed coordination is unphysical. [95] Instead, one could also ignore these slight deviations from the idealized tolerance factor model in terms of phase formation, as we are only interested in having a control over the crystal structure by maintaining a constant tolerance factor, which means that the absolute values of t are less relevant than changes in t. Nevertheless, the here-introduced method for calculating the tolerance factor leads to more accurate results, at least for the $SrMnO_{3-\delta}$-$SrFeO_{3-\delta}$ system. Therefore, we apply this method throughout this work.

Stability limits of rhombohedral/hexagonal and cubic perovskites

In section 4.3.2 it has been shown that the type of perovskite structure formed depends on the Goldschmidt tolerance factor and the related stability limits of different perovskites. In good agreement with the literature, [93, 173, 236] it has been demonstrated that ideal (undistorted) perovskite lattices are formed if the tolerance factor t is 1 or slightly higher, whereas orthorhombic and tetragonal perovskite phases are formed if t is below 1, and rhombohedral and hexagonal phases form if t is above ≈ 1.02-1.03. In section 2.2, we also discussed the possibility of phase transitions between these perovskite phases during the redox reaction if the tolerance factor changes due to a

change in the ionic radii of the transition metals in the perovskite. This behavior can be observed for $SrMnO_{3-\delta}$ - $SrFeO_{3-\delta}$ solid solutions with low Fe content. [92] Fig. 4.26 shows a thermogravimetric scan of the sample $SrMn_{0.95}Fe_{0.05}O_{3-\delta}$ at different oxygen partial pressure and temperature levels. As long as the mass changes are small (i.e., δ does not deviate strongly from the initial δ_0), an equilibrium state is reached while the temperature and oxygen partial pressure are constant ($\Delta T/dt = 0$ and $\Delta p_{O_2}/dt = 0 \rightarrow \Delta m/dt = 0$). Only this equilibrium data is used for the extraction of thermodynamic properties (see section 4.3.2). However, for strong reduction extents, the mass change increases suddenly and an equilibrium state is not reached within the given amount of time. This indicates a phase change, as the re-arrangement of atoms in this case is expected to require more time than the creation of vacancies in a purely non-stoichiometric reduction reaction.

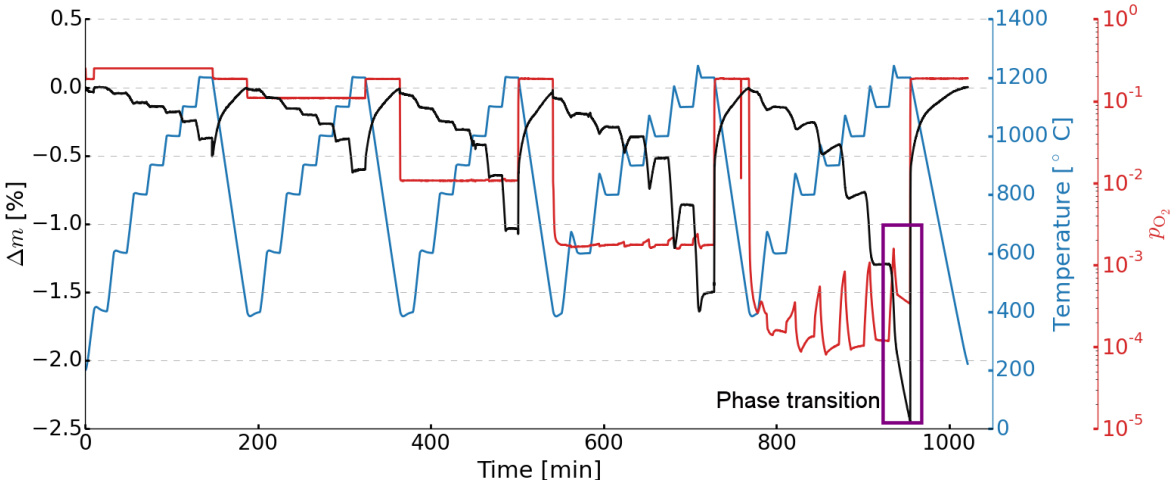

Fig. 4.26. Thermogravimetric scan of the $SrMn_{0.95}Fe_{0.05}O_{3-\delta}$ perovskite at different oxygen partial pressure (p_{O_2}) and temperature levels. An equilibrium state is reached for small values of mass change (Δm), whereas the strong non-equilbrium mass loss indicates a phase transition (highlighted in purple). Graph taken from Vieten *et al.* [92]

In a separate experiment, this phase change is induced at 1200 °C under Ar in the thermobalance, and the sample is cooled down to room temperature under Ar at the maximum cooling rate of the thermobalance after the phase transition is completed (i.e., $\Delta m/dt \rightarrow 0$). By this means, the reduced phase is preserved in a metastable state. An XRD analysis of this sample compared to its initial state and of a sample with x = 0.50 for comparison (Fig. 4.27) shows a good agreement between the X-Ray diffraction patterns of the metastable reduced phase and the phase with x = 0.50 in its initial ("oxidized") state. This shows that a phase transition from a hexagonal to a cubic perovskite phase occurred, as expected according to the tolerance factor, which is 1.033 for the oxidized phase with Fe content x = 0.05 (δ = 0, perovskite), and 0.978 for a completely reduced phase at δ = 0.5 (brownmillerite). The phase change occurs at $\delta \approx 0.1$ and a calculated tolerance factor of 1.023. Moreover, the strong mass change in Fig. 4.26 may imply that the cubic phase can be reduced more

readily than the hexagonal perovskite, i.e., the vacancy formation energy in this structure is lower, which means that the redox enthalpy change ΔH is lower. This has been suggested by Curnan *et. al.* through DFT calculations, which show that oxygen vacancy formation is less favorable in orthorhombic or rhombohedral perovskites w.r.t. cubic perovskites. [92, 237] Our experimental data appears to agree well with these theoretical predictions.

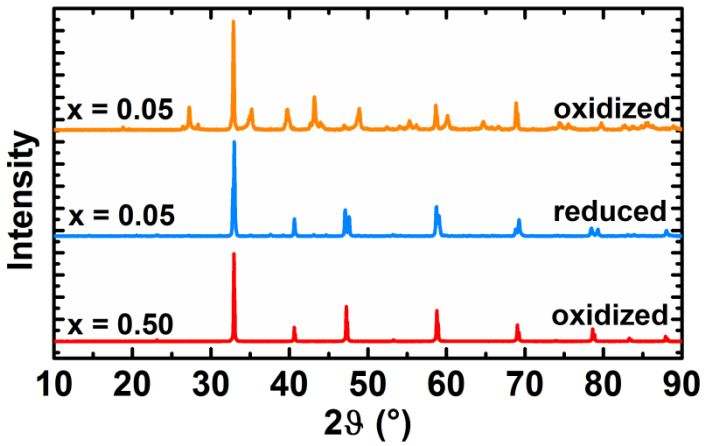

Fig. 4.27. X-Ray diffractograms of perovskite phases in the $SrMn_{1-x}Fe_xO_{3-\delta}$ system under different conditions with indicated Fe content x. The phase with $x = 0.50$ shows a cubic structure after synthesis in air ("oxidized", compare Fig. 4.21), whereas the as-synthesized phase with $x = 0.05$ has a hexagonal crystal structure. The latter material can be converted into a cubic phase through reduction, which can be preserved under ambient temperature and pressure in a metastable state. Taken from Vieten *et al.* [92]

Stability limits of orthorhombic perovskites

We have successfully shown that phase transitions between different perovskites may occur during reduction or oxidation, and we demonstrated that the stability limit of the cubic phase is defined by a tolerance factor slightly higher than 1.02. This, of course, may depend on the type of perovskite solid solution and the specific redox energetics in each system. However, many perovskites with rare earth metals on the *A* site and transition metals on the *M* site may show considerably low tolerance factor values, as the lanthanide ionic radii are smaller than those of most alkali earth metals. As mentioned before in section 2.2, a perovskite may not be formed if the tolerance factor is too low and other structure types are more favorable. In the following, we try to elucidate the stability limit of orthorhombic perovskite phases using $EuFeO_3$ and $EuCuO_3$ as reference materials, which show calculated tolerance factors of 0.907 and 0.879, respectively, assuming no oxygen non-stoichiometry being present after synthesis in air. The X-Ray diffraction patterns resulting from synthesis attempts of these two phases reveal significant differences (see Fig. 4.28).

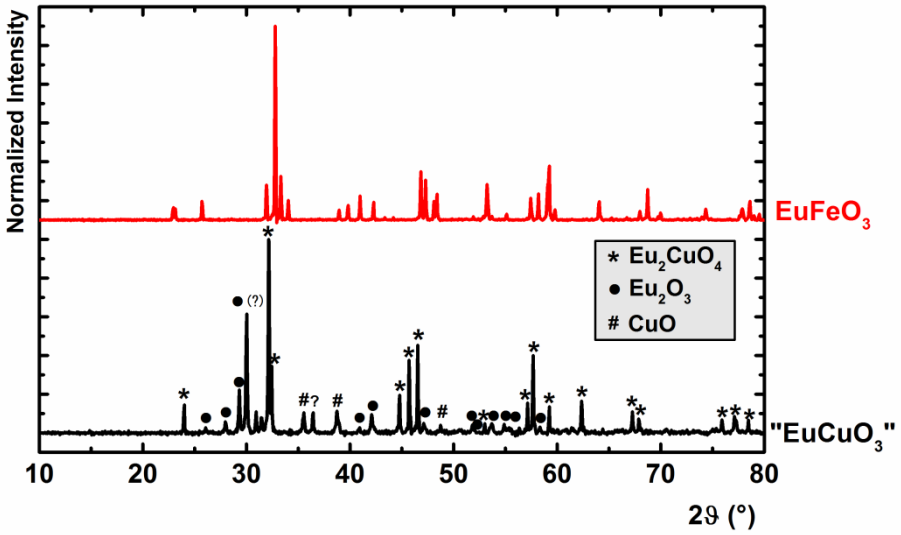

Fig. 4.28. X-Ray diffraction patterns of $EuFeO_3$ showing a pure orthorhombic perovskite, and the result of an attempt to synthesize $EuCuO_3$, which yields a mixture of Eu_2CuO_4, Eu_2O_3, and CuO, as indicated by the respective markers on the assigned reflections. $EuFeO_3$ has a calculated tolerance factor of $t = 0.907$, whereas the tolerance factor of $EuCuO_3$ is significantly lower ($t = 0.879$) due to the larger ionic radius of Cu^{3+} w.r.t. Fe^{3+}.

While the $EuFeO_3$ sample could be prepared successfully with no side phases (compare: literature data [238]), $EuCuO_3$ could not be prepared, and a mixture of Eu_2CuO_4, Eu_2O_3, and CuO is formed instead. Therefore, we can conclude that the stability limit of orthorhombic perovskites (at least in this perovskite system) is between 0.879 and 0.907. The Cu^{3+} in "$EuCuO_3$" may be partially reduced to Cu^{2+} in equilibrium at room temperature, as the calculated redox enthalpy per mol of oxygen for the reduction of $EuCuO_3$ to $Eu_2Cu_2O_5$ is rather low (DFT: 105 kJ/mol$_O$, data based on section 5.2/Materials Project [117], compare: $SrFeO_3$ with 87 kJ/mol$_O$ showing a $\delta_0 = 0.19$), which could lead to a slightly lower tolerance factor than 0.879. Different perovskite systems may have different stability limits, but within this work we from now on generally assume that compositions with $t < 0.90$ may not form stable perovskite phases. While we studied the stability limit of orthorhombic phases, we cannot give any specific stability limits for tetragonal phases. From the data on $SrMnO_{3-\delta}$ – $SrFeO_{3-\delta}$ solid solutions, it appears that tetragonal phases are formed if the tolerance factor is only slightly below 1.00, i.e., the degree of distortion is low. However, it is questionable whether this applies to all perovskite systems.

As a side note, it is worth discussing that perovskites with low tolerance factor (0.90 to approx. 0.95) may form a different type of orthorhombic structure than those with higher tolerance factor such as $CaMnO_{3-\delta}$. The so-called post-perovskite structure has first been discussed as a perovskite variant formed in earth's mantle under high pressure as a polymorph of $MgSiO_3$. [106, 107] However, this structure type can not only be formed at high pressures, but other perovskite systems may also show the same structure under ambient conditions, such as $CaIrO_3$. [239] The calculated tolerance factor of

$CaIrO_3$ is 0.924, and one could assume that the formation of such post-perovskite phases is tolerance-factor dependent. According to the literature, the post-perovskite $CaIrO_3$ crystallizes in space group $CmCm$ (No. 63, orthorhombic), [240] whereas the perovskite $EuFeO_3$ exhibits a structure which can be indexed in space group $Pbnm$ (No. 62, orthorhombic), [238] and the diffraction pattern of the literature structure of $EuFeO_3$ agrees well with our result. Therefore, a post-perovskite has not been observed, and the tolerance factor may not be a useful indicator to predict perovskite/post-perovskite formation. Moreover, Keawprak *et. al*. show that the preparation of post-perovskite $CaIrO_3$ in a single phase is very difficult in ambient atmosphere, and these authors report long sintering times for the formation of this phase. [239] Therefore, the preparation of these phases or inducing such phase transitions most likely has no practical application in two-step thermochemical cycles, but the possibility that post-perovskite phases are formed should always be kept in mind, as there may be systems in which this phase is formed more readily.

We now discussed the stability limits of orthorhombic and tetragonal perovskites, cubic perovskites, and rhombohedral/hexagonal perovskites, and found a relation between those and the Goldschmidt tolerance factor t. By mixing different alkali earth metal species on the A site, the formation of such phases may be controlled. Moreover, the expected decrease in the tolerance factor value due to reduction can be estimated. It is therefore possible to prepare perovskites which are stable in a large range of non-stoichiometry δ without showing phase transitions, allowing fast and reversible redox reactions. To accommodate the increased ionic radii of the transition metal cations in their reduced states, a tolerance factor around 1 or slightly above, but below 1.02 should be chosen. By this means, cubic perovskites are formed, which show a gradual orthorhombic or tetragonal distortion during reduction, but they neither decompose, nor form hexagonal or rhombohedral structures according to our data on some reference systems.

Potentially beneficial properties of phase transitions

Despite the main strategy of perovskite design within this work being based on the preparation of perovskites with high chemical stability, the effect of a targeted induction of phase transitions shall be studied briefly in the following as an outlook and motivation for future studies. For this purpose, the perovskite $Ca_{0.125}Sr_{0.875}Ti_{0.125}Mn_{0.875}O_3$ is synthesized, which should be on the verge of a phase transition at room temperature in air according to its tolerance factor t = 1.025. It should therefore form a hexagonal or rhombohedral structure, but a slight increase in the average M ionic radius should be enough to induce a phase change to a cubic perovskite. Fig. 4.29 shows that the material behaves exactly as expected. After synthesis, a mixture of a rhombohedral and a cubic phase is formed, which shows that both phases must be very similar in their formation enthalpy. After heating the sample under Ar to induce a phase transition and cooling the sample down quickly under Ar (compare Fig. 4.27), the metastable cubic phase is preserved.

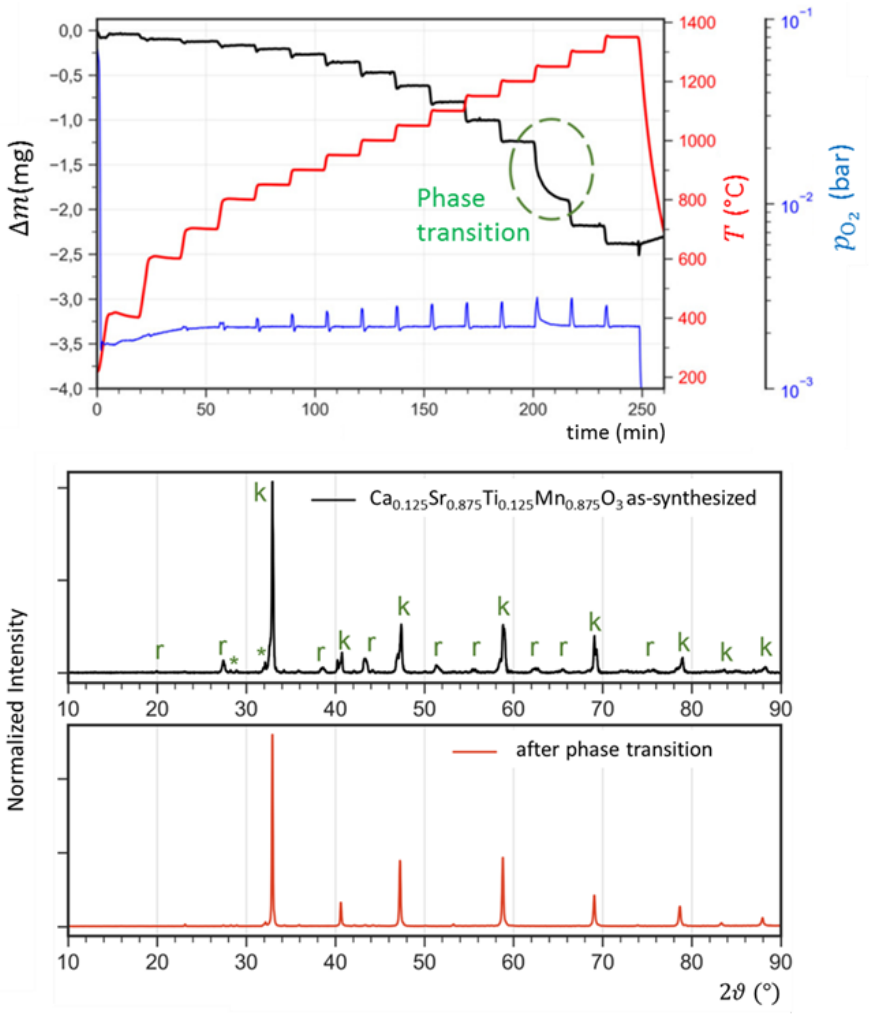

Fig. 4.29. X-Ray diffraction patterns of $Ca_{0.125}Sr_{0.875}Ti_{0.125}Mn_{0.875}O_3$ as-synthesized in air (bottom), and after reduction and quick cool-down under Ar in a thermobalance (top, initial mass: 110.64 mg). The as-synthesized phase contains both reflections assigned to a cubic (k) and rhombohedral (r) phase, whereas only the reflections of the cubic phase remain after the phase transition. Reflections marked with an asterisk could not be assigned, which indicates the formation of minor impurities. Adapted from Lebendig. [241]

The phase transition occurs at 1200-1250 °C at $p_{O_2} = 2 \cdot 10^{-3}$ bar. According to thermogravimetric data (see Fig. 4.29), the phase transition has its onset at about $\Delta\delta = 0.20$, and most likely, $\Delta\delta = \delta$ due to the high redox enthalpy of alkali earth manganate and titanate perovskites. This corresponds to a tolerance factor of 1.016 assuming Mn^{4+} reduction only, which is a bit lower than in the case of the hexagonal/rhombohedral – cubic phase transition in $SrMnO_{3-\delta}$ - $SrFeO_{3-\delta}$ solid solutions ($t = 1.023$).

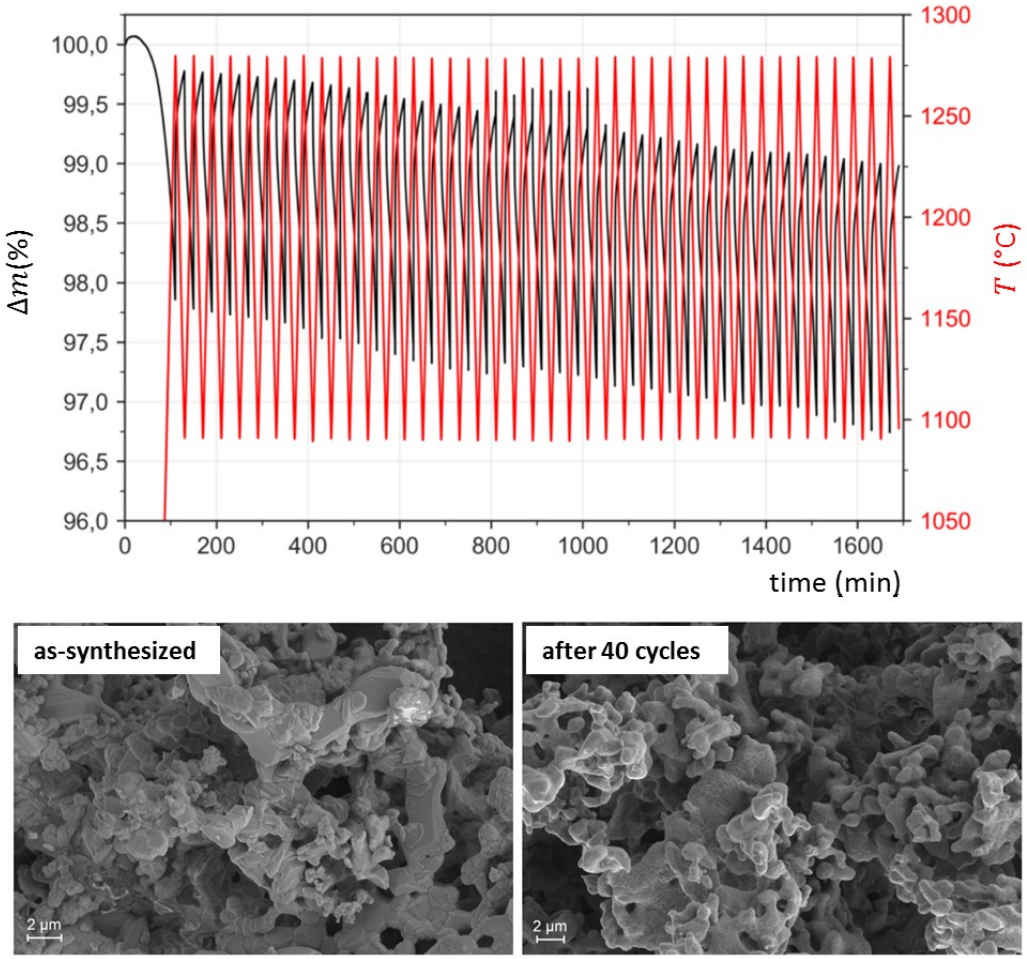

Fig. 4.30. Long term thermogravimetric scan (40 cycles) of $Ca_{0.125}Sr_{0.875}Ti_{0.125}Mn_{0.875}O_{3-\delta}$ (top) with oxidation at 1100 °C under synthetic air:Ar in 90:10 vol% mixture and reduction under Ar at 1280 °C showing a reversible phase transition between cubic and rhombohedral perovskite structures with constant mass change. The absolute value of Δm is subject to an instrument-induced drift which has been observed before and does not reflect an actual mass loss. [179] The microstructure of the samples (bottom) does not change significantly apart from sintering effects and a higher porosity after 40 cycles. Adapted from Lebendig. [241]

Thermogravimetric scans over 40 cycles within the $\Delta\delta$ window in which the phase transition occurs (see Fig. 4.30) do not reveal any measurable degradation of the redox activity, as indicated by the constant Δm. The microstructure of the samples shows sintering a after the long term study according to SEM scans along with what appears to be a higher porosity, but the particle size does not change significantly. The oxidation kinetics measured at $T \geq 500$ °C using relaxation experiments in the thermobalance (see data by Lebendig [241], compare section 4.2) reveal no significant decrease in the oxidation speed with respect to perovskites without phase transition, and the oxidation rate appears to limited by the gas supply only, as it appears to be temperature-independent. Further studies are necessary to characterize the oxidation reaction at lower temperatures. The reduction reaction, however, takes between approx. 5 and 15 min to complete

(compare Fig. 4.29), [241] which is significantly slower than in the case of perovskites without phase transition. The data by Lebendig moreover indicates that the mass change is increased during the phase transition, and preliminary studies using the van't Hoff method indicate that ΔH and ΔS both increase at δ values near the phase transition, [241] and the simultaneous increase of both properties may also be owing to enthalpy-entropy compensation. [197] It is likely that the higher mass change during the phase transition is induced by an increase in entropy and/or, as mentioned before, by a lower vacancy formation energy in the cubic structure, and further studies are required to clarify whether the thermodynamics of such perovskite phase change reactions are favorable for an application in thermochemical cycles. It appears to be a good option to operate a thermochemical cycle around the $\Delta\delta$ value at which the phase transition occurs to benefit from the increased Δm compared to materials without such phase transitions. This may allow decreasing the temperature swing necessary to operate such cycles. The temperature and/or oxygen partial pressure at which such phase transitions occur can be modified through tolerance factor engineering, i.e. by choosing a suitable mixture of constituents in a perovskite solid solution. However, it needs to be clarified whether the slower reduction reaction is a limiting factor for the operation of such cycles.

In summary, it has been demonstrated in this section that the tolerance factor is a good measure to estimate phase stability limits in perovskites. We have shown that by assuming mixed A site coordination, the calculated tolerance factors are in good agreement with our experiments and literature data. Above a tolerance factor of $t \approx 1.02$, rhombohedral and hexagonal perovskites are formed, at $1.00 \leq t \leq 1.02$ cubic perovskites form, and at $t < 1.00$, tetragonal and orthorhombic structures can be observed. Below $t \approx 0.90$, non-perovskite phases are more likely to be formed, and we explored the stability limit of perovskites with low tolerance factors by comparing $EuFeO_{3-\delta}$ to $EuCuO_{3-\delta}$. Within the stability limit of orthorhombic perovskites, we could not observe the formation of post-perovskite phases and the tolerance factor appears to be not sufficient to predict the formation of such structures. The stability limits of different perovskites differ slightly depending on the composition, but we did not observe any significant deviations from the above-stated stability rules. Phase transitions in perovskites can usually be identified by their non-equilibrium state in thermogravimetric scans during reduction in a certain window of non-stoichiometry δ, which is due to the slow kinetics of the reductive phase change. The phase change is fully reversible and does not lead to any observable degradation of the material. Due to the higher mass change during the phase change compared to perovskites without phase changes, the application of perovskites with phase changes could reduce the necessary temperature swing in thermochemical cycles or increase the oxygen storage capacity. Our preliminary results call for further studies of the thermodynamics and kinetics of such reactions. In the framework of this work, however, perovskites without phase changes are used, as their properties are well-known and controllable.

Within chapter 4 of this work, the redox reaction in perovskites and its thermodynamics and kinetics have been discussed in detail by starting with simple perovskites as prototype systems and gradually extending the range of properties by doping and solid solution formation. It has been shown that solid solutions can be formed as long as the differences in ionic radii are small, and that these mixed phases can be prepared in any mixture ratio. We elaborated a general synthesis route applicable for the synthesis of all perovskite solid solutions with in this work. The preparation of solid solutions with two different transition metals M changes their redox thermodynamics, whereas an adjustment of the A site composition can be used to control the tolerance factor and hence the phase stability. To avoid phase transitions, the tolerance factor should be chosen so it allows for an increase in ionic radii during reduction without decomposition of the perovskite, and the tolerance factor should be below 1.02 at all times to avoid phase transitions to rhombohedral or hexagonal phases. With this knowledge, we now have full control over the redox properties of perovskite solid solutions which are relevant for thermochemical cycles, which allows the targeted design of perovskite materials for different applications. In the following chapter, perovskite solid solutions with controlled crystal structure and thermodynamics are studied both theoretically and experimentally, especially with respect to their redox thermodynamics. The tunable properties of perovskites and their effect on the redox properties and phase stability are summarized in Table 4.3.

Table 4.3. Tunable properties of perovskites and their solid solutions and their effect on the redox properties.

Property	Effect
Variation of the A site composition	Change of the →tolerance factor Stabilization or destabilization (avoidance of decomposition reactions by using $Sr_{0.2}Ca_{0.8}MnO_{3-\delta}$ instead of $CaMnO_{3-\delta}$)
M site doping (small compositional variation)	Small changes in the oxygen capacity, dependent on the temperature and oxygen partial pressure Changes in redox kinetics (studied only for $SrFe_{1-x}Cu_xO_{3-\delta}$)
M site solid solution formation	Large changes in all redox properties and the oxygen capacity δ-dependent thermodynamics Significant changes in →ΔH and →ΔS
(Goldschmidt) Tolerance factor (t)	Depends on ionic radii and oxidation state of species Avoidance or induction of phase transitions during reduction/oxidation Change of the →perovskite phase
Differences in ionic radii in solid solutions	Small differences: solid solution formation Large differences (typically > 15%): Phase segregation
Perovskite phase	Describes the type of lattice arrangement of atoms in the perovskite, controlled mainly by the →tolerance factor t: Hexagonal or rhombohedral for t over ≈1.015 – 1.025 Cubic for t between 1.00 and 1.015 Tetragonal or orthorhombic for t between 0.90 and 1.00 Non-perovskite phases more stable typically for t below 0.90 Oxygen vacancy formation occurs more readily in cubic structures
ΔH (change in redox enthalpy upon reduction)	Governs reduction temperature and oxygen partial pressure
ΔS (change in redox entropy upon reduction)	Higher ΔS allows reduction at lower temperature or higher oxygen partial pressure if ΔH remains constant

5. Tolerance factor adjusted perovskite materials design

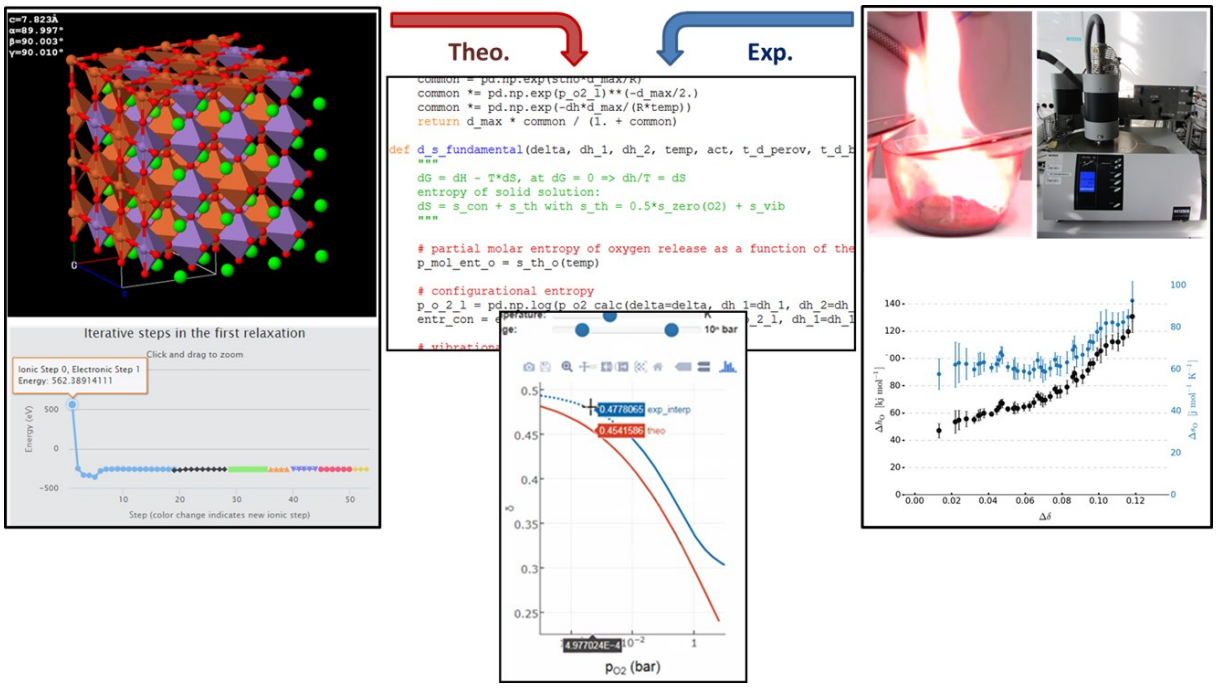

Fig. 5.1. The combination of theoretical data (left, from The Materials Project [116]) and experimental data (right) on perovskite solid solutions and their thermodynamics helps predict the redox properties of such materials and verify these predictions. The theoretical and experimental redox behavior is modelled computationally (middle) using a custom python package.

In the previous chapter, it has been shown that perovskite solid solutions can be prepared in a wide compositional range, and that properties such as the crystal structure and thermodynamics can be tuned by changing the composition of these perovskites. Based on this fundamental understanding of perovskite solid solutions, a wide range of materials is screened experimentally (24 perovskites) and theoretically (> 240 perovskites + the respective brownmillerites). The experimental thermodynamic data is discussed and an empirical model is presented to fit this data. Using density functional theory (DFT), this data is complemented by a theoretical screening, and both datasets are compared and discussed. Based on empirical and theoretical functions, the equilibrium states of these perovskites are calculated in the online tool *RedoxThermoCSP* as a contribution to MPContribs in the infrastructure of Materials Project.

This chapter is partially based upon the following peer-reviewed publication authored by the author of this work:

Vieten, J.; Bulfin, B.; Huck, P.; Horton, M.; Guban, D.; Zhu, L.; Youjun, L.; Persson, K.; Roeb, M.; Sattler, C., Materials design of perovskite solid solutions for thermochemical appplications, Energy & Environmental Science 2019, 12, 1369-1384.

5.1 Experimental materials screening and derivation of empirical models

5.1.1 Synthesis, thermodynamic data and fits

In this chapter, the redox properties of perovskite solid solutions with up to two different elements on both the *A* site and *M* site are discussed. As mentioned in chapter 2, these materials have the general composition $(A'_xA''_{1-x})^{(6-n)+}\left(M'_yM''_{1-y}\right)^{(n-2\delta)+}O_{3-\delta}$. As shown in chapter 4, perovskite solid solutions can be formed in any mixture ratio as long as the differences in ionic radii are small enough. We first discuss the synthesis and thermodynamic properties of these materials based on experimental data for 24 perovskite solid solutions, and later extend the materials screening to theoretical data of over 240 perovskites. The experimental and theoretical results are discussed and compared in order to validate theoretical models, and expressions for $\Delta H(\delta)$ and $\Delta S(\delta)$ are derived both based on experimental and theoretical datasets.

Synthesis and phase formation

The experimental materials screening is limited to alkali earth metal containing perovskites as a reference system with $n = 4$ and $\delta = 0…0.5$ (compare Fig. 2.5). These perovskite systems are mainly applicable as oxygen pump and air separation materials. To evaluate the effect of different tolerance factors (i.e., different *A* site compositions) on the redox thermodynamics, perovskites with three different target tolerance factor values *t* are prepared. In order to compare the results with the reference systems $SrFeO_{3-\delta}$ and $CaMnO_{3-\delta}$ (see chapter 4), we use $t = 1.006$ ($SrFeO_3$) and $t = 0.995$ ($CaMnO_3$). Additionally, three materials with $t = 1.015$ are synthesized, as we have shown before that these materials are at the upper limit of the stability range of the cubic perovskite phase in terms of their tolerance factor *t*. All 24 of the perovskite solid solutions prepared do not show any notable amounts of side phases according to X-Ray diffractograms (see Fig. 5.2). Perovskite solid solutions without miscibility gap have successfully been prepared. Out of the ion pairs used within the experimental screening (Ca^{2+}-Sr^{2+}, $Ti^{3/4+}$-$Mn^{3/4+}$, $Mn^{3/4+}$-$Fe^{3/4+}$, and $Fe^{3/4+}$-$Co^{3/4+}$), none show differences in ionic radii of more than 15 % (max. 12 %), which appears to be the critical limit for unrestricted solid solution formation according to the Goldschmidt rules (compare chapter 4). All XRD patterns show reflections of cubic perovskites or their distorted orthorhombic variants. The diffraction signals are shifted with respect to each other according to the different ionic radii of the species involved. By using tolerance factor engineering as described within this work, it was possible to avoid the formation of hexagonal, rhombohedral or mixed perovskite phases. The Co containing perovskites are synthesized at a maximum temperature of 1100 °C, as described in the experimental

section in chapter 3.1 to avoid side reactions with alumina and melting. All other phases are prepared at up to 1300 °C using the standardized preparation method presented within this work.

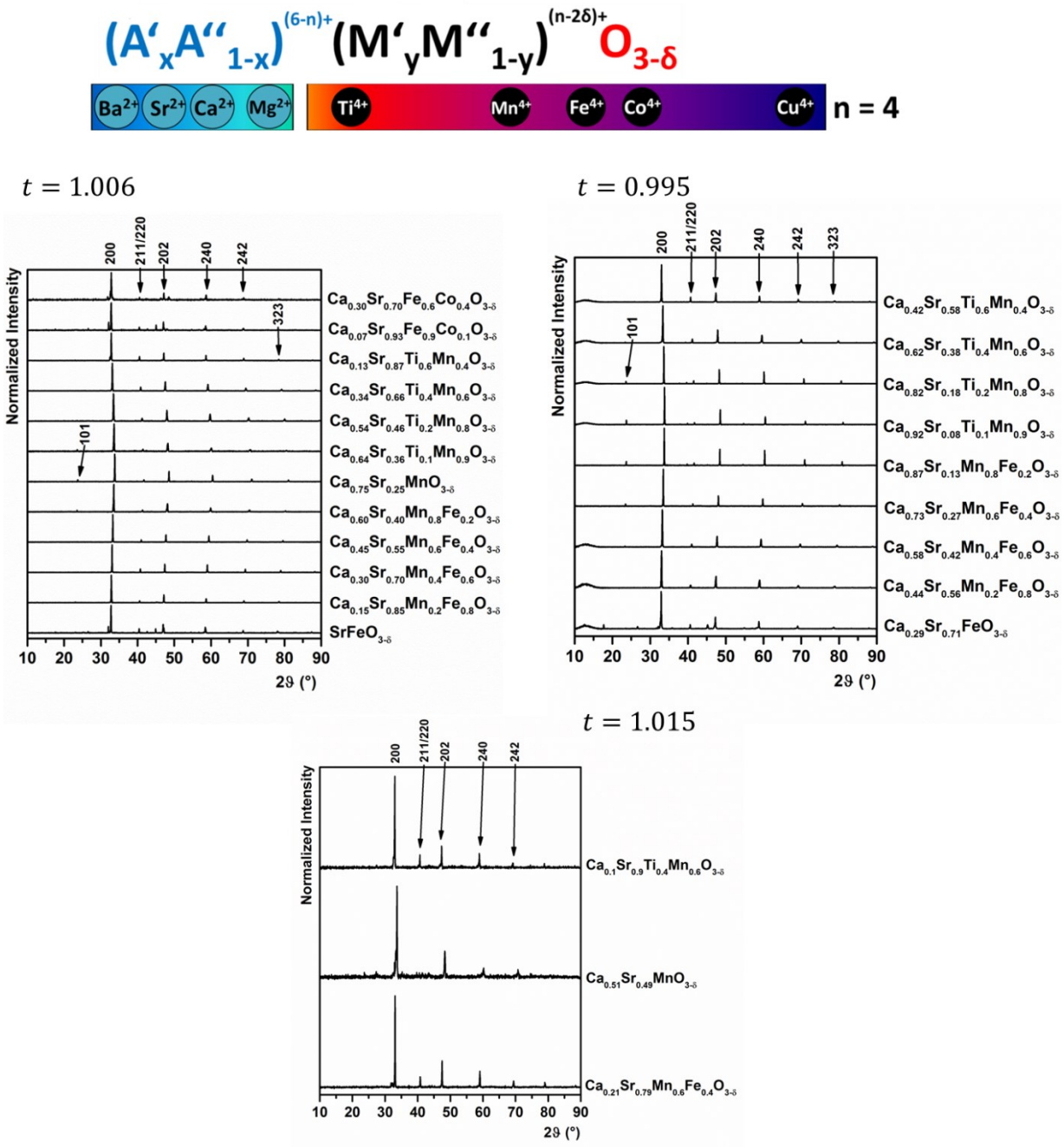

Fig. 5.2. X-Ray diffraction (XRD) patterns of the 24 perovskite solid solutions studied in the materials screening campaign presented within this work. The general composition of these perovskites is shown at the top (compare Fig. 2.5), and the use of Mg^{2+} or Ba^{2+} as cations was not necessary according to the target tolerance factors. The three graphs show the XRD patterns of perovskites with $n = 4$ and $t = 1.006$, 0.995, and 1.015 (with respect to the oxidized state). All perovskite solid solutions are formed without any significant amounts of side phases. Diffraction pattern indexing performed according to the orthorhombic phases presented in section 4.1 and Bulfin *et al.* [132] Adapted from Vieten *et. al.* (supporting information). [95]

Empirical fits of $\Delta H(\delta)$ and $\Delta S(\delta)$

Thermogravimetric experiments are carried out at different temperature and oxygen partial pressure levels to gather equilibrium values of $\Delta\delta$ under different conditions as explained in section 3.4 (van't Hoff method). Varied temperature ranges are used for different materials according to their expected reducibility. For all materials, we could observe a gradual mass change Δm when T and/or p_{O_2} were changed, and this mass change can be converted into $\Delta\delta$ values.

Fit of the redox enthalpy change $\Delta H(\delta)$: For solid solutions with only one transition metal species, we can observe only small changes of ΔH in dependence of δ, whereas these changes are more significant if two different transition metals species are present (compare section 4.3.2). These distinct differences are shown for two exemplary materials (both with t = 1.006 in the fully oxidized state) in Fig. 5.3, and the data shown here is in good agreement with our earlier findings presented in chapter 4, specifically section 4.3.2, where the change in redox enthalpy ΔH as a function of the oxygen non-stoichiometry δ is explained with the preferential reduction of Fe^{4+} ions over Mn^{4+}. In order to fit the experimental data, we derive empirical fit functions in the following, which are not or only partially based upon physical properties, but lead to a good fit of the experimental data with rather simple functions. Using these fit functions ΔG can be calculated for any set of conditions (T, p_{O_2}), even beyond the range of experimentally covered temperature and oxygen partial pressure values. Extrapolations beyond the range of measured δ values, however, may lead to inaccuracies.

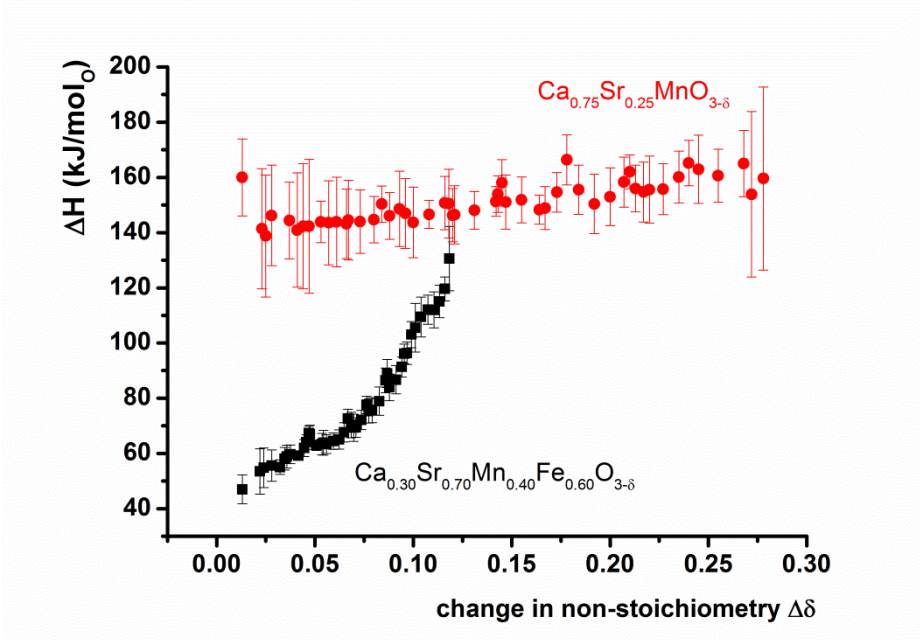

Fig. 5.3. Change in redox enthalpy ΔH shown as a function of $\Delta\delta$ for two exemplary perovskite solid solutions. Perovskites with only one transition metal species on the M site (red) show only small changes of ΔH with changing δ (or $\Delta\delta$), whereas those with two different species show a significant increase of ΔH with increasing reduction extent (black).

We first compare the results of our experimental materials screening to the theoretical considerations shown in section 2.5, especially Fig. 2.8. We have confirmed using experimental data for the $SrMnO_{3-\delta}$ - $SrFeO_{3-\delta}$ system (see section 4.3.2) that by assuming two limiting values of ΔH ($\Delta H_{\min}$ and $\Delta H_{\max}$) the experimental data is described well. We do not use the functions in section 2.5 to fit our experimental data, as they can only be solved numerically, and use a simpler model instead. The arctangent function ($\tan^{-1} x$) has two limiting values $\lim_{x\to-\infty}(\tan^{-1} x) = -\pi/2$ and $\lim_{x\to+\infty}(\tan^{-1} x) = +\pi/2$, and shows a sinusoidal increase of its value around $x = 0$. We empirically found that this function can be used very well to describe the increase of $\Delta H(\delta)$ in perovskite solid solutions, if its limiting values and slope are modified (see Fig. 5.4): [95]

$$\Delta H(\Delta\delta) = \frac{\Delta H_{\max} - \Delta H_{\min}}{\pi} \cdot \left(\tan^{-1}\left((\Delta\delta - sh)\cdot sl\right) + \frac{\pi}{2}\right) + \Delta H_{\min} \qquad (5.1)$$

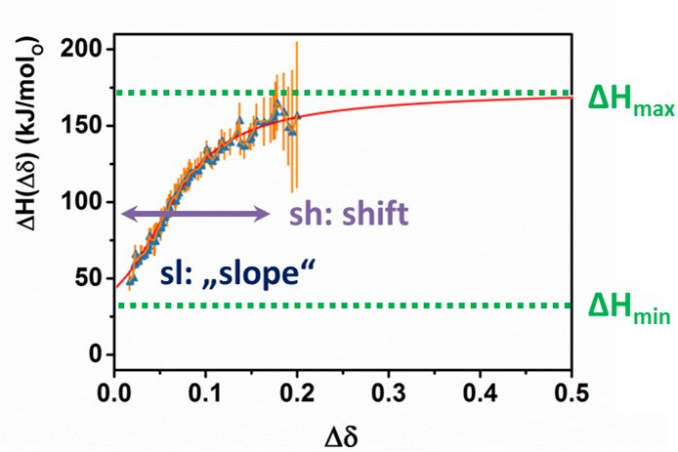

Fig. 5.4. Fit of the redox enthalpy change as a function of the change in non-stoichiometry ($\Delta H(\Delta\delta)$) for the perovskite $Ca_{0.21}Sr_{0.79}Mn_{0.6}Fe_{0.4}O_{3-\delta}$. The limiting values of the arctangent function $\Delta H_{\min}$ and $\Delta H_{\max}$ are shown, along with the fit function (red) and the experimental data (blue triangles) and its uncertainty (orange). The fit accurately describes the change of ΔH as a function of $\Delta\delta$ in perovskite solid solutions. Adapted from Vieten *et. al.* [95]

The transition between $\Delta H_{\min}$ and $\Delta H_{\max}$ is described using the variables sh and sl, where sh stands for a shift of the transition point in δ direction, i.e., the $\Delta\delta$ value where $\Delta H(\Delta\delta = \mathrm{sh}) = 1/2(\Delta H_{\min} + \Delta H_{\max})$, and sl describes the "slope" of the ΔH increase. [95] In the extreme case of $sl \to \infty$, $\Delta H(\Delta\delta)$ turns into a step function between $\Delta H_{\min}$ and $\Delta H_{\max}$. Fig. 5.4 shows an excellent agreement between the experimental data and the fit (red) for the system $Ca_{0.21}Sr_{0.79}Mn_{0.6}Fe_{0.4}O_{3-\delta}$. This empirical fit works well for the 24 solid solutions in our experimental campaign, but the values sh and sl do not represent any physical quantities and the choice of the arctangent function to describe the change of ΔH in dependence of $\Delta\delta$ in perovskite solid solution does not have any physical background. The fit parameters for all 24 perovskite solid solutions are summarized in the Appendix, section 8.2.

Despite the good agreement between this fit and the experimental data in most cases, there are important limitations to be considered. First of all, the fit only yields reliable results in the range of δ values covered experimentally. An interpolation between these values is reasonable, but the accuracy of extrapolated data beyond this range may be limited. This is especially important if the region where ΔH is close to ΔH_{min} or ΔH_{max} has not been covered experimentally, which means it is impossible to know the respective upper or lower limits of ΔH. This occurs in some cases in our data, as the range of temperature and oxygen partial pressure values which can be reached in the thermobalance is limited. If, for instance, the region near ΔH_{max} is not covered experimentally, the fit appears to be underdetermined and the resulting fit value for ΔH_{max} is highly inaccurate (and usually too large). This has to be considered when using this data. Another constraint is our model itself, which is suitable to describe solid solutions with two different transition metal species independent of the temperature. In the case of phases such as $Ca_{0.29}Sr_{0.71}FeO_{3-\delta}$, the difference between ΔH_{min} and ΔH_{max} is rather small as the system seems overdetermined, and the changes in ΔH are more related to temperature effects than δ. Therefore, we use a fixed ΔH_{min} value for $Ca_{0.29}Sr_{0.71}FeO_{3-\delta}$ and $SrFeO_{3-\delta}$ to stabilize the fit (see Appendix section 8.2).[95] One could also use a linear function to describe $\Delta H(\Delta\delta)$ in these cases with similar accuracy. Not accounting for temperature effects in our simplified empirical model may lead to an inaccuracy of the ΔH values, as the $\Delta\delta$ values have been determined using the van't Hoff method at different temperature levels. By doing so, we assume that ΔH and ΔS only depend on $\Delta\delta$, irrespective of how this oxygen release or uptake was reached (temperature variation, pressure variation, or both). However, to measure $\Delta H(\delta, T)$ instead of $\Delta H(\delta)$, the required measurement time increases by about an order of magnitude, as the amount of partial pressure and temperature steps would have to be significantly increased. One could imagine to perform measurements with 10 K temperature difference and to evaluate ΔH and ΔS at different temperature levels T by using all values recorded in the range of, for instance, $T \pm 50\ K$ for separate van't Hoff evaluations, and to repeat this for all values of T. It is obvious that, while this would yield an increase in the accuracy of the data, it is not practical to perform such an analysis within a large perovskite screening, as each material would require several weeks of thermogravimetric scans instead of two days. However, temperature effects on $\Delta H(\delta)$ for some exemplary materials could be covered in future experiments, and are also considered in our theoretical study.

Fit of the redox entropy change $\Delta S(\delta)$: For the redox entropy change ΔS, solid solutions with one and two different transition metal species on the M sites have to be differentiated. The simple case of one transition metal species can be described using a dilute species model as described in section 2.5. The redox entropy gradually decreases with increasing δ and changes more rapidly near the extreme values δ = 0.0 and δ = 0.5 due to the stronger changes in configurational entropy. In this case, it is important to consider $\Delta S(\delta)$ instead of $\Delta S(\Delta\delta)$, and a method to convert between these two values is introduced here. Fig. 5.5 shows $\Delta S(\delta)$ for two different non-stochiometric perovskite oxides from our study.

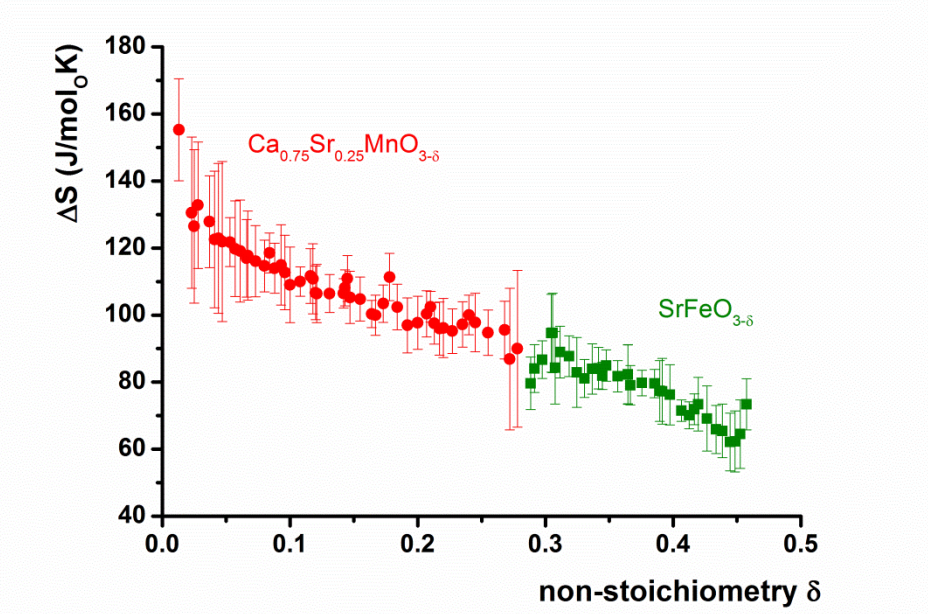

Fig. 5.5. Change in redox entropy ΔS shown as a function of δ for two exemplary perovskite solid solutions, both with only one transition metal species on the M site. An initial non-stoichiometry δ_0 at the reference point of the data of 0.237 is assumed for $SrFeO_{3-\delta}$ according to data shown later, and the measured $\Delta\delta$ values are converted to δ values using $\delta = \Delta\delta + \delta_0$. For $Ca_{0.75}Sr_{0.25}MnO_{3-\delta}$, it is assumed that $\Delta\delta = \delta$. The data illustrates the change in configurational entropy as a function of δ in good agreement with the dilute species model.

The dilute species model which can be used to fit data for perovskites with only one redox-active species is described by: [95, 129]

$$\Delta S(\delta) = \frac{1}{2} \cdot S_{O_2} + \Delta s_{\text{vib}} + 2 \cdot a \cdot R \cdot \left(\ln\left(\frac{1}{2} - \delta\right) - \ln(\delta) \right) \tag{5.2}$$

Eq. 5.2 in principle represents a summation of the partial molar entropy of oxygen, the vibrational entropy, and the configurational entropy. For the calculation of the partial molar entropy of oxygen S_{O_2}, which corresponds to the absolute entropy of the released oxygen, the average temperature is used at which the thermogravimetric data was recorded. Both the vibrational entropy change Δs_{vib} and the parameter a are fit using the experimental data. R is the ideal gas constant. Moreover, for all perovskites which follow the dilute species model, the initial non-stoichiometry δ_0 as a correction term can be fit using experimental data as well. As mentioned before, only $\Delta\delta$ can be determined in our thermogravimetric experiments. Therefore, measurements at T = 400 °C and p_{O_2} = 0.18 bar are included in our thermogravimetric scans as explained in section 3.4. $\Delta\delta$ is defined as zero at this point, and the absolute δ value at this point is defined as δ_0. To convert $\Delta\delta$ to δ, one can then use the relationship $\delta = \Delta\delta + \delta_0$. Please note that δ_0 does not necessarily agree with δ_i in section 4.3.2, as δ_i refers to the non-stoichiometry at ambient temperature in air, which may be

slightly lower than the δ_0 value at 400 °C and p_{O_2} = 0.18 bar. With $\Delta\delta = \delta - \delta_0$, , Eq. 5.2 can be converted to yield the entropy change as a function of the relative change in non-stoichiometry $\Delta\delta$ measured here: [95]

$$\Delta S(\Delta\delta) = \frac{1}{2} \cdot S_{O_2} + \Delta s_{vib} + 2 \cdot a \cdot R \cdot \ln\left(\left(\frac{1}{2} - (\Delta\delta + \delta_0)\right) - ln\,(\Delta\delta + \delta_0)\right) \quad (5.3)$$

This method of determining δ_0 works very well for our reference system $SrFeO_{3-\delta}$. The δ_0 value resulting from the fit is 0.2365, which is in excellent agreement to literature data on the non-stoichiometry of this perovskite at 400 °C in this oxygen partial pressure range in air, where stoichiometry values around 2.77-2.79 are reported. [61, 212] However, this method may be inaccurate for other cases. We apply this method only if Fe or Co are present in our solid solutions, and assume that $\Delta\delta = \delta$ in all other cases, as the extent of oxygen non-stoichiometry in $AMnO_3$ and $ATiO_3$ at 400 °C at near-ambient oxygen partial pressures is negligible. [173, 242-244] Using the so-determined values for δ_0, the enthalpy change $\Delta H(\Delta\delta)$ is converted to $\Delta H(\delta)$ as well. As mentioned before, one could also determine δ_0 using iodometry, thermogravimetric reduction using hydrogen/argon mixtures, or volumetric gas analysis. [234] For the purpose of a high-throughput materials screening with focus on determining the change in non-stoichiometry based on the thermodynamic properties, the fit presented here is a viable alternative, as it does not require any additional experiments.

In perovskite solid solutions with two transition metal species, the redox enthalpy change ΔS is significantly different. We have already shown in section 4.3.2 that the entropy change is lower when only one of the two transition metals is redox-active. We can determine which of the species is expected to be more redox-active from DFT data on binary oxides (see Fig. 2.5), and we define a material specific constant act here, which describes the stoichiometry of the redox-active species in the perovskite, i.e., $act = 0.4$ in $Ca_{0.45}Sr_{0.55}Mn_{0.6}Fe_{0.4}O_{3-\delta}$. For the increase of the entropy change ΔS as a function of δ in the transition region between the regime where only one species is redox-active and both species are involved, we can use an arctangent function similar to the one shown before. The lower limit of the arctangent function is then described by $act \cdot \Delta S_{ref}$, as the configurational entropy should scale linearly with the amount of atoms involved in the reaction. The upper limit is then given by ΔS_{ref}. As the reference system with entropy change ΔS_{ref}, we use $SrFeO_{3-\delta}$, for which the entropy change is accurately described using the dilute species model, and we denote the entropy change of this system by ΔS_{Fe}. As the vibrational entropy change does not necessarily depend on act and is different for every system, the entropy change may be shifted independent of δ or act, and we describe this shift by using a correction factor m, where $|m| < 15\ JK^{-1}mol^{-1}$. This arbitrary constraint of the maximum value of m is used to stabilize the fit, as very high deviations from the thermodynamics of $SrFeO_{3-\delta}$ are unlikely and we empirically get better fit result (i.e., a better

agreement between the fit and the experimental data) if the fit is repeated with a fixed value $m = 0$ in the cases where $m > 15\ \mathrm{JK^{-1}mol^{-1}}$ is found initially. Under all these assumptions, the fit function we apply is given by: [95]

$$\Delta S(\delta) = \underbrace{\frac{act \cdot \Delta S_{\mathrm{Fe}}(\delta + \delta_0)}{\pi}}_{\text{active species}} \cdot \underbrace{\left(\tan^{-1}\left[(\delta - \delta_0) \cdot s_{\mathrm{Ent}}\right] + \frac{\pi}{2}\right)}_{\text{transition}} + \underbrace{(1 - act) \cdot \Delta S_{\mathrm{Fe}}(\delta + \delta_0)}_{\text{less active species}} + \underbrace{m}_{\text{corr.}} \qquad (5.4)$$

Especially in this case, the resulting value of δ_0 may be highly inaccurate for some systems where not a large range of δ values is covered. As the relative changes in the non-stoichiometry are more relevant for the application than absolute values, we accept this uncertainty within this work. The entropy fits according to Eq. 5.3 for perovskites with one redox-active transition metal species and the fit according to Eq. 5.4 for solid solutions with two redox-active transition metals are illustrated for two reference systems in Fig. 5.6.

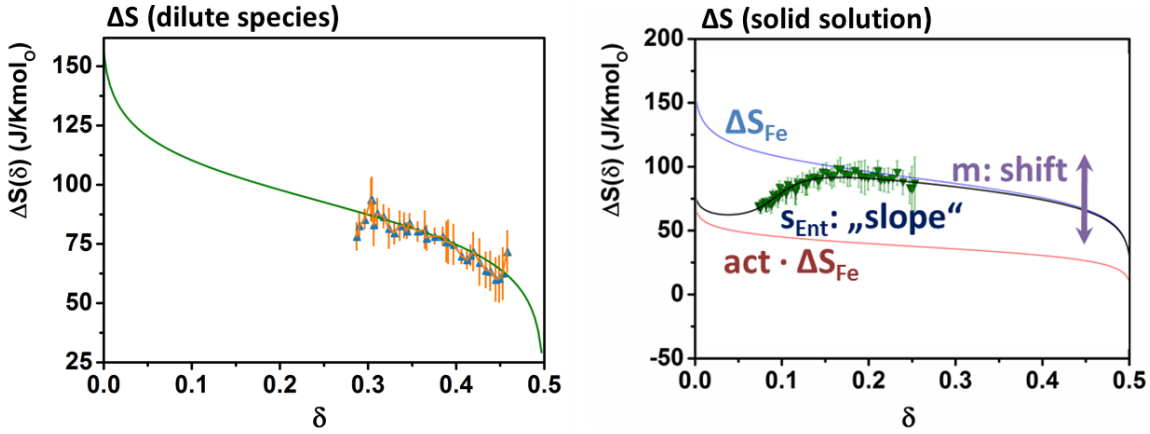

Fig. 5.6. Change in redox enthalpy ΔS and fit functions according to Eqn. 5.3 and 5.4. The graph on the left shows a fit according to the dilute species model for materials with only one redox active species (here: $SrFeO_{3-\delta}$), whereas the graph on the right shows the arctangent fit based on the content of the redox-active species (here: $act = 0.4$) and the redox entropy change of $SrFeO_{3-\delta}$ as a reference system (ΔS_{Fe}) as determined from the fits. Adapted from Vieten *et. al.* [95]

This fit works well for solid solutions containing Fe ($Mn^{3/4+}$-$Fe^{3/4+}$ and $Fe^{3/4+}$-$Co^{3/4+}$ systems). However, it appears to be not reliable for $Ti^{3/4+}$-$Mn^{3/4+}$ systems. For these perovskite solid solutions, we could only cover a small range of δ values experimentally, as these materials typically show high redox enthalpies. Therefore, the fit is overdetermined and unstable, leading to unphysical results. Within the temperature and oxygen partial pressure ranges covered in our study, a significant extent

of Ti^{4+} reduction is not expected. Therefore, we can approximate the redox entropy change by assuming that only one species is redox-active, and use the dilute species model instead. One also has to mention that due to the small range of δ values measured in some cases, the physical meaning of the found fit parameters a and Δs_{vib} can be questioned, but the solid solution model leads to a reasonable empirical fit of the measured data. As mentioned before, an extrapolation based on such fits may be inaccurate. Using the empirical fits introduced in this section, we can accurately represent the measured datasets within the range of experimentally covered δ values and extrapolate in a small range beyond. This can be done using relatively simple analytical expressions. By this means, we can calculate $\Delta G(\delta)$ for our systems at given T and $p_{\mathrm{O_2}}$ values using our expressions for $\Delta H(\delta)$ and $\Delta(S)$ and Eq. 2.12 (based on the Gibbs Helmholtz equation). Through finding where ΔG is zero, we can determine the equilibrium state of the system and predict the expected non-stoichiometry δ at a given set of T and $p_{\mathrm{O_2}}$ values in the same way as for the theoretical data (compare section 2.5 and the appendix, section 8.5). We have to note that this fit method is very material specific and has only been tested for the materials presented herein. Future studies are necessary to elucidate whether or not this fit can be applied to different systems. Moreover, the data itself is subject to measurement uncertainties.

While the thermodynamic properties, their dependence on δ, and fit functions to describe this dependence have been discussed in this section in a generalized way, the following three sections deal with specific solid solution systems investigated experimentally and their potential fields of application based on the gathered thermodynamic data. Some particularly interesting and relevant properties of this perovskites are shown in the following section. The raw thermodynamic data for all 24 materials can be found in the Appendix, section 8.6. Moreover, user-controlled interactive graphs showing equilibrium data (compare section 8.5) are shown in the *RedoxThermoCSP* interface, as mentioned before.

5.1.2 (Ca-Sr)(Ti-Mn) perovskite oxides as a means to reach low oxygen partial pressures

Redox enthalpy change $\Delta H(\delta)$: Perovskites containing titanium-manganate solid solutions are expected to show considerably high redox enthalpy changes per mol of oxygen (compare section 4.3.1). We first consider the redox enthalpy $\Delta H(\delta)$ and the corresponding fits for $t = 1.006$ as a reference in Fig. 5.7. It is noteworthy that the mean value of ΔH does not increase significantly if a small amount of Mn is replaced by Ti. To observe a significant increase in ΔH, 40 % or more of the M sites in the perovskites need to be occupied by Ti^{4+}. This effect has already been mentioned in section 4.3.1 and is further investigated using theoretical data in section 5.2. Part of this effect is certainly also due to the fact that Mn^{4+} is reduced preferentially. Since we only observe small δ-dependent changes of ΔH, it is very likely that Ti^{4+} is mostly redox-passive under the conditions applied in the thermobalance. Our empirical model leads to a good fit of the experimental data. At very low δ values (below 0.01-0.02), the measurement uncertainties and fluctuations of $\Delta H(\delta)$ increase significantly, which we attribute to the low mass changes observed and the corresponding measurement uncertainties of the thermobalance. This partially leads to unrealistic values for ΔH_{min} (see appendix section 8.2).

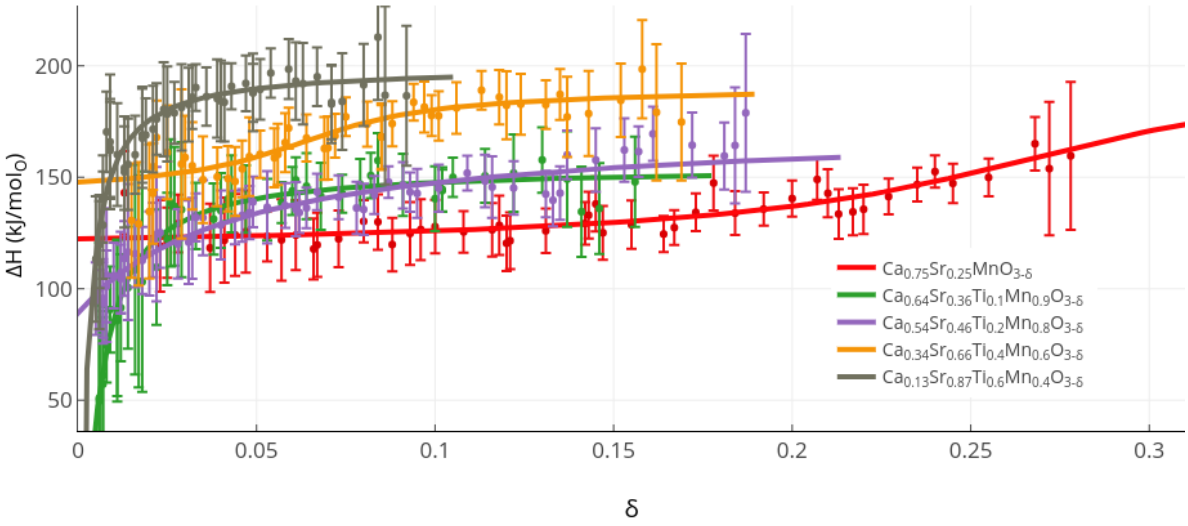

Fig. 5.7. Experimentally determined redox enthalpy change per mol of oxygen O as a function of the oxygen non-stoichiometry δ for (Ca,Sr)(Ti,Mn)$O_{3-\delta}$ perovskite solid solutions with t = 1.006 (at δ = 0), and empirical fits of the data using Eq. 5.1 assuming $\Delta\delta = \delta$. The redox enthalpy change ΔH only significantly increases if the Ti content is 40 at% or higher (w.r.t. M sites in the perovskite). The redox enthalpy does not show a strong dependence on δ within the experimentally covered data range. Generated using plotly from data in *RedoxThermoCSP* (https://contribs.materialsproject.org/redox_thermo_csp).

Redox enthalpy change $\Delta S(\delta)$: The redox entropy change ΔS generally increases for low values of δ in agreement with the dilute species model (see Fig. 5.8). However, this effect is not consistently observed for all (Ca,Sr)(Ti,Mn)$O_{3-\delta}$ solid solutions. In the case of samples with $t = 1.006$ and a Ti content of 20 and 40 at% (w.r.t. the M site), ΔS is essentially constant within the measured δ range. The measurement uncertainties do not allow unambiguous statements regarding the δ-dependence of ΔS, and the possibility that the measurement results are affected by entropy-enthalpy compensation adds to the uncertainty of the data.[197] The uncertainties and deviations from the dilute species model might be attributed to the nature of the Mn^{4+} and Ti^{4+} reduction process, the latter only occurring to a limited extent depending on the sample composition. It is very likely that Ti^{4+} is not reduced to a substantial amount under the applied conditions.

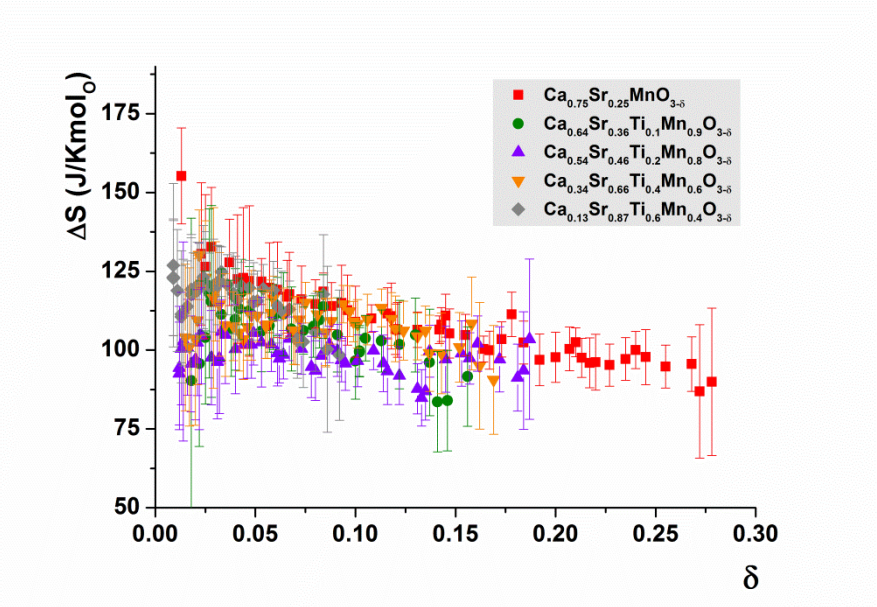

Fig. 5.8. Experimentally determined redox entropy change per mol of oxygen O as a function of the oxygen non-stoichiometry δ for (Ca,Sr)(Ti,Mn)$O_{3-\delta}$ perovskite solid solutions with $t = 1.006$ (at $\delta = 0$). In most cases, ΔS increases for small values of δ, which is in good agreement to the dilute species model, but deviations from this model may be attributed to the effect of the substitution of Mn^{4+} by Ti^{4+}.

Effect of the tolerance factor t: To study the effect of different tolerance factors on the redox thermodynamics, we use systems with 40 at% Ti content as a reference. Fig. 5.9 shows $\Delta H(\delta)$ and $\Delta S(\delta)$ for three of these systems with different tolerance factors, i.e., different Ca/Sr ratios. Our data reveals no significant differences in both $\Delta H(\delta)$ and $\Delta S(\delta)$ and confirms once more that the transition metal composition decides over the redox thermodynamics of perovskite solid solutions, while the redox-inactive A site metals play a minor role, if any. In the (Ca,Sr)(Ti,Mn) system, the Ca/Sr ratio does not affect the redox properties to any measureable extent, considering the measurement uncertainties.

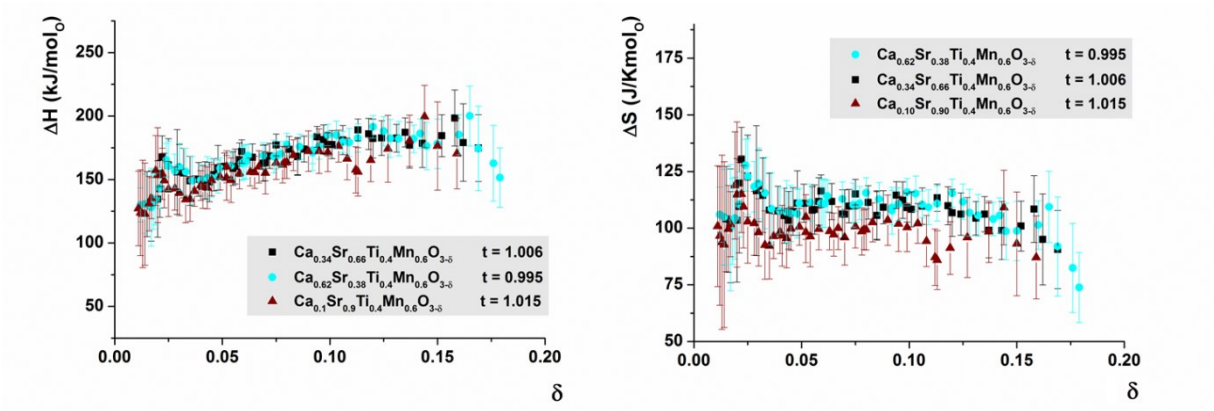

Fig. 5.9. $\Delta H(\delta)$ and $\Delta S(\delta)$ for three different (Ca,Sr)$Ti_{0.4}Mn_{0.6}O_{3-\delta}$ systems with different Ca/Sr ratio according to different target tolerance factors t = 0.995, 1.006, and 1.015 (at δ = 0). The redox thermodynamics of these materials are not affected by the Ca/Sr ratio to any measurable extent, considering the measurement uncertainties.

Isoredox graph and conclusions: (Ca,Sr)(Ti,Mn)$O_{3-\delta}$ perovskites show considerably high values of ΔH. This means that the amount of chemical energy necessary to reduce these perovskites per mol of oxygen released is rather high, and high temperatures and/or low oxygen partial pressures are required for their reduction (especially compared to the perovskites in sections 5.1.3 and 5.14). Nevertheless, using such perovskites in an air separation cycle can be advantageous. The high redox enthalpies for the reduction of the perovskite also mean that they show a high oxygen affinity in the reduced state (compare Fig. 4.2). In other words, the equilibrium oxygen partial pressure of such perovskite samples with the surrounding atmosphere is considerably low. Fig. 5.10 shows these oxygen partial pressures of the (Ca,Sr)(Ti,Mn)$O_{3-\delta}$ samples with t = 1.006 at a constant oxygen non-stoichiometry value of δ = 0.10 ("isoredox" plot, compare Appendix section 8.5), calculated using the derived empirical fit functions and fit parameters (section 8.2). The data and user-controlled interactive isoredox plots for each of the materials can also be found in the *Isographs* section of *RedoxThermoCSP*.[j] Four main findings can be read from this plot:

1. The reduction of (Ca,Sr)(Ti,Mn)$O_{3-\delta}$ perovskites occurs only at high temperatures and/or low oxygen partial pressures, as mentioned above. For instance, $Ca_{0.54}Sr_{0.46}Ti_{0.2}Mn_{0.8}O_{3-\delta}$ requires a temperature of over 1350 K to reach δ = 0.10 in air (p_{O_2} = 0.21 bar).
2. In turn, considerably low oxygen partial pressures can be achieved using the partially reduced materials. Fig. 5.10 shows p_{O_2} values below 10^{-20} bar for the Ti-rich (Ca,Sr)(Ti,Mn)$O_{3-\delta}$ perovskites below $T \approx 650$ K at δ = 0.10. The minimum achievable oxidation temperature may be limited by the oxidation kinetics, but nevertheless, oxygen pumping and air separation can be achieved down to very low oxygen partial pressures, allowing the production of extremely pure nitrogen for advanced applications.

[j] https://contribs.materialsproject.org/redox_thermo_csp/isographs/

3. In agreement with the $\Delta H(\delta)$ values presented above, the equilibrium thermodynamic properties of (Ca,Sr)(Ti,Mn)$O_{3-\delta}$ samples with 0-20 at% Ti content are not differing strongly from each other. The equilibrium oxygen partial pressure is only shifted significantly to lower values if the Ti content is 40 at% or higher.
4. Within the range of the experimentally studied (Ca,Sr)(Ti,Mn)$O_{3-\delta}$ solid solutions (0-60 at% Ti content), none of the materials is very well suitable for thermochemical water splitting. The achievable equilibrium oxygen partial pressures are still too high to reach substantial hydrogen yields (compare Fig. 2.10).

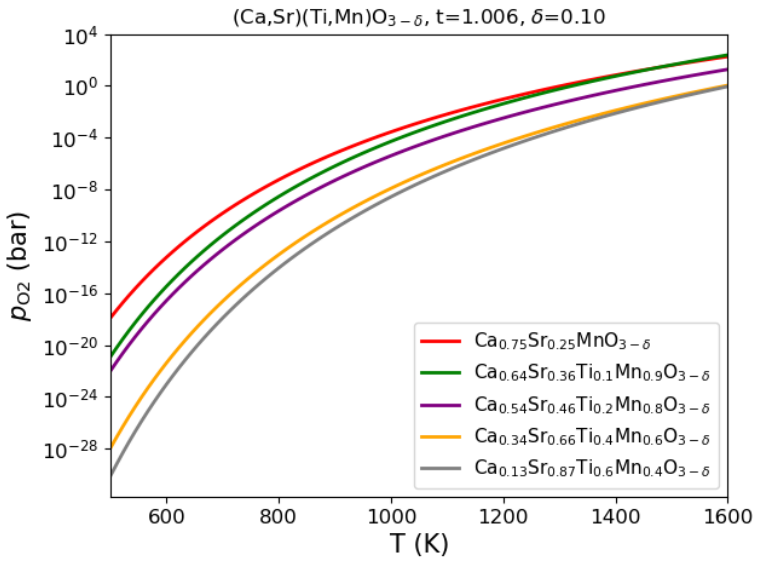

Fig. 5.10. Isoredox graphs (compare section 8.5) for different (Ca,Sr)(Ti,Mn)$O_{3-\delta}$ systems at a fixed δ = 0.10 showing the dependence of the equilibrium oxygen partial pressure on the temperature in K. Using (Ca,Sr)(Ti,Mn)$O_{3-\delta}$ solid solutions allows thermochemical air separation with very low residual oxygen levels. Based on data in *RedoxThermoCSP*.

In summary, (Ca,Sr)(Ti,Mn)$O_{3-\delta}$ perovskites are very well suitable as a means to reach considerably low oxygen partial pressures in thermochemical air separation due to their $\Delta H(\delta)$ values around 130-180 kJ/mol_O. In turn, the energy input for the reduction of such perovskites is rather high per mol of oxygen. A reasonable application scenario could involve a pre-purified gas feedstock containing trace amounts of oxygen, which is further purified using (Ca,Sr)(Ti,Mn)$O_{3-\delta}$ perovskites as redox materials. By this means, the molar amount of oxygen to be transported per unit volume of the total gas stream is lower. We also found that the thermodynamic redox properties are independent of the tolerance factor within the investigated range of t = 0.995 – 1.015. Furthermore, the replacement of Mn^{4+} by Ti^{4+} in such solid solutions only has a significant effect on the thermodynamic properties if 40% or more of the Mn^{4+} ions are replaced. In the following, we will consider a system with a larger effect of the substitution on the thermodynamics: the (Ca,Sr)(Mn,Fe)$O_{3-\delta}$ system.

5.1.3 (Ca-Sr)(Mn-Fe) perovskite oxides as versatile oxygen pump materials

Redox thermodynamics and tolerance factor effects: Literature data on Fe- and Mn- containing alkali earth metal perovskites [173] as well as the data in chapter 4 reveal the formation of oxygen vacancies at moderate temperatures. The dataset on (Ca-Sr)(Mn-Fe)$O_{3-\delta}$ perovskites shows very similar thermodynamics as observed for Sr(Mn-Fe)$O_{3-\delta}$ in section 4.3.2 (see thermodynamic data in the Appendix, section 8.6 and the *RedoxThermoCSP* interface). It is important to consider the effect of different tolerance factors on the thermodynamics, as this is the essential difference between the dataset in section 4.3.2 and the tolerance factor adjusted data shown here, where the Ca/Sr ratio is varied. Fig. 5.11 shows a comparison of three datasets with equal Fe/Mn ratio but varied Ca/Sr ratio (compare Fig. 5.9). All three samples show an increase of the redox enthalpy and entropy with increasing oxygen non-stoichiometry δ due to the rise in the Mn^{4+} redox activity (compare section 4.3.2). The δ_0 values obtained from the entropy fit are considered, which leads to a shift of the values in δ direction. The δ_0 values range from 0.064 to 0.125, which on average agrees well with the δ_i value of 0.09 derived from table 4.2 by linear interpolation for Ca-free solid solutions. However, one has to say that δ_i describes the equilibrium at room temperature, whereas δ_0 refers to our reference point at 400 °C and 0.18 bar p_{O_2}. The fluctuations of our δ_0 values indicate that our method of deriving δ_0 may be subject to a certain measurement uncertainty, or that the Ca content influences the obtained δ_0 value. Nevertheless, we can state that the redox behavior observed for tolerance-factor adjusted (Ca,Sr)(Mn,Fe)$O_{3-\delta}$ perovskites is mostly independent of the tolerance factor within the range of t = 0.995 – 1.015. An exception are the Mn-free phases $SrFeO_{3-\delta}$ and $Ca_{0.29}Sr_{0.71}FeO_{3-\delta}$, where a higher Ca content leads to a significantly lower average redox enthalpy according to our experiments (see section 8.6), a trend which is in good agreement with DFT data (see section 5.3). The reason for this behavior is still unknown.

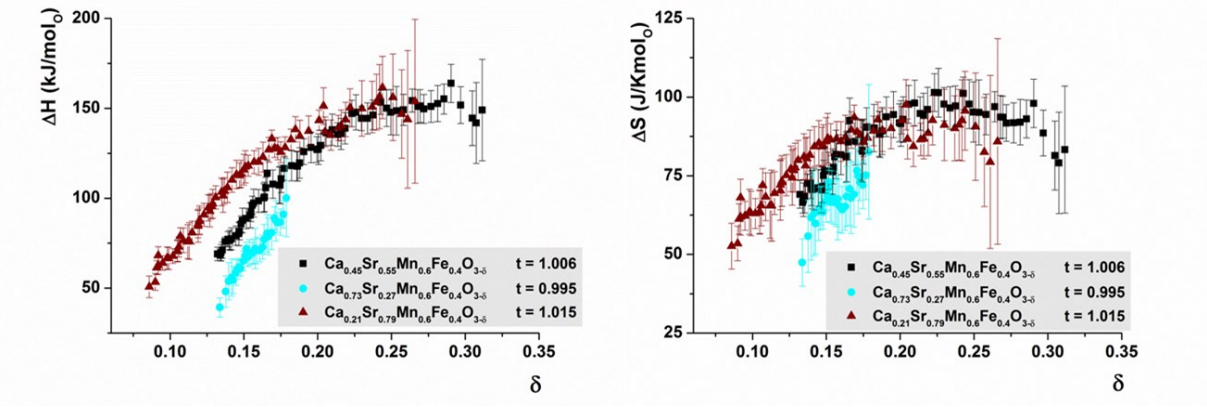

Fig. 5.11. $\Delta H(\delta)$ and $\Delta S(\delta)$ for three different (Ca,Sr)$Mn_{0.6}Fe_{0.6}O_{3-\delta}$ systems with different Ca/Sr ratio according to different target tolerance factors t = 0.995, 1.006, and 1.015 (at δ = 0). The measured $\Delta\delta$ values are corrected by the δ_0 values obtained from entropy fits.

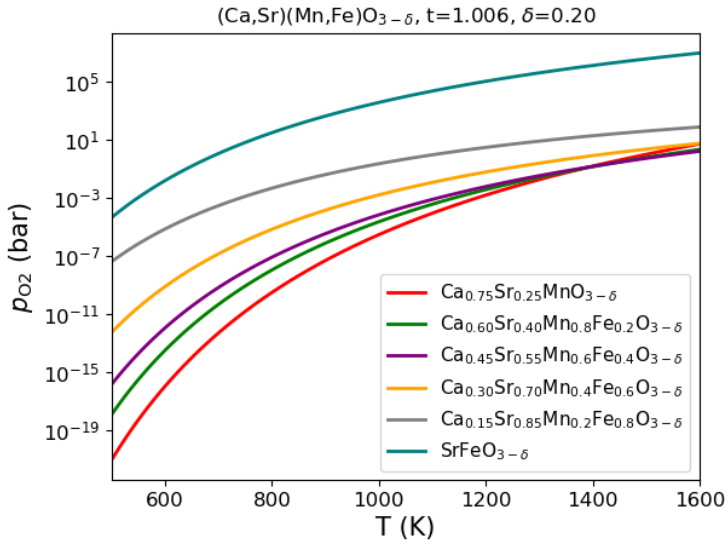

Fig. 5.12. Isoredox graphs for different (Ca,Sr)(Mn,Fe)$O_{3-\delta}$ systems at a fixed δ = 0.20 (with measured $\Delta\delta$ data corrected by δ_0) showing the dependence of the equilibrium oxygen partial pressure on the temperature in K. Using (Ca,Sr)(Mn,Fe)$O_{3-\delta}$ solid solutions allows thermochemical air separation over a large range of oxygen partial pressures. Based on data in *RedoxThermoCSP*.

Isoredox graph and conclusions: An "isoredox" plot depicting the state of the chemical equilibrium for δ = 0.20 is shown in Fig. 5.12. With increasing Mn content, the achievable lowest oxygen partial pressure increases. We can derive the following statements from an analysis of this data:

1. (Ca-Sr)(Mn-Fe)$O_{3-\delta}$ perovskite solid solutions can be applied for air separation at near ambient oxygen partial pressures, as well as at partial pressures below 10^{-15} bar. The application range of these materials can be tuned by adjusting the Mn content.
2. The Fe-rich materials can be applied for thermochemical air separation and oxygen pumping with air as a feedstock.
3. The Mn-rich materials can be used to further lower the oxygen content using a pre-purified gas feedstock. Both Mn-rich and Fe-rich materials can be combined in an oxygen pumping cascade (see section 6.2.2). Ti-containing materials (see section 5.1.2) ideally complement the (Ca-Sr)(Mn-Fe)$O_{3-\delta}$ solid solutions, as they extend the range of achievable oxygen partial pressures.

Moreover, it has to be noted that due to the strong δ-dependent changes in ΔH and ΔS, the redox properties are strongly dependent on the non-stoichiometry δ. For instance, at high values of δ, the Fe content becomes less relevant as Mn is redox-active in any case. Therefore, plots such as in Fig. 5.12 can be created for any set of given conditions in the *RedoxThermoCSP* interface, allowing application-based redox materials design.

5.1.4 (Ca-Sr)(Fe-Co) perovskite oxides as efficient air separation materials at high oxygen partial pressures

Phase stability and non-stoichiometry limits: Cobalt containing alkali earth metal perovskites can be reduced readily if their initial oxygen content is high. In turn, their oxygen affinity is not very high (compare literature data on $SrCoO_{3-\delta}$ [36]). Upon thermal reduction, the limiting value of $\delta = 0.50$ can be reached rather quickly. This limit in the oxygen non-stoichiometry, however, is not generally valid for all systems. $SrCoO_{3-\delta}$, for instance, can show an additional perovskite-like phase with the composition $SrCoO_{2.29}$. [245] Fig. 5.13 shows a thermogravimetric scan of the sample $Ca_{0.07}Sr_{0.93}Fe_{0.9}Co_{0.1}O_{3-\delta}$, where a non-equilbrium region can be observed in the first reduction cycle. This indicates a phase transition, as demonstrated earlier in this work (chapter 4). The onset of this phase transition occurs at 750 °C under an oxygen partial pressure of 0.9 bar. It is very likely that this phase transition is associated with the formation of a phase with $\delta > 0.50$. However, our thermodynamic models are only valid if $0.5 \leq \delta \leq 0.0$ holds true. Therefore, the temperature region above 600 °C is avoided in all further thermogravimetric scans used for the generation of thermodynamic data, and the sample analyzed in the scan shown in Fig. 5.13 is not re-used. Nevertheless, such phase transitions most likely occur during the synthesis of these perovskites at up to 1100 °C in air. For future studies, it appears promising to investigate the reversibility of this phase transition, its thermodynamics, and the formed phase(s), but due to the unusually high non-stoichiometry value which is in incompatible with our thermodynamic model, we restrict our analysis in the following to $(Ca,Sr)(Fe,Co)O_{3-\delta}$ solid solutions with $\delta \leq 0.5$. This limits the amount of available data significantly, but it is necessary to do so in order to obtain valid results.

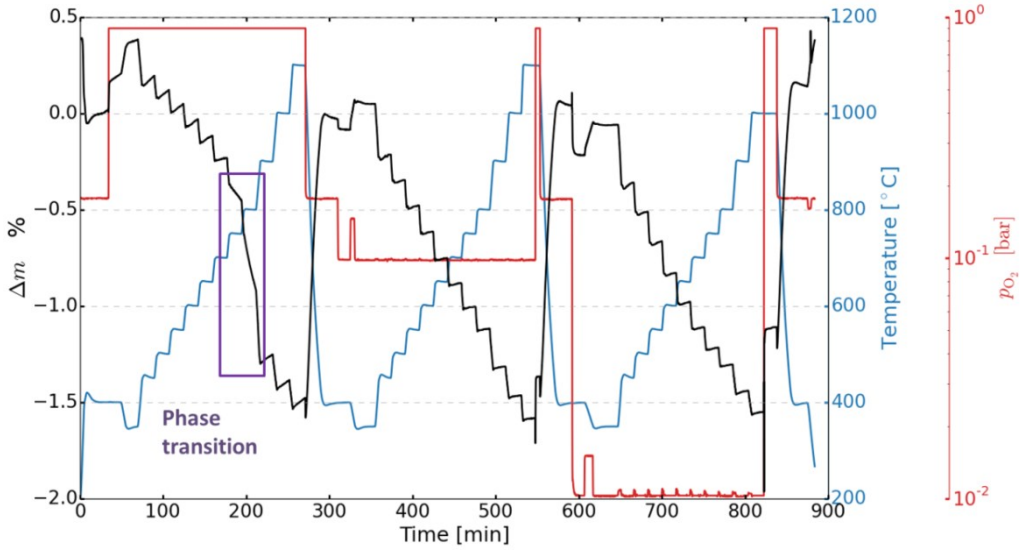

Fig. 5.13. Thermogravimetric scan of $Ca_{0.07}Sr_{0.93}Fe_{0.9}Co_{0.1}O_{3-\delta}$ showing a phase transition at 750 °C at an oxygen partial pressure of 0.9 bar indicated by the non-equilibrium state of the system. The phase transition is attributed to the formation of a phase with $\delta > 0.5$.

Redox thermodynamics: A similar phase transition is observed in both investigated Co containing samples (Co content 10 and 40 at%, t = 1.006). It is also noteworthy that these samples show a significant redox activity below 400 °C (see Fig. 5.13). This indicates a relatively low redox enthalpy change per mol of oxygen. Fig. 5.14 shows $\Delta H(\delta)$ and $\Delta S(\delta)$ for the Co-containing samples. The ΔH values decrease with increasing Co content and are in fact particularly low compared to the values for Mn-Fe or Ti-Mn solid solutions. Especially for the sample with 40 at% Co content (w.r.t. the M site in the perovskite), the redox entropy change decreases significantly for high values of δ, which is expected according to the dilute species model. The data also allows determining δ_0, which is as high as 0.45 for $Ca_{0.30}Sr_{0.70}Fe_{0.6}Co_{0.4}O_{3-\delta}$. Moreover, the decreasing ΔH in parallel to the decrease in ΔS is most likely an artefact induced by enthalpy-entropy compensation, [197] which means that ΔH and ΔS cannot be measured completely independent from each other, especially at these extreme points where small changes in $\Delta\delta$ are particularly relevant. At high values of δ, the enthalpy fit reaches a slope yielding almost a step-function (compare Eq. 5.1), but a sudden change in redox enthalpy cannot be explained physically.

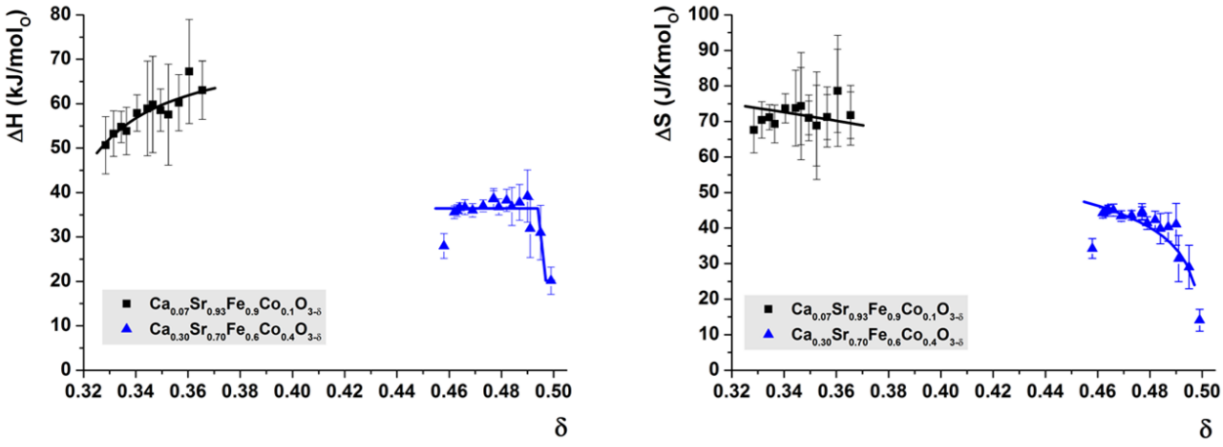

Fig. 5.14. $\Delta H(\delta)$ and $\Delta S(\delta)$ for the two studied (Ca,Sr)(Fe,Co)$O_{3-\delta}$ systems (both t = 1.006 w.r.t. $\delta = 0$) including empirical fits according to sections 5.11 and 8.2. The change in redox enthalpy is particularly low for these materials. The sample with higher Co content ($Ca_{0.30}Sr_{0.70}Fe_{0.6}Co_{0.4}O_{3-\delta}$) reaches the limiting value of $\delta = 0.5$ which is associated with a strong decrease in ΔS according to the dilute species model.

Despite the data being sensible in its mean values and in good agreement with our expectations, we also have to state that due to the temperature/decomposition limit, the range of measured data is rather low, and that extrapolations using our fit functions have to be used carefully. Nevertheless, we can use this data to create "isoredox" plots for these two samples to estimate the expected partial pressure and temperature range achievable with these materials (see Fig. 5.15). The plot is created for δ = 0.35, which means that extrapolated data is used for the $Ca_{0.30}Sr_{0.70}Fe_{0.6}Co_{0.4}O_{3-\delta}$ sample (compare Fig. 5.14). Moreover, potential decomposition reactions are not considered, but these are not expected at δ = 0.35 according to our fitted δ_0 values and the $\Delta\delta$ derived from Fig. 5.13.

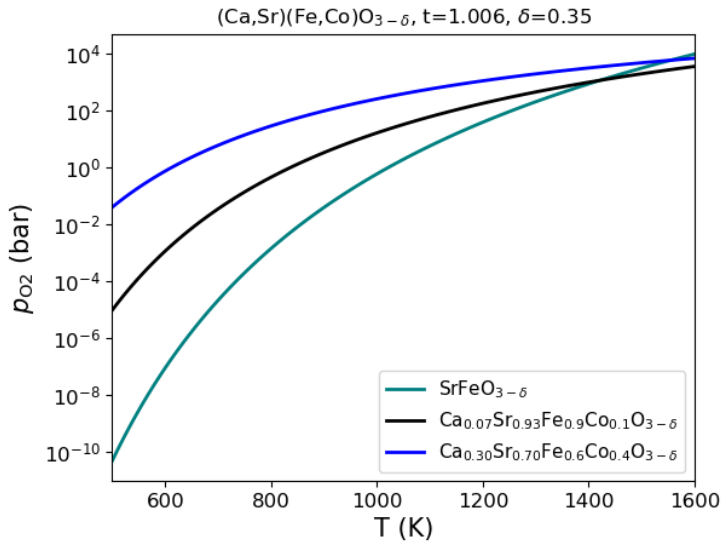

Fig. 5.15. Isoredox graphs for different (Ca,Sr)(Fe,Co)$O_{3-\delta}$ systems at a fixed δ = 0.35 (with measured $\Delta\delta$ data corrected by δ_0) showing the dependence of the equilibrium oxygen partial pressure on the temperature in K. Using (Ca,Sr)(Fe,Co)$O_{3-\delta}$ solid solutions allows thermochemical air separation with considerably low energy input at rather high oxygen partial pressures. Based on data in *RedoxThermoCSP*.

Isoredox graph and conclusions:

(Ca-Sr)(Fe-Co)$O_{3-\delta}$ perovskite solid solutions are reduced readily even at low temperatures (see Fig. 5.15). This lowers the energy input for thermochemical air separation significantly with respect to the materials discussed before.

1. The minimum achievable oxygen partial pressure is limited, as the rather low redox enthalpies of these materials are associated with a low oxygen affinity in the reduced state. Under most conditions, the (Ca-Sr)(Fe-Co)$O_{3-\delta}$ perovskites studied within this work cannot be used to generate nitrogen with an oxygen content sufficient for the Haber-Bosch process (which requires oxygen concentrations in the ppm range or below [66]). This is possible only with (Ca-Sr)(Mn-Fe)$O_{3-\delta}$ or (Ca-Sr)(Ti-Mn)$O_{3-\delta}$ perovskites. Nevertheless, a combination of Co-containing perovskites with another material for further purification in an air separation cascade could be beneficial.
2. At high temperatures, oxygen partial pressures higher than the oxygen partial pressure of air are required to limit the oxygen non-stoichiometry to the here-chosen value of δ = 0.35. As shown before, decomposition reactions may occur if δ is near 0.50. Therefore, these materials should be applied in air only at $T <$ 600-700 °C.

Of course, the redox properties also depend on the chosen δ value, which can be seen by comparing the data for $SrFeO_{3-\delta}$ in Fig. 5.12 and Fig. 5.15.

In summary, our experimental materials screening revealed details on phase formation and the redox thermodynamics of tolerance-factor adjusted perovskite solid solutions. Only perovskites with alkali earth metals on the *A* site have been studied within the experimental screening, as they are similar in composition to most of the perovskites presented in chapter 4 of this work. We have shown that all 24 prepared perovskite solid solutions are formed as single phases without any notable miscibility gaps. By adjusting the *A* site composition, we successfully prepared perovskites which do not show any notable phase transitions during the redox reactions. Exceptions are Co containing perovskites, where a phase with $\delta > 0.50$ may exist. We have shown that the tolerance factor (i.e., the Ca/Sr ratio) has little to no effect on the redox thermodynamics of most perovskites studied here with the exception of the materials $SrFeO_{3-\delta}$ and $Ca_{0.29}Sr_{0.71}FeO_{3-\delta}$. The redox thermodynamics of perovskites with two different transition metal species are essentially characterized by the different redox activity of these species. At higher values of the oxygen non-stoichiometry δ, both species in the solid solutions are redox-active, whereas at lower δ values, one of the species typically acts mostly redox-passive. This has implications on the redox enthalpy and entropy, which rise in an arctangent-like manner with increasing δ. This effect is most pronounced when Mn and Fe are mixed on the M site. Within this chapter, we developed empirical fit functions which accurately describe $\Delta H(\delta)$ and $\Delta S(\delta)$ within the experimentally covered δ range, and we also showed how the initial non-stoichiometry δ_0 at a reference point can be derived from the entropy data. By looking at three solid solution systems more in detail, we confirmed the suitability of the fit functions and created graphs describing the chemical equilibrium as a function of the temperature T and the oxygen partial pressure p_{O_2} at a given oxygen non-stoichiometry δ. By doing so, we show that these three solid solution systems ideally complement each other for application in thermochemical air separation and oxygen pumping processes. The achievable lowest oxygen partial pressures decrease between the systems in the order Fe-Co > Mn-Fe > Ti-Mn. By selecting an appropriate mixture ratio within this phase space, air separation and oxygen pumping processes can be carried out at any oxygen partial pressure between > 100 bar and < 10^{-20} bar. The necessary reduction temperatures consequently increase in the order Fe-Co < Mn-Fe < Ti-Mn, which means that selecting an appropriate material is a trade-off between the energy input per mol of oxygen transferred and the achievable oxygen partial pressure. It can therefore be advantageous to use a two-step cascade system for pumping with two different redox materials instead of one.

So far, we have only considered perovskites with $n = 4$ in the $(A'_xA''_{1-x})^{(6-n)+}\left(M'_yM''_{1-y}\right)^{(n-2\delta)+}O_{3-\delta}$ composition range, and 24 of these perovskites have been investigated experimentally. Theoretical materials screening using formation enthalpies and elastic properties calculated using density functional theory (DFT) and thermodynamic models as shown in sections 2.4 and 2.5 allows increasing the range of investigated materials significantly. In the next section, the result of a theoretical perovskite solid solution screening of over 240 redox materials is presented, which allows extending the range of studied perovskites to n = 3 and n = 5.

5.2 Theoretical materials screening using DFT in the framework of *Materials Project*

DFT calculations: Theoretical calculations using density functional theory (DFT) extend the range of covered materials in our materials screening. Using the supercells shown in section 2.4, we carry out mixed GGA and GGA + U calculations using the infrastructure of Materials Project.[117] Over 250 perovskite structures and the same amount of brownmillerites are submitted to the DFT workflow, and only a very small amount of the submitted structures lead to divergent results and errors. All successfully calculated materials (over 240 perovskites and the same amount of corresponding brownmillerites) are added to the Materials Project database and can be retrieved through www.materialsproject.org. For the perovskite materials studied within this work, a DOI has been generated (DOI: 10.17188/1475589), which resolves to a list of all corresponding perovskites, brownmillerites and their solid solutions.[199] The calculation workflow includes a duplicate check, which leads to some materials being not based on the supercells described in section 2.4 but existing Materials Project database entries. Moreover, some materials have unit cells smaller than the supercells. The materials added to Materials Project are assigned a so-called MP-ID, which is a unique identifier for each material. To look at the calculation process more in detail, we consider the perovskite solid solution $Sr_5Ca_3MnFe_7O_{24}$ (mp-1076079, https://materialsproject.org/materials/mp-1076079/) as an example. The used U values in the GGA + U calculation (see section 2.4 for the theoretical background) are 3.9 eV and 5.3 eV for Mn and Fe, respectively. Part of the calculation summary for the GGA + U structure optimization from Materials Project is shown in Fig. 5.16.

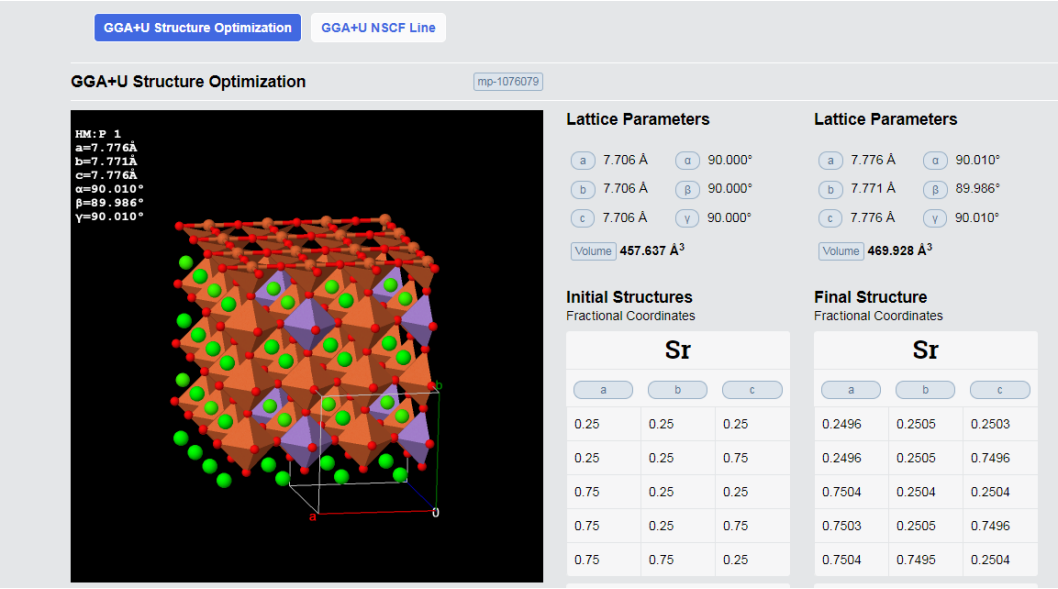

Fig. 5.16. Excerpt of the calculation summary for the exemplary perovskite solid solution $Sr_5Ca_3MnFe_7O_{24}$ from Materials Project (https://materialsproject.org/tasks/mp-1076079#mp-1076079) showing the crystal structure after optimization, the initial lattice parameters, and the final lattice parameters.

The initial lattice parameters are equal for all structures, as they are supercells based on the cubic $SrFeO_3$ structure according to the literature.[246] The final lattice parameters result after relaxation and energy minimization and reveal a near-cubic structure. Within this work, DFT is used as a "black box" tool with a pre-defined workflow, and it is not the objective of this work to optimize this workflow or develop new theoretical DFT methods. The evolution of the total energy of our exemplary system over multiple optimization cycles is shown in Fig. 5.17. It can be seen that the total energy of the system converges quickly. One reason for failed calculations can be non-convergent systems, but this occurs rarely in our dataset. The optimization workflow is using the Vienna ab-initio simulation package (VASP) and consists of electronic and ionic relaxation steps.[203] During the electronic optimization, the wavefunctions are refined to lead to the electronic ground state, whereas during the ionic steps, the atom positions are refined by minimizing the forces between them. Each color in Fig. 5.17 indicates a new ionic step, and multiple electronic steps are carried out within each ionic step. Two relaxation cycles are applied, the second one being based on the result of the first ("re-relaxation"). For further details on the VASP structural optimization process and the DFT calculation workflow, please refer to the literature [117, 200, 202, 203] and the documentation of Materials Project (https://materialsproject.org/docs/calculations).

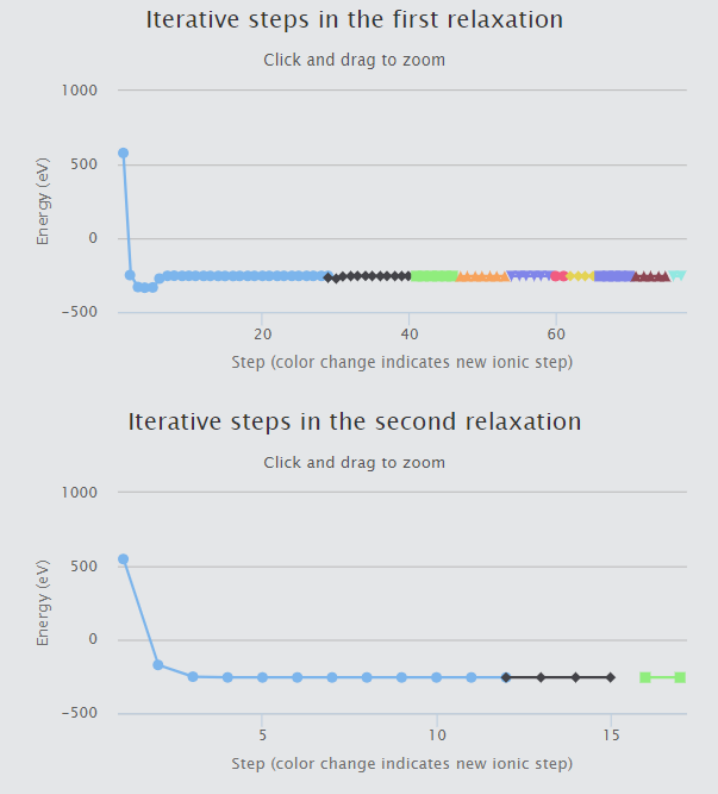

Fig. 5.17. Relaxation steps within the DFT calculations in Materials Project/VASP for the exemplary perovskite solid solution $Sr_5Ca_3MnFe_7O_{24}$. During the electronic optimization steps, the wavefunctions are refined, whereas the atom positions are refined in the ionic optimization. Taken from https://materialsproject.org/tasks/mp-1076079#mp-1076079.

Lattice parameters: The lattice parameters of solid solutions follow Vegard's law in most cases. However, the discretization necessary for performing DFT calculations with 2x2x2 supercells leads to deviations from the linear trend. Fig. 5.18 shows the unit cell volumes of the calculated perovskite supercells for the exemplary system (Ca,Sr)(Mn,Fe)O_3 with $t = 1.006 \pm 0.002$ depending on the Fe content. The standard deviation of t indicates that the tolerance factor could not be matched exactly in all cases due to the constraint of integer unit cell occupancies. For instance, due to the rounded occupancies, the systems $Ca_{0.125}Sr_{0.875}Mn_{0.125}Fe_{0.875}O_3$ and $Ca_{0.125}Sr_{0.875}Mn_{0.25}Fe_{0.75}O_3$ both have the same Ca/Sr ratio, whereas the next member of the solid solution series, $Ca_{0.25}Sr_{0.75}Mn_{0.375}Fe_{0.625}O_3$, does not. The Ca content needs to be increased with increasing Mn content to account for the smaller ionic radius of Mn^{4+} compared to Fe^{4+}, but it cannot be increased linearly due to the discretization. This explains the non-linearity of the unit cell volumes between these entries in Fig. 5.18. In general, however, the linear fit indicates a good agreement with Vegard's law. One has to note that the unit cell volumes have been normalized to the values for 2x2x2 supercells, as $Ca_{0.75}Sr_{0.25}MnO_3$ and $SrFeO_3$ have unit cells smaller than the supercell (1/2 and 1/8 of the supercell, respectively).

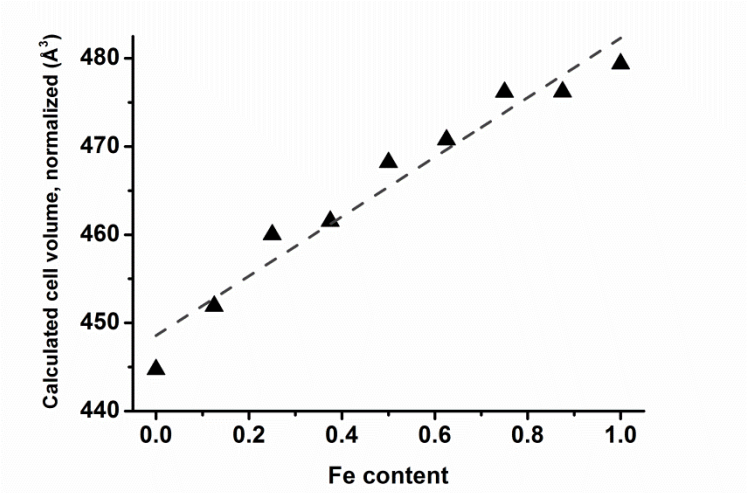

Fig. 5.18. Unit cell volume based on DFT data for the exemplary (Ca,Sr)(Mn,Fe)O_3 system with $t = 1.006 \pm 0.002$ normalized for 2x2x2 unit cells. The change in cell volumes agrees well with Vegard's law (linear fit: dashed line), with deviations attributed to the occupancy discretization. Taken from Vieten *et al.* (supporting information). [95]

Moreover, when comparing the cell parameters of experimentally studied phases such as to the theoretical results, discrepancies may arise. For instance, $SrFeO_3$ has a cell parameter $a = 3.85$ Å according to literature data (which actually describes $SrFeO_{2.96}$ to be exact), [246] but the calculated cell parameter is $a = 3.91$ Å. This could be explained both with the inherent inaccuracies of the DFT methods applied, as well as with potential experimental inaccuracies. The difference cannot be attributed to the non-stoichiometry in the experimental dataset, as it would counteract this effect. However, the results within the DFT study are consistent, as the change in lattice parameters between different perovskite compositions agrees well with the ionic radii and Vegard's law.

Energy of the systems: By means of DFT calculations, the formation enthalpies of all perovskite and brownmillerite phases are known. By calculating the difference in energies between the perovskite and the brownmillerite phase plus oxygen, we derive the redox enthalpy between the perovskite and brownmillerite phases. Moreover, one can estimate the stability of these phases by comparing the total energies of the systems to existing entries in the Materials Project database. The so-called energy above the convex hull (E_{hull}) describes the stability of a structure compared to the other phases with the same composition. E_{hull} = 0 means that a phase thermodynamically is the most stable material with the same composition and stoichiometry. According to these results, most phases investigated within this study are metastable, as E_{hull} is above zero. However, this does not mean that they cannot be formed, and moreover, the theoretical result does not necessarily describe the system accurately, as DFT calculations are never 100 % accurate for real systems, and by choosing ordered superstructures, we include some simplification in our simulations. Fig. 5.19 shows the energy above hull for all our calculated materials [199] and the calculated redox enthalpies for all pairs of perovskites and brownmillerites studied. 35 % of our calculated materials show E_{hull} values above 100 meV per atom. It is not possible to state one specific limiting value of E_{hull} above which materials should be considered unstable. Some authors use 25 meV/atom as a limiting value, [247] while others show exemplarily for binary oxides that 10 % of all experimentally observed polymorphs show theoretical E_{hull} values of 94 meV/atom or above. [95, 248] For this reason, we do not exclude any materials from our screening based on the E_{hull} values. One could derive a cutoff energy based on the so-called amorphous limit in future studies. [249] Nevertheless, one can use the E_{hull} value to estimate whether a calculated phase will be stable or not. For example, the E_{hull} for $Sr_7CaMnFe_7O_{24}$ is rather low at 13 meV/atom, and we synthesized similar solid solutions successfully as presented within this work. In contrast, phases like $K_4Na_4Mo_7WO_{20}$ with a significantly higher E_{hull} = 215 meV/atom are more likely to be unstable, and the literature in fact shows that synthesis of similar molybdenum and tungsten bronzes can be challenging and may require high pressures. [250]

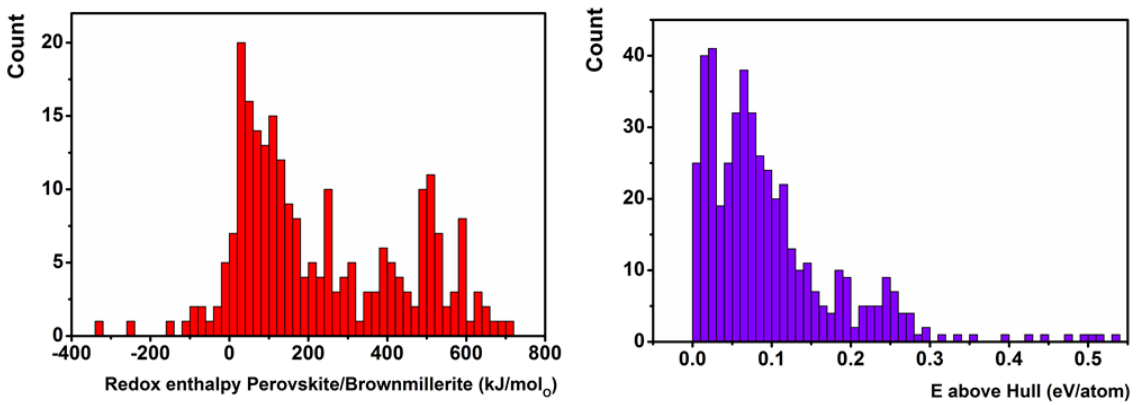

Fig. 5.19. Histograms of the redox enthalpy of the perovskite-brownmillerite redox pairs according to DFT (left) and the energy above the convex hull for all perovskite and brownmillerite phases (right). 35 % of the phases show E_{hull} values above 100 meV/atom.

The redox enthalpy can be calculated for 241 perovskite and brownmillerite redox pairs (both $(A'_xA''_{1-x})(M'_yM''_{1-y})O_{3/2.5}$ solid solutions and their $AMO_{3/2.5}$ endmembers), and is normalized in terms of kJ/mol of oxygen O. Kinetic limitations are not accounted for, and all reaction enthalpies are calculated for a temperature of 0 K, as usual in DFT. The materials cover a large range from -340 to 706 kJ/mol$_O$ for the reduction from perovskite to brownmillerite. A negative value indicates that the reduction occurs spontaneously at 1 bar p_{O_2} according to the thermodynamics, meaning that the materials are unstable and can only be prepared under high oxygen pressures. This is the case for 7 % of the studied redox pairs. Over 50 % of the redox material pairs are in the range between 50 and 400 kJ/mol$_O$, which is the most relevant range for thermochemical applications. [30, 95] In this enthalpy window, the maximum difference between two consecutive entries is 17 kJ/mol$_O$ with an average of 2.5 kJ/mol$_O$. A list of all redox pairs ordered by their redox enthalpy is included in the Appendix, section 8.3. Using this data, it is possible to select materials for a specific application, which means that we successfully designed redox materials based perovskite solid solutions applicable for different types of thermochemical cycles and under different operational parameters. The redox enthalpies for all studied perovskite solid solution systems are summarized in Fig. 5.20.

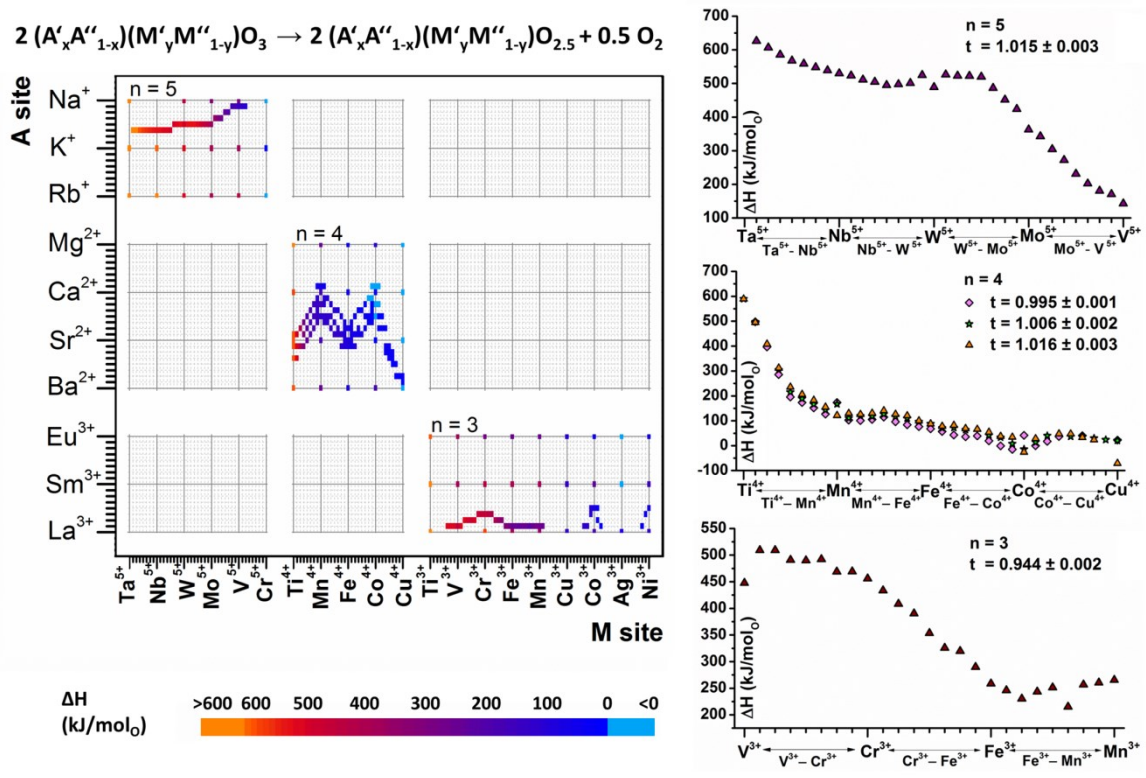

Fig. 5.20. Map of all perovskite-brownmillerite pairs studied using DFT within this work (left). The composition of the redox pairs is indicated on the *x* axis (*M* site) and on the *y* axis. Each dot represents one redox pair, and the color indicates the redox enthalpy from perovskite to brownmillerite. Solid solution endmembers are located on the intersections of solid lines indicating integer AMO_3 compositions. The redox enthalpies of selected tolerance-factor adjusted solid solutions are displayed on the right. Taken from Vieten *et. al.* [95]

Perovskite solid solutions with the general composition $(A'_xA''_{1-x})^{(6-n)+}(M'_yM''_{1-y})^{(n-2\delta)+}O_{3-\delta}$ with n = 3, 4, or 5 and δ = 0…0.5 are studied using DFT. While the experimental study was limited to systems with n = 4 (alkali earth metals on the *A* site), the theoretical dataset includes perovskites with alkali metals and lanthanides. These materials are particularly interesting, as some of them are in the enthalpy range suitable for water splitting, i.e., they show redox enthalpy changes close to the formation enthalpy of water. These include lanthanum ferrites and manganates, which are similar to materials suitable for water splitting reported in the literature. [33, 35, 251] Our theoretical study also includes unusual material compositions such as (Na,K)(Nb,W)$O_{3-\delta}$ or KVO_3. The synthesizability of some of these phases is questionable, as many of them are rather unstable. [250, 252] Moreover, KVO_3 is a material which is also known as potassium metavanadate, which does not show a perovskite structure but is a water soluble salt. This is in good agreement with the high E_{hull} of the perovskite phase, which is 216 meV/atom indicating that other phases may be more stable. Therefore, the data on such phases has to be considered carefully. Moreover, phases with very low tolerance factors (below 0.9 according to section 4.4) may not form stable perovskites. These include many Mg containing phases. Additionally, we have to consider the potential effect of the ionic radii on solid solution formation. Most of the ion pairs in our study have differences in ionic radii < 15 %, which should be an indicator for solid solution formation without phase segregation according to Goldschmidt's rules. [82] An exception for *A* site compositions (assuming 12-fold coordination) are Na^+-K^+ systems, with K^+ being 18 % larger than Na^+, and Mg^{2+}-Ca^{2+} systems, where Ca^{2+} is 26 % larger than the estimated ionic radius of Mg^{2+} in the same coordination (see table 2.2). For the *M* sites, Cu^{3+}-Co^{3+}, Cu^{4+}-Co^{4+}, Ag^{3+}-Co^{3+}, and Ag^{3+}-Ni^{3+} show differences in ionic radii over 15 %. These systems might show solubility gaps, which means that phase segregation may occur in these cases.

Effect of the tolerance factor *t* and linearity of Δ*H*: To study the effect of the tolerance factor on the redox enthalpy using theoretical data, we can consider the plots for n = 4 in Fig. 5.20. Our theoretical data reveals only small differences in the redox enthalpy for different tolerance factors for many phases, which is in good agreement with our experimental data. Most compositions seem to show lower slightly lower redox enthalpies for lower tolerance factors, but it is not possible to derive a general quantifiable trend. Moreover, if we look at the data for solid solutions more in detail and the dependence of the redox enthalpy on the *M* site composition, we can observe interesting trends. Exemplarily, (Ca,Sr,Ba)(Ti-Mn)$O_{3-\delta}$ phases are considered. Due to the higher redox enthalpy of $ATiO_3$ phases with respect to $AMnO_3$ phases (for the reduction to the brownmillerite), one would expect a linear increase in the redox enthalpy with increasing Ti content in these systems. Fig. 5.21 shows that this is not the case. Irrespective of the tolerance factor, replacing a small amount of Mn^{4+} by Ti^{4+} does not increase the redox enthalpy significantly according to our DFT calculations. While we do not know why this is the case, this result is in excellent agreement with our experimental data (see sections 4.3.1 and 5.1.2). This non-linear behavior is observed in some other cases in our DFT data of perovskite solid solutions. [95] Our results show two different regimes with a different Ti-content dependent slope of the Δ*H* increase, which overlap at 50 at% Ti.

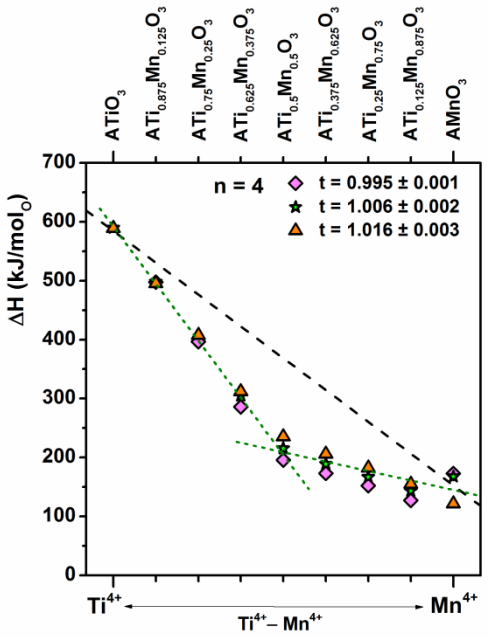

Fig. 5.21. Change in ΔH for the complete reduction from perovskite to brownmillerite for solid solutions containing Ti^{4+} and Mn^{4+}. The black dashed line indicates the expected redox enthalpy for a system where ΔH depends only on the Ti content. The real system does not show this behavior, but two different regimes (green dashed lines) with different Ti-content dependent enthalpy change. The replacement of a small amount of Mn^{4+} by Ti^{4+} has no significant effect on the redox enthalpy. This is in good agreement with our experimental data. The data is shown for different tolerance factors t, and the standard deviation of t is due to the occupancy discretization (2x2x2 supercells) in DFT. Taken from Vieten *et. al.* [95]

Perovskite solid solutions do not necessarily act like the sum of their constituents. The electronic structure of the solid solutions or changes in their unit cell sizes might impact their thermodynamics. Assuming an ideal random distribution of species, the amount of Ti atoms with other Ti atoms as next nearest neighbors is very low if the Ti concentration is small, and increases significantly only if Ti becomes the dominant species on the *M* sites of the perovskite. This may have implications on the thermodynamics and the electronic structure and might cause the observed effects. However, this is a speculative statement at this point. So far, we have only considered the extreme points in the non-stoichiometric phase space: the perovskite with $\delta = 0.0$ and the brownmillerite with $\delta = 0.5$. For some perovskites, it has been observed that stable vacancy-ordered structures are formed in-between these extreme values. [231] This may change the redox enthalpy and entropy. For instance, the entropy change may be lower due to vacancy ordering. In future studies, different vacancy-ordered structures could be considered along with structures with random vacancy distribution, and DFT calculations for each of these structures could reveal which one is the most stable structure by choosing the one with the lowest energy. A similar approach has been applied for locating vacancies in ceria as shown by Murgida *et. al.* [253] Moreover, the dilute species model describing the entropy change in the perovskite could be adjusted by changing the factor a (see Eq. 2.28). Another limitation of our data is given by the ordered superstructures which are used. Finding the lowest Ewald sum

does not necessarily lead to a realistic representation of the structure. The real perovskite solid solution does not behave like one ordered superstructure, but more like the overlap of all possible superstructures. One could calculate more than one superstructure and find which one is the most stable. In this process, other superstructures apart from the here-applied 2x2x2 phases could also be considered to account for potential long range ordering. This could be done using special quasirandom structures (SQS). [127, 128] Moreover, it could be advantageous to not just use the energy of one of these structures, but the weighted average. One also has to consider that the most stable structure at a temperature of 0 K is not necessarily the most stable structure at any given temperature, and the energetic barriers between different structures could be used to estimate which structure is most stable at which temperature. By calculating the enthalpy of these phase changes, one could estimate how likely they occur. The calculations suggested here, of course, would increase the computational power necessary to model these systems drastically. Another approach for modelling solid solutions in DFT can be so-called virtual crystals, where the electronic potentials of the constituents of the solid solution are averaged, and the creation of superstructures is not necessary. [254] Despite the limitations, the DFT calculations presented here allow a pre-selection of materials and give a good approximation of the expected redox thermodynamics and crystal structures. Further studies could focus on achieving a higher accuracy in DFT modelling for very few materials, and allow increasing the accuracy of the materials screening by deriving general trends in phase stability and order/disorder effects. Further studies could also consider a wider range of materials, such as perovskites with differently charged *A* site anions (for example, Sr^{2+} and La^{3+} [35, 112]). This, of course, would require an adjusted thermodynamic model due to the different maximum δ and the different changes in ΔH and ΔS as a function of δ. Non-perovskite redox materials could be studied as well.

In summary, we have shown a large dataset of DFT calculations of perovskite and brownmillerite solid solutions and their endmembers. For the most part, the DFT calculations converged quickly and lead to reasonable results. The lattice constants of the solid solutions follow Vegard's law. Most of the structures are metastable according to the E_{hull}, but most of them are likely to be synthesizable nevertheless. The redox enthalpies of the solid solutions for the reduction from the perovskite to the brownmillerite phases span over a wide range, with 50 % in the window between 0 and 400 $\mathrm{kJ/mol_O}$. We have demonstrated that through design of perovskite solid solutions, any ΔH value within this window can be achieved, and perovskites can be designed according to their intended field of application. Solid solutions do not necessarily act as the sum of their constituents, which we demonstrate using the example of Ti^{4+} and Mn^{4+} containing phases. The resulting dependence of ΔH on the Ti content is in good agreement with our experimental findings. The accuracy of the thermodynamic models may be improved in the future by considering a wider range of possible arrangements of the atoms and vacancies in the solid solutions phases by performing additional DFT calculations in an extended parameter space. This, however, increases the computational cost.

5.3 Comparison of theoretical and experimental data

In the previous section, it has already been mentioned that the observed dependence of the redox enthalpy change in Ti^{4+}-Mn^{4+} solid solutions is in good agreement with our experimental findings. We extend this comparison in the following to all experimentally studied materials and apply the functions for $\Delta H(\delta)$ and $\Delta S(\delta)$ to calculate the chemical equilibrium for any set of conditions (temperatures, oxygen partial pressures, and δ values). By this means, we create "isographs" based on experimental and theoretical data as shown in section 8.5. The data is combined in the online resource *RedoxThermoCSP* as part of the Materials Project infrastructure, and the user-controlled interactive graphs created with this tool are presented in this section.

Redox enthalpies for the full reduction from perovskite to brownmillerite

Firstly, we consider the redox enthalpies calculated using DFT compared to those based on experimental studies. Fig. 5.22 shows a plot comparing both datasets. Based on DFT, the redox enthalpy is calculated for the full reduction from perovskite to brownmillerite, whereas in the experimental studies, only a limited range of δ values is covered. This changes the result and limits the accuracy of this comparison. For our comparison, we use the average measured ΔH values. The upper graph in Fig. 5.22 shows the minimum and maximum absolute δ values (accounting for the δ_0) covered in our experimental study for different materials. Experimental thermodynamic data for $CaMnO_3$ is based on an earlier study (see section 4.1). [132]

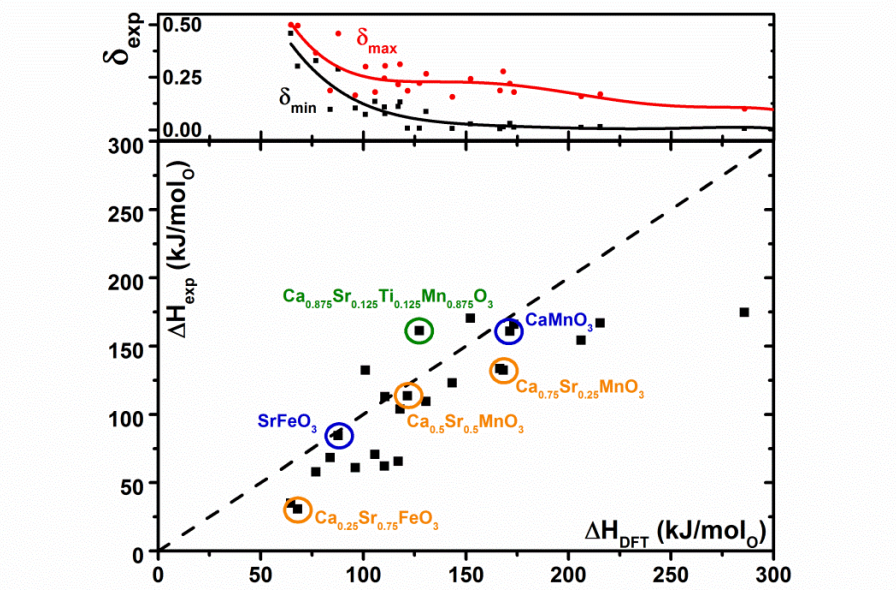

Fig. 5.22. Comparison of experimental (exp) and theoretical (DFT) values for the reduction of perovskite solid solutions. DFT values are calculated for the complete reduction from perovskite to brownmillerite, whereas experimental values only cover a limited range of δ values, as indicated by δ_{min} and δ_{max} in the upper plot. The dashed line indicates where $\Delta H_{exp} = \Delta H_{DFT}$. Some exemplary materials are highlighted. Taken from Vieten et. al. [95]

The experimental and theoretical phases are matched by finding the theoretical phases closest in composition to the experimental phases through a discretization of the experimental stoichiometry values by a factor of 1/8. For simple compositions of solid solution endmembers such as $SrFeO_3$ and $CaMnO_3$ (blue circles in Fig. 5.22), we can find a very good agreement between the experimental and theoretical ΔH values. This is not surprising, as the redox enthalpy of these phases should not depend on δ, and the limited range of experimentally covered δ values is therefore irrelevant. This should also hold true for solid solution phases with two different *A* species but only one *M* species (orange circles in Fig. 5.22), but we can find larger discrepancies in some cases. Larger deviations can be expected for phases with two different *M* species (one exemplary phase marked in green in Fig. 5.22). Especially in the case of phases with large ΔH_{DFT} values, the measured ΔH_{exp} is considerably smaller than the theoretical value. This is owing to the fact that only data for small δ values is covered experimentally. For solid solutions with two *M* species with different redox activity, the $\Delta H(\delta)$ for small δ values is below the average ΔH, as shown before in this work. In terms of the general trend, the calculated and experimental redox enthalpies correspond well, but the significant deviations of both values in many cases show that it is necessary to use a δ-dependent model also for the theoretical data, as introduced in sections 2.5 with limiting values ΔH_{min} and ΔH_{max} based on the redox enthalpies of the solid solution endmembers. These limiting values are tabulated in the Appendix, section 8.3.

RedoxThermoCSP: Using this data, the chemical equilibrium can be calculated by finding where ΔG is zero. This data is compiled through *RedoxThermoCSP*, a contribution of *MPContribs* within the infrastructure of Materials Project. [k] Access is free of charge after registration, which enables the re-use of the data by the entire scientific community. Fig. 5.23 shows the start page of RedoxThermoCSP. The package consists of a tool to plot chemical equilibrium data ("Generate Isographs"), an "Energy Analysis" tool for materials selection based on the expected energy consumption (see section 6.1), and a short documentation explaining the use of the data. We focus on the Isographs section in the following. After a click on "Generate Isographs", a page appears which shows a list of all materials within this study, and one specific material can be selected by clicking on the corresponding row. By doing so, the six user-controlled interactive graphs presented in section 8.5 appear and can be modified by changing the parameters. Each plot contains equilibrium data based on theoretical calculations as presented in this work, and experimental data, if available. Moreover, by clicking on the entries under "contribution", detailed thermodynamic data can be retrieved, such as the experimental data and fits, if available. Additionally, one of the raw thermogravimetric scans is shown exemplarily on this details page, and the raw computed data for the energy analysis (see section 6.1) is presented. Through the list of materials in the Isographs section, the corresponding entries (perovskite and brownmillerite) in the Materials Project database can also be retrieved.

[k] https://materialsproject.org/mpcontribs and https://contribs.materialsproject.org/redox_thermo_csp

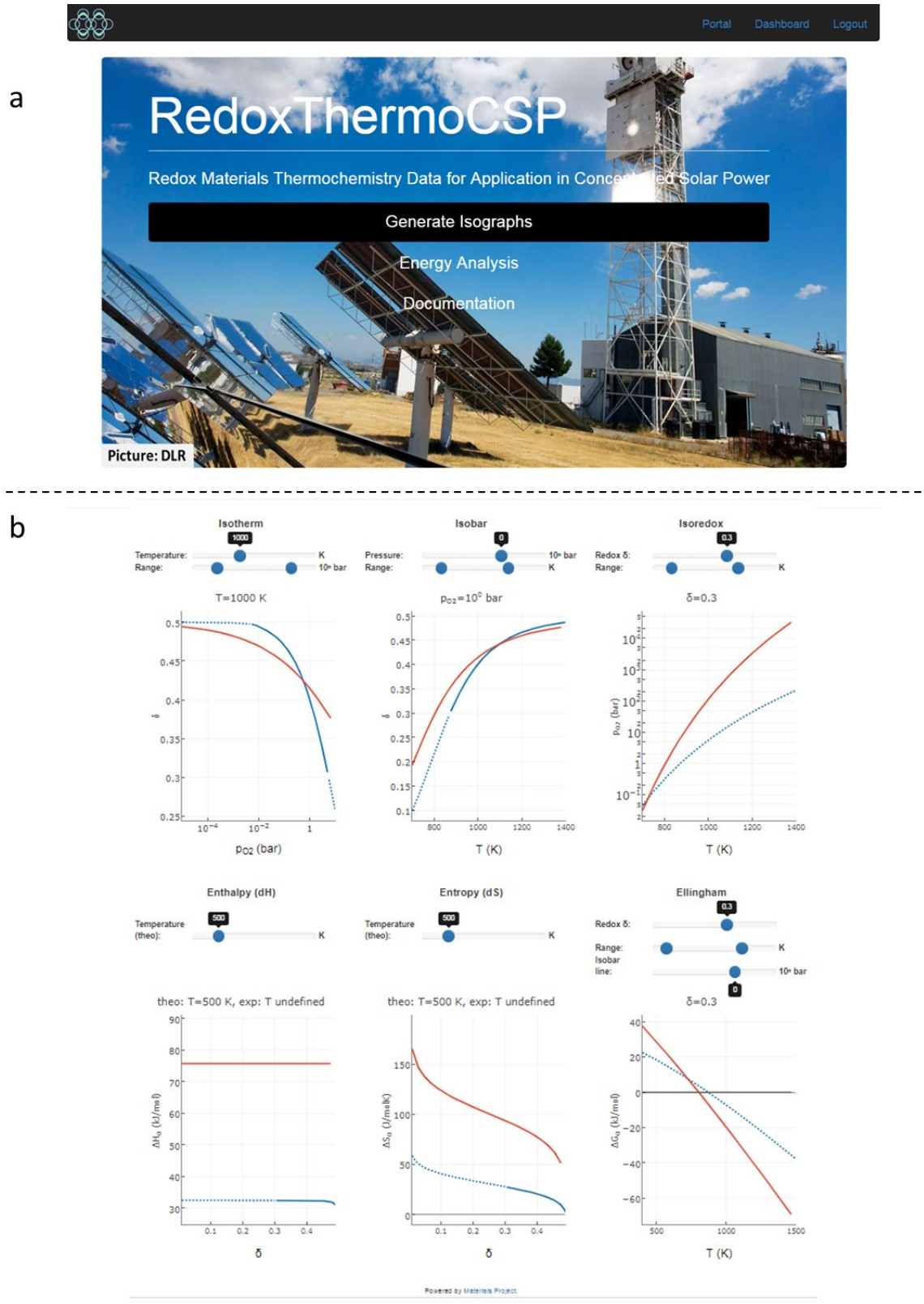

Fig. 5.23. RedoxThermoCSP database as of Oct 12th 2018. The start page (a) allows selecting one of the three main sections of the tool. By clicking on "Generate Isographs" and choosing one material on the next page, plots of the thermodynamic equilibrium can be created based on theoretical (red) and experimental (blue) data (b, here: $Ca_{0.25}Sr_{0.75}FeO_{3-\delta}$), see Appendix section 8.5, available through https://contribs.materialsproject.org/redox_thermo_csp).

The full source code is available through GitHub (see Appendix, section 8.4). [1]

Theoretical and experimental thermodynamics of species with one transition metal *M*

To compare experimental and theoretical equilibrium thermodynamic data, we first consider the case of $SrFeO_{3-\delta}$ as a simple reference material due to its well-known redox properties. [16, 61, 92] Three Isographs created in RedoxThermoCSP for this material are shown in Fig. 5.24. The experimental data is drawn as solid lines within the range of experimentally covered δ values, and as dashed lines to indicate extrapolations. Within the range of the measured data, the theoretical and experimental equilibrium positions are in good agreement. For extrapolated data, the experimental model shows a significantly higher δ value for low temperatures than the theoretical model. This may be due to kinetic limitations in the oxidation reaction at low temperature, so that the sample could not be oxidized to reach its equilibrium oxygen content. The Ellingham diagram shows the Gibbs free energy at standard conditions (1 bar oxygen partial pressure) and an isobar line to correct for the actual oxygen partial pressure ($-1/2\ RT \ln p_{O_2}$). The plot in Fig. 5.24 shows exemplarily that the system reaches the composition $SrFeO_{2.60}$ ($\delta = 0.40$) at approx. 750 K under $p_{O_2} = 10^{-5}$ bar (intercept of blue or red line with the grey line). A lower oxygen partial pressure leads to a lower reduction temperature, as the slope of the grey isobar line increases with decreasing p_{O_2}.

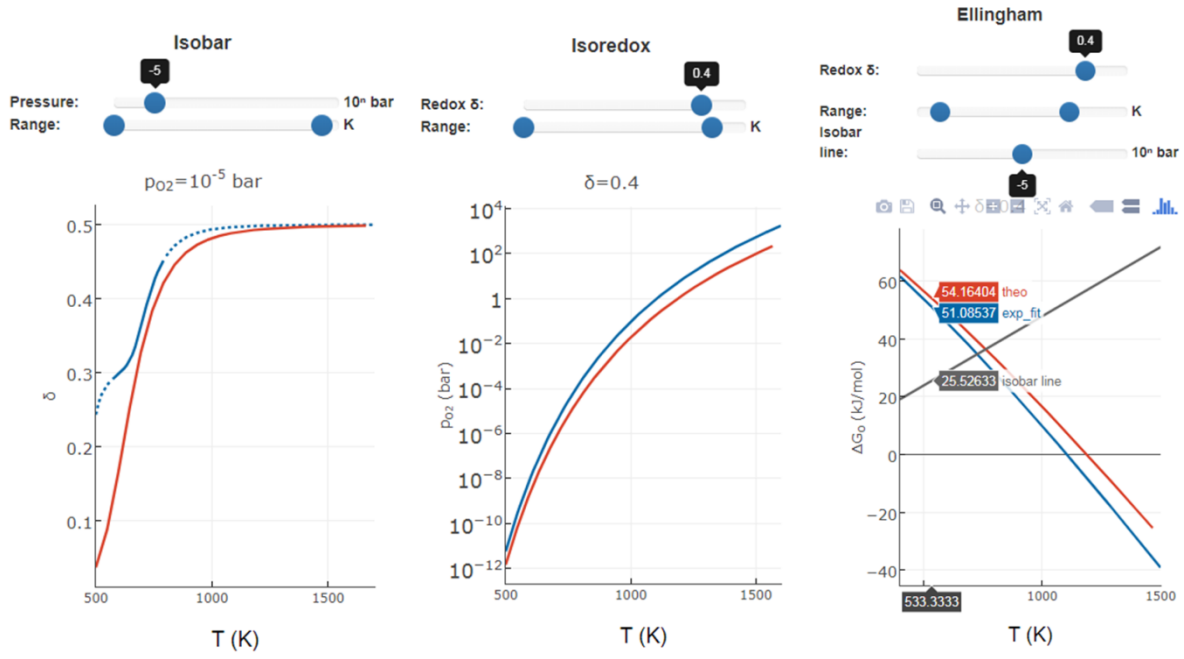

Fig. 5.24. Exemplary isographs as of Oct 12th 2018 created using RedoxThermoCSP for the system $SrFeO_{3-\delta}$. The equilibrium position is calculated based on theoretical data (red) and experimental data (blue). Dashed blue lines indicate where the experimental data is extrapolated, whereas solid blue lines indicate data within the range of measured δ values. Taken from Vieten *et al.* [95]

[1] https://github.com/materialsproject/MPContribsUsers/tree/master/redox_thermo_csp

In the theoretical model presented in section 2.5, the DFT-calculated enthalpy values and elasticity data are used to calculate $\Delta H(\delta, T)$ and $\Delta S(\delta, T)$. Opposed to this, our experimental data only contains functions for $\Delta H(\delta)$ and $\Delta S(\delta)$, as temperature effects on the entropy or enthalpy change are not determined in our experiments. It was not possible to measure $\Delta H(\delta)$ and $\Delta S(\delta)$ isothermally, as mentioned before. Therefore, it is difficult to compare both datasets. Fig. 5.25 shows a comparison of the experimental $\Delta H(\delta)$ and the theoretical $\Delta H(\delta, T)$ as well as a comparison of the respective entropy datasets. The theoretical data is given for isothermal conditions, whereas the experimental data has been measured over a broad temperature change. This may also explain the δ-dependent changes in $\Delta H(\delta)$ in the experimental dataset. The theoretical ΔH value is significantly higher than the value calculated through DFT (see section 8.3 or Fig. 5.22), as the redox enthalpy change increases with increasing temperature in our model (compare Eq. 2.23), which leads to higher ΔH values being used than the DFT-calculated values for 0 K. ΔS is calculated theoretically as the sum of the partial molar entropy of oxygen, the vibrational entropy, and the configurational entropy. The latter may be lowered by oxygen vacancy ordering, which is not considered in our theoretical model may explain the lower experimental $\Delta S(\delta)$ compared to the theoretical $\Delta S(\delta, T)$. A source of error in the experimental data is enthalpy-entropy compensation, which leads to ΔH and ΔS not being measurable completely independently. [197] Nevertheless, ΔG should be accurate, and Fig. 5.24 does show a good agreement between the experimental and theoretical ΔG values.

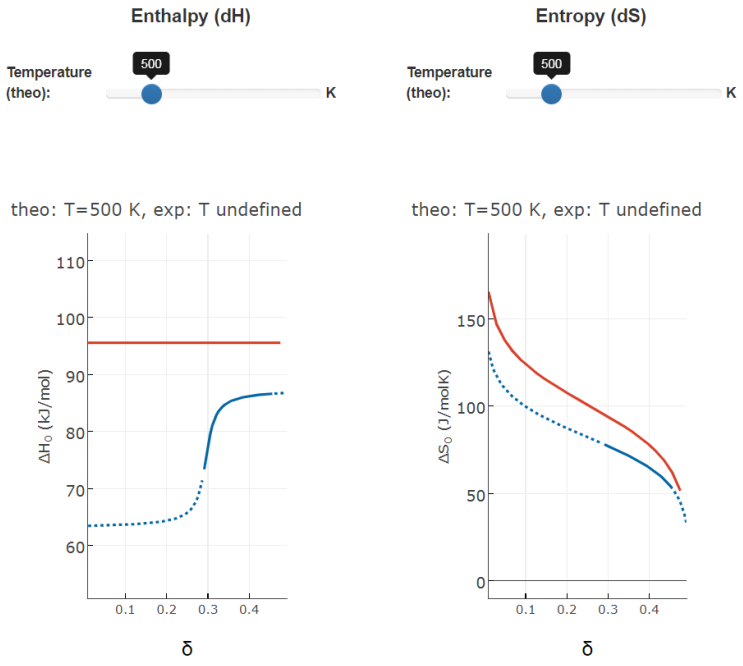

Fig. 5.25. Enthalpy and entropy change for the perovskite $SrFeO_{3-\delta}$ as a function of δ, based on experimental data ($\Delta H(\delta)$ and $\Delta S(\delta)$, blue lines) and theoretical data ($\Delta H(\delta, T)$ and $\Delta S(\delta, T)$, red lines) as of Oct 12th 2018 from RedoxThermoCSP. The fixed temperature only affects the theoretical dataset, as the experimental data could not be measured isothermally. Dashed blue lines indicate where the experimental data is extrapolated, whereas solid blue lines indicate data within the range of measured δ values.

Theoretical and experimental thermodynamics of species with two transition metals

If we look at data for perovskite solid solutions with more than one transition metal species *M*, the predicted equilibrium data based on the experimental and theoretical datasets agree well in many cases, but there are exceptions. Fig. 5.26 shows experimental data for $Ca_{0.21}Sr_{0.79}Mn_{0.6}Fe_{0.4}O_{3-\delta}$ and theoretical data for $Ca_{0.25}Sr_{0.75}Mn_{0.625}Fe_{0.375}O_{3-\delta}$. The equilibrium oxygen partial pressure agrees relatively well between the two datasets within the range of measured δ values (solid blue lines). The discrepancies in the ΔH and ΔS curve shapes may be attributed to the constant temperature in the theoretical datasets, whereas the temperature in the experimental datasets typically increased with increasing δ. Therefore, the theoretical ΔS is underestimated at high δ values. Nevertheless, experimental and theoretical data are in good overall agreement in this case.

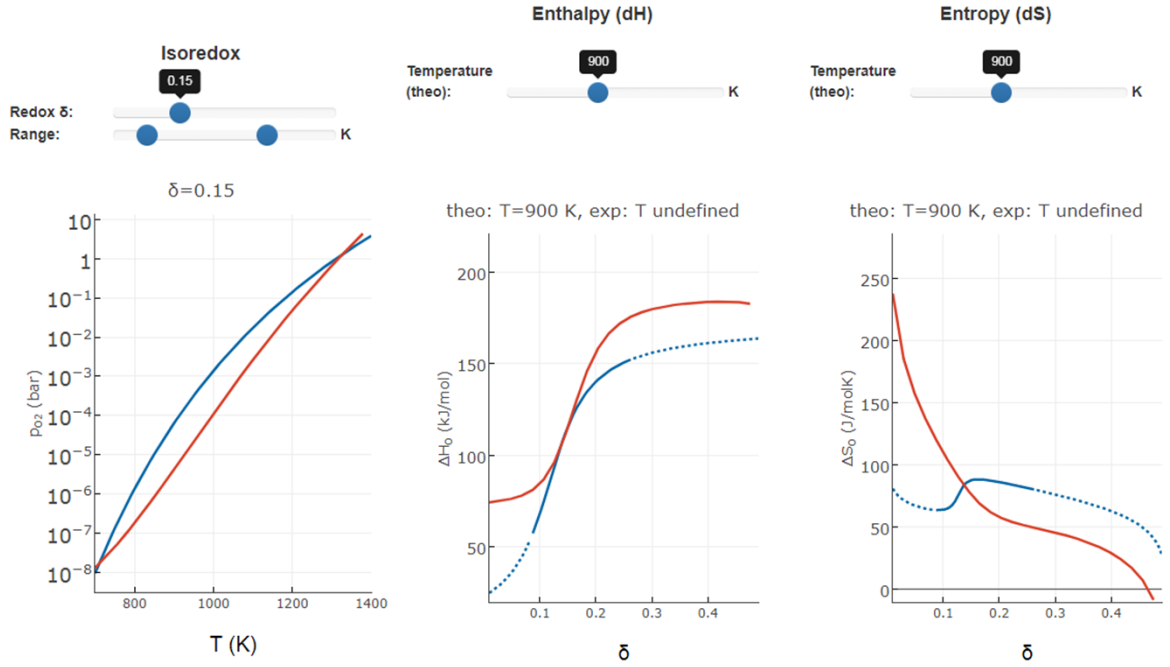

Fig. 5.26. Isoredox plot and enthalpy/entropy graphs for $Ca_{0.21}Sr_{0.79}Mn_{0.6}Fe_{0.4}O_{3-\delta}$ (experimental data, blue) and $Ca_{0.25}Sr_{0.75}Mn_{0.625}Fe_{0.375}O_{3-\delta}$ (theoretical data, red) as of Oct 12th 2018 from RedoxThermoCSP. Interpolated experimental data is indicated as dashed lines.

In other cases, however, the agreement between both datasets can appear less promising. This is especially the case for solid solutions with a large experimentally determined δ_0 value. In some cases, this value may be inaccurate, which leads to the $\Delta\delta$ values being correct while the absolute δ values are not. This, of course, is only true in most cases but not always, as ΔH and ΔS are different near absolute δ values of 0 and 0.5 compared to values in-between, and the absolute δ is not irrelevant for the model. Nevertheless, we compare the relative $\Delta\delta$ values predicted for different sets of oxygen partial pressures and temperatures in the following. The $\Delta\delta$ values can be used to determine how much oxygen is absorbed or released under given conditions, and are therefore the most relevant values for practical applications.

Comparison of the predicted $\Delta\delta$ values

By calculating the chemical equilibrium state as a function of T and p_{O_2} for different oxidation and reduction temperature and oxygen partial pressure levels, we can determine the respective δ_{red} and δ_{ox} values, and calculate the difference between them ($\Delta\delta$). As parameter sets for the temperatures and pressures, we use all possible combinations of the values as given in the matrices below see Fig. 5.27, These values represent a range of typical operating conditions of thermochemical air separation cycles. Values are only used if Eq. 2.43 is positive, as materials with a negative integral over ΔH in the selected range are either highly unstable, or $\delta_{red} < \delta_{ox}$, which is excluded by definition (the material would be oxidized instead of reduced under these conditions). This calculation is performed for all materials with both experimental and theoretical datasets. The result is a plot of over 27500 theoretical $\Delta\delta$ values which are coupled with the same amount of experimental $\Delta\delta$ values in Fig. 5.28 (black dots).

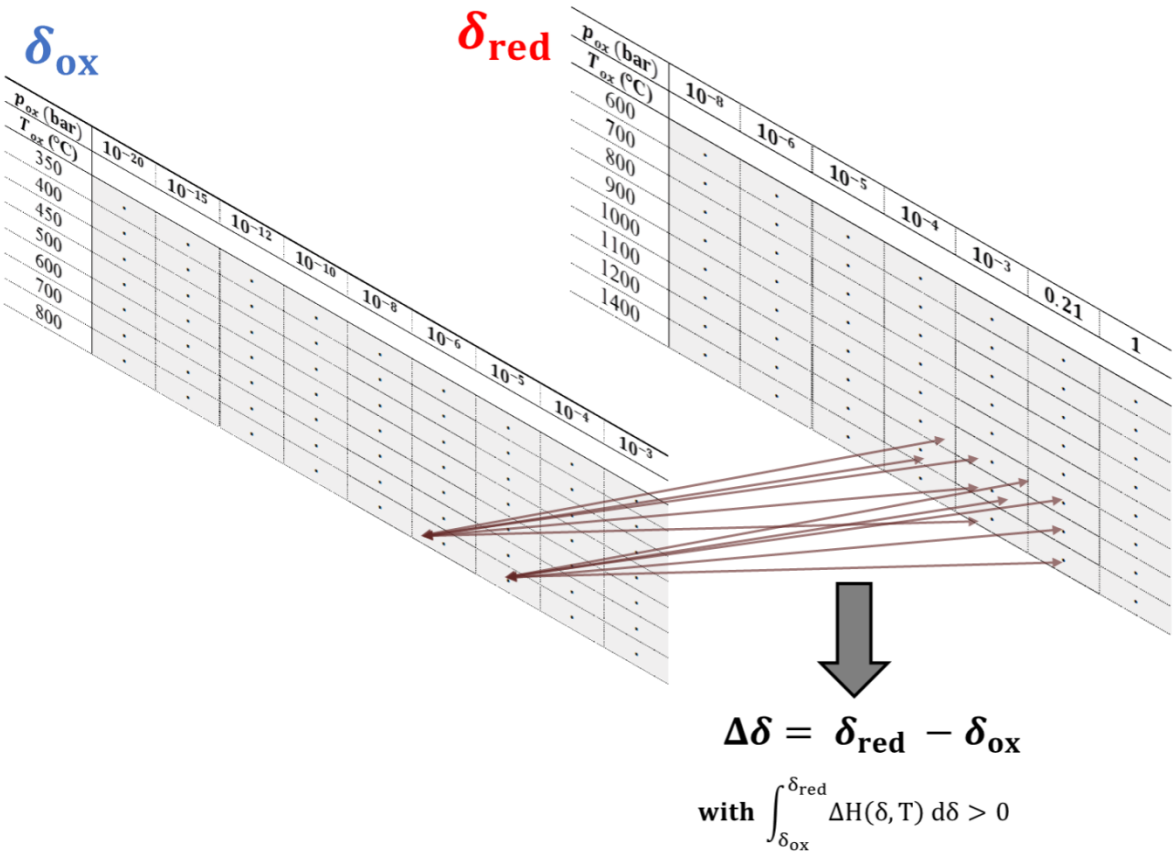

Fig. 5.27. Calculating $\Delta\delta$ for a large amount of pre-defined parameter sets (T, p_{O_2}) for typical air separation processes. The change in non-stoichiometry $\Delta\delta$ is calculated for equilibrium conditions under oxidation and the reduction conditions for all materials using experimental and theoretical data. The $\Delta\delta$ values are only used if the integral over ΔH in this range is positive, i.e. the reduction reaction is endothermic. An exothermic reduction reaction indicates highly unstable materials or that $\delta_{red} < \delta_{ox}$, which is excluded by definition. Compare Table 6.1.

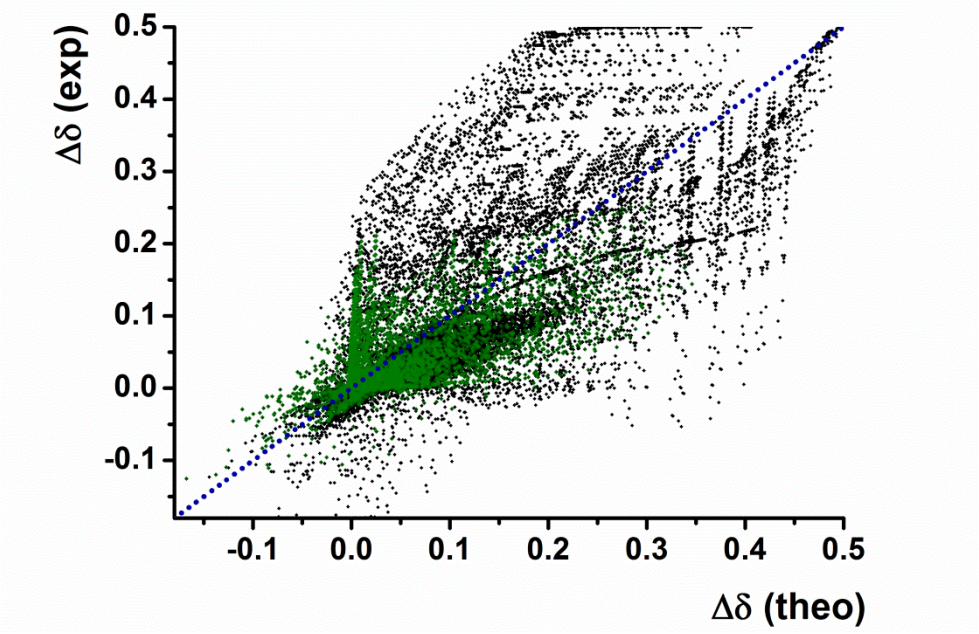

Fig. 5.28. Change in non-stoichiometry $\Delta\delta$ for the conditions according to Fig. 5.27 according to our empirical experimental model (exp) and our theoretical model (theo). Each data point corresponds to one set of redox parameters (oxidation and reduction temperatures and oxygen partial pressures) and one material. The data marked in black (> 27500 data points) indicates the complete data set, whereas the green data points (> 4500) are based on non-extrapolated δ values only, leading to a significant improvement in the accuracy of the experimental data. The dashed blue line indicates where theoretical and experimental data match. Taken from Vieten *et al.* [113]

In some cases, large differences between the values predicted using the theoretical and the experimental models can be observed. The agreement between both datasets is especially unsatisfactory for large values of $\Delta\delta$. It can be significantly improved by only considering data points where the experimentally predicted δ_{red} and δ_{ox} values are both within the range of experimentally covered δ values, i.e., extrapolated data is excluded (green data points in Fig. 5.28). As the range of calculated redox conditions spans temperature windows between 350 and 1400 °C and oxygen partial pressures between 10^{-20} and 1 bar, the here-calculated range of conditions is much larger than what was covered in the experiments. Hence, the extrapolated data may be highly inaccurate. The amount of oxygen released (which is proportional to $\Delta\delta$) is in the correct order of magnitude for many materials and sets of redox conditions, but its accuracy may be improved in future studies. It is important to note here that we are not comparing a model to measured data in Fig. 5.28., but an empirical model based on experimental data is compared to a theoretical model based mainly on DFT data. Moreover, the discretization of occupancies leads to slight differences in non-stoichiometry and may induce aliasing effects (step-wise increase of naturally linear properties). For these reasons, one cannot state that one value is more accurate than the other, but only compare the predicted values in both models and evaluate the agreement between them.

The large dataset of experimental and theoretical thermodynamic data allows predicting the expected mass change for a large range of redox conditions. By comparing the data based on empirical fits to the theoretical data, it can be estimated how accurate the predicted values are. The probability of an accurate prediction is higher if both values agree well. Additionally, if the relevant range of T and p_{O_2} values has been covered experimentally, it is possible to use the measured experimental $\Delta\delta$ values from section 8.6 to verify the data.

In summary, it has been shown within this chapter that it is possible to prepare stable perovskite solid solutions as redox materials over a large compositional range with adjustable thermodynamic properties and phase stability. The X-Ray diffractograms reveal solid solution formation for all 24 studied cases with 2ϑ shifts in agreement with the varied ionic radii. Thermogravimetric scans at different oxygen partial pressures and temperatures have been used to extract the change in redox enthalpy ΔH and the change in redox entropy ΔS in dependence of the change in non-stoichiometry $\Delta\delta$. For perovskite solid solutions with two different transition metals on the M sites, ΔH and ΔS are usually strongly dependent on δ. In most cases, the A site composition, however, only has small effects on the thermodynamics. This allows stabilizing perovskites with different M species by adjusting the A site composition without large changes in the redox thermodynamics ("tolerance factor engineering"). The thermodynamic data has been extracted using the van't Hoff method and empirical fit functions have been applied to create analytical functions describing $\Delta H(\delta)$ and $\Delta S(\delta)$. The fit functions also allow an extrapolation beyond the range of experimentally covered δ values, but this data may be highly inaccurate. The experimental data reveals that perovskites with alkali earth metals on their A sites can be applied for thermochemical air separation over a large range of temperatures and oxygen partial pressures. By changing the M site composition of these perovskites, the redox enthalpy change can be adjusted to tune the reducibility of the oxidized material and the oxygen affinity of the material in the reduced state. Materials containing Ti can be used to reach very low oxygen partial pressures (below $10^{-15} - 10^{-20}$ bar) at the expense of a high energy input per mol of oxygen released, whereas materials containing Co are at the opposite end of the spectrum with achievable equilibrium oxygen partial pressures typically not below 10^{-4} bar. Solid solutions both containing Mn and Fe are in-between these extremes, and the oxygen affinity can be adjusted through control of the Mn/Fe content.

The DFT calculations necessary for the theoretical model were successful in the vast majority of cases, as indicated by the convergence in the total energies of the calculated systems. The cell volumes based on the calculated structures are in good agreement with Vegard's law. However, minor non-linearities in the cell volumes of solid solutions are induced by discretizing partial occupancies in the 2x2x2 supercells, which leads to a discretization in the metal stoichiometries by a factor of 1/8. Most calculated materials are metastable according to the energy above the convex hull, but a large amount of them is expected to be synthesizable nevertheless. By calculating the

difference in formation enthalpies of the perovskite and brownmillerite phases, we determined the theoretical redox enthalpies per mol of oxygen released or absorbed for over 240 perovskite/brownmillerite pairs. The redox enthalpies are in good agreement with the experimental data, as long as the experimentally covered data range is large enough and representative for the complete spectrum of $\delta = 0 \dots 0.5$. Using the experimental data and empirical fit functions introduced in this chapter, as well as the theoretical data and the models introduced in section 2.5, we can derive equations describing the thermodynamic properties as a function of δ, and in the case of theoretical data, also as a function of the temperature T. By finding the chemical equilibrium position through a minimization of the Gibbs free energy, we can calculate the thermodynamic equilibrium position over a large range of conditions such as different oxygen partial pressures and temperatures. We derived "Isographs" from this data as explained in section 8.5 including isobars, isotherms, and "isoredox" plots. These are made publicly available within the infrastructure of Materials Project as the user contribution RedoxThermoCSP. We introduced the user-controlled interactive graphs available in this online resource within this chapter and evaluated the agreement between experimental and theoretical graphs. This agreement is good in many cases, especially as long as the data range is within the experimentally covered values. To study the agreement between both models more in detail, we compared predicted $\Delta\delta$ values for a large range of potential parameter sets for thermochemical air separation. By excluding interpolated values based on the empirical model (experimental data), we could show that the agreement between both models is significantly improved. Our models allow predicting the expected redox behavior of a large set of perovskites and their solid solutions for two-step (solar-) thermochemical cycles for many different potential application scenarios.

Despite the promising results, it is important to summarize the limitations of our models and give an outlook on potential improvements in future studies. Table 5.1 shows the strengths and weaknesses of both models. Our methods enable screening a large set of materials and allow the prediction of the redox extent in good accuracy under many different parameters and for many different materials. Therefore, these methods are ideal for a broad screening as a materials pre-selection study. The potential improvements of the materials screening process as suggested in Table 5.1 all significantly increase the complexity and cost of the experimental or theoretical screening process due to longer measurement times and computational times, and should therefore be applied to study a small amount of materials depending on the operating conditions after the initial screening presented here. Our generic process model as shown in section 2.6 as well as our thermodynamic functions and models allow calculating the amount of energy required to operate thermochemical cycles with different materials based on the process conditions. In the following chapter, we present a perovskite search engine based on this data which reveals which materials are expected to show the best performance under given conditions. Moreover, we discuss how the efficiency of these processes can be improved based on our data.

Table 5.1. Strengths and weaknesses of the applied models and potential improvements in the future. Both models complement each other, and a dataset is deemed reliable if the experimental and theoretical models are in good agreement. Many improvements can be made to further study the redox properties of perovskite solid solutions in the future. These should be carried out with a limited sample size due to the significantly increased experimental and computational effort.

Model		Strengths/Weaknesses and potential improvements
Experimental model	+	Based on experimentally measured thermogravimetric data
	+	Fit accurately describes $\Delta H(\delta)$ and $\Delta S(\delta)$ within the measured data range
	+	Relatively simple analytical fit functions allow fast equilibrium calculations
	+	Broad experimental screening of 24 materials with a standardized procedure
	–	Inaccurate extrapolations outside the measured data range **Improvement:** measurement over a larger data range for materials of interest (increases experimental effort, may require reaching very low and very high oxygen partial pressures in the thermobalance)
	–	Temperature dependence of ΔH and ΔS not covered **Improvement:** measurement of significantly more data points and evaluation of different temperature ranges to evaluate temperature effects (disadvantage: measurement time per material increases by one order of magnitude)
	–	Non-stoichiometry at the reference point (400 °C, oxygen partial pressure 0.18 bar) δ_0 only determined from fit, often not very accurate **Improvement:** measurement of δ_0 through experimental methods such as iodometry or thermogravimetric reduction in hydrogen
Theoretical model	–	Relies purely on theoretical considerations, may be biased by model
	+	Thermodynamic models describe $\Delta H(\delta, T)$ and $\Delta S(\delta, T)$ for any $\delta = 0 \ldots 0.5$ and are based on well-estabilished fundamental properties and physical models
	–	Complex thermodynamic functions which are solved numerically and DFT calculations require long computation times
	+	Includes a large set of materials (over 240 perovskite-brownmillerite pairs)
	+	Does not depend on limited experimental data ranges
	+	Temperature dependence of ΔH and ΔS is covered
	+	Absolute δ values are determined instead of relative $\Delta\delta$ values, no δ_0 values required
	–	Metal species occupancies normalized to 1/8 to allow integer occupancy values in a 2x2x2 supercell as required by DFT, this may lead to aliasing effects (step-wise change of properties which are changing gradually in nature) **Improvement:** use larger supercells (longer computation times) or virtual crystal approximation (VCA, potentially lower accuracy)
	–	Discretized supercells do not necessarily represent a solid solution with random site occupancy **Improvement:** use virtual crystal approximation (VCA) or averaging of more than one ordered structure (increases computational time), potentially use special quasirandom structures (SQS) to find representative ordered structures
	–	Potential ordering of solid solutions not considered (for instance: complex stacking variants in some perovskites along one or more crystal axes) **Improvement:** increase the size of the supercells and simulate more than one ordered structure (limited due to exponential increase in computational times)
	–	Oxygen vacancy ordering not considered **Improvement:** simulate oxygen vacancy ordered structures through DFT and select those with lowest total energy (limited due significant increase in computational times)
	–	DFT only yields results for 0K, accuracy of $\Delta H(T)$ and $\Delta S(T)$ may be limited **Improvement:** further experimental studies of temperature effects, calculation of energetic barriers between different similar structures

6. Application scenarios and energetic analysis

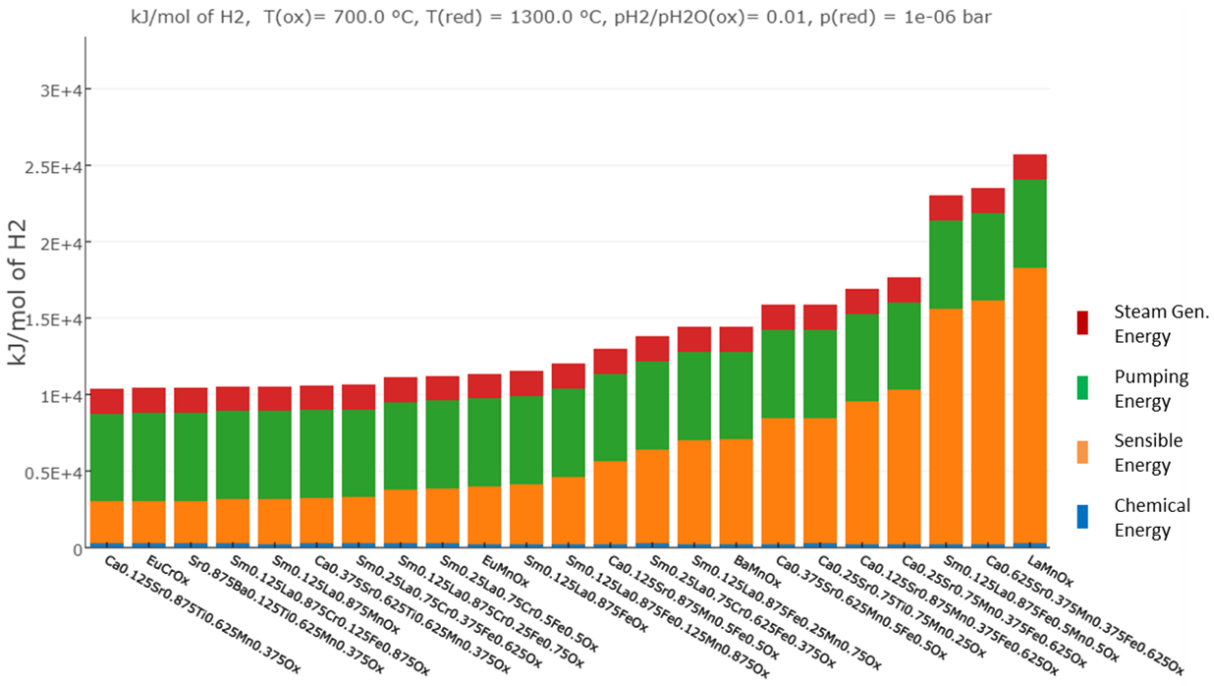

Fig. 6.1. Energetic analysis of a water splitting redox cycle as generated in RedoxThermoCSP based on theoretical data presented within this work. Our tool allows ranking materials according to the expected overall energy demand, for instance in terms of kJ per mol of product (here: H_2). The overall energy demand is calculated as the sum of the Chemical Energy, Sensible Energy, Pumping Energy, and Steam Generation Energy (if applicable). Taken from Vieten *et. al.* [113]

Experimental and theoretical thermodynamic data on tolerance-factor adjusted perovskite solid solutions has been presented in the previous chapter. Using this data, the change in non-stoichiometry can be predicted under a set of given parameters (oxidation and reduction temperatures and oxygen partial pressures). The use of this data is extended within this chapter by calculating the energy demand of such redox cycles using a generic process model. This allows creating a perovskite materials search engine which reveals the most efficient material for most application scenarios. Based on this data, we show which factors govern the energy demand of these cycles. We also present the advantages of using thermochemical cycles for different processes and show which aspects need to be improved based on our data to render such redox cycles energetically competitive with state-of-the-art technologies.

This chapter is partially based upon the following peer-reviewed publications authored and co-authored by the author of this work:

Vieten, J.; Bulfin, B.; Huck, P.; Horton, M.; Guban, D.; Zhu, L.; Youjun, L.; Persson, K.; Roeb, M.; Sattler, C., Materials design of perovskite solid solutions for thermochemical appplications, Energy & Environmental Science 2019, 12, 1369-1384.

Brendelberger, S.; Vieten, J.; Roeb, M.; Sattler, C., Thermochemical oxygen pumping for improved hydrogen production in solar redox cycles. International Journal of Hydrogen Energy 2019, 44, 9802-9810.

6.1 Perovskite search engine and redox cycle analysis

One tremendous benefit of creating equations describing the change in redox enthalpy and entropy under different conditions is being able to model the system under any of these conditions and find the thermochemical equilibrium state. In the previous chapter, we have shown how isographs can be prepared from this data which reveal the extent of oxygen uptake or release under different conditions (different oxygen partial pressures, temperatures, or oxygen non-stoichiometry δ). In section 2.6, we have introduced a generic model describing the energy demand of such redox cycles. The model predicts the materials specific aspects of the overall energy demand. It does not account for parameters such as the receiver type, re-radiation or other thermal losses, or the efficiency of the solar field if the sun is used as heat source. By assuming systems in thermochemical equilibrium and by deriving the energy necessary to bring the system from the reduced state in equilibrium to the equilibrium oxidized state and back, we can compare the suitability of different materials for such redox process under different pre-defined conditions. By this means, we can create a perovskite search engine. It is worth mentioning that a real system is not always in equilibrium. Since we apply thermodynamic models, we can only calculate the equilibrium state, and our simplified process model does not account for non-equilbrium conditions, as these would be reactor-dependent. Nevertheless, our model allows comparing different materials and gives an estimation of the total energy demand, which has to be corrected for different reactor types.

We have introduced the model to calculate the energy uptake or release by the individual process steps. By this means, the chemical energy, sensible energy, pumping energy, and steam generation energy (if applicable) can be calculated. The equilibrium state can be determined by finding under which conditions the Gibbs free energy is zero (compare section 8.5, Eq. 8.1). To calculate Eq. 8.1 we assume a linear change of T and $ln(p_{O_2})$ according to the operational case (c) mentioned in section 2.6, page 46, and define N equidistant sets of T and p_{O_2} between T_{ox}/p_{ox} and T_{red}/p_{red} at which the equilibrium state is calculated to yield ΔH_n and δ_n. The integral in Eq. 2.43 is then calculated stepwise to reduce the necessary calculation time: [113]

$$\int_{\delta_{ox}}^{\delta_{red}} \Delta H(\delta, T)\, d\delta \;\approx\; \sum_{N}^{N-1} \left[\frac{\Delta H_N + \Delta H_{N+1}}{2} \cdot (\delta_{N+1} - \delta_N) \right] \tag{6.1}$$

We use N = 20 to get an accurate approximation of the integral. For the experimental datasets, we can calculate the integral directly without using the approximation in Eq. 6.1, as the derived empirical fit functions can be solved analytically. The heat capacity values necessary to determine the sensible energy input are calculated analogously to Eq. 6.1, and the derived heat capacity is used both

within the experimental and theoretical models, as experimental heat capacity data has not been acquired within this study.

The numerical solution of equations in the case of the theoretical models requires some time for the calculations. Executing these for all of the materials studied theoretically would lead to response times of the search engine of about one minute whenever the operational parameters are changed. Therefore, we pre-define a set of reasonable conditions and pre-calculate the chemical equilibrium for each of the materials and each of these parameter sets. This data is then adapted in the search engine to account for different heat recovery efficiencies (and in the case of water splitting, the water feed temperature). The parameters for the air separation process are defined as shown in the previous chapter in Fig. 5.27. In analogy, the parameter sets used for different types of redox cycles are given in Table 6.1. Calculations are performed for all parameters once using experimental and once using theoretical data in the case of air separation. For water splitting and CO_2 splitting, we only use theoretical data, as the experimentally studied perovskites are typically not applicable in these processes (compare section 5.1.2). The result are over 10500 parameter sets used for calculating the chemical equilibrium in all given cases (≈ 7000 for air separation including calculations based on experimental and theoretical data, ≈ 2250 each for water splitting and CO_2 splitting). Even with the simplification in Eq. 6.1, calculating the chemical energy for each material and each parameter set at all 20 steps *N* requires finding the zero points of Eq. 8.1 over 38 million times for the theoretical dataset only, and a similar calculation effort is necessary to determine the sensible energy. The completion of the entire set of calculations therefore took 1.5 weeks on the jupyterhub server infrastructure (calculated using jupyter notebooks, see www.jupyter.org) of Materials Project.

Table 6.1. Equilibrium parameters used in the energy analysis for different process types. Water Splitting is denoted by "WS", CO_2 splitting by "CS", and air separation/oxygen pumping by "AS". Temperature values are given in °C for convenience and converted to K.

Process step	Parameters
Oxidation WS/CS	T_{ox} = [600, 700, 800, 900, 1000, 1050, 1100, 1150] °C $p(CO/H_2)$ / $p(CO_2/H_2O)$ = $[10^{-6}, 10^{-5}, 10^{-4}, 10^{-3}, 10^{-2}, 10^{-1}]$
Reduction WS/CS	T_{red} = [1100, 1200, 1250, 1300, 1350, 1400, 1450, 1500] °C p_{red} = $[10^{-6}, 10^{-5}, 10^{-3}, 0.21, 1.00]$ bar (oxygen partial pressure)
Oxidation AS	T_{ox} = [350, 400, 450, 500, 600, 700, 800] °C p_{ox} = $[10^{-20}, 10^{-15}, 10^{-12}, 10^{-10}, 10^{-8}, 10^{-6}, 10^{-5}, 10^{-4}, 10^{-3}]$ bar (oxygen partial pressure)
Reduction AS	T_{red} = [600, 700, 800, 900, 1000, 1100, 1200, 1400] °C p_{red} = $[10^{-8}, 10^{-6}, 10^{-5}, 10^{-4}, 10^{-3}, 0.21, 1.00]$ bar (oxygen partial pressure)

Based on the pre-calculated chemical and sensible energy values for all these cases, we can create a perovskite search engine with multiple user-defined process variables. The oxidation and reduction temperatures and oxygen partial pressures can be defined by the user within the constraints given in

Table 6.1 (only these values can be selected, no intermediate values). The actual chemical and sensible energy demand of the redox cycle are then calculated directly using the user-specified solid-solid heat recovery efficiency. The pumping energy and steam generation energy are also calculated directly based on user inputs. All calculations are performed as part of the "Energy Analysis" in RedoxThermoCSP, and the source code is available through GitHub (see Appendix, section 8.4). [m] Fig. 6.2 shows the user input of the energy analysis tool. The "process type" allows selecting air separation/oxygen pumping, water splitting, or CO_2 splitting. The "data source" describes whether experimental or theoretical datasets are used, and the experimental datasets cannot be selected if any other process type but air separation is chosen.

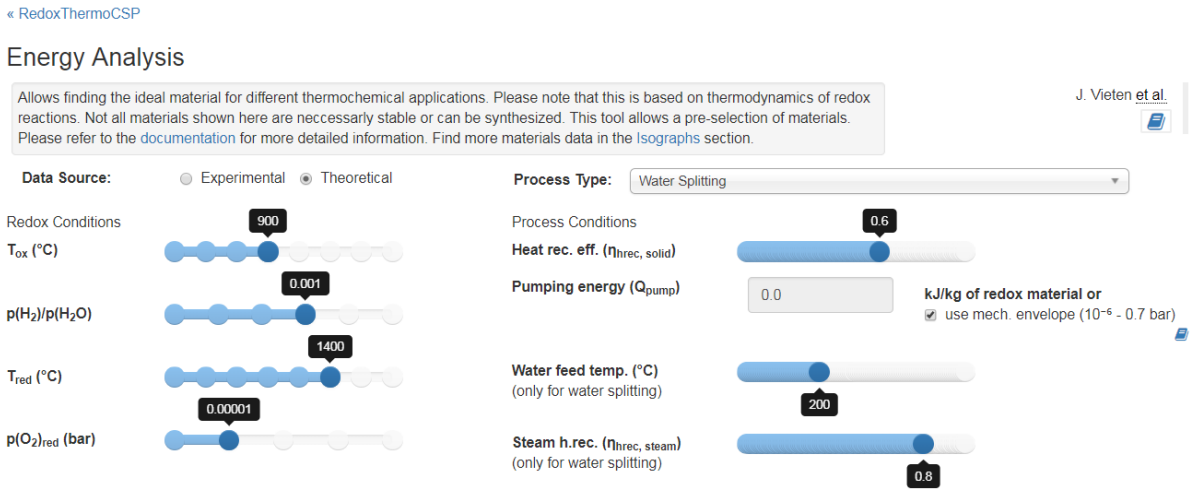

Fig. 6.2. User input of the "Energy Analysis" tool in RedoxThermoCSP. The parameters in the left column can only be set to pre-defined values as given in Table 6.1. The parameters on the right can be changed freely. The Energy Analysis tool uses pre-calculated sets of chemical and sensible energy data, which are corrected by the user-given solid-solid heat recovery efficiency. The pumping energy and steam generation energy are calculated based on user inputs (see section 2.6). Available on https://contribs.materialsproject.org/redox_thermo_csp.

In analogy to the analysis in section 5.3 (Fig. 5.27), the data is excluded if the calculated chemical energy is negative. In those cases, the parameters either do not indicate a reduction reaction (for instance, if the "reduction" temperature is below the oxidation temperature in our parameter set at equal oxygen partial pressure), or the material is highly unstable. The latter case means that it cannot be oxidized to any appreciable extent under the given parameters. Another possible explanation of such results is a negative $\Delta H_{\min}$ value in the empirical fit functions. Only the data for materials with positive chemical energy is displayed. Moreover, we exclude potentially unstable materials from our analysis. These include materials with tolerance factor below 0.9. Moreover, we exclude materials which most likely show covalent V-O bonds such as $NaVO_3$ (all materials containing V^{5+} ions), and

[m] https://github.com/materialsproject/MPContribsUsers/tree/master/redox_thermo_csp

materials with expected low melting points such as alkali molybdenates (all materials containing Mo^{5+} ions). [252] 36 out of the > 240 perovskite materials in this study are thus excluded from the energetic analysis in RedoxThermoCSP, but this data is available through isograph plots. Users should check the chemical and physical properties of these materials by checking the literature on similar phases and the energy above hull before attempting to use them as redox materials. Moreover, at low temperatures, the oxidation reaction may be kinetically limited. All these factors have to be taken into account when evaluating the output of the perovskite search engine. In the following, we look at some exemplary output data.

Air Separation

We first consider the result for an air separation process with oxidation at 500 °C and an oxygen partial pressure of 10^{-6} bar, and reduction at 1000 °C in air at an oxygen partial pressure of 0.21 bar (see Fig. 6.3). This could be a typical air separation process for the provision of a nitrogen feedstock in the Haber-Bosch process. All temperature and partial pressure values are given as equilibrium conditions, meaning that the target oxygen partial pressure is reached after the equilibrium is reached. Of course, real reactors are not always in equilibrium, [255] which may require choosing a lower target equilibrium partial pressure to reach an oxygen partial pressure of 10^{-6} bar on average. We cannot account for these reactor-specific effects in our materials screening study.

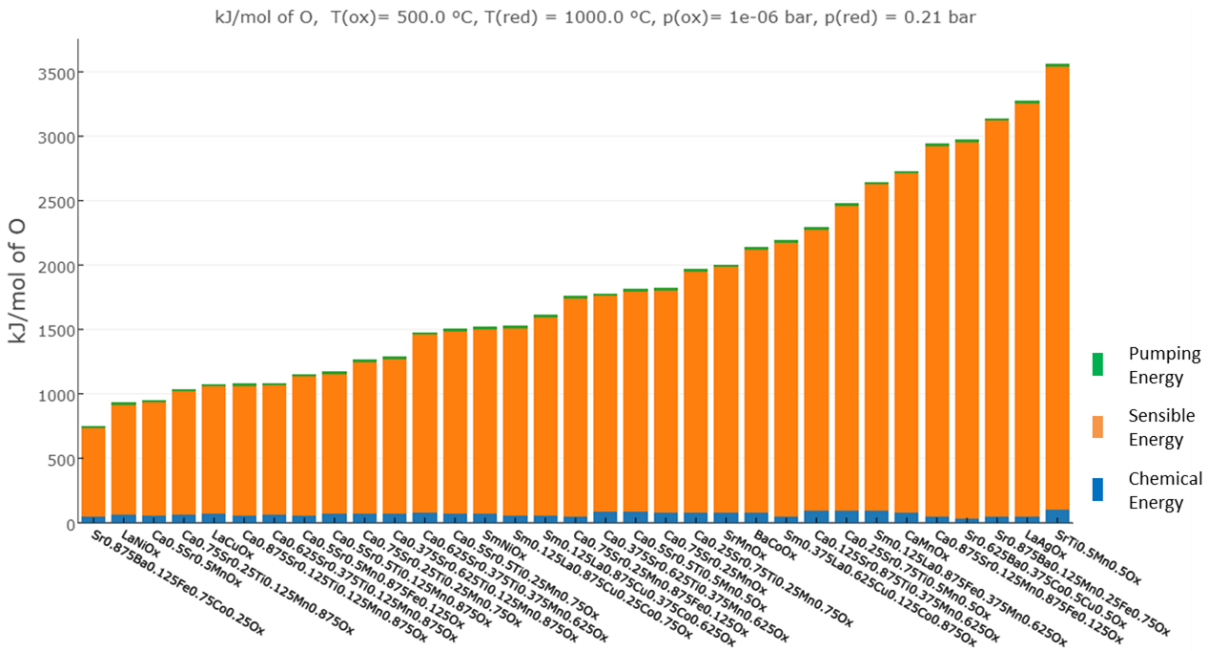

Fig. 6.3. Energy analysis for a typical air separation cycle ranking perovskite redox materials based on theoretical data. $\eta_{\mathrm{hrec,solid}} = 0.6$. The conditions are chosen to simulate a typical air separation process for the generation of mostly inert gas for application in the Haber-Bosch process. Many materials are similar to those studied in section 5.1, which shows that both datasets are in good agreement. Adapted from Vieten *et. al.* [113]

The analysis in Fig. 6.3 is based on theoretical data and has been generated assuming $\eta_{\mathrm{hrec,solid}} = 0.6$, and using the mechanical envelope function by Brendelberger *et al.* to calculate the pumping energy. [24] The 33 materials with the lowest energy demand of the redox cycle per mol of O are shown. In principle, the theoretical dataset contains much more materials, but only part of the data is displayed for clarity. The user can set the maximum amount of materials to be displayed in the RedoxThermoCSP tool.

The largest fraction of the energy input is attributed to the sensible energy in the case shown in Fig. 6.3. As perovskites typically show small mass changes and rather low oxygen storage capacities in the range of a few mass percent per mol of redox material, a substantial amount of material has to be used to generate oxygen in an appreciable amount. This also determines the overall energy demand. Materials show a very high energy input per mol of O produced if they only exhibit small non-stoichiometry changes under the given conditions. In this case, these would include materials with very high ΔH, which leads to very low δ values and means that they cannot be reduced to an appreciable amount under the conditions applied. For instance, $SmMnO_{3-\delta}$ with ΔH_{DFT} = 388.21 kJ/mol$_O$ shows $\Delta\delta = 2.75 \cdot 10^{-6}$ under the conditions specified in Fig. 6.3, which means that very large amounts of this material would be required to release one mol of oxygen. Moreover, materials with very low ΔH already show δ values near 0.5 in the oxidation step, which means that they cannot be reduced much further. In general, this means that the best performing materials show δ values far away from the extreme points $\delta = 0$ and $\delta = 0.5$ during the entire redox cycle, which means that the oxygen affinity of the material is neither too high nor too low for the chosen application. [256] While the sensible energy input per mol of redox material is widely independent of the thermodynamics as it is given by the Debye model, the value per mol of oxygen O strongly depends on the thermodynamic properties, as they define the $\Delta\delta$. The chemical energy input also depends on the thermodynamics, as it is directly proportional to ΔH. It can be seen as the average $\Delta H(\delta)$ between δ_{ox} and δ_{red} lowered by the solid-solid heat recovery efficiency $\eta_{\mathrm{hrec,solid}}$. The $\eta_{\mathrm{hrec,solid}}$ value does not affect the order of materials in the ranking, but only changes the absolute value of the total energy demand. The fictional case of $\eta_{\mathrm{hrec,solid}} = 1$ means that the chemical and sensible energy uptake are effectively zero over the whole cycle as all released heat is recovered, and only the pumping energy is left. However, under realistic assumptions (i.e, $\eta_{\mathrm{hrec,solid}} = 0.6$ [163]) the pumping energy input is very low at near-ambient oxygen partial pressures, but increases significantly if reduction at lower pressures is carried out. The pumping energy describes the energy required to maintain the reduction partial pressure in a closed system, which is very low if p_{red} is similar to the ambient oxygen partial pressure. However, if the reduction step is carried out at 10^{-5} bar or lower, the pumping energy constitutes the largest share in the total energy demand of the air separation cycle per mol O.

Despite the sensible energy demand being higher if the difference between reduction and oxidation temperature levels is larger, it can nevertheless be beneficial in terms of the process efficiency to operate such redox cycles with higher temperature differences. The sensible energy demand per mol of oxygen is inversely proportional to the change in non-stoichiometry and proportional to the temperature change (see Eq. 2.48 and the discussion thereafter). Since the non-stoichiometry change increases often overproportional to the temperature change, the overall energy demand can be lower despite the higher temperature change. This is especially the case if the differences in partial pressures are large between the oxidation and reduction step. If the difference in temperatures is small and the difference in partial pressures is large, the change in non-stoichiometry which can be achieved is rather small. Fig. 6.4 shows the demand in total energy per mol of O and redox cycle for different conditions for the respective materials with lowest predicted energy demand. It shows how there is a certain minimum temperature difference required to reach a process with low overall energy demand depending on the oxygen partial pressure difference.

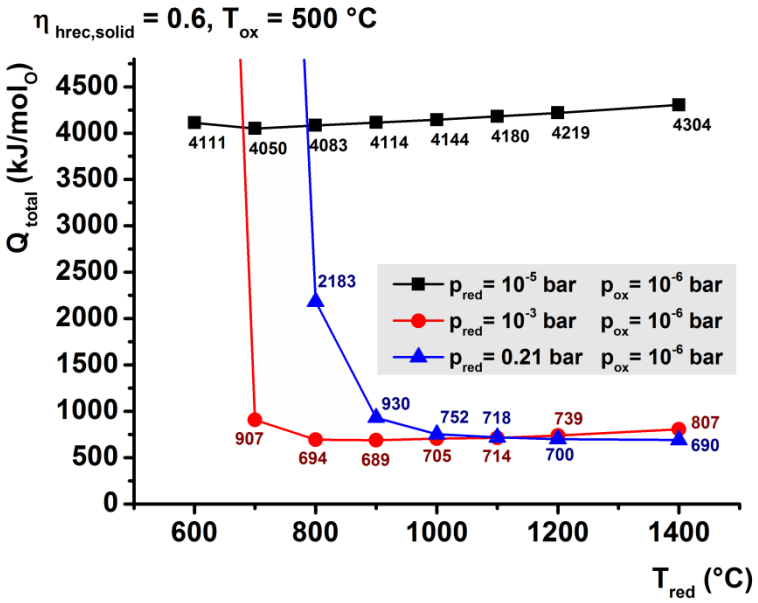

Fig. 6.4. Comparison of the total demand in thermal energy for air separation per redox cycle and mol O transferred under different oxidation and reduction oxygen partial pressures and temperatures. The indicated total energies are retrieved from the "Energy Analysis" search engine of RedoxThermoCSP based on theoretical data for the entry with lowest total energy. A large temperature change between reduction and oxidation step appears beneficial if the targeted oxygen partial pressure change is large as well. The pumping energy is predominant if the reduction step is carried out at 10^{-5} bar.

Instead of the energy demand per mol of oxygen, we can also calculate different properties and display them as a graph in the RedoxThermoCSP tool. The possible properties to select from are listed in Table 6.2. These can be converted as shown in Table 2.3. For instance, we can plot the change in non-stochiometry $\Delta\delta$ of these materials (see Fig. 6.5). As the sensible energy demand per mol of oxygen depends to a large extent on $\Delta\delta$ and the sensible energy is the largest factor in the total

energy demand, the list is very similar to the previous plot in Fig. 6.3. The order of some materials in the list changes, however, owing to the different chemical energy demand of different materials. We can clearly see that materials with high oxygen storage capacity under the pre-defined conditions (i.e., a high $\Delta\delta$) are usually also the best choice in terms of minimizing the energy demand of the redox cycle per mol of O. This is owing to the fact that the heat capacities of different perovskites are very similar according to the Debye model. Moreover, as mentioned in section 2.6, elastic tensors for many perovskite materials are not available yet in Materials Project and are constantly being added, leading to data for $SrFeO_{3-\delta}$ being used as an approximation (see section 2.6). As the heat capacity at temperatures significantly higher than the Debye temperature only depends on the amount of atoms in the lattice, no fundamental changes in heat capacity and the order of materials in the energetic analysis are expected.

Table 6.2. Available plot types in the "Energy Analysis" module of RedoxThermoCSP.

Plot type
kJ/mol redox material
kJ/kg redox material
Wh/kg redox material
kJ/mol of product
kJ/L of product
Wh/L of product
mol product per mol redox material
L product per mol redox material
g product per mol redox material
Change in non-stoichiometry between T_{ox} and T_{red}
Mass change between T_{ox} and T_{red}

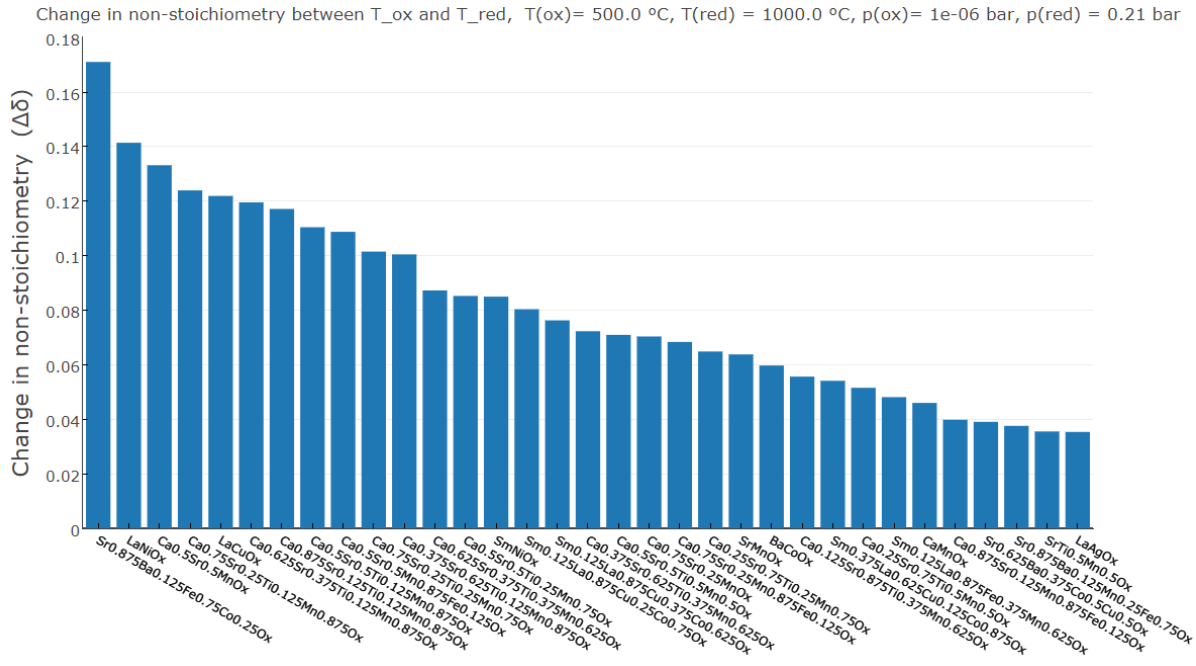

Fig. 6.5. Plot of the change in non-stoichiometry $\Delta\delta$ generated through RedoxThermoCSP based on theoretical data under the same conditions as in Fig. 6.3.

Among the predicted materials with best performance under the conditions used to create Fig. 6.3 and Fig. 6.5, many include calcium strontium manganates with some of the Mn being replaced by different amounts of Fe or Ti. This is in good agreement with our experimental study (section 5.1), which revealed that such materials are applicable in air separation for a large range of different conditions. The material with lowest calculated energy demand per redox cycle and mol O is $Sr_{0.875}Ba_{0.125}Fe_{0.75}Co_{0.25}O_{3-\delta}$, which also shows the highest expected $\Delta\delta$. This material could be seen as a substituted variant of $SrFeO_{3-\delta}$, but with a slightly lower redox enthalpy (81.8 vs. 87.8 kJ/mol_O for complete reduction from $\delta = 0$ to $\delta = 0.5$). [95, 113] $SrFeO_{3-\delta}$ and doped variants have been introduced in the literature and in this work as suitable redox materials for air separation. [16, 65, 213] Using our perovskite search engine and theoretical materials screening, we can find similar materials with redox properties adjusted for the specific application. The second best material according to our study shown in Fig. 6.3 and Fig. 6.5 is $LaNiO_{3-\delta}$. It is difficult to find literature data of the redox properties of this phase, but Silva *et. al.* show that Ni^{3+} is reduced readily to Ni^{2+} in this phase, which confirms its good reducibility. [257]

If we change the redox conditions in our search engine, we get further results in good agreement with our experimental study. For instance, we can leave the oxidation temperature at 500 °C but change the reduction temperature to 1400 °C in air (at 0.21 bar oxygen partial pressure) while the oxidation equilibrium oxygen partial pressure is set to 10^{-20} bar. The three best performing materials according to our search engine are then $ATi_{0.625}Mn_{0.375}O_{3-\delta}$ perovskites with different Ca/Sr/Ba ratios on the *A* site. This agrees well with the experimental results in section 5.1.2 (Fig. 5.10). Moreover, further materials with good predicted performance are (Sm/La)(Cr/Fe)-oxides and (Sm/La)(Fe/Mn)-oxides, as well as $EuMnO_{3-\delta}$. On the other hand, if we change the oxidation and reduction temperature levels to 400 and 600 °C, respectively, and assume reduction in air and oxidation at 10^{-3} bar, the three best performing materials are (in this order) $Sr_{0.875}Ba_{0.125}FeO_{3-\delta}$, $SrFeO_{3-\delta}$, and $BaFeO_{3-\delta}$. $(Ca/Sr)(Fe/Co)O_{3-\delta}$ perovskites with Co content of 25 at% or lower are also predicted to show low overall energy demands, which agrees well with the results in chapter 5.1.4, showing that such materials are suitable for air separation at higher oxygen partial pressures. Other interesting materials with predicted good performance in this application scenario are $LaAgO_{3-\delta}$ and $Sm_{0.5}La_{0.5}Cu_{0.125}Co_{0.875}O_{3-\delta}$. $LaAgO_{3-\delta}$ shows an energy above hull of over 200 meV/atom and is therefore most likely unstable in the perovskite phase. It would require the rather high Ag^{3+} oxidation state to be partially present in its oxidized state. Experimental studies could be carried out in the future to evaluate phase formation and stability for this material.

For 24 perovskite materials, experimental data is contained within this work. As the fit may be inaccurate beyond the measured data range, any evaluation of a redox cycle based on this data should be regarded critically. The total energy demand calculated based on the experimental fit and the corresponding model often deviates strongly from the result of the theoretical model. Users should always check the isographs, especially the $\Delta H(\delta)$ and $\Delta S(\delta)$ plots, to see whether the data is

reasonable and within the range of experimentally covered results. However, if we create plots within the range of the measured data, we get reasonable material rankings. For instance, if we apply the "high pressure" conditions mentioned before (400/600 °C at 10^{-3}/0.21 bar oxygen partial pressure), we only get results for four of the 24 materials studied. This is reasonable, as the other materials are not applicable within this data range and/or the fit functions predict negative changes in the chemical energy. The two most efficient materials are (in this order) $SrFeO_{3-\delta}$ and $Ca_{0.875}Sr_{0.125}Mn_{0.75}Fe_{0.25}O_{3-\delta}$. $SrFeO_{3-\delta}$ has also been predicted as a good redox material based on the theoretical data.

Water splitting and carbon dioxide splitting

For water splitting and carbon dioxide splitting, we only use the theoretical datasets as the experimentally studied materials are not well suitable for such processes. The energy demand of the overall process is strongly dependent on the target hydrogen or carbon monoxide conversion rate. This metric is expressed by the ratio in partial pressures between H_2 or CO and H_2O or CO_2, respectively. Ceria-based redox cycles have typically very high conversion rates, as the redox thermodynamics of this material favor the water or carbon dioxide splitting reaction due to its high redox enthalpy, but this also means that the reduction of ceria to an appreciable extent is difficult and requires very high temperatures or very low oxygen partial pressures. [258] On the other hand, many perovskites reported to split water in the literature favor the reduction reaction due to their lower redox enthalpy. [259] This means that the conversion rate in these cases is rather low, which requires a large excess of steam to yield reasonable amounts of hydrogen. The energy necessary to generate this steam is often neglected in studies reporting perovskites as water splitting materials. The challenge in terms of materials selection is to find the optimal balance between the reducibility of the perovskite and its water splitting ability. [256] This can be achieved by adjusting the redox thermodynamics accordingly, and our study offers a means to do so. As the redox entropy change for the reduction of ceria is in almost any case higher than in the case of perovskites, a perovskite with the same redox enthalpy change as ceria is expected to show a lower overall heat-to-fuel efficiency (compare Fig. 4.7). [30, 135] The strength of perovskites as redox materials could be a lower enthalpy change than ceria with slightly lower conversion rates, which in turn allows reduction at lower temperatures and/or higher oxygen partial pressures. This could be beneficial for practical and energetic reasons. Therefore, we focus on target conversion rates below 1 in our study and evaluate whether the higher energy demand of steam generation can be cancelled out by the lower demand in sensible and chemical energy.

We first study a water splitting cycle with a conversion rate of 1 % ($p(H_2)/p(H_2O) = 0.01$). In the following, we only look at water splitting cycles, as the thermodynamics of carbon dioxide splitting are very similar (see section 2.5). Plots for both water splitting and carbon dioxide splitting are available for many different operational conditions through RedoxThermoCSP. Fig. 6.6 shows a water splitting cycle with 1 % conversion rate, reduction at 1300 °C at 10^{-6} bar oxygen partial pressure and oxidation at 700 °C. Due to the low reduction pressure, the share of the pumping energy compared to the total energy demand is significant. Assuming $\eta_{\mathrm{hrec,steam}} = 0.8$ while $\eta_{\mathrm{hrec,solid}} = 0.6$ as before, the energy necessary to prepare the excess steam is still only the third largest factor in the total energy demand. However, we do not account for the separation work necessary to remove the produced hydrogen when the steam is recycled. As we assume a water feed temperature of 25 °C at the steam generator inlet, we can assume that the separation can be done by condensing the water and removing the hydrogen gas from the reactor. The materials predicted to perform well in our study include $ATi_{0.625}Mn_{0.375}O_{3-\delta}$, which is not very well suitable for water splitting according to our experimental data, and $BaMnO_{3-\delta}$, which does not split water to an appreciable extent according to the literature. [256] Other predicted materials such as (Sm,La)(Cr,Fe)-oxides and (Sm,La)(Fe,Mn)-oxides appear more reasonable, as the water splitting activity of similar materials has been reported in the literature. [33, 35, 251] It is possible that the entropy change is overestimated in our model, as it does not account for oxygen vacancy ordering, which could explain these discrepancies and would lead to lower hydrogen yields in the real application.

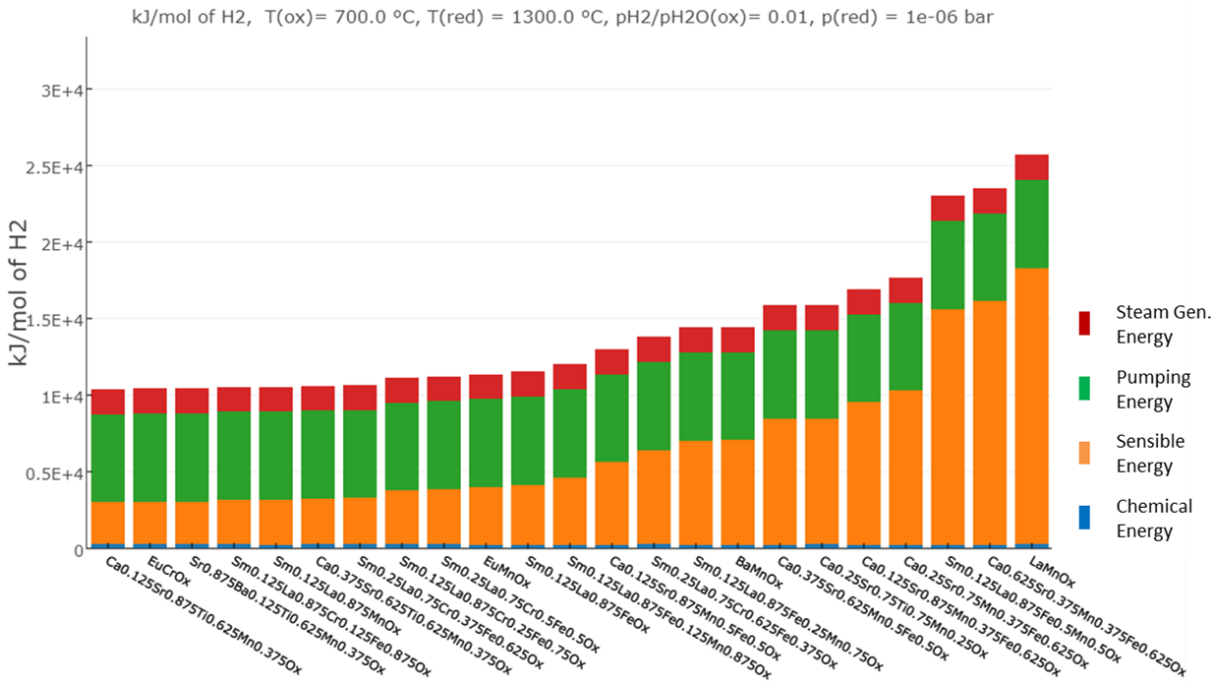

Fig. 6.6. Energy analysis for a water splitting cycle with 1 % conversion ranking perovskite redox materials based on theoretical data. $\eta_{\mathrm{hrec,solid}} = 0.6$, $\eta_{\mathrm{hrec,steam}} = 0.8$, water feed temperature: 25 °C. Adapted from Vieten *et. al.* [113]

We can compare the heat-to-fuel efficiency predicted by our model for these perovskites to the heat-to-fuel efficiency for ceria-based cycles as a reference. For this purpose, we use the analytical expression and data derived by Bulfin *et. al.* as well as enthalpy and elastic data from Materials Project to predict the heat-to-fuel efficiency for ceria-based cycles. [116, 134, 260, 261] The analytic expression describing the non-stoichiometry in ceria is given by: [260]

$$0 = 8700 \cdot \mathrm{p}_{\mathrm{O}_2}^{-0.217} \cdot e^{-\frac{195600\,\frac{\mathrm{J}}{\mathrm{mol}}}{RT}} - \frac{\delta}{0.35 - \delta} \tag{6.2}$$

We can determine the δ values by finding where Eq. 6.2 is zero. The chemical energy demand is calculated by using a constant redox enthalpy value of 381 $\mathrm{kJ/mol_O}$ according to the literature. [116, 261] Pumping and steam generation energy are calculated the same way as for the perovskites. The sensible energy is calculated by using elastic tensor data for CeO_2 and pymatgen. [113, 126] Under the same assumptions for heat recovery efficiencies, the hydrogen yield, and the oxidation and reduction temperature and partial pressure levels, we reach a heat-to-fuel efficiency for ceria-based cycles of 1.83 % for ceria, and the values shown in Fig. 6.7 for perovskites. Under the same conditions using similar theoretical models, perovskites allow increasing the heat-to-fuel efficiency by 50 %, as the maximum heat-to-fuel efficiency reaches 2.7 % in our analysis. The efficiency calculation shown in Fig. 6.7 is not available in the public version of RedoxThermoCSP as of Nov. 2018, but will be included in a later release. However, it is based on publicly available data such as shown in Fig. 6.6.

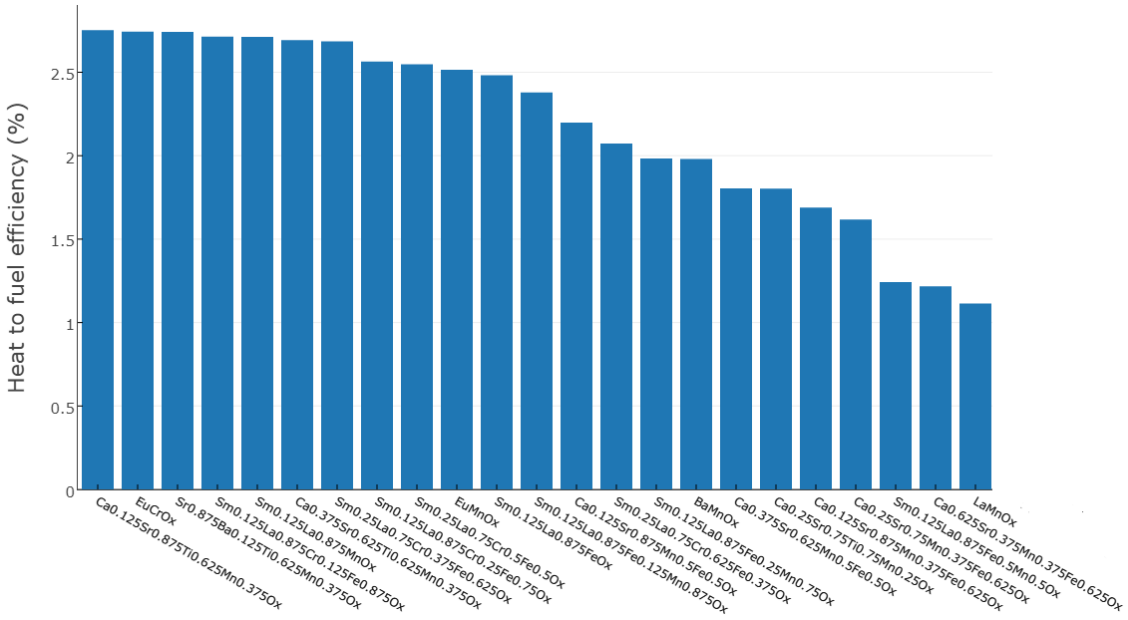

Fig. 6.7. Heat-to-fuel efficiency for a water splitting redox cycle based on the conditions in Fig. 6.6 using the higher heating value of hydrogen (HHV, see chapter 2.6).

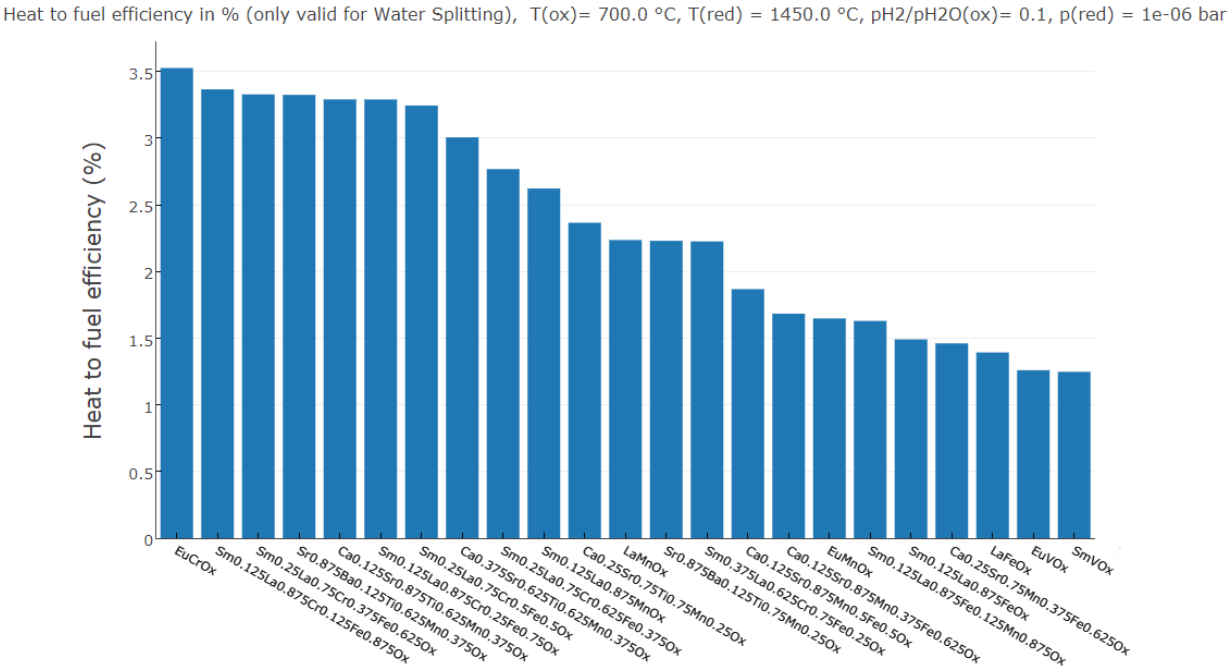

Fig. 6.8. Heat-to-fuel efficiency for a water splitting redox cycle with 10 % conversion, reduction at 1450 °C at 10^{-6} bar oxygen partial pressure, oxidation at 700 °C, with $\eta_{\mathrm{hrec,solid}} = 0.6$, $\eta_{\mathrm{hrec,steam}} = 0.8$, and a water feed temperature of 25 °C. Generated using RedoxThermoCSP.

If we assume higher conversion ratios in the case of ceria and higher reduction temperatures, the heat-to-fuel efficiency of ceria-based redox cycles peaks around 3-3.5 % under the assumptions made here in terms of heat recovery efficiencies. Perovskites can get close to this value in our study (see Fig. 6.8), but they do not significantly exceed the efficiency of ceria. This is due to the before-mentioned lower entropy change during the reduction of perovskites. This entropy change might be increased by inducing phase transitions (see section 4.4) or by introducing redox-active *A* cations such as $Ag^{+/2+}$ or $Bi^{3+/5+}$. Cerium ions might also be partially occupying *A* sites in solid solutions if the ionic radii of the other *A* site cations do not differ too much. Perovskites tolerate an *A* site non-stoichiometry to some extent. [215] It might even be possible to create systems where some of the *M* site cations switch to the *A* sites as they increase in ionic radii during reduction. Such systems would require new thermodynamic models, and experimental as well as theoretical studies on new types of perovskites are an appealing task for the future.

If the operational parameters are not fixed, the heat-to-fuel efficiency of perovskite-based redox cycles cannot significantly exceed the efficiency of ceria as state of the art. However, we have shown that under some conditions (low reduction temperatures), perovskites can be significantly more efficient than ceria. This may be advantageous for the design of such redox reactors on a larger scale. Lowering the reduction temperature to 1300-1350 °C for perovskites instead of 1450-1500 °C for ceria may allow using different reactor materials and improves their longevity. Moreover, re-

radiation and other thermal losses are significantly reduced by lowering the reduction temperature. According to Planck's law, the intensity of emitted radiation scales with the fourth power of the temperature, meaning that the emitted radiation decreases in intensity by 25 % if a black body is kept at 1350 °C instead of 1450 °C. Moreover, maintaining very high temperatures and low oxygen partial pressures throughout the bulk of the material can be very challenging. Therefore, perovskites as redox materials for solar fuels production may offer significant advantages compared to ceria in terms of reactor engineering while reaching comparable heat-to-fuel efficiencies. Considering the higher re-radiation losses at higher temperatures, the overall process efficiency of perovskite cycles may be even higher than with ceria. In-depth techno-economic studies are required to quantify the economic advantages of perovskite-based cycles over ceria as redox material.

Discussion of the data accuracy

The heat-to-fuel conversion efficiency values in our study are significantly lower than in many literature references. [255, 259] One reason for this is that many literature studies do not account for the steam generation or pumping energy, or they use fixed values for the energy demand which are not always realistic. [255] It is important to manage the expectations set in two-step thermochemical water splitting for fuels production. According to our data, it is very difficult to reach solar-to-fuel efficiency values with state-of-the art thermochemical routes competitive to existing technologies such as electrolysis. [30, 262] However, there are many ways in which this technology could be improved, and these are discussed in section 6.2.3. Moreover, there are important limitations in the data accuracy in our study. This study has been created to compare different materials in terms of the cycle energy demand based on materials-specific parameters. Some simplifications have been applied to be able to compare these materials, and the absolute values are influenced by our assumptions. Therefore, one should not overstate the accuracy of the absolute efficiency values reported here. Simplifications and limitations of our model include:

- **Overall process:**
    - The assumption of equilibrium conditions as final states for the reduction and oxidation process; we do not account for intermediate non-equilibrium states [255]
    - The assumption of negligible reaction times (fast reduction and oxidation at all times under all conditions)
    - The assumption of a scenario where temperature and oxygen partial pressure are continuously changed (scenario "c", compare section 2.6, page 46), other options may lead to a lower total energy demand
    - The limitations given by our fixed parameter sets of temperatures, oxygen partial pressures, and conversion rates

- **Chemical energy:**
  - The calculated ΔH values are limited in their accuracy due to the limitations of our DFT and experimental study (see Table 5.1)
  - Our model uses specific assumptions for the temperature- and δ-dependent change in ΔH which may not hold true for all materials

- **Sensible energy:**
  - Using the Debye model to calculate the heat capacity can be inaccurate, especially in cases where the materials exhibit second order phase transitions; this may lead to an underestimation of the sensible energy, especially at low temperatures
  - If the sensible energy is given as energy demand per mol of product, it depends on the predicted ratio mol of product produced per mol of perovskite, which is limited by the accuracy of the thermodynamic models (predicted $\Delta\delta$)

- **Pumping energy:**
  - Approximation of the pumping energy using the mechanical envelope function [24]; this may lead to an underestimation of the pumping energy
    - ⇨ Instead, the energy demand of the specific mechanical pump applied in the process could be used (this is possible in RedoxThermoCSP by using a manual input value)
  - Thermochemical pumps may lead to a lower energy demand at low oxygen partial pressures (below 10^{-3} bar oxygen partial pressure) [24]
  - Assuming a constant oxygen partial pressure for the entire reduction process may lead to an over- or underestimation of the pumping energy
    - ⇨ Instead, the pumping energy could be minimized by simulating different scenarios where not all of the oxygen is pumped at the final equilibrium reduction pressure, this could lower the necessary overall energy for pumping especially at low reduction oxygen partial pressures

- **Steam generation energy:**
  - The separation work of hydrogen from the steam product gas is not accounted for
  - The energy necessary to provide the CO_2 or air in carbon dioxide splitting or air separation cycles is considered negligible
  - The amount of oxidizer necessary may be lowered by not feeding the oxidizer continuously during cool-down (scenario “c”, see above) but by carrying out the oxidation reaction only at low temperature (on the other hand, the material may get partially re-oxidized by residual oxygen in the system during cool-down)

Moreover, we only consider the heat-to-fuel efficiency and do not account for generation of this heat or thermal losses, i.e. in a solar-thermochemical process.

The strength of this study is to offer thermodynamic data for a large set of materials and compare them in terms of their expected efficiency as redox materials in a two-step thermochemical process. The absolute values in terms of energy demand and efficiency may be biased by our assumption. Real reactor systems are much more complex than our idealized model systems can account for. Modelling these details is beyond the scope of this study and our RedoxThermoCSP search engine is meant as a materials pre-selection tool, and can by no means replace a process simulation.

We suggest the following route for developing redox cycles through materials design based on our tools:

1. Definition of a range of suitable parameters such as oxidation and reduction temperatures, partial pressures, and product yields based on the constraints and conditions given by reactor design and engineering
2. Use of the "Energy Analysis" search engine to find a set of 10-20 materials with the best expected efficiency under these conditions
3. Verification of the chemical stability of the selected materials based on the DFT data (energy above hull), literature reports, and initial experimental studies
4. Generation of "Isographs" for the most promising materials using our tools to estimate the expected change in non-stoichiometry and to fine-tune the redox conditions
5. Detailed process modelling and laboratory scale tests of the suggested materials

These steps can require multiple iterations and optimization loops to lead to satisfactory results. By using materials design to prepare perovskites with a large range of thermodynamic properties and through thermodynamic modelling and calculations, we offer a means to accelerate and rationalize the search for suitable redox materials significantly. Without such models and methods for materials design, step 2 would have to be replaced by a large set of experimental studies involving trial and error. While our model by no means offers absolute accuracy, it is a powerful tool for materials pre-selection and has the potential to replace many work hours of experimental materials development.

6.2 Discussion of potential improvements in the efficiency of thermochemical cycles

Within this work, we have shown that perovskites and their solid solutions are suitable redox materials for many different types of thermochemical processes and a variety of different operating conditions. In general, the achievable efficiency for solar fuels production can be equal or higher than that related to the state-of-the-art cerium dioxide (ceria), and the lower reduction temperatures of many perovskites are advantageous for reactor engineering. However, the absolute efficiency values reported in this study and other recent studies are too low to reach competitiveness with other fuels production technologies such as electrolysis (for hydrogen production). [255, 259, 262-265] Therefore, our study and the perovskite search engine allow finding possible optimization strategies for these processes. In the following, we discuss potential improvements of air separation, oxygen pumping, and water/carbon dioxide splitting routes separately, as these technologies have very different requirements.

6.2.1 Air separation

In the previous section, we have shown how the choice of different temperature levels affects the overall energy demand of the process (see Fig. 6.4). As an example, we can evaluate the energy demand of the process per mol O for the best predicted material ($Sr_{0.875}Ba_{0.125}Fe_{0.75}Co_{0.25}O_{3-\delta}$) with oxidation at 500 °C and 10^{-6} bar oxygen partial pressure and reduction at 0.21 bar oxygen partial pressure and 1000 °C at $\eta_{\mathrm{hrec,solid}} = 0.6$ (60% solid-solid heat recovery efficiency). The total energy demand of the process is 752 kJ/mol_O according to our model. This is significantly higher than the energy demand for cryogenic air separation. Banaszkiewicz *et. al.* give a value of 200 kWh/ton of O_2 as state of the art and a thermodynamic limit of 53.1 kWh/ton. [266] Converted to kJ per mol of O, the state-of-the-art energy demand is 11.5 kJ/mol_O. Li *et. al.* mention a similar value for preparing nitrogen (but per mol of N_2) in an air separation process (12 kJ/mol of N_2). [267] Accounting for the fact that thermochemical routes use thermal energy directly while cryogenic air separation suffers from inherent conversion and transport losses, we assume in the following that 30 % of the thermal energy generated in a solar plant could reach the cryogenic separation plant in the form of electricity, leading to a thermal energy demand of 38 kJ/mol_O. The most obvious way of getting closer to this value is to increase the heat recovery efficiency of the thermochemical process. For the following considerations, we assume that the reduction step is carried out in an open reactor, which allows the oxygen to be removed by exchange with the air and leads to a pumping energy of zero. Only chemical and sensible energy need to be supplied in this case. The chemical and sensible energy demand can be lowered by recovering heat from the solid materials. Fig. 6.9 shows the energy demand per mol of O for a thermochemical process with different solid-solid heat recovery efficiency values $\eta_{\mathrm{hrec,solid}}$.

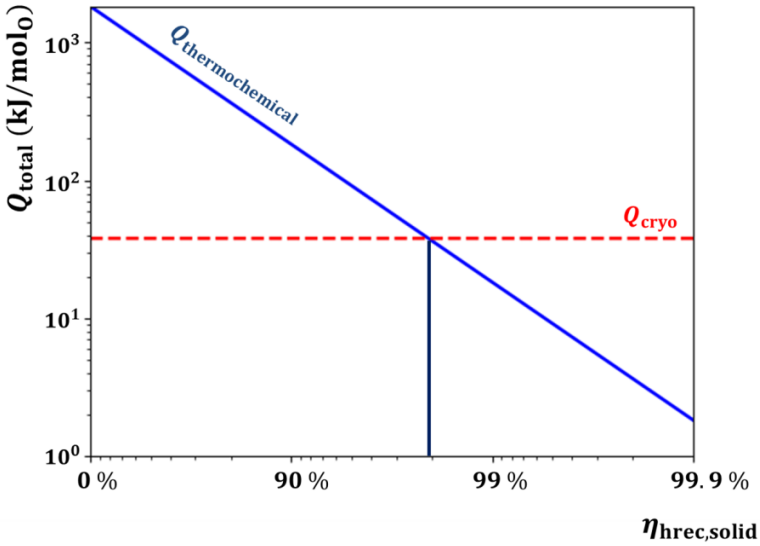

Fig. 6.9. Total thermal energy demand for an air separation cycle using the perovskite $Sr_{0.875}Ba_{0.125}Fe_{0.75}Co_{0.25}O_{3-\delta}$ as a redox material with oxidation at 500 °C and 10^{-6} bar oxygen partial pressure and reduction in ambient air (no pumping energy) at 1000 °C and 0.21 bar oxygen partial pressure. The solid-solid heat recovery efficiency $\eta_{hrec,solid}$ (in %) is shown on the x axis. The thermal energy demand is compared to state-of-the-art cryogenic air separation (see text, Q_{cryo}). In this reference case, the thermochemical air separation route is only more efficient than cryogenic air separation if the solid-solid heat recovery efficiency exceeds 98 %.

The perovskite-based thermochemical air separation route is less efficient than cryogenic air separation in many cases. Only if the solid-solid heat recovery efficiency exceeds 98 %, the thermochemical route becomes more efficient under the conditions assumed here. There is some uncertainty in the energy demand of state-of-the-art cryogenic air separation. Additionally, the energy demand for thermochemical air separation is given for the production of oxygen *and* a stream of mostly inert gas (N_2, Ar, CO_2) in one process. By this means, synergy effects could be reached in thermochemical fertilizer production, as the oxygen may be used to prepare nitric acid more efficiently (compare Fig. 2.2) There may also be oxygen partial pressure and temperature levels where thermochemical air separation is more efficient, and it could also be coupled to other techniques such as pressure swing absorption to reduce the energy demand in the high pressure region. [268, 269] This could increase the competitiveness of this technology significantly. Based on our data it appears unlikely that thermochemical air separation as a standalone technology is competitive with state-of-the-art technologies if the solid-solid heat recovery efficiency is below 90-95 %. It is challenging to reach such high values of the heat recovery efficiency, especially between two solids. Felinks *et al.* [163, 270], among others, have shown potential concepts for solid-solid heat recovery, and heat recovery efficiency values between 50 and 80 % appear achievable. With state-of-the-art technology, it is therefore more efficient for large scale air separation to first produce electricity through a solar plant and then use this electricity to cryogenically separate air. A significant improvement of solid-solid heat exchanger concepts is necessary.

However, the reference value we use for cryogenic air separation is given for large scale plants with typical purity levels of the resulting gases (Li *et. al.* assume 1 ppm of oxygen in nitrogen, i.e., 10^{-6} bar oxygen partial pressure). [267] For small scale air separation or very high purity levels, the cryogenic route is likely to be less efficient. Therefore, thermochemical processes based on perovskites may be a viable option for such specialized applications. Very high purity oxygen with contaminants in the sub-ppm range can be produced directly through thermochemical routes without any further purification steps. High purity gases find many applications in the chemical industry, and lowering the energy demand for their generation is appealing for economic and ecologic reasons.

To improve the efficiency of the air separation processes, an improvement of the solid-solid heat recovery efficiency is the most promising option, as shown above. By optimization of the reduction and oxidation temperature and partial pressure levels, the energy demand may also be lowered, but it will always be in the same order of magnitude or above (compare Fig. 6.4, we are already assuming one of the best cases). The heat recovery efficiency necessary for an efficient process cannot be lowered significantly by this means, but one may be able to optimize the temperature levels so the heat exchanger is most efficient. The amount of chemical energy necessary is determined by the thermodynamics of the material. Within our study, we optimized the thermodynamic properties. Unless the entropy change is unusually high during the redox process, the chemical energy demand cannot be significantly lower than the values found within this work. Moreover, the chemical energy demand is by far outweighed by the sensible energy demand. The oxygen-specific sensible energy demand can be significantly reduced if materials are used which show a higher molar oxygen storage capacity than perovskites. These materials could be other metal oxides, as well as gases such as the SO_3/SO_2 system. The thermodynamics and kinetics of such materials are beyond the scope of this work, but it is worth taking such materials into account in future studies. Gases and other fluids as redox materials could be especially appealing, as the heat recovery from such materials is typically much more efficient than between solids.

In summary, the following steps can be considered to improve the energy efficiency of thermochemical air separation processes (in descending order; the most effective measure is listed first):

- Improvement of the **solid-solid heat recovery efficiency** $\boldsymbol{\eta_{\mathrm{hrec,solid}}}$ between the material in its reduced state and its oxidized state to lower the **chemical** and **sensible** energy demand per redox cycle
- Finding materials with **higher molar oxygen storage capacity** (beyond perovskites, these may include gases or different metal oxides) to lower the oxygen-specific **sensible energy** demand and potentially improve the **heat recovery efficiency**

- **Coupling** of thermochemical air separation with other technologies such as **pressure swing absorption** to lower the **total energy demand** in the high pressure regime; application of this technology in processes which require **both nitrogen and oxygen** to increase the economic viability and efficiency
- Optimization of the **temperature** and **oxygen partial pressure** levels to optimize the efficiency of the heat exchanger and to minimize the **total energy demand**
- Finding materials with **higher entropy change** (phase change materials) to lower the **chemical energy** demand

Apart from the energy efficiency, other factors must also be taken into account, such as the required purity of the output gases, the plant size, and the capital cost of the plant. Many of the perovskites studied within this work consist of earth-abundant elements, allowing them to be produced at low cost.

6.2.2 Oxygen pumping

We now consider thermochemical oxygen pumping as an application scenario. Oxygen pumping is required to lower the oxygen partial pressure in any closed system. This is especially important for other thermochemical processes such as water splitting. Decreasing the oxygen partial pressure in the reduction step allows lowering the reduction temperature while reaching the same oxygen non-stochiometry or reduction extent in the redox material. Mechanical pumps can be used to do so, as they remove all gases. However, they are very inefficient (per mol of O transferred) at low oxygen partial pressures. Thermochemical pumps are a viable alternative and may be the only reasonable means to reach very low oxygen partial pressures (oxygen concentrations in the sub-ppm range). [24]

Many of the aspects discussed on the previous pages hold true both for air separation and thermochemical oxygen pumping. However, there are some important differences. The most important of these differences is the reference technology. For air separation, highly efficient and optimized technologies exist. In the case of oxygen pumping, however, only mechanical pumps can be used as a reference and their oxygen-specific energy demand is much higher than for cryogenic air separation. It is also important to point out that both technologies (air separation and oxygen pumping) cannot be considered interchangeably in terms of their competitiveness. Nitrogen can be produced with low energy input in air separation processes, but very high gas flow rates and amounts of nitrogen as a sweep gas are necessary to maintain a low oxygen partial pressure over a redox material. Therefore oxygen pumping is strongly preferred over sweep gas technologies for maintaining low partial pressures in thermochemical processes. [150] We can use the mechanical envelope function by Brendelberger *et. al.* to estimate the minimum energy demand of a mechanical pump and compare these values to thermochemical routes. [24]

In the following, we use a simplified theoretical model to approximate the energy demand of an oxygen pumping redox cycle in dependence of the target oxygen partial pressure and solid-solid heat recovery efficiency. This allows estimating the energy demand over a wide range of oxygen partial pressures instead of being limited to fixed values based on pre-defined parameter sets. We assume a constant heat capacity of 120 J/mol K, constant redox enthalpies according to our DFT calculations, and no vibrational entropy change (as a consequence of the constant heat capacity; compare: Debye model). The configurational entropy change and partial molar entropy change of oxygen are calculated as before. We use two reference materials for oxygen pumping, $SrFeO_{3-\delta}$ and $SrMnO_{3-\delta}$, and assume constant $\Delta\delta$ values of 0.2 and 0.05, respectively. The reduction temperature is fixed to 800 °C and the reduction reaction is carried out in air. Based on the chemical equilibrium according to the Gibbs free energy (see section 8.5), we can then calculate the oxidation temperature necessary to reach these $\Delta\delta$ values. We assume a kinetic limit of 250 °C, i.e., no oxidation reaction is possible below this temperature. $SrFeO_{3-\delta}$ can then be applied to reach oxygen partial pressures down to $10^{-6} - 10^{-5}$ bar, whereas $SrMnO_{3-\delta}$ is applicable for oxygen pumping at lower oxygen partial pressures (see Fig. 6.10). This is in good agreement with the results in section 5.1.3.

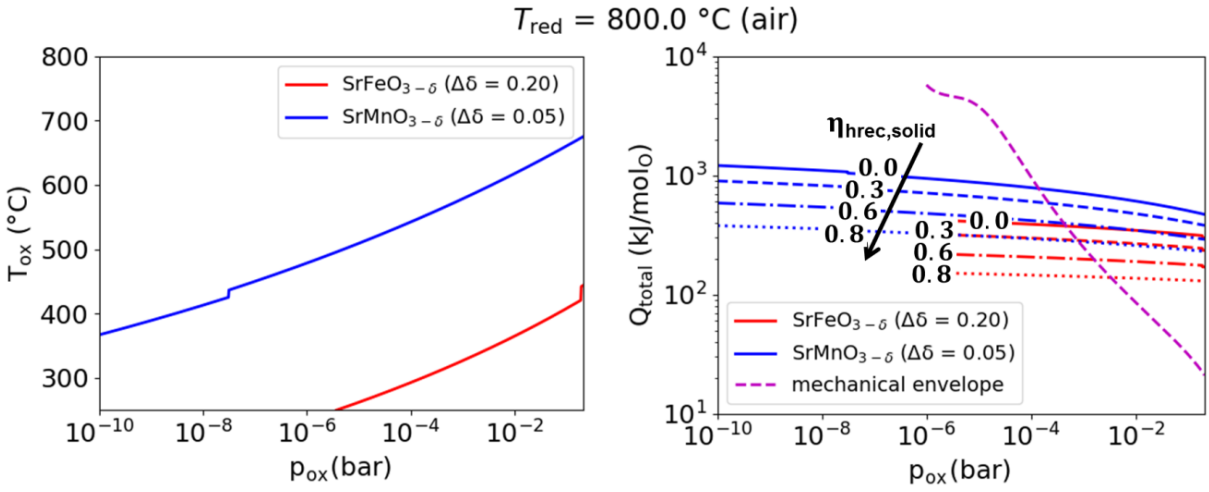

Fig. 6.10. Left: Oxidation temperature as a function of the oxidation oxygen partial pressure in a simplified theoretical model based on equilibrium conditions (see text) for two reference redox materials and reduction at 800 °C in air for fixed $\Delta\delta$ values. The steps are due to the switch of constants in the Shomate equation for calculating the partial molar entropy of oxygen according to the NIST thermochemical tables. Right: Total energy demand (sensible and chemical energy) for oxygen pumping according to the simplified model for the two reference materials compared to the mechanical envelope according to Brendelberger *et. al.* [24] The energy demand is calculated for different solid-solid heat recovery efficiencies ($\eta_{hrec,solid}$). Adapted from Vieten *et. al.* [271]

From these considerations, we can estimate the total energy demand for oxygen pumping per mol of oxygen O. While the absolute values are inaccurate due to the strong simplifications in this model, we can nevertheless estimate under which conditions thermochemical oxygen pumping may be advantageous. Even without heat recovery, thermochemical oxygen pumping requires less energy than a mechanical pump below approx. 10^{-3} bar when $SrFeO_{3-\delta}$ is used (see Fig. 6.10). This result is similar to those by Brendelberger *et. al.* who theoretically investigated a cobalt oxide based thermochemical oxygen pump. [24] In the case of $SrMnO_{3-\delta}$, this limit changes to about 10^{-4} bar oxygen partial pressure. By using a solid-solid heat exchanger, the energy demand of the pumping process decreases and it becomes competitive to mechanical pumping even at higher oxygen partial pressures. Moreover, the thermochemical pumps allow reaching very low partial pressures, for which the mechanical envelope is not defined as it is very difficult to reach such low oxygen partial pressures by mechanical pumping. The results shown here are in good agreement with those in Fig. 6.4. In our search engine, it is assumed that a mechanical pump is used to reach the reduction pressure. The cycle with reduction at 10^{-3} bar has a lower overall energy demand than the cycle with reduction in air under some conditions, as mechanical pumping is usually more energy efficient than thermochemical pumping at pressures above 10^{-3} bar. Therefore, it is reasonable to combine a mechanical pump and a thermochemical process by using a mechanical pump to reach oxygen partial pressures of 10^{-3} bar, whereas the redox material is used to further lower the oxygen partial pressure to 10^{-6} bar in the case shown in Fig. 6.4. This result is very similar to what has been shown in section 6.2.1, where we state that combining pressure swing absorption with a thermochemical air separator could be beneficial. In general, thermochemical pumps and air separators are not very efficient at oxygen partial pressures above approx. 1 mbar, but ideally complement efficient state-of-the art technologies for oxygen transport at higher pressures. One can also see that such a combination is not reasonable if the mechanical pump is used to reach 10^{-5} bar and the redox material is only used in the small range between 10^{-5} and 10^{-6} bar, as the total energy demand is significantly increased in this case. This is mainly due to the increased pumping energy.

We have seen that combined cycles in which both thermochemical and mechanical pumps are used can be more energy efficient than using only one of these technologies. It is very difficult to efficiently reach low oxygen partial pressures with physisorption techniques. [272] A thermochemical pump could ideally extend the range of potential applications. In addition or as an alternative, it may also be advantageous to use two different redox materials in a cascade. It has been explained in section 5 that each redox material has an ideal range of application. By combining one material suitable for high pressure application with a material which is suitable for reaching very low oxygen partial pressures, we can efficiently reach a broad range of oxygen partial pressures (see Fig. 6.11). For this purpose, we assume constant oxidation and reduction temperatures and vary the amount of material required according to the predicted $\Delta\delta$. To predict the chemical equilibrium state, we use the simplified model introduced before.

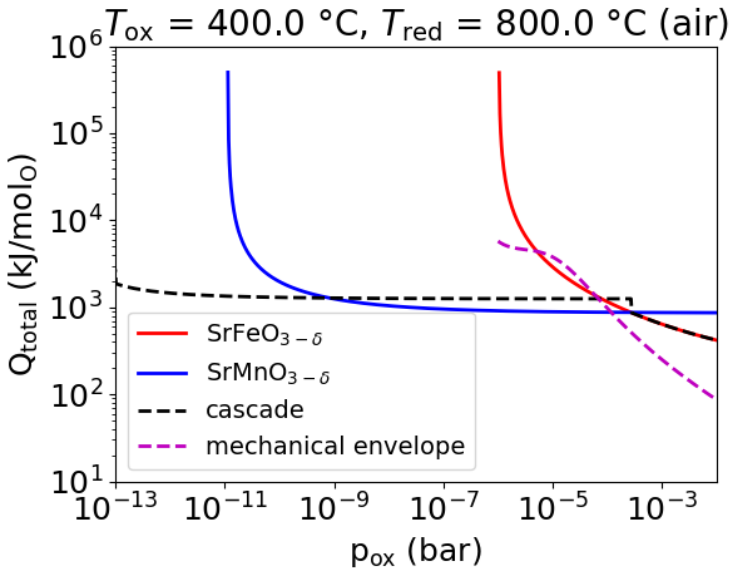

Fig. 6.11. Total energy demand (sensible and chemical energy) for oxygen pumping according to the simplified model for two reference materials with fixed oxidation and reduction temperatures. Due to a decrease in $\Delta\delta$ at low oxidation oxygen partial pressures, the energy demand per mol of O increases significantly in these cases. By combining two redox materials in a cascade system, the energy demand for thermochemical oxygen pumping can be very low over a large range of oxygen partial pressures. Adapted from Vieten *et. al.* [271]

The reduction reaction is carried out in air at 800 °C while the oxidation is performed at different oxygen partial pressure levels at 400 °C. With decreasing oxygen partial pressure, the amount of material necessary to pump one mol of oxygen increases as $\Delta\delta$ decreases. When $\Delta\delta$ approaches 0, the energy demand per mol of oxygen increases dramatically. We assume using only one reactor with $SrFeO_{3-\delta}$ at oxygen partial pressures where the energy demand of oxygen pumping with $SrFeO_{3-\delta}$ is lower than with $SrMnO_{3-\delta}$. At pressures where the energy demand of the $SrFeO_{3-\delta}$-based cycle is higher than with $SrMnO_{3-\delta}$, we assume using a second reactor with $SrMnO_{3-\delta}$. The oxidation pressure of the first reactor is the reduction pressure of the second reactor. By this means, $SrMnO_{3-\delta}$ is reduced by using $SrFeO_{3-\delta}$, which is exactly the same process as using a thermochemical pump to lower the oxygen partial pressure in another redox cycle. By this means, we can reach oxygen partial pressures between 10^{-4} bar and $< 10^{-13}$ bar with virtually the same energy demand per mol of oxygen as when using a mechanical pump to reach an oxygen partial pressure of 10^{-4} bar. Thereby, the reduction of materials for thermochemical fuels production such as ceria or perovskites should be possible at significantly lower temperatures while maintaining a constant pumping energy. [213] By using solid-solid heat recovery, the energy demand for oxygen pumping can be further reduced.

It has to be noted that the cascade concept only extends the range of oxygen partial pressures in which the thermochemical pump can be used efficiently, but it does not significantly reduce the minimum energy required to pump oxygen. The minimum energy demand is defined by the redox material with lowest redox enthalpy, and the sensible energy demand is very similar independent of the oxygen partial pressure. Even with a cascade system, thermochemical air separation at low purity levels cannot be competitive with cryogenic technology in terms of efficiency, unless the heat recovery efficiency or oxygen storage capacity are significantly improved. We have seen that, as opposed to thermochemical air separation, thermochemical oxygen pumping is energetically beneficial with respect to established methods using state-of-the-art technology, because state-of-the-art pumps require much more energy to transfer one mol of oxygen than state-of-the-art air separators. Thermochemical oxygen pumping is more energy efficient than mechanical pumps if the target oxygen partial pressure is below $10^{-3} - 10^{-4}$ bar, even without any means of heat recovery.

The steps necessary to further improve thermochemical oxygen pumping are essentially equal to the steps mentioned before for thermochemical air separation. In summary, the following steps can be considered to improve the energy efficiency of thermochemical oxygen pumping (in descending order; the most effective measure is listed first):

- Improvement of the **solid-solid heat recovery efficiency** $\boldsymbol{\eta_{hrec,solid}}$ between the material in its reduced state and its oxidized state and finding materials with **higher molar oxygen storage capacity** (see: air separation)
- **Coupling** of thermochemical oxygen pumping with other technologies such as **vacuum pumping** to lower the **total energy demand** in the high pressure regime
- Use of a **cascade** system with more than just one metal oxide to efficiently pump oxygen **over a larger pressure range**
- Optimization of the **temperature** and **oxygen partial pressure** levels to optimize the efficiency of the heat exchanger and to minimize the **total energy demand**
- Finding materials with **higher entropy change** (phase change materials) to lower the **chemical energy** demand

6.2.3 Water splitting and carbon dioxide splitting

In the case of water and CO_2 splitting, the main issue to be addressed is the low heat-to-fuel efficiency according to our study. Other authors have found higher heat-to-fuel efficiencies, but only under the assumption of a reduction step at extremely high temperatures such as 1900 K and/or by assuming significant improvements in vacuum pumping and heat recovery. [259, 273]

In practice, it is very difficult to reach such high temperatures, especially in an enclosed system which is required to maintain a low oxygen partial pressure. [57, 273] An optically transparent separation plate is required to allow highly concentrated solar radiation to enter the reactor, but this plate (usually quartz glass) will also heat up, which limits the temperature limit for its operation. Moreover, the interface between this glass plate and the reactor must be kept sealed at high temperature and at the same time withstand the thermal stress due to the different thermal expansion coefficients of different components. In addition, the commonly used redox material ceria and its doped variants show sublimation at high temperatures and low oxygen partial pressures. [274, 275] Perovskites may show similar phenomena, and the fact that we observed sintering of the perovskite particles in many cases after synthesis at 1300 °C suggests that the melting point of these perovskites does not exceed the melting point of ceria. Another issue is the temperature distribution throughout the redox material. Heating the material using concentrated sunlight may result in the front parts of the redox material structure being heated to a high temperature, while the rear parts remain significantly cooler. While it is not impossible to reach very high reduction temperatures, it appears extremely challenging and the necessary reactor materials which withstand such high temperatures on the long term are expensive. We therefore assume a maximum reduction temperature of 1500 °C in our study.

A low heat-to-fuel efficiency means that only a small part of the thermal energy input is stored chemically in the reaction product. The blue bars in Fig. 6.6 show how low the chemical energy input is, and not even all of the chemical energy is stored in the fuel, as the oxidation reaction is usually exothermic. Therefore, we need to find ways to reduce the energy input for the sensible, pumping, and (in case of water splitting) steam generation energy.

Firstly, it has to be pointed out again that the redox process is by no means optimized in our study and we are not modelling a real reactor but just the thermochemical equilibrium state. The order of pumping and temperature change as specified on page 46 may be optimized in order to reach a more efficient process. Our model only serves as a means of comparing different redox materials and is accurate in doing so, but the resulting heat-to-fuel efficiencies in the order of 2-4 % may be raised significantly by optimizing the redox process operation. Other authors find values between approx. 1 and 8 % for water splitting using ceria under realistic conditions. [57, 267] However, the amount of different modelling approaches and whether or not different energetic contributions are defined

realistically allows finding almost any value between 0.04 % and 40 % solar-to-fuel efficiency for thermochemical water splitting in the literature, which would correspond to even higher heat-to-fuel efficiencies. [267] The heat-to-fuel efficiencies in our model appear realistic and in the correct order of magnitude, considering that many models do not account for the sensible energy, pumping energy, and steam generation energy. Based on the literature, the commercialization threshold for thermochemical water splitting is around 35 % solar-to-fuel efficiency, which appears impossible to reach with current technology. [267, 276, 277] We are now using our model to investigate the effect of different optimization strategies on the heat-to-fuel efficiency and the different energy penalties in the system in order to see what could be possible through further technology and materials development.

Chemical and Sensible Energy: The material thermodynamics which determine the oxygen-specific chemical and sensible energy demand have been optimized within our model. It has been found that perovskites can be used to adjust the thermodynamics to specific process conditions and reach up to 50 % higher heat-to-fuel efficiencies at low reduction temperatures (1300 °C) with respect to ceria due to their lower redox enthalpy. The thermodynamics may be further optimized by increasing the entropy change in the redox material during the redox cycle. Initial studies using perovskites with phase changes by Lebendig indicate that the entropy change of perovskites might be increased to a magnitude comparable to ceria within a small window of $\Delta\delta$, but the initial tests need to be verified by more detailed studies. [241] As mentioned before, the configurational entropy may also be increased by introducing redox-active ions on the perovskite *A* sites. Moreover, other phase change materials beyond perovskites may be used, as long as they show appreciable kinetics and reversibility. [30, 32] These may include even non-solid oxides, but handling such materials is challenging. [30, 278] Besides optimizing the thermodynamics of the redox material, one could also shift the chemical equilibrium of the water splitting reaction by constantly removing hydrogen from the system. This may be achieved using hydrogen-conducting membranes, [279] or through capturing hydrogen in a hydride-based cycle (for instance using MgH_2 [280, 281]). The effect of such optimizations can be estimated by looking at the share of the chemical and sensible energy compared to the total energy demand of the cycle. According to our model, the chemical and sensible energy for a water splitting cycle with heat-to-fuel efficiency around 2 % account for approx. 10-90 % of the total energy demand, based on the chosen conditions. Redox cycles with high hydrogen yields and reduction at higher oxygen partial pressures show the largest share of sensible and chemical energy. Further optimizing the thermodynamics of the redox material and the water splitting reaction therefore has a tremendous potential in increasing the heat-to-fuel efficiency, but it has to be seen which of the discussed approaches is realistic. In addition to that, the process conditions can be optimized. Nevertheless, it appears highly unlikely that the commercialization threshold can be reached by optimizing the material thermodynamics and the process conditions only. Therefore, we study other effects additionally in the following.

Pumping Energy: The pumping energy has a large share in the total energy demand of the redox cycle if low oxygen partial pressures shall be reached. By modifying the process parameters, the pumping energy may be minimized. Moreover, thermochemical pumps could be used instead of mechanical pumps to reach low oxygen partial pressures, as recently demonstrated. [213] The pumping energy accounts for over 50 % of the total energy demand of the redox cycle in our exemplary case (see Fig. 6.6). According to Fig. 6.10 and the previous section, the pumping energy demand can be decreased by over 95 % through application of thermochemical pumps, which would double the heat-to-fuel efficiency in our exemplary redox cycle. Moreover, using thermochemical pumps, lower oxygen partial pressures may be reached in the reduction reaction. This allows reducing materials at lower temperature and/or with higher $\Delta\delta$, which lowers the sensible and chemical energy demand.

Steam Generation Energy/Carbon Dioxide Supply: The steam generation energy is very high if low product yields are assumed. These low product yields, however, help shift the chemical equilibrium to allow for reduction of the redox materials at lower temperatures. The most effective way of improving the overall process efficiency is therefore to improve the heat recovery efficiency from steam. Similar considerations hold true for carbon dioxide splitting and the recovery of heat from the reaction products, but the amount of energy necessary to heat the carbon dioxide to the reduction temperature is significantly lower than in the case of water and therefore neglected in our model. In principle, lower carbon monoxide yields therefore appear acceptable from this point of view. Low carbon monoxide yields, however, may not be beneficial for the overall process, as the separation of carbon monoxide and carbon dioxide can be challenging.

Optimization of the Heat Recovery Efficiency: This is typically the most effective method of improving the overall efficiency of the redox cycle. As the heat recovery efficiency from steam is already high in our reference case (80 %), a further optimization of this efficiency only has significant benefits if low product yields are assumed (where the steam generation energy has a significant share in the total energy demand). An optimization of the solid-solid heat recovery efficiency has a significantly larger effect. If the solid-solid heat recovery efficiency is high, we can choose a redox cycle which has a high share of sensible and chemical energy demand and effectively minimize the total energy demand by maximizing the solid-solid heat recovery efficiency. Theoretically and under idealized assumptions, we can reach heat-to-fuel efficiencies significantly closer to the commercialization limit using perovskites. Fig. 6.12 shows the output of RedoxThermoCSP for water splitting with an assumed $\eta_{\mathrm{hrec,solid}} = 0.9$, $\eta_{\mathrm{hrec,steam}} = 0.95$, oxidation at 600 °C and reduction at 1500 °C. The hydrogen conversion rate is assumed to be 10 %, and the use of a thermochemical oxygen pump is implied to reach 10^{-6} bar during reduction. Based on the results shown in sections 6.2.1 and 6.2.2, a value of 150 kJ/kg redox material for oxygen pumping is assumed exemplarily, leading to a pumping energy demand of 238 kJ/mol H_2 for the most efficient material. As

$n(H_2) = n(O)$ according to the stoichiometry of water, this value corresponds to the energy demand per mol of oxygen pumped, which appears realistic according to Fig. 6.9 and 6.10 if we assume $\eta_{\mathrm{hrec,solid}} = 0.9$. The chemical energy demand in this case is very similar for all materials, as it mainly consists of the formation enthalpy of water at this temperature.

It is questionable whether these idealized values can be reached in practice using these materials. The assumed solid-solid heat recovery efficiency is far beyond the state of the art. The temperature change between oxidation and reduction is very large, and the oxidation reaction has not yet been studied with respect to its low temperature kinetics for these materials. Moreover, we are assuming chemical equilibrium conditions. It is also yet to demonstrate that thermochemical oxygen pumps can in fact be operated efficiently on a larger scale and such low oxygen partial pressures can be maintained. Additionally, we have to rely on the accuracy of our models here. Nevertheless, we can demonstrate the theoretical limits of perovskite-based redox cycles by using our model under such idealized conditions. The commercialization of thermochemical fuels production appears achievable, but very challenging. The use of thermochemical oxygen pumps and very efficient solid-solid heat exchangers is required. It can also be beneficial to further optimize the material thermodynamics in order to reach higher entropy changes. Using technologies for hydrogen capture is an appealing option to shift the chemical equilibrium. The separation of the products from the remaining educts needs to be highly efficient. Further research and engineering will show whether the challenges in this technology can be overcome in practice. Competing technologies such as high temperature electrolysis are developed in parallel and some of these have already reached a technology readiness level (TRL). However, the direct use of heat on a large scale in concentrating solar plants in desert areas and the storage of this energy and its use in the transportation sector appear very appealing, which warrants ongoing research and development in this area. The avoidance of conversion losses from heat or light to electrical energy is a large benefit of this technology which must not be neglected.

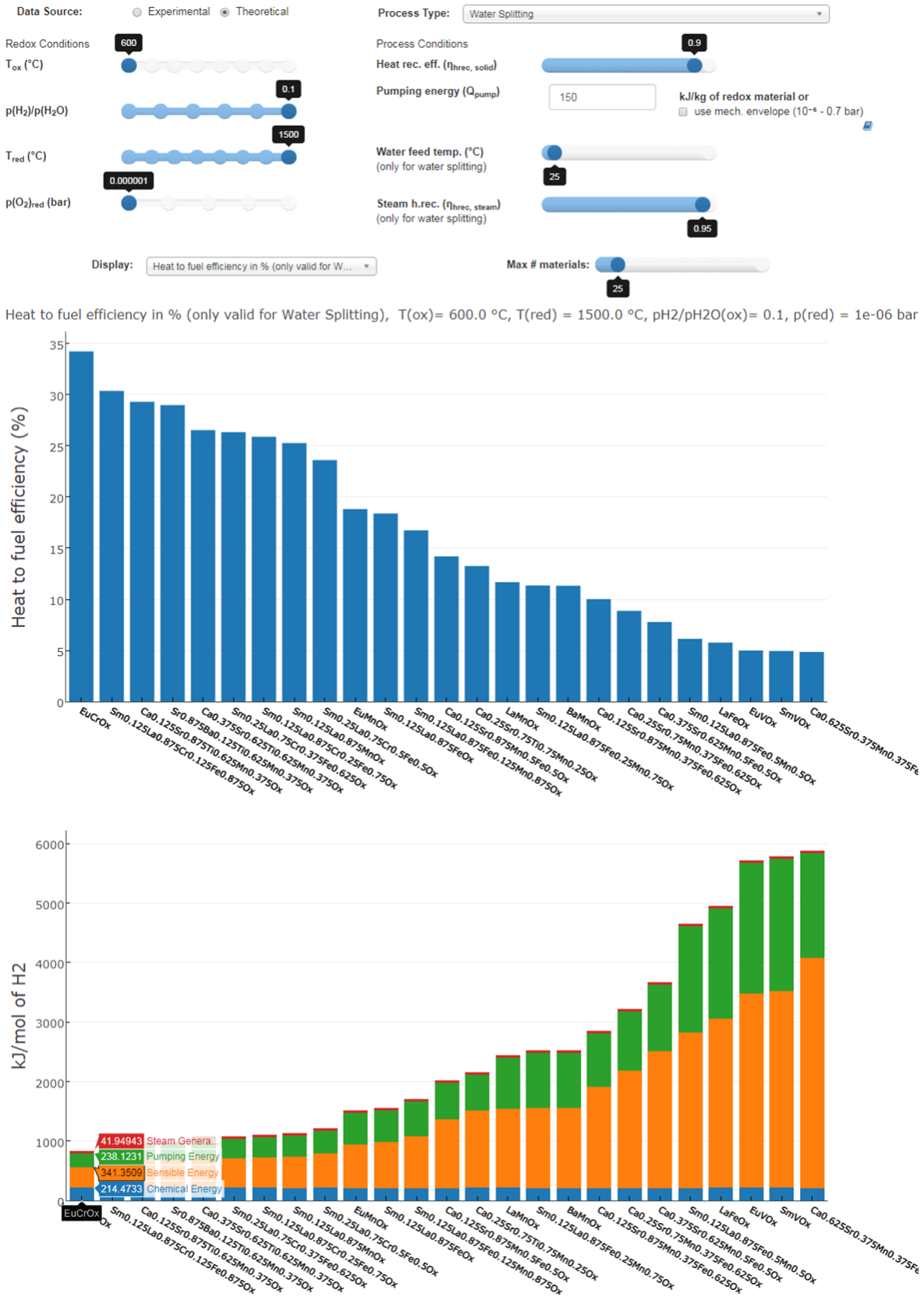

Fig. 6.12. Outputs from RedoxThermoCSP (contrast enhanced) for thermochemical water splitting using perovskites under highly idealized conditions and under the assumption of a thermodynamic equilibrium state. High heat recovery rates and the use of thermochemical pumps are implied. The theoretical maximum heat-to-fuel efficiency is as high as 34 %.

In summary, it has been shown within this section how the perovskite search engine can be used to find the perovskites with highest efficiency by optimizing their thermodynamics. As the theoretical dataset consists of a wide range of materials, ideal materials can be found for almost any set of conditions. For air separation and oxygen pumping, we find a good agreement between the suggested materials and the experimental results in section 5.1. Additionally, many new redox materials are predicted which have never been studied experimentally. For water and carbon dioxide splitting, we find many materials similar to those known from the literature. However, some materials are predicted to split water which may not actually be capable of doing so, or may have conversion rates lower than expected. We attribute this to the inaccuracies and uncertainties of our model (see table 5.1), especially with respect to the entropy calculation, but also the calculation of the temperature-dependent enthalpy change. The perovskite search engine also shows the different contributions of the chemical, sensible, pumping, and steam generation energy to the total energy demand and allows optimizing the overall energetics of the process by adjusting the heat recovery efficiencies. The redox conditions such as temperature and oxygen partial pressure levels can be fine-tuned according to the specific requirements set by the reactor and process design. The perovskite search engine is a powerful tool for materials pre-selection, and its limitations have been discussed. A general 5-step instruction to finding new redox materials has been included at the end of section 6.1 to help users apply the RedoxThermoCSP databases in the most beneficial and efficient way.

Based on the energetic analysis, we also discussed potential improvements in the efficiency of thermochemical cycles within this chapter, which potentially allow the commercialization of such processes, if technological advancements can be made. The most promising technology is oxygen pumping, as it is already energetically favorable at low oxygen partial pressures ($10^{-4} - 10^{-3}$ bar) using state-of-the-art technology. Thermochemical air separation is only commercially viable for specialized applications such as ultra-pure gases, or if it is combined with existing technologies such as pressure swing absorption. An increase of the solid-solid heat recovery efficiency is crucial for the success of this technology, and is also highly beneficial for the efficiency of thermochemical oxygen pumping. This also holds true for thermochemical fuels production. In fact, most thermochemical processes based on solid oxides stand and fall with their solid-solid heat recovery efficiency. Thermochemical fuels production based on perovskites can be more efficient than when ceria is used, if low reduction temperatures (1300-1400 °C are chosen). This is highly desirable due to the thermal stability of many materials used for reactor construction. With state-of-the-art technology, thermochemical fuels production (hydrogen or carbon monoxide) is far from being efficient enough to be commercially viable. However, this status could be reached in the future. We identified the following means to reach this goal: improvement of the solid-solid heat recovery efficiency, use of efficient thermochemical oxygen pumps, shifting the chemical equilibrium by constantly removing the products, and increasing the entropy change upon reduction of the redox materials.

7. Summary and outlook

Within this work, it has been demonstrated how perovskite solid solutions can be designed for a wide range of applications in two-step solar-thermochemical redox cycles. The phase formation can be adjusted through selection of the *A* site species in AMO_3 perovskites, whereas the thermodynamic properties are mainly influenced by the *M* site cations. These thermodynamic properties have been analyzed and made publicly available in an the online resource RedoxThermoCSP within the framework of MPContribs and Materials Project.

By applying the Goldschmidt tolerance factor and modifying it to account for solid solutions through using average ionic radii, we described the phase formation in the perovskite phase space rationally and accurately. Theoretical considerations were used to elaborate models describing the thermodynamics of such solid solutions and the heat capacity of these perovskites. Within initial studies on reference perovskite systems, we have shown that such perovskites can be used for reversible oxygen storage and we investigated the mechanisms behind these reactions by using *in-situ* investigations of the redox state. Moreover, the oxidation kinetic properties have been studied, revealing a very fast oxygen uptake of pre-reduced samples, even at temperatures well below 200-300 °C. We developed a standardized and simple method for the synthesis of perovskite solid solutions, including titanates. It has been found that solid solutions are formed in any mixture ratio if the involved species are comparable in terms of their ionic radii, and miscibility gaps exist if the ionic radii differ strongly. We investigated the tolerance-factor dependent stability limits of perovskites and associated phase transitions between them. Moreover, we confirmed our initial assumption that the thermodynamics of the redox reactions are mainly governed by the choice of *A* site cations and that their different reducibilities lead to a dependence of the thermodynamic properties on the oxygen non-stoichiometry δ. With this knowledge, we rationally designed perovskite solid solutions with two different *A* species and two different *M* species based on their tolerance factors and their expected reducibilities. Within a broad materials screening, 24 of these phases have been studied experimentally and over 240 perovskite-brownmillerite pairs were simulated using density functional theory (DFT). The energetics and stability of the perovskite phases have also been studied using DFT, and it has been shown that the vast majority of input phases is thermodynamically metastable, but likely to be synthesizable nevertheless. Based on the experimental data, we created empirical fit functions describing the thermodynamics as a function of δ, which we then compared to theoretical expressions describing the same properties. We found a good agreement between both datasets as long as δ was within the experimentally covered data range. Using the fit functions, we developed a python package to calculate thermodynamic equilibrium data for any set of temperatures, oxygen partial pressures, and/or the non-stoichiometry δ, which is used within the RedoxThermoCSP tool to create so-called “Isographs”, such as isobars and isotherms. These describe the release and uptake of oxygen of these materials under almost any conditions.

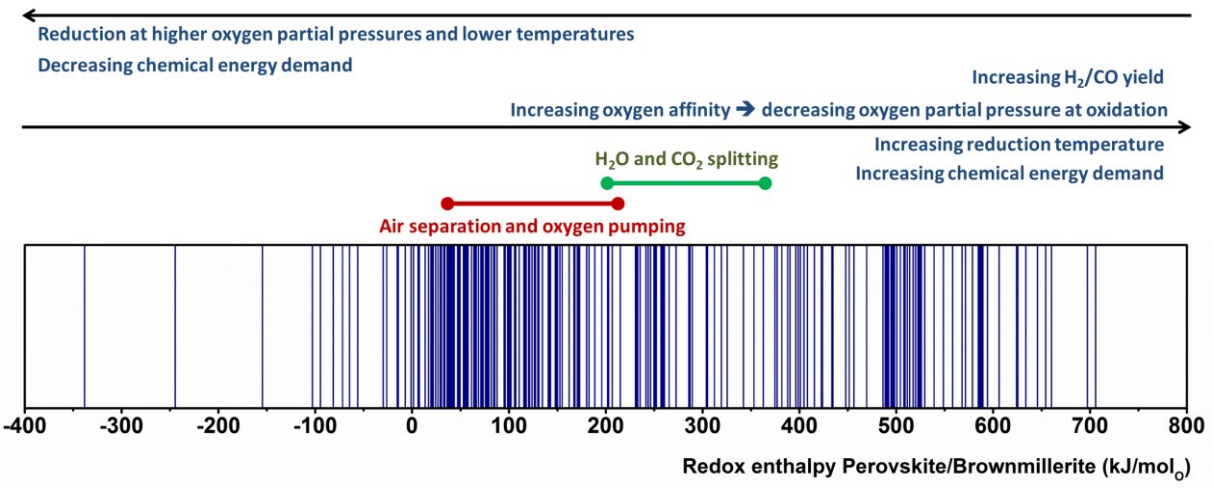

Fig. 7.1. Visualization of the enthalpy range covered within the experimental materials screening. Each line represents one of the > 240 perovskite/brownmillerite pairs studied using DFT. Some of the factors affecting the choice of materials are listed, and the approximate range of reduction enthalpies for different applications such as air separation or water splitting is shown. Depending on the conditions, different materials can be chosen.

The large range of redox enthalpies covered within the experimental study is visualized in Fig. 7.1. Each line represents one perovskite/brownmillerite pair, and important factors governing the choice of materials are shown. By making this data publicly available in user-controlled interactive graphs, we help accelerate the use and discovery of new materials for application in two-step thermochemical cycles. We have shown how oxygen pumping and air separation are possible over a large range of oxygen partial pressures and how the product conversion rate affects the choice of materials. We created a perovskite search engine based on pre-defined operational parameters which allows choosing an ideal perovskite solid solution for almost any imaginable process parameters. Based on this data, it has also been investigated which factors affect the efficiency of such thermochemical redox cycles. This is very important to estimate the potential of these technologies and to evaluate which steps are necessary for commercialization. Thermochemical oxygen pumping has been presented as a very appealing method for creating low oxygen partial pressures and is highly advantageous over state-of-the-art technologies. [213] Air separation processes can be appealing if coupled with existing technologies or to prepare ultra-pure gases. Water or carbon dioxide splitting for fuels production is currently far from being competitive with state-of-the-art technologies, but could reach competitiveness if technological advances can be made. Using perovskites, we can reach an increase in efficiency of up to 50 % with respect to ceria as a redox material at low temperatures (1300-1400 °C), which potentially allows building reactors at lower cost. The efficiency of all thermochemical cycles highly depends on the solid-solid heat recovery efficiency, which needs to be significantly improved to render these processes more efficient. Other methods of optimization include materials thermodynamics, shifting the chemical equilibrium, and an optimization of the process conditions. Thermochemical oxygen pumps help increase the efficiency of two-step thermochemical cycles significantly. In summary, the commercialization of

such redox cycles is challenging, but possible, and our method of materials design and the results of this work allow getting closer to this target.

Within future studies, the theoretical description of perovskite solid solutions can be further improved by simulating a larger amount of potential structures and arrangements of atoms. The accuracy of the thermodynamic models can be improved by accounting for oxygen vacancy ordering as well as long and short range ordering effects in solid solutions. More materials beyond perovskites, including fluids, could be studied as redox materials through theoretical means. The prediction of phase stability may be improved in DFT by investigating the amorphous limits. [249] Moreover, special quasirandom structures or the virtual crystal approximation may lead to a better description of solid solution phases. The experimental dataset can be extended in terms of the amount of the materials as well as in terms of the number of data points at different δ values. By these means, the accuracy of the applied models may be further increased, as suggested in Table 5.1.

In terms of a fundamental analysis of the perovskite properties and further materials development, it is appealing to study some materials more in detail, especially solid solutions with two different transition metal species. Phase formation and phase stability limits may be studied by preparing single crystals, and oxygen vacancy formation could be studied using advanced techniques such as *in-situ* neutron diffraction. [231] It is especially promising to investigate perovskite samples using Auger electron spectroscopy or X-Ray photoelectron spectroscopy. For perovskite solid solutions, these studies could reveal details on the electronic band structure and eludicate the oxidation state of the two transition metal species in a solid solution. The result of these studies can then be compared to our models and the results of the theoretical calculations in Materials Project, especially in terms of the electronic band structure. *In-situ* studies similar to those presented in this work could be helpful to study the properties of perovskite solid solutions, as they could further sustain our assumption of preferential reduction of one of the two species, and extend the analysis of solid solution redox properties beyond the experimentally studied systems. Moreover, phase changes between hexagonal/rhombohedral and cubic perovskite phases and their effects on the overall thermodynamics appear very promising as a means to increase the redox entropy change. The thermodynamics of these phase changes require more in-depth studies, and it is yet to prove that an increased entropy change is present to a substantial extent and that it can be harnessed as a means to increase the perovskite's non-stoichiometry change. The oxygen diffusion throughout the perovskite and its effect on the reaction kinetics could also be studied, for instance using molecular dynamics simulations.

As a means of process engineering, the equilibrium in water splitting reactions may be shifted by steadily removing hydrogen from the reaction chamber, and thermochemical pumps could be applied. Together with an improved heat recovery efficiency and process design, these steps may lead to the realization of solar fuels production plants. Moreover, thermochemical air separation and oxygen pumping techniques are applicable in industrial processes. These technologies can be an important factor for reaching a future with sustainable energy supply and conversion.

8. Appendix

8.1 Used starting materials

Table 8.1: Materials used for experiments within this thesis.

Substance	Properties	Supplier	Purity[n]
Metal nitrates			
$Ca(NO_3)_2 \cdot 4\ H_2O$	powder	Alfa Aesar	99 %
$Sr(NO_3)_2 \cdot 4\ H_2O$	powder	Alfa Aesar	> 99.0 %
$Eu(NO_3)_3 \cdot 6\ H_2O$	powder	Acros Organics	99.9 %
$Fe(NO_3)_3 \cdot 9\ H_2O$	powder	VWR Chemicals	99.0 – 101.0 %
$Mn(NO_3)_2 \cdot 4\ H_2O$	powder	Acros Organics	for analysis
$Cu(NO_3)_2 \cdot 2.5\ H_2O$	powder	Sigma-Aldrich	98 %
$Co(NO_3)_2 \cdot 6\ H_2O$	powder	Acros Organics	99 %
Liquids			
H_2O_2 (30% aqueous solution)	stabilized	Merck	for analysis
NH_3 (28-30% aqueous solution)	-	Merck	reagent grade
Other solids			
$C_6H_8O_7$ (citric acid, anhydrous)	powder	Merck	99 %
TiO (titanium monoxide)	powder, -325 mesh	Alfa Aesar	99.5 %
TiO_2 (titanium dioxide)	powder, -22 mesh	Alfa Aesar	99.995 %
$SrCO_3$	powder	Alfa Aesar	99.99 %
Reaction and protective gases			
Ar	compressed gas	Linde	5.0 (99.999 %)
synthetic air (80:20 N_2:O_2 mol%)	compressed gas	Linde	see reference [282]
O_2	compressed gas	Linde	4.5 (99.995 %)

[n] as specified by the suppliers

8.2 Perovskite samples prepared and empirical fit parameters

Table 8.2: Perovskites prepared for the initial studies in chapter 4 of this work. 5 mmol of each perovksite sample have been prepared.

Substance (nominal starting composition)
$CaMnO_{3-\delta}$
$Ca_{0.8}Sr_{0.2}MnO_{3-\delta}$
$SrFeO_{3-\delta}$
$Sr_{1.05}Fe_{0.95}Cu_{0.05}O_{3-\delta}$
$SrFe_{0.85}Cu_{0.15}O_{3-\delta}$
$SrFe_{0.75}Cu_{0.25}O_{3-\delta}$*
$SrFe_{0.67}Cu_{0.33}O_{3-\delta}$*
$CaTi_{0.2}Mn_{0.8}O_{3-\delta}$
$CaTi_{0.3}Mn_{0.7}O_{3-\delta}$
$CaTi_{0.4}Mn_{0.6}O_{3-\delta}$
$CaTi_{0.5}Mn_{0.5}O_{3-\delta}$
$CaTi_{0.6}Mn_{0.4}O_{3-\delta}$
$CaTi_{0.7}Mn_{0.3}O_{3-\delta}$
$CaTi_{0.8}Mn_{0.2}O_{3-\delta}$
$CaTiO_{3-\delta}$
$SrMn_{0.05}Fe_{0.95}O_{3-\delta}$*
$SrMn_{0.15}Fe_{0.85}O_{3-\delta}$
$SrMn_{0.33}Fe_{0.67}O_{3-\delta}$
$SrMn_{0.50}Fe_{0.50}O_{3-\delta}$
$SrMn_{0.67}Fe_{0.33}O_{3-\delta}$
$SrMn_{0.85}Fe_{0.15}O_{3-\delta}$
$SrMn_{0.95}Fe_{0.05}O_{3-\delta}$
$SrMnO_{3-\delta}$
$EuCuO_{3-\delta}$*
$EuFeO_{3-\delta}$

* synthesis of a pure phase failed

Table 8.3: Perovskites studied within the experimental materials screening presented in chapter 5 including the experimentally covered non-stoichiometry range, accounting for the non-stoichiometry at the reference point (400 °C, 0.18 bar oxygen partial pressure) δ_0 as determined from the entropy fits as explained within this work. Taken from Vieten *et. al.* (supporting information). [95]

Composition	δ_{exp} min	δ_{exp} max	δ_0 (from entropy fit*)	tolerance factor ($\delta = 0$)	molar_mass ($\delta = 0$), g/mol
$Ca_{0.15}Sr_{0.85}Mn_{0.2}Fe_{0.8}O_{3-\delta}$	0.1080	0.2450	0.0690	1.006	184.1505
$Ca_{0.30}Sr_{0.70}Mn_{0.4}Fe_{0.6}O_{3-\delta}$	0.1103	0.2153	0.0973	1.006	176.8378
$Ca_{0.45}Sr_{0.55}Mn_{0.6}Fe_{0.4}O_{3-\delta}$	0.1316	0.3116	0.1056	1.006	169.5251
$Ca_{0.60}Sr_{0.40}Mn_{0.8}Fe_{0.2}O_{3-\delta}$	0.0768	0.3038	0.0638	1.006	162.2124
$Ca_{0.75}Sr_{0.25}MnO_{3-\delta}$	0.0130	0.2780	0	1.006	154.8997
$Ca_{0.54}Sr_{0.46}Ti_{0.2}Mn_{0.8}O_{3-\delta}$	0.0050	0.1870	0	1.006	163.4694
$Ca_{0.34}Sr_{0.66}Ti_{0.4}Mn_{0.6}O_{3-\delta}$	0.0150	0.1690	0	1.006	171.5635
$Ca_{0.13}Sr_{0.87}Ti_{0.6}Mn_{0.4}O_{3-\delta}$	0.0050	0.0920	0	1.006	180.1332
$SrFeO_{3-\delta}$	0.2885	0.4575	0.2365	1.006	191.4632
$Ca_{0.87}Sr_{0.13}Mn_{0.8}Fe_{0.2}O_{3-\delta}$	0.0720	0.3000	0.0520	0.995	149.3761
$Ca_{0.73}Sr_{0.27}Mn_{0.6}Fe_{0.4}O_{3-\delta}$	0.1337	0.1787	0.1247	0.995	156.2134
$Ca_{0.58}Sr_{0.42}Mn_{0.4}Fe_{0.6}O_{3-\delta}$	0.1034	0.1694	0.0894	0.995	163.5261
$Ca_{0.44}Sr_{0.56}Mn_{0.2}Fe_{0.8}O_{3-\delta}$	0.0971	0.1871	0.0761	0.995	170.3633
$Ca_{0.29}Sr_{0.71}FeO_{3-\delta}$	0.3026	0.4976	0.2606	0.995	177.6760
$Ca_{0.92}Sr_{0.08}Ti_{0.1}Mn_{0.9}O_{3-\delta}$	0.0070	0.2220	0	0.995	146.1105
$Ca_{0.82}Sr_{0.18}Ti_{0.2}Mn_{0.8}O_{3-\delta}$	0.0270	0.2420	0	0.995	150.1576
$Ca_{0.62}Sr_{0.38}Ti_{0.4}Mn_{0.6}O_{3-\delta}$	0.0120	0.1790	0	0.995	158.2518
$Ca_{0.42}Sr_{0.58}Ti_{0.6}Mn_{0.4}O_{3-\delta}$	0.0060	0.1000	0	0.995	166.3460
$Ca_{0.07}Sr_{0.93}Fe_{0.9}Co_{0.1}O_{3-\delta}$	0.3285	0.3655	0.3215	1.006	188.4441
$Ca_{0.30}Sr_{0.70}Fe_{0.6}Co_{0.4}O_{3-\delta}$	0.4580	0.4990	0.4530	1.006	178.4359
$Ca_{0.64}Sr_{0.36}Ti_{0.1}Mn_{0.9}O_{3-\delta}$	0.0060	0.1560	0	1.006	159.4223
$Ca_{0.21}Sr_{0.79}Mn_{0.6}Fe_{0.4}O_{3-\delta}$	0.0859	0.2659	0.0639	1.015	180.9352
$Ca_{0.51}Sr_{0.49}MnO_{3-\delta}$	0.0070	0.1860	0	1.015	166.3098
$Ca_{0.1}Sr_{0.9}Ti_{0.4}Mn_{0.6}O_{3-\delta}$	0.0110	0.1590	0	1.015	182.9736

* Set to zero for the Ti-Mn system due to negligible non-stoichiometry at 400 °C and p_{O_2} = 0.18 bar.

Table 8.4: Enthalpy fit data for experimentally studied perovskites. Taken from Vieten *et. al.* (supporting information). [95]

Composition	dH_{max}	dH_{min}	sh	sl
$Ca_{0.15}Sr_{0.85}Mn_{0.2}Fe_{0.8}O_{3-\delta}$	24437.739	28.844	0.254	1772.649
$Ca_{0.30}Sr_{0.70}Mn_{0.4}Fe_{0.6}O_{3-\delta}$	20364.640	-20.095	0.200	602.646
$Ca_{0.45}Sr_{0.55}Mn_{0.6}Fe_{0.4}O_{3-\delta}$	202.021	-28183.726	-0.081	570.238
$Ca_{0.60}Sr_{0.40}Mn_{0.8}Fe_{0.2}O_{3-\delta}$	182.060	-28025.380	-0.114	652.266
$Ca_{0.75}Sr_{0.25}MnO_{3-\delta}$	199.639	115.776	0.265	15.148
$Ca_{0.54}Sr_{0.46}Ti_{0.2}Mn_{0.8}O_{3-\delta}$	173.523	-54594.202	-0.044	4652.384
$Ca_{0.34}Sr_{0.66}Ti_{0.4}Mn_{0.6}O_{3-\delta}$	190.733	141.082	0.063	35.227
$Ca_{0.13}Sr_{0.87}Ti_{0.6}Mn_{0.4}O_{3-\delta}$	199.827	-27222.407	-0.001	16954.431
$SrFeO_{3-\delta}$	87.441	63*	0.059	59.791
$Ca_{0.87}Sr_{0.13}Mn_{0.8}Fe_{0.2}O_{3-\delta}$	165.294	-17.616	0.020	33.042
$Ca_{0.73}Sr_{0.27}Mn_{0.6}Fe_{0.4}O_{3-\delta}$	144.528	-15054.692	-0.041	923.677
$Ca_{0.58}Sr_{0.42}Mn_{0.4}Fe_{0.6}O_{3-\delta}$	20685.743	-23.961	0.180	608.545
$Ca_{0.44}Sr_{0.56}Mn_{0.2}Fe_{0.8}O_{3-\delta}$	16532.294	25.542	0.206	998.139
$Ca_{0.29}Sr_{0.71}FeO_{3-\delta}$	32.521	22*	0.236	-293.341
$Ca_{0.92}Sr_{0.08}Ti_{0.1}Mn_{0.9}O_{3-\delta}$	166.550	108.510	0.019	373.552
$Ca_{0.82}Sr_{0.18}Ti_{0.2}Mn_{0.8}O_{3-\delta}$	304.780	-5753.333	-0.810	15.512
$Ca_{0.62}Sr_{0.38}Ti_{0.4}Mn_{0.6}O_{3-\delta}$	192.346	127.418	0.052	28.245
$Ca_{0.42}Sr_{0.58}Ti_{0.6}Mn_{0.4}O_{3-\delta}$	187.580	157.200	0.025	159.677
$Ca_{0.07}Sr_{0.93}Fe_{0.9}Co_{0.1}O_{3-\delta}$	74.133	-3273.552	-0.029	1281.024
$Ca_{0.30}Sr_{0.70}Fe_{0.6}Co_{0.4}O_{3-\delta}$	20.160	36.458	0.042	67702721.650
$Ca_{0.64}Sr_{0.36}Ti_{0.1}Mn_{0.9}O_{3-\delta}$	154.802	-234.439	0.001	174.027
$Ca_{0.21}Sr_{0.79}Mn_{0.6}Fe_{0.4}O_{3-\delta}$	171.225	-0.227	0.054	18.865
$Ca_{0.51}Sr_{0.49}MnO_{3-\delta}$	120.923	84.016	0.025	408.041
$Ca_{0.1}Sr_{0.9}Ti_{0.4}Mn_{0.6}O_{3-\delta}$	183.499	119.442	0.051	25.155

* dH_{min} fixed manually to stabilize the fit.

Table 8.5: Entropy fit data for experimentally studied perovskites. Taken from Vieten *et. al.* (supporting information). [95]

Composition	Fit type	Δs_{vib}	a	s_{Ent}	m
$Ca_{0.15}Sr_{0.85}Mn_{0.2}Fe_{0.8}O_{3-\delta}$	Solid Solution			3.2817	-13.8547
$Ca_{0.30}Sr_{0.70}Mn_{0.4}Fe_{0.6}O_{3-\delta}$	Solid Solution			31.0522	-6.7730
$Ca_{0.45}Sr_{0.55}Mn_{0.6}Fe_{0.4}O_{3-\delta}$	Solid Solution			41.5771	0
$Ca_{0.60}Sr_{0.40}Mn_{0.8}Fe_{0.2}O_{3-\delta}$	Solid Solution			76.0299	-12.8393
$Ca_{0.75}Sr_{0.25}MnO_{3-\delta}$	Dilute Species	-40.6063	0.4639		
$Ca_{0.54}Sr_{0.46}Ti_{0.2}Mn_{0.8}O_{3-\delta}$	Dilute Species	-26.2111	0.0125		
$Ca_{0.34}Sr_{0.66}Ti_{0.4}Mn_{0.6}O_{3-\delta}$	Dilute Species	-22.7249	0.2425		
$Ca_{0.13}Sr_{0.87}Ti_{0.6}Mn_{0.4}O_{3-\delta}$	Dilute Species	-8.4690	-0.0239		
$SrFeO_{3-\delta}$	Dilute Species	-28.0530	0.7567		
$Ca_{0.87}Sr_{0.13}Mn_{0.8}Fe_{0.2}O_{3-\delta}$	Solid Solution			319.9609	4.2984
$Ca_{0.73}Sr_{0.27}Mn_{0.6}Fe_{0.4}O_{3-\delta}$	Solid Solution			20.6839	0
$Ca_{0.58}Sr_{0.42}Mn_{0.4}Fe_{0.6}O_{3-\delta}$	Solid Solution			42.0604	0.9554
$Ca_{0.44}Sr_{0.56}Mn_{0.2}Fe_{0.8}O_{3-\delta}$	Solid Solution			1.6029	0.0000
$Ca_{0.29}Sr_{0.71}FeO_{3-\delta}$	Dilute Species	-79.3352	0.4334		
$Ca_{0.92}Sr_{0.08}Ti_{0.1}Mn_{0.9}O_{3-\delta}$	Dilute Species	-23.8004	0.6589		
$Ca_{0.82}Sr_{0.18}Ti_{0.2}Mn_{0.8}O_{3-\delta}$	Dilute Species	-24.9649	0.5865		
$Ca_{0.62}Sr_{0.38}Ti_{0.4}Mn_{0.6}O_{3-\delta}$	Dilute Species	-18.8441	0.1458		
$Ca_{0.42}Sr_{0.58}Ti_{0.6}Mn_{0.4}O_{3-\delta}$	Dilute Species	-27.7482	0.4430		
$Ca_{0.07}Sr_{0.93}Fe_{0.9}Co_{0.1}O_{3-\delta}$	Solid Solution			3748206.6430	0
$Ca_{0.30}Sr_{0.70}Fe_{0.6}Co_{0.4}O_{3-\delta}$	Solid Solution			21423185.5100	12.0446
$Ca_{0.64}Sr_{0.36}Ti_{0.1}Mn_{0.9}O_{3-\delta}$	Dilute Species	-7.6069	-0.3305		
$Ca_{0.21}Sr_{0.79}Mn_{0.6}Fe_{0.4}O_{3-\delta}$	Solid Solution			78.3719	-8.2539
$Ca_{0.51}Sr_{0.49}MnO_{3-\delta}$	Dilute Species	-51.1221	0.6084		
$Ca_{0.1}Sr_{0.9}Ti_{0.4}Mn_{0.6}O_{3-\delta}$	Dilute Species	-30.5018	0.1362		

Table 8.6: Assignment of experimentally studied perovskite compositions to the sample numbers used within the RedoxThermoCSP code, the tolerance factors t of the experimentally studied phases for δ = 0, and the composition of the corresponding phases in the DFT study.Taken from Vieten *et. al.* (supporting information). [95]

Composition (exp)	Sample number	*t*	Composition (theo)
$Ca_{0.15}Sr_{0.85}Mn_{0.2}Fe_{0.8}O_{3-\delta}$	75	1.006	$Ca_{0.125}Sr_{0.875}Mn_{0.25}Fe_{0.75}O_{3-\delta}$
$Ca_{0.30}Sr_{0.70}Mn_{0.4}Fe_{0.6}O_{3-\delta}$	76	1.006	$Ca_{0.25}Sr_{0.75}Mn_{0.375}Fe_{0.625}O_{3-\delta}$
$Ca_{0.45}Sr_{0.55}Mn_{0.6}Fe_{0.4}O_{3-\delta}$	77	1.006	$Ca_{0.5}Sr_{0.5}Mn_{0.625}Fe_{0.375}O_{3-\delta}$
$Ca_{0.60}Sr_{0.40}Mn_{0.8}Fe_{0.2}O_{3-\delta}$	78	1.006	$Ca_{0.625}Sr_{0.375}Mn_{0.875}Fe_{0.125}O_{3-\delta}$
$Ca_{0.75}Sr_{0.25}MnO_{3-\delta}$	79	1.006	$Ca_{0.75}Sr_{0.25}MnO_{3-\delta}$
$Ca_{0.54}Sr_{0.46}Ti_{0.2}Mn_{0.8}O_{3-\delta}$	93	1.006	$Ca_{0.5}Sr_{0.5}Ti_{0.25}Mn_{0.75}O_{3-\delta}$
$Ca_{0.34}Sr_{0.66}Ti_{0.4}Mn_{0.6}O_{3-\delta}$	94	1.006	$Ca_{0.25}Sr_{0.75}Ti_{0.5}Mn_{0.5}O_{3-\delta}$
$Ca_{0.13}Sr_{0.87}Ti_{0.6}Mn_{0.4}O_{3-\delta}$	95	1.006	$Ca_{0.125}Sr_{0.875}Ti_{0.625}Mn_{0.375}O_{3-\delta}$
$SrFeO_{3-\delta}$	100	1.006	$SrFeO_{3-\delta}$
$Ca_{0.87}Sr_{0.13}Mn_{0.8}Fe_{0.2}O_{3-\delta}$	106	0.995	$Ca_{0.875}Sr_{0.125}Mn_{0.75}Fe_{0.25}O_{3-\delta}$
$Ca_{0.73}Sr_{0.27}Mn_{0.6}Fe_{0.4}O_{3-\delta}$	107	0.995	$Ca_{0.75}Sr_{0.25}Mn_{0.625}Fe_{0.375}O_{3-\delta}$
$Ca_{0.58}Sr_{0.42}Mn_{0.4}Fe_{0.6}O_{3-\delta}$	108	0.995	$Ca_{0.625}Sr_{0.375}Mn_{0.375}Fe_{0.625}O_{3-\delta}$
$Ca_{0.44}Sr_{0.56}Mn_{0.2}Fe_{0.8}O_{3-\delta}$	109	0.995	$Ca_{0.5}Sr_{0.5}Mn_{0.25}Fe_{0.75}O_{3-\delta}$
$Ca_{0.29}Sr_{0.71}FeO_{3-\delta}$	110	0.995	$Ca_{0.25}Sr_{0.75}FeO_{3-\delta}$
$Ca_{0.92}Sr_{0.08}Ti_{0.1}Mn_{0.9}O_{3-\delta}$	111	0.995	$Ca_{0.875}Sr_{0.125}Ti_{0.125}Mn_{0.875}O_{3-\delta}$
$Ca_{0.82}Sr_{0.18}Ti_{0.2}Mn_{0.8}O_{3-\delta}$	112	0.995	$Ca_{0.75}Sr_{0.25}Ti_{0.25}Mn_{0.75}O_{3-\delta}$
$Ca_{0.62}Sr_{0.38}Ti_{0.4}Mn_{0.6}O_{3-\delta}$	113	0.995	$Ca_{0.625}Sr_{0.375}Ti_{0.375}Mn_{0.625}O_{3-\delta}$
$Ca_{0.42}Sr_{0.58}Ti_{0.6}Mn_{0.4}O_{3-\delta}$	114	0.995	$Ca_{0.375}Sr_{0.625}Ti_{0.625}Mn_{0.375}O_{3-\delta}$
$Ca_{0.07}Sr_{0.93}Fe_{0.9}Co_{0.1}O_{3-\delta}$	116	1.006	$SrFe_{0.875}Co_{0.125}O_{3-\delta}$
$Ca_{0.30}Sr_{0.70}Fe_{0.6}Co_{0.4}O_{3-\delta}$	118	1.006	$Ca_{0.25}Sr_{0.75}Fe_{0.625}Co_{0.375}O_{3-\delta}$
$Ca_{0.64}Sr_{0.36}Ti_{0.1}Mn_{0.9}O_{3-\delta}$	122	1.006	$Ca_{0.625}Sr_{0.375}Ti_{0.125}Mn_{0.875}O_{3-\delta}$
$Ca_{0.21}Sr_{0.79}Mn_{0.6}Fe_{0.4}O_{3-\delta}$	128	1.015	$Ca_{0.25}Sr_{0.75}Mn_{0.625}Fe_{0.375}O_{3-\delta}$
$Ca_{0.51}Sr_{0.49}MnO_{3-\delta}$	129	1.015	$Sr_{0.5}Ca_{0.5}MnO_{3-\delta}$
$Ca_{0.1}Sr_{0.9}Ti_{0.4}Mn_{0.6}O_{3-\delta}$	130	1.015	$Ca_{0.125}Sr_{0.875}Ti_{0.375}Mn_{0.625}O_{3-\delta}$

8.3 Perovskite-Brownmillerite pairs studied theoretically

Table 8.7: Theoretical data for the perovskite redox pairs investigated within this work. Solid solutions have the general composition $(A'_xA''_{1-x})^{(6-n)+}(M'_yM''_{1-y})^{(n-2\delta)+}O_{3-\delta}$ with n denoting the charge of the transition metal species M' and M'' in the fully oxidized state, and A' and A'' being two different alkali, alkali earth, or rare earth species. The tolerance factor of the perovskite is denoted by t and calculated with respect to the fully oxidized state as explained within this work. The redox enthalpies ΔH are calculated using DFT (GGA and GGA+U as explained in the main manuscript) as per mol of oxygen O for the complete reduction from the perovskite to the brownmillerite phase ($\delta = 0$ and $\delta = 0.5$, respectively). All materials are ranked according to their calculated redox enthalpies. More materials data including the energy above hull, the crystal structures, DFT calculation summaries, and simulated X-Ray diffractograms can be retrieved on www.materialsproject.org using the hyperlinks to the MP-IDs in each dataset.Taken from Vieten *et. al.* (supporting information). [95]

Redox Material	*n*	*t*	ΔH (kJ/mol$_O$)	perovskite (oxidized phase)		brownmillerite (reduced phase)	
$MgCuO_{3-\delta}$	4	0.827	-337.87	$MgCuO_3$	mp-1076317	$Mg_2Cu_2O_5$	mp-1076527
$SmAgO_{3-\delta}$	3	0.864	-244.17	$SmAgO_3$	mp-1075933	$Sm_2Ag_2O_5$	mp-1076848
$CaCuO_{3-\delta}$	4	0.920	-154.45	$CaCuO_3$	mp-1099873	$Ca_2Cu_2O_5$	mp-772813
$EuAgO_{3-\delta}$	3	0.863	-102.97	$EuAgO_3$	mp-1077622	$Eu_2Ag_2O_5$	mp-1099927
$RbCrO_{3-\delta}$	5	1.163	-95.16	$RbCrO_3$	mp-1076360	$Rb_2Cr_2O_5$	mp-1076401
$Mg_{0.125}Ca_{0.875}CoO_{3-\delta}$	4	0.983	-81.80	$Ca_7Mg(CoO_3)_8$	mp-1076128	$Ca_7Mg(Co_2O_5)_4$	mp-1076526
$BaCuO_{3-\delta}$	4	1.012	-71.24	$BaCuO_3$	mp-1076800	$Ba_2Cu_2O_5$	mp-772788
$Mg_{0.125}Ca_{0.875}Fe_{0.125}Co_{0.875}O_{3-\delta}$	4	0.980	-65.13	$Ca_7MgFeCo_7O_{24}$	mp-1076139	$Ca_7MgFeCo_7O_{20}$	mp-1099907
$Mg_{0.125}Ca_{0.875}Co_{0.875}Cu_{0.125}O_{3-\delta}$	4	0.973	-56.05	$Ca_7MgCo_7CuO_{24}$	mp-1076132	$Ca_7MgCo_7CuO_{20}$	mp-1099952
$NaCrO_{3-\delta}$	5	1.033	-30.37	$NaCrO_3$	mp-1076642	$Na_2Cr_2O_5$	mp-1099683
$Ca_{0.5}Sr_{0.5}CoO_{3-\delta}$	4	1.015	-25.93	$SrCa(CoO_3)_2$	mp-1075928	$SrCaCo_2O_5$	mp-1099694
$Ca_{0.875}Sr_{0.125}Fe_{0.125}Co_{0.875}O_{3-\delta}$	4	0.997	-15.35	$SrCa_7FeCo_7O_{24}$	mp-1076861	$SrCa_7FeCo_7O_{20}$	mp-1099847
$Ca_{0.75}Sr_{0.25}CoO_{3-\delta}$	4	1.006	-14.17	$SrCa_3(CoO_3)_4$	mp-1076096	$SrCa_3(Co_2O_5)_2$	mp-1076675
$SrCuO_{3-\delta}$	4	0.955	-7.35	$SrCuO_3$	mp-1076711	$Sr_2Cu_2O_5$	mp-21129
$Ca_{0.875}Sr_{0.125}Fe_{0.25}Co_{0.75}O_{3-\delta}$	4	0.994	-1.20	$SrCa_7Fe_2(CoO_4)_6$	mp-1076829	$SrCa_7Fe_2(Co_3O_{10})_2$	mp-1099745
$Ca_{0.75}Sr_{0.25}Co_{0.875}Cu_{0.125}O_{3-\delta}$	4	0.995	-0.57	$Sr_2Ca_6Co_7CuO_{24}$	mp-1099600	$Sr_2Ca_6Co_7CuO_{20}$	mp-1076470
$SrCoO_{3-\delta}$	4	1.035	0.82	$SrCoO_3$	mp-561952	$Sr_2Co_2O_5$	mp-556076
$Ca_{0.75}Sr_{0.25}Fe_{0.125}Co_{0.875}O_{3-\delta}$	4	1.002	6.06	$Sr_2Ca_6FeCo_7O_{24}$	mp-1076626	$Sr_2Ca_6FeCo_7O_{20}$	mp-1099653
$KCrO_{3-\delta}$	5	1.134	6.77	$KCrO_3$	mp-1076732	$K_2Cr_2O_5$	mp-1076696
$Ca_{0.625}Sr_{0.375}Fe_{0.125}Co_{0.875}O_{3-\delta}$	4	1.007	7.82	$Sr_3Ca_5FeCo_7O_{24}$	mp-1099827	$Sr_3Ca_5FeCo_7O_{20}$	mp-1076479
$Ca_{0.5}Sr_{0.5}Co_{0.875}Cu_{0.125}O_{3-\delta}$	4	1.005	13.73	$Sr_4Ca_4Co_7CuO_{24}$	mp-1099611	$Sr_4Ca_4Co_7CuO_{20}$	mp-1076175
$Ca_{0.5}Sr_{0.5}Co_{0.75}Cu_{0.25}O_{3-\delta}$	4	0.995	17.45	$Sr_2Ca_2Co_3CuO_{12}$	mp-1099844	$Sr_2Ca_2Co_3CuO_{10}$	mp-1076273
$Ca_{0.75}Sr_{0.25}Fe_{0.375}Co_{0.625}O_{3-\delta}$	4	0.995	19.14	$Sr_2Ca_6Fe_3Co_5O_{24}$	mp-1099890	$Sr_2Ca_6Fe_3(CoO_4)_5$	mp-1076198
$Sr_{0.125}Ba_{0.875}CuO_{3-\delta}$	4	1.005	20.46	$Ba_7Sr(CuO_3)_8$	mp-1099824	$Ba_7Sr(Cu_2O_5)_4$	mp-1099795
$Sr_{0.25}Ba_{0.75}CuO_{3-\delta}$	4	0.998	22.34	$Ba_3Sr(CuO_3)_4$	mp-1099602	$Ba_3Sr(Cu_2O_5)_2$	mp-1076189
$Sr_{0.25}Ba_{0.75}Co_{0.25}Cu_{0.75}O_{3-\delta}$	4	1.018	23.76	$Ba_3SrCo(CuO_4)_3$	mp-1099886	$Ba_3SrCoCu_3O_{10}$	mp-1100085
$Sr_{0.25}Ba_{0.75}Co_{0.125}Cu_{0.875}O_{3-\delta}$	4	1.008	23.79	$Ba_6Sr_2CoCu_7O_{24}$	mp-1076247	$Ba_6Sr_2CoCu_7O_{20}$	mp-1076296
$Ca_{0.5}Sr_{0.5}Fe_{0.125}Co_{0.875}O_{3-\delta}$	4	1.012	24.32	$Sr_4Ca_4FeCo_7O_{24}$	mp-1075997	$Sr_4Ca_4FeCo_7O_{20}$	mp-1100009
$Sm_{0.125}La_{0.875}Co_{0.75}Ag_{0.25}O_{3-\delta}$	3	0.943	26.19	$La_7SmCo_6(AgO_{12})_2$	mp-1076275	$La_7SmCo_6(AgO_{10})_2$	mp-1076866
$Ca_{0.25}Sr_{0.75}Co_{0.875}Cu_{0.125}O_{3-\delta}$	4	1.014	28.48	$Sr_6Ca_2Co_7CuO_{24}$	mp-1076741	$Sr_6Ca_2Co_7CuO_{20}$	mp-1076118
$Sm_{0.125}La_{0.875}Ag_{0.25}Ni_{0.75}O_{3-\delta}$	3	0.947	28.64	$La_7SmNi_6(AgO_{12})_2$	mp-1076723	$La_7SmNi_6(AgO_{10})_2$	mp-1099871
$Sr_{0.5}Ba_{0.5}Co_{0.25}Cu_{0.75}O_{3-\delta}$	4	1.003	30.08	$Ba_2Sr_2Co(CuO_4)_3$	mp-1099763	$Ba_2Sr_2CoCu_3O_{10}$	mp-1099812
$Sr_{0.5}Ba_{0.5}Co_{0.375}Cu_{0.625}O_{3-\delta}$	4	1.013	32.68	$Ba_4Sr_4Co_3Cu_5O_{24}$	mp-1076491	$Ba_4Sr_4Co_3(CuO_4)_5$	mp-1076896
$Ca_{0.5}Sr_{0.5}Fe_{0.25}Co_{0.75}O_{3-\delta}$	4	1.008	33.07	$Sr_2Ca_2Fe(CoO_4)_3$	mp-1099605	$Sr_2Ca_2FeCo_3O_{10}$	mp-1099665
$Sm_{0.5}La_{0.5}Co_{0.875}Ag_{0.125}O_{3-\delta}$	3	0.936	33.33	$La_4Sm_4Co_7AgO_{24}$	mp-1099698	$La_4Sm_4Co_7AgO_{20}$	mp-1076724
$Ca_{0.375}Sr_{0.625}Fe_{0.125}Co_{0.875}O_{3-\delta}$	4	1.016	34.36	$Sr_5Ca_3FeCo_7O_{24}$	mp-1076107	$Sr_5Ca_3FeCo_7O_{20}$	mp-1099816

Redox Material	*n*	*t*	ΔH (kJ/mol$_O$)	perovskite (oxidized phase)		brownmillerite (reduced phase)	
$Ca_{0.625}Sr_{0.375}Fe_{0.625}Co_{0.375}O_{3-\delta}$	4	0.993	35.90	$Sr_3Ca_5Fe_5(CoO_8)_3$	mp-1076802	$Sr_3Ca_5Fe_5Co_3O_{20}$	mp-1076614
$Ca_{0.25}Sr_{0.75}Co_{0.625}Cu_{0.375}O_{3-\delta}$	4	0.994	36.72	$Sr_6Ca_2Co_5(CuO_8)_3$	mp-1075901	$Sr_6Ca_2Co_5Cu_3O_{20}$	mp-1076678
$Sr_{0.75}Ba_{0.25}Co_{0.5}Cu_{0.5}O_{3-\delta}$	4	1.008	36.92	$BaSr_3Co_2(CuO_6)_2$	mp-1076528	$BaSr_3Co_2(CuO_5)_2$	mp-1100092
$Ca_{0.375}Sr_{0.625}Fe_{0.25}Co_{0.75}O_{3-\delta}$	4	1.013	37.34	$Sr_5Ca_3Fe_2(CoO_4)_6$	mp-1076260	$Sr_5Ca_3Fe_2(Co_3O_{10})_2$	mp-1099798
$Sr_{0.625}Ba_{0.375}Co_{0.375}Cu_{0.625}O_{3-\delta}$	4	1.006	37.84	$Ba_3Sr_5Co_3Cu_5O_{24}$	mp-1076600	$Ba_3Sr_5Co_3(CuO_4)_5$	mp-1076881
$Ca_{0.625}Sr_{0.375}Fe_{0.5}Co_{0.5}O_{3-\delta}$	4	0.996	39.01	$Sr_3Ca_5Fe_4(CoO_6)_4$	mp-1076602	$Sr_3Ca_5Fe_4(CoO_5)_4$	mp-1099708
$Sm_{0.25}La_{0.75}Co_{0.875}Ag_{0.125}O_{3-\delta}$	3	0.946	39.52	$La_6Sm_2Co_7AgO_{24}$	mp-1076287	$La_6Sm_2Co_7AgO_{20}$	mp-1076492
$Ca_{0.25}Sr_{0.75}Co_{0.75}Cu_{0.25}O_{3-\delta}$	4	1.004	40.17	$Sr_3CaCo_3CuO_{12}$	mp-1076688	$Sr_3CaCo_3CuO_{10}$	mp-1099678
$Sr_{0.75}Ba_{0.25}Co_{0.375}Cu_{0.625}O_{3-\delta}$	4	0.998	40.21	$Ba_2Sr_6Co_3Cu_5O_{24}$	mp-1076264	$Ba_2Sr_6Co_3(CuO_4)_5$	mp-1099742
$MgFeO_{3-\delta}$	4	0.871	40.85	$MgFeO_3$	mp-778717	$Mg_2Fe_2O_5$	mp-705864
$CaCoO_{3-\delta}$	4	0.996	41.41	$CaCoO_3$	mvc-3994	$Ca_2Co_2O_5$	mp-1099786
$Ca_{0.5}Sr_{0.5}Fe_{0.375}Co_{0.625}O_{3-\delta}$	4	1.004	41.82	$Sr_4Ca_4Fe_3Co_5O_{24}$	mp-1076674	$Sr_4Ca_4Fe_3(CoO_4)_5$	mp-1076502
$Ca_{0.5}Sr_{0.5}Fe_{0.75}Co_{0.25}O_{3-\delta}$	4	0.994	42.84	$Sr_2Ca_2Fe_3CoO_{12}$	mp-1075966	$Sr_2Ca_2Fe_3CoO_{10}$	mp-1076147
$Sr_{0.625}Ba_{0.375}Co_{0.5}Cu_{0.5}O_{3-\delta}$	4	1.016	47.17	$Ba_3Sr_5Co_4(CuO_6)_4$	mp-1075989	$Ba_3Sr_5Co_4(CuO_5)_4$	mp-1076683
$Sr_{0.75}Ba_{0.25}Co_{0.625}Cu_{0.375}O_{3-\delta}$	4	1.018	47.64	$Ba_2Sr_6Co_5(CuO_8)_3$	mp-1076429	$Ba_2Sr_6Co_5Cu_3O_{20}$	mp-1076893
$Sr_{0.875}Ba_{0.125}Co_{0.625}Cu_{0.375}O_{3-\delta}$	4	1.011	47.99	$BaSr_7Co_5(CuO_8)_3$	mp-1075982	$BaSr_7Co_5Cu_3O_{20}$	mp-1100068
$Sr_{0.875}Ba_{0.125}Co_{0.5}Cu_{0.5}O_{3-\delta}$	4	1.001	48.55	$BaSr_7Co_4(CuO_6)_4$	mp-1076054	$BaSr_7Co_4(CuO_5)_4$	mp-1099990
$EuCoO_{3-\delta}$	3	0.923	49.90	$EuCoO_3$	mp-1075975	$Eu_2Co_2O_5$	mp-1076123
$Sm_{0.375}La_{0.625}Ag_{0.125}Ni_{0.875}O_{3-\delta}$	3	0.945	52.78	$La_5Sm_3Ni_7AgO_{24}$	mp-1076249	$La_5Sm_3Ni_7AgO_{20}$	mp-1076656
$Ca_{0.25}Sr_{0.75}Fe_{0.375}Co_{0.625}O_{3-\delta}$	4	1.014	54.13	$Sr_6Ca_2Fe_3Co_5O_{24}$	mp-1076805	$Sr_6Ca_2Fe_3(CoO_4)_5$	mp-1076488
$CaFeO_{3-\delta}$	4	0.968	55.51	$CaFeO_3$	mvc-776	$Ca_2Fe_2O_5$	mp-25750
$Ca_{0.375}Sr_{0.625}Fe_{0.875}Co_{0.125}O_{3-\delta}$	4	0.995	56.98	$Sr_5Ca_3Fe_7CoO_{24}$	mp-1075955	$Sr_5Ca_3Fe_7CoO_{20}$	mp-1076516
$Mg_{0.125}Ca_{0.875}Mn_{0.875}Fe_{0.125}O_{3-\delta}$	4	0.980	57.56	$Ca_7MgMn_7FeO_{24}$	mp-1076214	$Ca_7MgMn_7FeO_{20}$	mp-1099831
$Mg_{0.125}Ca_{0.875}MnO_{3-\delta}$	4	0.983	61.05	$Ca_7MgMn_8O_{24}$	mp-1076485	$Ca_7MgMn_8O_{20}$	mp-1076897
$Ca_{0.25}Sr_{0.75}Fe_{0.625}Co_{0.375}O_{3-\delta}$	4	1.007	63.86	$Sr_6Ca_2Fe_5(CoO_8)_3$	mp-1076457	$Sr_6Ca_2Fe_5Co_3O_{20}$	mp-1076769
$Ca_{0.25}Sr_{0.75}Fe_{0.875}Co_{0.125}O_{3-\delta}$	4	1.000	64.86	$Sr_6Ca_2Fe_7CoO_{24}$	mp-1076399	$Sr_6Ca_2Fe_7CoO_{20}$	mp-1100030
$Ca_{0.125}Sr_{0.875}Fe_{0.5}Co_{0.5}O_{3-\delta}$	4	1.015	65.92	$Sr_7CaFe_4(CoO_6)_4$	mp-1076747	$Sr_7CaFe_4(CoO_5)_4$	mp-1076159
$Ca_{0.25}Sr_{0.75}FeO_{3-\delta}$	4	0.997	68.03	$Sr_3Ca(FeO_3)_4$	mp-1094055	$Sr_3Ca(Fe_2O_5)_2$	mp-1076761
$Ca_{0.125}Sr_{0.875}Fe_{0.625}Co_{0.375}O_{3-\delta}$	4	1.012	68.95	$Sr_7CaFe_5(CoO_8)_3$	mp-1076062	$Sr_7CaFe_5Co_3O_{20}$	mp-1100087
$Ca_{0.125}Sr_{0.875}Fe_{0.875}Co_{0.125}O_{3-\delta}$	4	1.005	71.48	$Sr_7CaFe_7CoO_{24}$	mp-1076858	$Sr_7CaFe_7CoO_{20}$	mp-1099946
$Ca_{0.125}Sr_{0.875}Fe_{0.75}Co_{0.25}O_{3-\delta}$	4	1.008	72.40	$Sr_7CaFe_6(CoO_{12})_2$	mp-1076372	$Sr_7CaFe_6(CoO_{10})_2$	mp-1076631
$EuNiO_{3-\delta}$	3	0.928	73.85	$EuNiO_3$	mp-32341	$Eu_2Ni_2O_5$	mp-1076223
$Sm_{0.5}La_{0.5}NiO_{3-\delta}$	3	0.949	76.16	$LaSm(NiO_3)_2$	mp-1076325	$LaSmNi_2O_5$	mp-1076810
$Ca_{0.375}Sr_{0.625}Mn_{0.125}Fe_{0.875}O_{3-\delta}$	4	0.995	76.32	$Sr_5Ca_3MnFe_7O_{24}$	mp-1076079	$Sr_5Ca_3MnFe_7O_{20}$	mp-1076199
$SrFe_{0.875}Co_{0.125}O_{3-\delta}$	4	1.009	76.87	$Sr_8Fe_7CoO_{24}$	mp-1077660	$Sr_8Fe_7CoO_{20}$	mp-1076165
$Sr_{0.875}Ba_{0.125}Fe_{0.875}Co_{0.125}O_{3-\delta}$	4	1.017	78.02	$BaSr_7Fe_7CoO_{24}$	mp-1075935	$BaSr_7Fe_7CoO_{20}$	mp-1076892
$Mg_{0.125}Ca_{0.875}Ti_{0.125}Mn_{0.875}O_{3-\delta}$	4	0.979	79.23	$Ca_7MgTiMn_7O_{24}$	mp-1076543	$Ca_7MgTiMn_7O_{20}$	mp-1077701
$Sr_{0.875}Ba_{0.125}Fe_{0.75}Co_{0.25}O_{3-\delta}$	4	1.021	81.84	$BaSr_7Fe_6(CoO_{12})_2$	mp-1099936	$BaSr_7Fe_6(CoO_{10})_2$	mp-1099862
$Ca_{0.5}Sr_{0.5}Mn_{0.25}Fe_{0.75}O_{3-\delta}$	4	0.994	83.80	$Sr_2Ca_2Mn(FeO_4)_3$	mp-1076410	$Sr_2Ca_2MnFe_3O_{10}$	mp-1076444
$Ca_{0.25}Sr_{0.75}Mn_{0.125}Fe_{0.875}O_{3-\delta}$	4	1.000	85.26	$Sr_6Ca_2MnFe_7O_{24}$	mp-1075969	$Sr_6Ca_2MnFe_7O_{20}$	mp-1099974
$SrFeO_{3-\delta}$	4	1.006	87.77	$SrFeO_3$	mp-1076585	$Sr_2Fe_2O_5$	mp-561589
$Sr_{0.875}Ba_{0.125}FeO_{3-\delta}$	4	1.013	88.00	$BaSr_7(FeO_3)_8$	mp-1099685	$BaSr_7(Fe_2O_5)_4$	mp-1076090
$BaFeO_{3-\delta}$	4	1.066	94.77	$BaFeO_3$	mp-19035	$Ba_2Fe_2O_5$	mp-654312
$Sm_{0.5}La_{0.5}CoO_{3-\delta}$	3	0.944	94.88	$LaSm(CoO_3)_2$	mp-1075930	$LaSmCo_2O_5$	mp-1076759
$Ca_{0.125}Sr_{0.875}Mn_{0.125}Fe_{0.875}O_{3-\delta}$	4	1.005	95.92	$Sr_7CaMnFe_7O_{24}$	mp-1099701	$Sr_7CaMnFe_7O_{20}$	mp-1076487
$Ca_{0.625}Sr_{0.375}Mn_{0.375}Fe_{0.625}O_{3-\delta}$	4	0.993	96.08	$Sr_3Ca_5Mn_3Fe_5O_{24}$	mp-1076854	$Sr_3Ca_5Mn_3(FeO_4)_5$	mp-1076482
$Sm_{0.5}La_{0.5}Cu_{0.125}Co_{0.875}O_{3-\delta}$	3	0.938	98.69	$La_4Sm_4Co_7CuO_{24}$	mp-1076219	$La_4Sm_4Co_7CuO_{20}$	mp-1076483
$LaAgO_{3-\delta}$	3	0.902	99.65	$LaAgO_3$	mp-768308	$La_2Ag_2O_5$	mp-1076119
$Sr_{0.875}Ba_{0.125}Mn_{0.125}Fe_{0.875}O_{3-\delta}$	4	1.017	99.89	$BaSr_7MnFe_7O_{24}$	mp-1076592	$BaSr_7MnFe_7O_{20}$	mp-1076473
$Ca_{0.875}Sr_{0.125}Mn_{0.75}Fe_{0.25}O_{3-\delta}$	4	0.994	101.07	$SrCa_7Mn_6(FeO_{12})_2$	mp-1077667	$SrCa_7Mn_6(FeO_{10})_2$	mp-1077691
$Ca_{0.875}Sr_{0.125}Mn_{0.875}Fe_{0.125}O_{3-\delta}$	4	0.997	102.62	$SrCa_7Mn_7FeO_{24}$	mp-1099696	$SrCa_7Mn_7FeO_{20}$	mp-1076449
$Na_{0.875}K_{0.125}V_{0.75}Cr_{0.25}O_{3-\delta}$	5	1.025	102.72	$KNa_7V_6Cr_2O_{24}$	mp-1099932	$KNa_7V_6Cr_2O_{20}$	mp-1099912
$EuCuO_{3-\delta}$	3	0.879	105.30	$EuCuO_3$	mp-1075902	$Eu_2Cu_2O_5$	mp-1099765
$Ca_{0.75}Sr_{0.25}Mn_{0.625}Fe_{0.375}O_{3-\delta}$	4	0.995	105.69	$Sr_2Ca_6Mn_5(FeO_8)_3$	mp-1076268	$Sr_2Ca_6Mn_5Fe_3O_{20}$	mp-1076862
$SrMn_{0.125}Fe_{0.875}O_{3-\delta}$	4	1.009	105.84	$Sr_8MnFe_7O_{24}$	mp-1076445	$Sr_8MnFe_7O_{20}$	mp-1076409
$Sm_{0.375}La_{0.625}Cu_{0.125}Co_{0.875}O_{3-\delta}$	3	0.943	106.73	$La_5Sm_3Co_7CuO_{24}$	mp-1076171	$La_5Sm_3Co_7CuO_{20}$	mp-1076874
$MgCoO_{3-\delta}$	4	0.895	110.14	$MgCoO_3$	mp-761524	$Mg_2Co_2O_5$	mp-1076088

Redox Material	*n*	*t*	ΔH (kJ/mol$_O$)	perovskite (oxidized phase)		brownmillerite (reduced phase)	
$Ca_{0.125}Sr_{0.875}Mn_{0.25}Fe_{0.75}O_{3-\delta}$	4	1.008	110.29	$Sr_7CaMn_2(FeO_4)_6$	mp-1076597	$Sr_7CaMn_2(Fe_3O_{10})_2$	mp-1076092
$Ca_{0.75}Sr_{0.25}Mn_{0.875}Fe_{0.125}O_{3-\delta}$	4	1.002	110.63	$Sr_2Ca_6Mn_7FeO_{24}$	mp-1099788	$Sr_2Ca_6Mn_7FeO_{20}$	mp-1099810
$Ca_{0.625}Sr_{0.375}Mn_{0.5}Fe_{0.5}O_{3-\delta}$	4	0.996	114.92	$Sr_3Ca_5Mn_4(FeO_6)_4$	mp-1075968	$Sr_3Ca_5Mn_4(FeO_5)_4$	mp-1076450
$Ca_{0.25}Sr_{0.75}Mn_{0.375}Fe_{0.625}O_{3-\delta}$	4	1.007	116.98	$Sr_6Ca_2Mn_3Fe_5O_{24}$	mp-1077670	$Sr_6Ca_2Mn_3(FeO_4)_5$	mp-1076177
$Ca_{0.5}Sr_{0.5}Mn_{0.625}Fe_{0.375}O_{3-\delta}$	4	1.004	117.88	$Sr_4Ca_4Mn_5(FeO_8)_3$	mp-1076058	$Sr_4Ca_4Mn_5Fe_3O_{20}$	mp-1076190
$Ca_{0.5}Sr_{0.5}Mn_{0.75}Fe_{0.25}O_{3-\delta}$	4	1.008	119.85	$Sr_2Ca_2Mn_3FeO_{12}$	mp-1099674	$Sr_2Ca_2Mn_3FeO_{10}$	mp-1076197
$Sm_{0.125}La_{0.875}Cu_{0.25}Co_{0.75}O_{3-\delta}$	3	0.948	119.91	$La_7SmCo_6(CuO_{12})_2$	mp-1077605	$La_7SmCo_6(CuO_{10})_2$	mp-1076871
$Sr_{0.875}Ba_{0.125}Mn_{0.25}Fe_{0.75}O_{3-\delta}$	4	1.021	120.66	$BaSr_7Mn_2(FeO_4)_6$	mp-1076408	$BaSr_7Mn_2(Fe_3O_{10})_2$	mp-1076181
$Ca_{0.5}Sr_{0.5}MnO_{3-\delta}$	4	1.015	121.61	$SrCaMn_2O_6$	mp-1076213	$SrCaMn_2O_5$	mp-1076496
$Na_{0.875}K_{0.125}V_{0.875}Cr_{0.125}O_{3-\delta}$	5	1.022	121.67	$KNa_7V_7CrO_{24}$	mp-1076665	$KNa_7V_7CrO_{20}$	mp-1076821
$Ca_{0.5}Sr_{0.5}Mn_{0.875}Fe_{0.125}O_{3-\delta}$	4	1.012	123.20	$Sr_4Ca_4Mn_7FeO_{24}$	mp-1076359	$Sr_4Ca_4Mn_7FeO_{20}$	mp-1076163
$Sm_{0.125}La_{0.875}Cu_{0.375}Co_{0.625}O_{3-\delta}$	3	0.942	123.90	$La_7SmCo_5(CuO_8)_3$	mp-1075961	$La_7SmCo_5Cu_3O_{20}$	mp-1076880
$Ca_{0.375}Sr_{0.625}Mn_{0.75}Fe_{0.25}O_{3-\delta}$	4	1.013	125.87	$Sr_5Ca_3Mn_6(FeO_{12})_2$	mp-1099603	$Sr_5Ca_3Mn_6(FeO_{10})_2$	mp-1076601
$Ca_{0.125}Sr_{0.875}Mn_{0.375}Fe_{0.625}O_{3-\delta}$	4	1.012	126.36	$Sr_7CaMn_3Fe_5O_{24}$	mp-1076651	$Sr_7CaMn_3(FeO_4)_5$	mp-1099661
$Ca_{0.375}Sr_{0.625}Mn_{0.5}Fe_{0.5}O_{3-\delta}$	4	1.006	126.88	$Sr_5Ca_3Mn_4(FeO_6)_4$	mp-1076796	$Sr_5Ca_3Mn_4(FeO_5)_4$	mp-1076141
$Ca_{0.875}Sr_{0.125}Ti_{0.125}Mn_{0.875}O_{3-\delta}$	4	0.996	127.33	$SrCa_7TiMn_7O_{24}$	mp-1077663	$SrCa_7TiMn_7O_{20}$	mp-1077688
$Ca_{0.375}Sr_{0.625}Mn_{0.875}Fe_{0.125}O_{3-\delta}$	4	1.016	130.00	$Sr_5Ca_3Mn_7FeO_{24}$	mp-1076080	$Sr_5Ca_3Mn_7FeO_{20}$	mp-1099672
$Ca_{0.25}Sr_{0.75}Mn_{0.625}Fe_{0.375}O_{3-\delta}$	4	1.014	130.54	$Sr_6Ca_2Mn_5(FeO_8)_3$	mp-1077671	$Sr_6Ca_2Mn_5Fe_3O_{20}$	mp-1076182
$Ca_{0.75}Sr_{0.25}Ti_{0.125}Mn_{0.875}O_{3-\delta}$	4	1.001	135.03	$Sr_2Ca_6TiMn_7O_{24}$	mp-1099702	$Sr_2Ca_6TiMn_7O_{20}$	mp-1076877
$Ca_{0.125}Sr_{0.875}Mn_{0.5}Fe_{0.5}O_{3-\delta}$	4	1.015	140.53	$Sr_7CaMn_4(FeO_6)_4$	mp-1099713	$Sr_7CaMn_4(FeO_5)_4$	mp-1099692
$LaNiO_{3-\delta}$	3	0.969	141.84	$LaNiO_3$	mp-19339	$La_2Ni_2O_5$	mp-1076121
$Na_{0.875}K_{0.125}VO_{3-\delta}$	5	1.018	142.67	$KNa_7V_8O_{24}$	mp-1099664	$KNa_7V_8O_{20}$	mp-1076630
$Ca_{0.625}Sr_{0.375}Ti_{0.125}Mn_{0.875}O_{3-\delta}$	4	1.005	143.35	$Sr_3Ca_5TiMn_7O_{24}$	mp-1076217	$Sr_3Ca_5TiMn_7O_{20}$	mp-1077695
$SmCuO_{3-\delta}$	3	0.880	147.50	$SmCuO_3$	mp-770767	$Sm_2Cu_2O_5$	mp-768866
$LaCuO_{3-\delta}$	3	0.919	149.59	$LaCuO_3$	mp-3474	$La_2Cu_2O_5$	mp-5696
$Ca_{0.5}Sr_{0.5}Ti_{0.125}Mn_{0.875}O_{3-\delta}$	4	1.010	149.66	$Sr_4Ca_4TiMn_7O_{24}$	mp-1076561	$Sr_4Ca_4TiMn_7O_{20}$	mp-1099799
$Ca_{0.75}Sr_{0.25}Ti_{0.25}Mn_{0.75}O_{3-\delta}$	4	0.996	152.20	$SrCa_3TiMn_3O_{12}$	mp-1076074	$SrCa_3TiMn_3O_{10}$	mp-1076776
$Ca_{0.375}Sr_{0.625}Ti_{0.125}Mn_{0.875}O_{3-\delta}$	4	1.015	155.01	$Sr_5Ca_3TiMn_7O_{24}$	mp-1075976	$Sr_5Ca_3TiMn_7O_{20}$	mp-1076192
$SmNiO_{3-\delta}$	3	0.928	162.20	$SmNiO_3$	mp-25588	$Sm_2Ni_2O_5$	mp-1099625
$Ca_{0.5}Sr_{0.5}Ti_{0.25}Mn_{0.75}O_{3-\delta}$	4	1.005	166.56	$Sr_2Ca_2TiMn_3O_{12}$	mp-1077669	$Sr_2Ca_2TiMn_3O_{10}$	mp-1076680
$Ca_{0.75}Sr_{0.25}MnO_{3-\delta}$	4	1.006	167.65	$SrCa_3Mn_4O_{12}$	mp-1094044	$SrCa_3Mn_4O_{10}$	mp-1076184
$Na_{0.875}K_{0.125}Mo_{0.125}V_{0.875}O_{3-\delta}$	5	1.014	170.32	$KNa_7V_7MoO_{24}$	mp-1076222	$KNa_7V_7MoO_{20}$	mp-1099669
$SrMnO_{3-\delta}$	4	1.035	170.33	$SrMnO_3$	mp-568977	$Sr_2Mn_2O_5$	mp-18798
$BaCoO_{3-\delta}$	4	1.096	172.09	$BaCoO_3$	mp-554938	$Ba_2Co_2O_5$	mp-1076439
$CaMnO_{3-\delta}$	4	0.996	173.13	$CaMnO_3$	mp-19201	$Ca_2Mn_2O_5$	mp-25008
$Ca_{0.625}Sr_{0.375}Ti_{0.375}Mn_{0.625}O_{3-\delta}$	4	0.996	173.40	$Sr_3Ca_5Ti_3Mn_5O_{24}$	mp-1076628	$Sr_3Ca_5Ti_3Mn_5O_{20}$	mp-1076134
$Na_{0.875}K_{0.125}Mo_{0.25}V_{0.75}O_{3-\delta}$	5	1.009	180.38	$KNa_7V_6(MoO_{12})_2$	mp-1076351	$KNa_7V_6(MoO_{10})_2$	mp-1099956
$Ca_{0.25}Sr_{0.75}Ti_{0.25}Mn_{0.75}O_{3-\delta}$	4	1.015	182.71	$Sr_3CaTiMn_3O_{12}$	mp-1099855	$Sr_3CaTiMn_3O_{10}$	mp-1076505
$Ca_{0.375}Sr_{0.625}Ti_{0.375}Mn_{0.625}O_{3-\delta}$	4	1.005	188.81	$Sr_5Ca_3Ti_3Mn_5O_{24}$	mp-1075962	$Sr_5Ca_3Ti_3Mn_5O_{20}$	mp-1099762
$Ca_{0.5}Sr_{0.5}Ti_{0.5}Mn_{0.5}O_{3-\delta}$	4	0.996	195.49	$SrCaTiMnO_6$	mp-1076384	$SrCaTiMnO_5$	mp-1099877
$Na_{0.75}K_{0.25}Mo_{0.375}V_{0.625}O_{3-\delta}$	5	1.017	202.11	$K_2Na_6V_5(MoO_8)_3$	mp-1099629	$K_2Na_6V_5Mo_3O_{20}$	mp-1076545
$LaCoO_{3-\delta}$	3	0.965	202.55	$LaCoO_3$	mp-19051	$La_2Co_2O_5$	mp-1076438
$Ca_{0.125}Sr_{0.875}Ti_{0.375}Mn_{0.625}O_{3-\delta}$	4	1.015	206.19	$Sr_7CaTi_3Mn_5O_{24}$	mp-1076827	$Sr_7CaTi_3Mn_5O_{20}$	mp-1076183
$Sm_{0.125}La_{0.875}Fe_{0.375}Mn_{0.625}O_{3-\delta}$	3	0.943	215.02	$La_7SmMn_5(FeO_8)_3$	mp-1099887	$La_7SmMn_5Fe_3O_{20}$	mp-1099861
$Ca_{0.25}Sr_{0.75}Ti_{0.5}Mn_{0.5}O_{3-\delta}$	4	1.005	215.45	$Sr_3CaTi_2Mn_2O_{12}$	mp-1076138	$Sr_3CaTi_2Mn_2O_{10}$	mp-1076875
$Sm_{0.125}La_{0.875}Fe_{0.75}Mn_{0.25}O_{3-\delta}$	3	0.943	230.08	$La_7SmMn_2(FeO_4)_6$	mp-1076598	$La_7SmMn_2(Fe_3O_{10})_2$	mp-1076418
$Na_{0.75}K_{0.25}Mo_{0.5}V_{0.5}O_{3-\delta}$	5	1.012	231.24	$KNa_3V_2(MoO_6)_2$	mp-1099867	$KNa_3V_2(MoO_5)_2$	mp-1099868
$SmCoO_{3-\delta}$	3	0.924	232.71	$SmCoO_3$	mp-24877	$Sm_2Co_2O_5$	mp-1076063
$SrTi_{0.5}Mn_{0.5}O_{3-\delta}$	4	1.015	235.38	Sr_2TiMnO_6	mp-1099881	Sr_2TiMnO_5	mp-1076627
$Sm_{0.125}La_{0.875}Mn_{0.875}Cu_{0.125}O_{3-\delta}$	3	0.939	241.55	$La_7SmMn_7CuO_{24}$	mp-1099832	$La_7SmMn_7CuO_{20}$	mp-1076513
$Sm_{0.125}La_{0.875}Fe_{0.625}Mn_{0.375}O_{3-\delta}$	3	0.943	243.35	$La_7SmMn_3Fe_5O_{24}$	mp-1075984	$La_7SmMn_3(FeO_4)_5$	mp-1076455
$EuFeO_{3-\delta}$	3	0.907	244.26	$EuFeO_3$	mp-540832	$Eu_2Fe_2O_5$	mp-1077617
$Sm_{0.125}La_{0.875}Fe_{0.875}Mn_{0.125}O_{3-\delta}$	3	0.943	245.84	$La_7SmMnFe_7O_{24}$	mp-1076610	$La_7SmMnFe_7O_{20}$	mp-1099902
$MgMnO_{3-\delta}$	4	0.895	250.13	$MgMnO_3$	mp-770618	$Mg_2Mn_2O_5$	mp-1099805
$Sm_{0.125}La_{0.875}Fe_{0.5}Mn_{0.5}O_{3-\delta}$	3	0.943	251.41	$La_7SmMn_4(FeO_6)_4$	mp-1076671	$La_7SmMn_4(FeO_5)_4$	mp-1076172
$BaMnO_{3-\delta}$	4	1.096	252.31	$BaMnO_3$	mp-19267	$Ba_2Mn_2O_5$	mp-1099904
$Sm_{0.125}La_{0.875}Fe_{0.25}Mn_{0.75}O_{3-\delta}$	3	0.943	256.80	$La_7SmMn_6(FeO_{12})_2$	mp-1076669	$La_7SmMn_6(FeO_{10})_2$	mp-1076797

Redox Material	*n*	*t*	ΔH (kJ/mol$_O$)	perovskite (oxidized phase)		brownmillerite (reduced phase)	
$Sm_{0.125}La_{0.875}Fe_1O_{3-\delta}$	3	0.943	258.54	$La_7Sm(FeO_3)_8$	mp-1076382	$La_7Sm(Fe_2O_5)_4$	mp-1076176
$EuMnO_{3-\delta}$	3	0.907	259.20	$EuMnO_3$	mp-25667	$Eu_2Mn_2O_5$	mp-1099747
$Sm_{0.125}La_{0.875}Fe_{0.125}Mn_{0.875}O_{3-\delta}$	3	0.943	260.34	$La_7SmMn_7FeO_{24}$	mp-1076792	$La_7SmMn_7FeO_{20}$	mp-1099704
$Sm_{0.125}La_{0.875}MnO_{3-\delta}$	3	0.943	265.38	$La_7SmMn_8O_{24}$	mp-1099923	$La_7SmMn_8O_{20}$	mp-1099865
$Na_{0.625}K_{0.375}Mo_{0.625}V_{0.375}O_{3-\delta}$	5	1.020	272.31	$K_3Na_5V_3Mo_5O_{24}$	mp-1099606	$K_3Na_5V_3(MoO_4)_5$	mp-1076888
$Ca_{0.375}Sr_{0.625}Ti_{0.625}Mn_{0.375}O_{3-\delta}$	4	0.996	285.80	$Sr_5Ca_3Ti_5Mn_3O_{24}$	mp-1077659	$Sr_5Ca_3Ti_5Mn_3O_{20}$	mp-1076557
$NaVO_{3-\delta}$	5	1.006	287.56	$NaVO_3$	mp-19083	$Na_2V_2O_5$	mp-1076048
$EuCrO_{3-\delta}$	3	0.921	289.00	$EuCrO_3$	mp-771930	$Eu_2Cr_2O_5$	mp-1076286
$Sm_{0.125}La_{0.875}Cr_{0.125}Fe_{0.875}O_{3-\delta}$	3	0.945	289.65	$La_7SmCrFe_7O_{24}$	mp-1099808	$La_7SmCrFe_7O_{20}$	mp-1076459
$Na_{0.625}K_{0.375}Mo_{0.75}V_{0.25}O_{3-\delta}$	5	1.015	304.18	$K_3Na_5V_2(MoO_4)_6$	mp-1076484	$K_3Na_5V_2(Mo_3O_{10})_2$	mp-1076637
$Ca_{0.125}Sr_{0.875}Ti_{0.625}Mn_{0.375}O_{3-\delta}$	4	1.005	304.86	$Sr_7CaTi_5Mn_3O_{24}$	mp-1075948	$Sr_7CaTi_5Mn_3O_{20}$	mp-1076202
$Sr_{0.875}Ba_{0.125}Ti_{0.625}Mn_{0.375}O_{3-\delta}$	4	1.018	311.78	$BaSr_7Ti_5Mn_3O_{24}$	mp-1099624	$BaSr_7Ti_5Mn_3O_{20}$	mp-1100246
$NaMoO_{3-\delta}$	5	0.971	319.41	$NaMoO_3$	mp-1076843	$Na_2Mo_2O_5$	mp-1099875
$Sm_{0.125}La_{0.875}Cr_{0.25}Fe_{0.75}O_{3-\delta}$	3	0.947	319.75	$La_7SmCr_2(FeO_4)_6$	mp-1076431	$La_7SmCr_2(Fe_3O_{10})_2$	mp-1076204
$Sm_{0.25}La_{0.75}Cr_{0.375}Fe_{0.625}O_{3-\delta}$	3	0.943	325.74	$La_6Sm_2Cr_3Fe_5O_{24}$	mp-1076529	$La_6Sm_2Cr_3(FeO_4)_5$	mp-1099892
$Na_{0.625}K_{0.375}Mo_{0.875}V_{0.125}O_{3-\delta}$	5	1.011	342.40	$K_3Na_5VMo_7O_{24}$	mp-1099938	$K_3Na_5VMo_7O_{20}$	mp-1076540
$LaMnO_{3-\delta}$	3	0.948	353.27	$LaMnO_3$	mp-629046	$La_2Mn_2O_5$	mp-1099627
$Sm_{0.25}La_{0.75}Cr_{0.5}Fe_{0.5}O_{3-\delta}$	3	0.945	353.33	$La_3SmCr_2(FeO_6)_2$	mp-1076611	$La_3SmCr_2(FeO_5)_2$	mp-1076194
$Na_{0.5}K_{0.5}MoO_{3-\delta}$	5	1.018	362.81	$KNa(MoO_3)_2$	mp-1076831	$KNaMo_2O_5$	mp-1076606
$KVO_{3-\delta}$	5	1.104	374.19	KVO_3	mp-18815	$K_2V_2O_5$	mp-1099837
$LaFeO_{3-\delta}$	3	0.948	377.56	$LaFeO_3$	mp-542920	$La_2Fe_2O_5$	mp-1099626
$EuVO_{3-\delta}$	3	0.910	381.81	$EuVO_3$	mp-769926	$Eu_2V_2O_5$	mp-1099750
$SmVO_{3-\delta}$	3	0.910	382.21	$SmVO_3$	mp-1099803	$Sm_2V_2O_5$	mp-1076055
$SmMnO_{3-\delta}$	3	0.908	388.21	$SmMnO_3$	mp-25026	$Sm_2Mn_2O_5$	mp-1076289
$Sm_{0.25}La_{0.75}Cr_{0.625}Fe_{0.375}O_{3-\delta}$	3	0.947	390.31	$La_6Sm_2Cr_5(FeO_8)_3$	mp-1099896	$La_6Sm_2Cr_5Fe_3O_{20}$	mp-1099978
$Ca_{0.25}Sr_{0.75}Ti_{0.75}Mn_{0.25}O_{3-\delta}$	4	0.996	396.73	$Sr_3CaTi_3MnO_{12}$	mp-1099703	$Sr_3CaTi_3MnO_{10}$	mp-1076170
$RbMoO_{3-\delta}$	5	1.093	398.52	$RbMoO_3$	mp-975304	$Rb_2Mo_2O_5$	mp-1099822
$SmFeO_{3-\delta}$	3	0.908	401.32	$SmFeO_3$	mp-24989	$Sm_2Fe_2O_5$	mp-1076463
$KMoO_{3-\delta}$	5	1.066	405.11	$KMoO_3$	mp-1076474	$K_2Mo_2O_5$	mp-1075956
$Sr_{0.875}Ba_{0.125}Ti_{0.75}Mn_{0.25}O_{3-\delta}$	4	1.013	407.83	$BaSr_7Ti_6Mn_2O_{24}$	mp-1075988	$BaSr_7Ti_6Mn_2O_{20}$	mp-1076196
$Sm_{0.375}La_{0.625}Cr_{0.75}Fe_{0.25}O_{3-\delta}$	3	0.943	408.22	$La_5Sm_3Cr_6(FeO_{12})_2$	mp-1076580	$La_5Sm_3Cr_6(FeO_{10})_2$	mp-1076203
$SmCrO_{3-\delta}$	3	0.922	415.04	$SmCrO_3$	mp-19257	$Sm_2Cr_2O_5$	mp-1099951
$RbVO_{3-\delta}$	5	1.133	422.16	$RbVO_3$	mp-19031	$Rb_2V_2O_5$	mp-1076354
$Na_{0.5}K_{0.5}W_{0.125}Mo_{0.875}O_{3-\delta}$	5	1.018	423.65	$K_4Na_4Mo_7WO_{24}$	mp-1076546	$K_4Na_4Mo_7WO_{20}$	mp-1076754
$Sm_{0.375}La_{0.625}Cr_{0.875}Fe_{0.125}O_{3-\delta}$	3	0.945	433.61	$La_5Sm_3Cr_7FeO_{24}$	mp-1075954	$La_5Sm_3Cr_7FeO_{20}$	mp-1100047
$NaWO_{3-\delta}$	5	0.966	434.58	$NaWO_3$	mp-1099918	$Na_2W_2O_5$	mp-1097724
$Sm_{0.125}La_{0.875}VO_{3-\delta}$	3	0.945	447.65	$La_7SmV_8O_{24}$	mp-1076131	$La_7SmV_8O_{20}$	mp-1076878
$Na_{0.5}K_{0.5}W_{0.25}Mo_{0.75}O_{3-\delta}$	5	1.017	451.70	$K_2Na_2Mo_3WO_{12}$	mp-1076836	$K_2Na_2Mo_3WO_{10}$	mp-1076891
$Sm_{0.375}La_{0.625}CrO_{3-\delta}$	3	0.947	455.88	$La_5Sm_3Cr_8O_{24}$	mp-1076603	$La_5Sm_3Cr_8O_{20}$	mp-1100028
$Sm_{0.375}La_{0.625}V_{0.25}Cr_{0.75}O_{3-\delta}$	3	0.944	468.90	$La_5Sm_3V_2Cr_6O_{24}$	mp-1099675	$La_5Sm_3V_2Cr_6O_{20}$	mp-1076879
$Sm_{0.375}La_{0.625}V_{0.125}Cr_{0.875}O_{3-\delta}$	3	0.945	469.00	$La_5Sm_3VCr_7O_{24}$	mp-1099724	$La_5Sm_3VCr_7O_{20}$	mp-1076766
$Na_{0.5}K_{0.5}W_{0.375}Mo_{0.625}O_{3-\delta}$	5	1.017	486.14	$K_4Na_4Mo_5(WO_8)_3$	mp-1099727	$K_4Na_4Mo_5W_3O_{20}$	mp-1076890
$Na_{0.5}K_{0.5}WO_{3-\delta}$	5	1.013	488.95	$KNa(WO_3)_2$	mp-1076224	$KNaW_2O_5$	mp-1099945
$Sm_{0.25}La_{0.75}V_{0.5}Cr_{0.5}O_{3-\delta}$	3	0.946	489.89	$La_3SmV_2Cr_2O_{12}$	mp-1076218	$La_3SmV_2Cr_2O_{10}$	mp-1099885
$Sm_{0.25}La_{0.75}V_{0.625}Cr_{0.375}O_{3-\delta}$	3	0.945	490.79	$La_6Sm_2V_5Cr_3O_{24}$	mp-1076253	$La_6Sm_2V_5Cr_3O_{20}$	mp-1099931
$Sm_{0.25}La_{0.75}V_{0.375}Cr_{0.625}O_{3-\delta}$	3	0.948	492.03	$La_6Sm_2V_3Cr_5O_{24}$	mp-1076584	$La_6Sm_2V_3Cr_5O_{20}$	mp-1076179
$Na_{0.375}K_{0.625}Nb_{0.5}W_{0.5}O_{3-\delta}$	5	1.020	494.87	$K_5Na_3Nb_4(WO_6)_4$	mp-1099943	$K_5Na_3Nb_4(WO_5)_4$	mp-1076208
$Sr_{0.625}Ba_{0.375}Ti_{0.875}Mn_{0.125}O_{3-\delta}$	4	1.023	495.35	$Ba_3Sr_5Ti_7MnO_{24}$	mp-1075974	$Ba_3Sr_5Ti_7MnO_{20}$	mp-1076186
$Na_{0.5}K_{0.5}Nb_{0.375}W_{0.625}O_{3-\delta}$	5	1.010	497.38	$K_4Na_4Nb_3W_5O_{24}$	mp-1099687	$K_4Na_4Nb_3(WO_4)_5$	mp-1076755
$Ca_{0.125}Sr_{0.875}Ti_{0.875}Mn_{0.125}O_{3-\delta}$	4	0.996	497.69	$Sr_7CaTi_7MnO_{24}$	mp-1076570	$Sr_7CaTi_7MnO_{20}$	mp-1099889
$Sr_{0.875}Ba_{0.125}Ti_{0.875}Mn_{0.125}O_{3-\delta}$	4	1.008	497.73	$BaSr_7Ti_7MnO_{24}$	mp-1076377	$BaSr_7Ti_7MnO_{20}$	mp-1076193
$Na_{0.5}K_{0.5}Nb_{0.25}W_{0.75}O_{3-\delta}$	5	1.011	500.92	$K_2Na_2Nb(WO_4)_3$	mp-1076812	$K_2Na_2NbW_3O_{10}$	mp-1076206
$Na_{0.375}K_{0.625}Nb_{0.625}W_{0.375}O_{3-\delta}$	5	1.019	504.46	$K_5Na_3Nb_5(WO_8)_3$	mp-1076481	$K_5Na_3Nb_5W_3O_{20}$	mp-1076886
$KWO_{3-\delta}$	5	1.061	508.05	KWO_3	mp-1099818	$K_2W_2O_5$	mp-1097834
$Sm_{0.25}La_{0.75}V_{0.75}Cr_{0.25}O_{3-\delta}$	3	0.943	509.16	$La_3SmV_3CrO_{12}$	mp-1076348	$La_3SmV_3CrO_{10}$	mp-1076191
$Sm_{0.125}La_{0.875}V_{0.875}Cr_{0.125}O_{3-\delta}$	3	0.947	509.22	$La_7SmV_7CrO_{24}$	mp-1076679	$La_7SmV_7CrO_{20}$	mp-1076889
$Sm_{0.125}La_{0.875}Ti_{0.25}V_{0.75}O_{3-\delta}$	3	0.942	509.53	$La_7SmTi_2V_6O_{24}$	mp-1099746	$La_7SmTi_2V_6O_{20}$	mp-1076595

Redox Material	*n*	*t*	ΔH (kJ/mol$_O$)	perovskite (oxidized phase)		brownmillerite (reduced phase)	
$Na_{0.375}K_{0.625}Nb_{0.75}W_{0.25}O_{3-\delta}$	5	1.018	510.96	$K_5Na_3Nb_6(WO_{12})_2$	mp-1076412	$K_5Na_3Nb_6(WO_{10})_2$	mp-1099913
$Sm_{0.125}La_{0.875}Ti_{0.125}V_{0.875}O_{3-\delta}$	3	0.944	511.97	$La_7SmTiV_7O_{24}$	mp-1075987	$La_7SmTiV_7O_{20}$	mp-1076664
$Sm_{0.125}La_{0.875}Ti_{0.375}V_{0.625}O_{3-\delta}$	3	0.940	514.30	$La_7SmTi_3V_5O_{24}$	mp-1076581	$La_7SmTi_3V_5O_{20}$	mp-1076885
$RbWO_{3-\delta}$	5	1.088	517.61	$RbWO_3$	mp-975156	$Rb_2W_2O_5$	mp-1075937
$Na_{0.5}K_{0.5}W_{0.5}Mo_{0.5}O_{3-\delta}$	5	1.016	519.41	$KNaMoWO_6$	mp-1076659	$KNaMoWO_5$	mp-1076195
$Na_{0.5}K_{0.5}W_{0.625}Mo_{0.375}O_{3-\delta}$	5	1.015	522.02	$K_4Na_4Mo_3W_5O_{24}$	mp-1099601	$K_4Na_4Mo_3(WO_4)_5$	mp-1076205
$Na_{0.5}K_{0.5}W_{0.75}Mo_{0.25}O_{3-\delta}$	5	1.015	522.72	$K_2Na_2Mo(WO_4)_3$	mp-1099821	$K_2Na_2MoW_3O_{10}$	mp-1099722
$Na_{0.375}K_{0.625}Nb_{0.875}W_{0.125}O_{3-\delta}$	5	1.016	523.02	$K_5Na_3Nb_7WO_{24}$	mp-1099622	$K_5Na_3Nb_7WO_{20}$	mp-1076894
$Na_{0.5}K_{0.5}Nb_{0.125}W_{0.875}O_{3-\delta}$	5	1.012	524.84	$K_4Na_4NbW_7O_{24}$	mp-1076751	$K_4Na_4NbW_7O_{20}$	mp-1099948
$Na_{0.5}K_{0.5}W_{0.875}Mo_{0.125}O_{3-\delta}$	5	1.014	526.37	$K_4Na_4MoW_7O_{24}$	mp-1076685	$K_4Na_4MoW_7O_{20}$	mp-1099972
$Na_{0.375}K_{0.625}NbO_{3-\delta}$	5	1.015	529.59	$K_5Na_3Nb_8O_{24}$	mp-1076335	$K_5Na_3Nb_8O_{20}$	mp-1076768
$Na_{0.375}K_{0.625}Ta_{0.125}Nb_{0.875}O_{3-\delta}$	5	1.015	538.93	$K_5Na_3TaNb_7O_{24}$	mp-1076363	$K_5Na_3TaNb_7O_{20}$	mp-1076887
$Na_{0.375}K_{0.625}Ta_{0.25}Nb_{0.75}O_{3-\delta}$	5	1.015	548.04	$K_5Na_3Ta_2Nb_6O_{24}$	mp-1099712	$K_5Na_3Ta_2Nb_6O_{20}$	mp-1076895
$Na_{0.375}K_{0.625}Ta_{0.375}Nb_{0.625}O_{3-\delta}$	5	1.015	558.23	$K_5Na_3Ta_3Nb_5O_{24}$	mp-1076512	$K_5Na_3Ta_3Nb_5O_{20}$	mp-1077704
$Na_{0.375}K_{0.625}Ta_{0.5}Nb_{0.5}O_{3-\delta}$	5	1.015	567.34	$K_5Na_3Ta_4Nb_4O_{24}$	mp-1076095	$K_5Na_3Ta_4Nb_4O_{20}$	mp-1099857
$LaCrO_{3-\delta}$	3	0.962	570.86	$LaCrO_3$	mp-19281	$La_2Cr_2O_5$	mp-1097715
$CaTiO_{3-\delta}$	4	0.959	578.97	$CaTiO_3$	mp-4019	$Ca_2Ti_2O_5$	mp-1096895
$Ca_{0.125}Sr_{0.875}TiO_{3-\delta}$	4	0.991	584.67	$Sr_7CaTi_8O_{24}$	mp-1075922	$Sr_7CaTi_8O_{20}$	mp-1076695
$Na_{0.375}K_{0.625}Ta_{0.625}Nb_{0.375}O_{3-\delta}$	5	1.015	585.41	$K_5Na_3Ta_5Nb_3O_{24}$	mp-1075953	$K_5Na_3Ta_5Nb_3O_{20}$	mp-1100247
$EuTiO_{3-\delta}$	3	0.896	586.90	$EuTiO_3$	mp-1079111	$Eu_2Ti_2O_5$	mp-1076037
$BaTiO_{3-\delta}$	4	1.055	588.75	$BaTiO_3$	mp-5020	$Ba_2Ti_2O_5$	mp-1076521
$Sr_{0.625}Ba_{0.375}TiO_{3-\delta}$	4	1.018	589.22	$Ba_3Sr_5Ti_8O_{24}$	mp-1075943	$Ba_3Sr_5Ti_8O_{20}$	mp-1099792
$Sr_{0.875}Ba_{0.125}TiO_{3-\delta}$	4	1.003	589.44	$BaSr_7Ti_8O_{24}$	mp-1099778	$BaSr_7Ti_8O_{20}$	mp-1099682
$SrTiO_{3-\delta}$	4	0.996	589.85	$SrTiO_3$	mp-4651	$Sr_2Ti_2O_5$	mp-1097778
$KNbO_{3-\delta}$	5	1.050	594.00	$KNbO_3$	mp-7375	$K_2Nb_2O_5$	mp-1076215
$Na_{0.375}K_{0.625}Ta_{0.75}Nb_{0.25}O_{3-\delta}$	5	1.015	606.41	$K_5Na_3Ta_6Nb_2O_{24}$	mp-1099860	$K_5Na_3Ta_6Nb_2O_{20}$	mp-1099903
$RbNbO_{3-\delta}$	5	1.077	624.20	$RbNbO_3$	mp-3283	$Rb_2Nb_2O_5$	mp-1076323
$Na_{0.375}K_{0.625}Ta_{0.875}Nb_{0.125}O_{3-\delta}$	5	1.015	625.94	$K_5Na_3Ta_7NbO_{24}$	mp-1076413	$K_5Na_3Ta_7NbO_{20}$	mp-1100141
$LaTiO_{3-\delta}$	3	0.937	633.41	$LaTiO_3$	mp-22013	$La_2Ti_2O_5$	mp-1097763
$NaTaO_{3-\delta}$	5	0.957	646.24	$NaTaO_3$	mp-3858	$Na_2Ta_2O_5$	mp-1075952
$SmTiO_{3-\delta}$	3	0.897	654.10	$SmTiO_3$	mp-22416	$Sm_2Ti_2O_5$	mp-1099757
$KTaO_{3-\delta}$	5	1.050	660.41	$KTaO_3$	mp-3614	$K_2Ta_2O_5$	mp-1099764
$MgTiO_{3-\delta}$	4	0.862	696.82	$MgTiO_3$	mp-3771	$Mg_2Ti_2O_5$	mp-1076652
$RbTaO_{3-\delta}$	5	1.077	705.99	$RbTaO_3$	mp-3033	$Rb_2Ta_2O_5$	mp-1076737

Table 8.8: Theoretical data for the perovskite redox pairs investigated within this work including the species and redox enthalpies of the endmembers. All redox enthalpies given per mol of oxygen O released (kJ/mol$_O$). ΔH_{DFT} corresponds to ΔH in table 8.7. The δ dependent redox enthalpy of a perovskite solid solution with two different redox-active species on the M site is calculated using the redox enthalpies for the limiting cases of $\delta \rightarrow 0$ (ΔH_{min}) and $\delta \rightarrow 0$ (ΔH_{max}). These are derived from the DFT-calculated redox enthalpies of the solid solution endmembers (EM) as explained in the main manuscript. The redox enthalpy of materials with only one species on the M site is assumed to be independent of δ and the endmember redox enthalpies are only given for comparison, as $\Delta H_{min} = \Delta H_{max} = \Delta H_{DFT}$ in these cases (marked in red). If the mean redox enthalpy calculated using the solid solution endmembers differs by more than 30 kJ/mol from the DFT-calculated value for the solid solution (diff > 30), $\Delta H_{min} = \Delta H_{max} = \Delta H_{DFT}$ is used instead. Taken from Vieten *et. al.* [95]

Redox Material	ΔH_{DFT}	ΔH_{min}	ΔH_{max}	diff>30	EM 1	ΔH_{EM1}	EM 2	ΔH_{EM2}	EM 3	ΔH_{EM3}	EM 4	ΔH_{EM4}
$MgCuO_{3-\delta}$	-337.87	-337.87	-337.87		$MgCuO_{3-\delta}$	-337.87						
$SmAgO_{3-\delta}$	-244.17	-244.17	-244.17		$SmAgO_{3-\delta}$	-244.17						
$CaCuO_{3-\delta}$	-154.45	-154.45	-154.45		$CaCuO_{3-\delta}$	-154.45						
$EuAgO_{3-\delta}$	-102.97	-102.97	-102.97		$EuAgO_{3-\delta}$	-102.97						
$RbCrO_{3-\delta}$	-95.16	-95.16	-95.16		$RbCrO_{3-\delta}$	-95.16						
$Mg_{0.125}Ca_{0.875}CoO_{3-\delta}$	-81.80	-81.80	-81.80		$MgCoO_{3-\delta}$	110.14	$CaCoO_{3-\delta}$	41.41				
$BaCuO_{3-\delta}$	-71.24	-71.24	-71.24		$BaCuO_{3-\delta}$	-71.24						
$Mg_{0.125}Ca_{0.875}Fe_{0.125}Co_{0.875}O_{3-\delta}$	-65.13	-65.13	-65.13	yes	$MgFeO_{3-\delta}$	40.85	$CaFeO_{3-\delta}$	55.51	$MgCoO_{3-\delta}$	110.14	$CaCoO_{3-\delta}$	41.41
$Mg_{0.125}Ca_{0.875}Co_{0.875}Cu_{0.125}O_{3-\delta}$	-56.05	-56.05	-56.05	yes	$MgCoO_{3-\delta}$	110.14	$CaCoO_{3-\delta}$	41.41	$MgCuO_{3-\delta}$	-337.87	$CaCuO_{3-\delta}$	-154.45
$NaCrO_{3-\delta}$	-30.37	-30.37	-30.37		$NaCrO_{3-\delta}$	-30.37						
$Ca_{0.5}Sr_{0.5}CoO_{3-\delta}$	-25.93	-25.93	-25.93		$CaCoO_{3-\delta}$	41.41	$SrCoO_{3-\delta}$	0.82				
$Ca_{0.875}Sr_{0.125}Fe_{0.125}Co_{0.875}O_{3-\delta}$	-15.35	-15.35	-15.35	yes	$CaFeO_{3-\delta}$	55.51	$SrFeO_{3-\delta}$	87.77	$CaCoO_{3-\delta}$	41.41	$SrCoO_{3-\delta}$	0.82
$Ca_{0.75}Sr_{0.25}CoO_{3-\delta}$	-14.17	-14.17	-14.17		$CaCoO_{3-\delta}$	41.41	$SrCoO_{3-\delta}$	0.82				
$SrCuO_{3-\delta}$	-7.35	-7.35	-7.35		$SrCuO_{3-\delta}$	-7.35						
$Ca_{0.875}Sr_{0.125}Fe_{0.25}Co_{0.75}O_{3-\delta}$	-1.20	-1.20	-1.20	yes	$CaFeO_{3-\delta}$	55.51	$SrFeO_{3-\delta}$	87.77	$CaCoO_{3-\delta}$	41.41	$SrCoO_{3-\delta}$	0.82

Redox Material	ΔH_{DFT}	ΔH_{min}	ΔH_{max}	diff>30	EM 1	ΔH_{EM1}	EM 2	ΔH_{EM2}	EM 3	ΔH_{EM3}	EM 4	ΔH_{EM4}
$Ca_{0.375}Sr_{0.625}Fe_{0.25}Co_{0.75}O_{3-\delta}$	37.34	28.77	63.04		$CaFeO_{3-\delta}$	55.51	$SrFeO_{3-\delta}$	87.77	$CaCoO_{3-\delta}$	41.41	$SrCoO_{3-\delta}$	0.82
$Sr_{0.625}Ba_{0.375}Co_{0.375}Cu_{0.625}O_{3-\delta}$	37.84	10.69	83.09		$SrCoO_{3-\delta}$	0.82	$BaCoO_{3-\delta}$	172.09	$SrCuO_{3-\delta}$	-7.35	$BaCuO_{3-\delta}$	-71.24
$Ca_{0.625}Sr_{0.375}Fe_{0.5}Co_{0.5}O_{3-\delta}$	39.01	25.91	52.11		$CaFeO_{3-\delta}$	55.51	$SrFeO_{3-\delta}$	87.77	$CaCoO_{3-\delta}$	41.41	$SrCoO_{3-\delta}$	0.82
$Sm_{0.25}La_{0.75}Co_{0.875}Ag_{0.125}O_{3-\delta}$	39.52	39.52	39.52	yes	$SmCoO_{3-\delta}$	232.71	$LaCoO_{3-\delta}$	202.55	$SmAgO_{3-\delta}$	-244.17	$LaAgO_{3-\delta}$	99.65
$Ca_{0.25}Sr_{0.75}Co_{0.75}Cu_{0.25}O_{3-\delta}$	40.17	40.17	40.17	yes	$CaCoO_{3-\delta}$	41.41	$SrCoO_{3-\delta}$	0.82	$CaCuO_{3-\delta}$	-154.45	$SrCuO_{3-\delta}$	-7.35
$Sr_{0.75}Ba_{0.25}Co_{0.375}Cu_{0.625}O_{3-\delta}$	40.21	21.09	72.08		$SrCoO_{3-\delta}$	0.82	$BaCoO_{3-\delta}$	172.09	$SrCuO_{3-\delta}$	-7.35	$BaCuO_{3-\delta}$	-71.24
$MgFeO_{3-\delta}$	40.85	40.85	40.85		$MgFeO_{3-\delta}$	40.85						
$CaCoO_{3-\delta}$	41.41	41.41	41.41		$CaCoO_{3-\delta}$	41.41						
$Ca_{0.5}Sr_{0.5}Fe_{0.375}Co_{0.625}O_{3-\delta}$	41.82	30.48	60.72		$CaFeO_{3-\delta}$	55.51	$SrFeO_{3-\delta}$	87.77	$CaCoO_{3-\delta}$	41.41	$SrCoO_{3-\delta}$	0.82
$Ca_{0.5}Sr_{0.5}Fe_{0.75}Co_{0.25}O_{3-\delta}$	42.84	20.16	50.40		$CaFeO_{3-\delta}$	55.51	$SrFeO_{3-\delta}$	87.77	$CaCoO_{3-\delta}$	41.41	$SrCoO_{3-\delta}$	0.82
$Sr_{0.625}Ba_{0.375}Co_{0.5}Cu_{0.5}O_{3-\delta}$	47.17	10.97	83.36		$SrCoO_{3-\delta}$	0.82	$BaCoO_{3-\delta}$	172.09	$SrCuO_{3-\delta}$	-7.35	$BaCuO_{3-\delta}$	-71.24
$Sr_{0.75}Ba_{0.25}Co_{0.625}Cu_{0.375}O_{3-\delta}$	47.64	15.78	66.76		$SrCoO_{3-\delta}$	0.82	$BaCoO_{3-\delta}$	172.09	$SrCuO_{3-\delta}$	-7.35	$BaCuO_{3-\delta}$	-71.24
$Sr_{0.875}Ba_{0.125}Co_{0.625}Cu_{0.375}O_{3-\delta}$	47.99	47.99	47.99	yes	$SrCoO_{3-\delta}$	0.82	$BaCoO_{3-\delta}$	172.09	$SrCuO_{3-\delta}$	-7.35	$BaCuO_{3-\delta}$	-71.24
$Sr_{0.875}Ba_{0.125}Co_{0.5}Cu_{0.5}O_{3-\delta}$	48.55	48.55	48.55	yes	$SrCoO_{3-\delta}$	0.82	$BaCoO_{3-\delta}$	172.09	$SrCuO_{3-\delta}$	-7.35	$BaCuO_{3-\delta}$	-71.24
$EuCoO_{3-\delta}$	49.90	49.90	49.90		$EuCoO_{3-\delta}$	49.90						
$Sm_{0.375}La_{0.625}Ag_{0.125}Ni_{0.875}O_{3-\delta}$	52.78	52.78	52.78	yes	$SmAgO_{3-\delta}$	-244.17	$LaAgO_{3-\delta}$	99.65	$SmNiO_{3-\delta}$	162.20	$LaNiO_{3-\delta}$	141.84
$Ca_{0.25}Sr_{0.75}Fe_{0.375}Co_{0.625}O_{3-\delta}$	54.13	39.77	78.06		$CaFeO_{3-\delta}$	55.51	$SrFeO_{3-\delta}$	87.77	$CaCoO_{3-\delta}$	41.41	$SrCoO_{3-\delta}$	0.82
$CaFeO_{3-\delta}$	55.51	55.51	55.51		$CaFeO_{3-\delta}$	55.51						
$Ca_{0.375}Sr_{0.625}Fe_{0.875}Co_{0.125}O_{3-\delta}$	56.98	27.00	61.26		$CaFeO_{3-\delta}$	55.51	$SrFeO_{3-\delta}$	87.77	$CaCoO_{3-\delta}$	41.41	$SrCoO_{3-\delta}$	0.82
$Mg_{0.125}Ca_{0.875}Mn_{0.875}Fe_{0.125}O_{3-\delta}$	57.56	57.56	57.56	yes	$MgMnO_{3-\delta}$	250.13	$CaMnO_{3-\delta}$	173.13	$MgFeO_{3-\delta}$	40.85	$CaFeO_{3-\delta}$	55.51
$Mg_{0.125}Ca_{0.875}MnO_{3-\delta}$	61.05	61.05	61.05		$MgMnO_{3-\delta}$	250.13	$CaMnO_{3-\delta}$	173.13				
$Ca_{0.25}Sr_{0.75}Fe_{0.625}Co_{0.375}O_{3-\delta}$	63.86	39.92	78.22		$CaFeO_{3-\delta}$	55.51	$SrFeO_{3-\delta}$	87.77	$CaCoO_{3-\delta}$	41.41	$SrCoO_{3-\delta}$	0.82
$Ca_{0.25}Sr_{0.75}Fe_{0.875}Co_{0.125}O_{3-\delta}$	64.86	31.35	69.65		$CaFeO_{3-\delta}$	55.51	$SrFeO_{3-\delta}$	87.77	$CaCoO_{3-\delta}$	41.41	$SrCoO_{3-\delta}$	0.82
$Ca_{0.125}Sr_{0.875}Fe_{0.5}Co_{0.5}O_{3-\delta}$	65.92	44.76	87.09		$CaFeO_{3-\delta}$	55.51	$SrFeO_{3-\delta}$	87.77	$CaCoO_{3-\delta}$	41.41	$SrCoO_{3-\delta}$	0.82

Redox Material	ΔH_{DFT}	ΔH_{min}	ΔH_{max}	diff>30	EM 1	ΔH_{EM1}	EM 2	ΔH_{EM2}	EM 3	ΔH_{EM3}	EM 4	ΔH_{EM4}
$Ca_{0.375}Sr_{0.625}Fe_{0.25}Co_{0.75}O_{3-\delta}$	37.34	28.77	63.04		$CaFeO_{3-\delta}$	55.51	$SrFeO_{3-\delta}$	87.77	$CaCoO_{3-\delta}$	41.41	$SrCoO_{3-\delta}$	0.82
$Sr_{0.625}Ba_{0.375}Co_{0.375}Cu_{0.625}O_{3-\delta}$	37.84	10.69	83.09		$SrCoO_{3-\delta}$	0.82	$BaCoO_{3-\delta}$	172.09	$SrCuO_{3-\delta}$	-7.35	$BaCuO_{3-\delta}$	-71.24
$Ca_{0.625}Sr_{0.375}Fe_{0.5}Co_{0.5}O_{3-\delta}$	39.01	25.91	52.11		$CaFeO_{3-\delta}$	55.51	$SrFeO_{3-\delta}$	87.77	$CaCoO_{3-\delta}$	41.41	$SrCoO_{3-\delta}$	0.82
$Sm_{0.25}La_{0.75}Co_{0.875}Ag_{0.125}O_{3-\delta}$	39.52	39.52	39.52	yes	$SmCoO_{3-\delta}$	232.71	$LaCoO_{3-\delta}$	202.55	$SmAgO_{3-\delta}$	-244.17	$LaAgO_{3-\delta}$	99.65
$Ca_{0.25}Sr_{0.75}Co_{0.75}Cu_{0.25}O_{3-\delta}$	40.17	40.17	40.17	yes	$CaCoO_{3-\delta}$	41.41	$SrCoO_{3-\delta}$	0.82	$CaCuO_{3-\delta}$	-154.45	$SrCuO_{3-\delta}$	-7.35
$Sr_{0.75}Ba_{0.25}Co_{0.375}Cu_{0.625}O_{3-\delta}$	40.21	21.09	72.08		$SrCoO_{3-\delta}$	0.82	$BaCoO_{3-\delta}$	172.09	$SrCuO_{3-\delta}$	-7.35	$BaCuO_{3-\delta}$	-71.24
$MgFeO_{3-\delta}$	40.85	40.85	40.85		$MgFeO_{3-\delta}$	40.85						
$CaCoO_{3-\delta}$	41.41	41.41	41.41		$CaCoO_{3-\delta}$	41.41						
$Ca_{0.5}Sr_{0.5}Fe_{0.375}Co_{0.625}O_{3-\delta}$	41.82	30.48	60.72		$CaFeO_{3-\delta}$	55.51	$SrFeO_{3-\delta}$	87.77	$CaCoO_{3-\delta}$	41.41	$SrCoO_{3-\delta}$	0.82
$Ca_{0.5}Sr_{0.5}Fe_{0.75}Co_{0.25}O_{3-\delta}$	42.84	20.16	50.40		$CaFeO_{3-\delta}$	55.51	$SrFeO_{3-\delta}$	87.77	$CaCoO_{3-\delta}$	41.41	$SrCoO_{3-\delta}$	0.82
$Sr_{0.625}Ba_{0.375}Co_{0.5}Cu_{0.5}O_{3-\delta}$	47.17	10.97	83.36		$SrCoO_{3-\delta}$	0.82	$BaCoO_{3-\delta}$	172.09	$SrCuO_{3-\delta}$	-7.35	$BaCuO_{3-\delta}$	-71.24
$Sr_{0.75}Ba_{0.25}Co_{0.625}Cu_{0.375}O_{3-\delta}$	47.64	15.78	66.76		$SrCoO_{3-\delta}$	0.82	$BaCoO_{3-\delta}$	172.09	$SrCuO_{3-\delta}$	-7.35	$BaCuO_{3-\delta}$	-71.24
$Sr_{0.875}Ba_{0.125}Co_{0.625}Cu_{0.375}O_{3-\delta}$	47.99	47.99	47.99	yes	$SrCoO_{3-\delta}$	0.82	$BaCoO_{3-\delta}$	172.09	$SrCuO_{3-\delta}$	-7.35	$BaCuO_{3-\delta}$	-71.24
$Sr_{0.875}Ba_{0.125}Co_{0.5}Cu_{0.5}O_{3-\delta}$	48.55	48.55	48.55	yes	$SrCoO_{3-\delta}$	0.82	$BaCoO_{3-\delta}$	172.09	$SrCuO_{3-\delta}$	-7.35	$BaCuO_{3-\delta}$	-71.24
$EuCoO_{3-\delta}$	49.90	49.90	49.90		$EuCoO_{3-\delta}$	49.90						
$Sm_{0.375}La_{0.625}Ag_{0.125}Ni_{0.875}O_{3-\delta}$	52.78	52.78	52.78	yes	$SmAgO_{3-\delta}$	-244.17	$LaAgO_{3-\delta}$	99.65	$SmNiO_{3-\delta}$	162.20	$LaNiO_{3-\delta}$	141.84
$Ca_{0.25}Sr_{0.75}Fe_{0.375}Co_{0.625}O_{3-\delta}$	54.13	39.77	78.06		$CaFeO_{3-\delta}$	55.51	$SrFeO_{3-\delta}$	87.77	$CaCoO_{3-\delta}$	41.41	$SrCoO_{3-\delta}$	0.82
$CaFeO_{3-\delta}$	55.51	55.51	55.51		$CaFeO_{3-\delta}$	55.51						
$Ca_{0.375}Sr_{0.625}Fe_{0.875}Co_{0.125}O_{3-\delta}$	56.98	27.00	61.26		$CaFeO_{3-\delta}$	55.51	$SrFeO_{3-\delta}$	87.77	$CaCoO_{3-\delta}$	41.41	$SrCoO_{3-\delta}$	0.82
$Mg_{0.125}Ca_{0.875}Mn_{0.875}Fe_{0.125}O_{3-\delta}$	57.56	57.56	57.56	yes	$MgMnO_{3-\delta}$	250.13	$CaMnO_{3-\delta}$	173.13	$MgFeO_{3-\delta}$	40.85	$CaFeO_{3-\delta}$	55.51
$Mg_{0.125}Ca_{0.875}MnO_{3-\delta}$	61.05	61.05	61.05		$MgMnO_{3-\delta}$	250.13	$CaMnO_{3-\delta}$	173.13				
$Ca_{0.25}Sr_{0.75}Fe_{0.625}Co_{0.375}O_{3-\delta}$	63.86	39.92	78.22		$CaFeO_{3-\delta}$	55.51	$SrFeO_{3-\delta}$	87.77	$CaCoO_{3-\delta}$	41.41	$SrCoO_{3-\delta}$	0.82
$Ca_{0.25}Sr_{0.75}Fe_{0.875}Co_{0.125}O_{3-\delta}$	64.86	31.35	69.65		$CaFeO_{3-\delta}$	55.51	$SrFeO_{3-\delta}$	87.77	$CaCoO_{3-\delta}$	41.41	$SrCoO_{3-\delta}$	0.82
$Ca_{0.125}Sr_{0.875}Fe_{0.5}Co_{0.5}O_{3-\delta}$	65.92	44.76	87.09		$CaFeO_{3-\delta}$	55.51	$SrFeO_{3-\delta}$	87.77	$CaCoO_{3-\delta}$	41.41	$SrCoO_{3-\delta}$	0.82

Redox Material	ΔH_{DFT}	ΔH_{min}	ΔH_{max}	diff>30	EM 1	ΔH_{EM1}	EM 2	ΔH_{EM2}	EM 3	ΔH_{EM3}	EM 4	ΔH_{EM4}
$Ca_{0.25}Sr_{0.75}FeO_{3-\delta}$	68.03	68.03	92.23		$CaFeO_{3-\delta}$	55.51	$SrFeO_{3-\delta}$	87.77				
$Ca_{0.125}Sr_{0.875}Fe_{0.625}Co_{0.375}O_{3-\delta}$	68.95	42.49	84.82		$CaFeO_{3-\delta}$	55.51	$SrFeO_{3-\delta}$	87.77	$CaCoO_{3-\delta}$	41.41	$SrCoO_{3-\delta}$	0.82
$Ca_{0.125}Sr_{0.875}Fe_{0.875}Co_{0.125}O_{3-\delta}$	71.48	34.45	76.78		$CaFeO_{3-\delta}$	55.51	$SrFeO_{3-\delta}$	87.77	$CaCoO_{3-\delta}$	41.41	$SrCoO_{3-\delta}$	0.82
$Ca_{0.125}Sr_{0.875}Fe_{0.75}Co_{0.25}O_{3-\delta}$	72.40	40.65	82.98		$CaFeO_{3-\delta}$	55.51	$SrFeO_{3-\delta}$	87.77	$CaCoO_{3-\delta}$	41.41	$SrCoO_{3-\delta}$	0.82
$EuNiO_{3-\delta}$	73.85	73.85	73.85		$EuNiO_{3-\delta}$	73.85						
$Sm_{0.5}La_{0.5}NiO_{3-\delta}$	76.16	76.16	76.16		$SmNiO_{3-\delta}$	162.20	$LaNiO_{3-\delta}$	141.84				
$Ca_{0.375}Sr_{0.625}Mn_{0.125}Fe_{0.875}O_{3-\delta}$	76.32	61.83	177.70		$CaMnO_{3-\delta}$	173.13	$SrMnO_{3-\delta}$	170.33	$CaFeO_{3-\delta}$	55.51	$SrFeO_{3-\delta}$	87.77
$SrFe_{0.875}Co_{0.125}O_{3-\delta}$	76.87	0.79	87.74		$SrFeO_{3-\delta}$	87.77	$SrFeO_{3-\delta}$	87.77	$SrCoO_{3-\delta}$	0.82	$SrCoO_{3-\delta}$	0.82
$Sr_{0.875}Ba_{0.125}Fe_{0.875}Co_{0.125}O_{3-\delta}$	78.02	1.17	89.00		$SrFeO_{3-\delta}$	87.77	$BaFeO_{3-\delta}$	94.77	$SrCoO_{3-\delta}$	0.82	$BaCoO_{3-\delta}$	172.09
$Mg_{0.125}Ca_{0.875}Ti_{0.125}Mn_{0.875}O_{3-\delta}$	79.23	79.23	79.23	yes	$MgTiO_{3-\delta}$	696.82	$CaTiO_{3-\delta}$	578.97	$MgMnO_{3-\delta}$	250.13	$CaMnO_{3-\delta}$	173.13
$Sr_{0.875}Ba_{0.125}Fe_{0.75}Co_{0.25}O_{3-\delta}$	81.84	15.97	103.79		$SrFeO_{3-\delta}$	87.77	$BaFeO_{3-\delta}$	94.77	$SrCoO_{3-\delta}$	0.82	$BaCoO_{3-\delta}$	172.09
$Ca_{0.5}Sr_{0.5}Mn_{0.25}Fe_{0.75}O_{3-\delta}$	83.80	54.74	170.96		$CaMnO_{3-\delta}$	173.13	$SrMnO_{3-\delta}$	170.33	$CaFeO_{3-\delta}$	55.51	$SrFeO_{3-\delta}$	87.77
$Ca_{0.25}Sr_{0.75}Mn_{0.125}Fe_{0.875}O_{3-\delta}$	85.26	70.82	186.34		$CaMnO_{3-\delta}$	173.13	$SrMnO_{3-\delta}$	170.33	$CaFeO_{3-\delta}$	55.51	$SrFeO_{3-\delta}$	87.77
$SrFeO_{3-\delta}$	87.77	87.77	87.77		$SrFeO_{3-\delta}$	87.77						
$Sr_{0.875}Ba_{0.125}FeO_{3-\delta}$	88.00	88.00	88.00		$SrFeO_{3-\delta}$	87.77	$BaFeO_{3-\delta}$	94.77				
$BaFeO_{3-\delta}$	94.77	94.77	94.77		$BaFeO_{3-\delta}$	94.77						
$Sm_{0.5}La_{0.5}CoO_{3-\delta}$	94.88	94.88	94.88		$SmCoO_{3-\delta}$	232.71	$LaCoO_{3-\delta}$	202.55				
$Ca_{0.125}Sr_{0.875}Mn_{0.125}Fe_{0.875}O_{3-\delta}$	95.92	81.53	196.70		$CaMnO_{3-\delta}$	173.13	$SrMnO_{3-\delta}$	170.33	$CaFeO_{3-\delta}$	55.51	$SrFeO_{3-\delta}$	87.77
$Ca_{0.625}Sr_{0.375}Mn_{0.375}Fe_{0.625}O_{3-\delta}$	96.08	52.37	168.94		$CaMnO_{3-\delta}$	173.13	$SrMnO_{3-\delta}$	170.33	$CaFeO_{3-\delta}$	55.51	$SrFeO_{3-\delta}$	87.77
$Sm_{0.5}La_{0.5}Cu_{0.125}Co_{0.875}O_{3-\delta}$	98.69	98.69	98.69	yes	$SmCuO_{3-\delta}$	147.50	$LaCuO_{3-\delta}$	149.59	$SmCoO_{3-\delta}$	232.71	$LaCoO_{3-\delta}$	202.55
$LaAgO_{3-\delta}$	99.65	99.65	99.65		$LaAgO_{3-\delta}$	99.65						
$Sr_{0.875}Ba_{0.125}Mn_{0.125}Fe_{0.875}O_{3-\delta}$	99.89	88.29	181.10		$SrMnO_{3-\delta}$	170.33	$BaMnO_{3-\delta}$	252.31	$SrFeO_{3-\delta}$	87.77	$BaFeO_{3-\delta}$	94.77
$Ca_{0.875}Sr_{0.125}Mn_{0.75}Fe_{0.25}O_{3-\delta}$	101.07	101.07	101.07	yes	$CaMnO_{3-\delta}$	173.13	$SrMnO_{3-\delta}$	170.33	$CaFeO_{3-\delta}$	55.51	$SrFeO_{3-\delta}$	87.77
$Ca_{0.875}Sr_{0.125}Mn_{0.875}Fe_{0.125}O_{3-\delta}$	102.62	102.62	102.62	yes	$CaMnO_{3-\delta}$	173.13	$SrMnO_{3-\delta}$	170.33	$CaFeO_{3-\delta}$	55.51	$SrFeO_{3-\delta}$	87.77

Redox Material	ΔH_{DFT}	ΔH_{min}	ΔH_{max}	diff>30	EM 1	ΔH_{EM1}	EM 2	ΔH_{EM2}	EM 3	ΔH_{EM3}	EM 4	ΔH_{EM4}
$Na_{0.875}K_{0.125}V_{0.75}Cr_{0.25}O_{3-\delta}$	102.72	102.72	102.72	yes	$NaVO_{3-\delta}$	287.56	$KVO_{3-\delta}$	374.19	$NaCrO_{3-\delta}$	-30.37	$KCrO_{3-\delta}$	6.77
$EuCuO_{3-\delta}$	105.30	105.30	105.30		$EuCuO_{3-\delta}$	105.30						
$Ca_{0.75}Sr_{0.25}Mn_{0.625}Fe_{0.375}O_{3-\delta}$	105.69	32.61	149.53		$CaMnO_{3-\delta}$	173.13	$SrMnO_{3-\delta}$	170.33	$CaFeO_{3-\delta}$	55.51	$SrFeO_{3-\delta}$	87.77
$SrMn_{0.125}Fe_{0.875}O_{3-\delta}$	105.84	95.52	178.08		$SrMnO_{3-\delta}$	170.33	$SrMnO_{3-\delta}$	170.33	$SrFeO_{3-\delta}$	87.77	$SrFeO_{3-\delta}$	87.77
$Sm_{0.375}La_{0.625}Cu_{0.125}Co_{0.875}O_{3-\delta}$	106.73	106.73	106.73	yes	$SmCuO_{3-\delta}$	147.50	$LaCuO_{3-\delta}$	149.59	$SmCoO_{3-\delta}$	232.71	$LaCoO_{3-\delta}$	202.55
$MgCoO_{3-\delta}$	110.14	110.14	110.14		$MgCoO_{3-\delta}$	110.14						
$Ca_{0.125}Sr_{0.875}Mn_{0.25}Fe_{0.75}O_{3-\delta}$	110.29	81.49	196.66		$CaMnO_{3-\delta}$	173.13	$SrMnO_{3-\delta}$	170.33	$CaFeO_{3-\delta}$	55.51	$SrFeO_{3-\delta}$	87.77
$Ca_{0.75}Sr_{0.25}Mn_{0.875}Fe_{0.125}O_{3-\delta}$	110.63	110.63	110.63	yes	$CaMnO_{3-\delta}$	173.13	$SrMnO_{3-\delta}$	170.33	$CaFeO_{3-\delta}$	55.51	$SrFeO_{3-\delta}$	87.77
$Ca_{0.625}Sr_{0.375}Mn_{0.5}Fe_{0.5}O_{3-\delta}$	114.92	56.63	173.20		$CaMnO_{3-\delta}$	173.13	$SrMnO_{3-\delta}$	170.33	$CaFeO_{3-\delta}$	55.51	$SrFeO_{3-\delta}$	87.77
$Ca_{0.25}Sr_{0.75}Mn_{0.375}Fe_{0.625}O_{3-\delta}$	116.98	73.66	189.18		$CaMnO_{3-\delta}$	173.13	$SrMnO_{3-\delta}$	170.33	$CaFeO_{3-\delta}$	55.51	$SrFeO_{3-\delta}$	87.77
$Ca_{0.5}Sr_{0.5}Mn_{0.625}Fe_{0.375}O_{3-\delta}$	117.88	45.24	161.46		$CaMnO_{3-\delta}$	173.13	$SrMnO_{3-\delta}$	170.33	$CaFeO_{3-\delta}$	55.51	$SrFeO_{3-\delta}$	87.77
$Ca_{0.5}Sr_{0.5}Mn_{0.75}Fe_{0.25}O_{3-\delta}$	119.85	32.69	148.91		$CaMnO_{3-\delta}$	173.13	$SrMnO_{3-\delta}$	170.33	$CaFeO_{3-\delta}$	55.51	$SrFeO_{3-\delta}$	87.77
$Sm_{0.125}La_{0.875}Cu_{0.25}Co_{0.75}O_{3-\delta}$	119.91	119.91	119.91	yes	$SmCuO_{3-\delta}$	147.50	$LaCuO_{3-\delta}$	149.59	$SmCoO_{3-\delta}$	232.71	$LaCoO_{3-\delta}$	202.55
$Sr_{0.875}Ba_{0.125}Mn_{0.25}Fe_{0.75}O_{3-\delta}$	120.66	97.46	190.27		$SrMnO_{3-\delta}$	170.33	$BaMnO_{3-\delta}$	252.31	$SrFeO_{3-\delta}$	87.77	$BaFeO_{3-\delta}$	94.77
$Ca_{0.5}Sr_{0.5}MnO_{3-\delta}$	121.61	121.61	121.61		$CaMnO_{3-\delta}$	173.13	$SrMnO_{3-\delta}$	170.33				
$Na_{0.875}K_{0.125}V_{0.875}Cr_{0.125}O_{3-\delta}$	121.67	121.67	121.67	yes	$NaVO_{3-\delta}$	287.56	$KVO_{3-\delta}$	374.19	$NaCrO_{3-\delta}$	-30.37	$KCrO_{3-\delta}$	6.77
$Ca_{0.5}Sr_{0.5}Mn_{0.875}Fe_{0.125}O_{3-\delta}$	123.20	123.20	123.20	yes	$CaMnO_{3-\delta}$	173.13	$SrMnO_{3-\delta}$	170.33	$CaFeO_{3-\delta}$	55.51	$SrFeO_{3-\delta}$	87.77
$Sm_{0.125}La_{0.875}Cu_{0.375}Co_{0.625}O_{3-\delta}$	123.90	123.90	123.90	yes	$SmCuO_{3-\delta}$	147.50	$LaCuO_{3-\delta}$	149.59	$SmCoO_{3-\delta}$	232.71	$LaCoO_{3-\delta}$	202.55
$Ca_{0.375}Sr_{0.625}Mn_{0.75}Fe_{0.25}O_{3-\delta}$	125.87	38.97	154.84		$CaMnO_{3-\delta}$	173.13	$SrMnO_{3-\delta}$	170.33	$CaFeO_{3-\delta}$	55.51	$SrFeO_{3-\delta}$	87.77
$Ca_{0.125}Sr_{0.875}Mn_{0.375}Fe_{0.625}O_{3-\delta}$	126.36	83.17	198.34		$CaMnO_{3-\delta}$	173.13	$SrMnO_{3-\delta}$	170.33	$CaFeO_{3-\delta}$	55.51	$SrFeO_{3-\delta}$	87.77
$Ca_{0.375}Sr_{0.625}Mn_{0.5}Fe_{0.5}O_{3-\delta}$	126.88	68.95	184.82		$CaMnO_{3-\delta}$	173.13	$SrMnO_{3-\delta}$	170.33	$CaFeO_{3-\delta}$	55.51	$SrFeO_{3-\delta}$	87.77
$Ca_{0.875}Sr_{0.125}Ti_{0.125}Mn_{0.875}O_{3-\delta}$	127.33	127.33	127.33	yes	$CaTiO_{3-\delta}$	578.97	$SrTiO_{3-\delta}$	589.85	$CaMnO_{3-\delta}$	173.13	$SrMnO_{3-\delta}$	170.33
$Ca_{0.375}Sr_{0.625}Mn_{0.875}Fe_{0.125}O_{3-\delta}$	130.00	28.61	144.48		$CaMnO_{3-\delta}$	173.13	$SrMnO_{3-\delta}$	170.33	$CaFeO_{3-\delta}$	55.51	$SrFeO_{3-\delta}$	87.77
$Ca_{0.25}Sr_{0.75}Mn_{0.625}Fe_{0.375}O_{3-\delta}$	130.54	58.34	173.86		$CaMnO_{3-\delta}$	173.13	$SrMnO_{3-\delta}$	170.33	$CaFeO_{3-\delta}$	55.51	$SrFeO_{3-\delta}$	87.77

Redox Material	ΔH_{DFT}	ΔH_{min}	ΔH_{max}	diff>30	EM 1	ΔH_{EM1}	EM 2	ΔH_{EM2}	EM 3	ΔH_{EM3}	EM 4	ΔH_{EM4}
$Ca_{0.75}Sr_{0.25}Ti_{0.125}Mn_{0.875}O_{3-\delta}$	135.03	135.03	135.03	yes	$CaTiO_{3-\delta}$	578.97	$SrTiO_{3-\delta}$	589.85	$CaMnO_{3-\delta}$	173.13	$SrMnO_{3-\delta}$	170.33
$Ca_{0.125}Sr_{0.875}Mn_{0.5}Fe_{0.5}O_{3-\delta}$	140.53	82.95	198.11		$CaMnO_{3-\delta}$	173.13	$SrMnO_{3-\delta}$	170.33	$CaFeO_{3-\delta}$	55.51	$SrFeO_{3-\delta}$	87.77
$LaNiO_{3-\delta}$	141.84	141.84	141.84		$LaNiO_{3-\delta}$	141.84						
$Na_{0.875}K_{0.125}VO_{3-\delta}$	142.67	142.67	142.67		$NaVO_{3-\delta}$	287.56	$KVO_{3-\delta}$	374.19				
$Ca_{0.625}Sr_{0.375}Ti_{0.125}Mn_{0.875}O_{3-\delta}$	143.35	143.35	143.35	yes	$CaTiO_{3-\delta}$	578.97	$SrTiO_{3-\delta}$	589.85	$CaMnO_{3-\delta}$	173.13	$SrMnO_{3-\delta}$	170.33
$SmCuO_{3-\delta}$	147.50	147.50	147.50		$SmCuO_{3-\delta}$	147.50						
$LaCuO_{3-\delta}$	149.59	149.59	149.59		$LaCuO_{3-\delta}$	149.59						
$Ca_{0.5}Sr_{0.5}Ti_{0.125}Mn_{0.875}O_{3-\delta}$	149.66	149.66	149.66	yes	$CaTiO_{3-\delta}$	578.97	$SrTiO_{3-\delta}$	589.85	$CaMnO_{3-\delta}$	173.13	$SrMnO_{3-\delta}$	170.33
$Ca_{0.75}Sr_{0.25}Ti_{0.25}Mn_{0.75}O_{3-\delta}$	152.20	152.20	152.20	yes	$CaTiO_{3-\delta}$	578.97	$SrTiO_{3-\delta}$	589.85	$CaMnO_{3-\delta}$	173.13	$SrMnO_{3-\delta}$	170.33
$Ca_{0.375}Sr_{0.625}Ti_{0.125}Mn_{0.875}O_{3-\delta}$	155.01	155.01	155.01	yes	$CaTiO_{3-\delta}$	578.97	$SrTiO_{3-\delta}$	589.85	$CaMnO_{3-\delta}$	173.13	$SrMnO_{3-\delta}$	170.33
$SmNiO_{3-\delta}$	162.20	162.20	162.20		$SmNiO_{3-\delta}$	162.20						
$Ca_{0.5}Sr_{0.5}Ti_{0.25}Mn_{0.75}O_{3-\delta}$	166.56	166.56	166.56	yes	$CaTiO_{3-\delta}$	578.97	$SrTiO_{3-\delta}$	589.85	$CaMnO_{3-\delta}$	173.13	$SrMnO_{3-\delta}$	170.33
$Ca_{0.75}Sr_{0.25}MnO_{3-\delta}$	167.65	167.65	168.35		$CaMnO_{3-\delta}$	173.13	$SrMnO_{3-\delta}$	170.33				
$Na_{0.875}K_{0.125}Mo_{0.125}V_{0.875}O_{3-\delta}$	170.32	170.32	170.32	yes	$NaMoO_{3-\delta}$	319.41	$KMoO_{3-\delta}$	405.11	$NaVO_{3-\delta}$	287.56	$KVO_{3-\delta}$	374.19
$SrMnO_{3-\delta}$	170.33	170.33	170.33		$SrMnO_{3-\delta}$	170.33						
$BaCoO_{3-\delta}$	172.09	172.09	172.09		$BaCoO_{3-\delta}$	172.09						
$CaMnO_{3-\delta}$	173.13	173.13	173.13		$CaMnO_{3-\delta}$	173.13						
$Ca_{0.625}Sr_{0.375}Ti_{0.375}Mn_{0.625}O_{3-\delta}$	173.40	173.40	173.40	yes	$CaTiO_{3-\delta}$	578.97	$SrTiO_{3-\delta}$	589.85	$CaMnO_{3-\delta}$	173.13	$SrMnO_{3-\delta}$	170.33
$Na_{0.875}K_{0.125}Mo_{0.25}V_{0.75}O_{3-\delta}$	180.38	180.38	180.38	yes	$NaMoO_{3-\delta}$	319.41	$KMoO_{3-\delta}$	405.11	$NaVO_{3-\delta}$	287.56	$KVO_{3-\delta}$	374.19
$Ca_{0.25}Sr_{0.75}Ti_{0.25}Mn_{0.75}O_{3-\delta}$	182.71	182.71	182.71	yes	$CaTiO_{3-\delta}$	578.97	$SrTiO_{3-\delta}$	589.85	$CaMnO_{3-\delta}$	173.13	$SrMnO_{3-\delta}$	170.33
$Ca_{0.375}Sr_{0.625}Ti_{0.375}Mn_{0.625}O_{3-\delta}$	188.81	188.81	188.81	yes	$CaTiO_{3-\delta}$	578.97	$SrTiO_{3-\delta}$	589.85	$CaMnO_{3-\delta}$	173.13	$SrMnO_{3-\delta}$	170.33
$Ca_{0.5}Sr_{0.5}Ti_{0.5}Mn_{0.5}O_{3-\delta}$	195.49	195.49	195.49	yes	$CaTiO_{3-\delta}$	578.97	$SrTiO_{3-\delta}$	589.85	$CaMnO_{3-\delta}$	173.13	$SrMnO_{3-\delta}$	170.33
$Na_{0.75}K_{0.25}Mo_{0.375}V_{0.625}O_{3-\delta}$	202.11	202.11	202.11	yes	$NaMoO_{3-\delta}$	319.41	$KMoO_{3-\delta}$	405.11	$NaVO_{3-\delta}$	287.56	$KVO_{3-\delta}$	374.19
$LaCoO_{3-\delta}$	202.55	202.55	202.55		$LaCoO_{3-\delta}$	202.55						

Redox Material	ΔH_{DFT}	ΔH_{min}	ΔH_{max}	diff>30	EM 1	ΔH_{EM1}	EM 2	ΔH_{EM2}	EM 3	ΔH_{EM3}	EM 4	ΔH_{EM4}
$Ca_{0.125}Sr_{0.875}Ti_{0.375}Mn_{0.625}O_{3-\delta}$	206.19	206.19	206.19	yes	$CaTiO_{3-\delta}$	578.97	$SrTiO_{3-\delta}$	589.85	$CaMnO_{3-\delta}$	173.13	$SrMnO_{3-\delta}$	170.33
$Sm_{0.125}La_{0.875}Fe_{0.375}Mn_{0.625}O_{3-\delta}$	215.02	215.02	215.02	yes	$SmFeO_{3-\delta}$	401.32	$LaFeO_{3-\delta}$	377.56	$SmMnO_{3-\delta}$	388.21	$LaMnO_{3-\delta}$	353.27
$Ca_{0.25}Sr_{0.75}Ti_{0.5}Mn_{0.5}O_{3-\delta}$	215.45	215.45	215.45	yes	$CaTiO_{3-\delta}$	578.97	$SrTiO_{3-\delta}$	589.85	$CaMnO_{3-\delta}$	173.13	$SrMnO_{3-\delta}$	170.33
$Sm_{0.125}La_{0.875}Fe_{0.75}Mn_{0.25}O_{3-\delta}$	230.08	230.08	230.08	yes	$SmFeO_{3-\delta}$	401.32	$LaFeO_{3-\delta}$	377.56	$SmMnO_{3-\delta}$	388.21	$LaMnO_{3-\delta}$	353.27
$Na_{0.75}K_{0.25}Mo_{0.5}V_{0.5}O_{3-\delta}$	231.24	231.24	231.24	yes	$NaMoO_{3-\delta}$	319.41	$KMoO_{3-\delta}$	405.11	$NaVO_{3-\delta}$	287.56	$KVO_{3-\delta}$	374.19
$SmCoO_{3-\delta}$	232.71	232.71	232.71		$SmCoO_{3-\delta}$	232.71						
$SrTi_{0.5}Mn_{0.5}O_{3-\delta}$	235.38	235.38	235.38	yes	$SrTiO_{3-\delta}$	589.85	$SrTiO_{3-\delta}$	589.85	$SrMnO_{3-\delta}$	170.33	$SrMnO_{3-\delta}$	170.33
$Sm_{0.125}La_{0.875}Mn_{0.875}Cu_{0.125}O_{3-\delta}$	241.55	241.55	241.55	yes	$SmMnO_{3-\delta}$	388.21	$LaMnO_{3-\delta}$	353.27	$SmCuO_{3-\delta}$	147.50	$LaCuO_{3-\delta}$	149.59
$Sm_{0.125}La_{0.875}Fe_{0.625}Mn_{0.375}O_{3-\delta}$	243.35	243.35	243.35	yes	$SmFeO_{3-\delta}$	401.32	$LaFeO_{3-\delta}$	377.56	$SmMnO_{3-\delta}$	388.21	$LaMnO_{3-\delta}$	353.27
$EuFeO_{3-\delta}$	244.26	244.26	244.26		$EuFeO_{3-\delta}$	244.26						
$Sm_{0.125}La_{0.875}Fe_{0.875}Mn_{0.125}O_{3-\delta}$	245.84	245.84	245.84	yes	$SmFeO_{3-\delta}$	401.32	$LaFeO_{3-\delta}$	377.56	$SmMnO_{3-\delta}$	388.21	$LaMnO_{3-\delta}$	353.27
$MgMnO_{3-\delta}$	250.13	250.13	250.13		$MgMnO_{3-\delta}$	250.13						
$Sm_{0.125}La_{0.875}Fe_{0.5}Mn_{0.5}O_{3-\delta}$	251.41	251.41	251.41	yes	$SmFeO_{3-\delta}$	401.32	$LaFeO_{3-\delta}$	377.56	$SmMnO_{3-\delta}$	388.21	$LaMnO_{3-\delta}$	353.27
$BaMnO_{3-\delta}$	252.31	252.31	252.31		$BaMnO_{3-\delta}$	252.31						
$Sm_{0.125}La_{0.875}Fe_{0.25}Mn_{0.75}O_{3-\delta}$	256.80	256.80	256.80	yes	$SmFeO_{3-\delta}$	401.32	$LaFeO_{3-\delta}$	377.56	$SmMnO_{3-\delta}$	388.21	$LaMnO_{3-\delta}$	353.27
$Sm_{0.125}La_{0.875}Fe_{1}O_{3-\delta}$	258.54	258.54	258.54		$SmFeO_{3-\delta}$	401.32	$LaFeO_{3-\delta}$	377.56				
$EuMnO_{3-\delta}$	259.20	259.20	259.20		$EuMnO_{3-\delta}$	259.20						
$Sm_{0.125}La_{0.875}Fe_{0.125}Mn_{0.875}O_{3-\delta}$	260.34	260.34	260.34	yes	$SmFeO_{3-\delta}$	401.32	$LaFeO_{3-\delta}$	377.56	$SmMnO_{3-\delta}$	388.21	$LaMnO_{3-\delta}$	353.27
$Sm_{0.125}La_{0.875}MnO_{3-\delta}$	265.38	265.38	265.38		$SmMnO_{3-\delta}$	388.21	$LaMnO_{3-\delta}$	353.27				
$Na_{0.625}K_{0.375}Mo_{0.625}V_{0.375}O_{3-\delta}$	272.31	272.31	272.31	yes	$NaMoO_{3-\delta}$	319.41	$KMoO_{3-\delta}$	405.11	$NaVO_{3-\delta}$	287.56	$KVO_{3-\delta}$	374.19
$Ca_{0.375}Sr_{0.625}Ti_{0.625}Mn_{0.375}O_{3-\delta}$	285.80	285.80	285.80	yes	$CaTiO_{3-\delta}$	578.97	$SrTiO_{3-\delta}$	589.85	$CaMnO_{3-\delta}$	173.13	$SrMnO_{3-\delta}$	170.33
$NaVO_{3-\delta}$	287.56	287.56	287.56		$NaVO_{3-\delta}$	287.56						
$EuCrO_{3-\delta}$	289.00	289.00	289.00		$EuCrO_{3-\delta}$	289.00						
$Sm_{0.125}La_{0.875}Cr_{0.125}Fe_{0.875}O_{3-\delta}$	289.65	289.65	289.65	yes	$SmCrO_{3-\delta}$	415.04	$LaCrO_{3-\delta}$	570.86	$SmFeO_{3-\delta}$	401.32	$LaFeO_{3-\delta}$	377.56

Redox Material	ΔH_{DFT}	ΔH_{min}	ΔH_{max}	diff>30	EM 1	ΔH_{EM1}	EM 2	ΔH_{EM2}	EM 3	ΔH_{EM3}	EM 4	ΔH_{EM4}
$Na_{0.625}K_{0.375}Mo_{0.75}V_{0.25}O_{3-\delta}$	304.18	304.18	304.18	yes	$NaMoO_{3-\delta}$	319.41	$KMoO_{3-\delta}$	405.11	$NaVO_{3-\delta}$	287.56	$KVO_{3-\delta}$	374.19
$Ca_{0.125}Sr_{0.875}Ti_{0.625}Mn_{0.375}O_{3-\delta}$	304.86	304.86	304.86	yes	$CaTiO_{3-\delta}$	578.97	$SrTiO_{3-\delta}$	589.85	$CaMnO_{3-\delta}$	173.13	$SrMnO_{3-\delta}$	170.33
$Sr_{0.875}Ba_{0.125}Ti_{0.625}Mn_{0.375}O_{3-\delta}$	311.78	311.78	311.78	yes	$SrTiO_{3-\delta}$	589.85	$BaTiO_{3-\delta}$	588.75	$SrMnO_{3-\delta}$	170.33	$BaMnO_{3-\delta}$	252.31
$NaMoO_{3-\delta}$	319.41	319.41	319.41		$NaMoO_{3-\delta}$	319.41						
$Sm_{0.125}La_{0.875}Cr_{0.25}Fe_{0.75}O_{3-\delta}$	319.75	319.75	319.75	yes	$SmCrO_{3-\delta}$	415.04	$LaCrO_{3-\delta}$	570.86	$SmFeO_{3-\delta}$	401.32	$LaFeO_{3-\delta}$	377.56
$Sm_{0.25}La_{0.75}Cr_{0.375}Fe_{0.625}O_{3-\delta}$	325.74	325.74	325.74	yes	$SmCrO_{3-\delta}$	415.04	$LaCrO_{3-\delta}$	570.86	$SmFeO_{3-\delta}$	401.32	$LaFeO_{3-\delta}$	377.56
$Na_{0.625}K_{0.375}Mo_{0.875}V_{0.125}O_{3-\delta}$	342.40	286.42	350.40		$NaMoO_{3-\delta}$	319.41	$KMoO_{3-\delta}$	405.11	$NaVO_{3-\delta}$	287.56	$KVO_{3-\delta}$	374.19
$LaMnO_{3-\delta}$	353.27	353.27	353.27		$LaMnO_{3-\delta}$	353.27						
$Sm_{0.25}La_{0.75}Cr_{0.5}Fe_{0.5}O_{3-\delta}$	353.33	353.33	353.33	yes	$SmCrO_{3-\delta}$	415.04	$LaCrO_{3-\delta}$	570.86	$SmFeO_{3-\delta}$	401.32	$LaFeO_{3-\delta}$	377.56
$Na_{0.5}K_{0.5}MoO_{3-\delta}$	362.81	362.81	362.81		$NaMoO_{3-\delta}$	319.41	$KMoO_{3-\delta}$	405.11				
$KVO_{3-\delta}$	374.19	374.19	374.19		$KVO_{3-\delta}$	374.19						
$LaFeO_{3-\delta}$	377.56	377.56	377.56		$LaFeO_{3-\delta}$	377.56						
$EuVO_{3-\delta}$	381.81	381.81	381.81		$EuVO_{3-\delta}$	381.81						
$SmVO_{3-\delta}$	382.21	382.21	382.21		$SmVO_{3-\delta}$	382.21						
$SmMnO_{3-\delta}$	388.21	388.21	388.21		$SmMnO_{3-\delta}$	388.21						
$Sm_{0.25}La_{0.75}Cr_{0.625}Fe_{0.375}O_{3-\delta}$	390.31	390.31	390.31	yes	$SmCrO_{3-\delta}$	415.04	$LaCrO_{3-\delta}$	570.86	$SmFeO_{3-\delta}$	401.32	$LaFeO_{3-\delta}$	377.56
$Ca_{0.25}Sr_{0.75}Ti_{0.75}Mn_{0.25}O_{3-\delta}$	396.73	396.73	396.73	yes	$CaTiO_{3-\delta}$	578.97	$SrTiO_{3-\delta}$	589.85	$CaMnO_{3-\delta}$	173.13	$SrMnO_{3-\delta}$	170.33
$RbMoO_{3-\delta}$	398.52	398.52	398.52		$RbMoO_{3-\delta}$	398.52						
$SmFeO_{3-\delta}$	401.32	401.32	401.32		$SmFeO_{3-\delta}$	401.32						
$KMoO_{3-\delta}$	405.11	405.11	405.11		$KMoO_{3-\delta}$	405.11						
$Sr_{0.875}Ba_{0.125}Ti_{0.75}Mn_{0.25}O_{3-\delta}$	407.83	407.83	407.83	yes	$SrTiO_{3-\delta}$	589.85	$BaTiO_{3-\delta}$	588.75	$SrMnO_{3-\delta}$	170.33	$BaMnO_{3-\delta}$	252.31
$Sm_{0.375}La_{0.625}Cr_{0.75}Fe_{0.25}O_{3-\delta}$	408.22	408.22	408.22	yes	$SmCrO_{3-\delta}$	415.04	$LaCrO_{3-\delta}$	570.86	$SmFeO_{3-\delta}$	401.32	$LaFeO_{3-\delta}$	377.56
$SmCrO_{3-\delta}$	415.04	415.04	415.04		$SmCrO_{3-\delta}$	415.04						
$RbVO_{3-\delta}$	422.16	422.16	422.16		$RbVO_{3-\delta}$	422.16						

Redox Material	ΔH_{DFT}	ΔH_{min}	ΔH_{max}	diff>30	EM 1	ΔH_{EM1}	EM 2	ΔH_{EM2}	EM 3	ΔH_{EM3}	EM 4	ΔH_{EM4}
$Na_{0.5}K_{0.5}W_{0.125}Mo_{0.875}O_{3-\delta}$	423.65	423.65	423.65	yes	$NaWO_{3-\delta}$	434.58	$KWO_{3-\delta}$	508.05	$NaMoO_{3-\delta}$	319.41	$KMoO_{3-\delta}$	405.11
$Sm_{0.375}La_{0.625}Cr_{0.875}Fe_{0.125}O_{3-\delta}$	433.61	433.61	433.61	yes	$SmCrO_{3-\delta}$	415.04	$LaCrO_{3-\delta}$	570.86	$SmFeO_{3-\delta}$	401.32	$LaFeO_{3-\delta}$	377.56
$NaWO_{3-\delta}$	434.58	434.58	434.58		$NaWO_{3-\delta}$	434.58						
$Sm_{0.125}La_{0.875}VO_{3-\delta}$	455.88	455.88	455.88		*missing data for $LaVO_{3-\delta}$*							
$Na_{0.5}K_{0.5}W_{0.25}Mo_{0.75}O_{3-\delta}$	451.70	451.70	451.70	yes	$NaWO_{3-\delta}$	434.58	$KWO_{3-\delta}$	508.05	$NaMoO_{3-\delta}$	319.41	$KMoO_{3-\delta}$	405.11
$Sm_{0.375}La_{0.625}CrO_{3-\delta}$	455.88	455.88	455.88	yes	$SmCrO_{3-\delta}$	415.04	$LaCrO_{3-\delta}$	570.86	$SmCrO_{3-\delta}$	415.04	$SmCrO_{3-\delta}$	415.04
$Sm_{0.375}La_{0.625}V_{0.25}Cr_{0.75}O_{3-\delta}$	468.90	468.90	468.90		*missing data for $LaVO_{3-\delta}$*							
$Sm_{0.375}La_{0.625}V_{0.125}Cr_{0.875}O_{3-\delta}$	469.00	469.00	469.00		*missing data for $LaVO_{3-\delta}$*							
$Na_{0.5}K_{0.5}W_{0.375}Mo_{0.625}O_{3-\delta}$	486.14	486.14	486.14	yes	$NaWO_{3-\delta}$	434.58	$KWO_{3-\delta}$	508.05	$NaMoO_{3-\delta}$	319.41	$KMoO_{3-\delta}$	405.11
$Na_{0.5}K_{0.5}WO_{3-\delta}$	488.95	488.95	488.95		$NaWO_{3-\delta}$	434.58	$KWO_{3-\delta}$	508.05				
$Sm_{0.25}La_{0.75}V_{0.5}Cr_{0.5}O_{3-\delta}$	489.89	489.89	489.89		*missing data for $LaVO_{3-\delta}$*							
$Sm_{0.25}La_{0.75}V_{0.625}Cr_{0.375}O_{3-\delta}$	490.79	490.79	490.79		*missing data for $LaVO_{3-\delta}$*							
$Sm_{0.25}La_{0.75}V_{0.375}Cr_{0.625}O_{3-\delta}$	492.03	492.03	492.03		*missing data for $LaVO_{3-\delta}$*							
$Na_{0.375}K_{0.625}Nb_{0.5}W_{0.5}O_{3-\delta}$	494.87	494.87	494.87		*missing data for $NaNbO_{3-\delta}$*							
$Sr_{0.625}Ba_{0.375}Ti_{0.875}Mn_{0.125}O_{3-\delta}$	495.35	495.35	495.35	yes	$SrTiO_{3-\delta}$	589.85	$BaTiO_{3-\delta}$	588.75	$SrMnO_{3-\delta}$	170.33	$BaMnO_{3-\delta}$	252.31
$Na_{0.5}K_{0.5}Nb_{0.375}W_{0.625}O_{3-\delta}$	497.38	497.38	497.38		*missing data for $NaNbO_{3-\delta}$*							
$Ca_{0.125}Sr_{0.875}Ti_{0.875}Mn_{0.125}O_{3-\delta}$	497.69	497.69	497.69	yes	$CaTiO_{3-\delta}$	578.97	$SrTiO_{3-\delta}$	589.85	$CaMnO_{3-\delta}$	173.13	$SrMnO_{3-\delta}$	170.33
$Sr_{0.875}Ba_{0.125}Ti_{0.875}Mn_{0.125}O_{3-\delta}$	497.73	497.73	497.73	yes	$SrTiO_{3-\delta}$	589.85	$BaTiO_{3-\delta}$	588.75	$SrMnO_{3-\delta}$	170.33	$BaMnO_{3-\delta}$	252.31
$Na_{0.5}K_{0.5}Nb_{0.25}W_{0.75}O_{3-\delta}$	500.92	500.92	500.92		*missing data for $NaNbO_{3-\delta}$*							
$Na_{0.375}K_{0.625}Nb_{0.625}W_{0.375}O_{3-\delta}$	504.46	504.46	504.46		*missing data for $NaNbO_{3-\delta}$*							
$KWO_{3-\delta}$	508.05	508.05	508.05		$KWO_{3-\delta}$	508.05						
$Sm_{0.25}La_{0.75}V_{0.75}Cr_{0.25}O_{3-\delta}$	509.16	509.16	509.16		*missing data for $LaVO_{3-\delta}$*							
$Sm_{0.125}La_{0.875}V_{0.875}Cr_{0.125}O_{3-\delta}$	509.22	509.22	509.22		*missing data for $LaVO_{3-\delta}$*							
$Sm_{0.125}La_{0.875}Ti_{0.25}V_{0.75}O_{3-\delta}$	509.53	509.53	509.53		*missing data for $LaVO_{3-\delta}$*							

Redox Material	ΔH_{DFT}	ΔH_{min}	ΔH_{max}	diff>30	EM 1	ΔH_{EM1}	EM 2	ΔH_{EM2}	EM 3	ΔH_{EM3}	EM 4	ΔH_{EM4}
$Na_{0.375}K_{0.625}Nb_{0.75}W_{0.25}O_{3-\delta}$	510.96	510.96	510.96		*missing data for $NaNbO_{3-\delta}$*							
$Sm_{0.125}La_{0.875}Ti_{0.125}V_{0.875}O_{3-\delta}$	511.97	511.97	511.97		*missing data for $LaVO_{3-\delta}$*							
$Sm_{0.125}La_{0.875}Ti_{0.375}V_{0.625}O_{3-\delta}$	514.30	514.30	514.30		*missing data for $LaVO_{3-\delta}$*							
$RbWO_{3-\delta}$	517.61	517.61	517.61		$RbWO_{3-\delta}$	517.61						
$Na_{0.5}K_{0.5}W_{0.5}Mo_{0.5}O_{3-\delta}$	519.41	519.41	519.41	yes	$NaWO_{3-\delta}$	434.58	$KWO_{3-\delta}$	508.05	$NaMoO_{3-\delta}$	319.41	$KMoO_{3-\delta}$	405.11
$Na_{0.5}K_{0.5}W_{0.625}Mo_{0.375}O_{3-\delta}$	522.02	522.02	522.02	yes	$NaWO_{3-\delta}$	434.58	$KWO_{3-\delta}$	508.05	$NaMoO_{3-\delta}$	319.41	$KMoO_{3-\delta}$	405.11
$Na_{0.5}K_{0.5}W_{0.75}Mo_{0.25}O_{3-\delta}$	522.72	522.72	522.72	yes	$NaWO_{3-\delta}$	434.58	$KWO_{3-\delta}$	508.05	$NaMoO_{3-\delta}$	319.41	$KMoO_{3-\delta}$	405.11
$Na_{0.375}K_{0.625}Nb_{0.875}W_{0.125}O_{3-\delta}$	523.02	523.02	523.02		*missing data for $NaNbO_{3-\delta}$*							
$Na_{0.5}K_{0.5}Nb_{0.125}W_{0.875}O_{3-\delta}$	524.84	524.84	524.84		*missing data for $NaNbO_{3-\delta}$*							
$Na_{0.5}K_{0.5}W_{0.875}Mo_{0.125}O_{3-\delta}$	526.37	526.37	526.37	yes	$NaWO_{3-\delta}$	434.58	$KWO_{3-\delta}$	508.05	$NaMoO_{3-\delta}$	319.41	$KMoO_{3-\delta}$	405.11
$Na_{0.375}K_{0.625}NbO_{3-\delta}$	529.59	529.59	529.59		*missing data for $NaNbO_{3-\delta}$*							
$Na_{0.375}K_{0.625}Ta_{0.125}Nb_{0.875}O_{3-\delta}$	538.93	538.93	538.93		*missing data for $NaNbO_{3-\delta}$*							
$Na_{0.375}K_{0.625}Ta_{0.25}Nb_{0.75}O_{3-\delta}$	548.04	548.04	548.04		*missing data for $NaNbO_{3-\delta}$*							
$Na_{0.375}K_{0.625}Ta_{0.375}Nb_{0.625}O_{3-\delta}$	558.23	558.23	558.23		*missing data for $NaNbO_{3-\delta}$*							
$Na_{0.375}K_{0.625}Ta_{0.5}Nb_{0.5}O_{3-\delta}$	567.34	567.34	567.34		*missing data for $NaNbO_{3-\delta}$*							
$LaCrO_{3-\delta}$	570.86	570.86	570.86		$LaCrO_{3-\delta}$	570.86						
$CaTiO_{3-\delta}$	578.97	578.97	578.97		$CaTiO_{3-\delta}$	578.97						
$Ca_{0.125}Sr_{0.875}TiO_{3-\delta}$	584.67	584.67	584.67		$CaTiO_{3-\delta}$	578.97	$SrTiO_{3-\delta}$	589.85				
$Na_{0.375}K_{0.625}Ta_{0.625}Nb_{0.375}O_{3-\delta}$	585.41	585.41	585.41		*missing data for $NaNbO_{3-\delta}$*							
$EuTiO_{3-\delta}$	586.90	586.90	586.90		$EuTiO_{3-\delta}$	586.90						
$BaTiO_{3-\delta}$	588.75	588.75	588.75		$BaTiO_{3-\delta}$	588.75						
$Sr_{0.625}Ba_{0.375}TiO_{3-\delta}$	589.22	589.22	589.22		$SrTiO_{3-\delta}$	589.85	$BaTiO_{3-\delta}$	588.75				
$Sr_{0.875}Ba_{0.125}TiO_{3-\delta}$	589.44	589.44	589.44		$SrTiO_{3-\delta}$	589.85	$BaTiO_{3-\delta}$	588.75				
$SrTiO_{3-\delta}$	589.85	589.85	589.85		$SrTiO_{3-\delta}$	589.85						

Redox Material	ΔH_{DFT}	ΔH_{min}	ΔH_{max}	diff>30	EM 1	ΔH_{EM1}	EM 2	ΔH_{EM2}	EM 3	ΔH_{EM3}	EM 4	ΔH_{EM4}
$KNbO_{3-\delta}$	594.00	594.00	594.00		$KNbO_{3-\delta}$	594.00						
$Na_{0.375}K_{0.625}Ta_{0.75}Nb_{0.25}O_{3-\delta}$	606.41	606.41	606.41		*missing data for $NaNbO_{3-\delta}$*							
$RbNbO_{3-\delta}$	624.20	624.20	624.20		$RbNbO_{3-\delta}$	624.20						
$Na_{0.375}K_{0.625}Ta_{0.875}Nb_{0.125}O_{3-\delta}$	625.94	625.94	625.94		*missing data for $NaNbO_{3-\delta}$*							
$LaTiO_{3-\delta}$	633.41	633.41	633.41		$LaTiO_{3-\delta}$	633.41						
$NaTaO_{3-\delta}$	646.24	646.24	646.24		$NaTaO_{3-\delta}$	646.24						
$SmTiO_{3-\delta}$	654.10	654.10	654.10		$SmTiO_{3-\delta}$	654.10						
$KTaO_{3-\delta}$	660.41	660.41	660.41		$KTaO_{3-\delta}$	660.41						
$MgTiO_{3-\delta}$	696.82	696.82	696.82		$MgTiO_{3-\delta}$	696.82						
$RbTaO_{3-\delta}$	705.99	705.99	705.99		$RbTaO_{3-\delta}$	705.99						

8.4 References: Python libraries

The thermodynamics and materials data for the experimentally and theoretically studied phases were evaluated using a python library created for this purpose in a collaborative effort between the Lawrence Berkeley National Laboratory (USA) and the author of this work. The package also includes javacript/HTML interfaces for user interaction to create "Isographs" and plot the energy analysis graphs for the perovskite search engine.
The full source code in its current and previous versions is available through GitHub in the MPContribs repository:
https://github.com/materialsproject/MPContribsUsers/tree/master/redox_thermo_csp

Please note that this python library is constantly being optimized and updated, which means that the version used to generate data shown in this work is not necessarily the latest version. To reproduce the data shown herein, the following back-up version as of November 2018 can be used:
https://github.com/josuav1/MPContribsUsers-Nov-2018-/tree/master/redox_thermo_csp

The efficiency calculation (heat-to-fuel efficiency) as shown within this work is not part of the public version of RedoxThermoCSP as of November 2018. It will be added in a later stage, as a more detailed coverage of this topic is part of ongoing studies. This data, however, can be generated manually using the RedoxThermoCSP code, or by using the product-specific energy demand and Eq. 2.55.

Part of this code and this work are also based on another python library called "solar_perovskite", which is not part of Materials Project. The solar_perovskite code also contains many functions not discussed within this work such as a plot showing the optimum temperature levels for reduction and oxidation and a script to create lists of redox enthalpies for all oxide phases in Materials Project (based on pymatgen [126]). Parts of these functionalities are still under development and may be made publicly available as a part of future studies. In that case, this library will be published in a later stage through:
https://github.com/josuav1/solar_perovskite/tree/master/solar_perovskite/ (not yet available to the public)

8.5 Generation of Isographs

We denote graphs describing the equilibrium state of perovskite solid solutions as “Isographs”. If functions describing $\Delta H(\delta, T, p_{O_2})$ and $\Delta S(\delta, T, p_{O_2})$ are known, one can draw six different plots defining the redox properties of the perovskite:

1. **Isotherms**

The temperature T is fixed and the non-stoichiometry δ is calculated as a function of p_{O_2}. The parameters ΔH_{min}, ΔH_{max}, act, and the Debye temperatures of the perovskite and brownmillerite $\Theta_{D,perov}$ and $\Theta_{D,brownm}$ are derived as described before, and are independent of δ, T, and p_{O_2}. $\Delta H(\delta, T)$ is calculated according to Eq. 2.23 and $\Delta S(\delta, T)$ is determined using Eq. 2.24. The change in Gibbs free energy is then given as (assuming $p^0 = 1$ bar):

$$\Delta G(\delta, T, p_{O_2}) = \Delta H(\delta, T) - T \cdot \Delta S(\delta, T) + \frac{1}{2} RT \cdot \ln(p_{O_2}) \tag{8.1}$$

For different values of p_{O_2} and a fixed T, δ values can be found so that the system is in equilibrium:

$$\Delta G(\delta, T, p_{O_2}) = 0 \tag{8.2}$$

Finding values so that 8.2 is true can be performed using Richard P. Brent’s algorithms, [283] or any other suitable method. This results in a plot of δ vs. p_{O_2} describing the chemical equilibrium. The plot can be drawn using any two functions of $\Delta H(\delta, T)$ and $\Delta S(\delta, T)$, for instance using fit functions derived for experimental data, or using a different theoretical model.

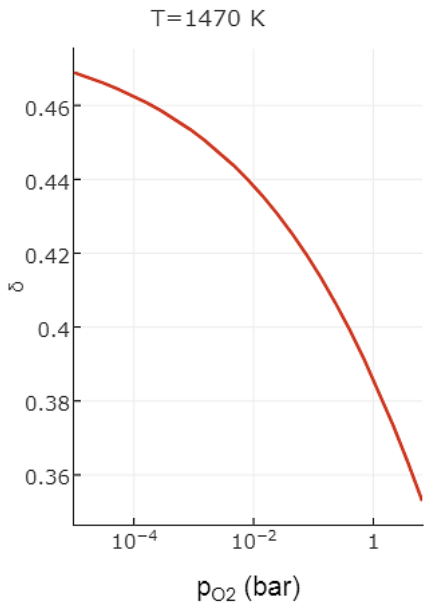

Fig. 8.1. Exemplary isothermal representation of the equilibrium between a perovskite solid solution and an atmosphere around it containing oxygen at different p_{O_2} levels.

2. Isobars

If the oxygen partial pressure is fixed and instead the temperature is a variable, Eq. 8.1 can be determined in analogy to the isothermal calculations, yielding equilibrium data where Eq. 8.2 is zero. This results in a plot of δ vs. T.

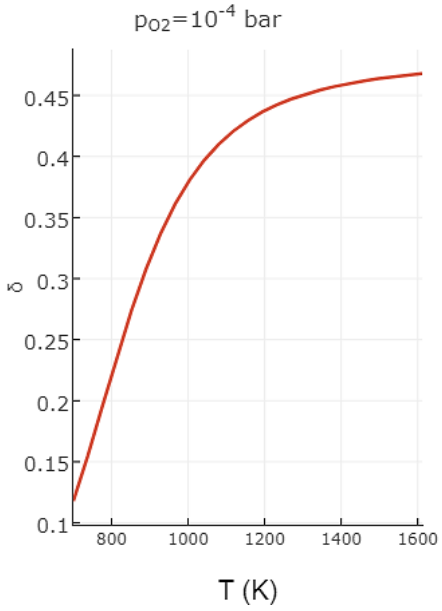

Fig. 8.2. Exemplary isobar describing the equilibrium of a perovskite solid solution with the surrounding atmosphere at $p_{O_2} = 10^{-4}$ bar and different temperatures.

3. Isoredox

In analogy to (1) and (2), the non-stoichiometry δ can be fixed, and Eq. 8.2 can be calculated for different T values, yielding a result for p_{O_2}. These plots are particularly relevant if the resulting δ after reduction of the perovskite has been measured or calculated and the oxygen partial pressure which can be reached during re-oxidation of the perovskite at lower temperature shall be determined.

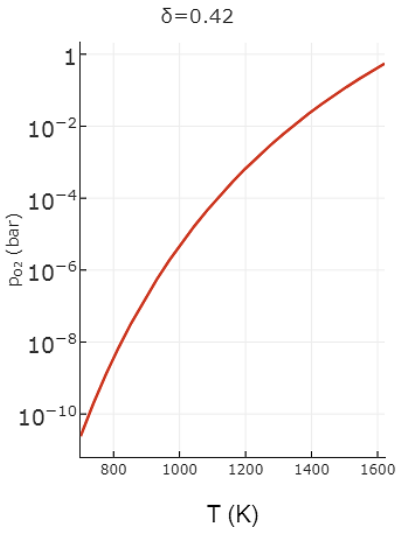

Fig. 8.3. Exemplary isoredox graph showing the dependence of T and p_{O_2} for a perovskite solid solution in equilibrium at constant non-stoichiometry δ.

4. ΔH(δ) at a fixed temperature

Using Eq. 2.23 or any other suitable function, the change of ΔH as a function of the non-stoichiometry δ can be determined. The temperature must be defined if temperature-dependent functions for ΔH are used, such as Eq. 2.23.

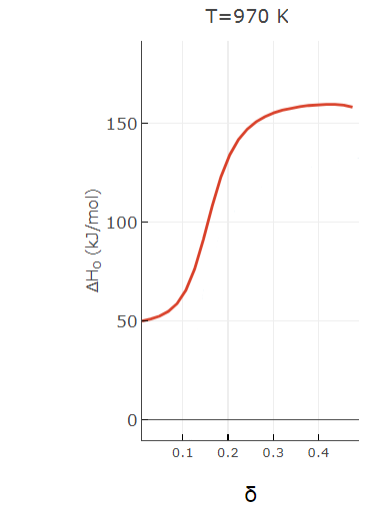

Fig. 8.4. The change in redox enthalpy per mol of oxygen ($\Delta H_O(\delta)$) as a function of the non-stoichiometry δ for an exemplary perovskite solid solution at constant temperature.

5. ΔS(δ) at a fixed temperature

Analogously, the change of ΔS as a function of the non-stoichiometry δ can be determined using a function such as Eq. 2.24.

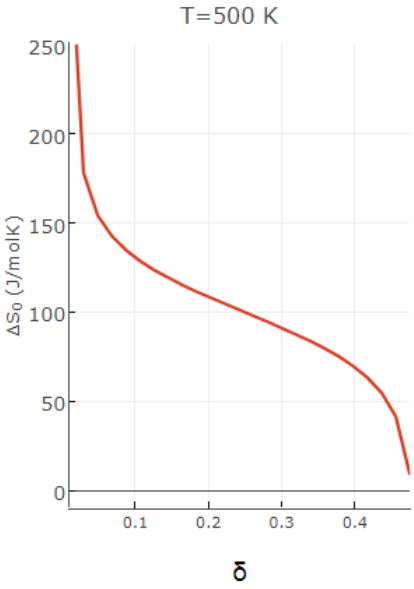

Fig. 8.5. The change in redox entropy per mol of oxygen ($\Delta S_O(\delta)$) as a function of the non-stoichiometry δ for an exemplary perovskite solid solution at constant temperature, consistent of the partial molar entropy of oxygen gas release, the change in vibrational entropy, and the change in configurational entropy.

6. Ellingham diagrams

Ellingham diagrams show the standard Gibbs free energy as a function of the temperature.. In our case, we have to calculate the Ellingham diagrams for a fixed non-stoichiometry δ. The standard Gibbs free energy is defined for p_{O_2} = 1 bar, which yields the following function for ΔG^0:

$$\Delta G^0(\delta, T) = \Delta H(\delta, T) - T \cdot \Delta S(\delta, T) \tag{7.3}$$

If p_{O_2} = 1 bar, the temperature where ΔG^0 is zero corresponds to the temperature at which the fixed non-stoichiometry value δ is reached in equilibrium. For $p_{O_2} \neq 1$ bar, one can draw an "isobar" function f_{iso}, which is defined by:

$$f_{iso}(p_{O_2}, T) = \frac{1}{2} RT \cdot \ln(p_{O_2}) \tag{8.4}$$

According to Eqn. 8.1 and 8.2, the non-stoichiometry value δ is reached where $\Delta G^0(\delta, T) = f_{iso}(p_{O_2}, T)$, i.e., at the intercept of both lines.

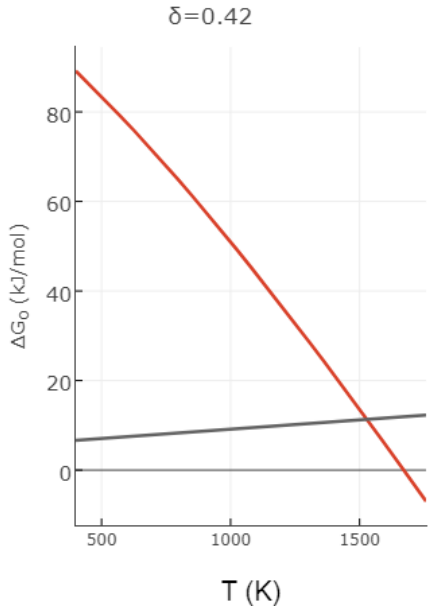

Fig. 8.6. Ellingham diagram for an exemplary perovskite solid solution at fixed non-stoichiometry showing the Gibbs free energy per mol of oxygen ΔG_O and an iso bar line (dark grey) for $p_{O_2} = 10^{-4}$ bar.

8.6 Raw experimental thermodynamic data

The following section is a reprint from part of the supplementary information in Vieten *et. al.* [95]

The thermodynamic data is extracted experimentally as explained in section 3. For all materials, we show plots of $\Delta\delta$ vs. p_{O_2} at constant pressure in the following, together with the resulting $\Delta H(\Delta\delta)$ and $\Delta S(\Delta\delta)$. The data is grouped using the materials composition and sample numbers as given in section 8.2.

For interactive plots including the fits of thermodynamic data, please refer to https://materialsproject.org/mpcontribs/redox_thermo_csp.

$Ca_{0.15}Sr_{0.85}Mn_{0.2}Fe_{0.8}O_{3-\delta}$	75

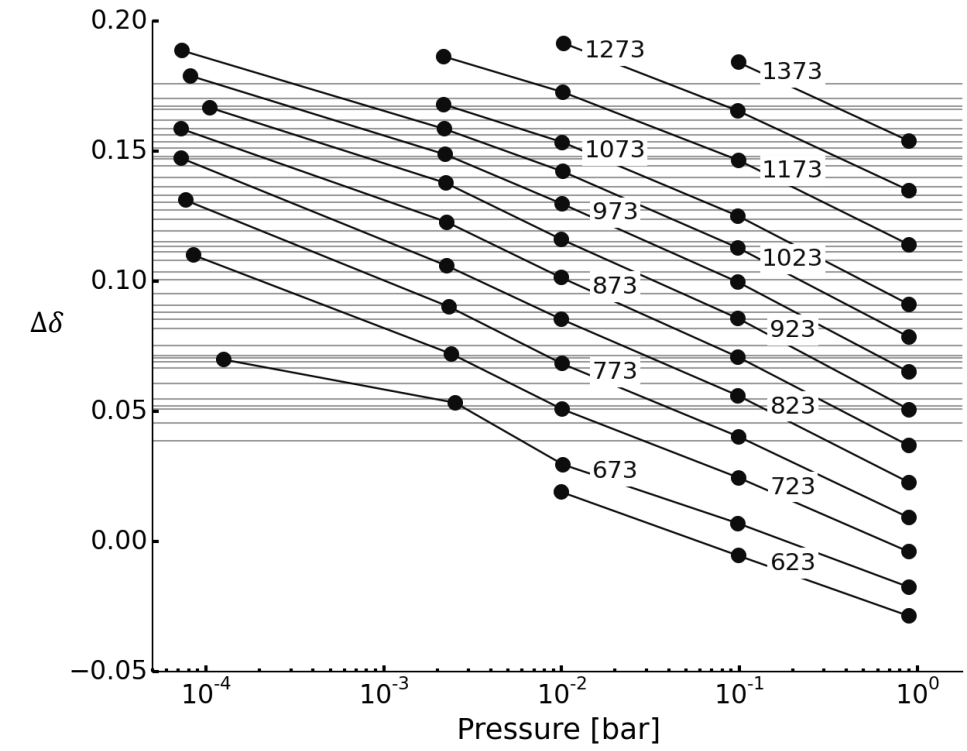

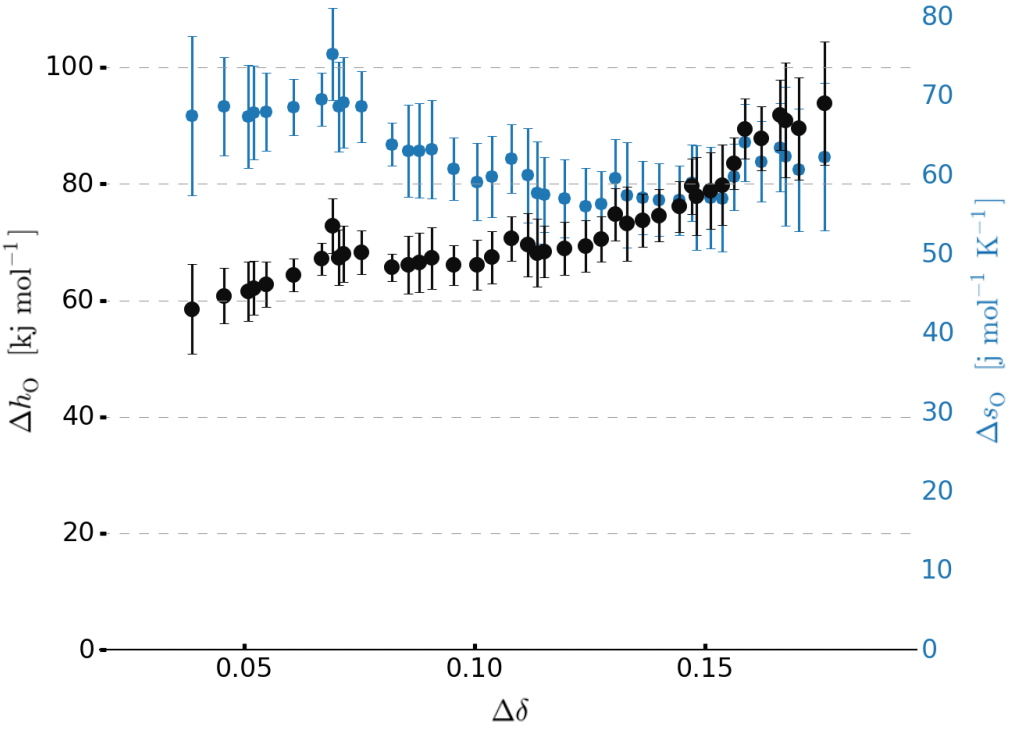

$Ca_{0.30}Sr_{0.70}Mn_{0.4}Fe_{0.6}O_{3-\delta}$	76

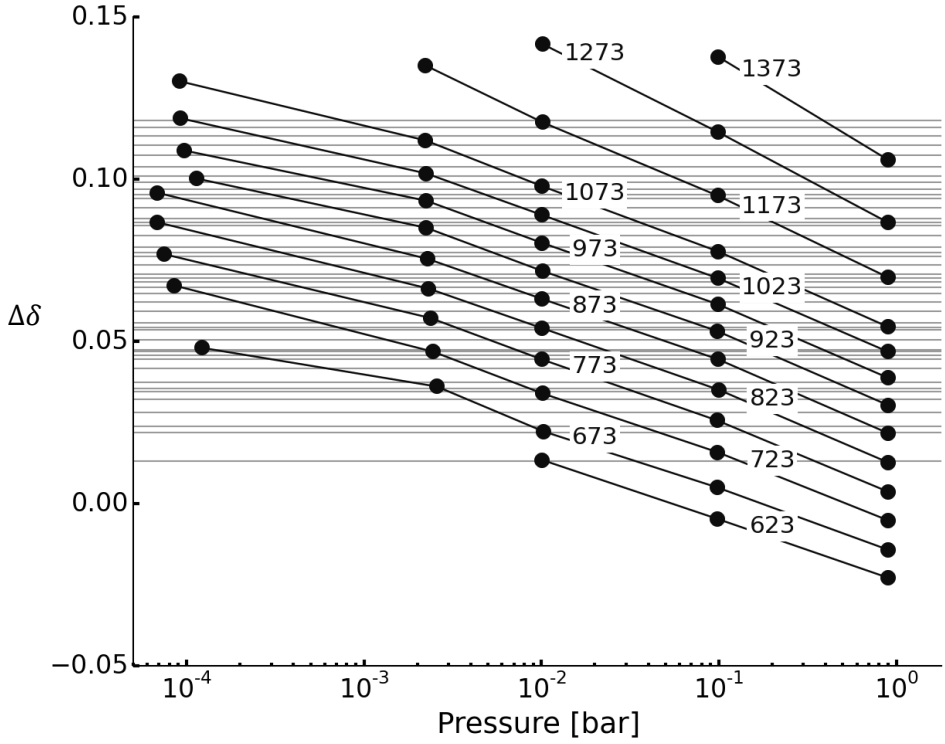

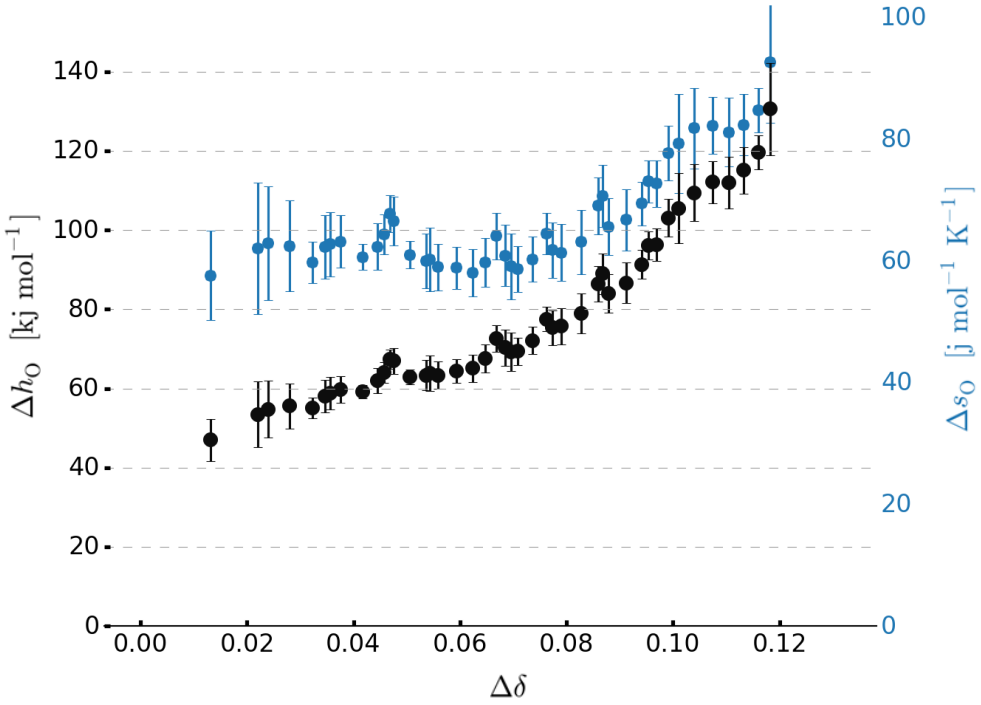

$Ca_{0.45}Sr_{0.55}Mn_{0.6}Fe_{0.4}O_{3-\delta}$	77

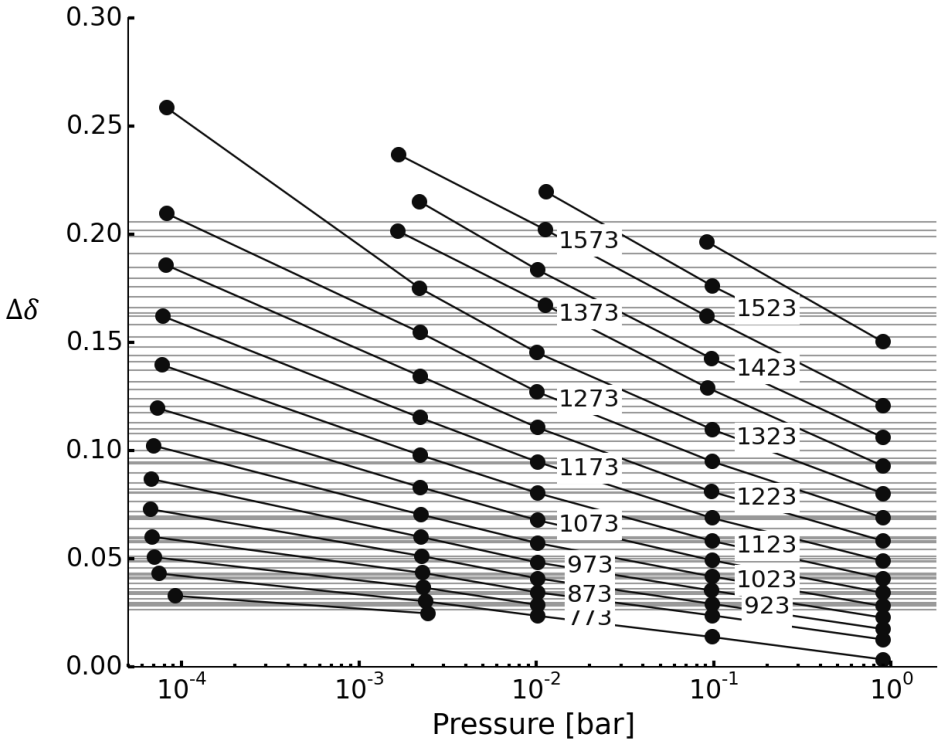

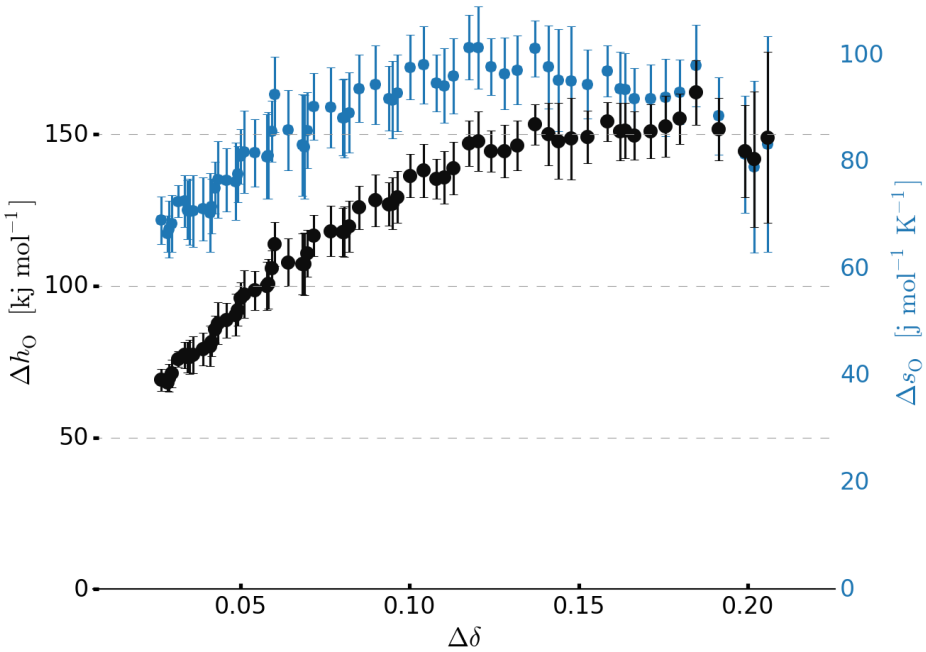

$Ca_{0.60}Sr_{0.40}Mn_{0.8}Fe_{0.2}O_{3-\delta}$	78

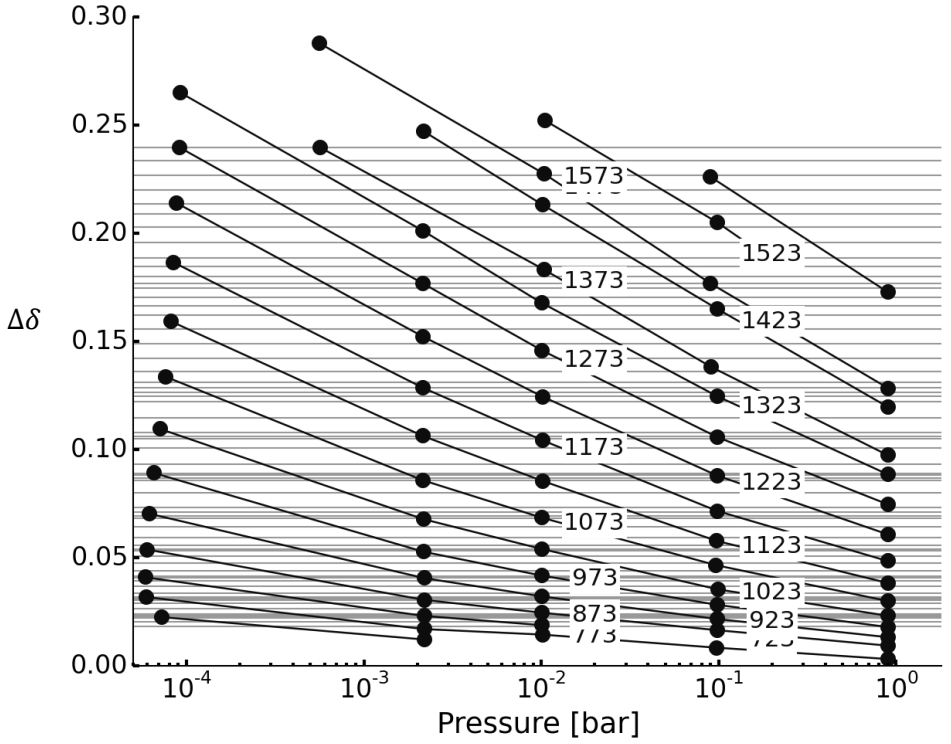

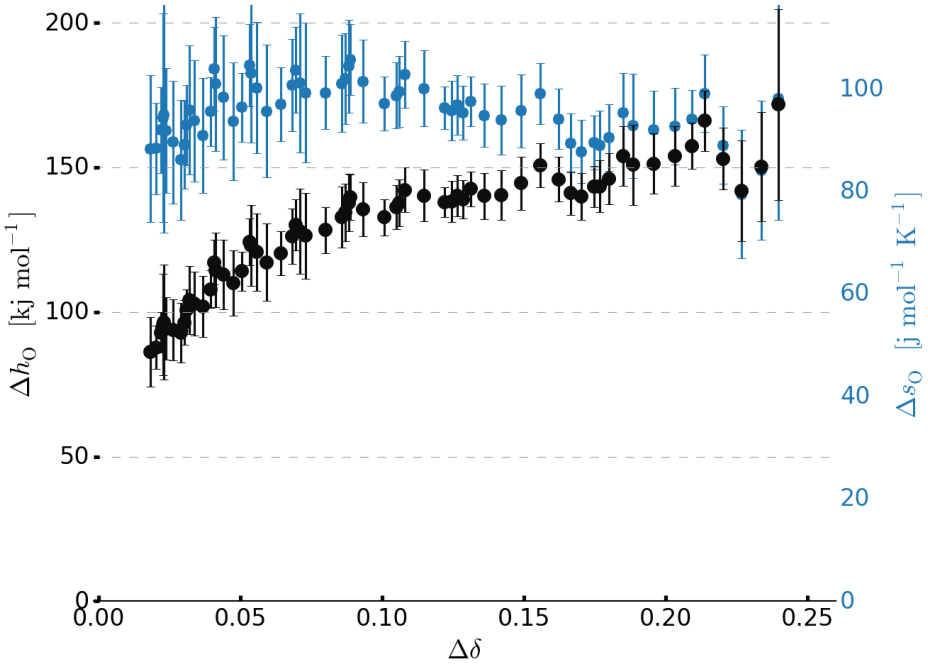

$Ca_{0.75}Sr_{0.25}MnO_{3-\delta}$	79

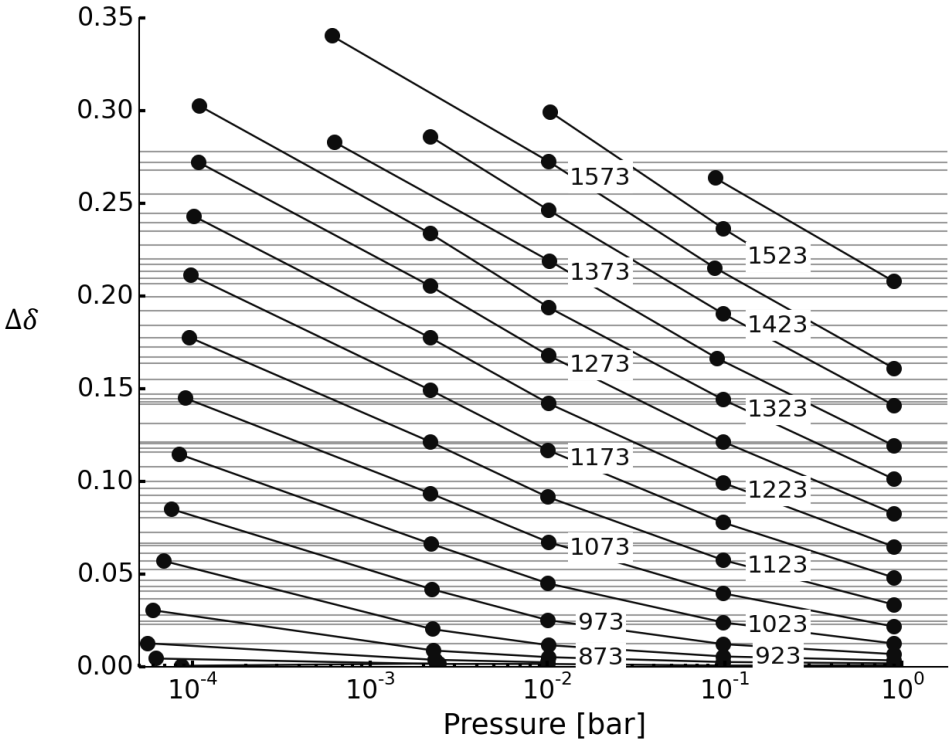

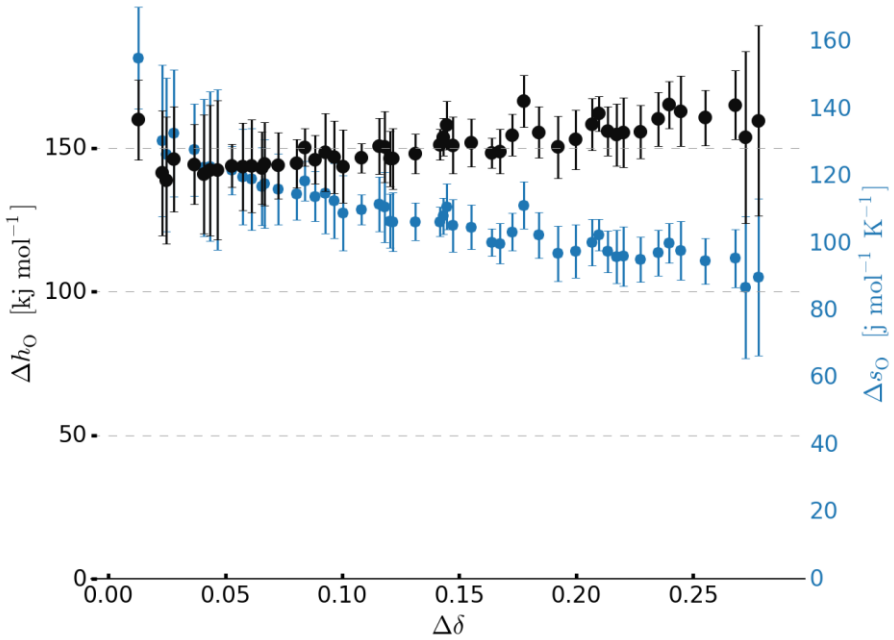

$Ca_{0.54}Sr_{0.46}Ti_{0.2}Mn_{0.8}O_{3-\delta}$	93

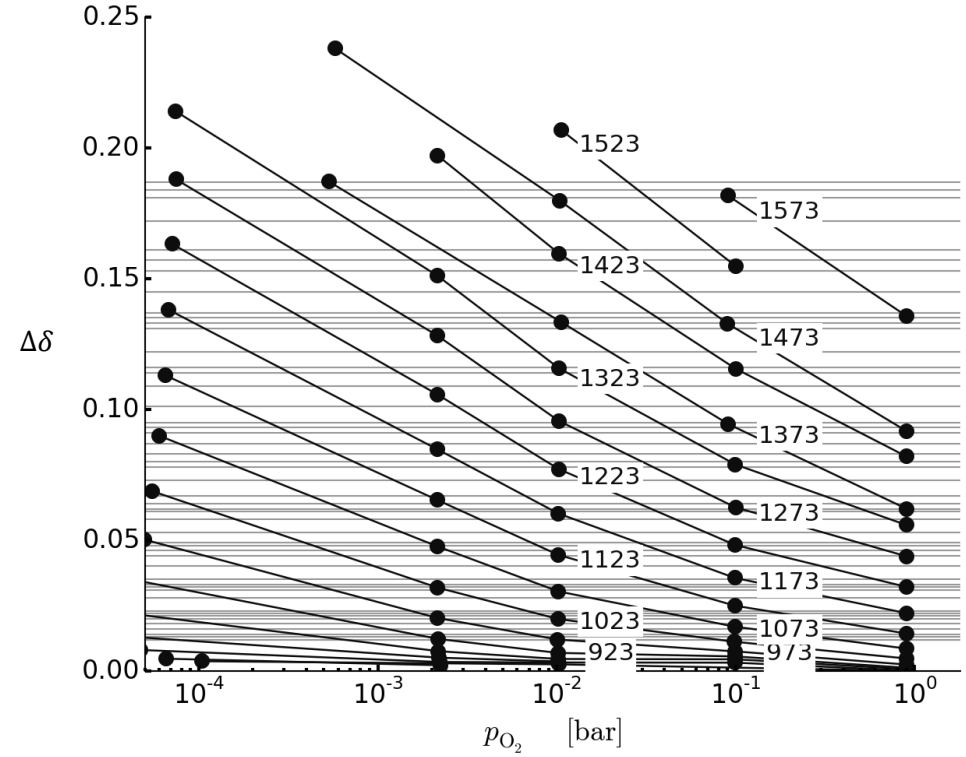

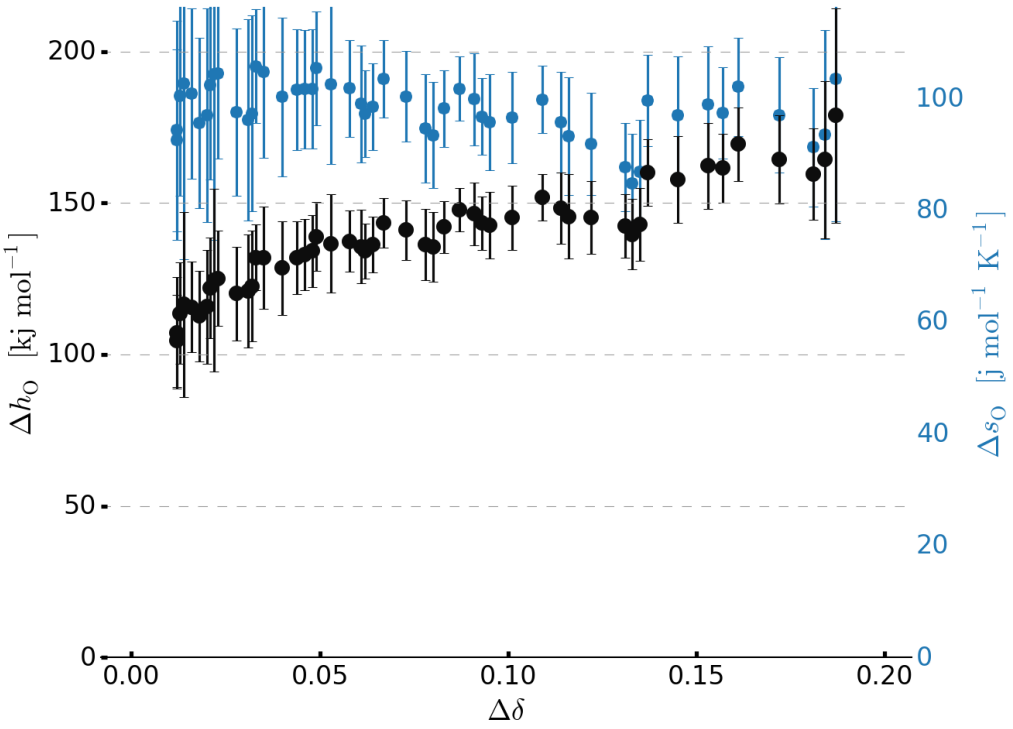

$Ca_{0.34}Sr_{0.66}Ti_{0.4}Mn_{0.6}O_{3-\delta}$	94

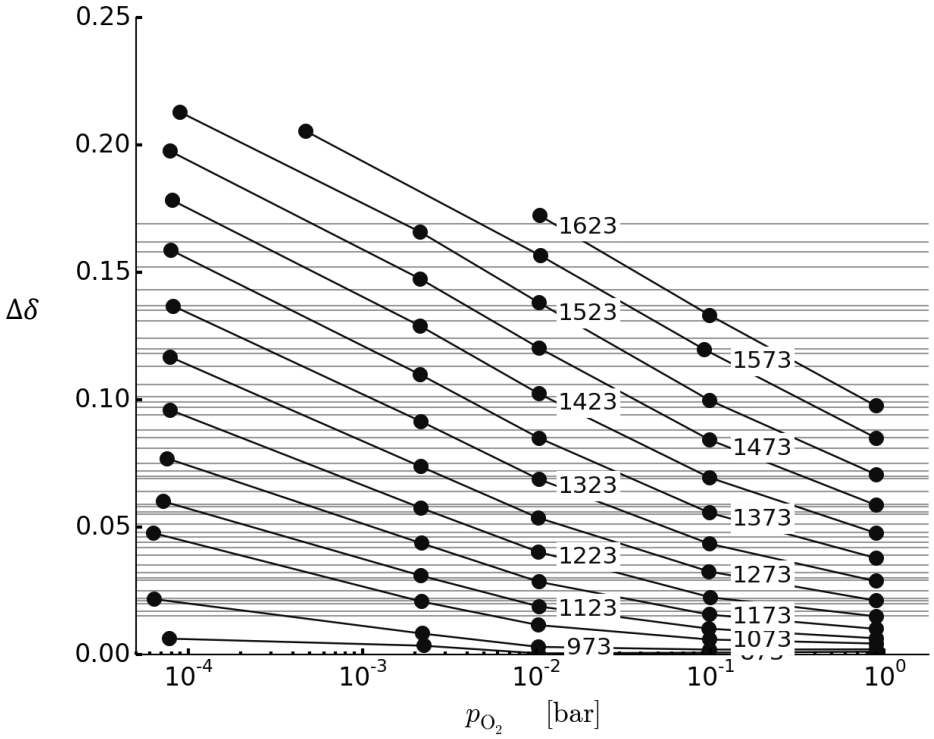

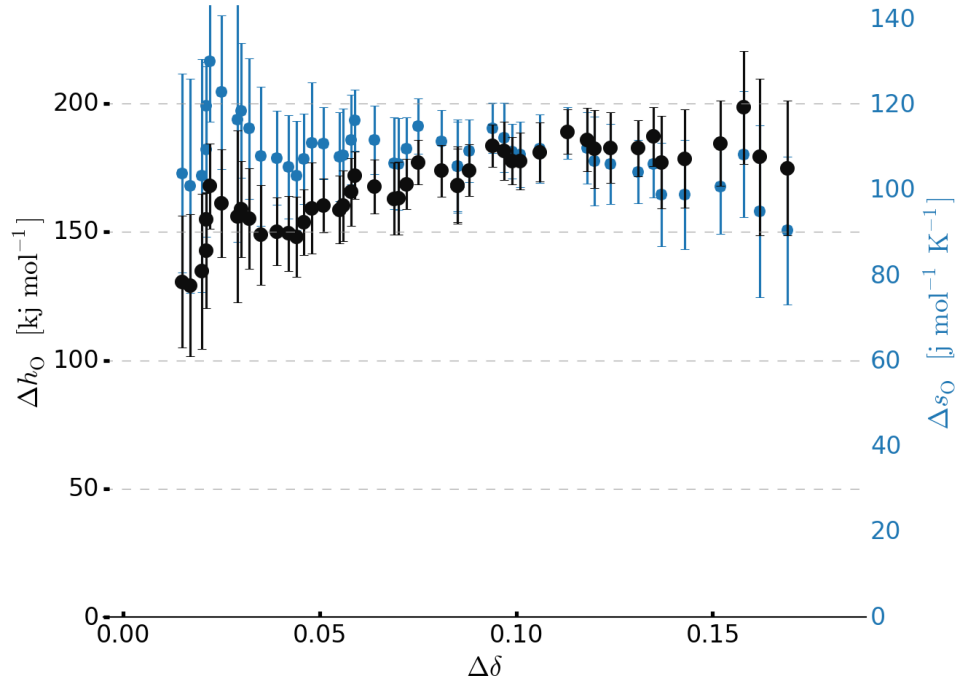

$Ca_{0.13}Sr_{0.87}Ti_{0.6}Mn_{0.4}O_{3-\delta}$	95

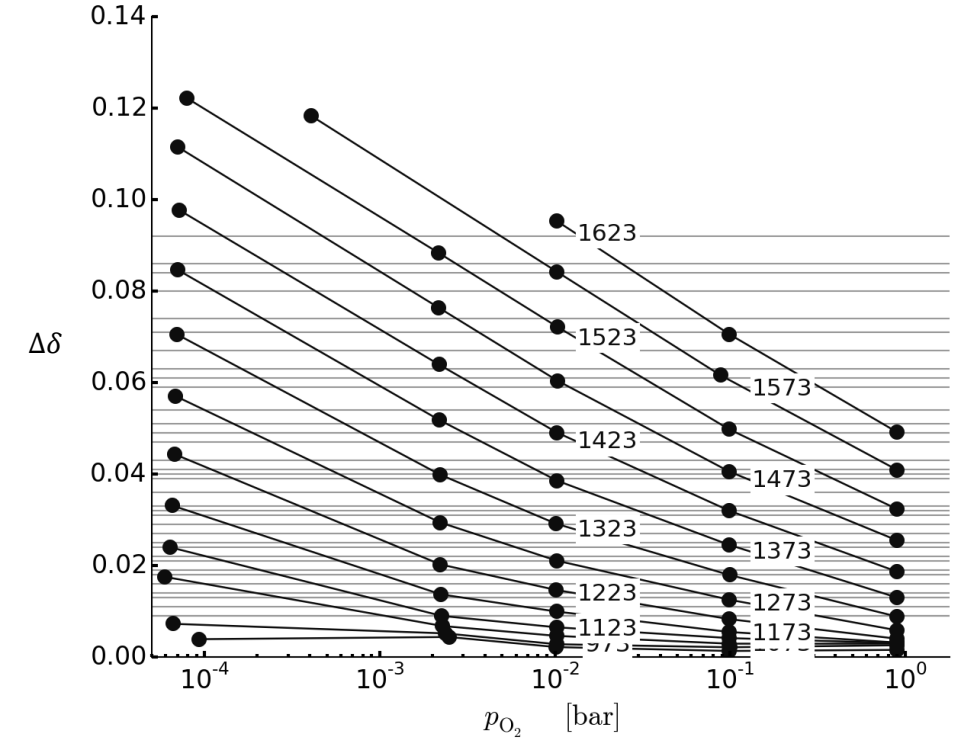

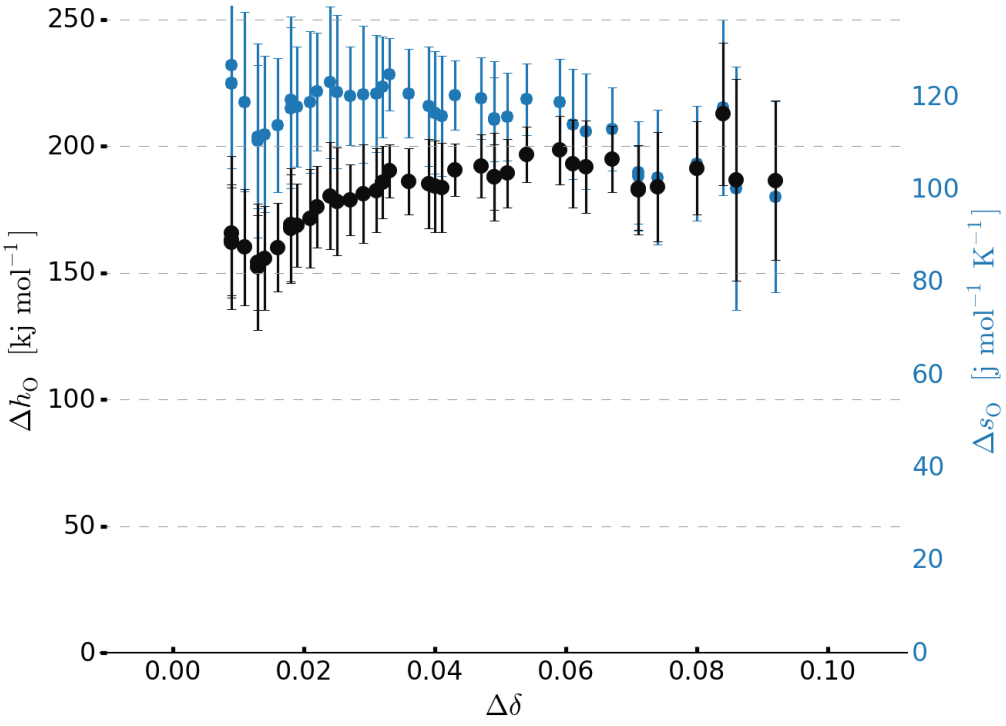

$SrFeO_{3-\delta}$	100

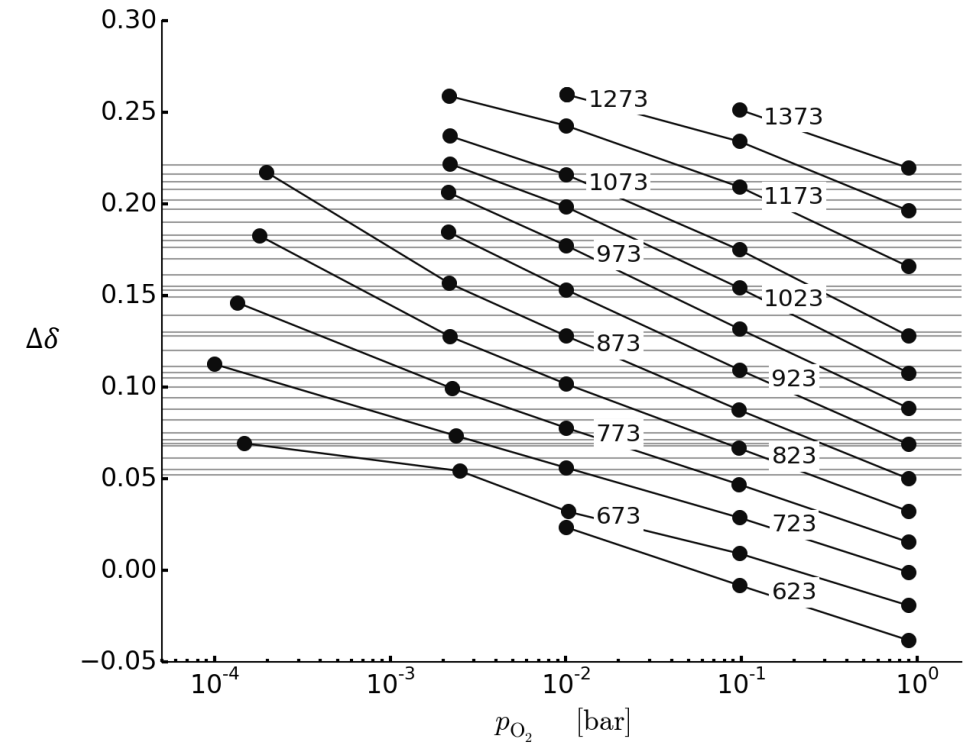

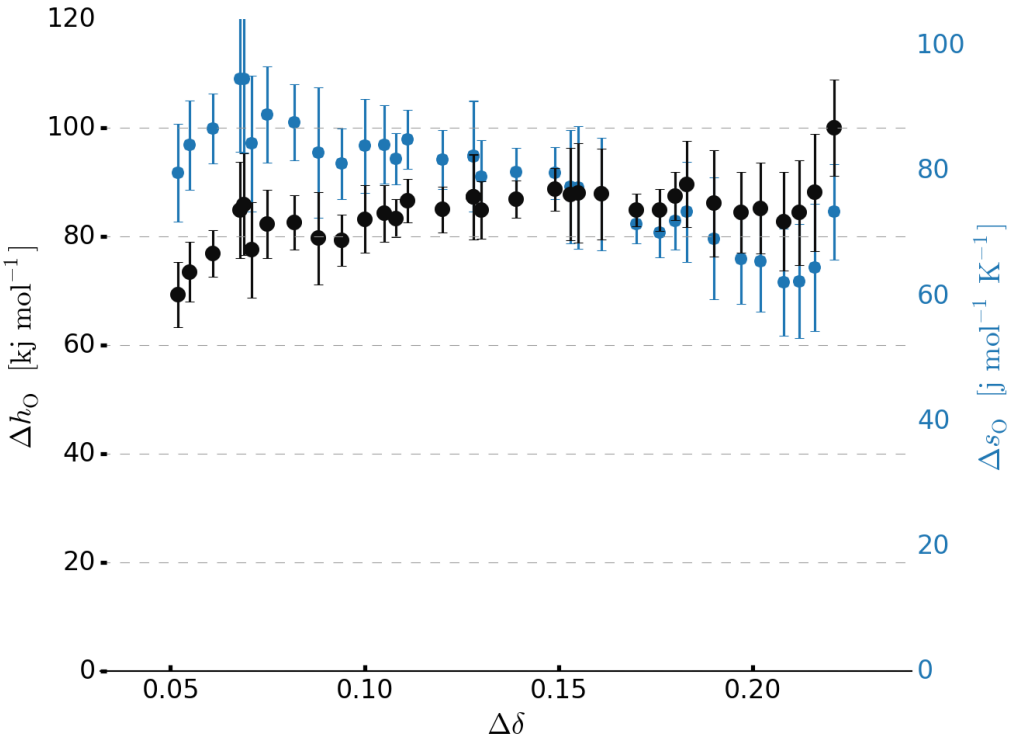

$Ca_{0.87}Sr_{0.13}Mn_{0.8}Fe_{0.2}O_{3-\delta}$	**106**

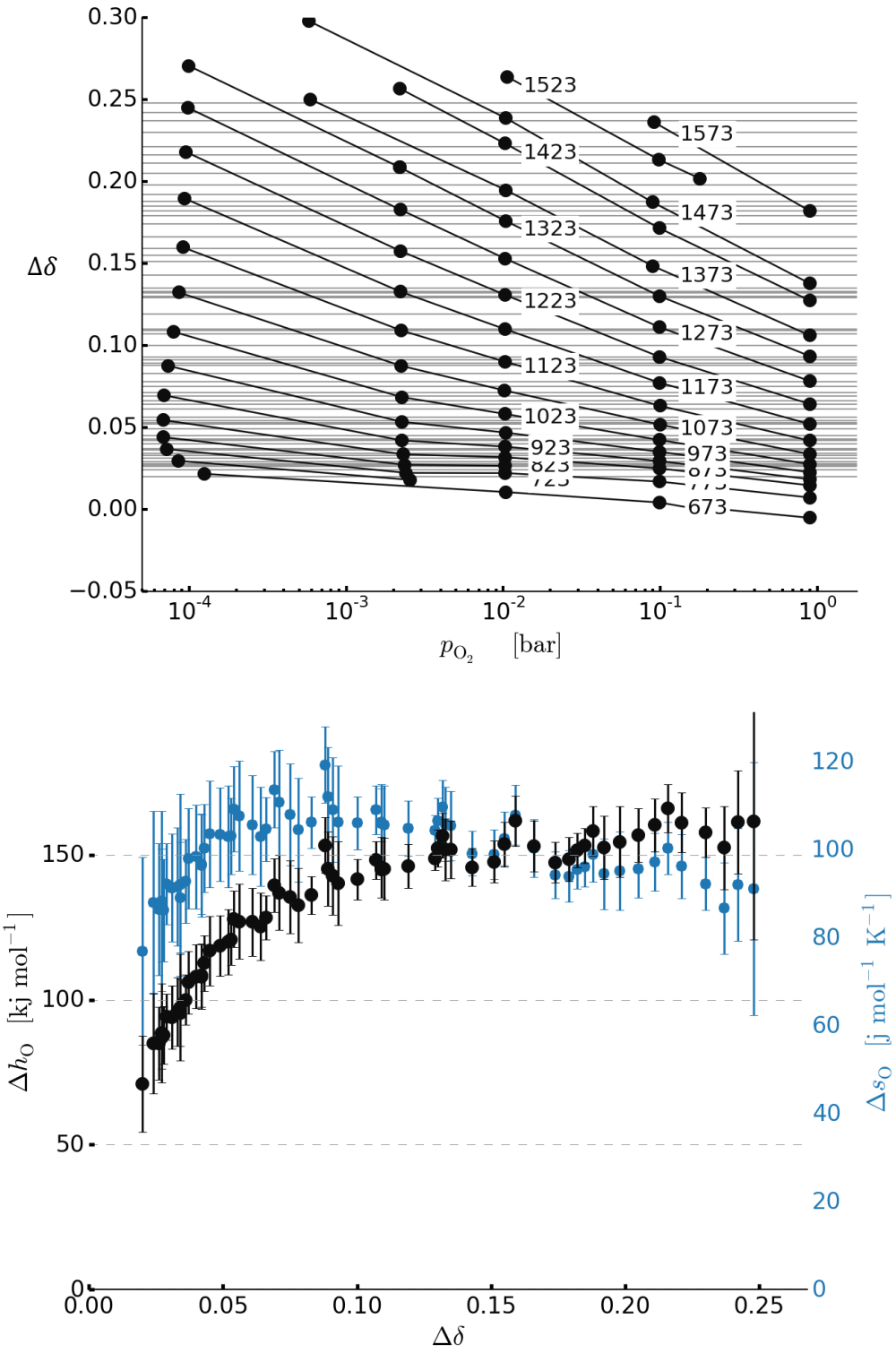

$Ca_{0.73}Sr_{0.27}Mn_{0.6}Fe_{0.4}O_{3-\delta}$	107

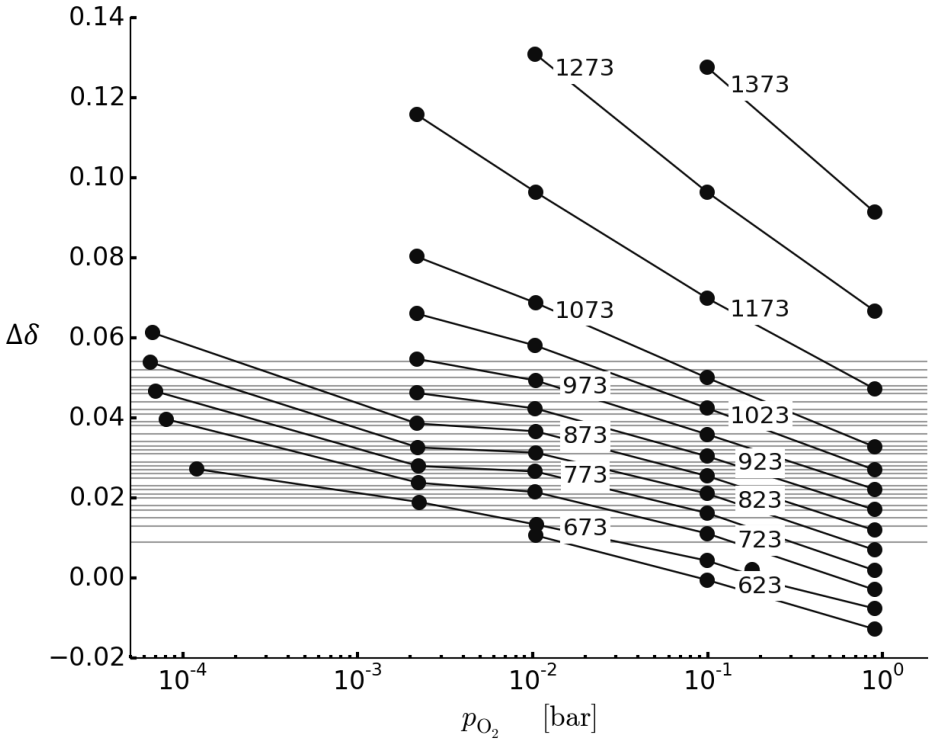

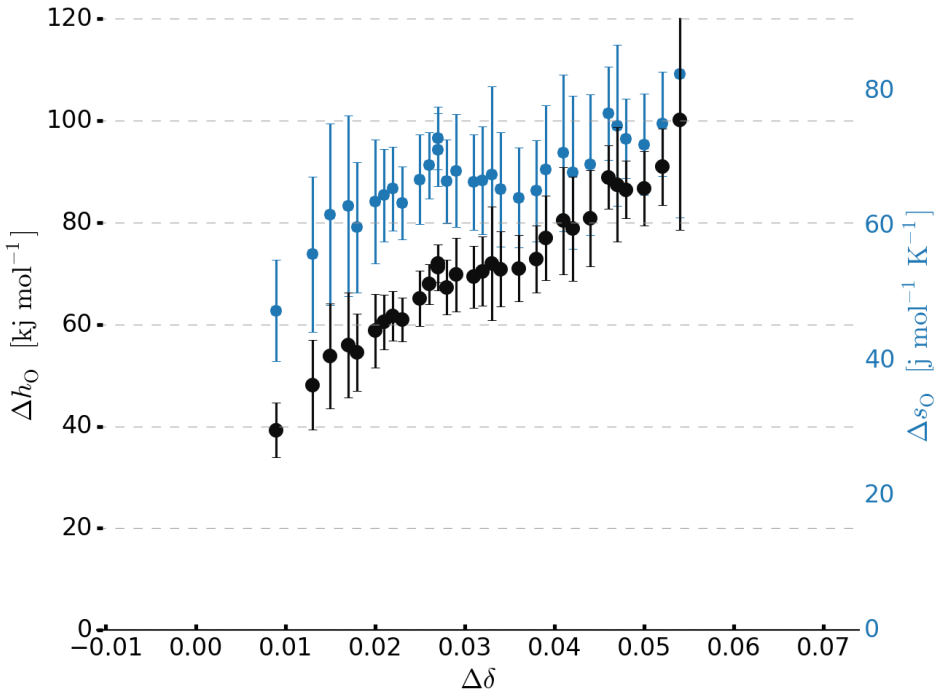

$Ca_{0.58}Sr_{0.42}Mn_{0.4}Fe_{0.6}O_{3-\delta}$	108

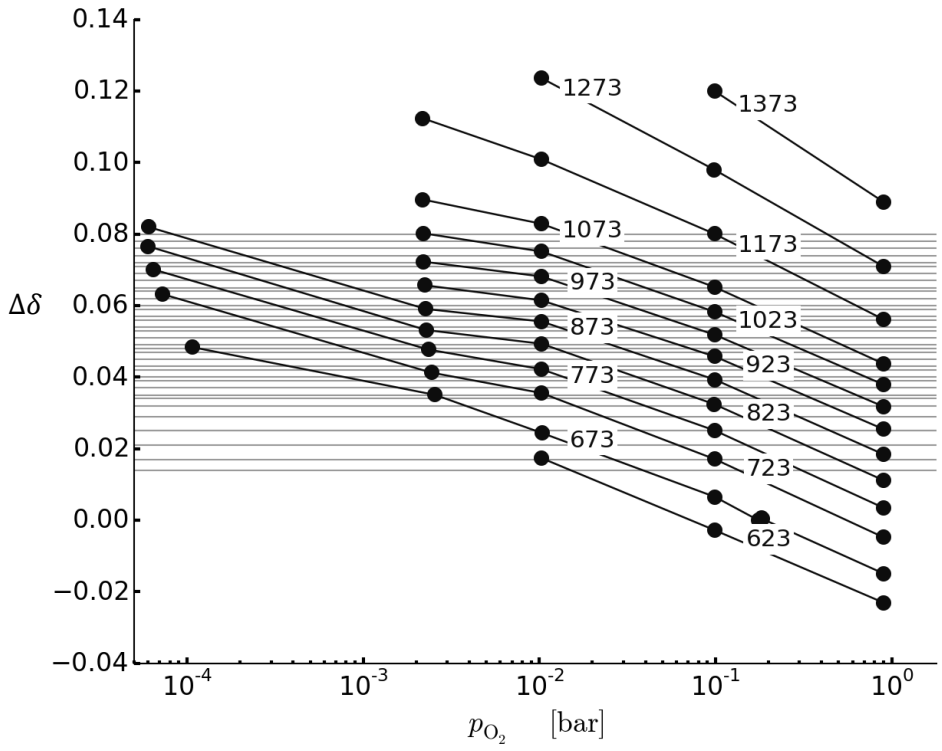

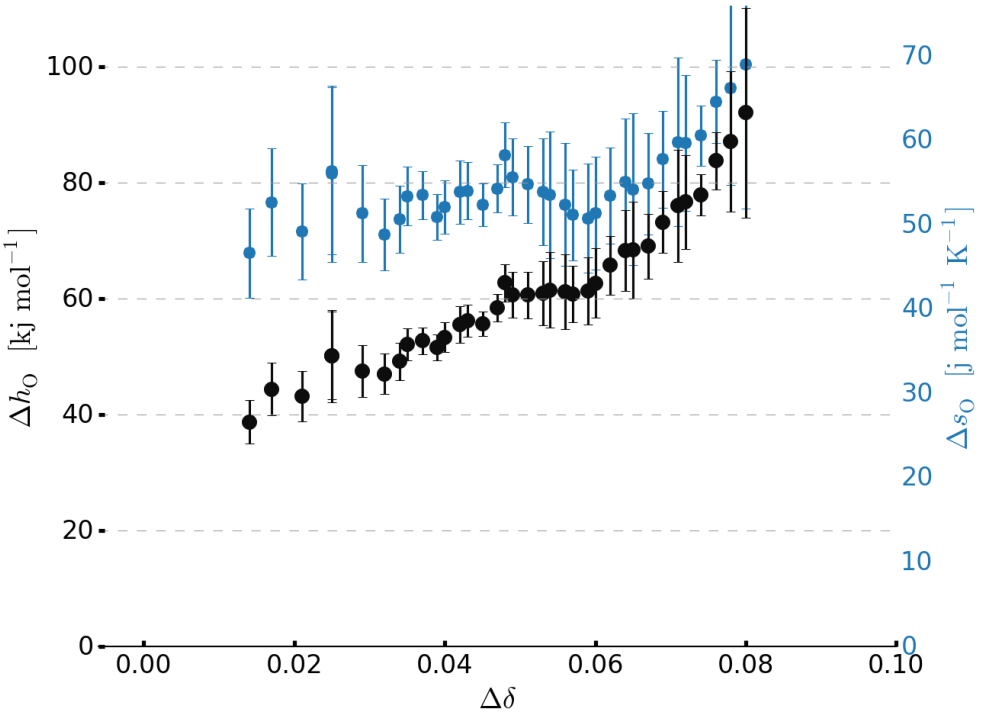

$Ca_{0.44}Sr_{0.56}Mn_{0.2}Fe_{0.8}O_{3-\delta}$	109

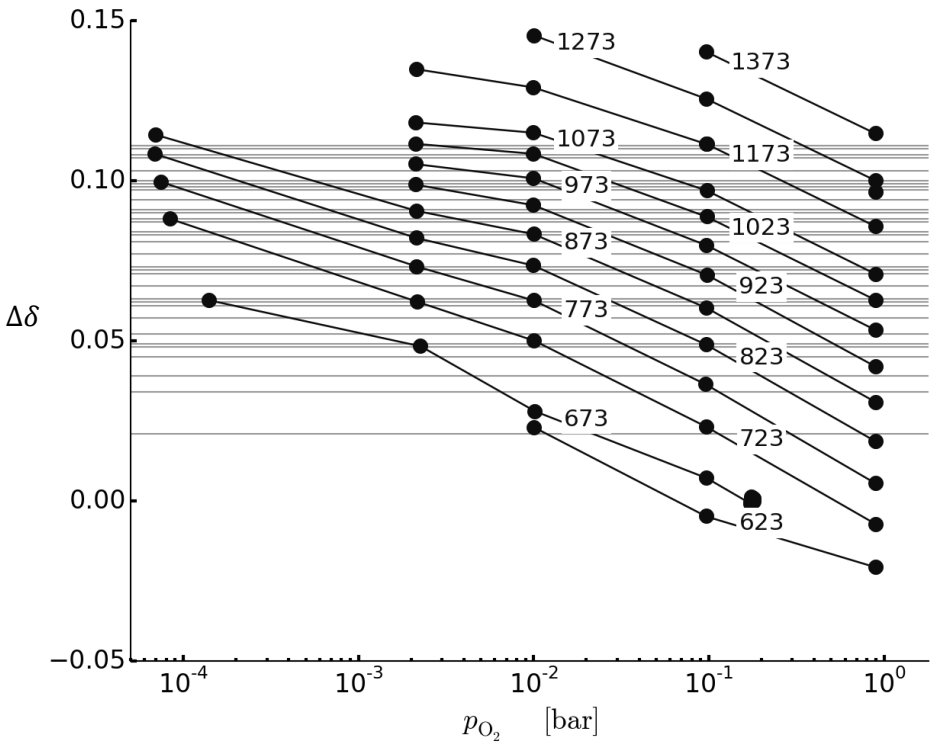

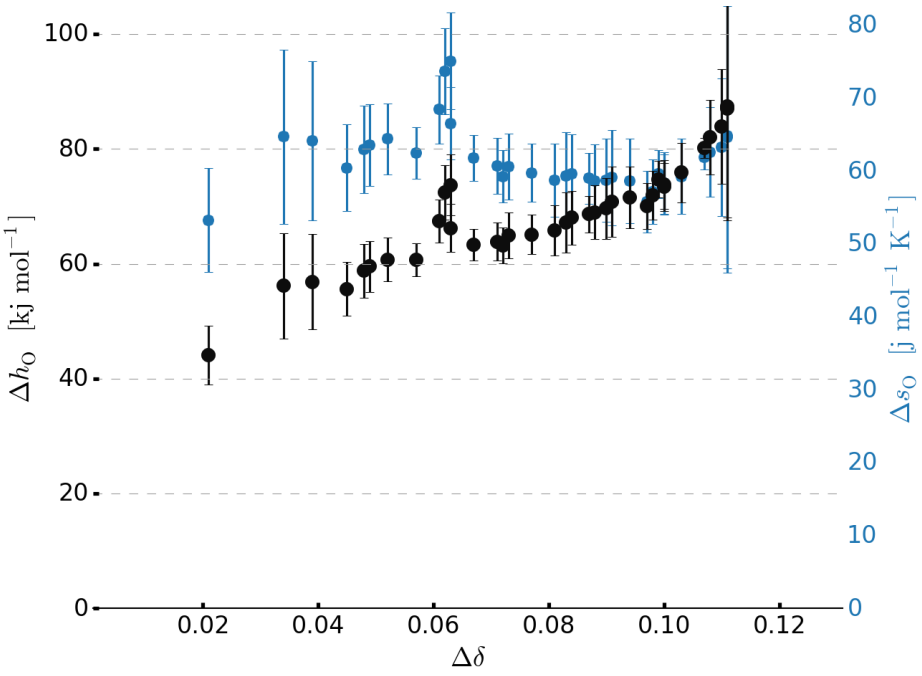

$Ca_{0.29}Sr_{0.71}FeO_{3-\delta}$	110

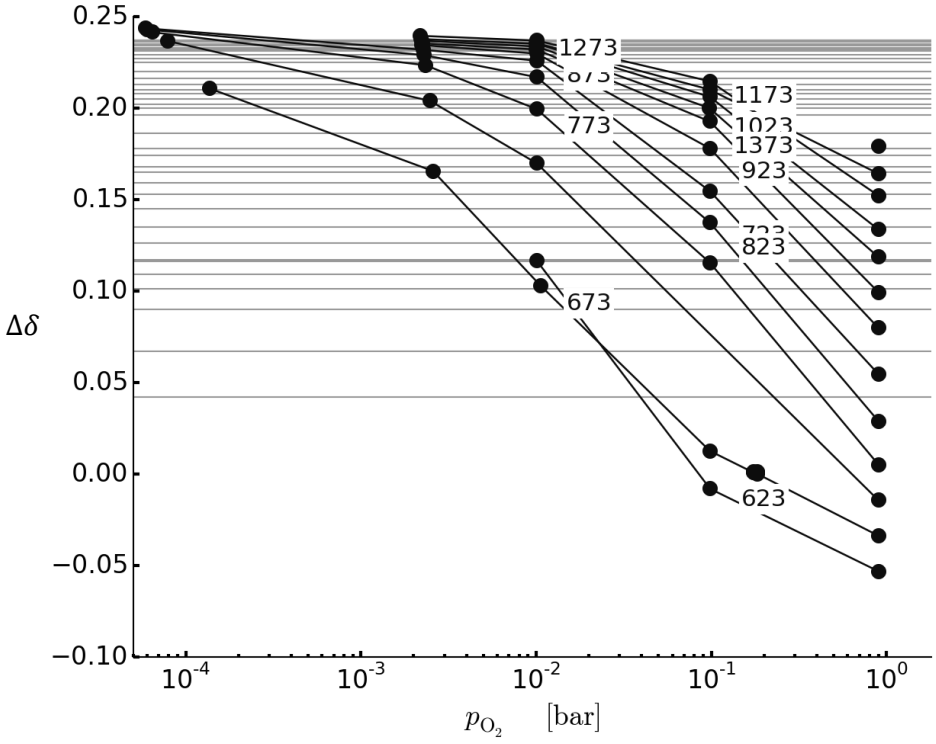

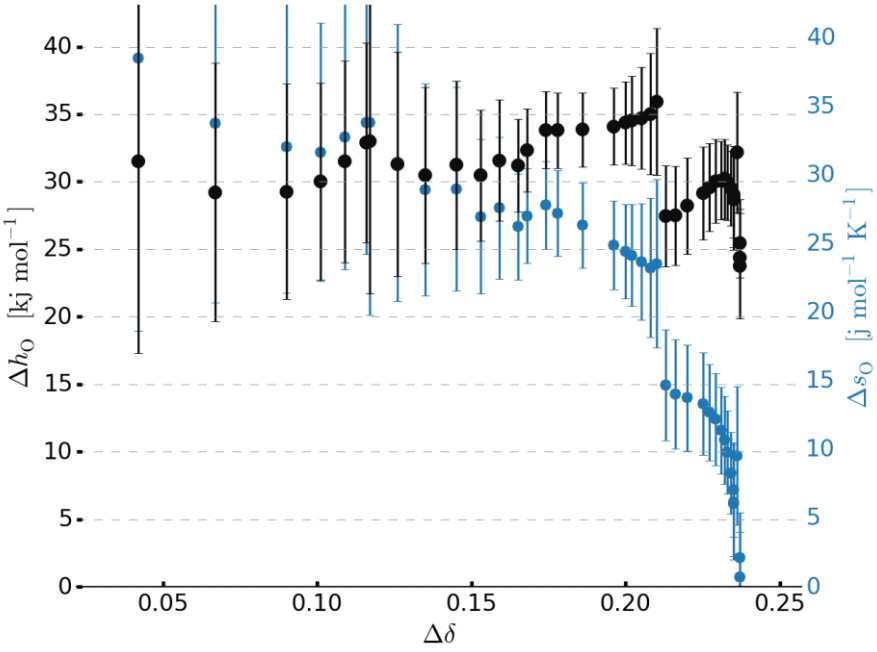

$Ca_{0.92}Sr_{0.08}Ti_{0.1}Mn_{0.9}O_{3-\delta}$	111

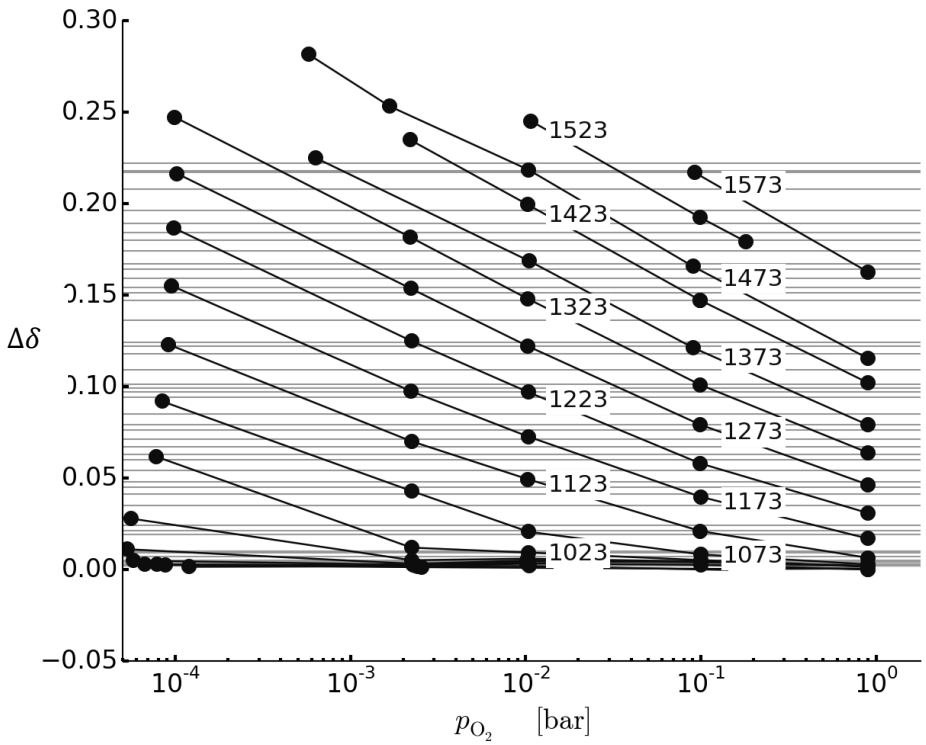

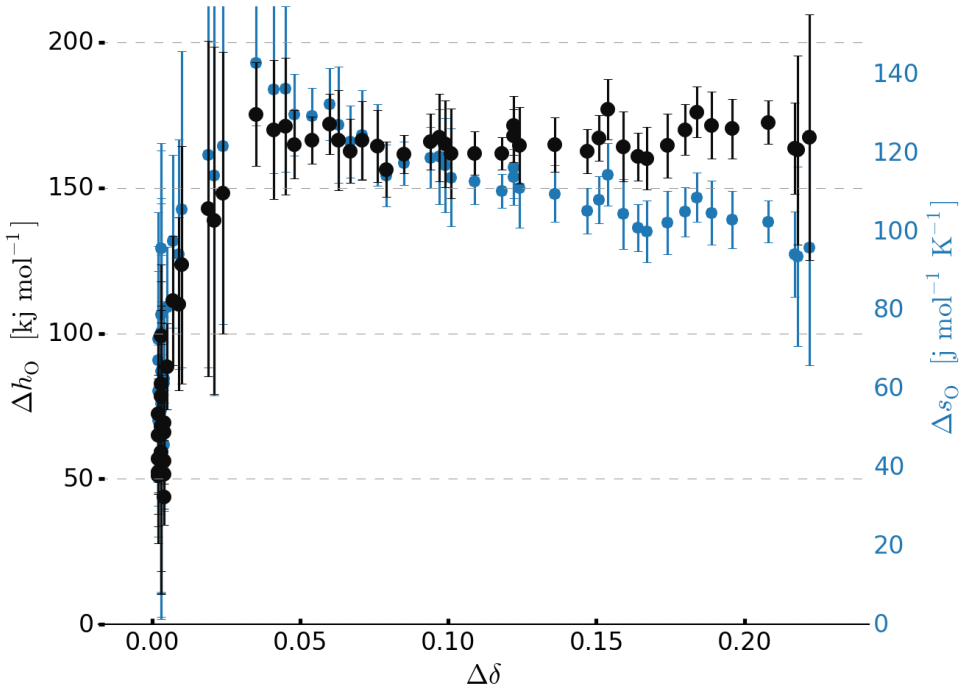

$Ca_{0.82}Sr_{0.18}Ti_{0.2}Mn_{0.8}O_{3-\delta}$	112

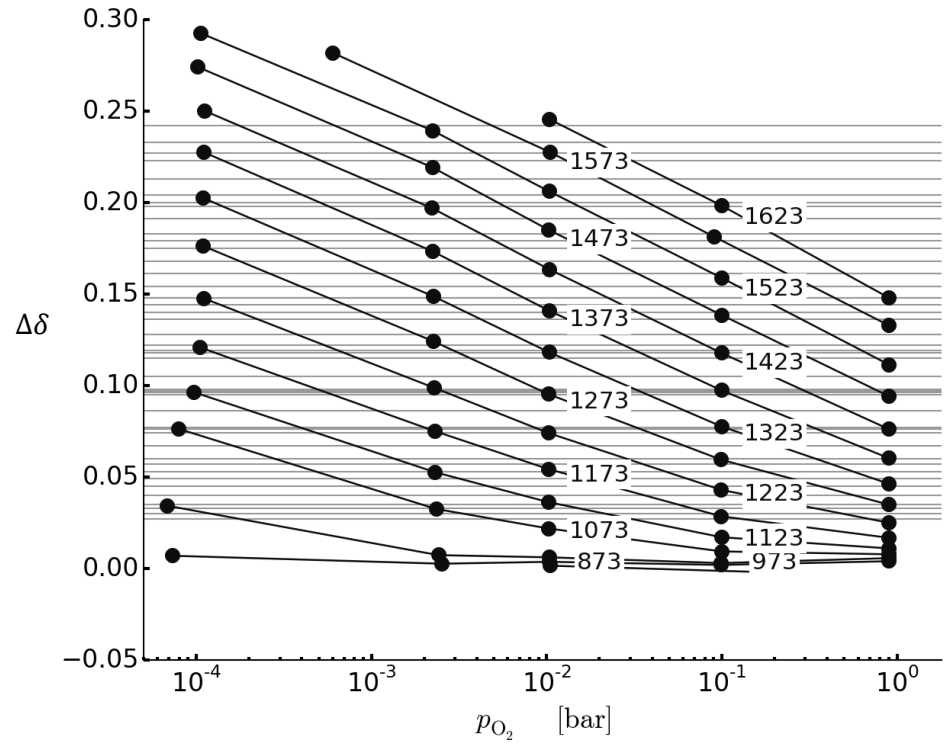

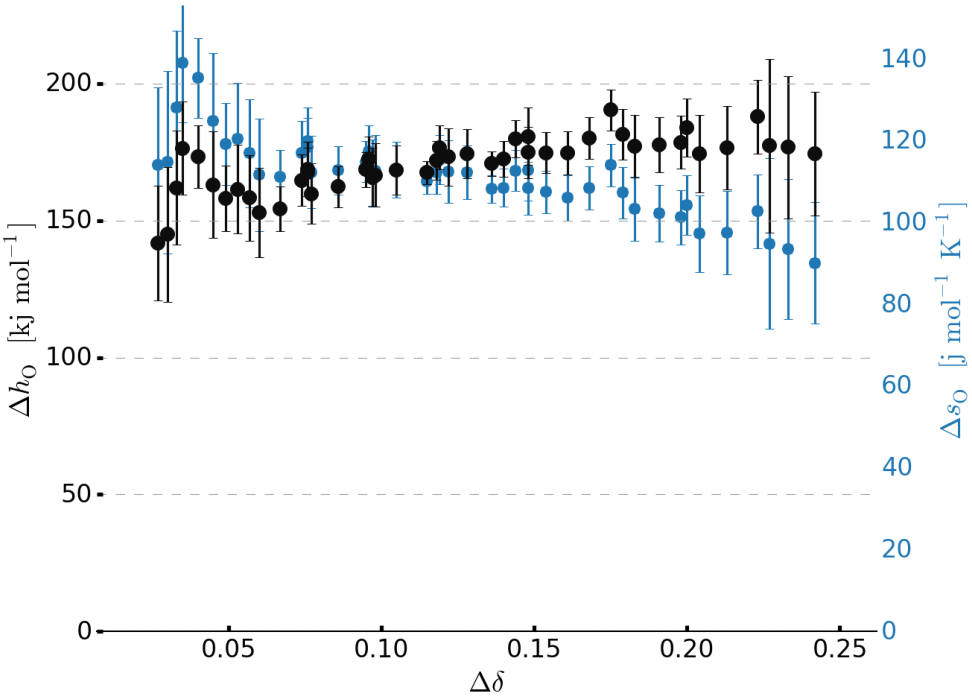

$Ca_{0.62}Sr_{0.38}Ti_{0.4}Mn_{0.6}O_{3-\delta}$	113

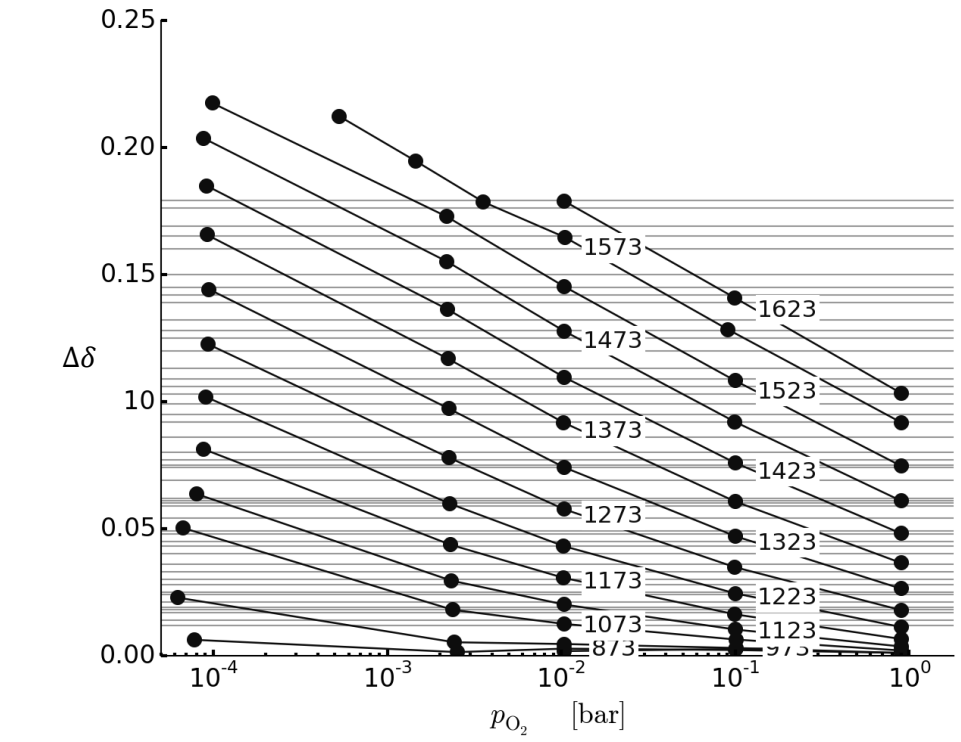

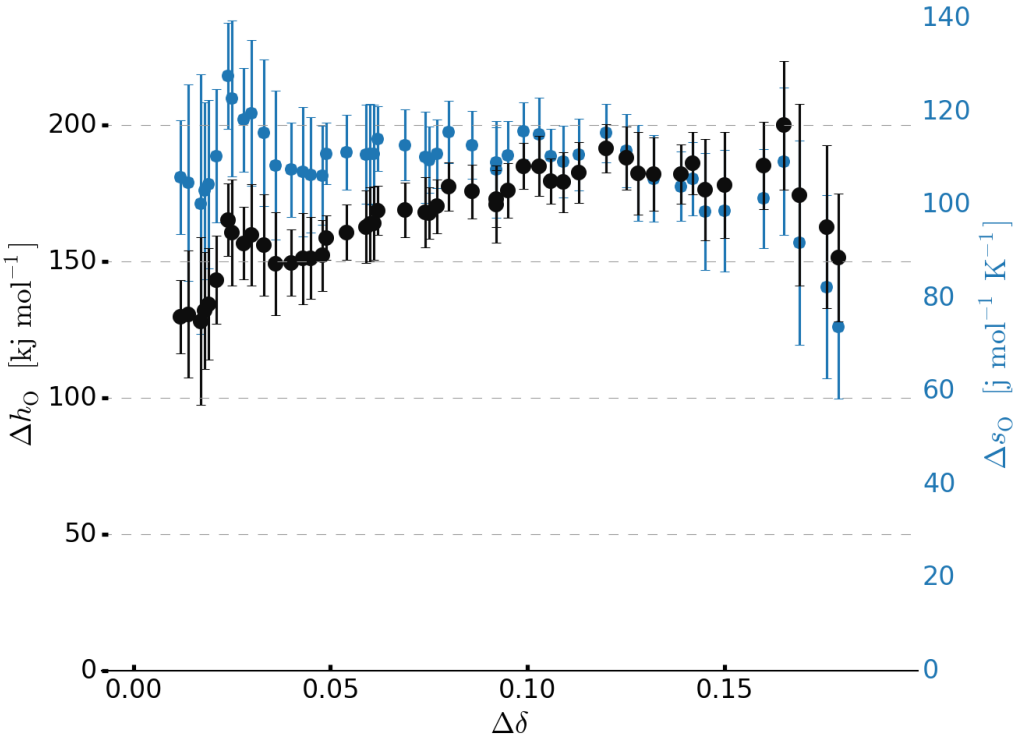

$Ca_{0.42}Sr_{0.58}Ti_{0.6}Mn_{0.4}O_{3-\delta}$	114

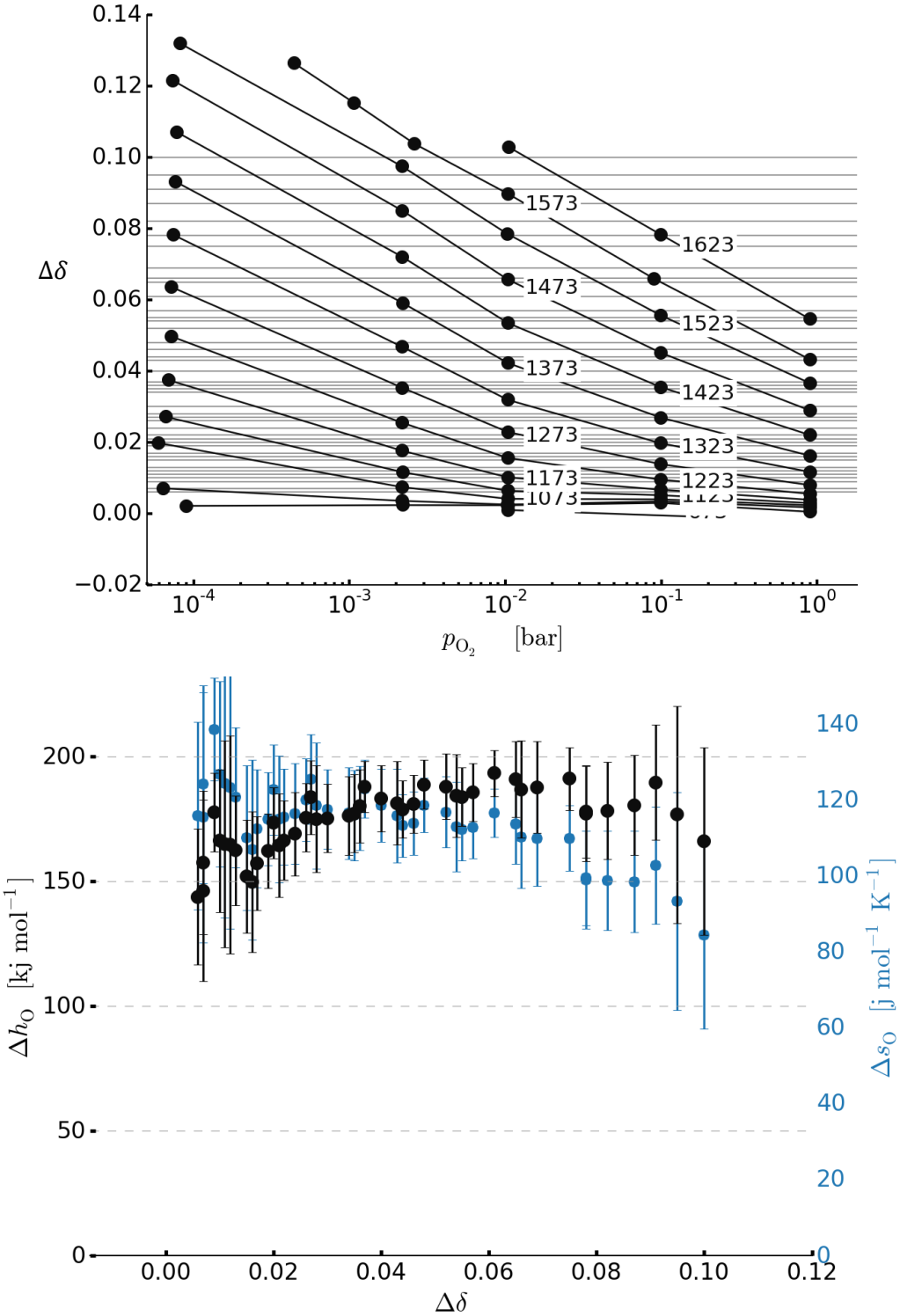

$Ca_{0.07}Sr_{0.93}Fe_{0.9}Co_{0.1}O_{3-\delta}$	116

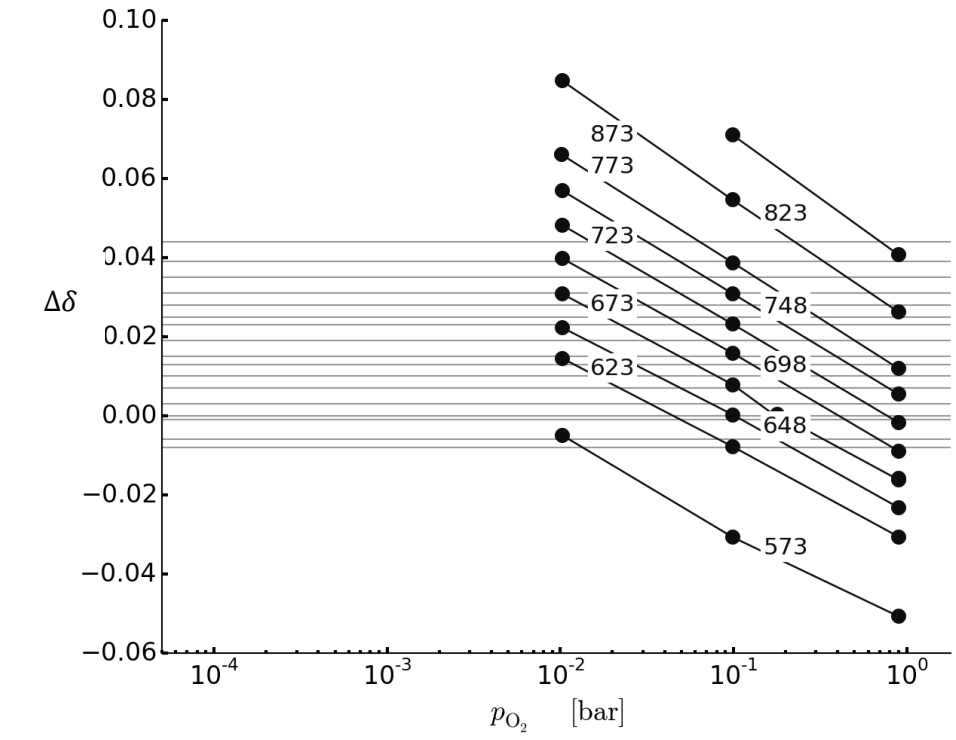

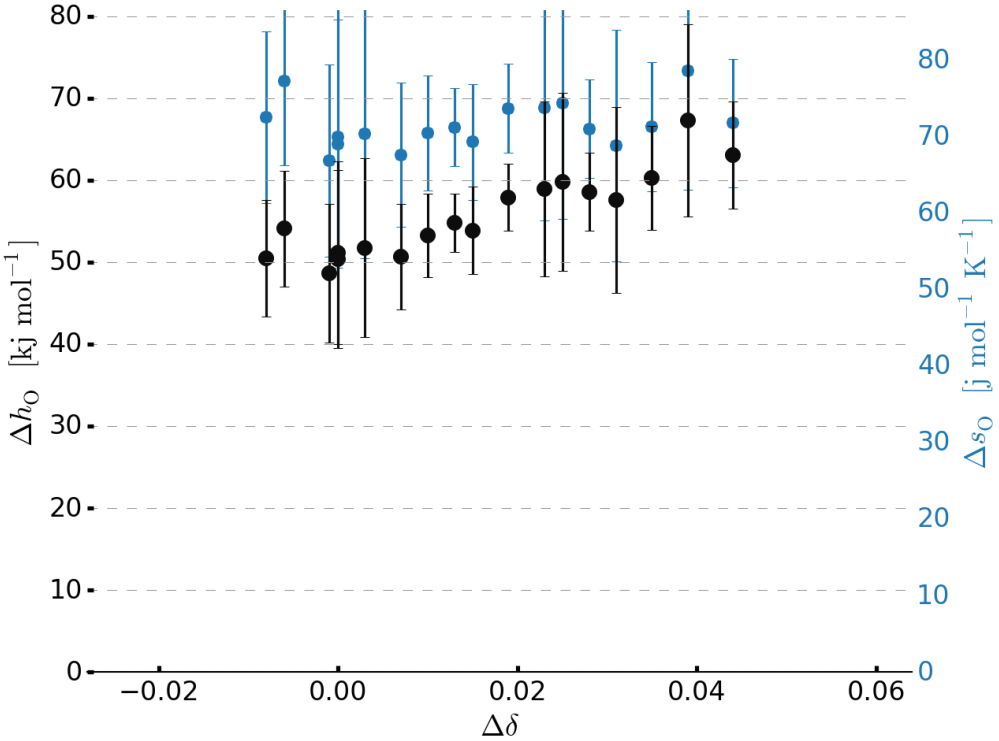

$Ca_{0.30}Sr_{0.70}Fe_{0.6}Co_{0.4}O_{3-\delta}$	118

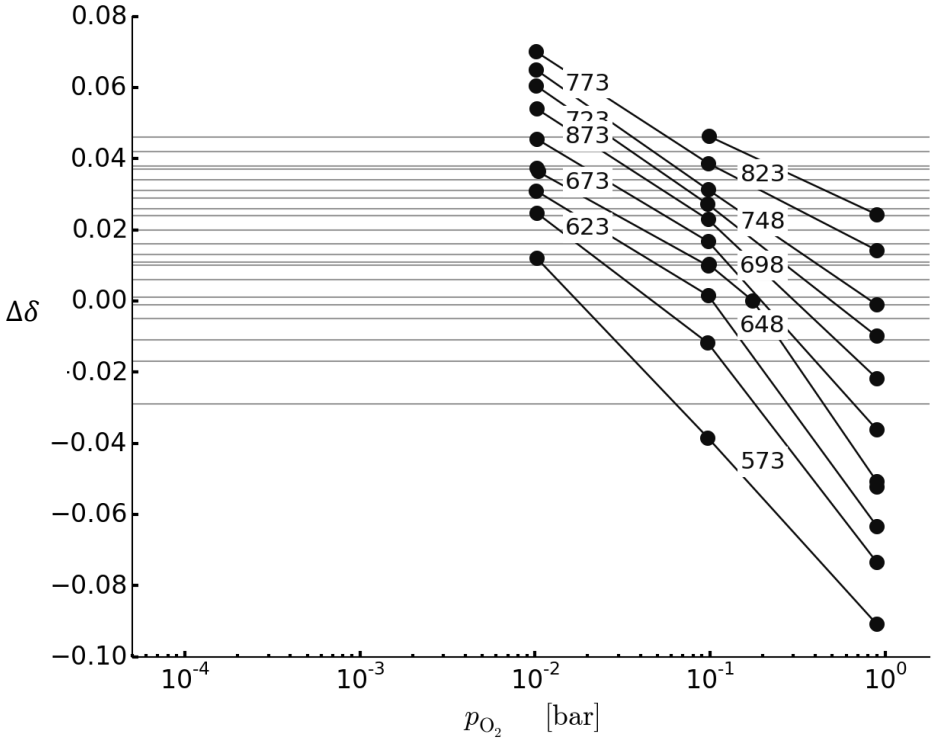

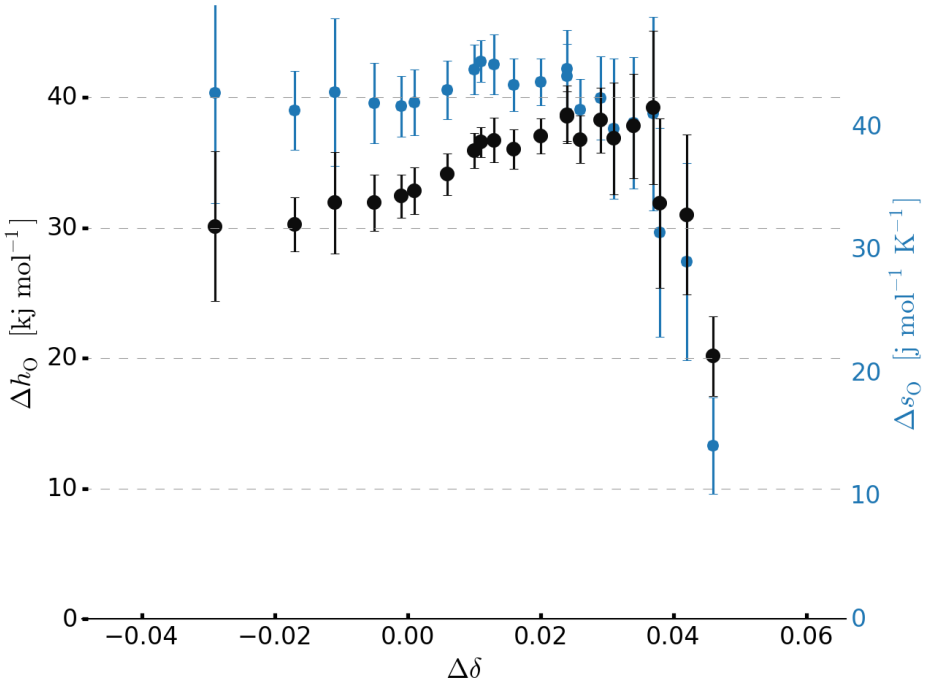

$Ca_{0.64}Sr_{0.36}Ti_{0.1}Mn_{0.9}O_{3-\delta}$	122

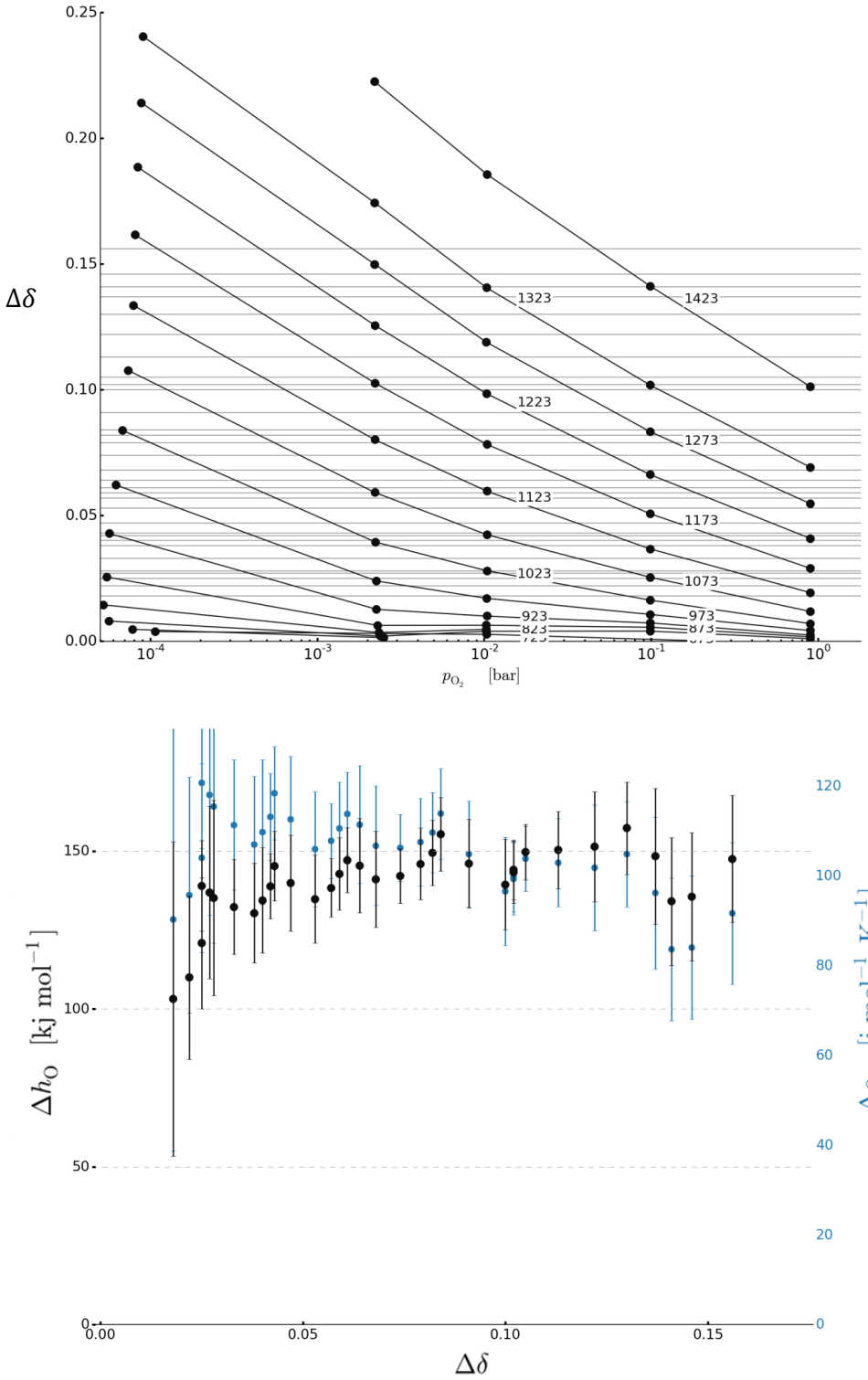

$Ca_{0.21}Sr_{0.79}Mn_{0.6}Fe_{0.4}O_{3-\delta}$	128

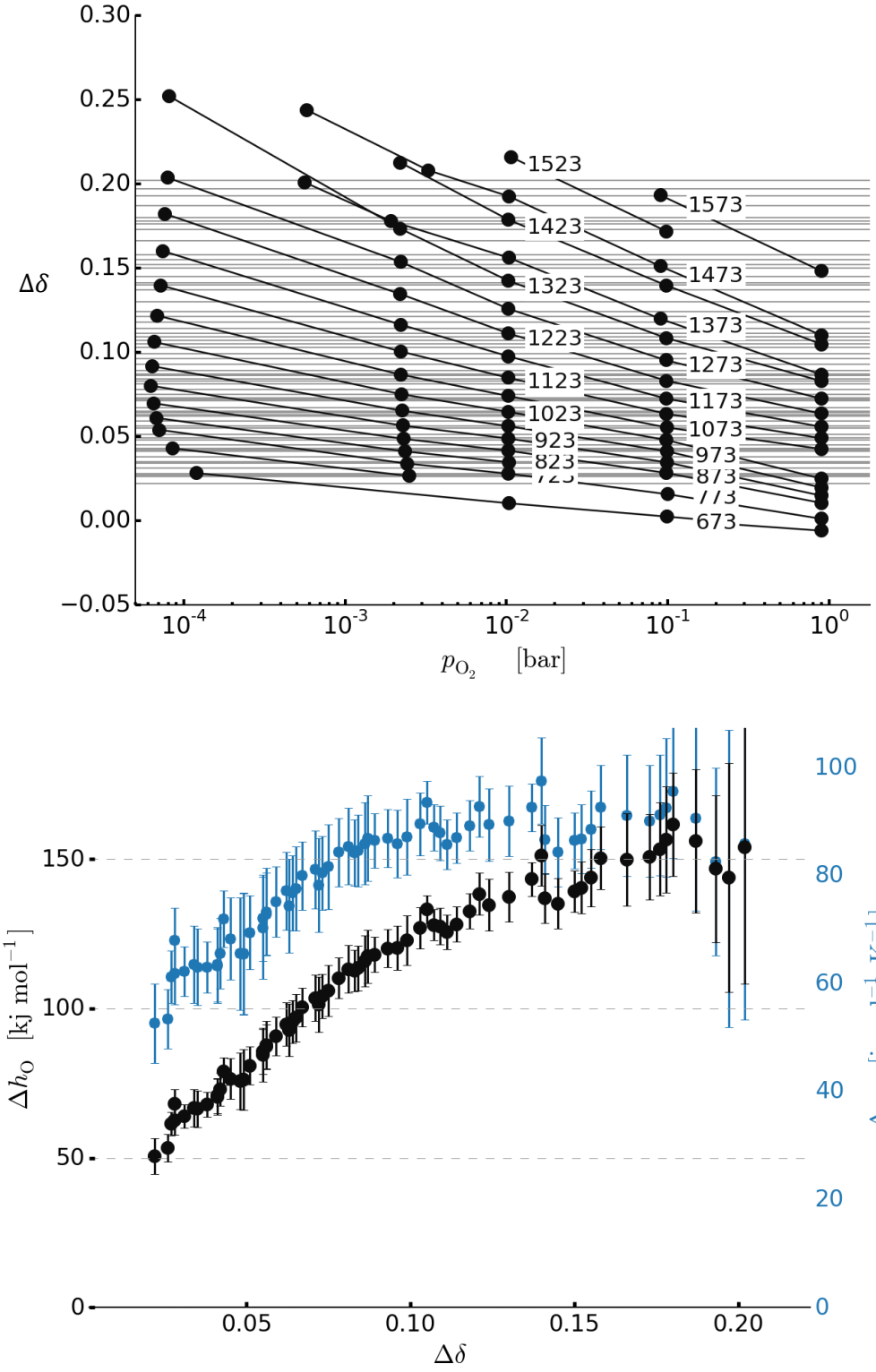

$Ca_{0.51}Sr_{0.49}MnO_{3-\delta}$	129

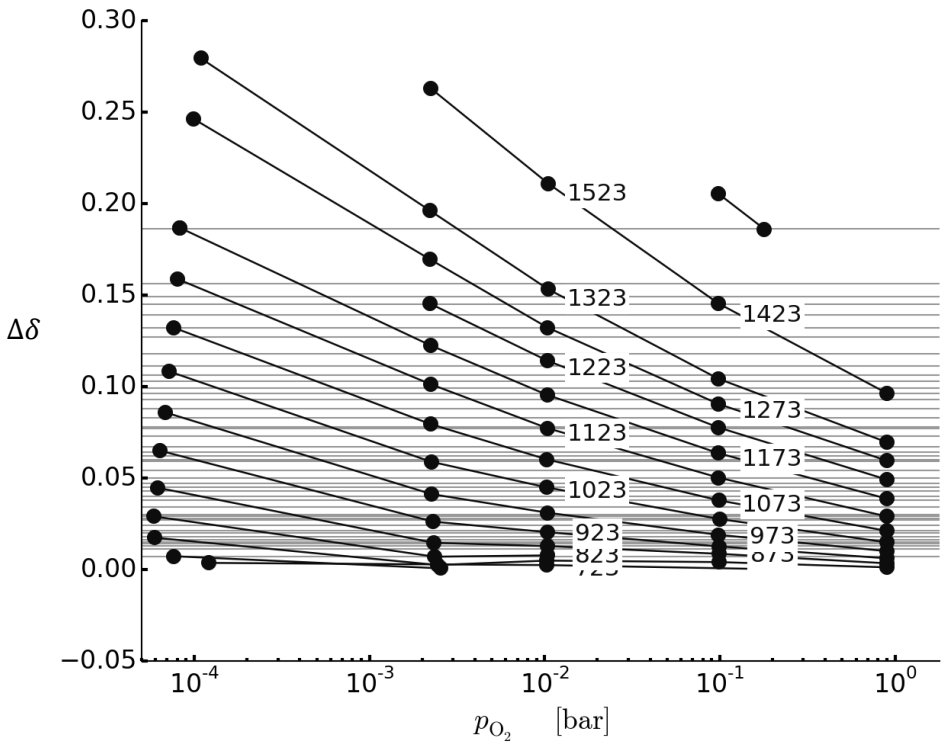

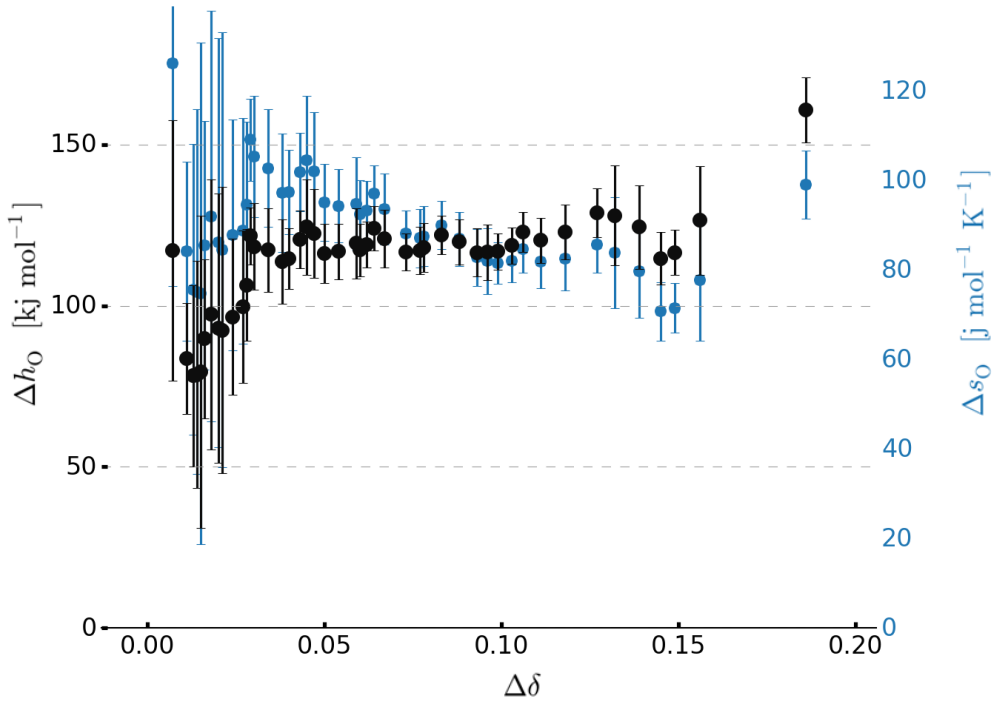

$Ca_{0.1}Sr_{0.9}Ti_{0.4}Mn_{0.6}O_{3-\delta}$	**130**

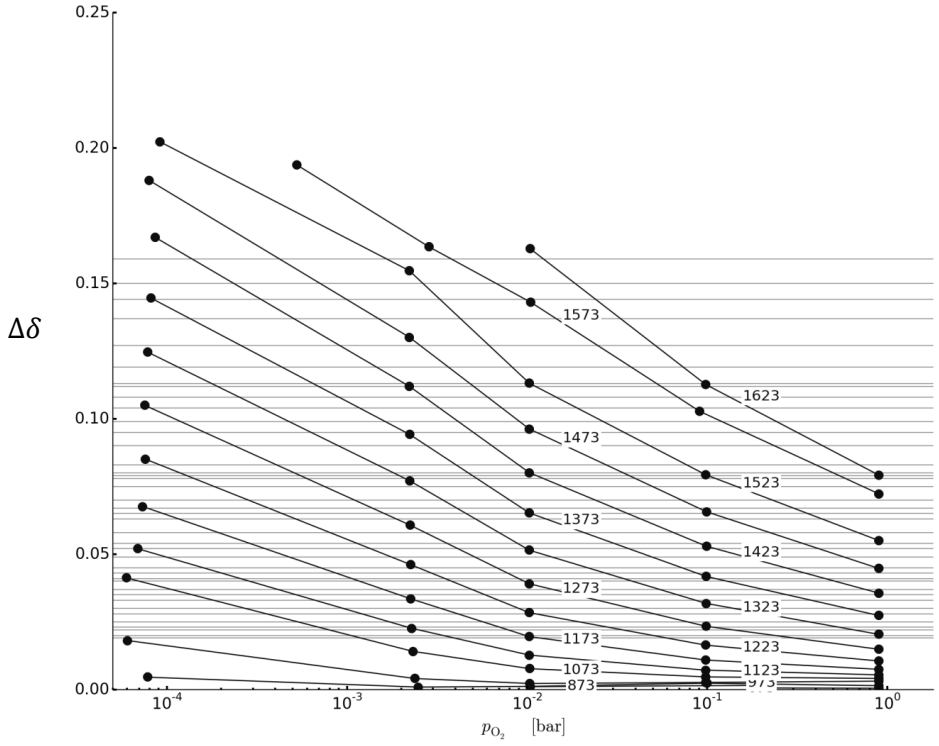

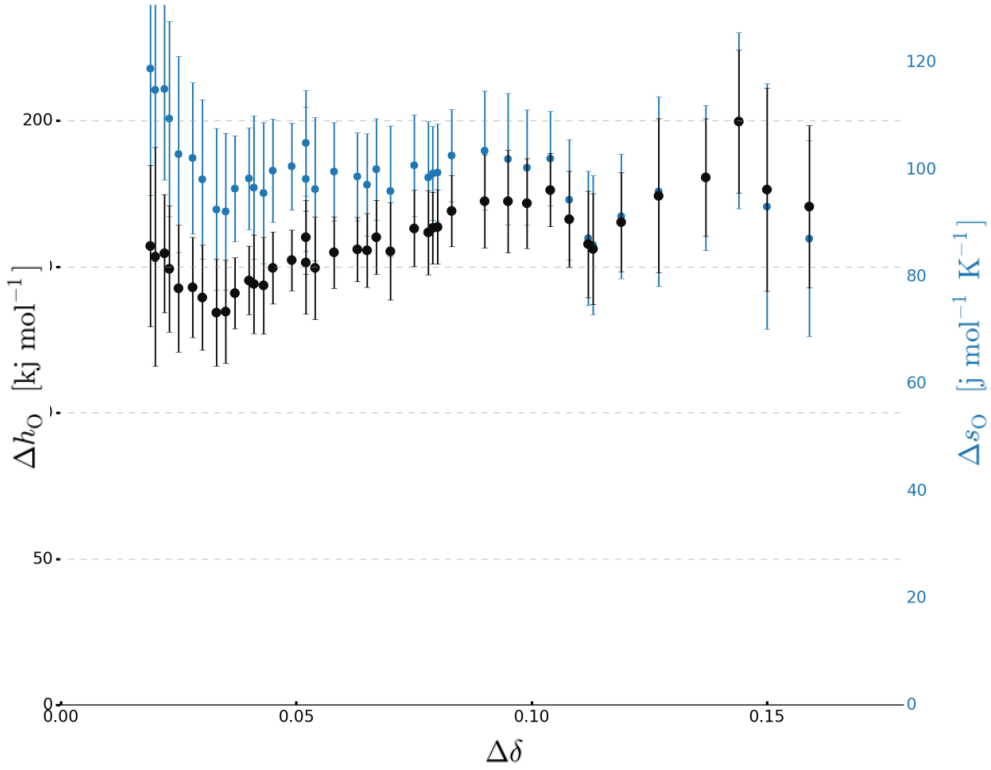

9. Acknowledgements

This work would not have been possible without the help and support of many people, and I highly appreciate all the effort and support provided by colleaugues and collaborators. I strongly believe that science can only advance in a collaborative environment and any research project stands and falls with the effort of the team, not only the achievements of individuals.

In particular, I would like to thank:

- My direct supervisor Dr. Martin Roeb and our department head Prof. Dr. Christian Sattler for their outstanding and professional guidance and support at all times, and for making it possible to collaborate with the Lawrence Berkeley National Laboratory within a research visit
- My dissertation advisors and correctors Prof. Dr. Christian Sattler and Prof. Dr. Gianaurelio for their valuable time spent in correcting this thesis and their very helpful advice.
- Dr. Brendan Bulfin (formerly DLR, now ETH Zurich) who was very supportive, especially in the early phase of my dissertation; he helped create thermodynamic models, gave me great advice in terms of writing scientific papers, and is now a good friend of mine
- Muralimohan Juttu Vidyasagar and Florian Lebendig who did their master's thesis under my supervision; I would like to thank them for their valuable help, especially in terms of experimental work
- All members of the Persson group at the Lawrence Berkeley National Laboratory (LBNL) for making my research visit a great success and their patience and help in developing our contribution to MPContribs/Materials Project, especially Dr. Patrick Huck, Dr. Matthew Horton, Dr. Joseph Montoya, Dr. Miao Liu, and Prof. Dr. Kristin Persson. I would also like to thank all others I met at LBNL for creating a great working environment and their support.
- Dr. Dorottya Guban, Liya Zhu, and Marion Senholdt for their valuable help in recording thermodynamic data and their advice and help in publishing our results
- The colleagues from the Insitute of Materials Research at DLR, especially Dr. Nicole Knoblauch, Alexander Francke, and Prof. Dr. Martin Schmücker for the great collaboration between our institutes and their help in materials analytics
- Our collaborators and beamline scientists at BESSY II in Berlin (Helmholtz Center Berlin and the Fritz Haber Insitute of the Max Planck society), namely Dr. David E. Starr, Dr. Anahita Azarpira, Dr. Carolin Zachäus, Dr. Michael Hävecker, and Dr. Katarzyna Skorupska for making our beam time at BESSY II a success by helping us conduct the experiments and evaluate the data
- Prof. Frank M. F. de Groot (Utrecht University) and Dr. Atsushi Hariki (TU Vienna) for their valuable help as experts in evaluating complex Cu XPS and XAS spectra

- All colleagues at DLR in the solar chemical engineering group and beyond for creating a collaborative and supportive working environment and being always there to help. I would especially like to thank all people I shared an office with for parts of my time at DLR, namely Dr. Brendan Bulfin, Mathias Pein, Lamark de Oliviera, and Dr. Martina Neises-von Putkamer. I would also like to thank Gkiokchan Moumin and Sebastian Richter for the great collaboration in organizing SOLLAB and working together. Moreover, I would like to thank Dr. Stefan Brendelberger for the great work together in terms of student supervision and the work on thermochemical oxygen pumping. You all were great colleagues who were always very helpful and made my time at DLR very enjoyable.
- The DLR Graduate Program and anybody who is in charge of organizing the dissertation program at DLR for giving me a broad education beyond the range of my field; I would also like to thank all colleagues in the “Doktorandenvertretung” for our great work together
- I would also like all technical, administrative and managing staff for their great work, including our heads of institute Prof. Dr. Robert Pitz-Paal and Prof. Dr. Bernhard Hoffschmidt
- Moreover, I would like to thank the dissertation board of TU Dresden and anybody else at TU Dresden who was involved in this work.

Last but not least, I would also like to personally thank my girlfriend and my friends for being always there for me and supporting me. This means a lot to me!

The author would like to acknowledge funding through the Helmholtz Association within the Virtual Institute SolarSyngas (VH-VI-509) and the project DÜSOL (EFRE-0800603) which is co-funded in the Klimaschutzwettbewerb "ErneuerbareEnergien.NRW" by the state of Northrhine-Westphalia, Germany, and the European EFRE fund. We thank HZB for the allocation of synchrotron radiation beamtime. The author would also like to acknowledge funding through the DLR programme “Competition of Visions”. Computational work was funded by the U.S. Department of Energy (DOE), Office of Science, Office of Basic Energy Sciences, Materials Sciences and Engineering Division under Contract No. DE-AC02-05-CH11231 (Materials Project program KC23MP). This research used resources of the National Energy Research Scientific Computing Center, a DOE Office of Science User Facility supported by the Office of Science of the DOE under contract no. DE-AC02-05CH1123.

10. References

1. BDEW Bundesverband der Energie- und Wasserwirtschaft e.V., Press Release. www.bdew.de/presse/presseinformationen/erneuerbare-ueberholen-erstmals-braun-und-steinkohle-bei-der-stromerzeugung/ (accessed 07/17/2018),
2. *Renewable Power Generation Costs in 2017*; IRENA: 2018.
3. Agora Energiewende, Press Release. www.agora-energiewende.de/fileadmin2/news/2017/Agora_PM_Kohleminimum_02052017.pdf (accessed 07/17/2018),
4. NREL, National Renewable Energy Laboratory. www.nrel.gov/csp/solarpaces/project_detail.cfm/projectID=4293 (accessed 07/17/2018),
5. Abanades, S.; Flamant, G. Thermochemical hydrogen production from a two-step solar-driven water-splitting cycle based on cerium oxides. *Solar Energy* **2006,** 80 (12), 1611-1623 DOI: https://doi.org/10.1016/j.solener.2005.12.005.
6. Gorensek, M. B.; Corgnale, C.; Staser, J. A.; Weidner, J. W. Solar Thermochemical Hydrogen (STCH) Processes. *The Electrochemical Society Interface* **2018,** 27 (1), 53-56.
7. Bozzano, G.; Manenti, F. Efficient methanol synthesis: Perspectives, technologies and optimization strategies. *Progress in Energy and Combustion Science* **2016,** 56, 71-105 DOI: https://doi.org/10.1016/j.pecs.2016.06.001.
8. Takeshita, T.; Yamaji, K. Important roles of Fischer–Tropsch synfuels in the global energy future. *Energy Policy* **2008,** 36 (8), 2773-2784 DOI: https://doi.org/10.1016/j.enpol.2008.02.044.
9. Bicer, Y.; Dincer, I. Life cycle evaluation of hydrogen and other potential fuels for aircrafts. *International Journal of Hydrogen Energy* **2017,** 42 (16), 10722-10738 DOI: https://doi.org/10.1016/j.ijhydene.2016.12.119.
10. Hepperle, M. Electric flight-potential and limitations. *German Aerospace Centre, Institute of Aerodynamics and Flow Technology, Germany* **2012**.
11. German Aerospace Center (DLR), Institute of Solar Research, Press Release. www.dlr.de/dlr/en/desktopdefault.aspx/tabid-10081/151_read-27203/desktopdefault.aspx/tabid-10081/151_read-27203/year-all/151_page-1/#/gallery/30470 (accessed 07/17/2018),
12. Cheng, W.-H.; Richter, M. H.; May, M. M.; Ohlmann, J.; Lackner, D.; Dimroth, F.; Hannappel, T.; Atwater, H. A.; Lewerenz, H.-J. Monolithic Photoelectrochemical Device for Direct Water Splitting with 19% Efficiency. *ACS Energy Letters* **2018**, 1795-1800 DOI: 10.1021/acsenergylett.8b00920.
13. Steinfeld, A. Solar thermochemical production of hydrogen––a review. *Solar Energy* **2005,** 78 (5), 603-615 DOI: http://dx.doi.org/10.1016/j.solener.2003.12.012.
14. Chueh, W. C.; Falter, C.; Abbott, M.; Scipio, D.; Furler, P.; Haile, S. M.; Steinfeld, A. High-Flux Solar-Driven Thermochemical Dissociation of CO2 and H2O Using Nonstoichiometric Ceria. *Science* **2010,** 330 (6012), 1797-1801 DOI: 10.1126/science.1197834.
15. E. Funk, J. Thermochemical hydrogen production: past and present. *International Journal of Hydrogen Energy* **2001,** 26 (3), 185-190 DOI: https://doi.org/10.1016/S0360-3199(00)00062-8.
16. Vieten, J.; Bulfin, B.; Starr David, E.; Hariki, A.; de Groot Frank, M. F.; Azarpira, A.; Zachäus, C.; Hävecker, M.; Skorupska, K.; Knoblauch, N.; Schmücker, M.; Roeb, M.; Sattler, C. Redox behavior of solid solutions in the SrFe1-xCuxO3-δ system for application in thermochemical oxygen storage and air separation. *Energy Technology* **2018,** 0 (ja), DOI: 10.1002/ente.201800554.
17. Call, F.; Roeb, M.; Schmücker, M.; Sattler, C.; Pitz-Paal, R. Ceria Doped with Zirconium and Lanthanide Oxides to Enhance Solar Thermochemical Production of Fuels. *The Journal of Physical Chemistry C* **2015,** 119 (13), 6929-6938 DOI: 10.1021/jp508959y.
18. Han, S. B.; Kang, T. B.; Joo, O. S.; Jung, K. D. Water splitting for hydrogen production with ferrites. *Solar Energy* **2007,** 81 (5), 623-628 DOI: https://doi.org/10.1016/j.solener.2006.08.012.
19. Yang, C.-J.; Jackson, R. B. China's growing methanol economy and its implications for energy and the environment. *Energy Policy* **2012,** 41, 878-884 DOI: https://doi.org/10.1016/j.enpol.2011.11.037.
20. Marxer, D.; Furler, P.; Takacs, M.; Steinfeld, A. Solar thermochemical splitting of CO2 into separate streams of CO and O2 with high selectivity, stability, conversion, and efficiency. *Energy & Environmental Science* **2017,** 10 (5), 1142-1149 DOI: 10.1039/c6ee03776c.
21. Kumabe, K.; Sato, T.; Matsumoto, K.; Ishida, Y.; Hasegawa, T. Production of hydrocarbons in Fischer–Tropsch synthesis with Fe-based catalyst: Investigations of primary kerosene yield and carbon mass balance. *Fuel* **2010,** 89 (8), 2088-2095 DOI: https://doi.org/10.1016/j.fuel.2010.02.018.
22. Moghtaderi, B. Application of Chemical Looping Concept for Air Separation at High Temperatures. *Energy & Fuels* **2010,** 24 (1), 190-198 DOI: 10.1021/ef900553j.
23. Vieten, J.; Bulfin, B.; Call, F.; Lange, M.; Schmucker, M.; Francke, A.; Roeb, M.; Sattler, C. Perovskite oxides for application in thermochemical air separation and oxygen storage. *Journal of Materials Chemistry A* **2016,** 4 (35), 13652-13659 DOI: 10.1039/c6ta04867f.
24. Brendelberger, S.; von Storch, H.; Bulfin, B.; Sattler, C. Vacuum pumping options for application in solar thermochemical redox cycles – Assessment of mechanical-, jet- and thermochemical pumping systems. *Solar Energy* **2017,** 141 (Supplement C), 91-102 DOI: https://doi.org/10.1016/j.solener.2016.11.023.
25. Nakamura, T. Hydrogen production from water utilizing solar heat at high temperatures. *Solar Energy* **1977,** 19 (5), 467-475 DOI: https://doi.org/10.1016/0038-092X(77)90102-5.
26. Parthasarathy, P.; Le Clercq, P. Heat Transfer Simulation in a High Temperature Solar Reactor. *Energy Procedia* **2015,** 69, 1810-1818 DOI: https://doi.org/10.1016/j.egypro.2015.03.154.
27. Singh, A.; Lapp, J.; Grobbel, J.; Brendelberger, S.; Reinhold, J. P.; Olivera, L.; Ermanoski, I.; Siegel, N. P.; McDaniel, A.; Roeb, M.; Sattler, C. Design of a pilot scale directly irradiated, high temperature, and low pressure moving particle cavity chamber for metal oxide reduction. *Solar Energy* **2017,** 157, 365-376 DOI: https://doi.org/10.1016/j.solener.2017.08.040.
28. Jarrett, C.; Chueh, W.; Yuan, C.; Kawajiri, Y.; Sandhage, K. H.; Henry, A. Critical limitations on the efficiency of two-step thermochemical cycles. *Solar Energy* **2016,** 123, 57-73 DOI: https://doi.org/10.1016/j.solener.2015.09.036.
29. Roeb, M.; Säck, J. P.; Rietbrock, P.; Prahl, C.; Schreiber, H.; Neises, M.; de Oliveira, L.; Graf, D.; Ebert, M.; Reinalter, W.; Meyer-Grünefeldt, M.; Sattler, C.; Lopez, A.; Vidal, A.; Elsberg, A.; Stobbe, P.; Jones, D.; Steele, A.; Lorentzou, S.; Pagkoura, C.; Zygogianni, A.; Agrafiotis, C.; Konstandopoulos, A. G. Test operation of a 100kW pilot plant for solar hydrogen production from water on a solar tower. *Solar Energy* **2011,** 85 (4), 634-644 DOI: https://doi.org/10.1016/j.solener.2010.04.014.
30. Bulfin, B.; Vieten, J.; Agrafiotis, C.; Roeb, M.; Sattler, C. Applications and limitations of two step metal oxide thermochemical redox cycles; a review. *Journal of Materials Chemistry A* **2017,** 5 (36), 18951-18966 DOI: 10.1039/c7ta05025a.

31. Panlener, R. J.; Blumenthal, R. N.; Garnier, J. E. A thermodynamic study of nonstoichiometric cerium dioxide. *Journal of Physics and Chemistry of Solids* **1975,** 36 (11), 1213-1222 DOI: http://dx.doi.org/10.1016/0022-3697(75)90192-4.

32. Zhai, S.; Rojas, J.; Ahlborg, N.; Lim, K.; Toney, M. F.; Jin, H.; Chueh, W. C.; Majumdar, A. The use of poly-cation oxides to lower the temperature of two-step thermochemical water splitting. *Energy & Environmental Science* **2018**, DOI: 10.1039/c8ee00050f.

33. Rao, C. N. R.; Dey, S. Solar thermochemical splitting of water to generate hydrogen. *Proceedings of the National Academy of Sciences of the United States of America* **2017,** 114 (51), 13385-13393 DOI: 10.1073/pnas.1700104114.

34. McDaniel, A. H.; Ambrosini, A.; Coker, E. N.; Miller, J. E.; Chueh, W. C.; O'Hayre, R.; Tong, J. Nonstoichiometric Perovskite Oxides for Solar Thermochemical H2 and CO Production. *Energy Procedia* **2014,** 49, 2009-2018 DOI: https://doi.org/10.1016/j.egypro.2014.03.213.

35. Scheffe, J. R.; Weibel, D.; Steinfeld, A. Lanthanum–Strontium–Manganese Perovskites as Redox Materials for Solar Thermochemical Splitting of H2O and CO2. *Energy & Fuels* **2013,** 27 (8), 4250-4257 DOI: 10.1021/ef301923h.

36. Ezbiri, M.; Allen, K. M.; Gàlvez, M. E.; Michalsky, R.; Steinfeld, A. Design Principles of Perovskites for Thermochemical Oxygen Separation. *ChemSusChem* **2015,** 8 (11), 1966-1971 DOI: 10.1002/cssc.201500239.

37. Yin, Q.; Kniep, J.; Lin, Y. S. High temperature air separation by perovskite-type oxide sorbents–Heat effect minimization. *Chemical Engineering Science* **2008,** 63 (24), 5870-5875 DOI: https://doi.org/10.1016/j.ces.2008.09.004.

38. Pishahang, M.; Erik Mohn, C.; Stølen, S. Density functional study on redox energetics of LaMO3−δ (M=Sc–Cu) perovskite-type oxides. *Journal of Solid State Chemistry* **2016,** 233, 62-66 DOI: http://dx.doi.org/10.1016/j.jssc.2015.10.013.

39. Lau, C. Y.; Dunstan, M. T.; Hu, W.; Grey, C. P.; Scott, S. A. Large scale in silico screening of materials for carbon capture through chemical looping. *Energy & Environmental Science* **2017,** 10 (3), 818-831 DOI: 10.1039/c6ee02763f.

40. Nikulshina, V.; Gebald, C.; Steinfeld, A. CO2 capture from atmospheric air via consecutive CaO-carbonation and CaCO3-calcination cycles in a fluidized-bed solar reactor. *Chemical Engineering Journal* **2009,** 146 (2), 244-248 DOI: https://doi.org/10.1016/j.cej.2008.06.005.

41. Charvin, P.; Abanades, S.; Flamant, G.; Lemort, F. Two-step water splitting thermochemical cycle based on iron oxide redox pair for solar hydrogen production. *Energy* **2007,** 32 (7), 1124-1133 DOI: https://doi.org/10.1016/j.energy.2006.07.023.

42. Agrafiotis, C.; Roeb, M.; Sattler, C. Cobalt Oxide-Based Structured Thermochemical Reactors/Heat Exchangers for Solar Thermal Energy Storage in Concentrated Solar Power Plants. **2014,** (45868), V001T02A005 DOI: 10.1115/es2014-6336.

43. Agrafiotis, C.; Tescari, S.; Roeb, M.; Schmücker, M.; Sattler, C. Exploitation of thermochemical cycles based on solid oxide redox systems for thermochemical storage of solar heat. Part 3: Cobalt oxide monolithic porous structures as integrated thermochemical reactors/heat exchangers. *Solar Energy* **2015,** 114, 459-475 DOI: http://dx.doi.org/10.1016/j.solener.2014.12.037.

44. Kun, W.; Qingbo, Y.; Qin, Q.; Wenjun, D. Feasibility of a Co Oxygen Carrier for Chemical Looping Air Separation: Thermodynamics and Kinetics. *Chemical Engineering & Technology* **2014,** 37 (9), 1500-1506 DOI: doi:10.1002/ceat.201400178.

45. Block, T.; Schmücker, M. Metal oxides for thermochemical energy storage: A comparison of several metal oxide systems. *Solar Energy* **2016,** 126, 195-207 DOI: http://dx.doi.org/10.1016/j.solener.2015.12.032.

46. Kodama, T.; Nakamuro, Y.; Mizuno, T. A Two-Step Thermochemical Water Splitting by Iron-Oxide on Stabilized Zirconia. *Journal of Solar Energy Engineering* **2004,** 128 (1), 3-7 DOI: 10.1115/1.1878852.

47. Abanades, S.; Charvin, P.; Lemont, F.; Flamant, G. Novel two-step SnO2/SnO water-splitting cycle for solar thermochemical production of hydrogen. *International Journal of Hydrogen Energy* **2008,** 33 (21), 6021-6030 DOI: https://doi.org/10.1016/j.ijhydene.2008.05.042.

48. Randhir, K.; Rhodes, N. R.; Li, L.; AuYeung, N.; Hahn, D. W.; Mei, R.; Klausner, J. F. Magnesioferrites for solar thermochemical fuel production. *Solar Energy* **2018,** 163, 1-15 DOI: https://doi.org/10.1016/j.solener.2017.12.006.

49. Wang, W.; Zhang, B.; Wang, G.; Li, Y. O2 Release of Mn-Based Oxygen Carrier for Chemical Looping Air Separation (CLAS): An Insight into Kinetic Studies. *Aerosol and Air Quality Research* **2016,** 16 (2), 453-463 DOI: 10.4209/aaqr.2014.07.0140.

50. Hänchen, M.; Stiel, A.; Jovanovic, Z. R.; Steinfeld, A. Thermally Driven Copper Oxide Redox Cycle for the Separation of Oxygen from Gases. *Industrial & Engineering Chemistry Research* **2012,** 51 (20), 7013-7021 DOI: 10.1021/ie202474s.

51. Kennedy, B. J.; Ting, J.; Zhou, Q.; Zhang, Z.; Matsuda, M.; Miyake, M. Structural characterisation of the perovskite series Sr0.9−xCaxCe0.1MnO3: Influence of the Jahn–Teller effect. *Journal of Solid State Chemistry* **2009,** 182 (4), 954-959 DOI: https://doi.org/10.1016/j.jssc.2008.12.032.

52. Islam, M. S.; Cherry, M.; Catlow, C. R. A. Oxygen Diffusion in LaMnO3and LaCoO3Perovskite-Type Oxides: A Molecular Dynamics Study. *Journal of Solid State Chemistry* **1996,** 124 (2), 230-237 DOI: https://doi.org/10.1006/jssc.1996.0231.

53. Holt, A.; Norby, T.; Glenne, R. Defects and transport in SrFe1−xCoxO3−δ. *Ionics* **1999,** 5 (5), 434-443 DOI: 10.1007/bf02376010.

54. Prado, F.; Armstrong, T.; Caneiro, A.; Manthiram, A. Structural Stability and Oxygen Permeation Properties of Sr3 − x La x Fe2 − y Co y O 7 − δ (0 ⩽ x ⩽ 0.3 and 0 ⩽ y ⩽ 1.0) *Journal of The Electrochemical Society* **2001,** 148 (4), J7-J14 DOI: 10.1149/1.1354605.

55. Bulfin, B.; Lowe, A. J.; Keogh, K. A.; Murphy, B. E.; Lübben, O.; Krasnikov, S. A.; Shvets, I. V. Analytical Model of CeO2 Oxidation and Reduction. *The Journal of Physical Chemistry C* **2013,** 117 (46), 24129-24137 DOI: 10.1021/jp406578z.

56. Abanades, S.; Legal, A.; Cordier, A.; Peraudeau, G.; Flamant, G.; Julbe, A. Investigation of reactive cerium-based oxides for H2 production by thermochemical two-step water-splitting. *Journal of Materials Science* **2010,** 45 (15), 4163-4173 DOI: 10.1007/s10853-010-4506-4.

57. Furler, P.; Scheffe, J.; Gorbar, M.; Moes, L.; Vogt, U.; Steinfeld, A. Solar Thermochemical CO2 Splitting Utilizing a Reticulated Porous Ceria Redox System. *Energy & Fuels* **2012,** 26 (11), 7051-7059 DOI: 10.1021/ef3013757.

58. Venstrom, L. J.; De Smith, R. M.; Hao, Y.; Haile, S. M.; Davidson, J. H. Efficient Splitting of CO2 in an Isothermal Redox Cycle Based on Ceria. *Energy & Fuels* **2014,** 28 (4), 2732-2742 DOI: 10.1021/ef402492e.

59. McIntosh, S.; Vente, J. F.; Haije, W. G.; Blank, D. H. A.; Bouwmeester, H. J. M. Structure and oxygen stoichiometry of SrCo0.8Fe0.2O3−δ and Ba0.5Sr0.5Co0.8Fe0.2O3−δ. *Solid State Ionics* **2006,** 177 (19–25), 1737-1742 DOI: http://dx.doi.org/10.1016/j.ssi.2006.03.041.

60. van Roosmalen, J. A. M.; Cordfunke, E. H. P. The Defect Chemistry of LaMnO3±δ: 4. Defect Model for LaMnO3+δ. *Journal of Solid State Chemistry* **1994,** 110 (1), 109-112 DOI: https://doi.org/10.1006/jssc.1994.1143.

61. Takeda, Y.; Kanno, K.; Takada, T.; Yamamoto, O.; Takano, M.; Nakayama, N.; Bando, Y. Phase relation in the oxygen nonstoichiometric system, SrFeOx (2.5 ≤ x ≤ 3.0). *Journal of Solid State Chemistry* **1986,** 63 (2), 237-249 DOI: http://dx.doi.org/10.1016/0022-4596(86)90174-X.

62. Johnsson, M.; Lemmens, P. In *Handbook of Magnetism and Advanced Magnetic Materials*; John Wiley & Sons, Ltd: 2007.

63. Eames, C.; Frost, J. M.; Barnes, P. R. F.; O'Regan, B. C.; Walsh, A.; Islam, M. S. Ionic transport in hybrid lead iodide perovskite solar cells. *Nat Commun* **2015,** 6, DOI: 10.1038/ncomms8497.

64. Yang, Z.; Lin, Y. S.; Zeng, Y. High-Temperature Sorption Process for Air Separation and Oxygen Removal. *Industrial & Engineering Chemistry Research* **2002,** 41 (11), 2775-2784 DOI: 10.1021/ie010736k.

65. Marek, E.; Hu, W.; Gaultois, M.; Grey, C. P.; Scott, S. A. The use of strontium ferrite in chemical looping systems. *Applied Energy* **2018,** 223, 369-382 DOI: https://doi.org/10.1016/j.apenergy.2018.04.090.

66. Jennings, J. R. *Catalytic Ammonia Synthesis: Fundamentals and Practice*. Springer US: 2013.

67. Lan, R.; Irvine, J. T. S.; Tao, S. Synthesis of ammonia directly from air and water at ambient temperature and pressure. *Scientific Reports* **2013,** 3, 1145 DOI: 10.1038/srep01145

http://www.nature.com/articles/srep01145#supplementary-information.

68. Erisman, J. W.; Sutton, M. A.; Galloway, J.; Klimont, Z.; Winiwarter, W. How a century of ammonia synthesis changed the world. *Nature Geosci* **2008,** 1 (10), 636-639.

69. Guban, D.; Bulfin, B.; Vieten, J.; Roeb, M.; Sattler, C., Sustainable production of ammonia using solar-thermochemical redox cycles. In *DLR Sonnenkolloquium 2018 (Poster)*, Cologne, Germany, 2018.

70. Sastre, D.; Carrillo, A. J.; Serrano, D. P.; Pizarro, P.; Coronado, J. M. Exploring the Redox Behavior of La 0.6 Sr 0.4 Mn 1− x Al x O 3 Perovskites for CO 2-Splitting in Thermochemical Cycles. *Topics in Catalysis* **2017,** 60 (15-16), 1108-1118.

71. Nalbandian, L.; Evdou, A.; Zaspalis, V. La1−xSrxMyFe1−yO3−δ perovskites as oxygen-carrier materials for chemical-looping reforming. *International Journal of Hydrogen Energy* **2011,** 36 (11), 6657-6670 DOI: http://dx.doi.org/10.1016/j.ijhydene.2011.02.146.

72. Emery, A. A.; Saal, J. E.; Kirklin, S.; Hegde, V. I.; Wolverton, C. High-Throughput Computational Screening of Perovskites for Thermochemical Water Splitting Applications. *Chemistry of Materials* **2016,** 28 (16), 5621-5634 DOI: 10.1021/acs.chemmater.6b01182.

73. Melo Jorge, M. E.; Correia dos Santos, A.; Nunes, M. R. Effects of synthesis method on stoichiometry, structure and electrical conductivity of CaMnO3−δ. *International Journal of Inorganic Materials* **2001,** 3 (7), 915-921 DOI: http://dx.doi.org/10.1016/S1466-6049(01)00088-5.

74. Dry, M. E. The Fischer–Tropsch process: 1950–2000. *Catalysis Today* **2002,** 71 (3), 227-241 DOI: https://doi.org/10.1016/S0920-5861(01)00453-9.

75. Fischer, F.; Tropsch, H. Über die direkte Synthese von Erdöl-Kohlenwasserstoffen bei gewöhnlichem Druck. (Erste Mitteilung). *Berichte der deutschen chemischen Gesellschaft (A and B Series)* **1926,** 59 (4), 830-831 DOI: 10.1002/cber.19260590442.

76. Khodakov, A. Y.; Chu, W.; Fongarland, P. Advances in the Development of Novel Cobalt Fischer—Tropsch Catalysts for Synthesis of Long-Chain Hydrocarbons and Clean Fuels. *ChemInform* **2007,** 38 (33), DOI: doi:10.1002/chin.200733255.

77. Keith, D. W.; Holmes, G.; St. Angelo, D.; Heidel, K. A Process for Capturing CO₂ from the Atmosphere. *Joule*, DOI: 10.1016/j.joule.2018.05.006.

78. Buhrer, C. F. Some properties of bismuth perovskites. *The Journal of Chemical Physics* **1962,** 36 (3), 798-803.

79. Liu, Z.; Zhang, T.; Wang, Y.; Wang, C.; Zhang, P.; Sarvari, H.; Chen, Z.; Li, S. Electronic Properties of a New All-Inorganic Perovskite TlPbI3 Simulated by the First Principles. *Nanoscale Research Letters* **2017,** 12 (1), 232 DOI: 10.1186/s11671-017-2015-y.

80. Bartesaghi, D.; Slavney, A. H.; Gélvez-Rueda, M. C.; Connor, B. A.; Grozema, F. C.; Karunadasa, H. I.; Savenije, T. J. Charge Carrier Dynamics in Cs2AgBiBr6 Double Perovskite. *The Journal of Physical Chemistry C* **2018,** 122 (9), 4809-4816 DOI: 10.1021/acs.jpcc.8b00572.

81. Wu, M. K.; Ashburn, J. R.; Torng, C. J.; Hor, P. H.; Meng, R. L.; Gao, L.; Huang, Z. J.; Wang, Y. Q.; Chu, C. W. Superconductivity at 93 K in a new mixed-phase Y-Ba-Cu-O compound system at ambient pressure. *Physical Review Letters* **1987,** 58 (9), 908-910 DOI: 10.1103/PhysRevLett.58.908.

82. Goldschmidt, V. M. Die Gesetze der Krystallochemie. *Naturwissenschaften* 14 (21), 477-485 DOI: 10.1007/bf01507527.

83. Liu, X.; Hong, R.; Tian, C. Tolerance factor and the stability discussion of ABO3-type ilmenite. *Journal of Materials Science: Materials in Electronics* **2008,** 20 (4), 323-327 DOI: 10.1007/s10854-008-9728-8.

84. Roth, R. S. Classification of perovskite and other ABO3-type compounds. *J. RES. NATL. BUR. STAN.* **1957,** 58 (2), 75 DOI: 10.6028/jres.058.010.

85. Bartel, C. J.; Sutton, C.; Goldsmith, B. R.; Ouyang, R.; Musgrave, C. B.; Ghiringhelli, L. M.; Scheffler, M. New Tolerance Factor to Predict the Stability of Perovskite Oxides and Halides. *arXiv preprint arXiv:1801.07700* **2018**.

86. Kieslich, G.; Sun, S.; Cheetham, A. K. An extended tolerance factor approach for organic–inorganic perovskites. *Chemical science* **2015,** 6 (6), 3430-3433.

87. Travis, W.; Glover, E. N. K.; Bronstein, H.; Scanlon, D. O.; Palgrave, R. G. On the application of the tolerance factor to inorganic and hybrid halide perovskites: a revised system. *Chemical science* **2016,** 7 (7), 4548-4556 DOI: 10.1039/c5sc04845a.

88. Shannon, R. Revised effective ionic radii and systematic studies of interatomic distances in halides and chalcogenides. *Acta Crystallographica Section A* **1976,** 32 (5), 751-767 DOI: doi:10.1107/S0567739476001551.

89. Chatzichristodoulou, C.; Norby, P.; Hendriksen, P. V.; Mogensen, M. B. Size of oxide vacancies in fluorite and perovskite structured oxides. *Journal of Electroceramics* **2015,** 34 (1), 100-107 DOI: 10.1007/s10832-014-9916-2.

90. Che, X.; Li, L.; Hu, W.; Li, G. Impact of hole doping on spin transition in perovskite-type cobalt oxides. *Dalton Transactions* **2016,** 45 (26), 10539-10545 DOI: 10.1039/c6dt00338a.

91. Sterne, P. A.; Gonis, A.; Borovoi, A. A. *Actinides and the Environment*. Springer Netherlands: 1998.

92. Vieten, J.; Bulfin, B.; Senholdt, M.; Roeb, M.; Sattler, C.; Schmücker, M. Redox thermodynamics and phase composition in the system SrFeO3 − δ — SrMnO3 − δ. *Solid State Ionics* **2017,** 308, 149-155 DOI: https://doi.org/10.1016/j.ssi.2017.06.014.

93. Dabrowski, B.; Chmaissem, O.; Mais, J.; Kolesnik, S.; Jorgensen, J. D.; Short, S. Tolerance factor rules for Sr1−x−yCaxBayMnO3 perovskites. *Journal of Solid State Chemistry* **2003,** 170 (1), 154-164 DOI: http://dx.doi.org/10.1016/S0022-4596(02)00056-7.

94. Kudoh, Y.; Prewitt, C.; Finger, L.; Ito, E. Ionic Radius-Bond Strength Systematics, Ionic Compressibilities, and an Application to (Mg, Fe) SiO3 Perovskites. *High-pressure research: Application to Earth and planetary sciences*, 215-218.

95. Vieten, J.; Bulfin, B.; Huck, P.; Horton, M.; Guban, D.; Zhu, L.; Youjun, L.; Persson, K.; Roeb, M.; Sattler, C. Materials design of perovskite solid solutions for thermochemical applications. *Energy & Environmental Science* **2019**, 12, 1369-1384.

96. Simon, A. Group 1 and 2 suboxides and subnitrides — Metals with atomic size holes and tunnels. *Coordination Chemistry Reviews* **1997,** 163, 253-270 DOI: https://doi.org/10.1016/S0010-8545(97)00013-1.

97. Colville, A. A.; Geller, S. The crystal structure of brownmillerite, Ca2FeAlO5. *Acta Crystallographica Section B* **1971,** 27 (12), 2311-2315 DOI: doi:10.1107/S056774087100579X.

98. Manimuthu, P.; Venkateswaran, C. Evidence of ferroelectricity in SrFeO 3−δ. *Journal of Physics D: Applied Physics* **2012,** 45 (1), 015303.

99. Hodges, J. P.; Short, S.; Jorgensen, J. D.; Xiong, X.; Dabrowski, B.; Mini, S. M.; Kimball, C. W. Evolution of Oxygen-Vacancy Ordered Crystal Structures in the Perovskite Series SrnFenO3n−1 (n=2, 4, 8, and ∞), and the Relationship to Electronic and Magnetic Properties. *Journal of Solid State Chemistry* **2000,** 151 (2), 190-209 DOI: http://dx.doi.org/10.1006/jssc.1999.8640.

100. Yusa, H.; Sata, N.; Ohishi, Y. Rhombohedral (9R) and hexagonal (6H) perovskites in barium silicates under high pressure. *American Mineralogist* **2007,** 92 (4), 648-654 DOI: 10.2138/am.2007.2314.

101. Battle, P. D.; Gibb, T. C.; Jones, C. W. The structural and magnetic properties of SrMnO3: A reinvestigation. *Journal of Solid State Chemistry* **1988,** 74 (1), 60-66 DOI: http://dx.doi.org/10.1016/0022-4596(88)90331-3.

102. Cussen, E. J.; Sloan, J.; Vente, J. F.; Battle, P. D.; Gibb, T. C. 15R SrMn1-xFexO3-δ (x ≈ 0.1); A New Perovskite Stacking Sequence. *Inorganic Chemistry* **1998,** 37 (23), 6071-6077 DOI: 10.1021/ic980802j.

103. Woodward, P. Octahedral Tilting in Perovskites. II. Structure Stabilizing Forces. *Acta Crystallographica Section B* **1997,** 53 (1), 44-66 DOI: doi:10.1107/S0108768196012050.

104. Glazer, A. Simple ways of determining perovskite structures. *Acta Crystallographica Section A* **1975,** 31 (6), 756-762 DOI: doi:10.1107/S0567739475001635.

105. Zhou, J. S.; Goodenough, J. B. Universal Octahedral-Site Distortion in Orthorhombic Perovskite Oxides. *Physical Review Letters* **2005,** 94 (6), 065501.

106. Murakami, M.; Hirose, K.; Kawamura, K.; Sata, N.; Ohishi, Y. Post-Perovskite Phase Transition in MgSiO₃. *Science* **2004,** 304 (5672), 855-858 DOI: 10.1126/science.1095932.

107. Oganov, A. R.; Ono, S. Theoretical and experimental evidence for a post-perovskite phase of MgSiO3 in Earth's D″ layer. *Nature* **2004,** 430, 445 DOI: 10.1038/nature02701.

108. KIRBY, S. H.; DURHAM, W. B.; STERN, L. A. Mantle Phase Changes and Deep-Earthquake Faulting in Subducting Lithosphere. *Science* **1991,** 252 (5003), 216-225 DOI: 10.1126/science.252.5003.216.

109. Takashi, N.; J., T. P. Effects of a perovskite-post perovskite phase change near core-mantle boundary in compressible mantle convection. *Geophysical Research Letters* **2004,** 31 (16), DOI: doi:10.1029/2004GL020648.

110. Ezbiri, M.; Takacs, M.; Theiler, D.; Michalsky, R.; Steinfeld, A. Tunable thermodynamic activity of LaxSr1-xMnyAl1-yO3-δ (0 ≤ x ≤1, 0 ≤ y ≤ 1) perovskites for solar thermochemical fuel synthesis. *Journal of Materials Chemistry A* **2017,** 5 (8), 4172-4182 DOI: 10.1039/c6ta06644e.

111. Cooper, T.; Scheffe, J. R.; Galvez, M. E.; Jacot, R.; Patzke, G.; Steinfeld, A. Lanthanum Manganite Perovskites with Ca/Sr A-site and Al B-site Doping as Effective Oxygen Exchange Materials for Solar Thermochemical Fuel Production. *Energy Technology* **2015,** 3 (11), 1130-1142 DOI: doi:10.1002/ente.201500226.

112. Jiang, S. P. Development of lanthanum strontium manganite perovskite cathode materials of solid oxide fuel cells: a review. *Journal of Materials Science* **2008,** 43 (21), 6799-6833 DOI: 10.1007/s10853-008-2966-6.

113. Vieten, J.; Huck, P.; Bulfin, B.; Horton, M.; Persson, K.; Roeb, M.; Sattler, C. Energetic analysis of two-step thermochemical cycles based on perovskite solid solutions, draft, merged with [95]

114. Burns, R. G.; Fyfe, W. S. Trace element distribution rules and their significance. *Chemical Geology* **1967,** 2, 89-104 DOI: https://doi.org/10.1016/0009-2541(67)90010-1.

115. Levason, W.; Spicer, M. D. The chemistry of copper and silver in their higher oxidation states. *Coordination Chemistry Reviews* **1987,** 76, 45-120 DOI: http://dx.doi.org/10.1016/0010-8545(87)85002-6.

116. Jain, A.; Ong, S. P.; Hautier, G.; Chen, W.; Richards, W. D.; Dacek, S.; Cholia, S.; Gunter, D.; Skinner, D.; Ceder, G.; Persson, K. A. Commentary: The Materials Project: A materials genome approach to accelerating materials innovation. *APL Materials* **2013,** 1 (1), 011002 DOI: doi:http://dx.doi.org/10.1063/1.4812323.

117. Jain, A.; Hautier, G.; Ong, S. P.; Moore, C. J.; Fischer, C. C.; Persson, K. A.; Ceder, G. Formation enthalpies by mixing GGA and GGA $+$ U calculations. *Physical Review B* **2011,** 84 (4), 045115.

118. Tschauner, O.; Ma, C.; Beckett, J. R.; Prescher, C.; Prakapenka, V. B.; Rossman, G. R. Discovery of bridgmanite, the most abundant mineral in Earth, in a shocked meteorite. *Science* **2014,** 346 (6213), 1100-1102 DOI: 10.1126/science.1259369.

119. Laing, M. Gadolinium: Central Metal of the Lanthanoids. *Journal of Chemical Education* **2009,** 86 (2), 188 DOI: 10.1021/ed086p188.

120. Parr, R. G.; Weitao, Y. *Density-Functional Theory of Atoms and Molecules*. Oxford University Press: 1994.

121. Hohenberg, P.; Kohn, W. Inhomogeneous Electron Gas. *Physical Review* **1964,** 136 (3B), B864-B871 DOI: 10.1103/PhysRev.136.B864.

122. Kieron, B.; O., W. L. DFT in a nutshell. *International Journal of Quantum Chemistry* **2013,** 113 (2), 96-101 DOI: doi:10.1002/qua.24259.

123. Becke, A. D. Perspective: Fifty years of density-functional theory in chemical physics. *The Journal of Chemical Physics* **2014,** 140 (18), 18A301 DOI: 10.1063/1.4869598.

124. Perdew, J. P.; Burke, K.; Ernzerhof, M. Generalized Gradient Approximation Made Simple. *Physical Review Letters* **1996,** 77 (18), 3865-3868.

125. Ewald, P. P. Die Berechnung optischer und elektrostatischer Gitterpotentiale. *Annalen der Physik* **1921,** 369 (3), 253-287 DOI: doi:10.1002/andp.19213690304.

126. Ong, S. P.; Richards, W. D.; Jain, A.; Hautier, G.; Kocher, M.; Cholia, S.; Gunter, D.; Chevrier, V. L.; Persson, K. A.; Ceder, G. Python Materials Genomics (pymatgen): A robust, open-source python library for materials analysis. *Computational Materials Science* **2013,** 68, 314-319 DOI: https://doi.org/10.1016/j.commatsci.2012.10.028.

127. van de Walle, A.; Tiwary, P.; de Jong, M.; Olmsted, D. L.; Asta, M.; Dick, A.; Shin, D.; Wang, Y.; Chen, L. Q.; Liu, Z. K. Efficient stochastic generation of special quasirandom structures. *Calphad* **2013,** 42, 13-18 DOI: https://doi.org/10.1016/j.calphad.2013.06.006.

128. Zunger, A.; Wei, S. H.; Ferreira, L. G.; Bernard, J. E. Special quasirandom structures. *Physical Review Letters* **1990,** 65 (3), 353-356 DOI: 10.1103/PhysRevLett.65.353.

129. Bulfin, B.; Hoffmann, L.; de Oliveira, L.; Knoblauch, N.; Call, F.; Roeb, M.; Sattler, C.; Schmucker, M. Statistical thermodynamics of non-stoichiometric ceria and ceria zirconia solid solutions. *Physical Chemistry Chemical Physics* **2016,** 18 (33), 23147-23154 DOI: 10.1039/c6cp03158g.

130. NIST, National Institute of Standards and Technology, http://webbook.nist.gov/cgi/cbook.cgi?ID=C7782447&Mask=1.

131. Chase, M. W.; National Institute of, S.; Technology. *NIST-JANAF thermochemical tables*. American Chemical Society ; American Institute of Physics for the National Institute of Standards and Technology: [Washington, D.C.]; Woodbury, N.Y., 1998.

132. Bulfin, B.; Vieten, J.; Starr, D. E.; Azarpira, A.; Zachäus, C.; Haevecker, M.; Skorupska, K.; Schmuecker, M.; Roeb, M.; Sattler, C. Redox chemistry of CaMnO3 and Ca0.8Sr0.2MnO3 oxygen storage perovskites. *Journal of Materials Chemistry A* **2017**, DOI: 10.1039/c7ta00822h.

133. Fultz, B. Vibrational thermodynamics of materials. *Progress in Materials Science* **2010,** 55 (4), 247-352 DOI: https://doi.org/10.1016/j.pmatsci.2009.05.002.

134. de Jong, M.; Chen, W.; Angsten, T.; Jain, A.; Notestine, R.; Gamst, A.; Sluiter, M.; Krishna Ande, C.; van der Zwaag, S.; Plata, J. J.; Toher, C.; Curtarolo, S.; Ceder, G.; Persson, K. A.; Asta, M. Charting the complete elastic properties of inorganic crystalline compounds. *Scientific Data* **2015,** 2, 150009 DOI: 10.1038/sdata.2015.9.

135. Naghavi, S. S.; Emery, A. A.; Hansen, H. A.; Zhou, F.; Ozolins, V.; Wolverton, C. Giant onsite electronic entropy enhances the performance of ceria for water splitting. *Nature Communications* **2017,** 8 (1), 285 DOI: 10.1038/s41467-017-00381-2.

136. Haavik, C.; Atake, T.; Kawaji, H.; Stolen, S. On the entropic contribution to the redox energetics of SrFeO3-[small delta]. *Physical Chemistry Chemical Physics* **2001,** 3 (17), 3863-3870 DOI: 10.1039/b104401j.

137. Lapp, J. L.; Rieping, R.; Bulfin, B.; Roeb, M.; Sattler, C. Mitigation methods for errors in oxygen measurement with redox cycling of materials for hydrogen and syngas production. *International Journal of Hydrogen Energy* **2018,** 43 (19), 9165-9180 DOI: https://doi.org/10.1016/j.ijhydene.2018.03.182.

138. Haber, J.; Grzybowska, B. Mechanism of the oxidation of olefins on mixed oxide catalysts. *Journal of Catalysis* **1973,** 28 (3), 489-492 DOI: https://doi.org/10.1016/0021-9517(73)90142-5.

139. Bielanski, A.; Haber, J. *Oxygen in catalysis*. CRC Press: 1990.

140. Merino, N. A.; Barbero, B. P.; Eloy, P.; Cadús, L. E. La1−xCaxCoO3 perovskite-type oxides: Identification of the surface oxygen species by XPS. *Applied Surface Science* **2006,** 253 (3), 1489-1493 DOI: https://doi.org/10.1016/j.apsusc.2006.02.035.

141. Ezbiri, M.; Takacs, M.; Stolz, B.; Lungthok, J.; Steinfeld, A.; Michalsky, R. Design principles of perovskites for solar-driven thermochemical splitting of CO2. *Journal of Materials Chemistry A* **2017,** 5 (29), 15105-15115 DOI: 10.1039/c7ta02081c.

142. De Souza, R. A. Oxygen Diffusion in SrTiO3 and Related Perovskite Oxides. *Advanced Functional Materials* **2015,** 25 (40), 6326-6342 DOI: doi:10.1002/adfm.201500827.

143. Goodenough, J. B.; Manthiram, A.; Kuo, J. F. Oxygen diffusion in perovskite-related oxides. *Materials Chemistry and Physics* **1993,** 35 (3), 221-224 DOI: https://doi.org/10.1016/0254-0584(93)90135-9.

144. Hanzig, J.; Zschornak, M.; Mehner, E.; Hanzig, F.; Münchgesang, W.; Leisegang, T.; Stöcker, H.; Meyer, D. C. The anisotropy of oxygen vacancy migration in SrTiO 3. *Journal of Physics: Condensed Matter* **2016,** 28 (22), 225001.

145. Mi-Young, Y.; Kuk-Jin, H.; Dae-Seop, B.; Joosun, K.; Hae-Jin, H.; Seong-Min, J. Computational Analysis of Oxide Ion Conduction in Orthorhombic Perovskite Structured La0.9A0.1InO2.95 (A = Ca, Sr and Ba). *Journal of the American Ceramic Society* **2015,** 98 (2), 515-519 DOI: doi:10.1111/jace.13294.

146. Steinfeld, A.; Sanders, S.; Palumbo, R. DESIGN ASPECTS OF SOLAR THERMOCHEMICAL ENGINEERING—A CASE STUDY: TWO-STEP WATER-SPLITTING CYCLE USING THE Fe3O4/FeO REDOX SYSTEM. *Solar Energy* **1999,** 65 (1), 43-53 DOI: https://doi.org/10.1016/S0038-092X(98)00092-9.

147. Ermanoski, I.; Siegel, N. P.; Stechel, E. B. A New Reactor Concept for Efficient Solar-Thermochemical Fuel Production. *Journal of Solar Energy Engineering* **2013,** 135 (3), 031002-031002-10 DOI: 10.1115/1.4023356.

148. Agrafiotis, C.; Roeb, M.; Sattler, C. A review on solar thermal syngas production via redox pair-based water/carbon dioxide splitting thermochemical cycles. *Renewable and Sustainable Energy Reviews* **2015,** 42, 254-285 DOI: https://doi.org/10.1016/j.rser.2014.09.039.

149. Grobbel, J.; Brendelberger, S.; Sattler, C.; Pitz-Paal, R. Heat transfer in a directly irradiated ceria particle bed under vacuum conditions. *Solar Energy* **2017,** 158, 737-745 DOI: https://doi.org/10.1016/j.solener.2017.10.022.

150. Brendelberger, S.; Roeb, M.; Lange, M.; Sattler, C. Counter flow sweep gas demand for the ceria redox cycle. *Solar Energy* **2015,** 122, 1011-1022 DOI: https://doi.org/10.1016/j.solener.2015.10.036.

151. Brendelberger, S.; Sattler, C. Concept analysis of an indirect particle-based redox process for solar-driven H2O/CO2 splitting. *Solar Energy* **2015,** 113 (0), 158-170 DOI: http://dx.doi.org/10.1016/j.solener.2014.12.035.

152. Scheffe, J. R.; Welte, M.; Steinfeld, A. Thermal Reduction of Ceria within an Aerosol Reactor for H2O and CO2 Splitting. *Industrial & Engineering Chemistry Research* **2014,** 53 (6), 2175-2182 DOI: 10.1021/ie402620k.

153. Bader, R.; Bala Chandran, R.; Venstrom, L. J.; Sedler, S. J.; Krenzke, P. T.; De Smith, R. M.; Banerjee, A.; Chase, T. R.; Davidson, J. H.; Lipiński, W. Design of a Solar Reactor to Split CO2 Via Isothermal Redox Cycling of Ceria. *Journal of Solar Energy Engineering* **2015,** 137 (3), 031007-031007-10 DOI: 10.1115/1.4028917.

154. Gokon, N.; Takahashi, S.; Yamamoto, H.; Kodama, T. Thermochemical two-step water-splitting reactor with internally circulating fluidized bed for thermal reduction of ferrite particles. *International Journal of Hydrogen Energy* **2008,** 33 (9), 2189-2199 DOI: https://doi.org/10.1016/j.ijhydene.2008.02.044.

155. Kaneko, H.; Miura, T.; Fuse, A.; Ishihara, H.; Taku, S.; Fukuzumi, H.; Naganuma, Y.; Tamaura, Y. Rotary-Type Solar Reactor for Solar Hydrogen Production with Two-step Water Splitting Process. *Energy & Fuels* **2007,** 21 (4), 2287-2293 DOI: 10.1021/ef060581z.

156. Roeb, M.; Sattler, C.; Klüser, R.; Monnerie, N.; de Oliveira, L.; Konstandopoulos, A. G.; Agrafiotis, C.; Zaspalis, V. T.; Nalbandian, L.; Steele, A.; Stobbe, P. Solar Hydrogen Production by a Two-Step Cycle Based on Mixed Iron Oxides. *Journal of Solar Energy Engineering* **2005,** 128 (2), 125-133 DOI: 10.1115/1.2183804.

157. Gokon, N.; Sagawa, S.; Kodama, T. Comparative study of activity of cerium oxide at thermal reduction temperatures of 1300–1550 °C for solar thermochemical two-step water-splitting cycle. *International Journal of Hydrogen Energy* **2013,** 38 (34), 14402-14414 DOI: https://doi.org/10.1016/j.ijhydene.2013.08.108.

158. Zhu, L.; Lu, Y.; Shen, S. Solar fuel production at high temperatures using ceria as a dense membrane. *Energy* **2016,** 104, 53-63 DOI: https://doi.org/10.1016/j.energy.2016.03.108.

159. Barin, I. *Thermochemical Data of Pure Substances, Third Edition*. 2008.

160. Körner, R. Untersuchung am System Cer-Sauerstoff, Thermische Ausdehnung im Bereich CeO2 bis CeO1,777 (German). Dissertation, Georg August Universität zu Göttingen, 1985.

161. Brendelberger, S.; Felinks, J.; Roeb, M.; Sattler, C. In *Solid Phase Heat Recovery and Multi Chamber Reduction for Redox Cycles*, Proceedings of the ASME 2014 8th International Conference on Energy Sustainability, Boston, June 30-July 2, 2014; Boston, 2014; pp ES2014-6421.

162. Felinks, J.; Richter, S.; Lachmann, B.; Brendelberger, S.; Roeb, M.; Sattler, C.; Pitz-Paal, R. Particle–particle heat transfer coefficient in a binary packed bed of alumina and zirconia-ceria particles. *Applied Thermal Engineering* **2016,** 101, 101-111 DOI: https://doi.org/10.1016/j.applthermaleng.2016.01.066.

163. Felinks, J.; Brendelberger, S.; Roeb, M.; Sattler, C.; Pitz-Paal, R. Heat recovery concept for thermochemical processes using a solid heat transfer medium. *Applied Thermal Engineering* **2014,** 73 (1), 1006-1013 DOI: https://doi.org/10.1016/j.applthermaleng.2014.08.036.

164. Grimvall, G. *Thermophysical Properties of Materials*. Elsevier Science: 1999.

165. Haavik, C.; Bakken, E.; Norby, T.; Stolen, S.; Atake, T.; Tojo, T. Heat capacity of SrFeO3-δ; δ= 0.50, 0.25 and 0.15 - configurational entropy of structural entities in grossly non-stoichiometric oxides. *Dalton Transactions* **2003,** (3), 361-368 DOI: 10.1039/b209236k.

166. Vieten, J.; Brendelberger, S.; Roeb, M.; Sattler, C., THERMOCCHEMICAL OXYGEN PUMPING FOR IMPROVED HYDROGEN PRODUCTION IN SOLAR REDOX CYCLES. In *9th International Conference on Hydrogen Production (ICH2P-2018)*, Zagreb, Croatia, 2018.

167. Barghouthi, S.; Tullis, K. Determination of the Vapor Pressure Curve of a Liquid in the Presence of a Nonvolatile Solute. *The Chemical Educator* **2000,** 5 (4), 183-186 DOI: 10.1007/s00897000396a.

168. Pacific Northwest National Laboratory, Lower and Higher Heating Values of Fuels. www.h2tools.org/hyarc/calculator-tools/lower-and-higher-heating-values-fuels (accessed May 8th 2018),

169. Vieten, J.; Bulfin, B.; Guban, D.; Zhu, L.; Huck, P.; Horton, M.; Persson, K.; Roeb, M.; Sattler, C., Materials Design and Characterization of Perovskites for Solar-thermochemical Redox Cycles. In *Poster at the Internal Helmholtz Evaluation*, Stuttgart, 2018.

170. Yu, X.; Long, W.; Jin, F.; He, T. Cobalt-free perovskite cathode materials SrFe1−xTixO3−δ and performance optimization for intermediate-temperature solid oxide fuel cells. *Electrochimica Acta* **2014,** 123, 426-434 DOI: https://doi.org/10.1016/j.electacta.2014.01.020.

171. Zuev, A. Y.; Tsvetkov, D. S. Oxygen nonstoichiometry, defect structure and defect-induced expansion of undoped perovskite LaMnO3 ± δ. *Solid State Ionics* **2010,** 181 (11–12), 557-563 DOI: http://doi.org/10.1016/j.ssi.2010.02.024.

172. Vieten, J.; Bulfin, B.; Roeb, M.; Sattler, C. Citric acid auto-combustion synthesis of Ti-containing perovskites via aqueous precursors. *Solid State Ionics* **2018,** 315, 92-97 DOI: https://doi.org/10.1016/j.ssi.2017.12.010.

173. Rørmark, L.; Mørch, A. B.; Wiik, K.; Stølen, S.; Grande, T. Enthalpies of Oxidation of CaMnO3-δ, Ca2MnO4-δ and SrMnO3-δ Deduced Redox Properties. *Chemistry of Materials* **2001,** 13 (11), 4005-4013 DOI: 10.1021/cm011050l.

174. Porta, P.; Cimino, S.; De Rossi, S.; Faticanti, M.; Minelli, G.; Pettiti, I. AFeO3 (A=La, Nd, Sm) and LaFe1−xMgxO3 perovskites: structural and redox properties. *Materials Chemistry and Physics* **2001,** 71 (2), 165-173 DOI: http://dx.doi.org/10.1016/S0254-0584(01)00273-5.

175. Delmon, B.; Droguest, J. Belgian Patent 735 476. 1969.

176. Danks, A. E.; Hall, S. R.; Schnepp, Z. The evolution of 'sol-gel' chemistry as a technique for materials synthesis. *Materials Horizons* **2016,** 3 (2), 91-112 DOI: 10.1039/c5mh00260e.

177. Deganello, F.; Marcì, G.; Deganello, G. Citrate–nitrate auto-combustion synthesis of perovskite-type nanopowders: A systematic approach. *Journal of the European Ceramic Society* **2009,** 29 (3), 439-450 DOI: http://doi.org/10.1016/j.jeurceramsoc.2008.06.012.

178. Pechini, M. P. Barium titanium citrate, barium titanate and processes for producing same, Patent US 3231328 A. 1966.

179. Vieten, J. *"Development of Materials for Solar Thermal Production of Nitrogen as a Basis for Regenerative Fertilizer Production", Master's thesis, DLR, TU Munich.* **2016**.

180. Marinšek, M.; Zupan, K.; Maèek, J. Ni–YSZ cermet anodes prepared by citrate/nitrate combustion synthesis. *Journal of Power Sources* **2002,** 106 (1), 178-188 DOI: https://doi.org/10.1016/S0378-7753(01)01056-4.

181. Holleman, A. F.; Wiberg, E.; Wiberg, N. *Lehrbuch der anorganischen Chemie*. Walter de Gruyter: 2007.

182. Ribeiro, P. C.; Costa, A. C. F. d. M. d.; Kiminami, R. H. G. A.; Sasaki, J. M.; Lira, H. L. Synthesis of TiO2 by the pechini method and photocatalytic degradation of methyl red. *Materials Research* **2013,** 16, 468-472.

183. Kao, C.-F.; Yang, W.-D. Preparation of barium strontium titanate powder from citrate precursor. *Applied Organometallic Chemistry* **1999,** 13 (5), 383-397 DOI: 10.1002/(sici)1099-0739(199905)13:5<383::aid-aoc836>3.0.co;2-p.

184. Kakihana, M.; Tada, M.; Shiro, M.; Petrykin, V.; Osada, M.; Nakamura, Y. Structure and Stability of Water Soluble (NH4)8[Ti4(C6H4O7)4(O2)4]·8H2O. *Inorganic Chemistry* **2001,** 40 (5), 891-894 DOI: 10.1021/ic001098l.

185. Schwarzenbach, G.; Muehlebach, J.; Mueller, K. Peroxo complexes of titanium. *Inorganic Chemistry* **1970,** 9 (11), 2381-2390 DOI: 10.1021/ic50093a001.

186. Dakanali, M.; Kefalas, E. T.; Raptopoulou, C. P.; Terzis, A.; Voyiatzis, G.; Kyrikou, I.; Mavromoustakos, T.; Salifoglou, A. A New Dinuclear Ti(IV)−Peroxo−Citrate Complex from Aqueous Solutions. Synthetic, Structural, and Spectroscopic Studies in Relevance to Aqueous Titanium(IV)−Peroxo−Citrate Speciation. *Inorganic Chemistry* **2003,** 42 (15), 4632-4639 DOI: 10.1021/ic0343051.

187. Patil, K. C.; Aruna, S. T.; Mimani, T. Combustion synthesis: an update. *Current Opinion in Solid State and Materials Science* **2002,** 6 (6), 507-512 DOI: http://doi.org/10.1016/S1359-0286(02)00123-7.

188. Barbooti, M. M.; Al-Sammerrai, D. A. Thermal decomposition of citric acid. *Thermochimica Acta* **1986,** 98, 119-126 DOI: http://dx.doi.org/10.1016/0040-6031(86)87081-2.

189. Merkle, R.; Maier, J. On the Tammann–Rule. *Zeitschrift für anorganische und allgemeine Chemie* **2005,** 631 (6-7), 1163-1166.

190. Pfaff, G. Synthesis of calcium titanate powders by the sol-gel process. *Chemistry of Materials* **1994,** 6 (1), 58-62 DOI: 10.1021/cm00037a013.

191. MAUD. *Materials Analysis Using Diffraction, Version 2.55* **2015**.

192. Gražulis, S.; Daškevič, A.; Merkys, A.; Chateigner, D.; Lutterotti, L.; Quirós, M.; Serebryanaya, N. R.; Moeck, P.; Downs, R. T.; Le Bail, A. Crystallography Open Database (COD): an open-access collection of crystal structures and platform for world-wide collaboration. *Nucleic Acids Research* **2012,** 40 (D1), D420-D427 DOI: 10.1093/nar/gkr900.

193. Rietveld, H. M., The Rietveld Method: A Retrospection. In *Zeitschrift für Kristallographie Crystalline Materials*, 2010; Vol. 225, p 545.

194. Rameshan, C.; Li, H.; Anic, K.; Roiaz, M.; Pramhaas, V.; Rameshan, R.; Blume, R.; Hävecker, M.; Knudsen, J.; Knop-Gericke, A.; Rupprechter, G. In situ NAP-XPS spectroscopy during methane dry reforming on ZrO 2 /Pt(1 1 1) inverse model catalyst. *Journal of Physics: Condensed Matter* **2018,** 30 (26), 264007.

195. Starr, D. E.; Liu, Z.; Havecker, M.; Knop-Gericke, A.; Bluhm, H. Investigation of solid/vapor interfaces using ambient pressure X-ray photoelectron spectroscopy. *Chemical Society Reviews* **2013,** 42 (13), 5833-5857 DOI: 10.1039/c3cs60057b.

196. Babiniec, S. M.; Coker, E. N.; Miller, J. E.; Ambrosini, A. Doped calcium manganites for advanced high-temperature thermochemical energy storage. *International Journal of Energy Research* **2016,** 40 (2), 280-284 DOI: 10.1002/er.3467.

197. Krug, R. R.; Hunter, W. G.; Grieger, R. A. Statistical interpretation of enthalpy–entropy compensation. *Nature* **1976,** 261, 566 DOI: 10.1038/261566a0.

198. Bulfin, B.; Call, F.; Vieten, J.; Roeb, M.; Sattler, C.; Shvets, I. Oxidation and Reduction Reaction Kinetics of Mixed Cerium Zirconium Oxides. *The Journal of Physical Chemistry C* **2016**, DOI: 10.1021/acs.jpcc.5b08729.

199. Vieten, J.; Persson, K.A., Materials Project DOI Collection 10.17188/1475589. **2018**.

200. Jain, A.; Ong, S. P.; Chen, W.; Medasani, B.; Qu, X.; Kocher, M.; Brafman, M.; Petretto, G.; Rignanese, G.-M.; Hautier, G.; Gunter, D.; Persson, K. A. FireWorks: a dynamic workflow system designed for high-throughput applications. *Concurrency and Computation: Practice and Experience* **2015,** 27 (17), 5037-5059 DOI: doi:10.1002/cpe.3505.

201. Mathew, K.; Montoya, J. H.; Faghaninia, A.; Dwarakanath, S.; Aykol, M.; Tang, H.; Chu, I.-h.; Smidt, T.; Bocklund, B.; Horton, M.; Dagdelen, J.; Wood, B.; Liu, Z.-K.; Neaton, J.; Ong, S. P.; Persson, K.; Jain, A. Atomate: A high-level interface to generate, execute, and analyze computational materials science workflows. *Computational Materials Science* **2017,** 139, 140-152 DOI: https://doi.org/10.1016/j.commatsci.2017.07.030.

202. Kresse, G.; Furthmüller, J. Efficiency of ab-initio total energy calculations for metals and semiconductors using a plane-wave basis set. *Computational Materials Science* **1996,** 6 (1), 15-50 DOI: https://doi.org/10.1016/0927-0256(96)00008-0.

203. Kresse, G.; Furthmüller, J. Efficient iterative schemes for ab initio total-energy calculations using a plane-wave basis set. *Physical Review B* **1996,** 54 (16), 11169-11186 DOI: 10.1103/PhysRevB.54.11169.

204. Zhou, Q.; Kennedy, B. J. Thermal expansion and structure of orthorhombic CaMnO3. *Journal of Physics and Chemistry of Solids* **2006,** 67 (7), 1595-1598 DOI: https://doi.org/10.1016/j.jpcs.2006.02.011.

205. Jain, A.; Hautier, G.; Moore, C. J.; Ping Ong, S.; Fischer, C. C.; Mueller, T.; Persson, K. A.; Ceder, G. A high-throughput infrastructure for density functional theory calculations. *Computational Materials Science* **2011,** 50 (8), 2295-2310 DOI: http://dx.doi.org/10.1016/j.commatsci.2011.02.023.

206. Bakken, E.; Norby, T.; Stølen, S. Nonstoichiometry and reductive decomposition of CaMnO3−δ. *Solid State Ionics* **2005,** 176 (1–2), 217-223 DOI: http://dx.doi.org/10.1016/j.ssi.2004.07.001.

207. Bevan, D. J. M.; Kordis, J. Mixed oxides of the type MO2 (fluorite)—M2O3—I oxygen dissociation pressures and phase relationships in the system CeO2Ce2O3 at high temperatures. *Journal of Inorganic and Nuclear Chemistry* **1964,** 26 (9), 1509-1523 DOI: http://dx.doi.org/10.1016/0022-1902(64)80038-5.

208. Sørensen, O. T. Thermodynamic studies of the phase relationships of nonstoichiometric cerium oxides at higher temperatures. *Journal of Solid State Chemistry* **1976,** 18 (3), 217-233 DOI: https://doi.org/10.1016/0022-4596(76)90099-2.

209. Hao, Y.; Yang, C.-K.; Haile, S. M. Ceria–Zirconia Solid Solutions (Ce1−xZrxO2−δ, x ≤ 0.2) for Solar Thermochemical Water Splitting: A Thermodynamic Study. *Chemistry of Materials* **2014,** 26 (20), 6073-6082 DOI: 10.1021/cm503131p.

210. Crumlin, E. J.; Mutoro, E.; Liu, Z.; Grass, M. E.; Biegalski, M. D.; Lee, Y.-L.; Morgan, D.; Christen, H. M.; Bluhm, H.; Shao-Horn, Y. Surface strontium enrichment on highly active perovskites for oxygen electrocatalysis in solid oxide fuel cells. *Energy & Environmental Science* **2012,** 5 (3), 6081-6088 DOI: 10.1039/c2ee03397f.

211. Efimov, K.; Czuprat, O.; Feldhoff, A. In-situ X-ray diffraction study of carbonate formation and decomposition in perovskite-type BCFZ. *Journal of Solid State Chemistry* **2011,** 184 (5), 1085-1089 DOI: https://doi.org/10.1016/j.jssc.2011.03.023.

212. Schmidt, M. Composition adjustment of non-stoichiometric strontium ferrite SrFeO3−δ. *Journal of Physics and Chemistry of Solids* **2000,** 61 (8), 1363-1365 DOI: https://doi.org/10.1016/S0022-3697(00)00002-0.

213. Brendelberger, S.; Vieten, J.; Vidyasagar, M. J.; Roeb, M.; Sattler, C. Demonstration of thermochemical oxygen pumping for atmosphere control in reduction reactions. *Solar Energy* **2018,** 170, 273-279 DOI: https://doi.org/10.1016/j.solener.2018.05.063.

214. Zhang, H.; Wang, T.; Dong, X.; Lin, W. Preparation and oxygen permeation properties of SrFe(Cu)O3−δ dense ceramic membranes. *Journal of Natural Gas Chemistry* **2009,** 18 (1), 45-49 DOI: https://doi.org/10.1016/S1003-9953(08)60084-5.

215. Li, M.; Zhang, H.; Cook, S. N.; Li, L.; Kilner, J. A.; Reaney, I. M.; Sinclair, D. C. Dramatic Influence of A-Site Nonstoichiometry on the Electrical Conductivity and Conduction Mechanisms in the Perovskite Oxide Na0.5Bi0.5TiO3. *Chemistry of Materials* **2015,** 27 (2), 629-634 DOI: 10.1021/cm504475k.

216. Mulmi, S.; Chen, H.; Hassan, A.; Marco, J. F.; Berry, F. J.; Sharif, F.; Slater, P. R.; Roberts, E. P. L.; Adams, S.; Thangadurai, V. Thermochemical CO2 splitting using double perovskite-type Ba2Ca0.66Nb1.34−xFexO6−δ. *Journal of Materials Chemistry A* **2017,** 5 (15), 6874-6883 DOI: 10.1039/c6ta10285a.

217. Kharton, V. V.; Kovalevsky, A. V.; Patrakeev, M. V.; Tsipis, E. V.; Viskup, A. P.; Kolotygin, V. A.; Yaremchenko, A. A.; Shaula, A. L.; Kiselev, E. A.; Waerenborgh, J. C. Oxygen Nonstoichiometry, Mixed Conductivity, and Mössbauer Spectra of Ln0.5A0.5FeO3−δ (Ln = La–Sm, A = Sr, Ba): Effects of Cation Size. *Chemistry of Materials* **2008,** 20 (20), 6457-6467 DOI: 10.1021/cm801569j.

218. Nenning, A.; Opitz, A. K.; Rameshan, C.; Rameshan, R.; Blume, R.; Hävecker, M.; Knop-Gericke, A.; Rupprechter, G.; Klötzer, B.; Fleig, J. Ambient Pressure XPS Study of Mixed Conducting Perovskite-Type SOFC Cathode and Anode Materials under Well-Defined Electrochemical Polarization. *The Journal of Physical Chemistry C* **2016,** 120 (3), 1461-1471 DOI: 10.1021/acs.jpcc.5b08596.

219. Darracq, S.; Kang, S. G.; Choy, J. H.; Demazeau, G. Stabilization of the Mixed Valence Cu(III)/Cu(IV) in the Perovskite Lattice of La1-xSrxCuO3 under High Oxygen Pressure. *Journal of Solid State Chemistry* **1995,** 114 (1), 88-94 DOI: http://dx.doi.org/10.1006/jssc.1995.1013.

220. Wu, X. J.; Laffez, P.; Yamauchi, H.; Môri, N. TEM study on a new Sr-Cu-O phase synthesized under high pressure. *Physica C: Superconductivity* **1994,** 228 (3), 292-298 DOI: http://dx.doi.org/10.1016/0921-4534(94)90418-9.

221. Sacher, E.; Klemberg-Sapieha, J. E.; Cambron, A.; Okoniewski, A.; Yelon, A. X-ray photoelectron spectroscopic evidence for CuIII in superconducting YBa2Cu3O7 ceramic. *Journal of Electron Spectroscopy and Related Phenomena* **1989,** 48 (2), C7-C12 DOI: https://doi.org/10.1016/0368-2048(89)80029-5.

222. Meyers, D.; Mukherjee, S.; Cheng, J. G.; Middey, S.; Zhou, J. S.; Goodenough, J. B.; Gray, B. A.; Freeland, J. W.; Saha-Dasgupta, T.; Chakhalian, J. Zhang-Rice physics and anomalous copper states in A-site ordered perovskites. **2013,** 3, 1834 DOI: 10.1038/srep01834

https://www.nature.com/articles/srep01834#supplementary-information.

223. Okada, K.; Kotani, A. Large-Cluster Effects on Core-Level Photoabsorption Spectrum of LaCuO 3. *Journal of the Physical Society of Japan* **1999,** 68 (2), 666-673 DOI: 10.1143/jpsj.68.666.

224. Qing, Z.; Yun-Yu, Y.; Jian-Hong, D.; Xi, S.; Zhi-Wei, H.; Jun-Ye, Y.; Qing-Tao, W.; Ri-Cheng, Y.; Xiao-Dong, L.; You-Wen, L. A -site ordered perovskite CaCu 3 Cu 2 Ir 2 O 12− δ with square-planar and octahedral coordinated Cu ions. *Chinese Physics B* **2016,** 25 (2), 020701.

225. Karppinen, M.; Yamauchi, H.; Suematsu, H.; Isawa, K.; Nagano, M.; Itti, R.; Fukunaga, O. Control on the Copper Valence and Properties by Oxygen Content Adjustment in the LaCuO3−ySystem (0≤y≤0.5). *Journal of Solid State Chemistry* **1997,** 130 (2), 213-222 DOI: https://doi.org/10.1006/jssc.1997.7296.

226. Vijayakumar, M.; Inaguma, Y.; Mashiko, W.; Crosnier-Lopez, M.-P.; Bohnke, C. Synthesis of Fine Powders of Li3xLa2/3-xTiO3 Perovskite by a Polymerizable Precursor Method. *Chemistry of Materials* **2004,** 16 (14), 2719-2724 DOI: 10.1021/cm049869x.

227. Kakihana, M.; Szanics, J.; Tada, M. Chemical design of highly water-soluble Ti, Nb and Ta precursors for multi-component oxides. *Bulletin of the Korean Chemical Society* **1999,** 20 (8), 893-896.

228. GONCALVES; #160; P.; CANALES-VAZQUEZ; J.; FIGUEIREDO; M., F. *Mecanosintesis de polvos nanocristalinos de CaTi[1-x]Mn[x]O[3-δ]*. Sociedad Espanola de Ceramica y Vidrio: Madrid, ESPAGNE, 2008; Vol. 47, p 5.

229. Buttner, R. H.; Maslen, E. N. Electron difference density and structural parameters in CaTiO3. *Acta Crystallographica Section B* **1992,** 48 (5), 644-649 DOI: doi:10.1107/S0108768192004592.

230. Leonowicz, M. E.; Poeppelmeier, K. R.; Longo, J. M. Structure determination of Ca2MnO4 and Ca2MnO3.5 by X-ray and neutron methods. *Journal of Solid State Chemistry* **1985,** 59 (1), 71-80 DOI: http://dx.doi.org/10.1016/0022-4596(85)90352-4.

231. Schmidt, M.; Campbell, S. J. In situ neutron diffraction study (300–1273 K) of non-stoichiometric strontium ferrite SrFeOx. *Journal of Physics and Chemistry of Solids* **2002,** 63 (11), 2085-2092 DOI: http://dx.doi.org/10.1016/S0022-3697(02)00198-1.

232. Fawcett, I. D.; Veith, G. M.; Greenblatt, M.; Croft, M.; Nowik, I. Properties of the perovskites, SrMn1−xFexO3−δ (x=1/3, 1/2, 2/3). *Solid State Sciences* **2000,** 2 (8), 821-831 DOI: http://dx.doi.org/10.1016/S1293-2558(00)01097-9.

233. Mizutani, N.; Kitazawa, A.; Ohkuma, N.; Kato, M. Synthesis of Strontium-Manganese Double Oxides. *The Journal of the Society of Chemical Industry, Japan* **1970,** 73 (6), 1097-1103 DOI: 10.1246/nikkashi1898.73.6_1097.

234. Conder, K.; Pomjakushina, E.; Soldatov, A.; Mitberg, E. Oxygen content determination in perovskite-type cobaltates. *Materials Research Bulletin* **2005,** 40 (2), 257-263 DOI: https://doi.org/10.1016/j.materresbull.2004.10.009.

235. Bakken, E.; Stølen, S.; Norby, T.; Glenne, R.; Budd, M. Redox energetics of SrFeO3−δ — a coulometric titration study. *Solid State Ionics* **2004,** 167 (3–4), 367-377 DOI: http://dx.doi.org/10.1016/j.ssi.2004.01.014.

236. Töpfer, J.; Pippardt, U.; Voigt, I.; Kriegel, R. Structure, nonstoichiometry and magnetic properties of the perovskites Sr1−xCaxMnO3−δ. *Solid State Sciences* **2004,** 6 (7), 647-654 DOI: https://doi.org/10.1016/j.solidstatesciences.2004.03.023.

237. Curnan, M. T.; Kitchin, J. R. Effects of Concentration, Crystal Structure, Magnetism, and Electronic Structure Method on First-Principles Oxygen Vacancy Formation Energy Trends in Perovskites. *The Journal of Physical Chemistry C* **2014,** 118 (49), 28776-28790 DOI: 10.1021/jp507957n.

238. Marezio, M.; Remeika, J. P.; Dernier, P. D. The crystal chemistry of the rare earth orthoferrites. *Acta Crystallographica Section B* **1970,** 26 (12), 2008-2022 DOI: doi:10.1107/S0567740870005319.

239. Keawprak, N.; Tu, R.; Goto, T. Thermoelectricity of CaIrO₃ ceramics prepared by spark plasma sintering. *Journal of the Ceramic Society of Japan* **2009,** 117 (1364), 466-469 DOI: 10.2109/jcersj2.117.466.

240. Martin, C. D.; Smith, R. I.; Marshall, W. G.; Parise, J. B. High-pressure structure and bonding in CaIrO3: The structure model of MgSiO3 post-perovskite investigated with time-of-flight neutron powder diffraction. *American Mineralogist* **2007,** 92 (11-12), 1912-1918 DOI: 10.2138/am.2007.2585.

241. Lebendig, F. Thermodynamische Untersuchung von Redoxmaterialien zur solarthermischen Wasserstoffherstellung, Master's Thesis (German). Department of Chemistry, University of Cologne, 2018.

242. Zhou, M.; Bak, T.; Nowotny, J.; Rekas, M.; Sorrell, C.; Vance, E. Defect chemistry and semiconducting properties of calcium titanate. *Journal of Materials Science: Materials in Electronics* **2002,** 13 (12), 697-704.

243. Chan, N. H.; Sharma, R. K.; Smyth, D. M. Nonstoichiometry in SrTiO3. *Journal of The Electrochemical Society* **1981,** 128 (8), 1762-1769 DOI: 10.1149/1.2127727.

244. Balachandran, U.; Eror, N. G. Oxygen non-stoichiometry of tantalum-doped SrTiO3. *Journal of the Less Common Metals* **1982,** 85, 11-19 DOI: https://doi.org/10.1016/0022-5088(82)90053-4.

245. Takeda, Y.; Kanno, R.; Takada, T.; Yamamoto, O.; Takano, M.; Bando, Y. Phase relation and oxygen-non-stoichiometry of Perovskite-like Compound SrCoOx (2.29 < x > 2.80). *Zeitschrift für anorganische und allgemeine Chemie* **1986,** 540 (9-10), 259-270 DOI: doi:10.1002/zaac.19865400929.

246. Blasco, J.; Stankiewicz, J.; García, J. Phase segregation in the Gd1−xSrxFeO3−δ series. *Journal of Solid State Chemistry* **2006,** 179 (3), 898-908 DOI: http://dx.doi.org/10.1016/j.jssc.2005.12.023.

247. Emery, A. A.; Wolverton, C. High-throughput DFT calculations of formation energy, stability and oxygen vacancy formation energy of ABO(3) perovskites. *Scientific Data* **2017,** 4, 170153 DOI: 10.1038/sdata.2017.153.

248. Sun, W.; Dacek, S. T.; Ong, S. P.; Hautier, G.; Jain, A.; Richards, W. D.; Gamst, A. C.; Persson, K. A.; Ceder, G. The thermodynamic scale of inorganic crystalline metastability. *Science Advances* **2016,** 2 (11), e1600225 DOI: 10.1126/sciadv.1600225.

249. Aykol, M.; Dwaraknath, S. S.; Sun, W.; Persson, K. A. Thermodynamic limit for synthesis of metastable inorganic materials. *Science Advances* **2018,** 4 (4), DOI: 10.1126/sciadv.aaq0148.

250. Bither, T. A.; Gillson, J. L.; Young, H. S. Synthesis of Molybdenum and Tungsten Bronzes at High Pressure. *Inorganic Chemistry* **1966,** 5 (9), 1559-1562 DOI: 10.1021/ic50043a020.

251. Nalbandian, L.; Evdou, A.; Zaspalis, V. La1−xSrxMO3 (M = Mn, Fe) perovskites as materials for thermochemical hydrogen production in conventional and membrane reactors. *International Journal of Hydrogen Energy* **2009,** 34 (17), 7162-7172 DOI: https://doi.org/10.1016/j.ijhydene.2009.06.076.

252. Kazuo, E.; Kouichi, F.; Fumikazu, H.; Sadao, T.; Noriyuki, S. Formation of Na0.9Mo6O17 in a Solid-Phase Process. Transformations of a Hydrated Sodium Molybdenum Bronze, Na0.23(H2O)0.78MoO3, with Heat Treatments in a Nitrogen Atmosphere. *Bulletin of the Chemical Society of Japan* **1991,** 64 (1), 161-164 DOI: 10.1246/bcsj.64.161.

253. Murgida, G. E.; Ferrari, V.; Ganduglia-Pirovano, M. V.; Llois, A. M. Ordering of oxygen vacancies and excess charge localization in bulk ceria: A DFT+U study. *Physical Review B* **2014,** 90 (11), 115120 DOI: 10.1103/PhysRevB.90.115120.

254. Ramer, N. J.; Rappe, A. M. Application of a new virtual crystal approach for the study of disordered perovskites. *Journal of Physics and Chemistry of Solids* **2000,** 61 (2), 315-320 DOI: https://doi.org/10.1016/S0022-3697(99)00300-5.

255. Li, S.; Wheeler, V. M.; Kreider, P. B.; Lipiński, W. Thermodynamic Analyses of Fuel Production via Solar-Driven Non-stoichiometric Metal Oxide Redox Cycling. Part 1. Revisiting Flow and Equilibrium Assumptions. *Energy & Fuels* **2018**, DOI: 10.1021/acs.energyfuels.8b02081.

256. Romero Barcellos, D.; Sanders, M. D.; Tong, J.; McDaniel, A. H.; O'Hayre, R. BaCe0.25Mn0.75O3-δ — A promising perovskite-type oxide for solar thermochemical hydrogen production. *Energy & Environmental Science* **2018**, DOI: 10.1039/c8ee01989d.

257. Silva, P. R. N.; Soares, A. B. Lanthanum based high surface area perovskite-type oxide and application in CO and propane combustion. *Eclética Química* **2009,** 34, 31-38.

258. McDaniel, A. H.; Debora R. Barcellos, C. S. o. M.; Michael Sanders, C. S. o. M.; Jianhua Tong, C. U.; Ryan O?Hayre, C. S. o. M. *A novel solar thermochemical water splitting material BaCe0.25Mn0.75O3 for hydrogen production*. ; Sandia National Lab. (SNL-CA), Livermore, CA (United States): 2017; p Medium: ED; Size: 16 p.

259. Muhich, C. L.; Blaser, S.; Hoes, M. C.; Steinfeld, A. Comparing the solar-to-fuel energy conversion efficiency of ceria and perovskite based thermochemical redox cycles for splitting H2O and CO2. *International Journal of Hydrogen Energy* **2018**, DOI: https://doi.org/10.1016/j.ijhydene.2018.08.137.

260. Bulfin, B.; Call, F.; Lange, M.; Lübben, O.; Sattler, C.; Pitz-Paal, R.; Shvets, I. V. Thermodynamics of CeO2 Thermochemical Fuel Production. *Energy & Fuels* **2015,** 29 (2), 1001-1009 DOI: 10.1021/ef5019912.

261. Kubaschewski, O.; Alcock, C. B.; Spencer, P. J. *Materials thermochemistry*. Pergamon Press: 1993.

262. Hauch, A.; Ebbesen, S. D.; Jensen, S. H.; Mogensen, M. Highly efficient high temperature electrolysis. *Journal of Materials Chemistry* **2008,** 18 (20), 2331-2340 DOI: 10.1039/b718822f.

263. Carmo, M.; Fritz, D. L.; Mergel, J.; Stolten, D. A comprehensive review on PEM water electrolysis. *International Journal of Hydrogen Energy* **2013,** 38 (12), 4901-4934 DOI: http://dx.doi.org/10.1016/j.ijhydene.2013.01.151.

264. Zeng, K.; Zhang, D. Recent progress in alkaline water electrolysis for hydrogen production and applications. *Progress in Energy and Combustion Science* **2010,** 36 (3), 307-326 DOI: http://dx.doi.org/10.1016/j.pecs.2009.11.002.

265. Mueller-Langer, F.; Tzimas, E.; Kaltschmitt, M.; Peteves, S. Techno-economic assessment of hydrogen production processes for the hydrogen economy for the short and medium term. *International Journal of Hydrogen Energy* **2007,** 32 (16), 3797-3810 DOI: http://dx.doi.org/10.1016/j.ijhydene.2007.05.027.

266. Banaszkiewicz, T.; Chorowski, M.; Gizicki, W. Comparative analysis of cryogenic and PTSA technologies for systems of oxygen production. *AIP Conference Proceedings* **2014,** 1573 (1), 1373-1378 DOI: 10.1063/1.4860866.

267. Li, S.; Wheeler, V. M.; Kreider, P. B.; Bader, R.; Lipiński, W. Thermodynamic Analyses of Fuel Production via Solar-Driven Non-stoichiometric Metal Oxide Redox Cycling. Part 2. Impact of Solid–Gas Flow Configurations and Active Material Composition on System-Level Efficiency. *Energy & Fuels* **2018,** 32 (10), 10848-10863 DOI: 10.1021/acs.energyfuels.8b02082.

268. Sircar, S. Pressure Swing Adsorption. *Industrial & Engineering Chemistry Research* **2002,** 41 (6), 1389-1392 DOI: 10.1021/ie0109758.

269. Shirley, A. I.; Lemcoff, N. O. Air Separation by Carbon Molecular Sieves. *Adsorption* **2002,** 8 (2), 147-155 DOI: 10.1023/a:1020486502889.

270. Felinks, J.; Lange, M.; Call, F., Thermo-chemical production of oxygen from air involves heating metal oxide by (in)direct concentrated solar radiation, and oxidizing metal oxide at lower temperature and in air atmosphere by partial/complete reduction of solar radiation. In Patent DE102013209658A1: 2014.

271. Vieten, J.; Brendelberger, S.; Roeb, M.; Sattler, C. Thermochemical Oxygen Pumping for Improved Hydrogen Production in Solar Redox Cycles. *International Journal of Hydrogen Energy* **2019**, 44, 9802-9810.

272. Ivanova, S.; Lewis, R. Producing nitrogen via pressure swing adsorption. *Chemical Engineering Progress* **2012,** 108 (6), 38-42.

273. Falter, C.; Pitz-Paal, R. Energy analysis of solar thermochemical fuel production pathway with a focus on waste heat recuperation and vacuum generation. *Solar Energy* **2018,** 176, 230-240 DOI: https://doi.org/10.1016/j.solener.2018.10.042.

274. Knoblauch, N.; Simon, H.; Dörrer, L.; Uxa, D.; Fielitz, P.; Wendelstorf, J.; Spitzer, K.-H.; Schmücker, M.; Borchardt, G. Ceria: Recent Results on Dopant-Induced Surface Phenomena. *Inorganics* **2017,** 5 (4), 76.

275. Knoblauch, N.; Simon, H.; Schmücker, M. Chemically induced volume change of CeO2−δ and nonstoichiometric phases. *Solid State Ionics* **2017,** 301, 43-52 DOI: https://doi.org/10.1016/j.ssi.2017.01.003.

276. Miller, J. E.; McDaniel, A. H.; Allendorf, M. D. Considerations in the Design of Materials for Solar-Driven Fuel Production Using Metal-Oxide Thermochemical Cycles. *Advanced Energy Materials* **2014,** 4 (2), 1300469 DOI: doi:10.1002/aenm.201300469.

277. Siegel, N. P.; Miller, J. E.; Ermanoski, I.; Diver, R. B.; Stechel, E. B. Factors Affecting the Efficiency of Solar Driven Metal Oxide Thermochemical Cycles. *Industrial & Engineering Chemistry Research* **2013,** 52 (9), 3276-3286 DOI: 10.1021/ie400193q.

278. Steinfeld, A. Solar hydrogen production via a two-step water-splitting thermochemical cycle based on Zn/ZnO redox reactions. *International Journal of Hydrogen Energy* **2002,** 27 (6), 611-619 DOI: https://doi.org/10.1016/S0360-3199(01)00177-X.

279. Balachandran, U.; Ma, B.; Lee, T. H.; Song, S.-J.; Chen, L.; Dorris, S. E. Mixed-Conducting Membranes for Hydrogen Production and Separation. *MRS Proceedings* **2006,** 972, 0972-AA02-01 DOI: 10.1557/proc-0972-aa02-01.

280. Gambini, M.; Stilo, T.; Vellini, M.; Montanari, R. High temperature metal hydrides for energy systems Part A: Numerical model validation and calibration. *International Journal of Hydrogen Energy* **2017,** 42 (25), 16195-16202 DOI: https://doi.org/10.1016/j.ijhydene.2017.05.062.

281. Wiberg, E.; Wiberg, N. *Inorganic Chemistry*. Academic Press: 2001.

282. Linde. http://produkte.linde-gase.de/db_neu/n2o2_kw-frei_0,20_o2_n2.pdf. *http://produkte.linde-gase.de/db_neu/n2o2_kw-frei_0,20_o2_n2.pdf* **2016**.

283. Brent, R. P. *Algorithms for minimization without derivatives*. Courier Corporation: 2013.